FERRITES

J. SMIT ★ H. P. J. WIJN

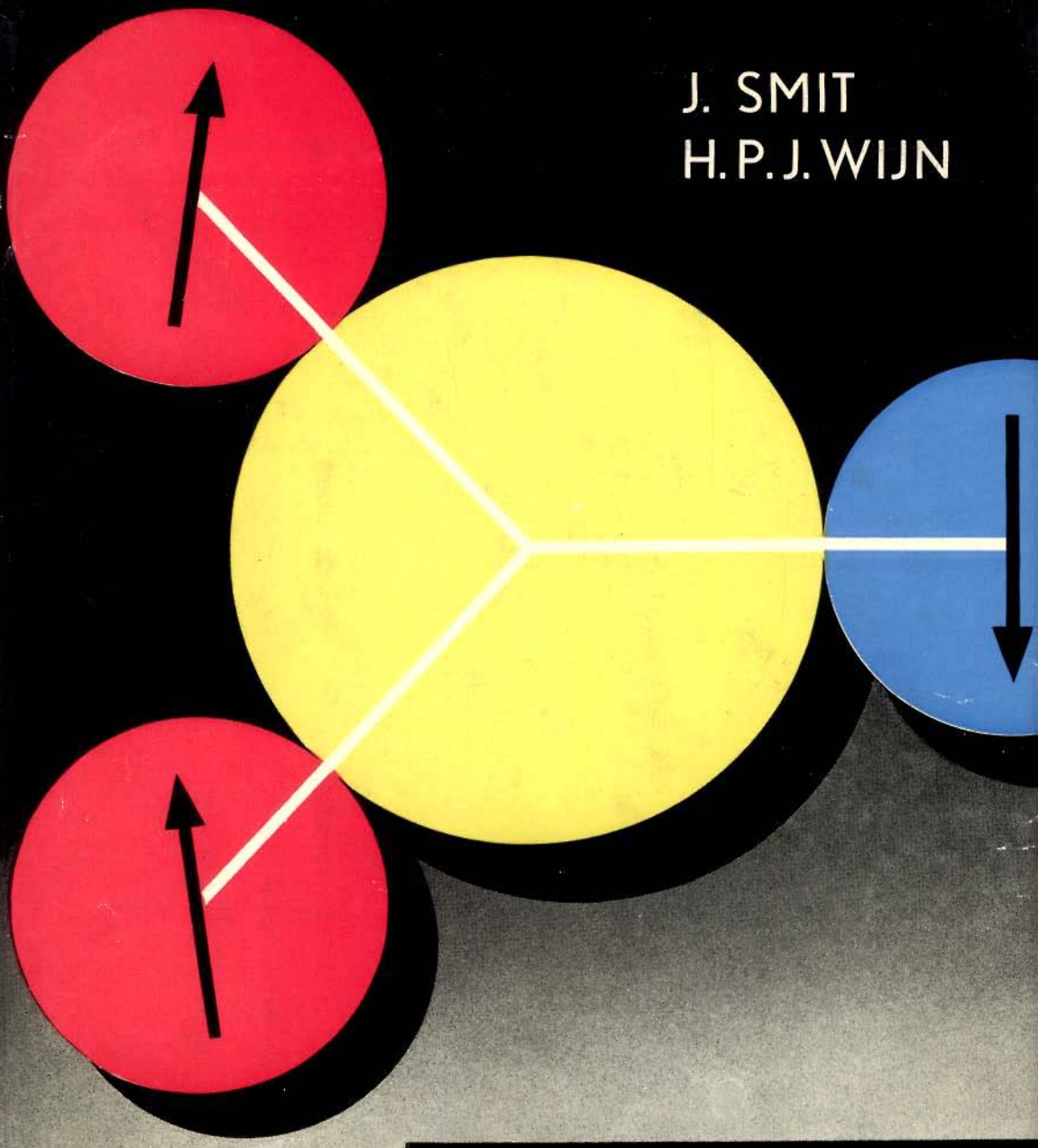

J. SMIT
H. P. J. WIJN

FERRITES

PHILIPS' TECHNICAL LIBRARY

About the book . . .

In recent years much effort has been put into research on ferrites, i.e. ferromagnetic oxides with iron as their main metallic component. This has resulted in many interesting and also essentially new applications of magnetic materials to electrical devices. Due to this research, many properties of ferrites are now better understood than corresponding properties of metallic ferromagnetics. In this book the characteristics of ferrites that are of importance for application purposes are presented and discussed and, whenever possible, explained in terms of intrinsic properties. These properties are in turn treated in relation to the chemical composition and crystal structures of the materials. The authors deal with many actual problems of the theory of phenomena occurring in various processes of magnetization. The subject is treated on an intermediate level and more use is made of simple physical models than of rigorous mathematical derivations.

About the authors . . .

J. Smit and H. P. J. Wijn are both Research Physicists in the Research Laboratories of the N.V. Philips' Gloeilampenfabrieken in Eindhoven, Netherlands. Dr. Smit received his physical engineering degree from Delft in 1948 and his doctorate in physics from Leiden University in 1956. Dr. Wijn took his degree in physics in 1948 at Utrecht University and his doctorate at Leiden in 1953.

FERRITES

Distributors for United Kingdom and Eire:
CLEAVER-HUME PRESS Ltd.
31, Wright's Lane, Kensington, London, W.8.

FERRITES

PHYSICAL PROPERTIES OF FERRIMAGNETIC OXIDES IN RELATION TO THEIR TECHNICAL APPLICATIONS

BY

J. SMIT

AND

H. P. J. WIJN

PHILIPS RESEARCH LABORATORIES
N.V. PHILIPS' GLOEILAMPENFABRIEKEN
EINDHOVEN – THE NETHERLANDS

1959

PHILIPS' TECHNICAL LIBRARY

Translated by: G. E. Luton, Eindhoven

Publisher's note:
This book is published in English, German and French editions

U.D.C. Nr. 538.221:621.318.124

This book contains 384 pages, 244 illustrations

Printed in the Netherlands

First published in 1959

J. L. SNOEK (1902-1950)

Foreword

The most important advances made in ferromagnetism in the years since the last war have been in the field of magnetic oxides. Their development into useful materials was initiated by the work of the late J. L. Snoek. The rapid expansion of technology, especially high-frequency engineering, has been a great stimulus to research on ferromagnetic oxides. Conversely the improvement of the characteristics of these materials has made increasingly refined applications possible. Much progress has been made towards the development of a theoretical description of the magnetic properties of these oxides. In this respect the work of L. Néel has been of fundamental importance. At the present time many of the properties of magnetic oxides are better understood than the corresponding properties of metallic ferromagnetics. For example the magnitude of the saturation magnetization of an oxide with given chemical composition can be predicted far more accurately than that of a metal or alloy.

The original literature in this new field is voluminous and readily accessible (it is to be found for example in the proceedings of the numerous conferences on magnetism of recent years). However, the authors felt that a definite need exists for a book which treats the subject of ferrites on an intermediate level. The term ferrites will be used to refer to all magnetic oxides containing iron as major metallic component. This book represents an attempt to meet this need and to provide readers in an informal way with an insight into the basic properties of ferrites. The treatment is not exhaustive as regards either the subject matter presented or the rigorousness of the theoretical development of basic concepts. The selection of material and manner of presentation have been governed by the special preferences and viewpoint of the authors.

The reader will perceive that some emphasis has been placed on work carried out in the Philips Laboratories. If history is not a sufficient justification for this fact, it may be recognized that the authors have first

hand information about these particular investigations and thus should be in a position to undertake a lively and penetrating discussion of them. A thorough familiarity with the experimental details is of especial importance since many properties of the ferrites strongly depend on their exact chemical composition and microscopic physical structure. These factors in turn are determined by the method of preparation.

The book is intended for all those who are actively interested in the properties of ferromagnetic oxides. It is hoped that the arrangement of the book will enable any member of this large group, whatever his line of specialization, to find some chapters of special interest to him. The practical c.g.s. system of units is employed, that is, the various parameters are expressed in terms of cm, ampere, volt, oersted, gauss and erg. The authors are indebted to many of their colleagues at Philips Research Laboratories, for useful criticism and suggestions, in particular to Dr. E. W. Gorter and Dr. G. H. Jonker. The manuscript has been translated into English by Mr. G. E. Luton, whose pleasant cooperation the authors gratefully acknowledge.

J. Smit H. P. J. Wijn.

May 1959

CONTENTS

Part A. Theory

Part B. Measurements

Part C. Intrinsic properties

Part D. Polycrystalline Ferrites

CHAPTER 1

ON THE PROPERTIES AND THE ORIGIN OF MAGNETIC FIELDS IN MATTER

§ 1. The Magnetic Field

A magnetic field is produced by electric currents. The magnetic field inside a toroid or long solenoid is

$$H = \frac{0.4\,\pi\,ni}{l} \tag{1.1}$$

and zero outside it. The field H is here expressed in oersteds, the current i in amperes and the length l in cm; n is the number of turns. For a circular current i with area A the magnetic moment is defined as

$$\mu = 0.1\,iA. \tag{1.2}$$

This is because the magnetic field at a distance many times greater than the radius of the circular current is equal to that of a mathematical dipole with a magnitude given by (1.2). Multiplying the numerator and denominator in (1.1) by A and then applying (1.2), we see that the field (1.1) can also be expressed in the magnetic moment per turn μ:

$$H = 4\pi\,\frac{n\mu}{V} \tag{1.3}$$

where V is the volume of the solenoid.

In matter, atomic circular currents may occur. Their strength is characterized by the magnetization M, which is the magnetic moment per cm^3. According to (1.3), then, matter can provide an extra contribution to the field of

$$H_{\text{mat}} = 4\pi M. \tag{1.4}$$

One can also say that a magnetization M is equivalent to a number of ampere turns

$$\left(\frac{ni}{l}\right)_{\text{mat}} = 10\,M. \tag{1.5}$$

The field given by (1.4) is only an averaged field; in reality there will be considerable fluctuations on an atomic scale. The total field arising from macroscopic currents (H_0) and microscopic currents together is called the induction B, so that for a toroid the induction in matter is

$$B = H_0 + 4\pi M. \tag{1.6}$$

B is expressed in gauss, a unit which is exactly the same, however, as the oersted.

The given derivation of (1.6) is valid only for a toroid or an infinitely long bar. If we compare a finite piece of matter, for example, an ellipsoid, with an infinitely long bar of the same cross-section (Fig. 1.1) we see that in the

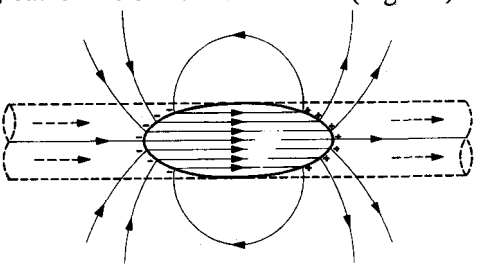

Fig. 1.1. Magnetized rotational ellipsoid compared with a magnetized bar of infinite length (dashed). In the latter there are only internal lines of force; with the ellipsoid the lines are closed around it. The stray fields and the internal demagnetizing field (in the opposite direction to the arrows) may also be assumed as originating from the fictitious poles (+ and −) at the ends.

ellipsoid the field due to the (microscopic) "ampere turns" of the rest of the bar is missing. This field would undoubtedly have been in the direction of the magnetization. On the other hand, the field outside the ellipsoid is not zero; we find there the fields of the magnetic moments in the ellipsoid which now are not cancelled out by those of the moments of the rest of the bar. The lines of force around the ellipsoid are closed loops. Leaving aside the field H_0, equation (1.6) would give $B = 4\pi M$ in the ellipsoid and zero outside it, and does not apply. We correct this equation by introducing an extra field H_D. In matter, H_D is called the demagnetizing field, because it is usually opposed to the magnetization; outside matter it is usually called the stray field. In all we have

$$B = H_0 + H_D + 4\pi M = H + 4\pi M. \tag{1.7}$$

Since the normal component of the induction, B_n, is equal at both sides of each surface element (continuity of the magnetic flux) the normal component of H_D makes at the edge of the specimen a jump of the magnitude $4\pi M_n$. This makes it possible to compare H_D with the electrostatic field arising from electric charges. The charges are here fictitious magnetic surface charges of the magnitude

$$\sigma = \Delta M_n \tag{1.8}$$

per cm², where ΔM_n is the jump in the normal component of the magnetization (see Fig. 1.1). Positive and negative charges are called north and south poles respectively, and they are always present in equal quantities. If the magnetization is not uniform, poles also appear inside the specimen. H_D makes no contribution to the integral of the tangential component of the magnetic field along a closed curve:

$$\oint H_{Dl}\,\mathrm{d}l = 0, \tag{1.9}$$

because the contributions of the atomic circular currents are cancelled out by those of $4\pi M$ in the integral of the total field along a closed path. For the H field of (1.7) we may therefore write

$$\oint H_l\,\mathrm{d}l = 0.4\pi ni \tag{1.10}$$

where i is the enclosed macroscopic current.

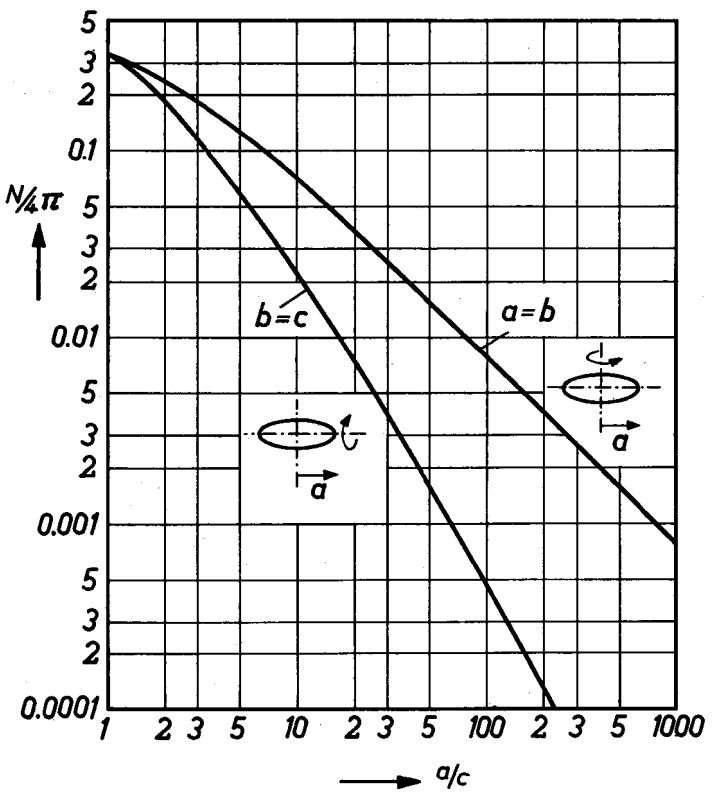

Fig. 1.2. Demagnetizing coefficient $N/4\pi$ of ellipsoid of revolution along the major axis (a) as a function of the ratio of the length of this axis to that of the minor axis (c), for prolate ellipsoids ($b = c$, needle) and oblate ellipsoids ($a = b$, disc).

It appears that only in a uniformly magnetized ellipsoid is H_D uniform and equal to

$$H_{Di} = -NM. \tag{1.11}$$

(The minus sign is used because H_{Di} is opposed to M.) In general, N will differ in the three principal directions, and will be smallest along the major axis, for there are then relatively fewer poles and moreover they lie farthest apart. The three demagnetizing coefficients (N_x, N_y and N_z) of an ellipsoid satisfy

$$N_x + N_y + N_z = 4\pi. \tag{1.12}$$

Some examples for special ellipsoids are:

sphere : $N_x = N_y = N_z = 4\pi/3$
infinitely long bar : $N_x = N_y = 2\pi \quad N_z = 0$
infinitely large flat plate: $N_x = N_y = 0 \quad N_z = 4\pi$.

Fig. 1.2 shows for ellipsoids of revolution the demagnetizing coefficients along the major axis (a) plotted as a function of the variable ratio of the major to the minor axes (a/c) as derived by Osborn [Os 1].

A uniformly magnetized ring has no demagnetizing field. It has, however, if the ring is broken by an air gap of width δ, which we assume to be small compared with the thickness of the ring d (see Fig. 1.3). Since B_n is continuous, the field in the narrow gap is uniform and equal to the induction B in the material. If no macroscopic currents are present, it follows from (1.9) that

$$H_D(l - \delta) + (H_D + 4\pi M)\delta = 0.$$

According to (1.11) this corresponds to a demagnetizing coefficient

$$N_{\text{ring}}/4\pi = \delta/l \quad (\delta \ll l) \tag{1.13}$$

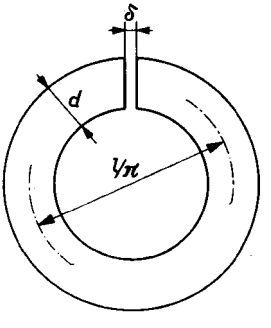

Fig. 1.3. Ring interrupted by an air gap.

2. Energy of the Magnetic Field

A change in the magnetic flux $\Phi = \int B_n \, dA$ surrounded by a closed turn gives rise to an e.m.f. in the winding equal to

$$e = -\frac{d\Phi}{dt} \times 10^{-8} \text{ volt} \tag{2.1}$$

(B_n is the normal component of B on an element dA of a surface through the winding.)

The presence of a magnetic field represents a certain quantity of energy, for work is performed in building it up with the aid of currents through coils. The Lenz opposing forces, then, are caused precisely by the voltages according to (2.1). If the current through the coil is i amperes, the energy supplied by the battery in the time δt is $ei\delta t = 0.1i\delta\Phi$ erg. The current i excites the magnetic field H_0, and it may easily be seen in the case of the solenoid, for example, that the energy required per cm³ in order to raise the induction in an arbitrary point by $\delta \boldsymbol{B}$ is equal to

$$\delta W = \frac{1}{4\pi} \boldsymbol{H}_0 \, \delta \boldsymbol{B}, \tag{2.2}$$

for which purpose the scalar product must be taken, *i.e.* the component of $\delta \boldsymbol{B}$ along $\boldsymbol{H}_0$. The total change of energy is found by integrating (2.2) over space. In the absence of matter, it follows that the total energy density per cm³ needed for building up the field is

$$W = \frac{1}{8\pi} H_0^2. \tag{2.3}$$

For the case of matter being present, $\delta \boldsymbol{B}$ consists of

$$\delta \boldsymbol{B} = \delta \boldsymbol{H}_0 + \delta \boldsymbol{H}_D + 4\pi \delta \boldsymbol{M}.$$

Since we are interested only in the total energy change, *i.e.* integrated over the whole space, the term with $\delta \boldsymbol{H}_D$ makes no contribution. This is a consequence of the general law in vector analysis that

$$\int \boldsymbol{ab} \mathrm{d}V = 0 \tag{2.4}$$

where the vector $\boldsymbol{a}$ is divergence-free (no sources or sinks), *i.e.* if for each closed surface $\int a_n \mathrm{d}A = 0$, as holds for each $\boldsymbol{B}$ field, and where the vector $\boldsymbol{b}$ is curl-free (no eddies), *i.e.* if for each closed curve $\int b_l \mathrm{d}l = 0$. According to (1.9), every demagnetizing field fulfils this condition. As a consequence, in (2.2) $\boldsymbol{H}_0$ may be replaced by the total field $\boldsymbol{H}$. In our case, $\boldsymbol{H}_0$ is the divergence-free vector ($\boldsymbol{H}_0 = \boldsymbol{B}$ in the absence of matter) and $\boldsymbol{H}_D$ is the curl-free vector (see (1.9)). The work performed on matter by the current is therefore

$$\delta W_{\mathrm{mat}} = \boldsymbol{H}_0 \delta \boldsymbol{M}. \tag{2.5}$$

By integrating to $\delta \boldsymbol{M}$ in (2.5) we can calculate the total work that must be performed to produce the magnetization. For this purpose we must know the relation between $\boldsymbol{H}_0$ and $\boldsymbol{M}$. Now, in the case of ferromagnetics the value of $\boldsymbol{M}$ is not determined by $\boldsymbol{H}_0$ but, as we shall see in Chapter V, by the field $\boldsymbol{H}$ which consists of $\boldsymbol{H}_0$ and $\boldsymbol{H}_D$ together. Thus

$$\delta W_{\mathrm{mat}} = \boldsymbol{H} \delta \boldsymbol{M} - \boldsymbol{H}_D \delta \boldsymbol{M}, \tag{2.6}$$

where $\boldsymbol{H}\delta\boldsymbol{M}$ does not depend upon the shape but solely upon the material. The last term of (2.6) is the demagnetizing energy. This can easily be calculated for an ellipsoid, since $H_D = -NM$ which, after integration, gives

$$W_{\text{dem}} = \tfrac{1}{2}NM^2 \tag{2.7}$$

per cm^3 of the ellipsoid. This energy therefore represents extra work to be performed. A more general expression for the demagnetizing energy, which also holds for arbitrary shapes, may be obtained by substituting $(1/4\pi)$ $\delta(\boldsymbol{B} - \boldsymbol{H}_0 - \boldsymbol{H}_D)$ for $\delta\boldsymbol{M}$ in the last term of (2.6). The terms with $\delta\boldsymbol{B}$ and $\delta\boldsymbol{H}_0$ integrated over space make no contribution, according to (2.4), so that there remains

$$W_{\text{dem}} = \frac{1}{8\pi} H_D^2 \tag{2.8}$$

which is comparable with (2.3). Equation (2.7) is valid for each point of the ellipsoid, while (2.8) is valid for each point of the space and must be integrated over it in order to find the total demagnetizing energy. The total field energy is then given by an expression like (2.3) or (2.8) for the field H.

We shall now consider the energy of a permanent magnetic dipole μ in a constant magnetic field $\boldsymbol{H}$. When a magnetic moment aligns itself in a magnetic field $\boldsymbol{H}$, the work performed on the dipole, according to (2.5), is $\boldsymbol{H}\delta\boldsymbol{\mu}$, where $\delta\mu$ is the change, due to rotation, in μ. In this case, as with the force of gravity for example, we can introduce a potential which is equal, to within a constant, to the opposite of the work performed on the dipole by the field during rotation of the vector. This then becomes

$$V = -\boldsymbol{\mu}\boldsymbol{H} \tag{2.9}$$

and is at minimum if $\boldsymbol{\mu}$ and $\boldsymbol{H}$ are parallel; this is the position of equilibrium of the dipole.

§ 3. The Nature of Magnetic Moments

In § 1 we calculated the magnetic field due to circular currents. We saw that in the example of an in finitely long bar a field $4\pi M$ is directly associated with a magnetic moment per unit volume M, so that the circular currents on which this field is based can and must be omitted from the field equation (1.10). In principle the magnetic moment can also be due to circulair currents on a macroscopic scale, as it is, for instance, in the case of eddy currents or

currents in a superconductor. In such cases it is not usually referred to as a magnetic moment, the currents being retained explicitlx in the equatione from which H can be determined. This separation is quite arbitrary, however.

The magnetic moments of interest to us come from the motion of the electrons in their atomic orbits (diameter $\cong 10^{-8}$ cm) or from their spin motion. It has been found that in ferromagnetics the magnetic moment due to orbital motion is of the order of only 10% of the total moment, the predominant part being due to spin. We shall therefore give a brief qualitative semi-classical treatment of the origin of electron spin.

3.1 SPIN MOMENT

After the existence of electron spin was postulated by Uhlenbeck and Goudsmit in 1925, in order to explain gas-discharge spectra, it was explained by Dirac in 1928 with the aid of relativity theory and quantum mechanics. In the theory of relativity the parameter pair E,t (energy, time) is treated in the same manner as the pair p,x (momentum, position); time is regarded as a fourth dimension and energy is the momentum conjugated with it. E,t should therefore occur in the equations in the same way as p,x. With the classical energy equation for a particle with mass m in a potential field V

$$E - \frac{p^2}{2m} - V = 0$$

this is not the case, for E occurs linearly and p quadratically. Dirac solved the difficulty by postulating a new equation in which p also occurs linearly, multiplied by a constant (really an operator). This constant can only be the velocity of the particle, because $v = \partial E_{\text{kin}}/\partial p$ is still valid, and is equal to the velocity of light c, so that, according to Dirac, the observable values (eigenvalues of the operator) of each component of the velocity can only be $\pm c$. Only one component can be "measured" at the same time, the others remaining then undetermined (*i.e.* $\pm c$). This is an unexpected result, but it leads directly to the existence of the spin. In order to visualize the spin of an electron we must assume that the path of a particle moving with a macroscopic velocity v ($\ll c$) is not straight, but is in some way spiralized, so that, although the microscopic velocity is c, the drift velocity is less. We thus have a translation plus a rotation, as shown schematically in Fig. 3.1. In general the sense of the rotational motion will not be defined, but with the application of a magnetic field the state with the one direction of rotation will have lower energy than the other and thus the electron has an angular momentum J and associated with it a magnetic moment μ. The magnitude of the angular momentum may be estimated

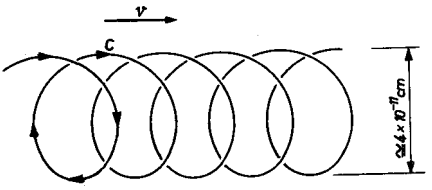

Fig. 3.1. Schematic representation of the internal motion of an electron. The electron moves in its path with a velocity c, while the translation velocity is v. The spin is in this case perpendicular to the plane of the figure.

in the following way. According to the theory of relativity, the energy of mass m, which actually moves with the velocity of light, is mc^2. We have seen that E is comparable with p. If, however, the momentum $+p$ occurs, then $-p$ is also possible. By analogy, therefore, a state with energy $-mc^2$ should equally be possible. With this statement, Dirac established the existence of a new state of the electron, which can be related to the positron, a particle which, as was later demonstrated experimentally, has the same mass as the electron but a charge of opposite sign. All that concerns us here is that in the description of the electron there occur two energy levels, $\pm mc^2$. According to Bohr, it is possible to cause transitions from the one state to the other by means of electromagnetic radiation of frequency ν, which follows from

$$h\nu = E_1 - E_2 = 2mc^2 \tag{3.1}$$

where h is Planck's constant (6.625×10^{-27} erg sec). Now it is reasonable to assume, because there are only two energy levels, that this ν will also be the frequency of the spin motion. A similar argument applies in the derivation of the precession frequency (see § 20). The angular momentum J is equal to the mass times the square of the velocity, divided by the angular frequency $\omega = 2\pi\nu$. The velocity here is c, so that, according to (3.1)

$$J = \frac{mc^2}{2mc^2/\hbar} = \hbar/2 \tag{3.2}$$

where $\hbar = h/2\pi$, corresponding to $S = \frac{1}{2}$ if $J = \hbar S$.

The frequency ν in (3.1) is very high ($\cong 2 \times 10^{20}$/sec) and corresponds to that of very hard gamma quanta (1 MeV). The average radius of the orbit may be taken as

$$r_{\text{spin}} = \frac{c}{\omega} = \frac{\hbar}{2mc} = 2 \times 10^{-11} \text{ cm},$$

known as the Compton wavelength. Of course, as in the case of the Bohr orbits in the hydrogen atom, we must not think here of a precise, sharp orbit. The spin motion is a zero point motion, just as that of the electron in the $1s$ state in the hydrogen atom. A difference is that in this lowest state the motion can show angular momentum, due to the fact that there is

always one component of the velocity which has the value c, so that the "orbits" cannot have reversal points. The size of the electron itself is probably of the order of 10^{-13} cm.

For a normal orbital motion the ratio γ between the magnetic moment and the angular momentum is equal to

$$\gamma_{\text{orbit}} = e/2mc. \tag{3.3}$$

For the spin motion, however, the relation is

$$\gamma_{\text{spin}} = e/mc \tag{3.4}$$

i.e. twice as large, as follows from Dirac's theory. This may also be expressed by the factor g in

$$\gamma = g\, e/2mc, \tag{3.5}$$

g being 2 for the free spin and 1 for the orbital motion. Owing to the fact that the charge e of the electron is negative, the magnetic moment and the angular momentum are of opposite sign. No simple explanation can be given for this deviating value of the g factor. The magnetic moment of the electron is called the Bohr magneton, and is given by the equation

$$\mu_B = \frac{e\hbar}{2mc} = 9.27 \times 10^{-21} \text{ erg/gauss}. \tag{3.6}$$

In § 19 we shall see that if spin and orbital motion are both present the g factor may have an arbitrary value.

3.2. QUENCHING OF THE ORBITAL ANGULAR MOMENTUM

In most magnetic materials containg elements of the first group of transition metals (Ti to Ni and also Cu) the resultant orbital moment of the electrons is much smaller than the spin moment; we say then that the orbital moment is "quenched". This is a consequence of the electric fields at the position of the ions, caused by the surrounding ions (known as the crystalline field). Disregarding magnetic effects, a state (orbit) in which an electron travels round in a certain sense has exactly the same energy as the same orbit with the opposite sense of rotation, *i.e.* such a state with an angular momentum is doubly degenerate (both states have the same energy). This degeneracy can be removed by the crystalline field. This field will be non-uniform; for instance it is strongly positive in the direction of negatively charged neighbouring ions (repulsion of the electron) and negative, or at least less positive, in directions in between. The above-mentioned indeterminancy in orbital motion can now be utilized in quantum mechanics by so superposing the

two states as to produce two different orbits. In the one state the positions of high potential will be avoided as much as possible (orbit *a* in Fig. 3.2) so that this state will have a lower energy than the original in this field. The other state is then left with precisely the unfavourable positions (orbit *b*) which results in an equally higher energy. The energy splitting ΔE is of the order of 10^{-12} erg. These new states can have no angular momentum. If they had — still disregarding magnetic effects — the opposite direction of motion would also be possible and we should have four states instead of two.

This superposition of states has some resemblance with the combination into one standing wave of two waves travelling in opposite directions. The average charge distribution of the travelling waves is uniform, that of the standing wave is non-uniform. According to old quantum theory the electron moving in a Bohr orbit is associated with a wave such that the length of the

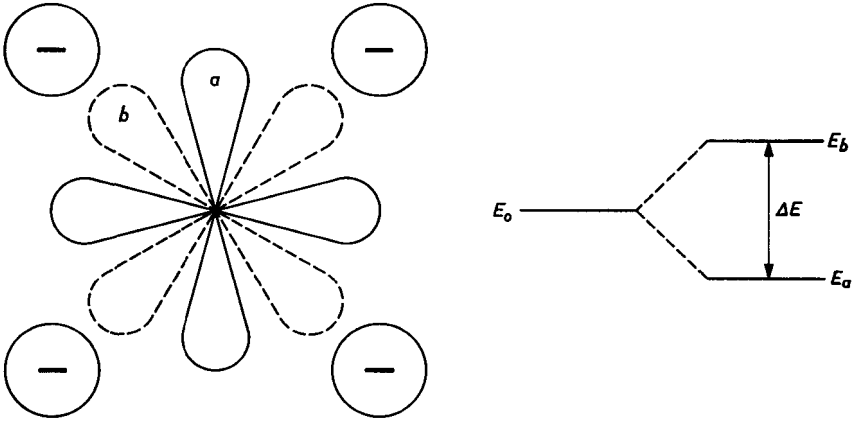

Fig. 3.2. Removal by the crystalline field of the orbital degeneracy caused by the four negatively charged ions in the corners. Orbits *a* and *b* are turned exactly 45° with respect to each other. The resultant energy change is shown.

circumference of the closed orbit is equal to an integral number l of wave lengths. The *s* state is additional and corresponds to $l = 0$, and should be regarded as a zero point motion. The state with $l = 1$ is a *p* state, $l = 2$ is a *d* state etc. When two such waves propagating in opposite directions (opposite values of angular momentum) are combined, a standing wave results with $2l$ nodes. It is clear that the energy of such a charge distribution will depend on its oriëntation in a non-uniform crystal field with the proper symmetry. For instance a *p* state does not combine with a field of cubic symmetry and the degeneracy is

not removed. A *d* state, however, is affected by such a field. The five fold energy level is split up into a doublet and a triplet. This partial degeneracy which still exists is due to the fact that equivalent orbits lying in different cube planes have equal energy. The degeneracy can be further removed by superimposed crystal fields of lower symmetry. If this is not the case a partial occupation of the triplet states by electrons leaves the lowest state of the total electronic system degenerate, which may possess orbital angular momentum. This situation occurs *e.g.* for divalent cobalt ions in octahedral sites in compounds. The states of the doublet are called non-magnetic and a combination of them does not give rise to angular momentum.

3.3. SPIN-ORBIT INTERACTION

If magnetic effects are present a reversal of electron velocity will also change the energy, and the above reasoning is no longer valid; even in the presence of a crystalline field there can still be some orbital angular momentum. Irrespective of the internal magnetic fields there is a magnetic effect due to what is known as spin-orbit interaction, which again has a relativistic origin. This interaction may be compared with the Lorentz force, which corresponds to an electrical field strength

$$\boldsymbol{E} = (\boldsymbol{v} \times \boldsymbol{H}).10.^{-8} \tag{3.7}$$

This follows from Maxwell's theory, or from the theory of relativity, which states that in a coordinate system moving with a velocity $\boldsymbol{v}$ relative to another system, an extra electrical field-strength prevails equal to (3.7), if $\boldsymbol{H}$ is the magnetic field-strength in that other system. By analogy with this, there exists in the one system a magnetic field-strength

$$\boldsymbol{H} = -(\boldsymbol{v} \times \boldsymbol{E})/9.10^{12}, \tag{3.8}$$

if $\boldsymbol{E}$ is the electrical field-strength in the other system. The spin of the moving electron is subject to this field, so that according to (2.9) the energy is

$$E_{\text{s.o.}} = \frac{1}{2}\boldsymbol{\mu}(\boldsymbol{v} \times \boldsymbol{E})/9.10^{12}, \tag{3.9}$$

to which a factor $\frac{1}{2}$, the Thomas factor, is added for reasons similar to those applying in the case of the g factor.

In general it may be assumed that the electrical potential of an atomic core is mainly spherically-symmetrical. The electric field is then radially oriented, so that

$$E_{\text{s.o.}} = \frac{1}{2mc}\frac{E}{r}\boldsymbol{\mu}(\boldsymbol{p} \times \boldsymbol{r})/9.10^{12}$$

and hence there is in the atom an interaction between spin and orbital moment of the form

$$E_{s.o.} = \lambda \boldsymbol{L}\,\boldsymbol{S}. \tag{3.10}$$

In this expression $\boldsymbol{L}$ is the orbital angular momentum and λ is an energy quantity which depends upon the ion concerned; for the transition metals of the iron group it is of the order of 10^{-13} erg. (See Table 3.1) (1 erg = 5.036×10^{15} cm^{-1}).

TABLE 3.I

SPIN-ORBIT PARAMETER λ FOR VARIOUS IONS OF THE IRON GROUP IN CM^{-1}

ion	Configuration	λ (cm^{-1})
Ti^{III}	$3d\ {}^2D_{3/2}$	154
V^{III}	$3d^2\ {}^3F_2$	150
Cr^{III}	$3d^3\ {}^4F_{3/2}$	87
$Cr^{II}Mn^{III}$	$3d^4\ {}^5D_0$	57
$Fe^{III}Mn^{II}$	$3d^5\ {}^6S_{5/2}$	
Fe^{II}	$3d^6\ {}^5D_4$	−100
Co^{II}	$3d^7\ {}^4F_{9/2}$	−180
Ni^{II}	$3d^8\ {}^3F_4$	−335
Cu^{II}	$3d^9\ {}^2D_{5/2}$	−852

The effect of an interaction (3.10) is that the original situation existing before the splitting action of the crystalline field is restored to some extent, so that the two states acquire a slight orbital moment again, amounting in first approximation to $\pm(\lambda/\Delta E)\ \hbar$, where the original orbital moment was $\hbar$ or a multiple thereof (max. 2 for the iron group). In the same approximation the spin orientation has not changed. If, therefore, only one of the states (that with the lower energy) is occupied by an electron, there will be some orbital moment present, the direction of which will depend upon the sign of λ. If both orbits are occupied by an electron, the orbital moments again offset each other, so that the interaction (3.10) has no effect. This occurs in filled shells, for example in Mn^{II} or Fe^{III}, in which all spins are parallel and all orbits of the $3d$ shell are singly occupied. Intermingling no longer has any effect in this case and the charge distribution is and remains spherically symmetrical.

The admixed orbital angular momentum is antiparallel to the spin moment ($\lambda > 0$). For more than half-filled shells, the direction of the resultant spin is determined by that of the half-filled shell. These do not, however, contribute to the orbital momentum, so that the resultant orbital momentum is parallel then to the resultant spin moment, corresponding to an effective negative λ.

3.4. ABSOLUTE MAGNITUDE OF THE ANGULAR MOMENTA

It was stated in § 3.1 that the actual velocity of the electron is $\pm c$, corresponding to an angular momentum of $\hbar/2$. Now this holds for each component of the velocity (along three axes perpendicular to each other) but we find that only one component can be measured at a time; the others remain indeterminate and are either $+c$ or $-c$. This is a consequence of Heisenberg's uncertainty principle. The square of the total velocity will not, therefore, be c^2 but $3c^2$. In the same way it appears, as a result of this, that each component of the angular momentum is $\pm\hbar/2$, but that only one component can be measured at one time. The square of the length of the angular momentum vector is then $\frac{3}{4}\hbar^2$, for $S = \frac{1}{2}$:

$$S_x^2 + S_y^2 + S_z^2 = S(S+1) \tag{3.11}$$

and not S^2. The expression postulated in (3.11) has general validity, and applies also to the spin moment of several coupled spins. Let there be $2S$ spins in the z direction, then

$$S_x^2 = (S_{x_1} + S_{x_2} + \ldots)^2 = S_{x_1}^2 + S_{x_2}^2 + \ldots = \tfrac{1}{2}S$$

since, owing to the lack of correlation between the motion of the individual spins, the double-product terms cancel out on the average. This applies also to the y direction, while $S_z^2 = S^2$, so that (3.11) follows here too. With increasing S the indeterminancy becomes relatively less.

For similar reasons, an expression analogous to (3.11) applies also in the case of pure orbital angular momenta:

$$L_x^2 + L_y^2 + L_z^2 = L(L+1). \tag{3.12}$$

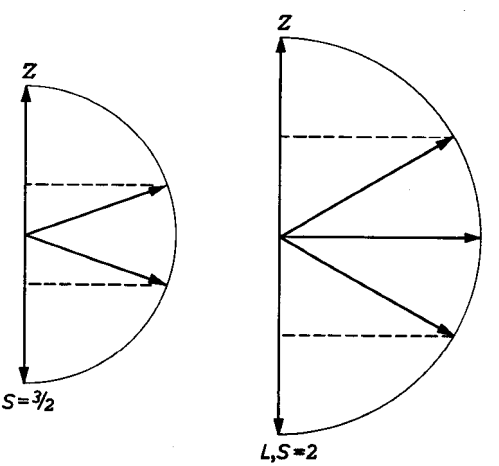

Fig. 3.3. Possible orientations of an angular momentum vector with respect to an axis of quantization (z axis).
The semi-integral numbers can occur only for spin ($S = {}^3/_2$ represents the case of three mutually parallel spins).

The values of S_z or L_z which can be determined by measurement, ascend in steps of 1, for example S, $S-1$, $S-2$, ... $(-S)$, thus totalling $(2S+1)$ or $(2L+1)$ which corresponds to as many positions of the resultant vector with respect to the z axis (see Fig. 3.3). The values of L are always integers. The positions of the vectors as drawn are only average positions. In reality there occurs as it were a zero point motion around them. Moreover, the whole figure should be thought of as arbitrarily rotating around the z axis.

CHAPTER II

THEORY OF FERROMAGNETISM

§ 4. Diamagnetism, Paramagnetism and Ferromagnetism

We have seen in Chapter I that a magnetization M can occur in matter as the result of a more or less parallel alignment of the elementary magnets present therein (electron orbits or electron spins). To produce this alignment it will generally be necessary to apply a magnetic field H. The magnetization M, when relatively small, is then often found to increase proportionally with H according to

$$M = \chi H, \tag{4.1}$$

where χ is the (constant) susceptibility per cm^3. In that case the induction B is found from (1.7) to be

$$B = (1 + 4\pi\chi)H = \mu H. \tag{4.2}$$

The constant μ is called the permeability. In vacuo, $\chi = 0$ and $\mu = 1$.

Depending upon the sign and the magnitude of χ, three cases may be distinguished:

a) *Diamagnetism* $\chi < 0$. For this phenomenon to occur there need be no permanent dipoles present. The magnetic field induces a magnetic moment that is opposed to H. This is really the most natural form of magnetism and occurs in principle in all substances. It is a direct consequence of one of the most fundamental laws of nature, which states that any change gives rise to forces which tend to counteract this change. This is here expressed in Lenz's law, according to which the magnetic flux contained by a closed circuit tends to remain constant, since the induced electromotive force (2.1) tries to change the current in such a way as to oppose the flux variation. The value of χ is usually of the order of -10^{-5}; it is very small compared with the other contributions to χ for the materials with which we are concerned here, and will therefore be disregarded.

b) *Paramagnetism* $\chi > 0$, but small (*e.g.* $\chi < 10^{-2}$). In this case magnetic moments which are already present (from electron orbits or spins) but which have a random orientation, are to a slight extent aligned in the field, this alignment being opposed by thermal agitation.

c) *Ferromagnetism.* In the so-called ferromagnetic materials, just as in paramagnetic materials, magnetic moments are also present, the difference being, however, that the spins of neighbouring ions are already more or less parallel. This does not mean that the whole specimen is necessarily uniformly magnetized (*i.e.* any arbitrary piece of soft iron is no magnet),

for if it were, the finite dimensions would give rise to large demagnetizing forces (see Fig. 1.1). Internally, too, a great deal of demagnetization would occur as a result of inhomogeneities and imperfections in the specimen. For this reason it is usually more favourable energetically for the material to subdivide itself magnetically into a large number of small regions, known as *Weiss domains*, after Pierre Weiss, who first postulated their existence in 1907. Within each domain, the size of which is of the order of 0.001 to 0.1 mm, the magnetization is uniform but the direction of this spontaneous magnetization varies from one domain to another such that, in the absence of an external field, there is usually no overall magnetization left.

The application of an external field of the order of 1 to 100 oersteds may often be sufficient to remove the domain structure and to bring the material practically to saturation. Thermal agitation has no effect on the magnetizing process of these large conglomerates of spins. Thus the material has a high permeability (maximum 10^6).

Another typical property of ferromagnetics is the occurrence of hysteresis, *i.e.* each value of the field H is not associated with one specific value of the induction B, the latter depending upon the previous history, that is upon the fields which have been applied previously. For example, with a given field the induction will be larger if the material is first saturated in a strong field in the direction of H than if the material were first saturated in the opposite direction. The graph which shows the relation between B and H is known as the hysteresis loop (Fig. 4.1). This hysteresis is the result of irreversible magnetization processes, which, since they cause energy dissipation, adversely affect the quality of coils in which these materials are employed as cores. On the other hand, the non-reversibility also has its useful side, because it is due to this phenomenon that after magnetization and subsequent reduction of the field to zero, there is still some magnetization left, which means that such a material has permanent magnet properties.

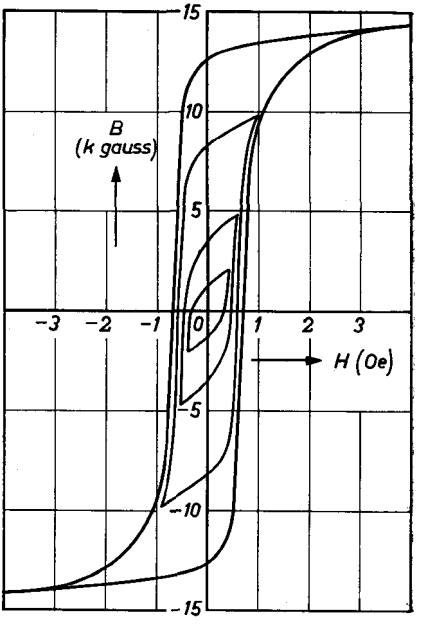

Fig. 4.1. Hysteresis loop of an annealed iron specimen.

§ 5. Exchange Interaction

The spontaneous magnetization of a Weiss domain is produced, as we have seen in § 3.3, mainly by the magnetic moments of electron spins. However, not all spins of the electrons of an atom or ion can be parallel. According to the Pauli principle two electrons in a system cannot be in the same state. The state of an electron is determined on the one hand by the orbit in which it moves, and on the other by the direction of its spin. As was shown in § 3.4, there exist only two states for the spin of one electron ($S = \frac{1}{2}$): parallel or anti-parallel to a certain direction. Each orbit, then, can be occupied by two electrons with opposite spin. In most atoms this is as far as possible the case, for reasons of economy in energy, so that there is no or only one uncompensated spin left. Exceptions are found in the transition metals, for example in the iron group (V to Ni) where the five circular orbits from the third shell (3*d* orbits) have equal energy. In these atoms it appears to be more advantageous, owing to quantum mechanical reasons, for the spins of the 3*d* electrons to be parallel (one of the Hund rules). The maximum magnetic moment per ion or atom is then 5 μ_B (*e.g.* Mn^{II} or Fe^{III}). For more than five electrons in the 3*d* shell the resultant moment decreases again; for instance, Co^{II} in the $3d^7$ state has a moment of $3\mu_B$. It may be said that, in consequence of the Pauli principle, the mutual spin orientation of the electrons imposes a restriction on their orbital motion. Since two electrons strongly repel each other (Coulomb force) this will certainly affect the energy. Now, in the more realistic case that the electron orbits are not separated, it appears that the mutual spin orientation also partly determines the stationary states of a system in which there are several electrons. As a result of the electrostatic interaction between the electrons the energy will depend upon the mutual orientation of the spins. The difference in energy of two electrons in a system with anti-parallel and parallel spins is called the exchange energy *J*. More generally, the interaction between two spin vectors $\boldsymbol{S}_1$ and $\boldsymbol{S}_2$ is given by

$$E_{\text{ex.}} = -2J\boldsymbol{S}_1.\boldsymbol{S}_2 = -2JS_1S_2\cos\phi, \tag{5.1}$$

where ϕ is the angle between $\boldsymbol{S}_1$ and $\boldsymbol{S}_2$. For $J > 0$ the parallel configuration is more favourable and for $J < 0$ the state with opposite spins has the lowest energy. The energy difference *J* can only differ from zero when the electrons come into each others' vicinity a great deal, that is to say when the orbits "overlap". Therefore we need only consider this effect for electrons belonging to the same or to neighbouring atoms.

Hund's rule is still usually applicable where the elements occur as ions in ionic crystals (as in the oxides). In itself this fact would merely give rise to strong paramagnetism. However, there also occurs an exchange interac-

tion between the spins of neighbouring ions. An interaction of this nature causes, for example, the formation of the hydrogen molecule and gives rise to binding between atoms of many other elements, both in the molecular form and in the solid state (valence bond). In this process the two interacting electrons always have opposite spins, corresponding to a negative exchange energy. In the ferromagnetic metals Fe, Co and Ni, on the other hand, the exchange energy between the $3d$ electrons of neighbouring ions is apparently positive. The conduction electrons, *i.e.* the electrons in the $4s$ orbits, presumably have no or only little part in this. Thus, for the ferromagnetism of the elements in the iron group, only the $3d$ electrons are of importance. In the rare earth elements corresponding conditions hold for the $4f$ shell and Gd and Dy are ferromagnetic.

It is found that the spontaneous magnetization M_s decreases with increasing temperature and vanishes fairly suddenly above a certain temperature, the Curie temperature T_C.

§ 6. Statistical Theory of Magnetism

6.1. LANGEVIN'S THEORY OF PARAMAGNETISM

In order to explain the temperature-dependence of the spontaneous magnetization we shall first treat Langevin's theory of paramagnetism, which was put into a quantum mechanical form by Brillouin. According to statistical mechanics the probability P that a system is in one of its possible states with energy E_i is equal to

$$P_i = \frac{e^{-E_i/kT}}{\sum_j e^{-E_j/kT}}, \tag{6.1}$$

where k is Boltzmann's constant ($k = 1.380 \times 10^{-16}$ erg/°K) and T is the absolute temperature. In (6.1) the sum of the probabilities over all states is equal to unity. At the absolute zero point of temperature, then, only the state with the lowest energy occurs, while at temperatures above that point there is a chance for states with a higher energy to occur. At very high temperatures all states have practically equal probability of occurring (total disorder). For one spin in a magnetic field H there are two possible states, parallel and antiparallel to the magnetic field. According to (2.9) the energies (in this case potential energies) are $-\mu_B H$ and $+\mu_B H$ respectively. The average magnetic moment μ in the direction of H can then be found by multiplying the moments in the two directions by their probability of occurrence (6.1) and subtracting one from the other:

$$<\mu> = \mu_B \frac{e^{\mu_B H/kT} - e^{-\mu_B H/kT}}{e^{\mu_B H/kT} + e^{-\mu_B H/kT}} = \mu_B \tanh \mu_B H/kT. \tag{6.2}$$

For a substance with N independent spins per cm^3 such that the maximum magnetization is $M_0 = N\mu_B$, we may therefore write

$$M/M_0 = \tanh \mu_B H/kT. \tag{6.3}$$

For high temperatures and weak fields the tanh in (6.3) can be replaced by its argument, and hence we may write for the paramagnetic susceptibility

$$M/H = \chi = \frac{\mu_B M_0}{kT} = \frac{C}{T}. \tag{6.4}$$

This is Curie's law, which states that χ^{-1} is proportional to the absolute temperature. The constant C is the Curie constant. This law is satisfied by many paramagnetic substances. For higher fields and low temperatures (6.4) is not valid ($\mu_B H = kT$ for $H = 1.5 \times 10^4$ oersteds and $T = 1$ °K) and M approaches the saturation value M_0. This saturation effect has been thoroughly investigated at low temperatures and high fields (H/T large) by Henry [He 1] (see Fig. 6.1) for various paramagnetic salts.

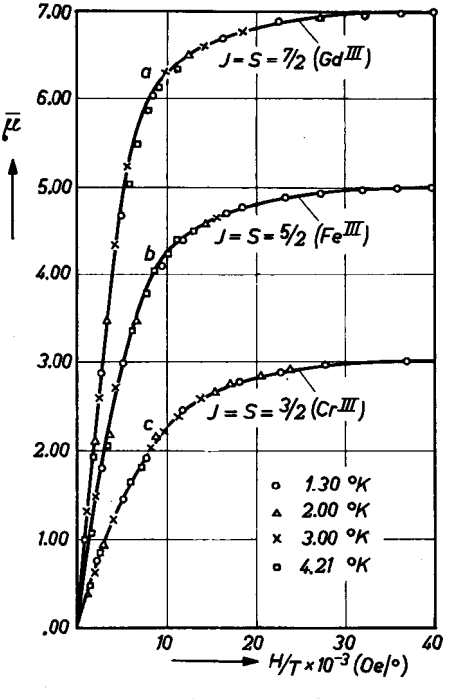

Fig. 6.1. Magnetic moment of some paramagnetic salts as a function of H/T. The solid lines are the theoretical Brillouin functions, according to (6.7). (After Henry [He 1]).

From (1.7) we might expect that H in (6.2) would not be equal to the externally applied field but equal to B. However, it is not the average field that must be taken, but the field produced at the position of the ion by the other ions. For a cubic crystal this is, according to Lorentz, $H + 4\pi M/3$. This correction can be neglected for paramagnetic materials, except at low temperatures (< 1 °K).

As a general rule the magnetic moment m of an ion will originate from more than one spin, which, according to Hund's rule, are parallel, while there can also be some orbital magnetism present; thus, where S is still a good quantum number (*i.e.* the value of S for an ion can still be measured without changing the orbital motion) the magnetic moment m is given by

$$m = Sg\mu_B, \tag{6.5}$$

where S is the spin angular momentum of the ion (see § 3.4). The Landé factor g is then given by

$$g = 2\frac{\text{total magnetic moment}}{\text{spin magnetic moment}} \tag{6.6}$$

For pure spin magnetic moments, $g = 2$; deviations occur if there is also some orbital magnetism present, in which case $g = 1$ (see § 3.1).

Where $S > \frac{1}{2}$ the moment will then have, as discussed in § 3.4, $(2S + 1)$ possible orientations in a magnetic field, so that (6.2) must be generalized and instead of (6.3) we find

$$M/M_0 = B_S(a) = \frac{2S+1}{2S}\operatorname{cotanh}\frac{2S+1}{2S}a - \frac{1}{2S}\operatorname{cotanh}\frac{a}{2S} \tag{6.7}$$

where B_S is the Brillouin function and a is given by

$$a = Sg\mu_B H/kT. \tag{6.8}$$

The measured points given in Fig. 6.1 are those of salts with $S = 3/2$, $5/2$ and $7/2$ respectively, and fall on the Brillouin functions concerned. Here, too, Curie's law applies, with a Curie constant C_S which is equal to the initial slope of the B_S curve and is given by

$$C_S = g\mu_B(S+1)M_0/3k = \frac{N\mu^2}{3k}, \tag{6.9}$$

where

$$\mu = \mu_B g\sqrt{S(S+1)} \tag{6.10}$$

is the absolute magnitude of the moment.

6.2. WEISS FIELD THEORY OF FERROMAGNETISM

If we keep all the spins in a ferromagnetic substance in one direction by means of a strong magnetic field, and we then try to turn one spin, or more generally the magnetic moment of one ion, out of that direction, this will be opposed not only by the external magnetic field but also by the exchange interaction with the spins of neighbouring ions. It is as if there were an extra field acting on each spin, the so-called Weiss field, H_W. It is not a true field, for that can be produced only by circular currents, but is simply a measure of the strength of the spin's interaction with its neighbours. This field is in general much stronger ($\simeq 10^7$ oersteds) than can normally be produced with coils *etc.* The classical dipole-dipole magnetic interaction is of no consequence here, for this would only give fields of the order of $4\pi M$, which can be no more than $\simeq 2.10^4$ oersteds. The Weiss field depends upon the magnitude of the average moment:

$$H_W = WM, \tag{6.11}$$

where W, the Weiss field constant, is assumed to be independent of M and T. If the interaction is caused by the z nearest neighbours, then according to (2.9) and (5.1) the energy change ΔE due to the reversal of one spin is

$$\Delta E = g\mu_B W M_0 = 2zJS, \tag{6.12}$$

where M_0 is the saturation moment at $T = 0°\text{K}$.

The temperature-dependence of the spontaneous magnetization can be found by applying the Langevin theory from § 6.1. The field H in (6.8) must then be replaced by $H + H_W$, where H_W is given by (6.11). For the calculation of the spontaneous magnetization we have to put $H = 0$. Equation (6.7) then becomes an equation in M which, at a given temperature, can have a solution, M_s, differing from zero. Thus, in Fig. 6.2, H/T is equal to WM/T. All points for which the quotient of M and H/T is equal to T/W lie on a straight line through the origin. The point where this intersects the drawn curve gives the sought-for value of the spontaneous magnetization. For low temperatures the straight line has a very small slope and in the point of intersection, for example A in Fig. 6.2, M_s/M_0 is almost equal to 1.

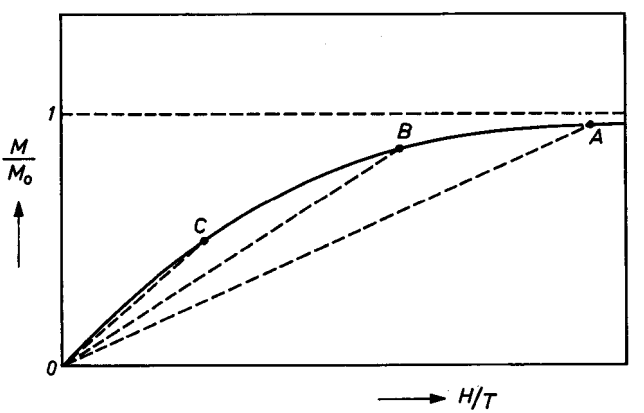

Fiig. 6.2. Magnetic moment as a function of H/T. The points where this curve intersects the broken straight lines represent possible spontaneous magnetizations at varous temperatures.

With rising temperature the point of intersection shifts towards B and C and M_s decreases. For that temperature where the point of intersection has arrived at the origin, and has hence become a tangential point, M_s is zero and remains so at still higher temperatures. This Curie temperature T_C is given, for an arbitrary value of S, by

$$T_C = C_S W = g\mu_B(S + 1)WM_0/3k, \tag{6.13}$$

as follows from (6.4) and (6.9) if the Weiss field H_W be inserted for H. Using (6.12) we may write for (6.13):

$$T_C = 2S(S + 1)zJ/3k. \tag{6.14}$$

The Curie temperature, then, increases with increasing S for constant interaction per spin (SJ or W) and magnetization (M_0). That is to say, if each ion has more than one uncompensated spin the Curie temperature is higher when these spins are coupled in one ion (following Hund's rule) than when this is not the case. This may be readily understood from the fact that in the latter case, the entropy is greater (more possibilities for orientation) with vanishing spontaneous magnetization than with coupled spins, where the maximum disorder has not yet been reached. The term $-TS$ (S is here the entropy) in the free energy is thus larger at the same temperature, and consequently the temperature (T_C) at which this large entropy can occur (corresponding to $M_s = 0$) will be lower.

For the ferromagnetic metals of the iron group the Curie temperatures and the saturation magnetizations at absolute zero are:

	Fe	Co	Ni	
T_C	770	1131	358	(°C)
$4\pi M_0$	21,805	18,150	6,394	(gauss)

The curve M_s/M_0 can now be plotted as a function of temperature, and is given in Fig. 6.3 for several values of S. The experimental curves for the metals iron and nickel are given, and it can be seen that they lie with good approximation on the curve $S = \frac{1}{2}$; this should indicate that the spins of the electrons inside one ion are in this case not coupled.

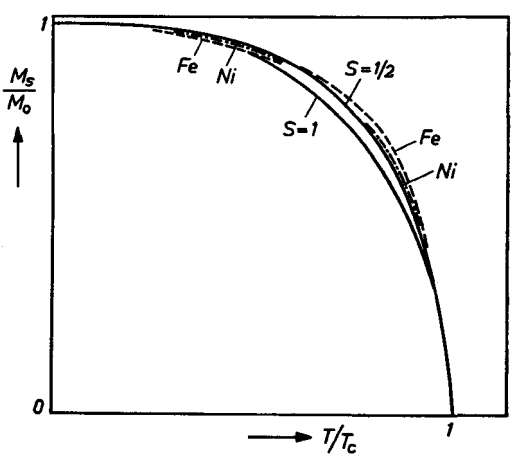

Fig. 6.3. Spontaneous magnetization as a function of temperature on reduced scales. The solid lines were found with the Weiss field theory for the cases $S = 1/2$ and $S = 1$. The experimental (dashed) curves for iron and nickel agree with the theoretical curve for $S = 1/2$ (uncoupled spins).

Above the Curie point the Weiss field is zero and there should therefore no longer be any parallel alignment of neighbouring ions. For $T > 0$ it is possible to enlarge M somewhat by an applied field; from the Weiss field theory it follows that

$$\partial M/\partial H = -(T/WM)\partial M/\partial T \tag{6.15}$$

According to the Weiss field theory the magnetization decreases only very slowly at low temperatures. For example, for $S = \frac{1}{2}$ the relative decrease of M_s, where $T/T_C = 0.2$, is only 2×10^{-4}. At higher values of S the decrease is faster (*e.g.* for $S = 1$ it amounts to 6×10^{-4} at the same temperature). The reason for this faster decline of the magnetization at greater values of S is that at low temperatures there occur only the state of the ion with $S_z = S$ and to a slight extent the state with $S_z = S - 1$. The energy of this excited state is practically $g\mu_B WM_0$. The deviation of the magnetization from that in the total saturated state will then be proportional to:

$$\frac{\Delta M}{M_0} \sim (1/S)e^{-g\mu_B WM_0/kT}, \tag{6.16}$$

as follows from (6.7). (Compare 6.1)). The number of individual moments is proportional to $1/S$. Irrespective of this factor the magnetization thus decreases in the same way for different values of S for increasing T. However, at the same value of the reduced temperature the decrease of M/M_0 will then be greater for the higher value of S, for which according to (6.13) the Curie temperature is highest. As this is manifest in the exponent of (6.16) the $1/S$ term in (6.16) can not compensate for it at low temperatures.

At $T = 0$, $dM_s/dT = 0$, which is not merely a property of the model but follows from general thermodynamic considerations. Using (2.5) we may write for the variation of the free energy F of the magnetic material

$$dF = -SdT + HdM.$$

From this F the free enthalpy G is found by adding a potential similar to (2.9), *i.e.*

$$G = F - HM, \tag{6.17}$$

so that

$$dG = -SdT - MdH.$$

In the state of equilibrium G is minimum for constant T and H, as was remarked after (2.9). By differentiation we get

$$(\partial S/\partial H)_T = (\partial M/\partial T)_H. \tag{6.18}$$

According to Nernst, at $T = 0$ the entropy S is zero, irrespective of all parameters and hence also of H; therefore in (6.18), $\partial S/\partial H = 0$ at $T = 0$, and accordingly $\partial M/\partial T = 0$. Curie's law, then, does not satisfy this, and it can be said with certainty that, owing to the order of the magnetic moments, Curie's law is not valid near $T = 0$. How low the transition temperature is does not, of course, follow from such thermodynamic considerations.

6.3. PARAMAGNETISM ABOVE THE CURIE POINT

Although the spontaneous magnetization has vanished above the Curie point, the interaction between the magnetic moments is nevertheless still noticeable if a magnetic moment is induced by the external field. This induced moment, too, gives rise to a Weiss field H_W of (6.11) which must be added to the external field, so that M can now be found by substituting $H + WM$ in (6.4) for H. With the aid of (6.13) we may therefore write

$$\chi = \frac{C}{T - T_C}. \tag{6.19}$$

The Weiss field is then

$$H_W = \frac{T_C}{T - T_C} H.$$

The susceptibility now becomes infinite at $T = T_C$, indicating that a spontaneous magnetization sets in at this point (finite M for $H = 0$). The part of the $1/\chi$ axis cut off by the extrapolated $1/\chi$ *versus* T straight line is equal to $-W$.

6.4. CRITICISM OF THE WEISS FIELD THEORY

In the Weiss field theory the interaction of a single spin with its neighbour was approximated by the interaction with a uniform field parallel to the magnetization. In reality, at least if we still represent the interaction in this way, such a field will vary from place to place in direction as well as in magnitude, just as the magnetization does. At low temperatures, slowly varying deviations in the spin orientation take place, as follows from the rigorous spin-wave theory applicable in that region, which we shall discuss in more detail in § 22.3. The exchange energy per reversed spin is, according to the spin-wave theory, much smaller than $2zJS$ and for long-wave interferences is given by:

$$E_{ex} = 2\,JS\,a^2k^2, \tag{6.20}$$

where a is the lattice constant and k the magnitude of the wave vector $k = 2\pi/\lambda$. For $k = 0$ it costs no energy to reverse a spin. The entire uniform

magnetization is turned through a small angle out of the direction of the field, so that all spins remain mutually parallel. For a small value of k the angle between the neighbouring spins (proportional to ak) is very small; the exchange energy (5.1) is therefore very little increased, the increase being in first approximation proportional to the square of the angle of deviation ($\propto a^2k^2$) in agreement with (6.20) (cos $\phi \cong 1 - \frac{1}{2}\phi^2$). These low energy states can thus readily be excited at low temperatures (cf. (6.1)) so that the magnetization decreases much more rapidly than follows from the Weiss theory (6.16). The theory gives for this case:

$$M = M_0\left[1 - (T/T_B)^{3/2}\right], \tag{6.21}$$

with

$$T_B = 21\, S^{5/3} J/k \tag{6.22}$$

for the b.c.c. lattice. Equation (6.21) is the so-called Bloch $T^{3/2}$ law. For $S = \frac{1}{2}$ it follows from (6.14) that $T_B = 1.7\, T_C$. Experimentally it appears from the temperature-dependence of M_s at low temperatures for Ni and Fe that $T_B \cong 4T_C$, so that for $T/T_C = 0.2$ the relative decrease in magnetization is 10^{-2}, as compared with 2×10^{-4} according to the Weiss theory. A $T^{3/2}$ dependence for the decrease in magnetization is found experimentally at temperatures below approximately 0.3 T_C, where only the spin-wave theory can be applicable.

However, the Weiss field theory is also incorrect at high temperatures

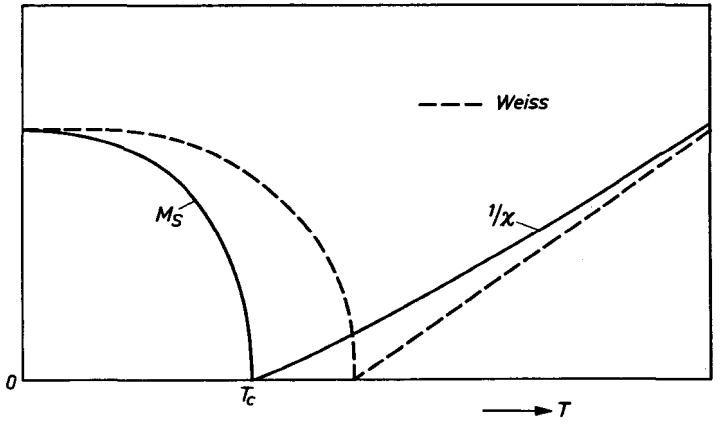

Fig. 6.4. Spontaneous magnetization M_s and the reciprocal susceptibility $1/\chi$ as a function of temperature. The broken curves are in accordance with the Weiss field theory. Better approximations steadily reduce the Curie point (cf. full curve) and make the $1/\chi$ *versus* T curve concave. The latter has as asymptote the Curie-Weiss line.

(in the region of the Curie point and higher). For example, the Weiss theory predicts that for $T > T_C$, in the absence of an external field, the spin order will have vanished completely. This would mean that there would no longer be any correlation between the orientations of two neighbouring spins. According to (5.1) and (6.1), however, there is an $e^{J/kT}$ greater chance of the spins being parallel than antiparallel. At the Curie point this factor, according to (6.14), is $e^{\frac{1}{2}} \simeq 1.3$ for a b.c.c. lattice. The order, however, will only be noticeable over a short distance (short range order) so that the magnetization will nevertheless disappear above the Curie point, which can only exist if there is long range order. More rigorous theories which deal in an approximate way with this correlation also above the Curie point all arrive at the result that the Curie temperature is lower than that given by (6.14). At very high temperatures ($T \gg T_C$) the correlation between the orientations of neighbouring spins is negligible and the Curie-Weiss straight line (6.19) is found as the asymptote of the actual $1/\chi$ *versus* T curve. However, the $1/\chi$ *versus* T line is now curved (see Fig. 6.4), the slope always being smaller than that of the asymptote (6.19). An expression for this slope can be found from the differential of F:

$$-\left(\frac{\partial S}{\partial M}\right)_T = \left(\frac{\partial H}{\partial T}\right)_M,$$

which can be written as:

$$\frac{\partial(1/\chi)}{\partial T} = -2\frac{\partial S}{\partial(M^2)}. \tag{6.23}$$

This slope is therefore related to the decrease of the entropy as a result magnetization. Since in the Weiss field approximation the state for $M = 0$ is in complete disorder, $\partial S/\partial(M^2)$ is constant as a function of temperature, and hence also $\partial(1/\chi)/\partial T$. In reality the entropy is smaller owing to the cluster formation and the change in it, caused by magnetization, will also be smaller (see Fig. 6.5). The orientation of the clusters is to some extent comparable with the orientation of the spin moments with greater S. Thus, the $1/\chi$ *versus* T curve will always be above the Curie-Weiss line (6.19) and therefore the Curie point will be lower. From the Bloch $T^{3/2}$ law, it also follows that the experimentally found Curie temperature is lower than that given by (6.14). This curvature of the $1/\chi$ *versus* T line is actually found, and is expressed as a difference between the ferromagnetic and the extrapolated paramagnetic Curie temperature; this difference is, however, rather small in most cases (20 to 30° for nickel). According to the theory the difference could amount to several tens per cent of the Curie temperature. In practice,

because the temperatures reached are not high enough, the true asymptote will probably not be drawn in most instances, but one with too low a slope. In fact, for nickel this slope agrees better with $S = 1$ than with $S = \frac{1}{2}$. It is therefore dangerous to draw conclusions from the $1/\chi$ *versus* T curve.

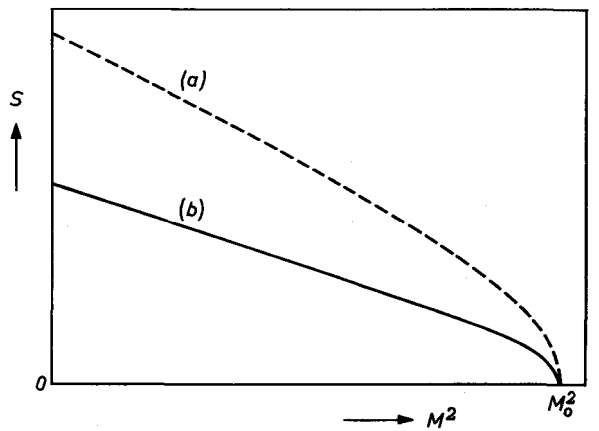

Fig. 6.5. Entropy as a function of the square of the magnetization. Curve (*a*) is according to Weiss field theory, whereas for curve (*b*) correlations between the spin directions of neighbouring ions have been taken into account.

§ 7. Caloric Properties

7.1. SPECIFIC HEAT

Owing to the decrease of M_s the change of the total exchange energy with the temperature is accompanied by an extra contribution to the specific heat which, in the absence of external fields, is given in the Weiss approximation by

$$c_M = \tfrac{1}{2} W \mathrm{d}(M_s^2)/\mathrm{d}T. \tag{7.1}$$

Just below the Curie temperature, c_M is maximum and above it c_M is zero, *i.e.* there occurs per spin a jump equal to

$$\Delta c_M = \frac{5S(S+1)}{S^2 + (S+1)^2} . k . \tag{7.2}$$

A finite jump of this kind in the specific heat is characteristic of what is called a second order transition. Transitions such as from the solid to the liquid state are first order transitions, where there occurs a finite transition heat which must be supplied in an infinitely small temperature interval;

in other words this corresponds to an infinitely high value of specific heat at the transition point. In a first order transition there is a jump in the entropy (a different phase) but not in a second order transition. Fig. 7.1 shows the specific heat curve of nickel in the region of $T = T_C$, in which

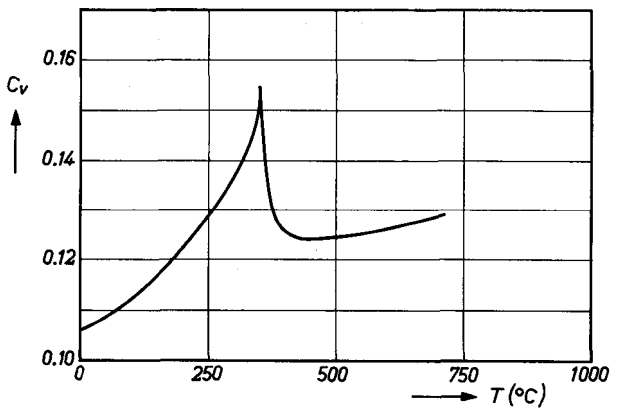

Fig. 7.1. Specific heat of nickel in the region of the Curie temperature. (After Moser [Mo 1]).

the magnetic contribution is in fairly good agreement with the theory. The drop, however, is not so sudden as predicted by the Weiss field theory according to which the magnetic contribution to the specific heat should be zero above the Curie point. However, all order has not yet disappeared above this point, as is manifest in the magnetic contribution to the entropy change

$$\Delta S_M = c_M \Delta T/T. \tag{7.3}$$

The "tail" of the specific heat curve is thus a measure of the short range order above the Curie point.

7.2. MAGNETOCALORIC EFFECT

In all thermodynamic systems a change of temperature takes place during an adiabatic change of an intensive parameter (potential, field). In the magnetic case an increase of the field reduces the magnetic entropy according to

$$\Delta S_M = (\partial S/\partial H)_T \Delta H.$$

In order to keep the total entropy constant the temperature is increased (greater disorder), so that the entropy is increased (cf. (7.3)) by:

$$\Delta S = c_H \Delta T/T,$$

where c_H is the specific heat of the whole system, the external field remaining constant. Making use of (6.18) we find for the temperature change:

$$\Delta T = -(T/c_H)\,(\partial M/\partial T)_H \Delta H, \tag{7.4}$$

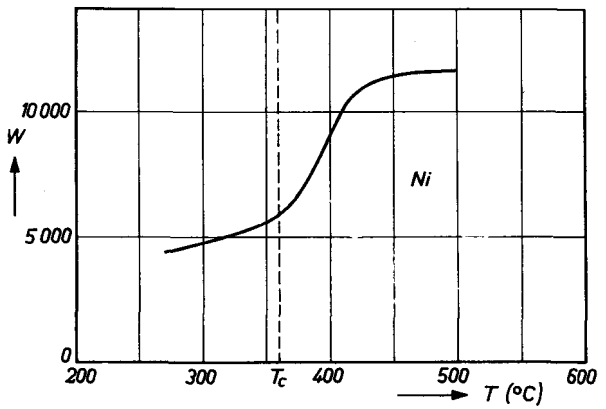

Fig. 7.2. Weiss field constant W for nickel, as determined from the magnetocaloric effect. According to the simple theory this should not be temperature-dependent. (After Weiss *et al.* [We 1]).

which has the correct sign, since $\partial M/\partial T < 0$. Owing to the use of thermodynamic relations, equation (7.4) holds only for reversible changes, *i.e.* for the change of the intrinsic magnetization and for those magnetization processes which take place without hysteresis. For $\Delta H = 10{,}000$ oersteds the temperature increase in the case of nickel and iron is of the order of 1 °K at the Curie point, and 0.1 °K at $T \cong 0.5\ T_C$.

Using (6.15) and applying the Weiss field theory, we can express T in the accompanying change of M:

$$\Delta T = \frac{WM}{c_H} \cdot \Delta M = \tfrac{1}{2}\frac{W}{c_H}\,\Delta M^2, \tag{7.5}$$

so that W can be calculated from the experimental values for ΔM and ΔT. Experiments by Weiss *et al.* [We 1] have demonstrated that ΔT is in fact proportional to the change of the square of the magnetization, but that W depends upon the temperature, especially in the region of T_C (see Fig. 7.2).

CHAPTER III

FERRIMAGNETISM

§ 8. Origin of Ferrimagnetism

8.1. INDIRECT EXCHANGE INTERACTION

In many ionic crystals, as in the majority of oxides to be discussed, the exchange energy J between the spins of the neighbouring metal ions is found to be negative, so that antiparallel alignment gives the lowest energy. In these substances, however, the metal ions are more or less separated by the negatively charged antions, which, like the inert gases, have a closed shell configuration in the ground state. For example, the electron structure of the O^{II} ion is like that of neon ($2s^2 2p^6$). The distance between the metal ions is usually much too great for a direct exchange interaction to be possible, since the extent of overlapping of the wave functions (orbitals) decreases exponentially with distance. Various magnetic interaction mechanisms have therefore been proposed [Va 1] in which the interlying anion plays an essential part (super exchange). In the ground state with the inert gas configuration the ion is inert and can produce no spin coupling. The surrounding ions will, however, disturb this state somewhat, so that the extra electrons will for a small part of the time belong to the neighbouring ions. In quantum mechanics this is expressed by the principle of the superposition of states. That is to say the state of the oxygen ion with the lowest energy is a superposition of the ground state O^{II} and (for a small amount) the state O^{I} and possibly that of the neutral O atom. In reality a whole variety

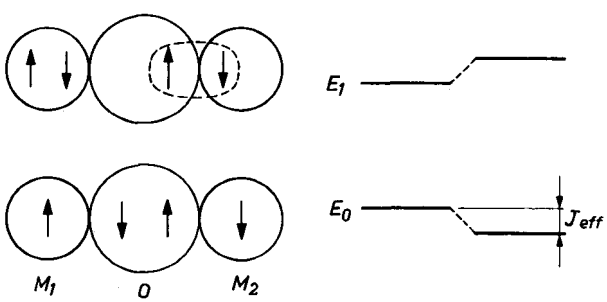

Fig. 8.1. Ground state and excited state of two metal ions, M_1 and M_2, with an oxygen ion between them. The spin configurations as drawn become intermingled, causing an extra reduction of ground state energy; this does not occur if M_1 and M_2 have parallel spins.

of excited states will be mixed together, but we shall consider only those which can be of use in explaining magnetic interaction. The electron separated from the oxygen will return to one of the surrounding metal ions from which it originally came (M_1 in Fig. 8.1.). Within this metal ion there exists a strong exchange interaction between the spins (Hund's rule). The electron can only be there if its spin has a given orientation with respect to the resultant spin moment of the ion, and that depends upon the orbit in which the electron in this excited state chooses to move. Where this (according to Anderson) is the $3d$ orbit, the spin will be parallel to the resultant moment if the shell was less than half occupied (five or less $3d$ electrons); otherwise it must occupy an orbit with antiparallel spin. The electron under consideration has come from a $2p$ oxygen orbit since this has the highest energy. According to the Pauli principle, an orbit can contain two electrons with opposite spins. The remaining, now unpaired, electron can interact with another metal ion. There are also many other possibilities, but these excited states will certainly be intermingled to a small extent. According to Anderson the second electron interacts with one of the metal ion electrons as in the covalent bond or hydrogen molecular bond, in which the two associated electrons constantly jump to and fro between the ions concerned and continually exchange their (antiparallel) spins. The latter will now only take place to a more limited extent, since the spins at the position of the ions are not free to orient themselves. In that case the energy gain will therefore only be half as large.

Where these states are admixed and then cause a reduction of energy, it means that an effective coupling has arisen between the spin moments of the two metal ions. For if the moments had been parallel there would have been no intermingling and hence no reduction of energy. This reduction of energy occurs because, owing to the intermingling of excited states, the total charge distribution can adapt itself with more economy of energy to the potential occurring in the lattice. Accordingly we can again speak of an effective exchange energy J. In this case we may therefore expect positive exchange energy for the d^1 to d^4 configuration and negative exchange energy for d^5 to d^9.

One of the other possibilities, according to Anderson and Hasegawa [An 1], is that the equivalent state, in which the other electron is transferred to the other metal ion, also occurs simultaneously, leading to a reduction in energy. This is only possible if the two metal ions have their resultant spin moments antiparallel, so that in this case only a negative effective exchange energy can exist ($J < 0$).

Which states are most strongly admixed will depend upon the distances

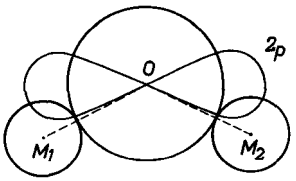

Fig. 8.2. Diagram showing the orientation of the $2p$ orbit of the oxygen ion with respect to the metal ions, which is responsible for the indirect exchange.

and the distribution of the surrounding ions. At all events, this interaction will also largely depedend depend — for the same reasons as in the case of direct interaction — upon the distance between the metal and oxygen ions, and will rapidly diminish with increasing distance. Apart from this dependence upon distance, there is also dependence upon direction to be considered. The orbits of the oxygen electrons in question are, as we have seen, the stretched $2p$ orbits. Since the interaction or the transition to the metal ions can take place only if there is some overlap with the orbits in these ions, it will take place most favourably if the oxygen ion lies centrally on the line connecting the two metal ions, so that the axis of the p orbit under consideration can coincide exactly with this line. If the angle M_1-O-M_2 in Fig. 8.2. is in the region of 90°, the interaction will be smaller. Such considerations are also frequently of importance for determining molecular configurations.

Experimentally, negative exchange energy is found in most cases, as in the ferromagnetic oxides, although some cases of positive J have been reported.

8.2. SPIN ORDER

In the case of negative exchange interaction one would expect the spins of neighbouring ions to be antiparallel, giving the sample a zero magnetic moment. A simple two-dimensional model is shown in Fig. 8.3. The spin order depends not only upon the crystalline structure but also upon the ratios of the magnitudes of the interactions. The order occurring will be that with the lowest energy. In Fig. 8.3*a*), for example, the interaction between the nearest neighbours A and B is stronger than that between the next nearest neighbours A and C. In Fig. 8.3*b*) the converse is true. The latter case will be found, for example, when the joining antion lies in the centre of the square elementary cell. Only the distances between cation and anion are important, and not those between the metal ions. In Fig. 8.3*a*), then, the bond A-C is the strongest because of the 180° angle between the connecting lines, although the distance between the metal ions is greater. The spin order in the MnO crystal is indicated in Fig. 8.4.

An antiferromagnetic order in which the elementary magnets are not purely antiparallel occurs for example in Fig. 8.3.*c*) in the two-dimensional trigonal lattice [Ya 1]. If a purely antiparallel order were to appear, each spin would

at the most be surrounded by four antiparallel neighbours, the other two being parallel. The exchange energy would then be $2J$. According to (5.1) the exchange energy in the situation as drawn, in which all spins make angles of 120° with each other, will be $-6J \cos 120° = 3J$, this being lower for $J < 0$.

In the cases *a*) and *b*) in Fig. 8.3, the lattice can be split up into two sublattices, each possessing uniform magnetization. In the case of *c*) there are three.

If the sublattices are occupied by identical ions, the resultant moment will be zero (antiferromagnetism). If the magnetic moments of both sublattices differ in magnitude a net moment will result. This case is known as ferrimagnetism, a name given to it by Néel [Ne 1].

In the cases with which we are concerned we can split the crystal lattice into a number of sublattices; these are not, however, crystallographically equivalent and moreover generally contain different numbers of ions

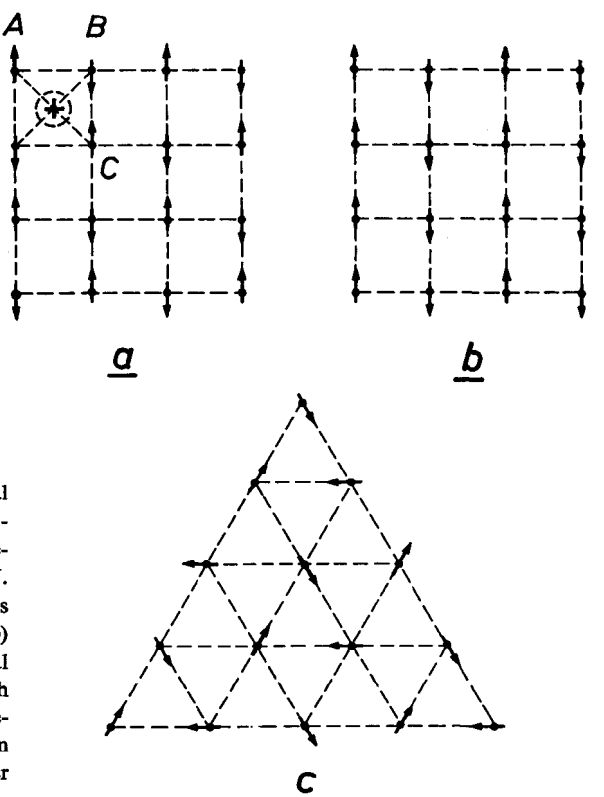

Fig. 8.3. Two-demensional representation of some modes of spin order for negative exchange energy J. In *a*) the *A*-*B* coupling is stronger than *A*-*C*, in *b*) it is weaker. In the trigonal lattice *c*) the spin order with three sublattices, the magnetizations of which make an angle of 120° with each other has the lowest energy.

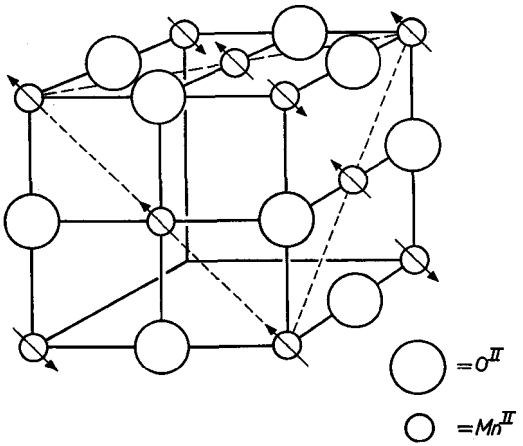

Fig. 8.4. Antiferromagnetic spin order in the cubic MnO crystal. The nearest neighbours but one have antiparallel spins.

(*e.g.* two sublattices for the spinel structure and five for the magnetoplumbite structure). In most such cases it is then possible for each of them to have uniform magnetization, so that it is not necessary to split up these sublattices again for the magnetic spin order.

§ 9. Weiss Field Theory Applied to Ferrimagnetism

9.1. STRETCHED CONFIGURATION

Néel [Ne 1] has shown that the Weiss field theory can also be applied to ferrimagnetism, albeit in a somewhat more complicated form. An ion of a given sublattice is surrounded by a number of neighbours, some of which belong to the same sublattice and some to others, so that the Weiss field acting on this ion depends upon the magnetizations of all sublattices, according to

$$H_{Wi} = \sum_{j=1}^{n} W_{ij}\, M_j. \tag{9.1}$$

The Weiss field coefficients W_{ij} are a measure of the strength of the exchange interaction between the spins of an ion from the ith sublattice with that of an ion from the jth sublattice. Thus, in the cases in which we are interested these W_{ij} values are negative. Since action is equal to reaction, $W_{ij} = W_{ji}$.

Formula (5.10) is now valid for each sublattice, and H in (5.11) must be augmented by the corresponding Weiss field from (9.1). In this way we obtain n simultaneous equations, the unknown quantities being the magnetizations of the n sublattices. Here, too, the Curie point is found by substituting the Weiss fields from (9.1) for H in (5.7), which equation now holds for each sublattice separately. For the i th sublattice this results in the equation:

$$T_C M_i - C_i \sum_{j=1}^{n} W_{ij} M_j = 0, \tag{9.2}$$

where T has been replaced by the Curie temperature T_C, since the equation applies to that only. These n linear, uniform equations in the magnetizations M_j of the sublattices cannot all be independent and they only give a solution differing from zero for the sublattice magnetizations if the determinant of the coefficients of M_i is zero. This gives an equation of the nth degree in T_C with n roots. For example, where $n = 2$:

$$\begin{vmatrix} (W_{11} - \frac{T_C}{C_1}) & W_{12} \\ W_{21} & (W_{22} - \frac{T_C}{C_2}) \end{vmatrix} = 0. \tag{9.3}$$

This does not mean that every sublattice has its own Curie temperature; that is the same for all of them, for the one sublattice magnetization exists solely by virtue of the others. It means only that there are n different M_s *versus* T curves for the resultant magnetization with n Curie points. Generally speaking, a number of these roots of the determinant equation will be negative or imaginary, so that in these cases there will be no spontaneous magnetization. Where there is more than one real, positive root for T_C only the state with the highest Curie temperature will occur; the others have a higher free energy and are unstable. For $n = 2$, we find according to (9.3)

$$T_C = \tfrac{1}{2}\left[C_1W_{11} + C_2W_{22} + \sqrt{(C_1W_{11} - C_2W_{22})^2 + 4C_1C_2W_{12}^2}\right]. \tag{9.4}$$

For antiferromagnetism (both sublattices identical and $W_{12} < 0$) it then follows that

$$T_N = C_1(W_{11} - W_{12}), \tag{9.5}$$

in which case the transition point is referred to as the Néel point.

In addition to the Weiss field coefficients which indicate the interaction between the spins associated with two different sublattices, equation (9.1) also contains those for the interaction originating from spins in the same sublattice. If this interaction is negative, which is usually the case, it will try to upset the parallel alignment of the spins within this sublattice. However, if the interaction with the other sublattices is stronger this will not happen. In Fig. 9.1 a schematic

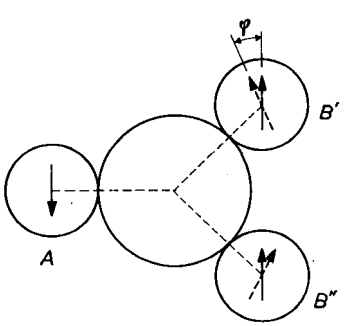

Fig. 9.1. Ion configuration in a ferrimagnetic crystal. The ion in the centre is the non-magnetic anion; A, B' and B'' are metal ions.

representation is given of this situation, which is characteristic of ferrimagnetism. The metal ion A belongs to the one lattice, and the two metal ions B' and B'' belong to the other lattice ($n = 2$). There is thus an unequal number of ions on the two lattices, so that in the case, for example, of occupation by identical ions a net moment can result. The ion A is separated from B' and B'' by an oxygen ion, which is responsible for the negative interaction between A and B' and B'' as well as between B' and B'' mutually. If the latter interaction is relatively weak, the A-B interaction produces the antiparallel alignment of both B' and B'' with A, so that B' and B'' are parallel with each other. This applies as long as J_{AB} is greater than $2J_{B'B''}$, where J_{AB} is the exchange energy between ion A and B' or B'', and $J_{B'B''}$ that between B' and B''.

Proceeding from these principles, Néel developed his theory of ferrimagnetism for two sublattices and determined the various possible forms of the M_s *versus* T curves, giving a very satisfactory explanation of the magnetizations observed in ferrites with spinel structure, as well as of their paramagnetic susceptibility above the Curie point. Depending upon the magnitude of the sublattice magnetizations at $T = 0$ and the ratios of the magnitudes of the interactions, the M_s *versus* T curve can assume very different forms. Although in general the sublattice magnetizations monotonically decrease with increasing temperature, the form of the resultant magnetization curve can be anomalous in view of the fact that it is obtained by subtraction of two magnetizations. For example, the magnetization can pass through zero or show a maximum as a function of temperature. The former case, which was first reported by Gorter and Schulkes [Go 1] (Fig. 9.2), is one of the most direct proofs of the existence of ferrimagnetism. Measurement of the saturation moment would reveal no reversal of sign; this takes place only in the measurement of the remanence established after the application and return to zero of a strong field.

The occurrence of magnetization curves of this kind, which are typical of ferrimagnetism, may be understood in the following way. Let the negative interaction between the two lattices be $W_{AB} = -n$, while

$$W_{AA} = \alpha W_{AB} = -\alpha n \qquad W_{BB} = \beta W_{AB} = -\beta n.^{*}) \tag{9.6}$$

Take first the case that $M_{B0} > M_{A0}$, with β large and α small. The effective Weiss field constant in the B lattice $n(M_{A0}/M_{B0} - \beta)$ is then small at $T = 0$ compared with that in the A lattice $n(M_{B0}/M_{A0} - \alpha)$. The magnetization

*) We have chosen α and β positive where the exchange interaction is negative, in contrast to the practice in most existing literature.

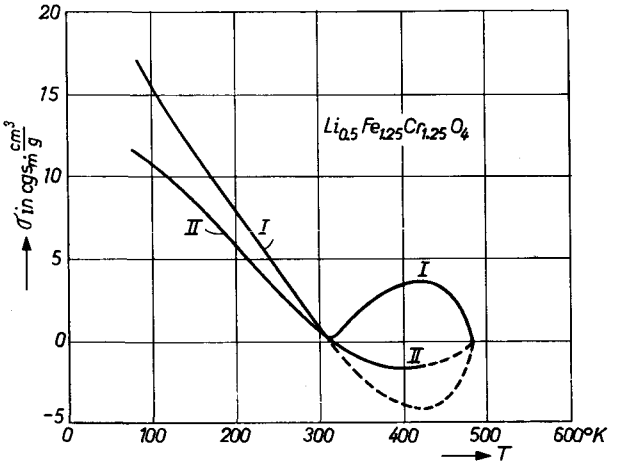

Fig. 9.2. Magnetization *versus* temperature curve for $Li_{0.5}Cr_{1.25}Fe_{1.25}O_4$. Curve II represents the remanence and curve I the spontaneous magnetization.

in the B lattice therefore begins to decrease faster than that in the A lattice (see Fig. 9.3*a*), as if the Curie point of the B lattice were lower than that of the A lattice. At increasing temperatures both sublattice magnetizations vanish, but at the same Curie point. Consequently the M_A *versus* T curve is more convex than that for M_B, and it is possible that below the Curie point $M_A - M_B$ will be equal to zero. In order to explain a magnetization curve with a maximum, a curve which is also found experimentally, we must assume that β is small and α large. Then M_A decreases less rapidly than M_B (Fig. 9.3*b*).

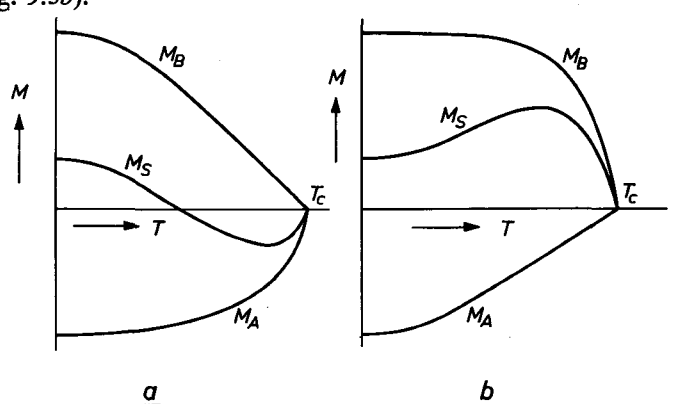

Fig. 9.3. Examples of the cause of anomalous M_s *versus* T curves. In a) β is greater than α and in *b*) α is greater than β. The M_s curves represent the resultant magnetization.

The above theory for $n = 2$ is applicable to the spinel lattice, for which in fact it was originally developed (see Chapter VIII). For more than two sublattices, such as occur in the hexagonal structures (Chapter IX) no such simple statements can be made about the form of the M_s *versus* T curves.

The existence of antiparallel- oriented magnetizations has been demonstrated in various cases by slow-neutron diffraction [Sh 1]. Because of the fact that these particles carry no charge they are able readily to penetrate matter; owing to their spin they undergo in matter an extra interaction with the ion cores, from which conversely the magnetic moment of the latter can be determined in magnitude and direction.

9.2. TRIANGULAR CONFIGURATION

Where, in the case of Fig. 9.1, $J_{AB} < 2J_{B'B''}$, the parallel alignment of B' and B'' is perturbed and the angle ϕ becomes such that $\cos\phi = J_{AB}/2J_{B'B''}$. This follows directly by minimizing the total exchange energy

$$E_{ex} = 2J_{AB}\cos\phi + J_{B'B''}\cos 2\phi.$$

An extension of the Weiss field theory for triangular configurations, as indicated above, has been developed by Yafet and Kittel [Ya 1]. If, for example, $W_{AA} < 0$ ($\alpha > 0$) then, where $W_{AB} = 0$, an antiferromagnetic order will occur in the A lattice, *e.g.* with two antiparallel sublattices. Analogous to the case described above, this splitting into sublattices, depending upon the relative magnitude of the interactions, will sometimes occur for $W_{AB} \neq 0$, but the two sublattice magnetizations will make an angle with each other differing from 0° or 180°. The Weiss fields are then:

$$\begin{aligned} \boldsymbol{H}_{WA'} &= -n\left[\alpha_1\boldsymbol{M}_{A'} + \alpha_2\boldsymbol{M}_{A''} + \boldsymbol{M}_B\right] = -n\left[(\alpha_1-\alpha_2)\boldsymbol{M}_{A'} + \alpha_2\boldsymbol{M}_A + \boldsymbol{M}_B\right] \\ \boldsymbol{H}_{WA''} &= -n\left[\alpha_2\boldsymbol{M}_{A'} + \alpha_1\boldsymbol{M}_{A''} + \boldsymbol{M}_B\right] = -n\left[(\alpha_1-\alpha_2)\boldsymbol{M}_{A''} + \alpha_2\boldsymbol{M}_A + \boldsymbol{M}_B\right] \end{aligned} \tag{9.7}$$

Similar equations apply to the B lattice:

$$\begin{aligned} \boldsymbol{H}_{WB'} &= -n\left[\boldsymbol{M}_A + \beta_1\boldsymbol{M}_{B'} + \beta_2\boldsymbol{M}_{B''}\right] = -n\left[\boldsymbol{M}_A + \beta_2\boldsymbol{M}_B + (\beta_1-\beta_2)\boldsymbol{M}_{B'}\right] \\ \boldsymbol{H}_{WB''} &= -n\left[\boldsymbol{M}_A + \beta_2\boldsymbol{M}_{B'} + \beta_1\boldsymbol{M}_{B''}\right] = -n\left[\boldsymbol{M}_A + \beta_2\boldsymbol{M}_B + (\beta_1-\beta_2)\boldsymbol{M}_{B''}\right] \end{aligned} \tag{9.8}$$

A splitting up of this kind will only occur where $\alpha_2 > \alpha_1$, or $\beta_2 > \beta_1$. This is also the reason for the angle formation: ions between which the greatest negative interaction prevails are no longer in parallel alignment. It further holds that

$$\boldsymbol{M}_{A'} + \boldsymbol{M}_{A''} = \boldsymbol{M}_A \qquad \boldsymbol{M}_{B'} + \boldsymbol{M}_{B''} = \boldsymbol{M}_B, \tag{9.9}$$

and for α and β from (9.6) that

$$\alpha = \tfrac{1}{2}(\alpha_1 + \alpha_2) \qquad \beta = \tfrac{1}{2}(\beta_1 + \beta_2). \tag{9.10}$$

The equations (9.9) are now essentially vector equations, like those for the Weiss fields (9.7) and (9.8). It is evident that the magnetization of a given sublattice must be parallel to the Weiss field concerned, as follows also from minimization of the energy [Ya 1]. From the first equation of (9.7) it follows then that the vector $(\alpha_2 \boldsymbol{M}_A + \boldsymbol{M}_B)$ is parallel to $\boldsymbol{M}_A'$, and from the second equation it would follow that this vector would be parallel to $\boldsymbol{M}_A''$. Thus, if angle formation occurs in the A lattice, it necessarily holds that

$$\alpha_2 \boldsymbol{M}_A + \boldsymbol{M}_B = 0 \tag{9.11}$$

Likewise for angle formation in the B lattice we may write

$$\boldsymbol{M}_A + \beta_2 \boldsymbol{M}_B = 0. \tag{9.12}$$

In general, $\alpha_2 \beta_2 \neq 1$, and therefore angle formation will only be able to occur on one of the two sublattices at one time. In that case we may write for the Weiss fields where, for example, angle formation occurs in the B lattice,

$$\begin{aligned} \boldsymbol{H}_{WA} &= n\left(\frac{1}{\beta_2} - \alpha\right)\boldsymbol{M}_A \\ \boldsymbol{H}_{WB}' &= n(\beta_2 - \beta_1)\boldsymbol{M}_B', \end{aligned} \tag{9.13}$$

while

$$\boldsymbol{M} = \left(1 - \frac{1}{\beta_2}\right)\boldsymbol{M}_A. \tag{9.14}$$

In the A lattice, then, the Weiss field depends only upon $\boldsymbol{M}_A$, so that according to (9.14) the M_s *versus* T curve will have the same form as for normal ferromagnetism. The angle ϕ (see Fig. 9.4) between the magnetizations of the sublattices B' or B'' and A follows from

$$\cos\phi = \boldsymbol{M}_A / 2\beta_2 \boldsymbol{M}_B' \leqslant \boldsymbol{M}_A / \beta_2 \boldsymbol{M}_B, \tag{9.15}$$

where $\boldsymbol{M}_A$ and $\boldsymbol{M}_B$ are determined by (9.13). If angle formation occurs, then according to (9.12) the last term of (9.15) is equal to one.

For fixed α_2 and fixed $\boldsymbol{M}_A$ and $\boldsymbol{M}_B$ (*e.g.* at $T = 0$ and calculated without angle formation) and variable β_2, configurations are obtained as shown in Fig. 9.5. For $\beta_2 < \boldsymbol{M}_A / \boldsymbol{M}_B$, we see from (9.12) that no angle forma-

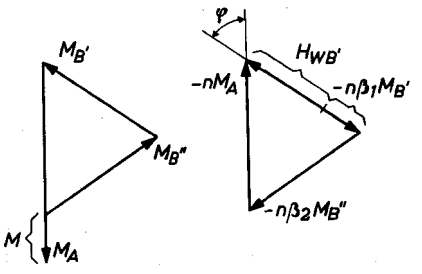

Fig. 9.4. Triangular configuration of the sublattice magnetizations (left) together with that of the Weiss fields on the B' lattice.

tion can occur in the B lattice. It does occur for larger values of β_2, whereby the angle ϕ from (9.15) becomes steadily smaller. Where $\beta_2 = 1/\alpha_2$, it follows from (9.11) and (9.12) that angle formation is possible in both sublattices; in that case the configuration becomes unstable and, at larger values of β_2, it changes discontinuously into an antiferromagnetic configuration (ϕ jumps to zero). Up to the point $\beta_2 = 1/\alpha_2$ the Weiss field H_{WA} from (9.13) is still positive, since $\alpha_2 > \alpha$. In Fig. 9.5 it can be seen that $1/\alpha_2$ is greater than M_A/M_B, but according to (9.11) this is precisely the condition with which we started, namely that no angle formation should occur in the A lattice.

With increasing temperature the configuration can change. For instance, if at $T = 0$ the parallel configuration appears, because, $\beta_2 < M_A/M_B$, but M_A decreases faster with increasing temperature than M_B, a temperature can be reached for which (9.12) is applicable, and therefore angle formation occurs. However, this configuration cannot go over into the pure paramagnetic one when the temperature is further increased, for (9.13) determines separately the Curie point of the sublattices A and B' or B'', *i.e.* T_{CA} and $T_{CB'}$ or $T_{CB''}$ respectively. These will generally not be the same (they will only be the same if $\beta_2^{-1} - \alpha = \beta_2 - \beta_1$ with equal Curie constants of the ions on both sublattices). If $T_{CA} > T_{CB'}$, then $M_{B'}$ would be zero sooner than M_A, but in that case cos ϕ from (9.15) would be greater than one, so that at lower temperature the stretched configuration occurs ($\phi = 0°$). On the other hand, if the Curie point of the A lattice is the lower, the A lattice will become paramagnetic at this Curie point, while the B lattice will be antiferromagnetic ($\phi = 90°$). This lattice does not become para-

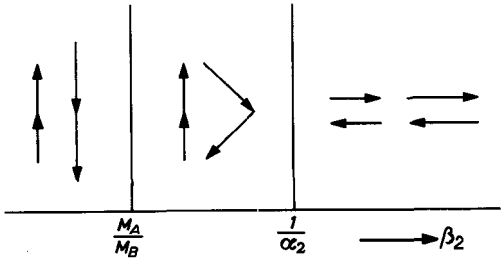

Fig. 9.5. Spin configurations for variable β_2.

magnetic until above the Néel point, which is determined by the second equation of (9.13). We have here, then, the special circumstance that there is a Néel point above the Curie point. Thus, the case of both sublattices being antiferromagnetic occurs only when $\alpha_2\beta_2 > 1$.

The transition of the triangular configuration to the stretched one, or *vice versa*, with variable temperature is comparable with the ferromagnetic-paramagnetic transition at the Curie point. It is also a second order transition. The magnetization and entropy are continuous, but with increasing temperature $\mathrm{d}M_s/\mathrm{d}T$ shows a positive jump, accompanied by a jump in the specific heat. These jumps, however, have never yet been found experimentally.

An example worked out by Lotgering [Lo 1] for the spinel lattice with occupation by identical ions ($M_B = 2M_A$) is given in Fig. 9.6, which shows some possible forms of M_s *versus* T curves for variable α and β. In this case

$$\alpha_1 = 0, \qquad \alpha_2 = 2\alpha, \qquad \beta_1 = {}^2/_3\beta, \qquad \beta_2 = {}^4/_3\beta, \tag{9.16}$$

so that the boundary line for ferrimagnetism is given by $\alpha\beta = \frac{3}{8}$.

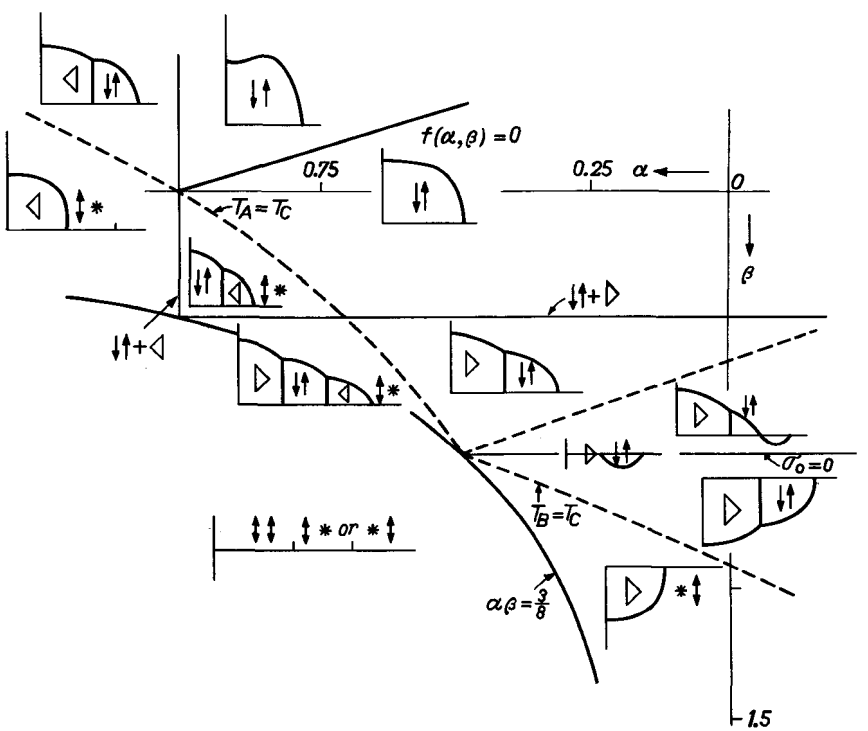

Fig. 9.6. Possible forms of magnetization-temperature curves for variable values of α and β for the spinel lattice. (After Lotgering [Lo 1]).

Although some of the spins are antiparallel in a ferrimagnetic substance without angle formation at $T = 0$, an applied field has nevertheless no effect, *i.e.* $\chi(T = 0) = 0$, because the exponents $\mu(H + H_W)/kT$ of the exponentials (6.1) do not change ($\pm\infty$), at least as long as the effective fields remain parallel to the sublattice magnetizations. That will be the case if the applied field is smaller than the Weiss field. Where angle formation occurs, this angle will be changed by an applied field, resulting in $\chi \neq 0$. A simple calculation shows in the case of angle formation in the B lattice that

$$\chi = \frac{1}{n\beta_2}, \tag{9.17}$$

irrespective of the magnitude of the angle. This is the same susceptibility that would be found for a purely antiferromagnetic B lattice. Measurement of χ at low temperatures above saturation should show whether angle formation occurs.

§ 10. Paramagnetism above the Curie Point

The paramagnetic susceptibility above the Curie point can again be found by expanding the Brillouin functions for a small argument as in (9.2), so that in the absence of an applied field H we may write for each i:

$$TM_i - C_i \sum_{j=1}^{n} W_{ij}M_j = C_iH. \tag{10.1}$$

From this we can find $M = \sum_{j=1}^{n} M_i$. For $n > 1$, the $1/\chi$ *versus* T curve is not a straight line. For $T \gg T_C$ the curve has an asymptote which can readily be found from (10.1) by first neglecting the Weiss field terms, so that $M_i = C_iH/T$, and then filling in these values in the Weiss field terms. For the asymptote we then find

$$\lim_{T\to\infty} 1/\chi = \frac{1}{C}(T - T_a), \tag{10.2}$$

where

$$C = \sum_{i=1}^{n} C_i \tag{10.3}$$

and T_a is the asymptotic Curie temperature, which is given by

$$T_a = \sum_{i=1}^{n}\sum_{j=1}^{n} C_iW_{ij}C_j/C. \tag{10.4}$$

For antiferromagnetic interactions ($W_{ij} < 0$), T_a is negative. In general, T_a is a measure of the average magnitude of the exchange interaction. For antiferromagnetism it follows that

$$T_a = C_1(W_{11} + W_{12}), \tag{10.5}$$

which may be compared with (9.5). Therefore, $T_a = -T_N$ only if $W_{11} = 0$. Formula (10.2) holds for antiferromagnetism not only asymptotically but also strictly above the Néel point, as follows from (10.1). Thus for $T > T_N$ the $1/\chi$ *versus* T curve is straight, as it is in the case of a ferromagnetic material. At $T = T_N$, then, χ is not infinite but is given by

$$\chi(T_N) = \frac{1}{W_{12}}, \tag{10.6}$$

which is the same value as that resulting from the deflection of the antiparallel magnetization vectors in (9.17). Below the transition point T_N the susceptibility depends upon the orientation of the sublattice magnetizations with respect to the applied field. Roughly speaking in a cubic or polycrystalline substance two-thirds of the substance is perpendicularly oriented and one third parallel. In the latter case a moment can only result if the absolute magnitude of the sublattice magnetizations changes owing to the field. At $T = T_N$, the susceptibility resulting from this process is apparently equal to that in the perpendicular orientation, the latter being independent of the temperature. At low temperature the parallel susceptibility becomes zero, so that in this case the resulting χ is only two thirds of that at $T = T_N$. Thus, the $1/\chi - T$ curve shows a dip at $T = T_N$, which is also found experimentally, although the ratio $\chi(0)/\chi(T_N)$ differs in most cases from 2/3, except for MnO.

For ferrimagnetism, T_a is also negative in most cases, but $1/\chi$ becomes zero at the Curie point; above the Curie point the $1/\chi$ *versus* T curve is therefore convex towards the T axis. As in the ferromagnetic case (compare § 6.3) the Weiss fields immediately above the Curie point are large compared with the applied field. As a result the ferrimagnetic state with antiparallel oriented sublattices is then restored by the application of the field. With increasing temperatures the magnetization of the antiparallel lattice decreases and at a given temperature becomes zero. In the case of two sublattices this temperature, for which $M_2 = 0$, is according to (10.1) equal to

$$T(M_2 = 0) = C_1(W_{11} - W_{12}).$$

In the case of an antiferromagnetic this temperature coincides, according to (9.5), exactly with T_N, which agrees with the fact that for $T > T_N$ the sublattice magnetizations in antiferromagnetic substances, too, are parallel.

Fig. 10.1 shows the various forms of the $1/\chi$ *versus* T curves for equal values of C. The curves, for anti ferromagnetism and ferrimagnetism (above the temperature of (10.7)) thus lie above the curve for pure paramagnetism be-

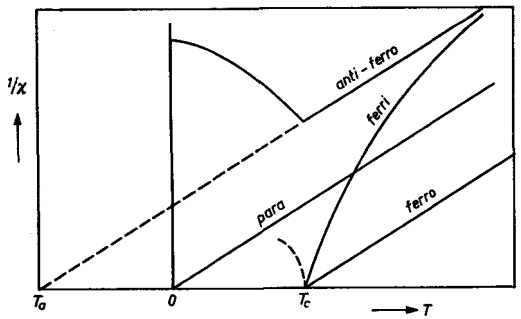

Fig. 10.1. $1/\chi$ *versus* T curves for $J = 0$ (paramagnetism), $J > 0$ (ferromagnetism) and $J < 0$ (antiferromagnetism and ferrimagnetism).

cause the Weiss fields oppose the applied field. The curve for a ferrimagnetic with a Néel point above the Curie point is given in Fig. 10.2.

The fact that the $1/\chi$ *versus* T curves for ferrimagnetics are concave and for ferromagnetics and antiferromagnetics straight — at least to the first approximation — follows also from more general thermodynamic considerations with reference to (5.23). In this respect an antiferromagnetic does not differ from a ferromagnetic. In the Weiss field approximation there is complete disorder above the transition point. The establishment of a magnetization caused by an applied field is then quite distinct, that is to say the $\mathrm{d}S/\mathrm{d}(M^2)$ is independent of the temperature. In a ferrimagnetic, on the other hand, the antiparallel order is restored just above T_c when the field is applied. One of the sublattice magnetizations is then larger than the resultant magnetization. There arises, then, a relatively large order, *i.e.* $\mathrm{d}S/\mathrm{d}(M^2)$ is large, and becomes smaller with increasing temperature where the Weiss fields decrease.

The Weiss field approximation as applied to ferrimagnetism is subject to the same criticism as when it is applied to ferromagnetism. For instance, Kaplan [Ka 1] has worked out that at low temperatures a Bloch $T^{3/2}$ law, analogous to (5.22), must also apply to the change of magnetization with temperature. In this approximation the spins of neighbouring A and B ions remain essentially antiparallel during thermal agitation and therefore the ratio M_A/M_B should remain constant. The resultant magnetization

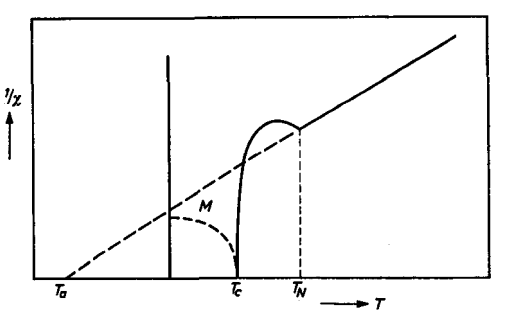

Fig. 10.2. $1/\chi$ *versus* T curve for a ferrimagnetic substance which, at $T > T_c$ becomes antiferromagnetic.

therefore can only decrease with increasing temperature, also in the case of Fig. 9.3*b*. Moreover, above the Curie point, short range order will persist. The influence of this on the susceptibility has been calculated by Smart [Sm 1] (Fig. 10.3). Here, again, the slope of the $1/\chi$ *versus* T curve is less steep than the Weiss field approximation would have led one to expect. This can again be explained with the aid of (5.23), for in consequence of the short-range order, S will be smaller and hence $dS/d(M^2)$ also. In this case, too, the result will be a lowering of the Curie point.

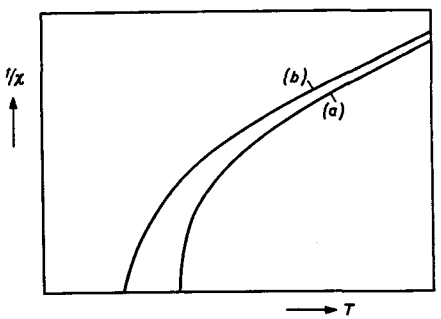

Fig. 10.3. $1/\chi$ *versus* T curve for a ferrimagnetic substance (*a*) in accordance with the classic Weiss field approximation and (*b*) in accordance with more exact methods. (After Smart [Sm 1].)

CHAPTER IV

MAGNETIC ANISOTROPIES

§ 11. Description of Magnetic Anisotropies

11.1 MAGNETOCRYSTALLINE ANISOTROPY

So far we have discussed only the mutual orientation of the spins, and have regarded the orientation in the crystal of the resultant magnetization or of the sublattice magnetizations as arbitrary. A ferromagnetic substance in which this were the case would be perfectly soft, that is it could be magnetized by an infinitely small field. In reality the magnetization vector in a ferromagnetic specimen is always bound to a certain preferred direction and a finite field is required to turn it from that direction. This behaviour is described by an anisotropy energy, *i.e.* by the value of the magnetization energy $\int \boldsymbol{H}\mathrm{d}\boldsymbol{M}$ from (2.5) required to turn the vector from a preferred direction into a so-called difficult direction. This anisotropy energy can have various causes and hence can also appear in various forms.

It has been found experimentally that the crystal anisotropy can be described by the first two or three terms of an infinite power series in the direction cosines of the magnetization vector with respect to the crystal axes. It must have the symmetry of the crystal lattice. Thus, for cubic crystals we have, for reasons of symmetry, the following expression to a second approximation apart from a constant:

$$F_K = K_1(\alpha_1^2\alpha_2^2 + \alpha_2^2\alpha_3^2 + \alpha_3^2\alpha_1^2) + K_2\alpha_1^2\alpha_2^2\alpha_3^2 + \ldots \qquad (11.1)$$

in which the coordinate axes coincide with the crystal axes. For the three principal directions this energy is given in Table 11.I.

TABLE 11.I

Energy conditions for a preferred direction of magnetization and anisotropy field for cubic crystals

	[100]	[110]	[111]
F_K	0	$\frac{1}{4}K_1$	$\frac{1}{3}K_1 + \frac{1}{27}K_2$
Preferred direction if	$K_1 \begin{cases} >0 \\ >-\frac{1}{9}K_2 \end{cases}$	$0 > K_1 > -\frac{4}{9}K_2$	$K_1 \begin{cases} <-\frac{4}{9}K_2 \\ <-\frac{1}{9}K_2 \end{cases}$
H^A	$2K_1/M_s$	$\begin{cases} (100)\colon -2K_1/M_s \\ (110)\colon (K_1+K_2)/M_s \end{cases}$	$-(\frac{4}{3}K_1 + \frac{4}{9}K_2)/M_s$

The conditions given in this table for the appearance of a preferred direction of magnetization are represented graphically in Fig. 11.1, in which K_1 and K_2 are plotted along the axes. On the semi-axis $K_1 = 0$, $K_2 > 0$, *i.e.* on the boundary between the [100] and the [110] domains the magnetization vector is freely rotatable in the cube planes in this approximation. Such planes can be called preferred planes of magnetization.

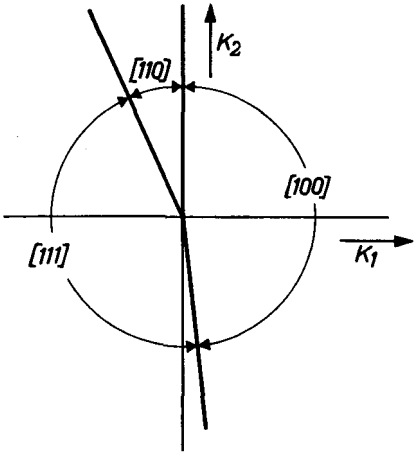

Fig. 11.1. The preferred directions of the magnetization vector in a cubic crystal for variable anisotropy contants K_1 and K_2 from (11.1).

An important factor in magnetizing processes is the stiffness with which the magnetization is bound to the preferred directions, defined as

$$c = \left(\frac{\partial^2 F_K}{\partial \theta^2}\right) \theta = 0, \qquad (11.2)$$

where θ is the angle of rotation from the position of equilibrium. For the [100] and the [111] directions this stiffness is isotropic and equal to

$$c[100] = 2K_1 \qquad c[111] = -\frac{4}{3}K_1 - \frac{4}{9}K_2. \qquad (11.3)$$

For the [110] direction the stiffness is anisotropic, and for deflections in the cube plane we find:

$$c_{(100)}\,[110] = -2K_1,$$

and in the (110) plane:

$$c_{(110)}\,[110] = K_1 + K_2. \qquad (11.4)$$

These stiffnesses may be compared with that of the magnetic moment M_s in a field H, where the energy is equal to

$$E = -HM_s \cos\theta,$$

and θ is the angle between H and M_s. In this case, $c = HM_s$, so that (11.3) and (11.4) can also be expressed as anisotropy fields H^A

$$H^A = (1/M_s)\partial^2 F_K/\partial\theta^2 \qquad (11.5)$$

which are included in table 11.I.

The anisotropy energy in hexagonal crystals must have sixfold symmetry around the c axis; with the same approximation as (11.1), we may therefore write for the energy

$$F_K = K_1 \sin^2\theta + K_2 \sin^4\theta + K_3' \sin^6\theta + K_3 \sin^6\theta \cos 6(\phi + \psi) \qquad (11.6)$$

This energy is now expressed, as is conventional, in the polar angles θ and ϕ, where the c axis coincides with the z axis, so that

$$\alpha_1 = \sin\theta \cos\phi, \quad \alpha_2 = \sin\theta \sin\phi, \quad \alpha_3 = \cos\theta.$$

The phase angle ψ can be made zero for suitably chosen axes. The constants K_1 and K_2 are not related to those in (11.1). Equation (11.6) can be understood only by starting from the direction cosines, in which it must be possible to express every analytical angular function (one might also proceed from spherical harmonics, which would give the same result). The energy can contain only even powers of α_i, so that cos θ and hence also sin θ appear in (11.6) with even powers only. The factor $\sin^6\theta$ for the cos 6ϕ term is due to the fact that cos 6ϕ is a polynomial of the 6th degree in α_1 and α_2.

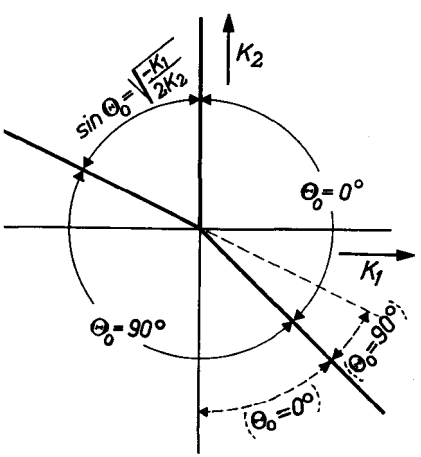

Fig. 11.2. The preferred directions of the magnetization vector in a hexagonal crystal for variable anisotropy constants K_1 and K_2 from (11.6). For $\theta_0 = 90°$ the basal plane is the preferred plane for the magnetization, while in the sector for which $\sin\theta_0 = \sqrt{\frac{-K_1}{2K_2}}$ all directions on the shell of a cone have the lowest energy (preferred cone).

If the term with K_1 is predominant, which is often the case, the preferred direction for $K_1 > 0$ is along the c axis ($\theta_0 = 0$) and for $K_1 < 0$ it is perpendicular thereto, *i.e.* in the basal plane ($\theta_0 = 90°$). If, in the latter case, $K_3 = 0$, the basal plane is a preferred plane of magnetization. Where K_1 is not predominant, stable positions in arbitrary directions are possible, as follows by minimizing (11.6). For the case where only K_1 and K_2 are taken into consideration, the stable position follows as

$\theta_0 = 0$, if $K_1 + K_2 > 0$ and $K_1 > 0$,

whereas for

$$0 < -K_1 < 2K_2$$

a stable position appears with

$$\sin^2\theta_0 = -K_1/2\,K_2,$$

having an energy $-K_1^2/4K_2$, which in the domain under consideration is lower than that for $\theta = 0$ or $\theta = 90°$. In this case each generatrix of a cone of revolution is a preferred direction for the magnetization vector. For all other ratios of K_1 and K_2 the basal plane is the preferred plane of magnetization. This is indicated in Fig. 11.2. In the region $-2K_2 > K_1 > 0$ metastable positions of M_s occur. According to measurements by Sucksmith [Su 1] the preferred cone should occur in cobalt between about 200° and 300°C.

For the anisotropy fields we find

$$\begin{aligned} \theta_0 = 0 \quad &: H^A = 2K_1/M_s \\ \theta_0 = 90° \quad &: H_\theta^A = -2(K_1 + 2K_2)/M_s \\ \sin\theta_0 = \sqrt{\frac{-K_1}{2K_2}} \quad &: H_\theta^A = 2(K_1/K_2)(K_1 + 2K_2)/M_s \end{aligned} \tag{11.7}$$

where H_θ^A represents the effective field for rotations of the magnetic vector in the direction in which only θ changes, while H_ϕ^A, given by

$$H_\phi^A = 36|K_3| \sin^4\theta_0/M_s, \tag{11.8}$$

represents that for rotations on the surface of the cone.

It appears from experiments that in most cases the crystal anisotropy is very strongly dependent upon temperature. This can also be expressed in terms of dependence upon the spontaneous magnetization. The experiments for iron, for example, then give $K_1 \propto M_s^{10}$, and for nickel even $K_1 \propto M_s^{20}$. Van Vleck's [Va 2] theory indicates a less strong dependence upon temperature. Zener [Ze 1], however, has evolved a classical theory from which this strong temperature-dependence does follow. According to this, the uniaxial anisotropy constants K_1 from (11.6) should vary more slowly proportionally to M_s^3. Zener's theory proceeds from the premise that M_s changes with temperature as a result of random variations in direction in small regions; the length of the vector remains constant, all that changes being the projection in the direction of the bulk magnetization. This will be approximately true at low temperatures, at which only slowly variable spin deviations occur (spin waves of large wavelength). Zener assumed that the macroscopic equations (11.1) or (11.6) remain valid for the direction variations due to thermal agitation. Since M_s is proportional to $\cos\theta$, fairly large variations in direction can occur, and hence large changes in energy, without the magnetization changing appreciably. The change in crystal energy with temperature will also be greater the faster this energy changes with the angle, like the K_2 terms in (11.1) and (11.6). Zener assumed a diffusion process (random walk) for the local variations of the magnetization vector in direction, and

calculated for the variation of the n^{th} power term in the crystal energy (really the n^{th} spherical harmonic)

$$K(n) \propto M_s^{n(n+1)/2},$$

i.e. with an exponent of 3, 10 and 21 for $n = 2$, 4 and 6 respectively. Keffer [Ke 1] has shown that Van Vleck's theory is better applicable at high temperatures.

11.2. INDUCED UNIAXIAL ANISOTROPY IN CUBIC CRYSTALS

In many disordered alloys, and also in various ferrites with cubic crystal structure, a uniaxial magnetic anisotropy can be brought about by subjecting the material to an annealing treatment in a magnetic field. A condition for the occurrence of the anisotopy is that the ions in the crystal should exhibit no complete ordering and that the Curie point should be sufficiently high to allow the ion diffusion below that point to take place rapidly enough. The fact that the ion diffusion takes place appears from the curve of the treatment time plotted against temperature; from this curve an activation energy can be derived of the order of 1 to 2 eV. The applied magnetic field need be no stronger than is necessary to orient the magnetization at the temperature at which the treatment is carried out; increasing the field above this value has no effect. Upon slow cooling in the field to room temperature the high temperature state is then frozen-in, which manifests itself in a preferred direction of magnetization.

The induced anisotropy energy in cubic crystals can be represented by the formula:

$$\begin{aligned} E_m = &-F(\alpha_1^2\beta_1^2 + \alpha_2^2\beta_2^2 + \alpha_3^2\beta_3^2) + \\ &-G(\alpha_1\alpha_2\beta_1\beta_2 + \alpha_1\alpha_3\beta_1\beta_3 + \alpha_2\alpha_3\beta_2\beta_3), \end{aligned} \tag{11.9}$$

where α_i are the direction cosines of the magnetization during the measurement and β_i are the direction cosines of the magnetization during the magnetic annealing at elevated temperatures. For $G = 2F$ the induced anisotropy is independent of the direction of the annealing field with respect to the crystal orientation, *i.e.* it is of the form

$$E_m = K_u \sin^2(\theta - \theta_u) \tag{11.10}$$

where $\theta - \theta_u$ is the angle which the magnetization during the measurement makes with the annealing field. This equation applies to polycrystalline specimens.

We have seen that an anisotropy of the form $\sin^2\theta$ cannot exist in a cubic crystal. The contributions of the interactions of the neighbouring atoms around a given atom cancel each other out. This condition can be eliminated by deformation of the crystal, as occurs with magnetostriction (§ 13.2). Néel [Ne 2] and Taniguchi and Yamamoto [Ta 1] have pointed out that, as regards the bonds, this cubic symmetry is also cancelled in cubic alloys if anisotropy occurs in the number of bonds between similar atoms, for example when the connecting lines between neighbouring atoms dissolved in a diluted alloy are all, or for the greater part, parallel to a particular direction. In that case a magnetic anisotropy may be expected of the form $E = \mathrm{K}\sin^2\theta$, in which the sign of K can still be arbitrary. In alloys, θ is the angle which the spin makes with the line connecting the atoms. The magnitude of K is proportional to the number of pairs of neighbours, which, for a disordered alloy, is proportional to x^2, where x is the (low) concentration of the foreign atoms. If the atoms are free to diffuse, as they are at elevated temperatures, a specific spin direction will conversely have a preference for that orientation of the pairs which reduces the energy. The probability of a pair occurring with an axis which makes an angle θ_a with the direction of the magnetization is then proportional to

$$P(\theta) \propto \exp. -\epsilon_a \sin^2\theta_a/kT \simeq 1 - \epsilon_a \sin^2\theta_a/kT \qquad (11.11)$$

where ϵ_a is the magnitude of the anisotropy energy per bond ($\ll kT$). If this configuration is frozen in, an axial magnetic anisotropy will be found at low temperatures which is proportional to $\epsilon_a\epsilon_T$, where ϵ_T is the magnitude of the anisotropy at the temperature of the measurement. In general ϵ_a and ϵ_T have the same sign, so that, irrespective of the sign of ϵ, a preferred direction is in fact always found, *i.e.* F, G in (11.9) and K_u in (11.10) are positive. Néel brought the magnitude of ϵ into relation with the magnetostriction of cubic material and showed that ϵ, converted per cm^3, is of the order of magnitude of λE (see § 13.2). This may amount to 10^8— 10^9 erg/cm^3. corresponding to several cm^{-1} per bond. It can happen, depending upon the crystal structure, that for a given orientation of the field during the heat treatment all bonds will have the same orientation with respect to the field, as for example for the bonds in a [111] direction in a simple cubic (s.c.) lattice or in the [100] direction in a b.c.c. lattice. In that case the annealing does not give rise to anisotropy. The term with F in (11.8) represents the field-cooling energy for an s.c. lattice and that with G for a b.c.c. lattice; for an f.c.c. lattice (11.8) will apply with $G = 4F$. The above applies, then, if it is assumed that the anisotropy axis of the magnetic energy coincides with the line connecting similar neighbours.

§ 12. Origin of Crystal Anisotropy

12.1. DIPOLE-DIPOLE INTERACTION

The classical interaction energy between two magnetic dipoles μ_1 and μ_2 is given by

$$E(1,2) = \frac{\mu_1\mu_2}{r^3} - \frac{3(\mu_1 r)\,(\mu_2 r)}{r^5}, \tag{12.1}$$

in which r indicates the distance apart of the dipoles. Where μ_1 and μ_2 are parallel or antiparallel, (12.1) reduces to

$$E(1,2) = \pm\frac{\mu_1\mu_2}{r^3}\,(1 - 3\cos^2\theta_{12}) \tag{12.2}$$

where θ_{12} is the angle between the direction of the dipoles and the connecting line. The + sign applies to the parallel orientation and the − sign to the antiparallel. For a crystal, (12.2) must be summated over all dipole pairs. Because of the relatively slow decrease with distance of (12.2) the interaction between all pairs must be taken into consideration. The total dipole energy is therefore dependent upon the shape of the crystal. For a uniformly magnetized sphere of a substance with a cubic crystalline structure, (12.2) is exactly zero; this can readily be seen for a dipole in the centre point. Over each shell of the sphere, $<\cos^2\theta> = {}^1/_3$. The field h_l acting on a dipole l, in the direction of the dipole l is

$$h_l = -\sum_i \frac{\mu_i}{r_{il}^3}\,(1 - 3\cos^2\theta_{il}), \tag{12.3}$$

the potential (12.2) being of the form (2.9). The field h_l of (12.3) is the sum of the Lorentz field (see § 5.2) and the demagnetizing field. In a general ellipsoid both are uniform. For the special case of a sphere these fields exactly cancel each other out.

In non-cubic crystals, (12.1) will not be isotropic, even for a sphere, *i.e.* it will depend upon the direction of magnetization. It can be said that the Lorentz field is then anisotropic. The dipoles within a sphere having a radius of a few atomic diameters now produce a resultant field at the site of the dipole in the centre point. The contributions of dipoles at large distances apart again cancel each other out, as for the sphere of a cubic substance. Consider therefore the dipoles in a spherical shell the thickness of which is at least equal to several times the lattice spacing, but still small compared with the radius. The spherical shell then contains per unit solid angle an equal number of dipoles at every part, so that irrespective of the structure

the contribution to the field in the centre point is zero. The dipole energy can be calculated by a method reported by Kornfeld (see Kittel [Ki 1]). What interests us is the dependence of this energy upon the orientation of the magnetization in a ferromagnetic material. Owing to the fact that (12.2) is a quadratic form in $\cos\theta$, the resultant energy will also be only a quadratic form of the direction cosines. The most general form of this dipole energy is thus

$$E_{\text{dipole}} = \sum_{i=1}^{3} \sum_{j=1}^{3} E_{ij}\ \alpha_i \alpha_j \tag{12.4}$$

This energy can make a contribution to the K_1 of (11.6) in hexagonal crystals, in which then only $E_{33} \neq 0$, (c axis in the z direction); *viz*: $E_{33} = -K_1$.

In the case of a cubic ferromagnetic crystal, (12.4) cannot, for reasons of symmetry, be anisotropic. It can, however, in the case of a cubic antiferromagnetic crystal. Apart from a slight deformation, which is discussed in the next section, the ion order has cubic symmetry, but not necessarily the spin order. This is the case for example in the MnO crystal (see Fig. 8.4) in which the spins in planes normal to the [111] direction are parallel, as is found by neutron diffraction. In the case of MnO the energy (12.4) for the spin configuration as drawn will have the form:

$$E_{\text{dip}} = 2\,E_{12}(\alpha_1\alpha_2 + \alpha_1\alpha_3 + \alpha_2\alpha_3), \tag{12.5}$$

which has an extreme value in the [111] direction (ellipsoid of revolution about the [111] axis). The spin order in cubic ferrites with spinel structure also has cubic symmetry, so that the dipole interaction cannot result in anisotropy in these either.

So far we have given a purely classical treatment of the dipole energy on the basis of equation (12.2). Quantum mechanically there is yet another effect to be considered, since in consequence of the general expression (12.1) for the dipole interaction some energy can be gained when the spins are not in purely parallel alignment; this can happen when mingling takes place with a state in which the component of the spin moment in the direction of the total magnetization is smaller by an amount $\hbar$. For $S = \frac{1}{2}$ this means the state with opposite spin, so that the angular deviation may be considerable. For large values of S the angular deviation is relatively small. We are concerned here then with a purely quantum mechanical effect. The intermingling will differ for different orientations of the magnetization vector with respect to the crystal axes, resulting in anisotropy of the energy. Although usually much smaller, this is of the same form as that due to spin-orbit interaction, which we shall now consider.

12.2. SPIN-ORBIT INTERACTION

As we have seen in § 12.1, the classical dipole energy can only give a term with $\sin^2\theta$ in (11.6). The occurrence of anisotropy in cubic materials and the additional terms in (11.6) must therefore be explained by spin-orbit interaction, which was discussed in § 3.3. The result of this spin-orbit interaction is [Va 2] that the total orbital angular momentum is no longer quenched and that the charge distribution will acquire an anisotropy depending upon the direction of spin. This can contribute to the magnetic anisotropy in two distinct ways.

(*a*) The indirect exchange depends upon the overlapping of the wave functions (orbits) of the electrons of the anion and the metal ion. Thus, owing to spin-orbit interaction, this overlapping can vary as it makes spherical charge clouds slightly ellipsoidal, and the extent to which it does so differs with differing spin orientations. The energy difference ΔE with a given excited state (corresponding to the jumping of an electron from the anion to the metal ion) can vary in a similar way. This mechanism is described as anisotropic exchange; for a substance with uniaxial anisotropy it is in the order of magnitude per ion of $J(\lambda/\Delta E)^2$, where J is the effective exchange energy. It will be shown in § 20 that $\lambda/\Delta E$ is approximately equal to the deviation of the g factor from 2, so that $K \cong J(g-2)^2$. Usually, $g-2 \cong 0.1$, so that for $T_c \cong 1000$ °K the constant K_1 from (11.5) should be of the order of $10^7 - 10^8$ erg/cm^3, which is rather large. Higher approximations yield the next terms in the series expansion for the energy. It appears that subsequent terms should differ by a factor $(\lambda/\Delta E)^2$, which is quite small. In practice a greater ratio is often observed. This may be due to the fact that ΔE is a fluctuating quantity in inhomogeneous media, which favours the higher terms.

(*b*) One may also consider only the interaction of the metal ion in the ground state with the crystalline field (see § 3.2), having due regard to spin-orbit interaction. In that case the exchange interaction from the surrounding ions is taken only indirectly into consideration, in order to ensure that the magnetic moment of the ion is preferentially parallel to the bulk magnetization. For the rest, the treatment is similar to that for a paramagnetic ion. The mingling of states with an orbital angular momentum will depend, like the energy, upon the orientation of the spin vector with respect to the crystal axes. For the case that the ground state is non-degenerate, the result is of the same order of magnitude as under (*a*), where J is replaced by some energy splitting due to the crystalline field. Which of the mechanisms (*a*) or (*b*) is more important, or which mode of description is the correct one, is in general difficult to say.

§ 13. Magnetostriction

13.1. VOLUME MAGNETOSTRICTION

The thermal expansion of a ferromagnetic substance shows a change in slope at the Curie point (see Fig. 13.1) and at low temperatures the dimensions of the body differ by a fraction 10^{-3} from those which it would have if it had not become ferromagnetic; this appears from extrapolation of the curve above the Curie temperature (curve (*a*) in Fig. 13.1). For a ferromagnetic material with cubic crystal structure, this strain — which we shall for the moment assume to be independent of the spin orientation — can only be isotropic, that is to say it is purely a change of volume. In the case of hexagonal ferromagnetics, for example, this need not be so, the strain then representing a change of volume plus a change of shape (*e.g.* greater strain along the *c* axis). In cubic antiferromagnetics, in which the magnetic ordering is non-cubic (*e.g.* as in MnO), a change of shape (trigonal deformation) also occurs, which is likewise of the order of magnitude of 10^{-3}.

The cause of the expansion anomaly is to be found in the dependence of the exchange energy upon interatomic spacing; this appears with metals, for example, in the so-called Slater curve (see Fig. 13.2), in which the exchange energy is plotted as a function of the ratio of inter-ionic distance to the shell diameter of the electrons responsible for ferromagnetism (the 3*d* shell for the iron group). This curve shows a maximum; for small distances the interaction is negative. In a material for which the representative point lies to the left of the maximum, additional expansion will occur below the Curie point, since in that case the exchange energy will increase (lowering of energy). Fig. 12.1, then, applies to a material with relatively large interatomic spacing. The change of exchange energy with interatomic distance $\mathrm{d}J/\mathrm{d}a$ can be found by minimizing the total energy:

$$E = N \frac{\mathrm{d}J}{\mathrm{d}a} (a - a_0) + \tfrac{1}{2}c \left(\frac{a - a_0}{a_0} \right)^2$$

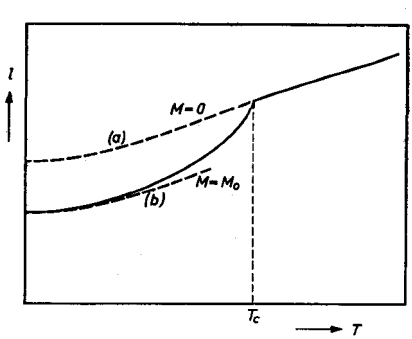

Fig. 13.1. Anomalous thermal expansion of ferromagnetics. The broken curve is for the hypothetical paramagnetic substance, while (*b*) would apply if the magnetization were to remain equal to that at $T = 0$, $(M = M_0)$.

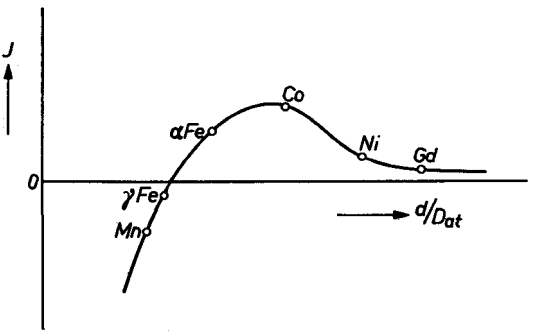

Fig. 13.2. Dependence of exchange energy upon the ratio of the inter-ionic spacing and the diameter of the shell of the magnetic electrons.

where N is the number of atoms per cm^3, a_0 the interatomic distance for $M_s = 0$ and c the elastic constant. We then find

$$\frac{a - a_0}{a_0} = -\frac{Na_0}{c}\frac{\mathrm{d}J}{\mathrm{d}a}.$$

For $\frac{a - a_0}{a_0} = 10^{-3}$, $a_0 = 3\times10^{-8}$ cm, $c = 10^{12}$ dyne/cm^2 and $J = 3\times10^{-14}$ erg, it follows that

$$\frac{\mathrm{d}J}{\mathrm{d}a} \simeq -\frac{J}{3\times10^{-8}},$$

which is of the right order of magnitude.

If a ferromagnetic substance at $T > 0$ °K is subjected to a very strong field, a small change of volume occurs, which is known as volume magnetostriction. The strong field causes a slight increase in the intrinsic magnetization (cf. (6.15)), so that in Fig. 12.1 the curve sags in the direction of curve (*b*), which would apply if the spontaneous magnetization were to remain constant as a function of temperature. However, the change of volume (and, in non-cubic ferromagnetics, also the change of shape) is relatively small, owing to $\partial M/\partial H$ being so small. There must therefore be a relation between the position on the Slater curve, the expansion anomaly and the volume magnetostriction [Sh 2]. This relation is satisfied in the case of the metals iron, cobalt and nickel. In gadolinium the magnetic $4f$ shell lies well inside the atom, and therefore the point in question should lie to the right of the maximum on the Slater curve. However, the expansion anomaly has the opposite sign, and an expansion occurs below the Curie point [Ba 4]. For alloys, too, this relation is not always satisfied. This may be due to the fact that there are several interactions, which do not always contribute in the same ratio for variations in temperature and the application of a field.

The indirect exchange energy, too, may be expected to be strongly dependent upon distance. Here too, then, volume magnetostriction and expansion anomalies may be expected.

13.2. LINEAR MAGNETOSTRICTION

Experiments have shown that the deformation discussed in 13.1 depends furthermore upon the direction of the magnetization. For a cubic crystal magnetized in the direction given by the direction cosines a_1, a_2 and a_3 (defined with respect to the cube axes) this deformation, expressed in strain components $\epsilon_{ij}(i,j = x,y,z)$ becomes in first approximation

$$\epsilon_{xx} = {}^3/_2\,\lambda_{100}(a_1{}^2 - {}^1/_3), \epsilon_{yy} = {}^3/_2\,\lambda_{100}(a_2{}^2 - {}^1/_3), \epsilon_{zz} = {}^3/_2\,\lambda_{100}(a_3{}^2 - {}^1/_3), \quad (13.1)$$

$$\epsilon_{xy} = {}^3/_2\,\lambda_{111}a_1a_2,\ \epsilon_{yz} = {}^3/_2\,\lambda_{111}a_2a_3,\ \epsilon_{zx} = {}^3/_2\,\lambda_{111}a_3a_1.$$

The extra terms $-{}^1/_3$ make the total change of volume nil (trace of the matrix is zero). The factors ${}^3/_2$ ensure that the strain in the direction of magnetization with respect to the non-magnetized state ($a_1{}^2 = a_2{}^2 = a_3{}^2 = {}^1/_3$) is λ_{100} and λ_{111} in the [100] and [111] directions respectively. The strain in a direction perpendicular thereto is then $-\frac{1}{2}\lambda_{100}$ and $-\frac{1}{2}\lambda_{111}$ respectively. In an arbitrary direction we then have parallel to the magnetization

$$\lambda(a_1,a_2,a_3) = \lambda_{100} + 3(\lambda_{111} - \lambda_{100})\,(a_1{}^2a_2{}^2 + a_2{}^2a_3{}^2 + a_3{}^2a_1{}^2). \quad (13.2)$$

For a polycrystalline substance the average λ will be:

$$\lambda_s = {}^2/_5\,\lambda_{100} + {}^3/_5\lambda_{111}. \quad (13.3)$$

For hexagonal crystals the λ values of the deformation components ϵ_{zz} and $\epsilon_{xz,yz}$ will be different from those of $\epsilon_{xx,yy}$ and ϵ_{xy} respectively. For the ferromagnetic metals the values of λ at room temperature (for Co parallel and perpendicular to the c axis) are found to be:

Fe	Ni	Co
$\lambda_{100} = +25\times10^{-6}$	$\lambda_{100} = -46\times10^{-6}$	$\lambda// = -60\times10^{-6}$
$\lambda_{111} = -19\times10^{-6}$	$\lambda_{111} = -25\times10^{-6}$	$\lambda_\perp = +16\times10^{-6}$

(13.4)

The origin of linear magnetostriction is closely related to that of crystal anisotropy. If a cubic crystal is deformed it is no longer cubic, so that there may also be present a uniaxial crystal anisotropy as in (11.6), which is proportional to the deformation. The total energy caused by the deformation consists, then, of this crystal energy and the elastic energy.

For a cubic crystal the deformation energy may, in first approximation, be written as:

$$\begin{aligned} F = {} & B_1\{\epsilon_{xx}(a_1{}^2 - \tfrac{1}{3}) + \epsilon_{yy}(a_2{}^2 - \tfrac{1}{3}) + \epsilon_{zz}(a_3{}^2 - \tfrac{1}{3})\} + \\ & + B_2(\epsilon_{xy}a_1a_2 + \epsilon_{yz}a_2a_3 + \epsilon_{zx}a_3a_1) + \tfrac{1}{2}c_{11}(\epsilon_{xx}{}^2 + \epsilon_{yy}{}^2 + \epsilon_{zz}{}^2) + \\ & + c_{12}(\epsilon_{xx}\epsilon_{yy} + \epsilon_{yy}\epsilon_{zz} + \epsilon_{zz}\epsilon_{xx}) + \tfrac{1}{2}c_{44}(\epsilon_{xy}{}^2 + \epsilon_{yz}{}^2 + \epsilon_{zx}{}^2), \end{aligned} \quad (13.5)$$

from which it follows by minimizing with respect to ϵ_{ij} and using (13.1):

$$\lambda_{100} = -\frac{2}{3}\frac{B_1}{c_{11}-c_{12}}, \quad \lambda_{111} = -\frac{2}{3}\frac{B_2}{c_{44}}. \tag{13.6}$$

The linear magnetostriction stands in the same relation to the crystal anisotropy as the volume magnetostriction (or rather the expansion anomaly) to the exchange energy. The same mechanisms that give rise to crystal energy will also be able to produce magnetostriction. The temperature dependence of λ or of B_1 and B_2 in (13.5) will thus be as of K_1 of uniaxial crystals, *i.e.* as M_s^3, according to Zener, provided the elastic constants do not change appreciably with temperature. Experimentally, $\lambda \propto M_s^2$ is found for nickel. Since the B's are of the order of magnitude of $K_1(10^7$ erg/cm$^3)$, λ should be about 10^{-5}, as is found experimentally.

Substituting the values of the ϵ's found by minimizing (13.5), the equation (13.5) gives an expression in terms of the α's which has cubic symmetry, and thus is to be regarded as a cubic crystal anisotropy like the first term in (11.1). This represents the difference in anisotropy energy between the states of constant stress and constant strain of the crystal. The order of magnitude of this contribution to K_1 is $c\lambda^2$; for $c = 10^{12}$ dyne/cm^2 and $\lambda = 10^{-5}$, this is equal to 10^2 erg/cm^2, which is usually much smaller than K_1. For cobalt ferrite, however, λ_{100} is 540×10^{-6}, so that this contribution to K_1 is of the order of 3×10^5 erg/cm^3, which is no longer negligible as against the observed K_1 of 4×10^6 erg/cm^3.

An extra deformation can be brought about by means of an external stress σ. This can be brought formally into the calculation by adding to (13.5) — analogous to the $+pV$ term in thermodynamics — a potential energy due to the stresses:

$$E_{\text{stress}} = -\sigma\epsilon = -\sigma_{xx}\epsilon_{xx} - \sigma_{yy}\epsilon_{yy} - \sigma_{zz}\epsilon_{zz} + \\ -\sigma_{xy}\epsilon_{xy} - \sigma_{yz}\epsilon_{yz} - \sigma_{zx}\epsilon_{zx}. \tag{13.7}$$

By minimizing the total energy we find the deformations, which now consist of the magnetostrictive deformation plus that due to the stress. This deformation substituted in the energy gives, in addition to the cubic term in ϵ, a non-cubic term resulting from the deformation due to stresses:

$$E_{\text{stress}} = -{}^3/_2\,\lambda_{100}\{\sigma_{xx}(\alpha_1^2 - {}^1/_3) + \sigma_{yy}(\alpha_2^2 - {}^1/_3) + \sigma_{zz}(\alpha_3^2 - {}^1/_3)\} + \\ -{}^3/_2\,\lambda_{111}\{\epsilon_{xy}\alpha_1\alpha_2 + \epsilon_{yz}\alpha_2\alpha_3 + \epsilon_{zx}\alpha_3\alpha_1\}. \tag{13.8}$$

We can interpret (13.8) by saying that the magnetostrictive deformations

must perform extra work against the applied stress. For a tensile stress $\sigma_{zz} = \sigma$ in the z axis, we may write (13.8), apart from a constant, as:

$$E_{\text{stress}} = {}^3/_2 \lambda\sigma \sin^2 \theta, \tag{13.9}$$

which is of the same form as the K_1 term in (11.6). One can think of a rod loaded in the (vertical) z direction by a weight. If we change from transversal to longitudinal magnetization, the length of the rod changes by ${}^3/_2\lambda$, so that an extra energy of ${}^3/_2\lambda\sigma$ must be supplied, in accordance with (13.9).

If we insert Young's modulus E for σ in (13.9), corresponding to a doubling of the length of the rod, we have made the material essentially non-cubic. The anisotropy energy (13.9) must then be of the same order of magnitude as the quadratic term in (11.6), *i.e.* $\lambda E \simeq K_1$, which comes down to the qualitative relation between λ and K_1 given above. The order of magnitude of (13.9) for $\sigma = 1000$ kg/cm^2 (10^9 dyne/cm^2) is approximately 10^4 to 10^5 erg/cm^3, which is in the region of the energy of cubic crystalline anisotropy.

CHAPTER V

MAGNETIZATION PROCESSES

§ 14. Weiss Domain Structure

In consequence of the demagnetizing energy it is usually more advantageous for a ferromagnetic body, rather than to be uniformly magnetized, to divide itself into a number of Weiss domains, in which the magnetization vectors are parallel to a preferred direction such that the demagnetizing fields, and hence the energy (2.8), are as small as possible. These uniformly magnetized domains are separated by a thin layer in which the direction of the magnetization gradually changes from one orientation to another. This transition boundary, known as a "Bloch wall", will be discussed in § 15. For the division into Weiss domains to be effective, no magnetic poles must form on the wall, that is to say the component of the magnetization perpendicular to the plane of the wall must, according to (1.8), be equal at both sides, *i.e.* $M_{n1} = M_{n2}$ in Fig. 14.1. The requirement is that the wall should be parallel to the difference vector $(\boldsymbol{M}_1 - \boldsymbol{M}_2)$. With two directions of magnetization, then, there are associated an infinite number of wall orientations. If the above requirement is not satisfied, demagnetizing fields will still appear and the Weiss domains will have lost, in part, their reason for existence. Fig. 14.2 gives some examples of Weiss domain structure with so-called 90° and 180° walls in which there is flux closure, that is to say no magnetic flux leaves the structure and hence there is no demagnetization. Weiss domains also occur in order to eliminate internal demagnetizing forces. This was predicted by Néel [Ne 3] and later found by experiment. In Fig 14. 3*a* the Weiss domain structure is given around a hole or non-magnetic inclusion in a cubic material. Demagnetization is not entirely absent since there is always some charge present on the walls that are not perfectly parallel. This need not be the case if there is

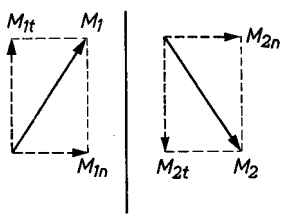

Fig. 14.1. Orientation of the magnetization vectors $\boldsymbol{M}_1$ and $\boldsymbol{M}_2$ at each side of a Bloch wall.

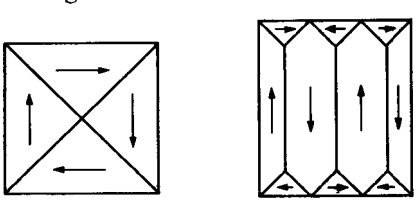

Fig. 14.2. Examples of Weiss domain configurations in which flux closure occurs.

a 180° wall near by (Fig. 14.3*b*). As was first remarked by Landau and Lifshitz [La 1], the geometry of the Weiss domain structure is determined by the requirement that the total energy must be minimum. In addition to magnetostatic energy and crystal energy or other anisotropy energy, this also includes the wall energy. Inside the wall the spins are not parallel, and, because they are not aligned in the most favour-

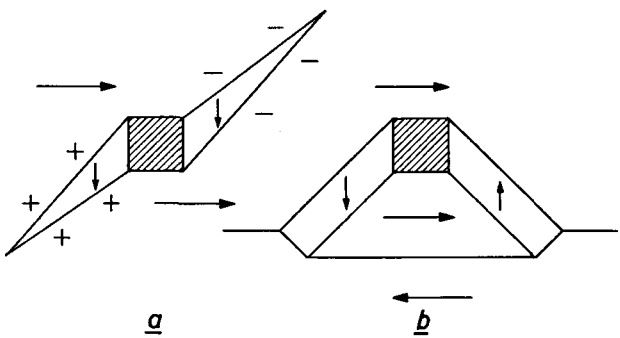

Fig. 14.3*a*) Formation of extra Weiss domains around an inclusion to avoid demagnetization energy. In *b*) there is a Bloch wall near the inclusion.

able direction, this costs exchange energy and crystal anisotropy energy. The result is that the wall has a finite energy per unit area, which we shall designate σ_w. This will be dealt with more in detail in § 15. Owing to the occurrence of these two kinds of energy, the width of the domains, *e.g.* in Fig. 14.2*b*, will have a specific value, corresponding to a minimum of the total energy, and also the configuration in Fig. 14.3*b* will change to that of Fig. 14.3*a* if the 180° wall is too far away. The wall area is reduced at the expense of some demagnetization energy. Furthermore, if the magnetostriction is finite, strain energy has to be taken into account, for, except in the case of a 180° wall, the magnetostriction differs at each side of the wall, giving rise to strains.

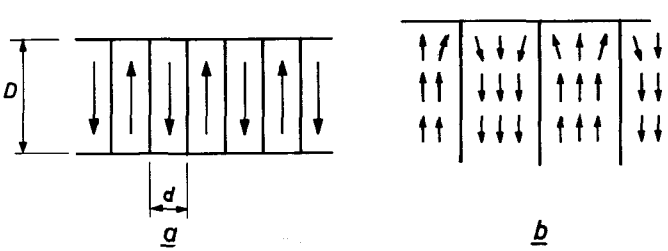

Fig. 14.4. Weiss domain formation in a thin plate.

We shall determine, by approximation, the thickness d of the Weiss domains for the configuration of Fig. 14.4*a*, *i.e.* the same as Fig. 14.1*b*, but without closure domains. The demagnetizing energy is proportional to the ratio d/D of the Weiss domains, where the values are not too large, D being the thickness of the specimen plate. Calculations show [Ki 2] that the demagnetization energy per unit volume of the plate of ferromagnetic material is $1.7\ M_s^2 d/D$. The wall energy per cm³ is σ_w/d, and hence the total energy is

$$E = 1.7\ M_s^2 \frac{d}{D} + \frac{\sigma_w}{d}\,. \tag{14.1}$$

Putting the differential of E with respect to d equal to zero gives:

$$d = \left(\frac{\sigma_w D}{1.7\ M_s^2}\right)^{\frac{1}{2}} \tag{14.2}$$

$$E = 2\left(\frac{1.7 M_s^2 \sigma_w}{D}\right)^{\frac{1}{2}}. \tag{14.3}$$

We have here assumed a uniaxial crystal anisotropy. Where $K = K_1 + K_2$ is not too large, the configuration from Fig. 14.2*b* will also be possible; there will then be some competition between the crystal energy and the wall energy. The crystal energy is $Kd/2D$ per cm³, while for $d \ll D$ the wall energy is practically unchanged; in (14.1), then, the first term on the right hand side is replaced by $Kd/2D$. If the latter is smaller, the configuration from Fig. 14.2*b* will appear, that is if $K < 3.4 M_s^2$. For cobalt at room temperature, $K \cong 5 \times 10^6$ erg/cm³, and $M_s = 1430$ gauss; hence $3.4\ M_s^2 = 7 \times 10^6$ erg/cm³. The above calculation holds good for the case where the magnetization outside the walls cannot deviate from the preferred direction. In reality this will not be the position of equilibrium, owing to the demagnetizing fields arising. Consequently, the spins will no longer be mutually parallel and will fan out slightly near the surface (Fig. 14.4*b*). If the variation in direction is slow compared with that in a domain boundary, which is the case when the Weiss domains are thicker than the walls, the change in exchange energy is negligible. If the permeability due to rotations is μ_{rot}, the demagnetization energy is reduced by a factor $(\mu_{\text{rot}} + 1)/2$. It will be seen in § 17 that μ_{rot} is equal to $1 + 2\pi M_s^2/K$, so that the demagnetization energy for cobalt is reduced to about 3.1×10^6 erg/cm³; for cobalt, therefore, the configuration in Fig. 14.4 should appear. This is in agreement with experiments by Germer [Ge 1], who, with the aid of electron bombardment (cathode rays), demonstrated fields of the order of 10^4 oersteds on a surface perpendicular to the c axis.

From (14.2) it follows that $d/D \propto D^{-\frac{1}{2}}$, so that the Weiss domains become

less slender as the thickness D diminishes. The derivation is then no longer valid. If $K < 2\pi M_s^2$, the magnetization will rotate in the plane of the plate at a thickness

$$D_{\text{rot}} < \frac{6.8\ M_s^2 \sigma_w}{K^2}, \tag{14.4}$$

as follows by putting the energy (14.3) equal to K.

For every finite body there is a critical dimension below which no Weiss domains can exist. If the dimensions of a given configuration be reduced uniformly by a factor f, the demagnetizing energy will change by a factor f^3, but the wall energy by f^2. As regards a sphere one has to compare the configurations in Fig. 14.5*a* and *b*, in order to calculate the critical diameter in a material with uniaxial anisotropy. The demagnetizing energies differ by about a factor 2. The gain, then, is about $(\pi^2/18)\ M_s^2 D^3$. The loss in wall energy is $\pi D^2 \sigma_w/4$, so that for the sphere

$$D_{\text{cr}} \cong 1.4\ \sigma_w / M_s^2. \tag{14.5}$$

In the next section we shall see that in most materials σ_w is of the order of magnitude of 1 erg/cm^2; for $M_s = 1000$ gauss, then, the critical dimension is $D_{\text{cr}} \cong 10^{-6}$ cm. This is very small, being in most cases of the same order of magnitude as the wall thickness, and the calculation is no longer valid. Where D is smaller than the wall thickness, single domain be-

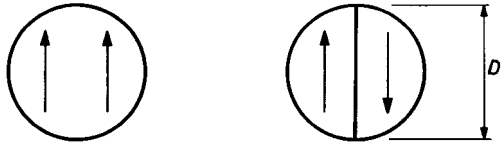

Fig. 14.5. Magnetization in a small sphere without and with Bloch wall.

haviour is the result. In some permanent magnetic oxides in which σ_w is fairly large and M_s small, D_{cr} may be of the order of 10^{-4} cm.

With the same assumptions for σ_w and M_s, we can estimate the thickness of the Weiss domains. According to (14.2) where $D = 0.1$ cm, it follows that $d = 3 \times 10^{-4}$ cm. If the size of the non-magnetic inclusion or hole in Fig. 14.3 is several times smaller than that given by (14.5), no extra Weiss domains will appear here either.

The Weiss domain structure can be made visible on a surface under the microscope with the aid of a Fe_3O_4 powder colloidally suspended in a soap solution. This powder coagulates at the position where the strongest field

prevails. Even though the magnetizations in the Weiss domains are parallel to the surface, so that no stray fields can be expected, these nevertheless appear at the position of the wall, thereby making the walls visible. An example of a powder pattern on a crystal oriented sample of $BaFe_{12}O_{19}$ is given in Fig. 14.6. In the case of metals the surface must be thoroughly destressed, for example by electrolytic polishing and annealing, otherwise the Weiss domain structure appearing on the surface will not be representative of that inside the material. Owing to the occurrence of closure domains this pattern can differ from the simpler domain structure below the surface.

Another way of making ferromagnetic domains visible is to analyse the light that has passed through a ferromagnetic body. As a result of the optical Faraday effect the plane of polarization of plane-polarized light will be rotated differently when the light passes a thin sample parallel to the magnetization of oppositely oriented Weiss domains. Fig. 14.7*a* and *b* gives pictures obtained by Kooy [Ko 1] with the help of a polarizing microscope with not completely perpendicularly oriented nicols. The sample is a single crystal disc of $BaFe_{12}O_{19}$ with a thickness of about 1 micron. The magnetization of the domains is perpendicular to the surface of the disc. The light and dark regions are domains with oppositely oriented magnetizations. Fig. 14.7*a* applies to the demagnetized state, Fig. 14.7*b* to a state after complete magnetization perpendicular to the plane and allowing the field to return to zero.

A third method is that which makes use of the magneto-optical Kerr effect. The reflection of light on the surface of a magnetic material depends on the permeability. Results for the compound MnBi have been obtained by Roberts [Ro 1].

§ 15. The Domain Boundary (Bloch wall)

The transition of the spin direction from one Weiss domain to another does not take place abruptly, since that would cost too much exchange energy. Instead, there is a gradual rotation of the spin vectors, as shown schematically in Fig. 15.1. To prevent demagnetization the normal component of the magnetization remains continuous inside the wall also. An exact calculation of a 180° wall has been given by Landau and Lifshitz [La 1]. To estimate roughly the wall energy σ_w and the effective wall thickness δ_w, we shall approximate the spin configuration inside the wall by assuming the (small) angle $\Delta\phi$ between the spins in successive atomic layers parallel to the wall to be constant. According to (5.1) (with $\cos \Delta\phi \simeq 1 - \frac{1}{2}(\Delta\phi)^2$) and (6.14), the exchange energy per cm^2 of the wall will be of the order of

$$\sigma_{ex} \simeq kT_C/a\delta_w,$$

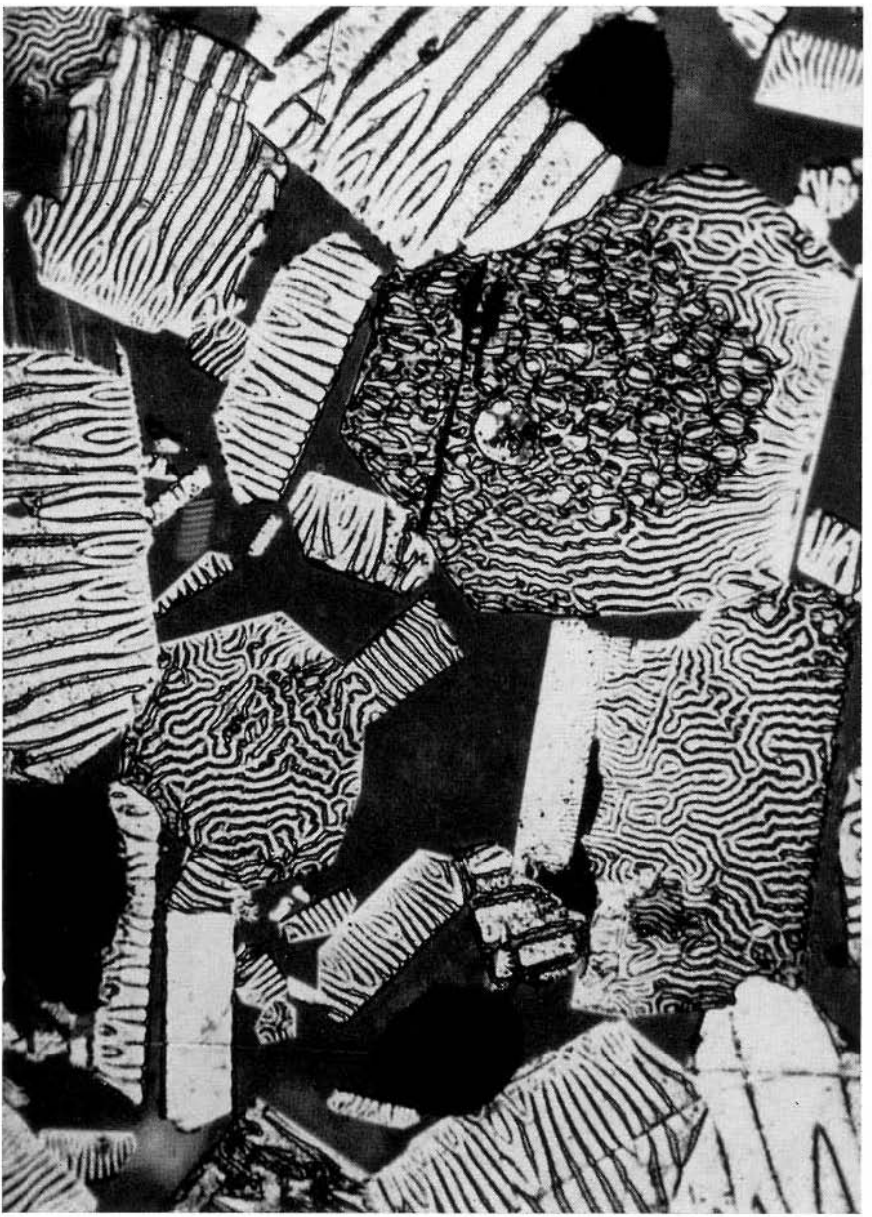

Fig. 14.6. Powder pattern of polycrystalline $BaFe_{12}O_{19}$.

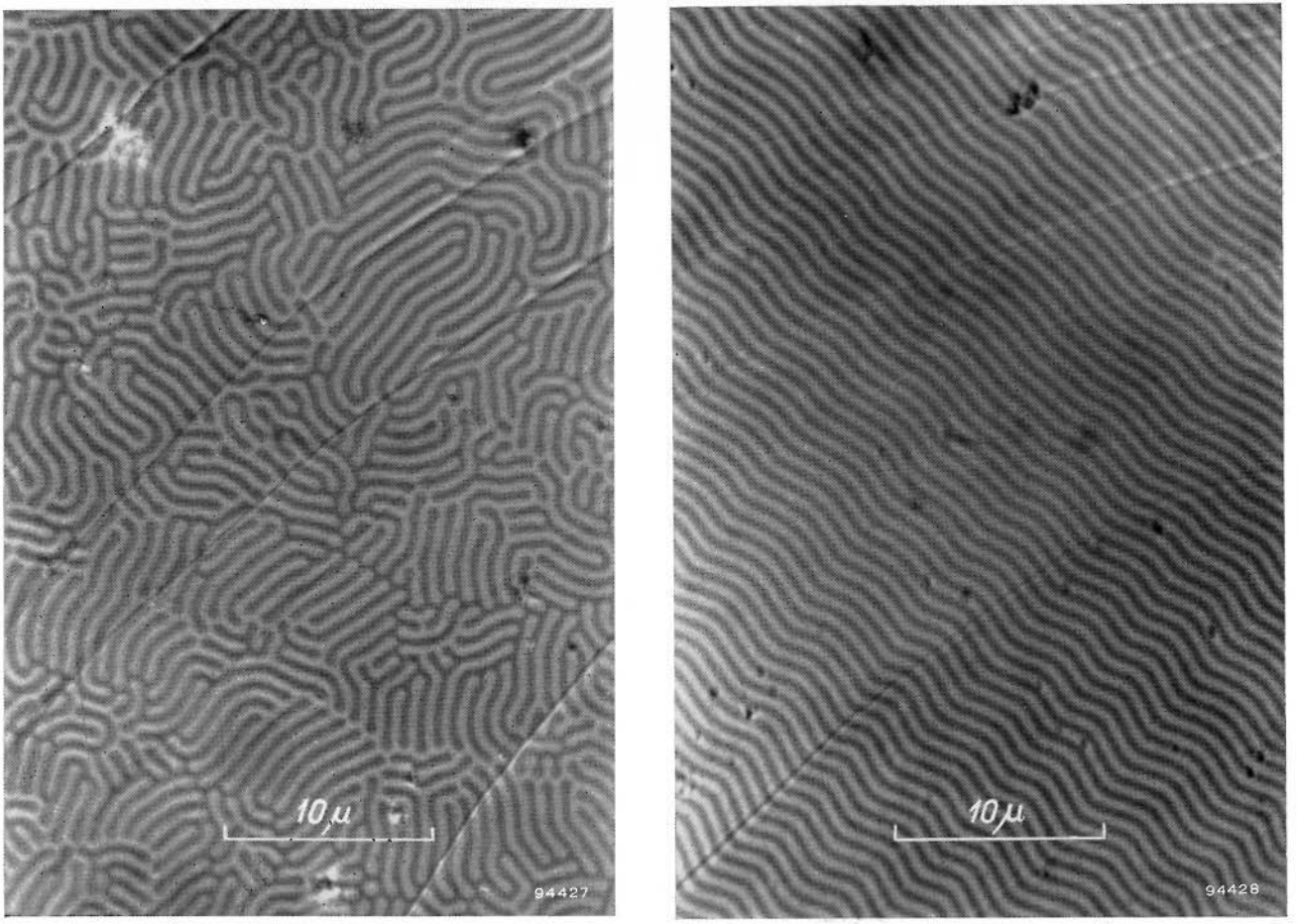

a) *b)*

Fig. 14.7. *a*. Single-crystal platelet ($<1\mu$ thick) of $BaFe_{12}O_{19}$ in the virgin state, as seen under a polarizing microscope with the nicols not quite exactly crossed. The light and dark bands are elongated Weiss domains.
b. The same platelet as in fig. *a*, after magnetizing. The domain pattern has assumed a much simpler form. (From scratches

where a is the lattice constant. The exchange interaction will thus tend to make the wall as thick as possible. This is opposed by the crystal energy, which will be of the order of magnitude of

$$\sigma_K \simeq \tfrac{1}{2} K \delta_w.$$

Hence a stable equilibrium will appear where

$$\delta_w \simeq \sqrt{\frac{2kT_C}{aK}} \tag{15.1}$$

and therefore the total wall energy per cm^2 is

$$\sigma_w \simeq \sqrt{\frac{2kT_C.K}{a}} \simeq K\delta_w. \tag{15.2}$$

This wall energy, then, consists for one half of crystal energy and for the other half of exchange energy. For $T_C \simeq 1000$ °K, $K \simeq 10^5$ erg/cm^3 and $a \simeq 2 \times 10^{-8}$ cm, σ_w is of the order of 1 erg/cm^2 and $\delta_w \simeq 10^{-5}$ cm, corresponding to several hundreds of inter-atomic spacings. We see immediately that the assumed configuration cannot be the correct one if we consider the equilibrium of one individual spin. If the angles made by this spin with

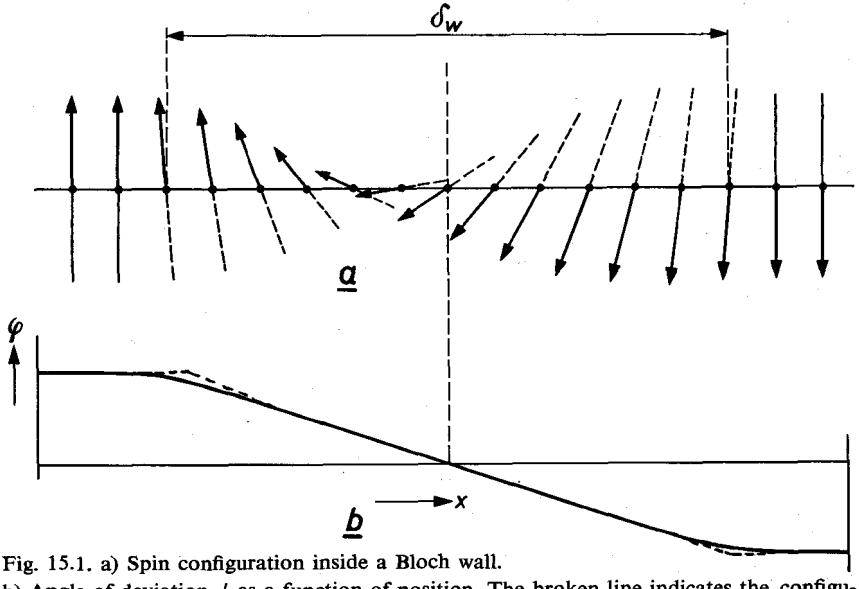

Fig. 15.1. a) Spin configuration inside a Bloch wall.
b) Angle of deviation ϕ as a function of position. The broken line indicates the configuration on which the calculation was based.

the preceding and the succeeding spin are equal and opposite, the same will hold for the torques acting on the central spin, so that owing to the exchange interaction the total torque acting on the spin is zero. This is not the case with the crystal energy, since the spin is not in the easy direction. This crystal anisotropy couple must be cancelled by a difference in exchange couples caused by the inequality of successive angles. The difference should be smaller the nearer the spin approaches the preferred position (the crystal anisotropy couple is then proportional to the angle of deviation from the preferred direction) from which it follows that $\phi \propto -\delta_w \partial\phi/\partial z$, so that for $z > \delta_w$, $\phi \propto \exp. -z/\delta_w$. Actually it is found that

$$\sin \phi = 1/\cosh (z/\delta_w). \tag{15.3}$$

The energy is not much affected by this erroneous assumption of the configuration, owing to the fact that we have minimized it. The term wall thickness, then, has a meaning similar to that of the skin depth of electromagnetic waves in conductors.

From (15.2) we see that the wall energy is proportional to $\sqrt{K}$. For two materials with approximately the same Curie temperature and lattice constant the wall energy will thus be greater for the material having the larger crystal anisotropy, whereas the thickness of the wall will be smaller. In general, a variation in K is also caused by a variation in temperature. However, it must be borne in mind in that case that the expression for the energy of exchange interaction, which we have put equal to kT_C, is no longer valid at high temperatures, where the exchange energy is smaller. According to (5.1) it seems reasonable to put the exchange interaction energy as proportional to M_s^2, so that kT_C in (15.1) and (15.2) must be multiplied by M_s^2/M_0^2, where M_0 is the saturation magnetization at the absolute zero of temperature. As a function of temperature, then, we find according to (15.2) that $\sigma_w \propto M_s\sqrt{K}$, and according to (14.5)

$$D_{cr} \propto \sqrt{K}/M_s. \tag{15.4}$$

In many cases K decreases faster with increasing temperature than M_s^2 (see § 11.1) and hence the critical diameter for wall formation, owing to the relative cheapening of the walls, will become smaller with higher temperatures. From (14.2) it follows that also the dimensions of the Weiss domains — and this will apply to most other configurations too — will change in proportion to $\sqrt{K}/M_s$, exactly like the critical diameter. Thus, in most substances the subdivision into Weiss domains will become increasingly finer with higher temperature.

§ 16. Magnetization due to Domain Boundary Movement

16.1. PERMEABILITY

An externally applied magnetic field will try to alter the Weiss domain structure and, if it is strong enough, will cause the Weiss domains to vanish. A magnetic field exerts pressure on a Bloch wall. Consider, for example, a 180° wall and a field parallel to the magnetization. If the 180° wall has moved by a slight amount Δx, then the total magnetic moment has increased by $2\,M_s\Delta x$ per cm^2 wall area. As a result, the potential energy has decreased by $-2\,HM_s\Delta x$. The same change of energy would occur if the wall were subjected to a pressure equal to

$$p = 2\,HM_s. \tag{16.1}$$

This pressure pushes the wall in such a direction that the domain with the magnetization in the same sense as H becomes larger. Here $2M_s$ is understood as the difference between the tangential components of the magnetization at either side of the wall. For other types of walls (*e.g.* 90° walls) the pressure changes accordingly. The pressure thus originates solely from the field $H = H_0 + H_D$ (see 1.7)). The internal fields $B - H$ or the Lorentz fields $4\pi M_s/3$ are parallel to the local spin vectors and change with the movement of the wall, so that there is no change of energy. These internal fields therefore have no influence on the wall movement.

As a general rule the wall will not be entirely free to move. In the foregoing sections we have seen that a particular configuration of the Weiss domain structure will establish itself in a crystal. That configuration corresponds to a minimum of free energy, consisting of demagnetizing energy, crystal energy, wall energy and possibly magnetostrictive energy. This means that the walls are bound with a certain stiffness to their positions of equilibrium. For small amplitudes of the field this gives rise to a permeability μ which is inversely proportional to that stiffness. We shall demonstrate this with a few examples. If the body is irregular in shape, for instance a grain with a constriction, then owing to the surface stress the wall will prefer to extend over the smallest cross-section, like a soap bubble, and will have a stiffness for displacement of $\sigma_w \mathrm{d}^2A/\mathrm{d}x^2$, where A is the area of the cross-section. This tendency to reduce the wall area is also of importance when non-magnetic inclusions or holes are present, as is frequently the case in technical ferromagnetic substances. Attention was first drawn to this by Kersten [Ke 1], who assumed that the walls would stretch from hole to hole (Fig. 16.1*a*), resulting in the smallest possible wall area. However, it was shown by Néel [Ne 4] that the reduction of the demagnetizing energy is much

more important than that of the wall energy. This case is comparable with that of Fig. 14.5, where the sphere is magnetized but not its environment; although the reverse is true here, there is no difference as regards energy. The reduction of demagnetizing energy, then, will be more important than the reduction of wall energy if the inclusion is larger than the critical diameter (14.5). According to Néel it is then possible to reduce the demagnetizing energy still further, or to eliminate it, by the formation of extra domains (Fig. 16.1*b*). If the wall moves, the situation arises as shown in Fig. 14.3, in which the wall area is larger, so that the wall is held firm by the inclusion.

Where the dimensions of the inclusion or the hole are smaller than the critical diameter (14.5) or the wall thickness, no extra wall formation will take place, but the wall will nevertheless prefer to contain the inclusion. The reason is that the exchange energy and the crystal energy are greater in the wall than outside it, and therefore if the inclusion is inside the wall this extra energy will not be called for. The demagnetizing fields will try to turn the magnetization, causing the pole strength to decrease. For inclusions smaller then the wall thickness this will not occur to any appreciable extent since it would cost too much exchange energy. In effect, the dimensions may be compared with a wall thickness formula in which K is substituted by a demagnetizing energy, *i.e.* with approximately $(\sqrt{K}/M_s)\delta_w$. For a change of direction on this scale the exchange energy is comparable with the demagnetizing energy. Dijkstra and Wert [Di 1] have shown that the wall-immobilizing effect is greatest for inclusions of Fe_3C in iron with dimensions equal to the wall thickness.

The wall movement is also hindered by physical imperfections in the crystal, such as dislocations. Where the atomic ordering is imperfect the exchange and crystal energy will also be smaller. Inhomogeneities on an atomic scale, such as vacancies, and deviations from periodicity as in disordered alloys, are of less importance since the concentration fluctuations over the distance of a wall thickness

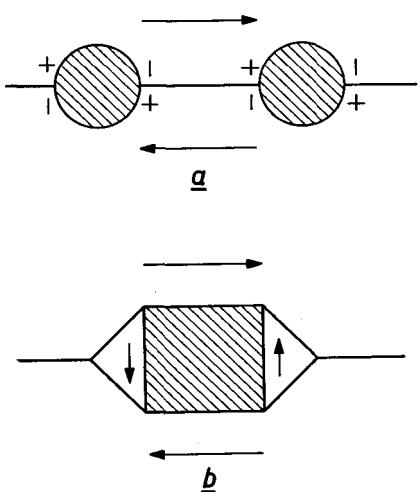

Fig. 16.1. *a*) Wall formation between inclusions, whereby free poles can appear. *b*) Extra Weiss domains are formed, so that no or only very few poles appear.

are small. The deviations from the periodic structure in a dislocation are important up to about ten lattice spacings from the centre. However, a line dislocation extends in one direction over a considerable distance, so that if a wall contains the whole line it will, according to Kersten [Ke 2], be strongly bound to that line.

Finally, the wall can also be bound by irregular internal mechanical stresses, for if the magnetostriction $\lambda \neq 0$, according to (13.8) there will be an extra uniaxial magnetic anisotropy present, which is equivalent to the crystal energy. According to Becker and Kersten the wall energy changes because K in (15.2) must be augmented by a term of the order of $K\delta = {}^3/_2\lambda\sigma$, which can thus be either positive or negative, irrespective of the sign of the stress (compressive or tensile stress). The wall will prefer to be at a position where the wall energy is lowest. Néel [Ne 4] has pointed out that these stresses cause the preferred direction of magnetization to vary from place to place. Consequently, the magnetization will not be uniform and poles and stray fields will appear. In the state so produced the total energy, consisting of crystal energy, stress energy and demagnetizing energy, will be at minimum. Due to stresses the preferred direction will make an angle of the order of $K_\sigma/K = \theta$ with the original preferred direction for $K_\sigma < K$. The angle of deviation of the magnetization will be of the order of $(K/NM_s^2)\ \theta = K_\sigma/NM_s^2$, where N is a demagnetizing factor of the order $4\pi/3$. This applies to the case where $\frac{1}{2}NM_s^2 < K$. The demagnetizing energy will then be of the order of K_σ^2/NM_s^2 per cm^3. This energy can now be reduced by a wall since a 180° wall reverses the polarity of the charge (see Fig. 16.2). In a domain having a dimension perpendicular to the wall of l, being the correlation distance or period of the internal stresses, the energy is then changed by an amount of $K_\sigma^2 l/NM_s^2$ per cm^2 of the wall. This change in energy density (K_σ^2/NM_s^2) is thus much smaller than K_σ itself, but since the former change of energy takes place over a much larger volume than the latter, which occurs only inside the wall, the effect of the magnetic poles, as suggested by Néel, can be more important than the direct change of the wall energy if

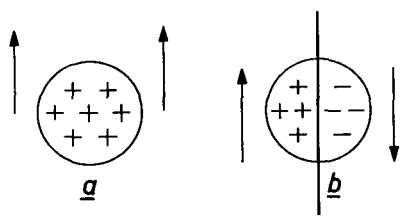

Fig. 16.2. Owing to inclusions or internal stresses, the material contains free poles (*a*). If a domain having a uniform polarity is intersected by a wall, the sign of the poles will reverse in the domain in which the magnetization has reversed, resulting in a reductjon in magnetostatic energy (*b*).

$$l > \frac{NM_s^2}{K_\sigma}\,\delta_w. \tag{16.2}$$

For example, where $NM_s^2 \cong 3\times10^5$ erg/cm^3, $K_o \cong 2\times10^4$, $\delta_w \cong 5\times10^{-6}$, then $l > 10^{-4}$ cm, as is usually the case, although this distance must be smaller than the linear dimension of a Weiss domain.

In the foregoing case, the exchange energy was disregarded even though the magnetization was not uniform. This is permissible if $l \gg \delta_w$, which was the condition for the derivations given.

So far we have discussed the factors that determine the position of a single plane wall. A Weiss domain structure, however, is stable only as a whole, that is to say the walls are strongly coupled to each other, and in general a particular wall will only be able to move provided that all the others — or at least a number of them — move too. If that were not the case, poles would appear which would give rise to large opposing fields. The magnetization process caused by wall movement should accordingly be regarded as being a cooperative phenomenon. This is of particular importance for explaining the coercive force.

If the walls are strongly coupled to each other or to imperfections in the crystal, individual wall movement is nevertheless possible though the bulging of a wall held at the edges. Kersten regards this as the most important magnetization process in small fields in many alloys. If in the bulging process the difference vector of the magnetizations at each side of the wall does not remain tangential to the surface of the wall, poles will appear on the wall which will hinder the bulging. Where the walls are held by straight lines parallel to the difference vector of the magnetizations this will not be the case, and the opposing force will then be exerted only by the surface stress of the wall, as in the example of a soap bubble. In this case it is easy to calculate the permeability resulting from a number of these walls at a distance d apart, and we find

$$\mu \cong 4\frac{M_s^2D^2}{\sigma_w d}, \tag{16.3}$$

in which D is the span of the wall. For example, where $M_s^2 = 10^5$ gauss^2, $D = d = 10^{-3}$ cm and $\sigma_w = 1$ erg/cm^2, we find $\mu \cong 400$. The temperature dependence for constant d is as $M_s/\sqrt{K}$, hence in most cases it rises sharply with temperature. If d changes as D_{cr} in (14.5), μ would change as M_s^2/K.

Where the wall is held on all sides, pole formation is unavoidable during the bulging process. Consider a ring of diameter D, in which the wall is spanned. If we approximate to the volume V through which the wall moves by an ellipsoid of revolution having major axes D and a minor axis p, the demagnetizing energy can be simply calculated (see Fig. 16.3); it is found to be about $(20\,p/D)\,M_s^2V$, where $V = (\pi/6)\,pD^2$. Here again,

the demagnetizing fields will slightly rotate the magnetization vectors, so that fewer poles will appear. It can be estimated that the pole strength will change by a factor $K/2\pi M_s^2$ (< 1) and therefore the demagnetizing energy (including crystal energy, which will be of the same order of magnitude) will now be

$$\Delta E_d \cong K^2 pV/M_s^2 D.$$

This energy is still greater than that due to the increase of the wall area

$$\Delta E_w \cong \pi p^2 \sigma_w \cong \frac{p.6V}{D^2}\,\sigma_w \cong 6K.\frac{p}{D}.\frac{\delta_w}{D}.\,V,$$

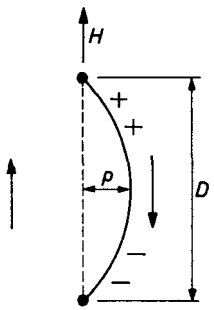

Fig. 16.3. Bulging of a wall held in position at the edges, under the influence of an external field H. The magnetic poles appearing are indicated.

since $\delta_w \ll D$. We need therefore only take into account the demagnetizing energy. The magnetostatic energy is $-2HM_s.V$, so that by minimizing we find for the permeability, at a wall spacing d,

$$\mu \cong 20\, M_s^4 D/K^2 d. \tag{16.4}$$

Where $M_s^2 = 10^5$ gauss^2, $D = d = 10^{-3}$ and $K = 10^5$ erg/cm^2, it follows that $\mu = 10$. In this case the temperature dependence is thus as M_s^4/K^2 if d remains constant, or as $M_s^5/K^{5/2}$ if d also varies.

16.2. COERCIVE FORCE

If we plot the energy of a wall, no matter how it may be caused, as a function of its coordinate of position, the result will be a fluctuating curve as shown in Fig. 16.4*a*. In the absence of an external field the wall will be in a minimum (A) and the susceptibility is then proportional to $\mathrm{d}^2E_w/\mathrm{d}x^2$ in that minimum. Upon a field being applied the wall will move until the pressure balances the opposing force:

$$2\,MH = \mathrm{d}E_w/\mathrm{d}x. \tag{16.5}$$

With increasing H the wall goes on moving until the maximum value of $\mathrm{d}E_w/\mathrm{d}x$ is reached (tangent point B of the curve in Fig. 16.4*a*). If H increases still further, a stable equilibrium is no longer possible and the wall moves irreversibly to a position where $\mathrm{d}E_w/\mathrm{d}x$ does have a large enough value (C). It may also happen that a wall has already come from the other side, so that the two walls eliminate each other, *i.e.* the Weiss domain disappears. If, the wall having arrived at C, the field is now allowed to decrease, the

wall then returns reversibly to the minimum D for $H = 0$, after which, upon the application of an opposing field, the wall goes to the tangent point E and then moves irreversibly to point F. If we now let H approach zero again, the wall returns reversibly to A. In this way a hysteresis loop is obtained as shown in Fig. 16.4*b*, in which the magnetization M of the sample is put proportional to the change of x. (The loop in this case is turned 90° with respect to the normal representation.) The area of the loop $\int HdM$ is the energy dissipated during the irreversible movements; this is absorbed as heat, caused by for example eddy currents produced by the rapidly changing magnetization. In a non-conductive medium the retarding of the wall by direct coupling of the spins with the lattice (spin-orbit interaction) is the most important mechanism.

The critical field-strength, then, is determined by the maximum value of dE_w/dx:

$$H_c = \tfrac{1}{2}M_s\,(dE_w/dx)_{\max}. \tag{16.6}$$

It can be calculated for the various mechanisms which hold the Bloch wall in position and which have been discussed in § 16.1. Statistical treatment is then necessary in order to obtain a representative maximum value from this fluctuating quantity.

In most cases the process described reverses the resultant magnetization,

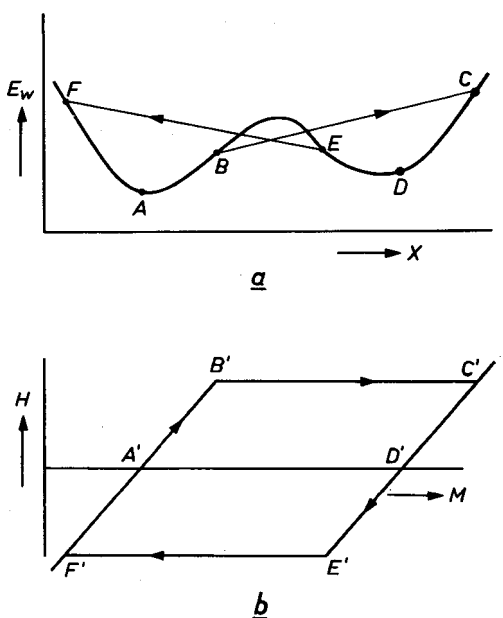

Fig. 16.4. *a*) Schematic representation of the wall energy as a function of the position x of the wall. For $H = 0$, the wall is either in A or in D.
b) The change of magnetization caused by the wall movement as a function of the field H.

and accordingly H_c is to be identified with the so-called coercive force, *i.e.* the field strength for which $M = 0$. Néel has computed the coercive force on the basis of minimum demagnetizing energy for the case where an internal stress σ prevails in a volume fraction v of the material.

$$H_c \cong (1.05\ v\lambda\sigma/M_s)\,[2.23 + \ln(M_s/\sqrt{\tfrac{3}{2}\lambda\sigma}] \text{ for } \tfrac{3}{2}\lambda\sigma \gg K$$

$$H_c \cong (0.191\ v\lambda^2\sigma^2/KM_s)\,[1.79 + \ln(M_s/\sqrt{K})] \text{ for } \tfrac{3}{2}\lambda\sigma \ll K. \qquad (16.7)$$

For the case of a volume fraction v consisting of non-magnetic material in cubic crystals with $K_1 > 0$, Néel finds:

$$H_c \cong \frac{8|K_1|v}{4\pi M_s}\left[0.39 + \tfrac{1}{2}\ln\frac{2\pi M_s^2}{|K_1|}\right]. \qquad (16.8)$$

For $K_1 < 0$, K_1 has to be replaced by $^2/_3\ K_1$ in (16.8).

§ 17. Magnetization due to Rotation of the Magnetization Vector

If there are no Bloch walls present (almost complete saturation, or small grains) or if the walls, under the influence of the fields discussed, are unable to move, magnetizing will take place as a result of the uniform rotation of all spins in the domain in question. We may represent the magnetization of this domain as a rigid vector $\boldsymbol{M}$. The torque $\boldsymbol{T}$ exerted thereon by a magnetic field $\boldsymbol{H}$ is given by

$$\boldsymbol{T} = \boldsymbol{M} \times \boldsymbol{H}, \qquad (17.1)$$

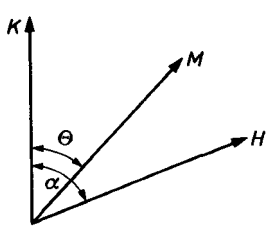

Fig. 17.1. Mutual orientations of the easy direction (K), the applied field $\boldsymbol{H}$ and the magnetization vector $\boldsymbol{M}$.

where the vector product must be taken, *i.e.* $\boldsymbol{T}$ is at right-angles to both $\boldsymbol{M}$ and $\boldsymbol{H}$ (this means the moment is in the plane of $\boldsymbol{M}$ and $\boldsymbol{H}$) and has the magnitude $HM \sin\theta$, where θ is the angle between $\boldsymbol{M}$ and $\boldsymbol{H}$. The equilibrium orientation is reached when this torque is equal and opposite to that exerted by the crystal anisotropy, *etc.* We see from (17.1) that the effective field is again H, because the internal fields $B - H$ or $4\pi M_s/3$ exert no torque on the magnetization vector. This may well be the case with an anisotropic Lorentz field, but this we include in the crystal

anisotropy. In general, then, it may be said that in ferromagnetic substances the effective field for magnetization processes is equal to H.

The position of equilibrium of the magnetization vector is found by minimizing the total energy. For the case of uniaxial crystalline anisotropy and a magnetic field H that makes an angle α with the easy direction, this energy per cm³ (see Fig. 17.1) is:

$$F = K \sin^2 \theta - HM \cos (\alpha - \theta). \tag{17.2}$$

For the position of equilibrium the condition is that $\partial F/\partial \theta = 0$, that is the resultant couple must be zero. With this relation we can calculate θ, which we shall do for two simple cases.

$\alpha = 90°$. The position of equilibrium is then given by:

$$\sin \theta_0 = HM/2K = H/H^A, \tag{17.3}$$

where H^A is the anisotropy field defined in (11.5). Equation (17.2) holds for $H < H^A$; for higher fields, M remains directed along H. The resultant susceptibility is

$$\chi = M/H^A, \tag{17.4}$$

which is constant for $H < H^A$ (Fig. 17.2*a* curve). The value (17.4) holds for all H^A fields from (11.7).

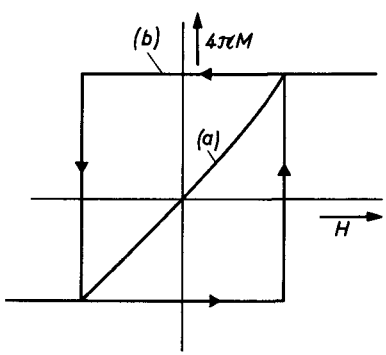

Fig. 17.2. Magnetization curves for a crystal having uniaxial anisotropy with the field perpendicular (*a*) and parallel (*b*) to the preferred direction of magnetization.

$\alpha = 180°$. In this case, a stable position can appear only when $\sin\theta_0 = 0$ ($\theta_0 = 0$ or 180°); the position with $\cos\theta = H/H^A$ is always labile. In order to see readily for what field the magnetization vector will turn over, we may write in this case for (17.2):

$$F = HM + 2 \sin^2 \frac{\theta}{2} (2K \cos^2 \frac{\theta}{2} - HM).$$

The position $\theta = 0$ will no longer be stable if, where θ is small, the factor between brackets becomes negative. This is the case if the field exceeds a critical field strength

$$H_c = H^A. \tag{17.5}$$

With this field, then, there also occurs an irreversible magnetization process and a hysteresis loop is obtained which is perfectly rectangular (Fig.

17.2, curve *b*). This is contrary to the case for $\alpha = 90°$, where there is always equilibrium for every field strength and no hysteresis loop appears.

Where $90° < \alpha < 180°$, the magnetization vector turns over for $\frac{1}{2}H^A < H_c < H^A$. The value $H_c = \frac{1}{2}H^A$ appears for $\alpha = 135°$. After turning over, and in the case of $\alpha < 90°$, the magnetization vector rotates gradually in the direction of the field; this direction can only be reached, however, in an infinitely strong field. This approach to saturation has been calculated for an isotropic distribution of the preferred directions over a sphere, and one finds for the series expansion in $1/H$:

$$\Delta M/M_s = \frac{8\ K^2}{105\ H^2 M_s^2} + \frac{192\ K^3}{5005\ H^3 M_s^3} + \qquad (17.6)$$

The fact that the term with $1/H$ does not occur is evident, since the total energy difference, consisting of $H\Delta M$ and the difference in crystal energy, must vanish with respect to the total saturated state for a very large field. Néel [Ne 5] has shown that for a polycrystalline specimen, for which (17.6) was derived, H must be substituted by

$$H_i = H + \frac{4\pi M_s}{3}. \qquad (17.7)$$

This is, as it were, a macroscopic Lorentz field. The grain concerned is assumed to be spherical, with a preferred direction not parallel to H. The surrounding material then induces in the direction of H a field $4\pi M/3$, in which M is practically equal to the saturation magnetization. This field can, therefore, exert a torque on the magnetization in the sphere, whereas its own demagnetizing field, which commonly compensates the induced field, can not.

CHAPTER VI

DYNAMICS OF MAGNETIZATION PROCESSES

§ 18. Ferromagnetic Resonance Conditions

18.1. RESONANCE IN UNIFORMLY MAGNETIZED FERROMAGNETICS

In the last chapter we dealt with the statics of magnetization processes and calculated the energetically most favourable configuration after the application of the field. We shall now consider how the transition takes place from the one state to the other. First of all we shall deal with the rotation processes and inquire into the resonance phenomena that can occur during these processes.

Consider a static field $\boldsymbol{H}$ in the z direction and a magnetic moment $\boldsymbol{M}$ making an angle θ with it (Fig. 18.1). Owing to the field a torque (17.1) is exerted on $\boldsymbol{M}$, which does not, however, rotate $\boldsymbol{M}$ towards $\boldsymbol{H}$. This is because of the gyroscopic properties of the magnetic moment. In § 3.1 it was shown that the magnetic moment is associated with an angular momentum $\boldsymbol{J}$ according to

$$M = g(e/2mc)J = \gamma J. \tag{18.1}$$

The equation of motion is

$$\dot{\boldsymbol{J}} = \boldsymbol{T} = \boldsymbol{M} \times \boldsymbol{H}. \tag{18.2}$$

In very good approximation we can take for the J in (18.2) only the spin angular momentum in (18.1), so that

$$\dot{\boldsymbol{M}} = \gamma \boldsymbol{M} \times \boldsymbol{H}. \tag{18.3}$$

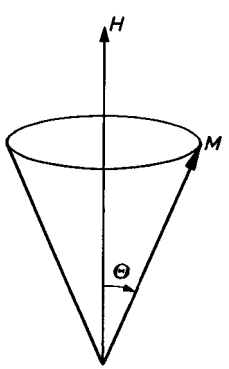

Fig. 18.1. Schematic representation of the precession of a magnetization vector $\boldsymbol{M}$ in a magnetic field $\boldsymbol{H}$.

from which it follows that the change of the magnetization vector is always at right-angles to both $\boldsymbol{M}$ itself and to $\boldsymbol{H}$. The $\boldsymbol{M}$ vector precesses over the surface of a circular cone with an angular frequency

$$\omega = \gamma H, \tag{18.4}$$

irrespective of the magnitude of the precession angle θ. For the spin of a free electron the resonance frequency f in Mc/s is according to this equation

$$f = 2.80\, H \quad \text{Mc/s} \tag{18.5}$$

if the applied field H is expressed in oersteds. As a rough estimate, $H\lambda \cong 10^4$ oersteds cm, where λ is the wavelength in free space.

By substituting (18.1) into (18.2) we neglect the change with time of the angular momentum of the electron in the directions at right-angles to the spin axis. The contribution of this change of angular momentum during the precession, which classically should give rise to nutation, is a fraction which at the most is of the order of the precession frequency divided by the spin frequency of the angular momentum due to the precession. Now the frequency (18.5) is usually not greater than 10^{11} c/s, while the spin frequency according to (3.1) is of the order of 2×10^{20} c/s, and so nutation can be neglected. If the angular momentum were due only to orbital motion, the associated frequency would be of the order of 10^{14} c/s.

So far we have been discussing the free vibration of the magnetization vector. In reality the oscillation will be damped, so that the magnetization vector will move in a spiral towards the equilibrium position in the z direction, in which process the magnetic energy (here only the potential energy $-\boldsymbol{HM}$) will be lost to the lattice.

For every free vibration there must be at least two degrees of freedom. In the mechanical case these are the kinetic and the potential energy, described respectively by a coordinate of momentum and a coordinate of position which, during the vibration, alternately merge one into the other. The natural frequency is then the geometric mean of the two stiffnesses

$$\omega_r = \sqrt{c/m}, \tag{18.6}$$

where c is the normal stiffness $(\partial^2 E/\partial x^2)$ and $1/m$ can be regarded as the kinetic stiffness $(\partial^2 E/\partial p^2)$. For ferromagnetic resonance there is only one form of energy (magnetostatic $-\boldsymbol{HM}$) in the case discussed, but because the movement is in more than one dimension there are nevertheless two degrees of freedom: the deflection in the x direction, defined by the (small) angle ϕ_x, and that in the y direction, ϕ_y.

We shall show that an expression similar to (18.6) exists for ferromagnetic resonance. To do so we shall start from the most general form of the equation of motion (18.2):

$$\dot{J}_x = \partial E/\partial \phi_y \ , \ \dot{J}_y = -\partial E/\partial \phi_x. \tag{18.7}$$

The minus sign is important and is connected with the fact that the second equation in (18.7) follows from the first owing to a rotation of the z axis by 90°, hence $x \rightarrow y$ but $y \rightarrow -x$. In the equilibrium position the energy is at minimum and so the first derivatives are zero. Thus, according to Taylor,

one finds for small angles:

$$E = E_0 + \tfrac{1}{2}E_{xx}\phi_x^2 + E_{xy}\phi_x\phi_y + \tfrac{1}{2}E_{yy}\phi_y^2 + \ldots, \tag{18.8}$$

where the second derivatives $E_{ij} = \partial^2 E/\partial\phi_i\partial\phi_j$ relate to the equilibrium position. For a harmonic oscillation of the magnetization vector with angular frequency ω one then finds for (18.8), using the complex notation and omitting the factor $e^{i\omega t}$:

$$\begin{aligned} -i(\omega M/\gamma)\phi_y &= E_{xx}\phi_x + E_{xy}\phi_y \\ i(\omega M/\gamma)\phi_x &= E_{xy}\phi_x + E_{yy}\phi_y. \end{aligned} \tag{18.9}$$

These equations can be solved for finite $\phi_{x,y}$ if ω is equal to the resonance frequency

$$\omega_r = (\gamma/M)\,(E_{xx}E_{yy} - E_{xy}^2)^{\frac{1}{2}}. \tag{18.10}$$

If the energy is on the principal axes ($E_{xy} = 0$) then (18.10) is analogous to (18.6), where E_{xx} and E_{yy} are now the stiffnesses. The energy is found alternately in the deflections in the x and y directions. This expression holds even if the energy is formed by the crystal energy or the demagnetizing energy. For the general case of the equilibrium position not coinciding with the z axis, we may write (18.10) in spherical coordinates (θ, ϕ), hence

$$\omega_r = (\gamma/M\sin\theta)\,(E_{\theta\theta}\,E_{\phi\phi} - E_{\phi\theta}^2)^{\frac{1}{2}}, \tag{18.11}$$

where the second derivatives again relate to the equilibrium position, found by putting the first derivatives equal to zero ($\partial E/\partial\theta = \partial E/\partial\phi = 0$). The expression (18.11) is singular for $\sin\theta = 0$, which points must therefore be avoided as equilibrium positions in (18.11).

As an example we shall take an ellipsoid in a uniform magnetic field H_x which is strong enough to orient the magnetization in the field direction. The coordinate system coincides with the axes of the ellipsoid, which has demagnetizing factors N_x, N_y and N_z, so that $H_x > (N_x - N_{y,z})M_s$. The energy is then, according to (2.7):
$E = -HM_s\sin\theta\cos\phi + \tfrac{1}{2}M_s^2\{N_x\sin^2\theta\cos^2\phi + N_y\sin^2\theta\sin^2\phi + N_z\cos^2\theta\}$
and the equilibrium position is given by $\theta = \pi/2$, $\phi = 0$. We then find for the resonance frequency the formula first given by Kittel [Ki 3]

$$\omega_r = \gamma\sqrt{\{H_x + (N_y - N_x)M_s\}\{H_x + (N_z - N_x)M_s\}} \tag{18.12}$$

which, for a sphere, reduces to (18.4). The first ferromagnetic resonance experiments were carried out by Griffith [Gr 1] on a thin plate of nickel, for which $N_x = N_z = 0$, $N_y = 4\pi$, and hence for the flat plate

$$\omega_r = \gamma\sqrt{BH}. \tag{18.13}$$

In (18.12) $N_x M_s$ represents the static demagnetizing field to be subtracted from H_x, while the terms $N_y M_s$ and $N_z M_s$ are caused by the alternating magnetization in the y and z directions respectively, which raise the resonance frequency.

Where only crystal anisotropy is present, with a preferred direction along the x axis such that $F_k \cong K\theta^2$ holds for small a deflection angle θ, it follows that

$$\omega_r = \gamma H_\theta^A, \tag{18.14}$$

where the anisotropy field H_θ^A is given by (11.5). For cubic crystal anisotropy (18.14) again holds with the relevant anisotropy fields from Table 11.I. In some cases the application of a magnetic field can give rise to a lowering of the resonance frequency, as in the case where the field coincides with the difficult direction for the crystal energy. For uniaxial crystal anisotropy, with the preferred direction along the z axis and the field in the x direction, the energy is

$$E = K \sin^2 \theta - HM \sin \theta \cos \phi.$$

The field turns the magnetization vector out of the preferred direction, and the equilibrium position is reached when

$$\sin \theta = H/H^A, \qquad (H < H^A),$$

as follows if the differential from E with respect to θ (or to $\sin \theta$) is equated to zero. When $H > H_A$ the magnetization vector is parallel to H. For the resonance frequency we find

$$\begin{aligned} (\omega_r/\gamma)^2 &= (H^A)^2 - H^2 \qquad (H < H^A) \\ (\omega_r/\gamma)^2 &= H(H - H^A) \qquad (H > H^A), \end{aligned} \tag{18.15}$$

(see Fig. 18.2). When $H = H^A$ the resonance frequency is zero. This obvious, because with the application of the field in the x direction the symmetry for the energy with respect to this axis remains unchanged. For small fields it is a direction of maximum energy, for large fields one of minimum energy. In between, and precisely when the magnetization arrives in the x direction, the equilibrium position is neutral, so that one of the stiffnesses is zero, and hence ω_r is also zero. This method can be used to generate ferromagnetic resonance in strongly anisotropic crystals at relatively low frequencies [Su 2, Sm 2]. Resonance can then be found at more than one field strength.

In general, eq. (18.11) enables one to calculate the resonance conditions for all cases in which combinations of field energy, crystal or stress anisotropy and shape anisotropy occur. The equilibrium position is found first by equating to zero the first derivatives of the energy with respect to the

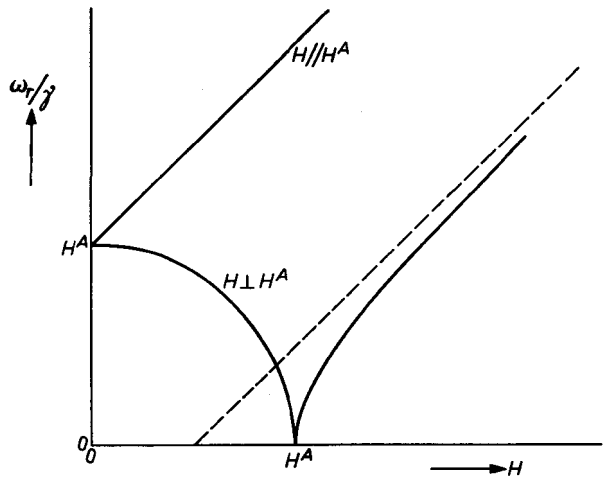

Fig. 18.2. Resonance frequency as a function of the applied field H both parallel and perpendicular to the preferred axis in a material having uniaxial anisotropy

angles, and the second derivatives are then calculated at that point. As a general rule the stiffnesses in directions at right-angles to each other will not in that case be equal, and as a result the precession will no longer be over the surface of a circular cone but over that of an elliptical cone, having an axial ratio $\sqrt{E_{yy}} : \sqrt{E_{xx}}$, as follows from the constancy of the energy (18.8) during the precession ($E_{xy} = 0$).

18.2. INFLUENCE OF THE WEISS DOMAIN STRUCTURE ON THE RESONANCE CONDITIONS

In § 18.1 we have seen that a free oscillation of the magnetization vector (resonance) can also occur in the absence of an externally applied magnetic field. The fictitious anisotropy field H^A then takes the place of the external field. Resonance is therefore also possible in a non-saturated specimen, *i.e.* in a specimen still divided into Weiss domains, as was first recognized by Snoek [Sn 1]. We shall now show that the Weiss domain structure can very strongly influence the resonance conditions. Let us consider the simplest case of an ellipsoid which is divided up into Weiss domains in the form of thin slabs each oppositely magnetized to the next. The magnetization vectors of the two kinds of domains can now be regarded as two systems coupled to each other by demagnetizing fields. The two vectors will precess in opposite sense, and consequently they cannot be in phase in two mutually perpendicular directions. For the two modes of oscillation (natural reso-

nance) of the system the alternating magnetization vectors are in phase either in a direction at right-angles to the domain boundaries or parallel thereto (cases (*a*) and (*b*) of Fig. 18.3 respectively). We shall now calculate the associated (natural) resonant frequencies. In case (*a*) the alternating

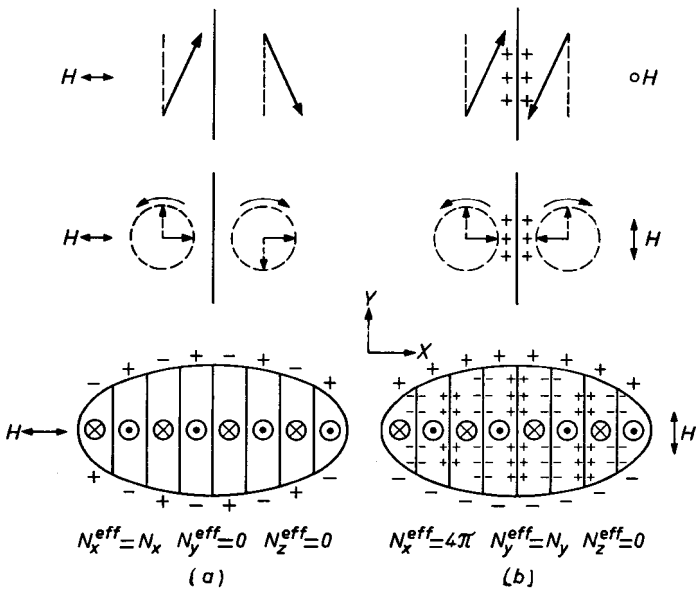

Fig. 18.3. Resonance modes in unsaturated ellipsoids; (*a*) with the a.c. field perpendicular to the walls; (*b*) with the a.c. field parallel to the walls.

magnetization in a direction at right-angles to the domain boundaries is continuous (x direction), and so for this case the boundaries have no particular consequence: $N_x^{\text{eff}} = N_x$, in which N_x is the demagnetizing coefficient of the ellipsoid along the x axis. In the y direction, however, the alternating poles at the edge of the ellipsoid are oppositely oriented in adjacent domains. At spacings greater than the thickness of the domains they will therefore cancel out each other's effect. For thin Weiss domains we can accordingly put $N_y^{\text{eff}} = 0$. For the same reason, but then for static fields, $N_z^{\text{eff}} = 0$, so that, summarizing, for case (*a*)

$$N_x^{\text{eff}} = N_x, \quad N_y^{\text{eff}} = 0, \quad N_z^{\text{eff}} = 0. \tag{18.16}$$

These effective demagnetizing factors must be inserted in (18.12) in order to find ω_r. However, x and z in that formula must be interchanged, and H_x now becomes an anisotropy field H^A.

In case (*b*) the alternating magnetizations in the x direction are in anti-phase. On the boundaries there are then alternating poles which, if the thickness of the Weiss domains is small compared with the other dimensions, will give rise to demagnetizing alternating fields at right-angles to the boundaries of the order of $4\pi m$, where m is the alternating component of the magnetization. Hence $N_x^{\text{eff}} = 4\pi$. In the y direction the alternating magnetizations are in phase, so that the domain structure has no special consequence and $N_y^{\text{eff}} = N_y$. Again, $N_z^{\text{eff}} = 0$, so that for case (*b*)

$$N_x^{\text{eff}} = 4\pi, \quad N_y^{\text{eff}} = N_y, \quad N_z^{\text{eff}} = 0. \tag{18.17}$$

Evidently, (1.12) no longer holds for the effective demagnetizing factors; what now holds is the inequality

$$0 \leqslant N_x^{\text{eff}} + N_y^{\text{eff}} + N_z^{\text{eff}} \leqslant 8\pi.$$

The extreme limits are reached for an ellipsoid in the form of a flat plate ($N_x = N_y = 0$, $N_z = 4\pi$), and therefore in case (*a*), according to (18.16), the sum is zero, and in case (*b*), according to (18.17), the sum is equal to 8π. The corresponding extreme resonance frequencies are, according to (18.12),

$$(a): \quad \omega_r = \gamma H^A \qquad (b): \quad \omega_r = \gamma(H^A + 4\pi M_s) \tag{18.18}$$

18.3. MAGNETOSTATIC MODES

It has been shown theoretically by Walker [Wa 1] and experimentally by Solt *et al* [Sol] that there also exist resonance modes of a uniformly magnetized ellipsoid, whereby the alternating component of the magnetization is not uniform. For example, it can happen that the crystal is divided into parts in which the precession movements of the magnetization vectors are 180° out of phase. This gives rise to additional demagnetizing fields, while in other directions the dynamic demagnetizing fields are reduced. As a result the resonance frequency will change and will lie in general between $\gamma(H - 4\pi M)$ and $\gamma(H + 2\pi M)$, as for the uniform precession. The resultant alternating magnetization vector will, as a general rule, be zero, and therefore these modes can only be excited with a non-uniform alternating field.

§ 19. Ferrimagnetic Resonance

In ferrimagnetic substances the magnetization vector is the sum of the various magnetization vectors of the sublattices. Generally speaking, these sublattices differ crystallographically and are also occupied by different

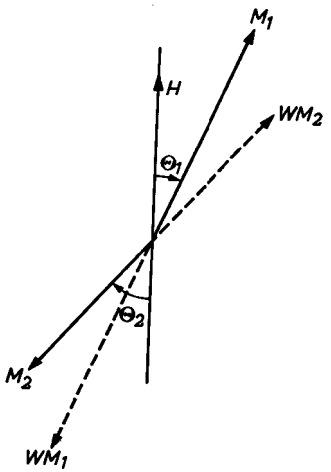

Fig. 19.1. Orientation of the sublattice magnetization vectors $\boldsymbol{M}_1$ and $\boldsymbol{M}_2$ at ferromagnetic resonance, for the case where $\boldsymbol{M}_1 > \boldsymbol{M}_2$ and $\gamma_1 < \gamma_2$. The torques caused by the Weiss fields $W\boldsymbol{M}_1$ and $W\boldsymbol{M}_2$ are then opposed to the torques exerted by the field $\boldsymbol{H}$ on the magnetization vectors.

ions. The intrinsic properties of these ions, as manifested by the individual g factor of the ions in the crystalline field, will therefore vary accordingly. In the foregoing we have seen that the magnetic properties of ionic crystals can be described in terms of the properties of individual ions. The latter are only modified with respect to the properties of the free ion by the crystalline fields. Each sublattice magnetization $\boldsymbol{M}_i$ is given its own factor γ_i. According to (18.4), then, the resonance frequency differs for each of the sublattices. Owing to their strong mutual coupling, however, the sublattices do not resonate individually but altogether at the same frequency and in the same sense.

Let us confine ourselves, for the convenience of the argument, to two sublattice magnetizations $\boldsymbol{M}_1$ and $\boldsymbol{M}_2$, which we assume to be opposite to each other. The difference in resonance conditions is eliminated by the fact that $\boldsymbol{M}_1$ and $\boldsymbol{M}_2$ do not remain strictly antiparallel during precession (Fig. 19.1) and that $\boldsymbol{M}_1$ is subjected to the torque not only of the field $\boldsymbol{H}$ but also of the Weiss field $\boldsymbol{H}_{21} = W\boldsymbol{M}_2$. For example, if $\gamma_1 < \gamma_2$, the torque on $\boldsymbol{M}_1$ would have to be increased and on $\boldsymbol{M}_2$ decreased. This is, however, not possible. From Fig. 19.1 it can be seen that both torques are increased or decreased simultaneously. However, since the Weiss field torques are equal whereas the field torques differ (because $M_1 \neq M_2$) the relative changes of the torques are unequal, and hence the resonance conditions can still be equal. It follows from this that $\Delta\theta/\theta$ will be of the order of magnitude of $(\Delta\gamma/\gamma)$ (H/WM), where $\Delta\gamma = \gamma_1 - \gamma_2$, $\Delta\theta = \theta_1 - \theta_2$, and $M = M_1 - M_2$. For a relatively small resultant magnetization there can be relatively considerable differences

between θ_1 and θ_2. In the situation as drawn, for $M_1 > M_2$ and $\gamma_1 < \gamma_2$, the torque acting on M_1 is reduced relatively less than that on M_2. The effective γ, then, will in this case be smaller than γ_1 or γ_2. The resonance conditions for each sublattice are (for small angles θ) given by

$$\begin{aligned} \omega_r M_1\theta_1 &= \gamma_1[HM_1\theta_1 + WM_1M_2(\theta_1 - \theta_2)] \\ \omega_r M_2\theta_2 &= \gamma_2[HM_2\theta_2 + WM_1M_2(\theta_1 - \theta_2)] \end{aligned} \tag{19.1}$$

The vector equation reduces in this case to a scalar, since all vectors are at right-angles to the plane through $\boldsymbol{M}$ and $\boldsymbol{H}$. These are homogeneous equations in θ_1 and θ_2, which have a solution only if

$$\left(\frac{\omega_r}{\gamma_1} - H - WM_2\right)\left(\frac{\omega_r}{\gamma_2} - H + WM_1\right) + W^2M_1M_2 = 0. \tag{19.2}$$

As we have assumed two sublattices we find here a quadratic equation with two roots for ω_r. By approximation the lower one can easily be found directly from (19.1). If we divide the first equation by γ_1 and the second by γ_2, and then subtract one from the other, the Weiss field torques drop out and we find

$$\omega_r = \frac{M_1\theta_1 - M_2\theta_2}{(M_1/\gamma_1)\theta_1 - (M_2/\gamma_2)\theta_2} H. \tag{19.3}$$

Where $H \ll W(M_1 - M_2)$, as is normally the case ($WM \cong 10^6$ oersteds) then θ_1 and θ_2 will be practically equal and cancel each other out in (19.3), and we then find for the corresponding g value:

$$g^{\text{eff}} = \frac{M_1 - M_2}{(M_1/g_1) - (M_2/g_2)} = \frac{g_1 + g_2}{2} + \frac{g_1 - g_2}{2} \cdot \frac{(M_1/g_1) + (M_2/g_2)}{(M_1/g_1) - (M_2/g_2)} \tag{19.4}$$

Since the absolute value of the factor after $\frac{1}{2}(g_1 - g_2)$ is greater than unity the value of g_{eff} never lies between g_1 and g_2, as has already been argued in the foregoing.

The other root for ω_r is very high, and in this case the Weiss field torques predominate since the small angles θ_1 and θ_2 are quite different. In first instance, then, we may neglect the torque due to the external field, *i.e.* we may put $H = 0$ in (19.2). We then find

$$\omega_r \cong W(\gamma_1 M_2 - \gamma_2 M_1), \tag{19.5}$$

which thus normally corresponds to a wavelength of about 0.1 mm, in the infra-red region. Now the form between brackets in (19.5) is equal, except for a factor $\gamma_1\gamma_2$, to the denominator of (19.4); the minus sign indicates that the precession of (19.3) is in the opposite sense to that of (19.5).

If this denominator becomes small, ω_1 increases and ω_2 decreases, so that the resonance frequencies approach one another, as also appears from a more exact analysis [Wa 2].

From (19.4) it follows that $g^{\text{eff}} = 0$ or ∞, according to whether the numerator ($M = 0$) or the denominator ($J = 0$) is zero. These phenomena occur at different temperatures in the Li-Cr ferrites, discussed in § 9.1, resulting in hyperbolic g *versus* T curves (Fig. 19.2). A similar effect also

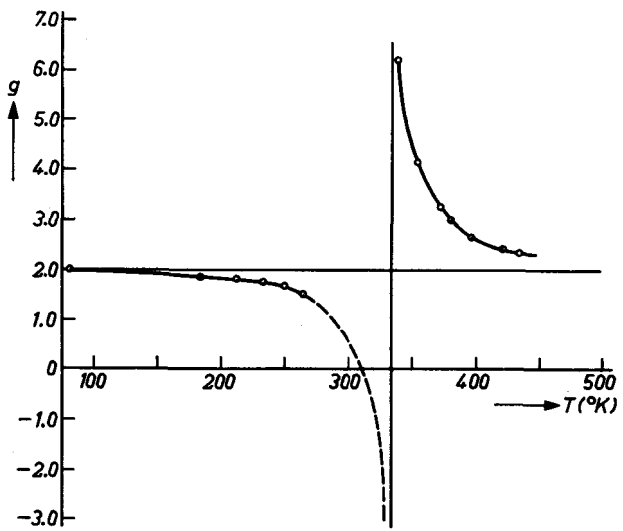

Fig. 19.2. Change of the g factor as a function of temperature for LiCr ferrite (after van Wieringen [Wi 1]).

occurs in Ni-Al ferrites as a function of the composition [Gu 1], while in the vicinity of the compensation point even the second resonance (19.5) has been observed.

The form of (19.5) might lead one to suppose that this second resonance would also occur if $g_1 = g_2$. This is not so because, as appears from (19.1), the dynamic components of $\boldsymbol{M}_1$ and $\boldsymbol{M}_2$ then compensate each other exactly, so that the resonance becomes unobservable and therefore physically meaningless. It also follows from the generally applicable equation (19.3) that there is only one resonance frequency for $g_1 = g_2$.

Just as with ferromagnetic resonance, the influence of anisotropies can also be taken into account in ferrimagnetics. As regards demagnetization there is no difference from the ferromagnetic case: the dynamic demagnetizing fields, caused by the total precessing magnetization vector, produce a torque that depends solely upon the orientation of the resultant magnetization

vector. In other words, we have the ferromagnetic case with $g = g_{\text{eff}}$. The uniaxial crystalline anisotropy energies for each sublattice are given by the constants K_1 and K_2 respectively, which are equivalent to the fields $H_1^A = 2K_1/M_1$ and $H_2^A = 2K_2/M_2$, analogous to (11.7). These fields, then, are in opposite alignment (always in the same direction as the magnetizations) hence if H is along the easy direction the effective fields are $H + H_1^A$ and $H - H_2^A$. Apart from a difference in g factor, the resonance conditions now differ once again for the two sublattices. The relative difference between the precession angles for the low-frequency mode of resonance will now be of the order of H^A/WM, which again, generally speaking, is small. If, as before, we neglect this difference, we can again speak of the precession of one rigid magnetization vector in a crystal having an anisotropy of $K = \mathrm{K}_1 + K_2$ or $H^A = (H_1^A M_1 + H_2^A M_2)/(M_1 - M_2)$. Once more we have $g = g_{\text{eff}}$ from (19.4). The second resonance frequency is again approximately given by (19.5) for small H^A.

All this follows again from equations analogous to (19.1) with the H's changed in the manner described above. To conclude we can say that the resonance conditions for the low frequency mode of normal ferrimagnetic substances may be calculated just as for ferromagnetic substances.

§ 20. Spectroscopic Splitting Factor g

For pure spin magnetism, the gyromagnetic ratio γ governing ferromagnetic resonance is equal to the γ of (3.4), but where orbital magnetism is also present, it will differ, as we already assumed in § 19. It cannot be said *a priori* that the corresponding g factors are equal to the Landé factors introduced in (6.6). Kittel [Ki 4] has shown, however, that this is in fact the case as regards the g factor in ferromagnetic resonance (called the spectroscopic splitting factor), but not as regards that g factor which governs the Barnett experiment or the Einstein-de Haas effect.

We must calculate the frequency ω of the precession. According to quantum mechanics, $\hbar\omega$ is equal to the difference in energy of the two states between which the transition takes place. In the present case this is the reversal of one spin. In a ferromagnetic material, in which the spins are very strongly coupled, there is no complete reversal of one specific spin but rather a slight tilting of all spins together, such that they remain in mutually parallel alignment and the exchange energy is unchanged. For a ferromagnetic substance in a field H we thus have the equation

$$\hbar\omega = H(\Delta M_{\text{spin}} + \Delta M_{\text{orbit}}). \tag{20.1}$$

We shall again, as in § 3.3, consider the case in which, in first approximation, the orbital angular momentum is quenched, this state being only slightly perturbed by the spin-orbit interaction. As we saw, the spin orientation in that case remains unchanged in first approximation, and therefore it can only be purely parallel or antiparallel to the magnetic field, *i.e.*

$$\Delta J_{\text{spin}} = \hbar, \tag{20.2}$$

so that from (20.1) we obtain for γ:

$$\gamma = \frac{\Delta M_{\text{spin}} + \Delta M_{\text{orbit}}}{\Delta J_{\text{spin}}}.$$

Since all composite vectors remain parallel to each other, we also obtain:

$$g = 2\,(M_{\text{spin}} + M_{\text{orbit}})/M_{\text{spin}}. \tag{20.3}$$

This is thus the same as (6.6), which governs the paramagnetic susceptibility and the saturation moment.

In (20.1) the change in the mechanical energy of the lattice (rotation) is neglected owing to its large moment of inertia. The change of angular momentum of the lattice ($\Delta J_{\text{lattice}}$) need not necessarily be small (compare with a ball bouncing from a rigid wall). Since evidently in this case $\Delta J = \Delta J_{\text{spin}} = \hbar$, then $\Delta J_{\text{orbit}} + \Delta J_{\text{lattice}} = 0$.

In § 3.3 we saw that J_{orbit} is of the order of $(\lambda/\Delta E)\hbar$, hence $(g-2) \cong \lambda/\Delta E$, which is of the order of 0.1 or 0.2. For more than half-filled shells the spin and orbital momenta are parallel so that g is greater than 2. Since the magnitude of the orbital angular momentum will also depend on the direction of the spin momentum with respect to the crystal axes, g can still be anisotropic.

There is another type of g factor, which also determines the ratio between a magnetic and a mechanical moment and which is known as the magneto-mechanical ratio g'. This is the governing factor in the Einstein-de Haas effect and the Barnett experiment, in which the change of angular momentum associated with a change of magnetization is measured by suspending a bar of ferromagnetic material from a thin wire. The bar is magnetized in the long axis (which is also the direction of the wire) by a surrounding coil The current is then reversed and this causes the bar to rotate. The g' factor is now defined as follows:

$$(e/2mc)g' = -(\Delta M_{\text{spin}} + \Delta M_{\text{orbit}})/\Delta J_{\text{lattice}},$$

where $\Delta J_{\text{lattice}}$ is the change in the angular momentum of the lattice, *i.e.* the observable change in the angular momentum of the bar, while

$\Delta M_{\text{spin}} + \Delta M_{\text{orbit}}$ is the change of M. Since the bar is suspended torsion-free, it follows that

$$\Delta J_{\text{lattice}} + \Delta J_{\text{spin}} + \Delta J_{\text{orbit}} = 0,$$

and therefore, if again we omit Δ,

$$g' = 2\frac{M_{\text{spin}} + M_{\text{orbit}}}{M_{\text{spin}} + 2M_{\text{orbit}}}, \tag{20.4}$$

because the ratio between M and J is smaller for orbital than for spin motion by a factor of 2. Evidently, then, there exists between the g of (20.3) and the g' of (20.4) the simple relation

$$\frac{1}{g} + \frac{1}{g'} = 1. \tag{20.5}$$

Thus if $g > 2$, then $g' < 2$, and *vice versa*. With most substances, for which both g and g' are known, this is indeed the case, but quantitatively (20.5) is not entirely satisfied, as appears from Table 20.I.

TABLE 20.I

VALUES OF g AND g' FOR A NUMBER OF FERROMAGNETIC MATERIALS

	g	g'	$\frac{1}{g} + \frac{1}{g'}$
Iron	2.12-2.17	1.93	0.980-0.990
Cobalt	2.22	1.97	0.986
Nickel	2.19	1.84	0.996
Magnetite Fe_3O_4	2.2	1.93	0.973
Heusler alloy Cu_2MnAl	2.01	2.00	0.998
Permalloy Ni78 Fe22	2.07-2.14	1.91	0.991-1.006

For the lowest resonance frequency of ferrimagnetics, (20.1) still holds for the total moment, since the change of exchange energy can be neglected. This means that (20.3) also holds for the ferrimagnetic materials. In (19.1) the γ_i's of the different sublattices were introduced phenomenologically. We see that (19.4) and (20.3) are indentical if we also take for the g's of the sublattices

$$g_i = 2\frac{(M_i)_{\text{spin}} + (M_i)_{\text{orbit}}}{(M_i)_{\text{spin}}}. \tag{20.6}$$

For low-frequency resonance, then, we may take in (19.4) the values for g_1 and g_2 according to (20.6), but this has not been proved for the high-fre-

quency case according to (19.5). It would only be so if we were able to treat each sublattice quite separately, such that (20.2) would apply to each. In view of the strong coupling between sublattices, which is much stronger than that with the external field, it is doubtful whether such a procedure would be possible.

Instead of (20.5) the relation usually given in the literature is

$$g - 2 = 2 - g', \tag{20.7}$$

which is only equivalent to (20.5) if $M_{\text{orbit}} \ll M_{\text{spin}}$. Thus (20.5) has a more general validity; the only approximation made to it is (20.2), *i.e.* the spin of the electron in an orbit is always purely parallel or antiparallel to the field. This is only true as regards normal ferromagnetics if the above restriction, $M_{\text{orbit}} \ll M_{\text{spin}}$ is obeyed, but as regards ferrimagnetics this is not necessary for the total moment, provided it is the case for the sublattice magnetizations. This difference is particularly apparent with such nearly compensated ferrimagnetics as the Li-Cr spinels already discussed. In these substances g can assume very high values in the vicinity of the compensation point. It can be seen that $g' \to 1$, which is evident since then, according to (20.3), $M_{\text{spin}} \to 0$, and therefore only orbital magnetism is present.

§ 21. Rotational Susceptibility

In this section we shall examine the off-resonance behaviour of the magnetization vector. Rotation can be caused by applying an alternating magnetic field $\boldsymbol{h}$ at right-angles to the equilibrium position (z axis) of the magnetization vector. This produces an alternating torque whose vector is at right-angles to the magnetization vector, the latter being, apart from a constant factor, equal to the angular momentum vector. The equation of motion (18.9), in the case of the energy (18.8) being on principal axes ($E_{xy} = 0$), can be written for small angles as:

$$\begin{aligned} -i\omega M\phi_y &= \gamma E_{11}\phi_x + \gamma M h_x \\ i\omega M\phi_x &= \gamma E_{22}\phi_y - \gamma M h_y, \end{aligned} \tag{21.1}$$

which follows by adding to (18.8) the term $-M(h_x\phi_x + h_y\phi_y)$. From this we obtain

$$M\phi_x = \frac{E_{22}h_x - (i\omega M/\gamma)h_y}{(\omega_r^2 - \omega^2)/\gamma^2}, \qquad M\phi_y = \frac{(i\omega M/\gamma)h_x + E_{11}h_y}{(\omega_r^2 - \omega^2)/\gamma^2},$$

where $\omega_r^2 = \gamma^2 E_{11}E_{22}/M^2$, corresponding to a susceptibility tensor of

$$\begin{aligned} \chi_{xx} &= \gamma^2 E_{22}/(\omega_r^2 - \omega^2) & \chi_{xy} &= -i\omega\gamma M/(\omega_r^2 - \omega^2) \\ \chi_{yx} &= i\omega\gamma M/(\omega_r^2 - \omega^2) & \chi_{yy} &= \gamma^2 E_{11}/(\omega_r^2 - \omega^2) \end{aligned} \tag{21.2}$$

The tensor is Hermitian and thus has real eigenvalues, in accordance with the fact that we have not taken damping into account. The off-diagonal elements are opposed. For elliptically polarized signals one finds from (21.1) the combinations

$$(\phi_x/\sqrt{E_{22}}) \pm i\,(\phi_y/\sqrt{E_{11}}) = \gamma \frac{(h_x/\sqrt{E_{11}}) \pm i\,(h_y/\sqrt{E_{22}})}{\omega \mp \omega_r} \tag{21.3}$$

It follows from this that an elliptically polarized field with axial ratio $\sqrt{E_{11}}/\sqrt{E_{22}}$ excites an elliptical rotation with exactly the opposite axial ratios (the largest field being required in the stiffest direction). It depends upon the sense of rotation whether, at a specific frequency, resonance will occur ($\chi = \infty$) or not. Resonance will always be excited in the case of a linearly polarized signal, since we may look on this as the superposition of two opposing elliptical rotations, in agreement with (21.3). For a linearly polarized magnetic field h_x, practically all that is excited at low frequency is an m_x in phase with h_x. At higher frequencies the alternating magnetization is elliptically polarized owing to the fact that one of the ellipses becomes predominant, m_x still being in phase with h_x. At resonance, one of the ellipses then being practically infinitely large, m_x goes over into antiphase after which m_x decreases faster than m_y, so that at very high frequencies the magnetization is linearly polarized in a plane at right-angles to the field. The latter phenomenon can be interpreted according to (21.3) by saying that at low frequencies the two oppositely rotating elliptical vibrations are in phase with the field, while at very high frequencies only one of the two has passed resonance and has rotated 180° in phase, so that superposition now yields a linear signal at right-angles to the first.

§ 22. Wave Propagation in Magnetized Media

22.1. THE WAVE EQUATION

The consequences of the non-diagonal form of the susceptibility tensor (21.2) as regards wave propagation were first studied by Polder [Po 1]. The wave equation, as found from the Maxwell equations, can be written for an infinite medium having a dielectric constant ϵ:

$$\Delta \boldsymbol{H} - \text{grad div } \boldsymbol{H} - \frac{\epsilon}{c^2} \frac{\partial^2 \boldsymbol{B}}{\partial t^2} = 0. \tag{22.1}$$

Since the magnetic permeability is not isotropic, div $\boldsymbol{H} = 0$ does not hold. In order to solve (22.1) we must know the relation between $\boldsymbol{B}$ and $\boldsymbol{H}$. In agreement with (21.2) we assume for the alternating components of $\boldsymbol{B}$ and $\boldsymbol{H}$ (indicated by small letters):

$$\boldsymbol{b} = \begin{pmatrix} \mu & -i\kappa & 0 \\ i\kappa & \mu & 0 \\ 0 & 0 & 1 \end{pmatrix} \boldsymbol{h} \tag{22.2}$$

corresponding to $E_{11} = E_{22}$ in (21.2). In (22.2), $\boldsymbol{b}$ and $\boldsymbol{h}$ are the alternating components of the internal field-strengths, and therefore external demagnetization, for example, is left out of consideration in determining μ and κ. The solution we calculate for (22.1) has the form of a travelling wave and hence we assume that the time and place dependence of $\boldsymbol{b}$ and $\boldsymbol{h}$ can be represented by that of a factor $\exp i(\boldsymbol{kr} - \omega t)$, in which $\boldsymbol{k}$ is the wave vector of magnitude $2\pi/\lambda$. This is no restriction, because any function of place and time can be expanded in these waves with the aid of Fourier analysis. For the three components of $\boldsymbol{h}$ eq. (22.1) then becomes:

$$\left.\begin{aligned} \left(\frac{\omega^2\epsilon\mu}{c^2} - k_y{}^2 - k_z{}^2\right) h_x + \left(k_xk_y - i\frac{\omega^2\epsilon\kappa}{c^2}\right) h_y + k_xk_zh_z = 0 \\ \left(k_xk_y + i\frac{\omega^2\epsilon\kappa}{c^2}\right) h_x + \left(\frac{\omega^2\epsilon\mu}{c^2} - k_x{}^2 - k_z{}^2\right) h_y + k_yk_zh_z = 0 \\ k_xk_zh_x + k_yk_zh_y + \left(\frac{\omega^2\epsilon}{c^2} - k_x{}^2 - k_y{}^2\right) h_z = 0 \end{aligned}\right\} \tag{22.3}$$

These are three homogeneous equations in h_x, h_y and h_z, and thus they only yield a solution if the determinant of the coefficients is zero, which gives a relation between $\boldsymbol{k}$ and ω.

We shall now examine some simple examples, taking first the case in which the wave is propagated in the direction of the magnetization ($k_x = k_y = 0$, $k_z = k$). We then find

$$k^2 = \frac{\omega^2\epsilon}{c^2}(\mu \pm \kappa). \tag{22.4}$$

These two solutions correspond to circularly polarized waves with a rotation respectively equal and opposite to that of the natural precession of the magnetization vector, as follows from substitution of (22.4) in (22.3). The quantity $(\mu \pm \kappa)$ is the permeability for circularly polarized fields, so that (22.4) has the same form as for a medium with isotropic μ.

We shall determine μ and κ occurring in (22.4) for the simple case in

which a static field H is present in the z direction, possibly to be substituted by an anisotropy field H^A. For a uniformly precessing magnetization vector we can then calculate μ and κ from (21.2), in which $E_{11} = E_{22} = HM$ and $\omega_r = \gamma H$, hence

$$\mu \pm \kappa = 1 + \frac{4\pi M}{H \pm \omega/\gamma} = \frac{B \pm \omega/\gamma}{H \pm \omega/\gamma}. \tag{22.5}$$

Owing to wave motion, however, the magnetization is no longer uniform, and a given spin will be subjected not only to the torque exerted by the magnectic field but also to a torque caused by exchange interaction. As a result the motion of the spin vector is changed, and with it the susceptibility. We shall examine this quantitatively for slow variations of the spin orientation ($2\pi/k$ being much larger than the lattice parameter). The exchange energy between two neighbouring spins 1 and 2 is according to (5.1) proportional to the scalar product $\boldsymbol{S}_1\boldsymbol{S}_2$. The torque $\boldsymbol{T}$ which they exert on each other will be proportional to the vector product of $\boldsymbol{S}_1$ and $\boldsymbol{S}_2$:

$$\boldsymbol{T} \propto \boldsymbol{S}_1 \times \boldsymbol{S}_2$$

The total torque acting on the magnetic moment of an atom follows from summation of the torques exerted by the moments of the surrounding atoms. In the case of the neighbouring spin $\boldsymbol{S}_2$ at a distance $\boldsymbol{R}$ we can write for a slow variation of the spin orientation

$$\boldsymbol{S}_2 = \boldsymbol{S}_1 + (\boldsymbol{R}\boldsymbol{\nabla})\boldsymbol{S} + \tfrac{1}{2}(\boldsymbol{R}\boldsymbol{\nabla})^2\boldsymbol{S} + \ldots$$

where $\boldsymbol{S}$ is taken to be a continuous function of position in the lattice and where the derivatives at the position of the central atom must be taken. In the summation of the torques the odd terms in $\boldsymbol{R}$ cancel each other out for a lattice with a centre of symmetry. For a cubic lattice in particular the torque, now expressed in terms of the magnetization, assumes the simple form

$$\boldsymbol{T} = A\boldsymbol{M} \times \Delta\boldsymbol{M}, \tag{22.6}$$

where Δ is again the Laplace operator, and A a constant. The torque for the travelling waves considered here is

$$\boldsymbol{T} = Ak^2\boldsymbol{M} \times \boldsymbol{m}, \tag{22.7}$$

where $\boldsymbol{m}$ is the variable part of the magnetization vector. The torque (22.7) would also be produced by a static magnetic field parallel to the magnetization of the magnitude

$$H_{ex} = Ak^2M.$$

The resultant permeability can be found quite simply, then, by substituting $H + H_{ex}$ for H. If this is done in (22.5) we obtain for (22.4) in this case:

$$k^2 = \frac{\omega^2 \epsilon}{c^2}\left(1 + \frac{4\pi M}{\mathrm{H} + AMk^2 \pm \omega/\gamma}\right), \tag{22.8}$$

which is now a quadratic equation for k^2. If the half wave length is equal to the lattice parameter, it then follows from an impermissible extrapolation that the field AMk^2 is of the order of the Weiss field $\cong 10^7$ oersteds, hence $AM \cong 10^{-9}$ oersteds cm^2. If the denominator in (22.8) is not nearly zero, *i.e.* for values of $\omega < \gamma H$, the form between brackets in (22.8) is of the order of magnitude 2. For microwaves ($\omega \cong 10^{11}$/sec), where $\epsilon = 10$, k^2 is of the order of 10^2, so that the exchange field is only $\cong 10^{-7}$ oersteds, which is negligible compared to H ($\cong 10^3$ oersteds). If ω approaches γH, then without the exchange field the right-hand side of (22.8) with the minus sign would be infinite, and with it k^2. The exchange field prevents this. If $\omega > \gamma H$, the denominator in the right-hand side of (22.8), without exchange field, is negative for this resonance mode. In that case it can be made positive again by the exchange field. This happens for fairly large values of k^2, larger than that for $\omega = \gamma H$ which, according to (22.8), is of the order of 10^7. Consequently the factor between brackets in (22.8) must be at least of the order of 10^5 for $\omega > \gamma H$. This means that, in very good approximation, the denominator is zero, hence

$$\omega = \gamma(H + AMk^2). \tag{22.9}$$

This is the frequency of the so-called spin-waves, first introduced by Bloch, and it thus depends quadratically on k. For $\omega > \gamma B$ the right-hand side of (22.8), also without exchange field, becomes positive again — see (22.5) — and therefore there is again a solution with small k^2, in which the exchange field is negligible. For the oppositely precessing mode, (22.8) is always positive, *i.e.* k^2 is small and again of the order of $\omega^2\epsilon/c^2$, so that in this case, too, the exchange field can be neglected. We have shown, then, that (22.8) gives two kinds of waves as solution, namely electromagnetic waves, for which the exchange energy can be neglected, and spin waves, for which the electromagnetic energy is negligibly small and only magnetic and exchange energy enter into account. Both kinds of waves, which we now propose to examine separately, gradually merge (see Fig. 22.1).

22.2. ELECTROMAGNETIC WAVES

For electromagnetic waves in the z direction (22.8) becomes

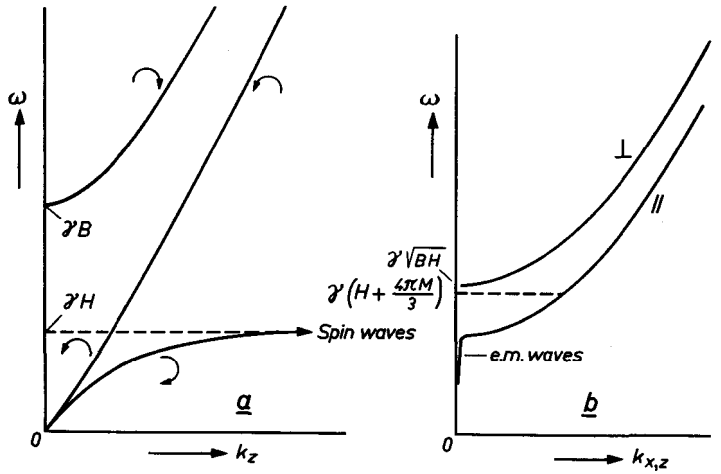

Fig. 22.1. Frequency of electromagnetic waves (*a*) and of spin waves (*b*) as a function of the wave number k. The scale for k in (*b*) is at least a factor 10^6 smaller than in (*a*).

$$k_x^2 = \frac{\omega^2 \epsilon}{c^2} \frac{B \pm \omega/\gamma}{H \pm \omega/\gamma} \tag{22.10}$$

Above resonance ($\omega > \gamma H$), the magnetization is in antiphase with the field and therefore the rotational susceptibility is negative. Where $\omega < \gamma B$ this also results in a negative permeability and, apart from spin waves, no wave propagation is possible, Where $\omega = \gamma B$, according to (22.5) the permeability becomes zero (antiresonance). Above this point, wave propagation is again possible. The oppositely rotating mode exhibits no resonance and here, therefore, the magnetization is always in phase with the field. The permeability varies continuously from B/H at low frequencies to unity at high frequencies.

A linearly polarized electromagnetic field can be split up into two oppositely rotating circularly polarized fields. For propagation in a direction parallel to the static magnetization vector, the wavelength of these two components will differ. Over a distance l the magnetization vector of the one component will thus have rotated through a different angle from that of the other. If, then, we again combine them into a linearly polarized signal, the polarization plane will have rotated through an angle β, which is given by

$$\beta/l = \tfrac{1}{2}(k_+ - k_-) \tag{22.11}$$

Below resonance ($\omega < \gamma H$) a rotation thus takes place which is in the

opposite sense to that above antiresonance ($\omega > \gamma B$). This so-called Faraday rotation (22.11) can be computed from (22.10) as a function of the frequency. For high frequencies ($\omega \gg \gamma B$) we find

$$\beta/l \cong \gamma \,.\, 4\pi M \,.\, \sqrt{\epsilon}/c, \tag{22.12}$$

which is independent of the frequency and proportional to the magnetization. For many ferrites $4\pi M_s \cong 4000$ gauss and $\epsilon \cong 10$, which means that in ferrites a Faraday rotation may occur of the order of 360°/cm.

Consider now the case of waves which propagate in a direction at right-angles to the direction of magnetization, *e.g.* $k_y = k_z = 0$, $k_x \neq 0$. We then find apart from a non-magnetic mode with $k_x^2 = \omega^2\epsilon/c^2$, a mode with

$$k_x^2 = \frac{\omega^2\epsilon}{c^2}\,\frac{\mu^2 - \kappa^2}{\mu} = \frac{\omega^2\epsilon}{c^2}\,\frac{B^2 - \omega^2/\gamma^2}{BH - \omega^2/\gamma^2}\,. \tag{22.13}$$

Resonance occurs here for $\omega = \gamma\sqrt{BH}$, which is a consequence of the fact that the magnetization, owing to the wave motion in the x direction, is subjected to a demagnetizing field corresponding to a demagnetizing coefficient of 4π. Here, too, an electromagnetic wave at resonance goes over into a spin wave, with, for cubic materials, the same dependence on k^2 as in the case of spin waves in the z direction. Electromagnetic waves in the x direction give rise to the Cotton-Mouton effect [Du 1], also familiar in optics.

Up to now we have calculated the propagation only in an infinitely large medium, without taking account of boundary conditions. These are the normal boundary conditions of Maxwell's theory, namely that on any surface the tangential components of $\boldsymbol{H}$ and $\boldsymbol{E}$ and the normal components of $\boldsymbol{B}$ and $\boldsymbol{D}$ are continuous. As was first shown by Van Trier [Tr 1], these conditions can radically modify the properties of wave propagation. For example, in the case of a thin rod, whose thickness is small compared with the wavelength and which is magnetized along its long axis, the resonance frequency for waves propagating along the axis of the rod is equal to $\gamma(H + 2\pi M)$, corresponding to the frequency for ferromagnetic resonance. In the latter case the wavelength is also assumed to be large in comparison with the dimensions of the body.

22.3. SPIN WAVES

In § 22.1 we saw that for small k a spin wave has a frequency between γH and $\gamma\sqrt{BH}$, depending upon its direction of propagation. In this case the wavelength is much smaller than the dimensions of the body ($k > 10^3$)

and therefore the boundary conditions are unimportant. Nevertheless, we must take into account here that the fields used in Fig. 22.1 are the internal static fields, H_i, *i.e.*

$$H_i = H_e - N_z M, \tag{22.14}$$

where the external field H_e always lies between H_i and $\sqrt{B_i H_i}$.

Spin waves describe the internal motion of the magnetic moments. In this respect they may be compared to sound waves (Debye waves) or to lattice vibrations in solids. The sound waves form, as it were, a Fourier spectrum of the individual movements of the atoms. Owing to the mutual coupling of the atoms, their movements are to some extent correlated. This coupling, together with the mass properties, gives rise to wave propagation. In the case of spin waves the same coupling exists between neighbours, but the mass properties are lacking. Instead, the motion of the spin vectors is now essentially more dimensional (see § 18), so that there are still two degrees of freedom, and therefore free oscillation is possible and hence also wave propagation. In the case of electromagnetic waves it are the electric and magnetic energies which, at each point, periodically go over one into the other.

The lattice vibrations are quantized, that is to say the amplitude of a wave with a certain frequency can only increase in certain finite steps, so that the energy of the wave increases by equal amounts $\hbar\omega$. The energy is then

$$E_n = (n + \tfrac{1}{2})\hbar\omega, \tag{22.15}$$

where $n \geqslant 0$. The lowest state for $n = 0$ corresponds to the zero-point vibration of a crystal, *i.e.* of the individual atoms, since, having regard to Heisenberg's uncertainty principle, an atom cannot stand still ($\Delta x = \Delta p = 0$). Even if we assume no correlation with the movement of neighbouring atoms, an atom still moves in a potential well, *i.e.* it has positive energy with respect to the state with zero amplitude and velocity because the energy quadratically contains the coordinate and the velocity. This energy appears to be $\frac{1}{2}\hbar\omega$ for the Fourier component with angular frequency ω. From an exact calculation of the spin waves it appears that a similar quantization occurs for these also. This is connected with the fact that, as we saw in § 3.4, the z component of the total angular momentum can only change by an integral multiple of $\hbar$. The zero-point vibration of spin waves corresponds to the zero-point motion of the individual spin moments, which is discussed in § 3.4. Although spin waves have a zero-point vibration, it makes no contribution to the energy since this, apart from the magnetostatic energy, consists of the exchange energy between the spins of neighbouring

atoms:

$$E_{ex} = -2J(S_{1x}S_{2x} + S_{1y}S_{2y} + S_{1z}S_{2z}) . \tag{22.16}$$

In the ground state the average value (expectation value) of $S_{1z} = S_{2z}$ is $\frac{1}{2}$, while the expectation value of S_x and S_y for both spins is zero. Owing to the essential lack of correlation between the zero point motion of the individual spins, the deviations from these values make no contribution to (22.16), since this equation only contains products of the spin components of different electrons. Similar reasoning applies to the magnetostatic energy $-HM$, which is proportional to $-H\Sigma S_{iz}$.

The energy with respect to the ground state then becomes

$$E_n = n\hbar\omega = n\hbar\gamma(H + H_{ex}) = 2n\mu_B(H + H_{ex}). \tag{22.17}$$

The reduction of the spontaneous magnetization with increasing temperature can be described in terms of spin waves. The creation of each spin wave (increase of n by 1 in (22.17)) causes the magnetization to change by $2\mu_B$, and therefore a spin wave can be thought of as a reversed spin moving through the crystal. Since a spin can be reversed once only, spin waves tend to repel each other. In the given phenomenological derivation this interaction is neglected, so that the spin wave theory applies only to temperatures far below the Curie temperature, where the spontaneous magnetization M_s still differs but little from the magnetization M_0 at $T = 0$ and there are very few spin waves. The degree of spin-wave excitation is then governed by the so-called Bose-Einstein statistics, just as for lattice vibrations, and is given by

$$n_k = [\exp(\hbar\omega_k/kT) - 1]^{-1}. \tag{22.18}$$

The reduction of the magnetization is equal to

$$M_0 - M_s = 2 \sum_k n_k\mu_B .$$

The possible values of k are uniformly distributed over the k space. According to (22.18), at low temperatures only those states are notably excited (*i.e.* where n is of the order of unity) for which $\hbar\omega_k \ll kT$. The number of excited spin waves, then, is approximately proportional to k_0^3, where k_0 is the wave number for which $\hbar\omega_k = kT$. From this and (22.18) is derived the Bloch $T^{3/2}$ law (6.21) for the magnetization-temperature curve. The magnetic component of specific heat has also to obey a $T^{3/2}$ law as has been found experimentally for magnetite by Kouvel [Ko 2].

§ 23. Damping

23.1. GENERAL PROPERTIES OF COMPLEX SUSCEPTIBILITY

Owing to the damping a phase shift occurs between the applied alternating field and the alternating magnetization to which it gives rise. As a result the alternating magnetization is not purely in phase or in antiphase and it is possible, therefore, that an energy dissipation $\int \boldsymbol{h}.\dot{\boldsymbol{m}}\, \mathrm{d}V$ will occur. If the complex notation is applied for the sinusoidally varying quantities, the damping and hence the phase shift find expression in the susceptibility becoming complex:

$$\chi = \chi' - i\chi'' \tag{23.1}$$

in which χ' and χ'' are real functions of ω. Here χ' is proportional to the component of $\boldsymbol{m}$ which is in phase or in antiphase with $\boldsymbol{h}$, while χ'' gives the 90° phase-shifted component of m. In principle, (23.1) holds for each component of the susceptibility tensor. For linearly polarized signals the energy dissipation per cm³ is:

$$\frac{\mathrm{d}W}{\mathrm{d}t} = \tfrac{1}{2}\omega\chi'' h^2. \tag{23.2}$$

If there is no damping, χ'' is zero for all frequencies, except at resonance, when χ'' becomes infinitely large. Owing to damping, this peak function is widened and lowered. Further, $\chi'' = 0$ where $\omega = 0$, *i.e.* for very slow variations the energy dissipation per cycle is zero. This holds for those processes in which equilibrium always prevails throughout very slow variations, that is to say we exclude hysteresis, as we can do for small amplitudes. Before discussing the mechanism of damping, we shall first consider some phenomenological relations.

If the applied field h varies arbitrarily with time the resultant m can be found by expanding h in a Fourier integral. For each Fourier component the magnetization can then be found with (23.1), so that by integration over ω the total magnetization follows as a function of time. If in particular we apply a field which is zero for $t < 0$, the same must also hold for m, irrespective of the further trend of h. This establishes a certain relation between χ' and χ'' which can be represented by the Kramers-Kronig relations:

$$\chi'(\omega) = \frac{2}{\pi}\int_0^\infty \frac{\omega_1\chi''(\omega_1)}{{\omega_1}^2 - \omega^2}\,\mathrm{d}\omega_1 \qquad \chi''(\omega) = \frac{-2}{\pi}\int_0^\infty \frac{\omega\chi'(\omega_1)}{{\omega_1}^2 - \omega^2}\,\mathrm{d}\omega_1 \tag{23.3}$$

Thus, if either χ' or χ'' is given as a function of frequency, χ'' or χ' is then determined. The relations (23.3) hold for each of the tensor elements of

(22.2) separately, since the above considerations are equally valid if $\boldsymbol{m}$ and $\boldsymbol{h}$ are not in the same direction. The tensor element χ_{xy} in (22.2) is already imaginary without damping. If the stiffness is anisotropic and the x and y axes do not coincide with the principal axes of the energy, an equal, real part is added to χ_{xy} and χ_{yx}, so that these are then respectively of the form $a - ib$ and $a + ib$. Where damping is present, a changes into $a' - ia''$ and b into $b' - ib''$. As a result the matrix is no longer Hermitian (it had already ceased to be Hermitian when (23.1) was introduced for the diagonal elements) and therefore the eigenvalues are complex, corresponding to signals decreasing exponentially with time and to energy dissipation. While (23.3) holds for a' and a'', the relations for b' and b'' are

$$b'(\omega) = \frac{2}{\pi}\int_0^\infty \frac{\omega b''(\omega_1)}{\omega_1{}^2 - \omega^2}\,\mathrm{d}\omega_1 \quad b''(\omega) = -\frac{2}{\pi}\int_0^\infty \frac{\omega_1 b'(\omega_1)}{\omega_1{}^2 - \omega^2}\,\mathrm{d}\omega_1 \tag{23.4}$$

that is where

$$\tfrac{1}{2}(\chi_{xy} + \chi_{yx}) = a' - ia'' \text{ and } \tfrac{1}{2}(\chi_{xy} - \chi_{yx}) = b' - ib''. \tag{23.5}$$

In (23.3), χ'' is automatically zero for $\omega = 0$, in agreement with the above. In (23.5) this is not the case for the damping term b''; here b' is automatically zero for $\omega = 0$. Nevertheless, b'' must also be zero for $\omega = 0$, as follows from the more general formula for the energy dissipation

$$\frac{\mathrm{d}W}{\mathrm{d}t} = \tfrac{1}{2}\mathrm{Re}\; i\omega\left[\chi_{xx}|h_x|^2 + \chi_{xy}h_x{}^*h_y + \chi_{yx}h_xh_y{}^* + \chi_{yy}|h_y|^2\right]. \tag{23.6}$$

The cross term according to (23.5) is

$$\omega\mathrm{Re}(a'' - ib'')h_x{}^*h_y. \tag{23.7}$$

If $b'' \neq 0$ for $\omega = 0$, then (23.7) is the only remaining term. The losses for elliptically polarized signals are then proportional to b'' (since $h_x{}^*h_y$ is imaginary for this term). By, for example, changing the sign of h_y (opposite sense of rotation) we change the energy dissipation into a generation of energy per cycle, so that b'' must be zero for $\omega = 0$. For $\omega \neq 0$ this generation of energy as a result of the b'' term is indeed possible, but in that case the other terms in (23.6) ensure that there will still be dissipation in the total result (eq. (23.6) is positive definite). For rotational fields in an isotropic medium the energy dissipation is

$$\frac{\mathrm{d}W}{\mathrm{d}t} = \omega h^2(\mu'' \pm \kappa''). \tag{23.8}$$

A useful expression for the area of the absorption peak follows from the first equation of (23.3) for $\omega = 0$:

$$\int_{\omega=0}^{\infty} \chi''(\omega)\, \mathrm{d}\,(\ln \omega) = \frac{\pi}{2}\, \chi'(0). \tag{23.9}$$

A magnetization process that contributes by a given fraction to $\chi'(0)$ will contribute by the same fraction to the area of the absorption peak if the frequency is plotted logarithmically.

23.2. PHENOMENOLOGICAL DESCRIPTION OF DAMPING

In order to describe damping, various terms are proposed which must be added to the equation of motion. In their classical paper [La 1], Landau and Lifshitz originally put the equation of motion as:

$$\dot{\boldsymbol{M}} = \gamma(\boldsymbol{M}\times\boldsymbol{H}) - (a\gamma/M)\boldsymbol{M}\times(\boldsymbol{M}\times\boldsymbol{H}) \tag{23.10}$$

which, as can easily be seen, is equivalent to

$$\dot{\boldsymbol{M}} = \gamma(1 + a^2)\,(\boldsymbol{M}\times\boldsymbol{H}) - (a/M)\,(\boldsymbol{M}\times\dot{\boldsymbol{M}}). \tag{23.11}$$

In (23.10) the damping term consists of a vector at right-angles to $\boldsymbol{M}$ in the direction of the resultant magnetic field $\boldsymbol{H}$ and proportional to the sine of the deflection angle of the magnetization from the direction of $\boldsymbol{H}$, so that the magnetization vector is forced back towards the direction of the field. In (23.11) the viscous character of the damping term comes more to the fore. Both damping terms leave the absolute magnitude of $\boldsymbol{M}$ unchanged, as appears from the scalar multiplication of both sides of the equation by $\boldsymbol{M}$. The correction to γ in (23.11) is in the main unimportant, since a is of the order of 10^{-2}. The damping constant a can also be a function of the static field H_0.

The damping terms from Bloch's theory of nuclear spin resonance were applied by Bloembergen [Bl 1] to ferromagnetic resonance. The damping torque is put proportional to the deviation of $\boldsymbol{M}$ from the equilibrium position. The Bloch-Bloembergen equation is

$$\dot{\boldsymbol{M}} = \gamma(\boldsymbol{M}\times\boldsymbol{H}) - a\gamma(\boldsymbol{M}H - M\boldsymbol{H}) \tag{23.12}$$

corresponding to a relaxation time $\tau = 1/a\gamma H$.

The damping term in (23.10) can be written as

$$-a\gamma\left[\boldsymbol{M}\frac{\boldsymbol{H}M}{M} - M\boldsymbol{H}\right].$$

We shall see in § 24.2 that the damping terms discussed here only apply when the rotations of the magnetization vector are small; when they are large there can no longer be any question of a rigid magnetization vector. Without loss of generality, then, we may put $\boldsymbol{HM}$ equal to HM, so that for small α the damping terms of Landau and Lifshitz, the viscous damping term and that of Bloch-Bloembergen are all identical. For the sake of simplicity of notation, we shall henceforth use only (23.11), in which the α^2 term is neglected. In the case of a non-cubic medium, different values of α may occur in the x and y directions. For the susceptibility tensor we then find

$$\begin{aligned} \chi_{xx} &= \gamma M\left[\frac{(\omega_1\omega_2-\omega^2)\omega_2}{(\omega_1\omega_2-\omega^2)^2+\omega^2(\Delta\omega)^2}-i\frac{\omega\omega_2\Delta\omega}{(\omega_1\omega_2-\omega^2)^2+\omega^2(\Delta\omega)^2}\right] \\ \chi_{xy} &= -i\gamma M\left[\frac{(\omega_1\omega_2-\omega^2)\omega}{(\omega_1\omega_2-\omega^2)^2+\omega^2(\Delta\omega)^2}-i\frac{\omega^2\Delta\omega}{(\omega_1\omega_2-\omega^2)^2+\omega^2(\Delta\omega)^2}\right] \end{aligned} \tag{23.12}$$

and similar expressions for χ_{yx} and χ_{yy}. Here $\omega_1 = \gamma E_{11}/M$ and $\omega_2 = \gamma E_{22}/M$ and

$$\alpha_1\omega_1 + \alpha_2\omega_2 = \Delta\omega \tag{23.13}$$

which is the line width measured between the points where χ'' has dropped to half the maximum value. This maximum value of χ_{xx}'' is related to the line width according to

$$(\chi_{xx}'')_{\max} \cdot \Delta\omega = \gamma M\sqrt{\frac{\omega_2}{\omega_1}}. \tag{23.14}$$

23.3 DAMPING THEORY

The microscopic theory on the damping of ferromagnetic precession was first put forward by Akhieser [Ak 1]. The deviation from the equilibrium position is described in terms of spin waves. On the other hand the thermal agitation of the atoms in the lattice is described in terms of lattice waves, and thus they may both be regarded as the terms of a Fourier series of the non-periodic perturbations of the magnetization and of the atomic ordering, respectively. Quantization gives these waves the character of particles with an energy $\hbar\omega$. These energies can be of the same order of magnitude, namely at maximum kT_C and kT_D, where T_C is the Curie temperature and T_D the Debye temperature. The wave numbers multiplied by $\hbar$ are to be regarded as the momenta of the particles.

The atomic magnetic moments are coupled by exchange interaction and dipole-dipole interaction. Moreover, the spin-orbit interaction gives rise

to an effective coupling between the magnetic moments which is somewhat similar to dipole-dipole interaction, and to which Van Vleck [Va 2] therefore gave the name "pseudo dipolar interaction". Owing to the fact that the above-mentioned interactions are strongly dependent on the interatomic spacing, interaction will result in a deformed crystal between the spin waves and the lattice waves. As a consequence, the spin waves may vanish and lattice waves be created, or conversely. The two most important processes can be represented schematically as

$$s + s \rightleftarrows l \text{ and } s + l \rightleftarrows s. \tag{23.15}$$

In the first, two spin waves are annihilated and one lattice wave is created, or *vice versa*, and in the second a spin wave and a lattice wave together go over into another spin wave. In these processes the total energy as well as the total momentum must be conserved, which implies a severe restriction of the number of possible processes. For this reason, to give an example, it is not possible for a single spin wave to go over into a single lattice wave, since if the wave number is the same the energy will be different and *vice versa*. There must, then, always be at least three "particles" involved in the process. The magnitude of the interaction is connected with that of macroscopic phenomena. Thus, the dependence of the exchange energy on the interatomic spacing gives rise to volume magnetostriction (see § 13.1), and that of dipolar and pseudo dipolar energy gives rise to linear magnetostriction. Volume magnetostriction being essentially a much larger effect than linear magnetostriction, it was found by Akhieser to give the more important coupling mechanism. In fact, Akhieser took only the true dipolar energy into account, but multiplication by a factor of 50, which gives approximately the ratio between pseudo and true dipolar energy, leaves this conclusion unchanged.

The interactions described above can cause a state of non-equilibrium to return to the state of equilibrium, and in the process the magnetostatic and exchange energies are converted into lattice vibration energy. For a return to the state of equilibrium it is necessary that the spin waves should vanish. This is only possible via the first process of (23.15). The variation of the exchange energy with interatomic spacing cannot give rise to these processes, since the exchange energy depends solely on the mutual orientation of the spins and not on the orientation in space of the resultant spin. Conversely, therefore, the exchange cannot change this orientation. The relaxation time is accordingly governed *via* processes which are connected with linear magnetostriction, as treated in the theory of Kittel and Abrahams [Ki 5]. The calculated relaxation time τ, which can be identified with $(\alpha\gamma H)^{-1}$ in a resonance experiment, appears to be of the correct order of magnitude

if one assumes that in the non-equilibrium state the occupation of all levels differs from that in the equilibrium state, such as for example the distribution pertaining to a temperature different from the ambient temperature. Polder [Po 1] has pointed out that this does not correspond to the circumstances in a resonance experiment performed on a small specimen within which the externally applied alternating field is uniform. One then excites, as it were, spin waves with $k = 0$, so that in the first instance only the distribution of these spin waves will deviate from the state of equilibrium. The interactions described above cannot then occur, since to do so the wave number as well as the energy of the other spin wave and the lattice vibration would have to be equal. The energy transfer would then have to take place in processes involving more than three particles, which is improbable. In such a case the relaxation time would become much longer.

It has been pointed out by Clogston *et al* [Cl 1] that, apart from dynamic perturbations, static deviations from lattice periodicity can give rise to transitions. These are found, for example, in ferrites in which two different magnetic ions occur disordered at equivalent lattice points, resulting in non-periodic perturbing magnetic fields of appreciable magnitude. These can change the wave number of a spin wave, but the energy remains constant thereby, comparable with the scattering of conduction electrons on an impurity in a solid. For a sphere, ferromagnetic resonance occurs when $\omega = \gamma H_e$, where H_e is the external field. Owing to the demagnetization in the z direction, (22.14) applies. The fields used in Fig. 22.1 are the internal fields H_i, which is to say that the frequency for ferromagnetic resonance lies between the values of the two ω *versus* k curves extrapolated to $k = 0$, and the value $\omega = \gamma H_e$ is degenerate with a large number of spin waves with a finite k value. This difference in behaviour between spin waves and the $k = 0$ waves at ferromagnetic resonance is due to the fact that the ferromagnetic resonance frequency is increased by the dynamic poles arising at the edges of the specimen. These also arise in the case of spin waves propagated in the z direction, but they then change sign with a wavelength equal to that of the spin wave. The demagnetizing fields thus practically cancel each other out at distances that are large with respect to the wavelength, so that in effect the frequency of the spin waves is not influenced by the finiteness of the crystal.

Once these spin waves with the ferromagnetic resonance frequency are excited, the excitation spreads out rapidly by the normal Akhieser processes over the entire spin wave spectrum, and interaction with the lattice can take place. The bottleneck lies in this first transition, which is believed to determine the relaxation time. Owing to the increase in perturbing fields when

the magnetization is increased as a result of lowering the temperature, there occurs an increase in $1/\tau$ and hence in line width.

Apart from a dependence upon the degree of ordering, this theory also predicts a dependence of τ on the shape of the specimen. For the flat disc which is magnetized at right-angles to the plane of the disc, the resonance field is equal to the internal field, since the poles on the edges are of no significance here. In other words, this frequency coincides with the lowest spin wave frequency and no degeneracy occurs. With this shape of specimen, therefore, a longer relaxation time and hence a narrower line will be found.

23.4. INSTABILITY AT LARGE AMPLITUDES

The qualitative considerations discussed above were applicable to the damping mechanism described by (23.11), *i.e.* where the constant α is independent of the amplitude of the signal. If this equation were also to apply to large amplitudes, the maximum value of χ'' would then be independent of the deviation from static equilibrium until the angle of deviation of the magnetization vector had reached 90°. This is the case when the amplitude of the alternating field is equal to the line width $\Delta H = 2\alpha H$ (see (23.13)). From experiments by Bloembergen *et al* [Bl2] it appears that non-linear phenomena already occur at amplitudes of the alternating field of the order of 1/50th of that value. The absorption curve then becomes lower and wider, as if α had become larger. Suhl [Su 3] has shown that this is the consequence of a stronger coupling of the ferromagnetic resonance mode with some of the spin waves having the same frequency, which coupling already existed owing to the Clogston mechanism. A spin wave superimposed on the uniformly precessing magnetization vector, having the same frequency and being propagated along the z axis, becomes unstable and grows larger at a specific amplitude of the alternating field. It appears that if $4\pi\Delta M_z \cong \Delta H$, where ΔM_z is the change in the z component of the magnetization as a result of the precession and ΔH is the line width, standing waves are created, *i.e.* the magnetization vector no longer remains stretched during precession. For the magnitude of the microwave field h_c this condition is

$$h_c \cong \Delta H \sqrt{\Delta H / 4\pi M} \,. \tag{23.16}$$

It further appears that these demagnetizing fields in the direction of propagation of a spin wave may also give rise to spin waves with a frequency equal to half the frequency of the external field, if the alternating amplitude m^+ of the still uniformly rotating magnetization vector satisfies

$$4\pi m^+ \sin\theta \cos\theta > \Delta H,$$

where θ is the wave vector angle of the spin wave with the z axis. This is first satisfied for $\theta = 45°$. The instability, which manifests itself as an extra absorption peak, is noticeable with static fields that are some hundreds of oersteds lower than the resonance field. In first approximation we may write for the critical value of the external field

$$h_c \simeq (\omega - \omega_r)\Delta H/\gamma \,.\, 2\pi M. \tag{23.17}$$

§ 24. Dynamics of Domain Boundary (Bloch Wall) Movement

24.1. WALL INERTIA

The applied field, parallel to the magnetization on one side of a 180° wall, exerts a torque on the spin vectors inside the wall. This does not, however, directly cause wall displacement, since the spin vectors are turned by the external field in a direction at right-angles to the plane of the wall, whereas in order to move the wall a rotation of the spin vectors is necessary in a plane parallel to the wall. The angle of movement from the plane of the wall obeys the relation

$$\dot{\theta} = \gamma H \sin \phi, \tag{24.1}$$

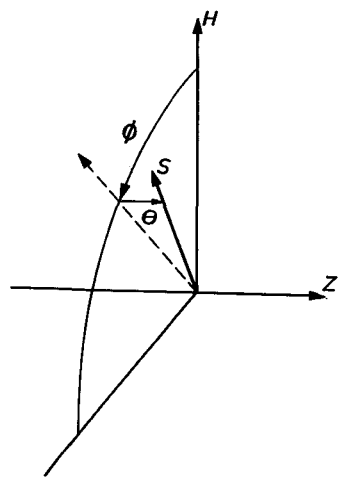

Fig. 24.1. Schematic representation of a spin vector S, inside a moving wall, moving out of the plane of the wall.

(see Fig. 24.1). This movement can give rise to a torque, represented by a vector in the plane of the wall, which may turn the magnetization vector in that plane and so cause the wall to move. This torque, for small values thereof, will be proportional to θ, hence

$$M\dot{\phi} = M\frac{\partial \phi}{\partial z} \,.\, v = C \,.\, \theta, \tag{24.2}$$

where C is a constant of proportionality, which can still be a function of the position (z) in the wall. In (24.2) it is assumed that, apart from θ, the wall moves undeformed. By differentiating (24.2) with respect to time we find, with the aid of (24.1), that the acceleration ($\dot{v}$) of the wall is proportional to the applied pressure 2 HM. This means that the wall has inertia [Do 1] and therefore mass can be attributed to it. We shall not give the calculation in detail, but simply explain its results.

The torque $C\theta$ in (24.2) consists of three parts, due to exchange energy, crystal energy and, as an extra contribution, a torque caused by demagnetization. In the z direction a magnetization $M\theta$ is present only inside the wall. Outside the wall we have $M_z = B_z = 0$, and therefore inside the wall, too, B_z must be equal to zero. As a consequence of this, a demagnetizing field arises of the order of

$$H_z = -4\pi M_z = -4\pi M_s \,.\, \theta.$$

This gives a torque MH_z at right-angles to the magnetization vector at the position of the wall. The torque of the exchange interaction is of the form of (22.6) which for the component considered here, becomes $AM^2\mathrm{d}^2\theta/\mathrm{d}z^2$. The crystal anisotropy torque is $2K\,\theta\cos^2\phi$. As explained in § 15, we may write for the exact 180° wall configuration in a uniaxial crystal

$$\sin\phi = \delta_w \,.\, (\partial\phi/\partial z) = 1/\cosh(z/\delta_w), \tag{24.3}$$

where δ_w is the wall thickness. A short time t after applying the field the applicable expression, according to (24.1) is

$$\theta = \gamma H\, t \,.\, \sin\phi. \tag{24.4}$$

If, using (24.3), we calculate with this value the component of the total torque in the plane of the wall, we find

$$T_\phi = (H^A + 4\pi M_s + H\cos\phi)M_s \,.\, \theta. \tag{24.5}$$

The part H^A in the form between brackets originates from the exchange energy and the crystal energy together, while the term $4\pi M_s$ originates from the demagnetizing field in the z direction. The term originating from the external field is negligible for the calculation of the acceleration. According to (24.3) and (24.4), $\partial\phi/\partial z$ and θ depend in the same way upon z, so that the notation in (24.2) with a uniform v is permissible. From (24.2) and (24.5), then, we obtain for the velocity v of the wall, for short times t,

$$v = \gamma^2\delta_w H(H^A + 4\pi M_s)t, \tag{24.6}$$

and therefore the mass per cm² of the wall is

$$m_w = [2\pi\gamma^2\delta_w(1 + H_A/4\pi M_s)]^{-1}. \tag{24.7}$$

The special point to be noted here is that the mass is inversely proportional to the thickness of the wall.

24.2. DAMPING OF THE WALL MOVEMENT

The movement of the domain boundary is subject to damping, so that some

time after the application of the field a stationary state will be reached, in which the wall moves with constant velocity. We assume that the rotation of the magnetization vectors inside the wall can be described by a damping term as in (23.11). However, it is not certain that α will have the same value as for ferromagnetic resonance, since in the latter case the magnetization is practically uniform. For wall movement the description with spin waves is no longer adequate, and therefore the Akhieser theory cannot be applied here. If nonetheless we use the damping term from (23.11), then in the stationary state this torque must be neutralized by the torque exerted by the external field H, as indicated in (24.5). The damping torque in this direction becomes $\alpha M_s \partial\theta/\partial t = \alpha M_s(\partial\theta/\partial z) \,.\, v$, hence

$$H \cos \phi \,.\, \theta = \alpha(\partial\theta/\partial z)v.$$

Now in the stationary state, too, θ is proportional to $\sin \phi$, as in (24.4), and therefore in the stationary state the relation between the velocity of the wall and the applied field is

$$v = (\gamma\delta_w/\alpha)H. \tag{24.8}$$

If we put for the equation of motion of a 180° wall

$$m_w\ddot{z} + \beta_w\dot{z} = 2M_sH, \tag{24.9}$$

where $\beta_w\dot{z} = \beta_w v$ represents the damping term, it then follows from (25.8) that

$$\beta_w = 2\alpha M_s/\gamma\delta_w. \tag{24.10}$$

Where $\alpha = 10^{-2}$, $H = 10$ oersteds and $\delta_w = 10^{-5}$ cm, the velocity of the wall follows from (24.8) as approximately 2000 m/s, which is thus of the order of magnitude of the speed of sound. Inside the wall the magnetization is not uniform and deformation will occur of the same kind as volume magnetostriction. The wall movement, then, will be associated with the propagation of a sound wave. Accordingly, the velocity of the wall will show a dispersion near the speed of sound in the material. The maximum value of the angle θ in the centre of the wall is of the order

$$\theta_{\max} \cong H/\alpha(H^A + 4\pi M_s),$$

which, where $H^A \cong 0$ and $4\pi M_s \cong 4000$ gauss, is here of the order of 15°. For larger fields the given derivation is thus no longer valid and an increase in β_w may be expected.

24.3. WALL RESONANCE

It may be assumed that the wall is bound to its equilibrium position with a certain stiffness. The equation of motion (24.9) then becomes

$$m_w\ddot{z} + \beta_w\dot{z} + \alpha z = 2M_sH \tag{24.11}$$

For small damping ($\beta_w{}^2 \ll \alpha m_w$) this equation predicts the occurrence of wall resonance with an angular frequency

$$\omega_r = \sqrt{\alpha/m_w} \tag{24.12}$$

The stiffness α is related to the low frequency permeability μ_0 by

$$\alpha \simeq 16\pi M_s{}^2/l(\mu_0 - 1) \tag{24.13}$$

where l is the thickness of the domains.

CHAPTER VII

METHODS OF MEASURING FERROMAGNETIC PROPERTIES

§ 25. Measurement of Magnetization

25.1. INDUCTIVE METHOD

For measuring magnetization several methods can be used which are based on the various physical laws. One of these is the induction law (2.1). The most common method of measuring magnetization is the ballistic method. The specimen takes the form of a prolate ellipsoid, since in that case, when the external field is uniform, the internal field is also uniform and hence the magnetization too. The experimental set-up is shown in Fig. 25.1. Inside the large coil which supplies the static field H_0 is mounted a short

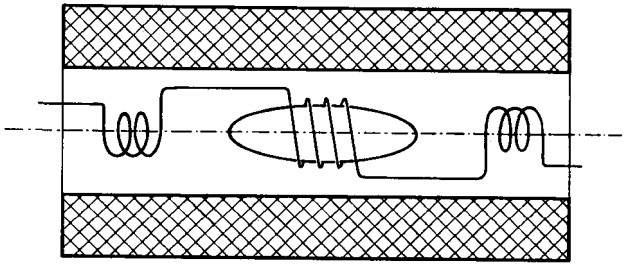

Fig. 25.1. Arrangement for ballistically measuring the magnetization of a prolate ellipsoid.

coil which encloses the specimen as narrowly as possible and which is connected to a ballistic galvanometer. In series with this small coil is an identical but oppositely wound coil, which is set up at some distance from the specimen but is nevertheless still in the static field. Changes in this field then produce no flux change in the galvanometer circuit. The specimen is now withdrawn from the coil so as to give rise to a flux change per turn of:

$$\Delta\Phi = \int (B - H_0)\mathrm{d}A,$$

where

$$B = H_0 + H_D + 4\pi M.$$

The field H_D is proportional to M (see Fig. 1.2) so that M can be calculated

from the maximum deflection of the galvanometer. If the measuring coil does not tightly enclose the specimen, the measured flux will also include some stray field outside the specimen. When the diameter of the measuring coil is small compared with the length of the specimen, we may assume to a good approximation that the external stray field inside the measuring coil is still practically equal to the demagnetizing field H_D inside the ellipsoid so that the correction can easily be applied.

This method can also be used for making an alternating current measurement by letting the specimen vibrate at the boundary between two oppositely wound measuring coils; this induces in the coils an alternating voltage which is proportional to the magnetization and the velocity of the specimen:

$$E \propto (\partial M/\partial z)v_z.$$

This method can be used [Oo1] for measuring the magnetization of very small specimens. The magnetic moment can be treated as that of a point dipole, in which case the field inside the measuring coils can easily be calculated with the aid of (12.3). It is also possible to calibrate with a specimen having a known magnetization.

So far it has been assumed that the magnetizing field is constant. The field can also be varied, for example stepwise by abrupt changes. The induced voltage is then due not only to the change in the magnetization of the specimen, but also to the change in the primary field. If the measuring coil fits exactly around the specimen, the change of B in the specimen is measured directly. This method has to be used when the specimen cannot be pulled out, as for example when measuring hard magnetic material between the poles of an electromagnet. To prevent eddy currents appearing during rapid field variations, the specimen and the yoke must be laminated. If the specimen is not perfectly in contact with the pole surfaces, the field in the specimen will not be equal to that in the gap when the specimen is not present. For example, with an air-gap between the specimen and the pole-piece equal to 1% of the thickness of the specimen, the value of $4\pi M$ being 10,000 gauss, the internal field is 100 oersteds smaller than the external. The internal field must therefore be measured separately. This can be done by making use of the continuity at a surface of the tangential component of the magnetic field. The field directly adjacent to the specimen is measured with a small coil. In this way, however, one measures the field at the distance equal to the radius of the coil around the specimen, which can differ appreciably from the internal field. In this case it is advantageous to use a magnetic potentiometer; see Fig. 25.2. This is a semi-circular, uniformly wound coil. The total enclosed flux is then propor-

tional to $\int H_t dl$ along the centre-line of the coil, which, when placed on the surface of the specimen, is equal to $\int H_t dl$ along its surface between the two ends of the coil, the field being measured exactly along the edge.

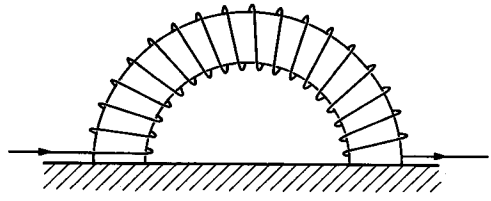

Fig. 25.2. Magnetic potentiometer or Rogowski coil.

In the case of ring-shaped specimens (principally suitable for soft magnetic materials) the total induction is also measured. If the field coil is uniformly wound around the specimen, the internal field is uniform, and the field outside the ring is exactly zero; therefore no correction whatsoever need be applied and the field is found directly from equation (1.1). In the case of straight rods, where the permeability would be too much restricted by the demagnetization, the magnetic circuit of the rod is closed with a yoke of soft magnetic material. If the cross-section of the yoke is large with respect to that of the specimen, the effect of the permeability of the yoke is negligible.

With measurements on a closed magnetic circuit, such as for instance a ferrite ring, only changes in B can be measured. In order to measure magnetization curves it is necessary to start from a known state, which is for instance obtained if the specimen is demagnetized; this can be done by placing it in an alternating field the amplitude of which is gradually reduced from a very high value (sufficient to saturate the specimen) to zero. For measuring hysteresis loops the saturated state is taken as the starting point and measurements are continued until the specimen is saturated in the opposite direction.

Hysteresis loops can be recorded on an x-y recorder with the aid of an integrating circuit [Br 1]. This calls for the use of d.c. amplifiers of high sensitivity, galvanometers with photoelectric cells being suitable for the purpose (see Fig. 25.3).

If the magnetization does not reach its final value immediately after the field is applied (which may be the case, for example, when eddy currents are present) wrong results may be obtained when measuring the hysteresis loop if demagnetization occurs [Sn 2]. The internal field $H_i = H_e - NM$ is then temporarily too large at certain places, and therefore, as a result of hysteresis, there will ultimately be too great a change in the magnetization. A consequence of this can be that the virgin curve (commutation curve)

falls outside the hysteresis loop (Fig. 25.4). With non-conductive ferromagnetic rings errors can occur owing to the fact that, because of the presence of stray capacitances, oscillations appear in the field after interruption of the current. In measurements of the remanent magnetization, for example, this can give rise to appreciable opposing fields, which result in an apparently lower value of the remanence. These oscillations can be adequately damped by applying a resistor R parallel to the primary winding L_x through which

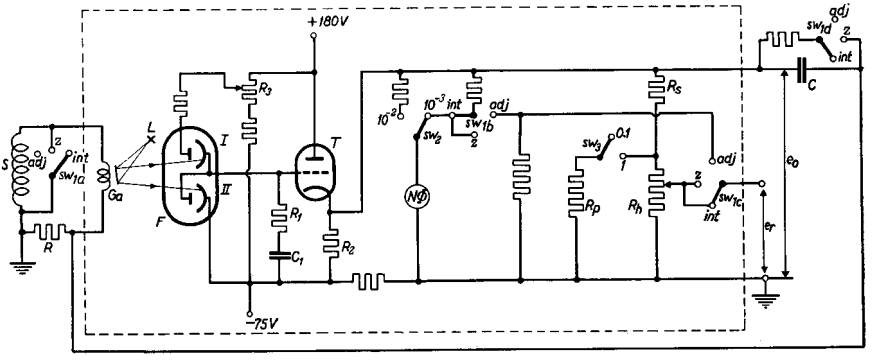

Fig. 25.3. Basic diagram of an integrator for measuring B-H loops. S search coil; R integrating resistor; Ga galvanometer; L Light source for galvanometer; F gas-filled twin phototube; $N\Phi$ meter giving a direct reading of the change of flux linked by the search coil. See [Br 1].

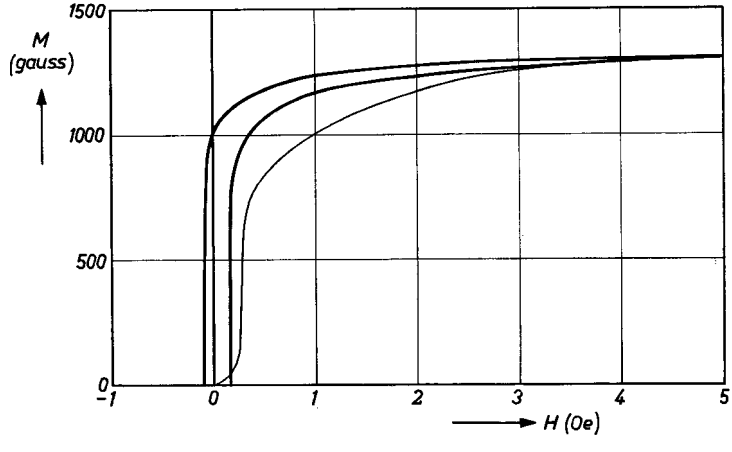

Fig. 25.4. Main loop of a wire of carbonyl iron, as measured by switching on and off the current in the usual way. The virgin curve measured by the "step by step" method, in which the current is increased in small steps, lies outside the loop. (After [Sn 2]).

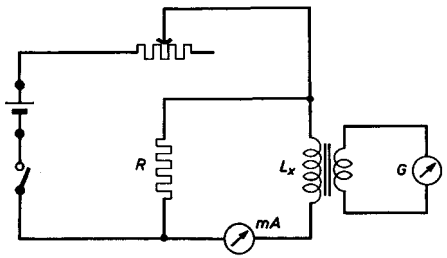

Fig. 25.5. Damping of oscillations by a resistance R parallel to the primary coil of a circuit for measuring magnetization ballistically.

about 10% of the current flows (Fig. 25.5); this makes the L_x/R time of the circuit sufficiently long.

25.2. METHODS UTILIZING THE FORCE ACTING ON A BODY IN A NON-UNIFORM FIELD

Magnetic moments of paramagnetic salts are generally measured by determining the force on the specimen in a non-uniform magnetic field, of which the component in the x direction is equal to:

$$F_x = M\partial H/\partial x = \chi H\partial H/\partial x. \tag{25.1}$$

The magnetic moment is then generally too small to be measured ballistically. However, the forces are soon large enough to be measured accurately. For example where $\chi = 10^{-4}/\text{cm}^3$ and $H = 1000$ Oe and $\partial H/\partial x = 1000$ Oe/cm, the force is 100 dyne per cm^3, although M is still only 0.1 gauss. The force is generally compensated with, say, a spring balance. For ferromagnetics the forces are very considerable.

A method of measuring magnetization exists [Ra1] in which use is made of the second derivative of the field with respect to position; the first derivative may then be zero, *i.e.* the specimen is placed at a position where the field is maximum in the x direction. For deflections in at least one direction at right angles thereto the field is then minimum. However, the specimen is suspended on a pendulum, (Fig. 25.6) so that it can only move in the x direction. Suppose that the field in the vicinity of the maximum can be descibed as

$$H = H_0 - \tfrac{1}{2}ax^2. \tag{25.2}$$

The force $f_x = aMx$ acting on the specimen is thus a harmonic force. Hence the period of oscillation will change according to:

$$\frac{1}{\tau^2} = \frac{1}{\tau_0^2} + \frac{aMV}{4\pi^2 m}, \tag{25.3}$$

where V is the volume of the specimen and m the mass of the pendulum. In most cases it is the weight of the sample that is determined, so that according to (25.3) the magnetization σ per gramme is measured. This method is used only for measuring the moment in high fields. The demagnetizing fields of the often irregularly shaped specimen are therefore unimportant.

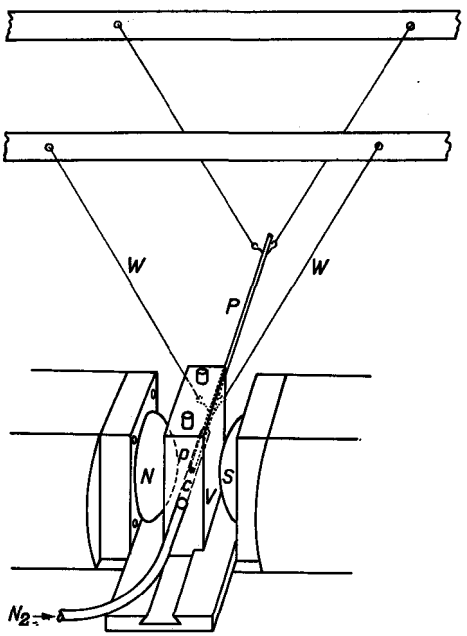

Fig. 25.6. Pendulum device for measuring the magnetization of a specimen in a non-uniform field (after [Ra 1]). Specimen p, pole pieces N and S, horizontal pendulum P, cooling vessel V and nitrogen current N_2.

§ 26. Measurements of Magnetocrystalline Anisotropy Energy

26.1. MEASUREMENT OF MAGNETIC ENERGY

The magnetocrystalline anisotropy energy can be measured from the different trend of the magnetization curves *versus* the field in the easy and difficult directions of magnetization in a crystal. The anisotropy is then equal to the difference in magnetic energy:

$$F_K = \Delta \int H \mathrm{d}M. \tag{26.1}$$

It is not possible from this relation alone to determine the different constants from (11.1) or (11.6). To do this it is first necessary to analyse the form of the M *versus* H curve in the difficult direction. For example, we have seen in § 17 that if we have only $K_1 \neq 0$ in (11.6) for a hexagonal crystal, the M *versus* H curve in the difficult direction is a straight line up to saturation

at $H = H^A$. If K_2 is also taken into consideration, for a preferred direction with the field H in the basal plane the component M_H of M along H satisfies:

$$\frac{2K_1}{M_s} M_H + \frac{4K_2}{M_s^3} M_H^3 = M_s H. \tag{26.2}$$

Thus, if HM_s/M_H is plotted [Su 1] as a function of M_H^2, astraight line is obtained whose point of intersection with the vertical axis is equal to $2K_1/M_s$, the slope being equal to $4K_2/M_s^2$.

For cubic crystalline anisotropy the *M versus H* curves are always curved. The anisotropy constants K_1 and K_2 can then be separately determined from measurements of M as a function of H in different directions, for example in the [100], [110] and [111] directions. The area enclosed between the magnetization *versus* field curves in the [111] and [100] directions is equal to $K_1/3 + K_2/27$, and that between the [110] and [100] directions is equal to $K_1/4$.

26.2. TORQUE METHOD

In the torque method of magnetic anisotropy measurement the specimen is suspended on a torsion spring in a uniform magnetic field H. If this is much stronger than the anisotropy field H^A the magnetization vector will be practically parallel to H. The torque acting on the specimen can then be found simply by differentiation of the crystal anisotropy with respect to the angle concerned. For fields comparable to or smaller than H^A the equilibrium position must first be calculated by, for example in (17.2), putting $\partial F/\partial\theta$ equal to zero. The torque is then

$$T = \mathrm{d}F/\mathrm{d}\alpha = \partial F/\partial\alpha + (\partial F/\partial\theta)\mathrm{d}\theta/\mathrm{d}\alpha,$$

where the last term is zero. For cubic materials and for strong fields we find in the (110) plane

$$T(\theta) = \frac{K_1}{8}(2\sin 2\theta + 3\sin 4\theta) + \frac{K_2}{64}(\sin 2\theta + 4\sin 4\theta - 3\sin 6\theta), \tag{26.3}$$

where θ is the angle of the magnetization with the [100] direction. By harmonic analysis of the measured curve the constants K_1 and K_2 can be determined. For rotation of the magnetization in a (111) plane, only K_2 gives rise to anisotropy owing to the hexagonal symmetry in that plane:

$$T(\theta) = \frac{K_2}{18}\sin 6\theta. \tag{26.4}$$

This method offers advantages and leads to simple results if the applied

field is much larger than the anisotropy fields. If this is not the case the magnetization can only be turned through a small angle out of the preferred orientation, and what in fact is measured is the stiffness with which the magnetization is bound to the preferred direction. In this case the stiffness can more easily be measured by the method described in § 26.3.

26.3. TORSION PENDULUM METHOD

An analogon for the pendulum method of measuring magnetization also exists for the determination of crystal anisotropy. This consists in determining the frequency of the torsional vibration of the specimen around the state of equilibrium in a uniform magnetic field. The stiffness c is then given by (see Fig. 17.1):

$$c = \mathrm{d}^2F/\mathrm{d}\alpha^2 = \partial^2F/\partial\alpha^2 + 2(\partial^2F/\partial\alpha\partial\theta)\mathrm{d}\theta/\mathrm{d}\alpha + (\partial^2F/\partial\theta^2)(\mathrm{d}\theta/\mathrm{d}\alpha)^2 \qquad (26.5)$$

If the moment of inertia of the torsion pendulum is I this magnetic stiffness changes the square of the reciprocal period of oscillation by an amount:

$$\Delta(1/\tau^2) = c/4\pi^2 I. \qquad (26.6)$$

For uniaxial anisotropy described with a constant K_1, equation (26.5) becomes:

$$c = \left(\frac{1}{HM_s\cos(\alpha-\theta)} + \frac{1}{2K_1\cos 2\theta}\right)^{-1}.$$

In weak fields ($H < H^A$) the relation between c^{-1} and H^{-1} is in first approximation linear:

$$c^{-1} \cong \frac{1}{HM_s\cos\alpha} + \frac{\cos 2\alpha}{2K_1\cos^2\alpha}, \qquad (26.7)$$

while for an infinitely strong field the limit value reached is:

$$c_\infty = 2K_1\cos 2\alpha. \qquad (26.8)$$

At $0 < \alpha < 45°$ the stiffness passes through a maximum. These values of α differing from zero can be obtained with a stiff torsion wire. At $\alpha = 0$ the relation is linear for all fields:

$$c^{-1} = \frac{1}{HM_s} + \frac{1}{2K_1} = \frac{1}{M_s}\left\{H^{-1} + (H^A)^{-1}\right\}. \qquad (26.9)$$

The slope of the c^{-1} *versus* H^{-1} straight line is equal to $1/M_s$; for $\alpha \neq 0$ it is generally equal to $1/M_s\cos\alpha$.

26.4. DETERMINATION OF CRYSTAL ANISOTROPY FROM FERROMAGNETIC RESONANCE

With the aid of the general expression (18.10) for the resonance frequency, an anisotropy energy can be determined by measuring the resonance frequency at different orientations of the static magnetic field with respect to the crystal axes. An example of this is given for uniaxial anisotropy in § 18.1. For cubic anisotropy this method has been applied by Bickford [Bi 1], among others. The method determines not only the crystal energy but also the g factor. If for the same resonance frequency the field strengths H_1, H_2 and H_3 have to be applied in the [100], [111] and [110] directions respectively, then the resulting effective field strengths are given by:

$$\begin{aligned}
&[110]\colon\ H_{\text{eff}} = H_1 + \frac{2K_1}{M_s} \\
&[111]\colon\ H_{\text{eff}} = H_2 - \frac{4}{3}\frac{K_1}{M_s} - \frac{4}{9}\frac{K_2}{M_s} \\
&[110]\colon\ H_{\text{eff}} = \left(H_3 - \frac{2K_1}{M_s}\right)^{\frac{1}{2}} \left(H_3 + \frac{K_1}{M_s} + \frac{K_2}{2M_s}\right)^{\frac{1}{2}}.
\end{aligned} \tag{26.10}$$

From the magnitudes of H_{eff} and M_s the quantities g, K_1 and K_2 can be determined. In the case of uniaxial crystals, in which both K_1 and K_2 differ from zero, the g factor can also be anisotropic. By measuring at only one frequency the crystal anisotropy cannot then be determined, and measurements must accordingly be made at more than one frequency.

§ 27. Magnetostriction

27.1. DISPLACEMENT MEASUREMENTS

The magnetostriction of a rod can be measured by the displacement of one of the ends of the rod with respect to the other. There are various methods of doing this, which can also be used for displacements of a non-magnetic nature. First of all there is the purely optical method, in which the displacement is first increased mechanically by for instance a factor of 10 with the aid of a lever, after which the translation is converted into the rotation of a thin spindle on which a mirror is mounted. In this way displacements of the order of 10^{-7} cm can be measured. The method has the advantage that the magnification factor depends only on mechanical quantities, determined by the construction. In principle the method can also be employed at temperatures differing from room temperature. There are also several electrical methods that can be used, in which the displacement is converted into a

change in the capacitance of a condenser or into the change in the mutual inductance between two coils (differential transformer). In the first case a circuit can be detuned so as to produce a different frequency. The beat frequency produced with a signal of the original frequency is then a measure of the displacement. In most cases a null method is made of this device by compensating the variation in capacitance with a variable condenser connected in parallel. The disadvantage here is that the measurement cannot be carried out quickly; quick measurements are usually necessary because of temperature variations. An increase in temperature of about 0.1° gives rise to a strain of 10^{-6}. The differential transformer can be made as a direct-reading instrument. With such small deflections several interfering effects can arise as for example a magneto-caloric effect when the field is switched on rapidly. This can produce temporary changes in temperature of 0.1° C.

27.2. STRAIN MEASUREMENTS

In 1947 Goldman [Go 2] reported how strain gauges, at that time just introduced, could be used for magnetostriction measurements. A folded metal wire, which can have a resistance of the order of 100 ohms, is affixed to the specimen. The magnetostrictive strain causes changes in the resistance of the wire, which can be measured with the help of a Wheatstone bridge. Similar strain gauges are in the other branches to compensate as far as possible for temperature influences. The measurement can be carried out with direct current or low-frequency alternating current ($f < 100$ c/s) since the magnetic material to which the current-carrying wires are affixed can give rise to an inductive effect which changes during magnetization. This method is also very sensitive, being capable of measuring strains up to 10^{-8}. The advantage is that no long rods or rings are needed, an important point in the measurement of single crystals. The minimum dimensions of strain gauges are approximately 2 mm. Additional errors that can occur in this measurement are caused in the first place by the magneto resistance of the wire. At room temperature this is not greater than 10^{-7}. When more than one strain gauge is used in a Wheatstone circuit this effect is approximately eliminated if care is taken to ensure that all the strain gauges are in the same magnetic field.

Strain gauges are not readily usable at low temperatures. In the first place, the temperature coefficient of the resistivity ρ has been made very small at room temperature, $(\Delta\rho/\rho)/°C \simeq 2.10^{-5}$. This is only possible in a small range of temperatures, and at low temperature this coefficient can be a factor of 10 larger. A temperature coefficient as low as this is obtained by

using an alloy with a transition element (*e.g.* Cu-Ni alloy). Even though they do not become ferromagnetic at low temperatures, these alloys nevertheless become strongly paramagnetic and exhibit a very considerable change in resistance ($\Delta\rho/\rho = 10^{-3}$) in a magnetic field. The use of strain gauges at high temperatures imposes restrictions on the paper and the cement employed, so that the upper temperature limit for practical purposes is 50 °C. To sum up, it can be said that strain gauges provide a good method for measuring magnetostriction on single crystals at room temperature, it then being easy to vary the angle between the direction of measurement and the applied voltage.

27.3. STRESS MEASUREMENT

In order to measure the dynamic magnetostriction in small alternating fields (small enough to cause no heating) the rod of magnetic material can be clamped against a piece of piezo-electric material so that the total length remains constant. If the length of the piezo-electric material is small and the cross-section large with respect to the same dimensions of the magnetic specimen, the length of the latter will also remain constant and the magnetostrictive stresses of the magnetic specimen can be measured from the polarization of the piezo-electric material.

§ 28. Methods of Measuring Complex Initial Permeability in Various Frequency Ranges

28.1. INFLUENCE OF DEMAGNETIZATION ON THE APPARENT PERMEABILITY

The relation between the apparent permeability μ_{app} of an ellipsoid and the true permeability μ of the material is:

$$\mu_{app} = \frac{\mu}{1 + \frac{N}{4\pi}(\mu - 1)}, \tag{28.1}$$

where N is the demagnetizing factor of the ellipsoid in the direction of the measuring field, see § 1. High-permeability materials are preferably measured in the shape of ring cores in order to avoid excessively large corrections for demagnetization. The demagnetizing factor of a sample can be determined from the ideal magnetization curve, which is measured by superimposing an alternating magnetic field on a constant magnetic field H in the core. The amplitude of the alternating field is gradually reduced from a high value to zero. The curve which gives the relation between the magnetization obtained in this way and the intensity of the constant magnetic

field is called the ideal magnetization curve. If no demagnetization is present, the curve touches in the origin the magnetization axis, $(dH/dM)_{H=0} = 0$. Owing to demagnetization the curve will make an angle β with the magnetization axis determined by $\tan\beta = dH/dM = N$, where N is the effective demagnetizing factor; see (1.11) and Fig. 28.1. Apart from the demagnetization caused by the shape of the sample, internal demagnetization exists which is related to the presence of a second, non-magnetic phase or pores; see § 43.3. With sintered ferrites, for instance, the angle β gives an impression of the magnitude of the porosity: the angle increases with the porosity. In this case $N_i = \tan\beta$ is called the internal demagnetizing factor. For a ring with a small air gap, (1.13) gives the relation between the relative length of the gap and the corresponding demagnetizing factor.

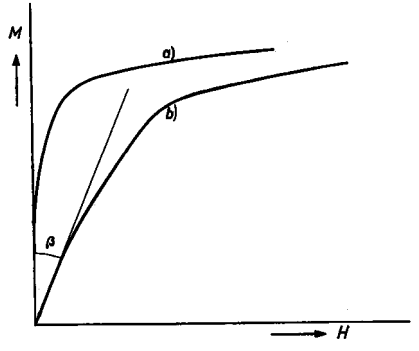

Fig. 28.1. Ideal magnetization curves: *a*) no demagnetization; *b*) demagnetizing factor $N = \tan\beta$

In § 23.1 a complex susceptibility was introduced which describes the linear relationship between an alternating magnetic field and the alternating magnetization which it produces in a ferromagnetic core. The susceptibility is complex owing to damping of the ferromagnetic rotator. Irrespective of the nature of the magnetization process and the nature of the damping, we write for the complex permeability

$$\mu = \mu' - i\mu''. \tag{28.2}$$

The real and the imaginary part of the permeability determine respectively the induction which changes in phase and that which changes 90° out of phase with the field. The phase angle δ or the loss factor $\tan\delta$ is given by

$$\tan\delta = \mu''/\mu'. \tag{28.3}$$

The influence of demagnetization on the magnitude of $\tan\delta$ can easily be calculated. The relation between the externally applied field strength H_e and the internal field strength H is:

$$H = H_e - NM. \tag{28.4}$$

Dividing (28.4) by M gives the general expression:

$$\frac{1}{\chi} = \frac{1}{\chi_{app}} - N, \tag{28.5}$$

where χ_{app} is the apparent susceptibility of the magnetic core. If follows from (28.5) that:

$$\frac{\chi''_{app}}{|\chi_{app}|^2} = \frac{\chi''}{|\chi|^2}. \tag{28.6}$$

Expressed in the permeability this becomes:

$$\frac{\tan \delta_{app}}{\mu'_{app}(1 - \tan^2 \delta_{app}) - 1} = \frac{\tan \delta}{\mu'(1 - \tan^2 \delta) - 1}, \tag{28.7}$$

or in the case of high permeabilities and small loss angles:

$$\frac{\tan \delta_{app}}{\mu_{app}} = \frac{\tan \delta}{\mu}. \tag{28.8}$$

This equation states that if the permeability of a magnetic core is reduced as a result of an air gap or as a result of internal demagnetization, then the loss factor is reduced proportionally.

28.2. BRIDGE METHODS AT LOWER FREQUENCIES

With soft magnetic core materials it is important to know the frequency-dependence of the initial permeability. For lower frequencies, up to about 50 Mc/s, this quantity is generally measured by winding a coil around a core of the material to be investigated. The properties of such lumped impedances are determined with the aid of bridge or resonance circuits. In order to measure the permeability and the dielectric constant of the material from frequencies of about 50 Mc/s up to the centimetric wave range, methods of measurement have been developed in which the magnetic core is incorporated in cavity resonators or transmission lines. From the resultant perturbations the properties of the ferrites can be determined.

A toroidal ferromagnetic core with permeability μ, cross-section A and average diameter D, provided with a winding of N turns, can be treated as an impedance Z consisting of a self-inductance L_s and a resistance R_s in series:

$$\begin{aligned} Z &= R_s + j\omega L_s \\ R_s &= \omega(N^2A/D)\mu'' \cdot 10^8 \text{ ohm} \\ L_s &= (N^2A/D)\mu' \cdot 10^{-8} \text{ henry}. \end{aligned} \tag{28.9}$$

With the aid of bridge circuits, such as the Maxwell and Schering bridge

or a mutual inductance bridge, the two components R_s and L_s of the impedance Z can be measured at low frequencies (below about 50 Mc/s) and μ' and μ'' calculated from the results. Measurements of the quantity μ' alone can be performed with great precision with an Owen bridge. A quick resonance method, which can be used at frequencies between about 50 kc/s and 5 Mc/s in cases where the loss angle is smaller than approximately 0.1 radian, is described in [Bu 1].

When measuring the permeability of ferrite cores at high frequency, the high electric resistance of these materials generally precludes the troublesome skin effect found with metals. However, the cross-section of the ferrite core to be measured may have to be kept small in order to avoid dimensional resonance phenomena. The reason is that, owing to the high dielectric constant of some ferrites, it is possible that at the measuring frequency the wave length in the ferrite will be of the order of magnitude of a linear dimension, which can give rise to standing-wave phenomena in the core (see § 29.1).

In the bridge measurements the ring core must be provided with a winding, which sets a limit to the measuring range. At low frequencies and low magnetic losses in the core the d.c. resistance of the winding can so predominate that there can be no question of an accurate measurement of R_s. A method of eliminating this d.c. resistance is that using the mutual inductance bridge described under (*b*). At higher frequencies a correction can be made for the d.c. resistance, provided it is known at this frequency. To avoid an increase in resistance owing to skin effect, braided copper wire should be used at frequencies higher than 100 kc/s, the thickness of the separate wire strands being adapted to the measuring frequency; up to about 10 Mc/s the rule of thumb is that the wire thickness in microns must be smaller than the wavelength in metres.

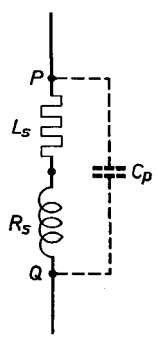

Fig. 28.2. Equivalent circuit of a coil with ferrite core. The stray capacitance is indicated by C_p.

Besides the earlier-mentioned self-inductance L_s and resistance R_s, the complete equivalent circuit also contains the stray parallel capacitance C_p shown in Fig. 28.2. Between the terminals P and Q apparent values R_s' and L_s' are thus measured, which for small values of C_p are related to the true values R_s and L_s by the equations:

$$\begin{aligned} R_s' &\cong R_s/(1 - 2\omega^2 L_s C_p) \\ L_s' &\cong L_s/(1 - \omega^2 L_s C_p) \\ \tan\delta' &\cong (\tan\delta)/(1 - \omega^2 L_s C_p). \end{aligned} \tag{28.10}$$

Consequently the values of μ' and μ'' derived from

L_s' and R_s' according to (28.9) will differ all the more from the real values the larger the value of $\omega^2 L_s C_p$. This is particularly the case at higher frequencies, at which C_p and L_s must therefore be kept as small as possible. To make C_p small the ring can be provided with a special low-capacitance winding, in the manner illustrated in Fig. 28.3. The number of sections can be extended to more than two. Moreover, in cases where the ferrite core has a high dielectric constant, the stray capacitance can be reduced by winding the ferrite core beforehand with an insulating material of low ϵ. The self-inductance L_s cannot be arbitrarily small, since otherwise the stray self-inductances of the supply leads would become relatively important. In that case the core can be wound with metal strip, but it is even better to use a single coaxial winding, a kind of box fitting closely around the ferrite ring.

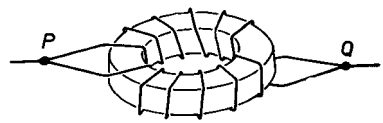

Fig. 28.3. Low-capacitance winding of six turns on ferrite core.

We shall now outline some commonly used methods of measurement with lumped impedances.

(a) Owen Bridge for Accurately Measuring μ' up to a Frequency of about 20 kc/s

The Owen bridge as in Fig. 28.4 is particularly suitable for the accurate measurement of self-inductances [Ow 1]. The conditions of balance are:

$$L_x = R_1 R_3 C_2$$
$$R_x = R_1 C_2 / C_3. \qquad (28.11)$$

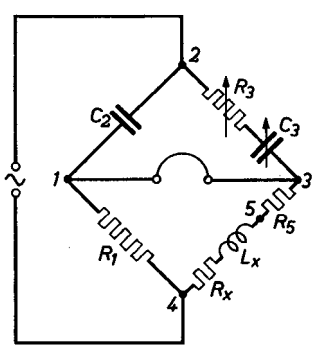

Fig. 28.4. Basic diagram of Owen bridge for measuring self-inductances up to a frequency of about 20 kc/s; see [Ow 1].

Both these conditions can be satisfied by adjusting R_3 and C_3 independently of each other, a facility which makes the bridge most convenient to work with in practice. The value of the self-inductance can be very accurately ascertained if C_2 is a well-calibrated condenser. The equivalent resistance R_x cannot properly be measured with this bridge, since closer analysis of the bridge reveals that the adjustment of C_3 is partly determined by the magnitude of L_x if R_1 is not a pure resistance and the loss factor of C_2 is not zero. Conversely, the setting of R_3 is not influenced by the magnitude of R_x. A difference measurement, carried out by short-circuiting points 4 and 5 and by inserting

between them the unknown self-inductance, shows that there are two settings of R_3 from which L_x immediately follows.

(b) Hartshorn bridge for frequencies from about 30 to 2000 c/s

The principle of the bridge is that the voltages induced in the secondary windings (see Fig. 28.5) by the mutual inductances M_F (with ferromagnetic core) and M_0 (with air core) cancel each other out. The mutual inductance M_0 is variable, and if its magnitude in the compensated state is M, the permeability of the ferrite ring is given by:

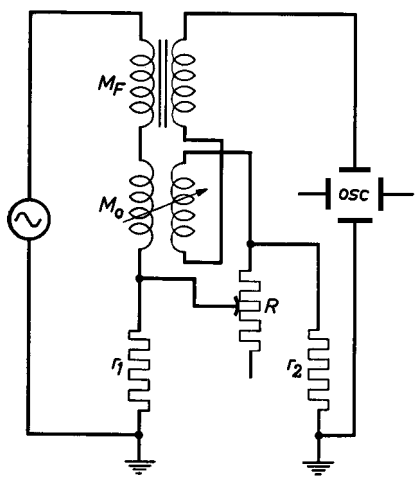

Fig. 28.5. Principle of Hartshorn bridge.

$$\mu = \frac{MD}{0.4\,N_1N_2A} \cdot 10^8, \quad (28.12)$$

where D is the average diameter of the ring and A its cross-section, and N_1 and N_2 are the numbers of primary and secondary turns around the ring respectively. The secondary voltages in M_F and M_0 can never entirely compensate each other, since magnetic losses in the ferrite core cause a phase shift. In order to compensate the resultant voltage component, which is 90° out of phase with the secondary voltage of M_0, another voltage is introduced into the secondary circuit which is proportional to the current I in the primary circuit. The resistances r_1 and r_2 and R in Fig. 28.5 can be replaced by an equivalent resistance r (see [Kl 1]) according to:

$$r = r_1r_2/(r_1 + r_2 + R).$$

By making R large with respect to r_1 and r_2, the value of r can be made small quite simply; hence the voltage Ir, used as compensation voltage in the secondary circuit, can also be arbitrarily small. The loss angle of the ferrite core is then given by

$$\tan \delta = r/\omega M, \quad (28.13)$$

where ω is the angular frequency at which the measurement is performed. The advantage of this method is that the d.c. resistance of the winding around the ferrite core plays no part.

Example: f = 100 c/s $N_1 = 13$, $N_2 = 57$, $D = 2.4$ cm and $A = 0.16$ cm^2.
$M = 16.5$ μH and $r = 0.000{,}9$ ohm
$\mu' = 91$ and $\tan \delta = 0.09$.

(c) Maxwell Bridge for Frequencies up to about 100 kc/s and Modified Schering Bridge up to about 60 Mc/s

The conditions of balance of the Maxwell bridge shown in Fig. 28.6 are:

$$\begin{aligned} L_x &= R_1 R_2 C \\ R_x &= R_1 R_2 / R_4 . \end{aligned} \tag{28.13}$$

Resistances R_1 and R_2 with very small time constants have been described by Köhler and Koops [Ko 3]. All the connections and switches of the bridge should have a very low resistance and reactance. Moreover, all parts must be well screened. A construction with Wagner earth is represented in [Ko4]. Self-inductances of 200 μH and a loss factor $\tan\delta$ of about 0.22 can be measured by this bridge with an accuracy of 0.1% in the range from 0.5 to 100 kc/s.

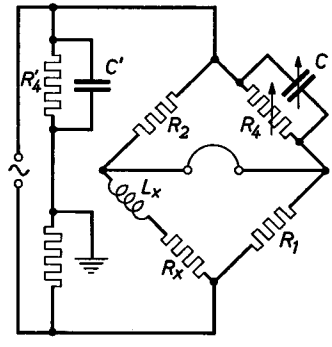

Fig. 28.6. Principle of Maxwell bridge with Wagner earth.

For higher frequencies a modified Schering bridge has been developed by Sinclair (Radio-Frequency Bridge Type 916-A, General Radio Company), by means of which reactances can be measured in the frequency range between 300 kc/s and 60 Mc/s, [Si 1].

28.3. WAVE METHODS AT HIGHER FREQUENCIES

(a) Coaxial Resonator from 10 Mc/s to 2000 Mc/s

At higher frequencies the accurate measurement of the properties of lumped impedances is almost impossible owing to the self-inductance and stray capacitances of the leads. One of the commonly used devices for measurements at these frequencies is a quarter-wavelength resonator. A coaxial line of a certain length l (see Fig. 28.7) is magnetically coupled via a small loop to an oscillator. The voltage appearing at the top of the resonator is measured with a crystal detector D mounted near the top of the inner conductor. The couplings between the coaxial resonator and the oscillator and between the detector and the resonator must be so weak as to make the amplitude and the frequency of the oscillator independent of the tuning

of the resonator and also to prevent the detector from influencing the resonator. The principle of the measuring method is that a ferrite ring F is inserted in the coaxial line at a position where the magnetic field strength has a maximum and where the electric field strength is approximately zero. For small disturbances of the line the displacement of the resonance frequency is proportional to $\mu' - 1$ of the ferrite. Also the width of the resonance line of the loaded cavity is broadend due to the losses in the ferrite. This line broadening is proportional to μ'' of the ferrite. In practice the resonance frequency is kept constant, while the length of the line is varied (see Fig. 28.8). In principle we now have all the information which, together with a knowledge of the dimensions of the ring and the line, is required for calculating the complex permeability. The equations are greatly simplified if the displacement of the resonance frequency is also determined for the case where a copper ring of the same dimensions [Li 1] is

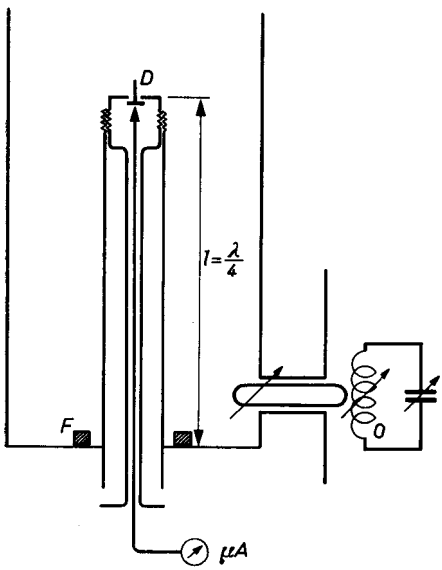

Fig. 28.7. Coaxial line ($l = \lambda/4$) for measuring μ' and μ'' at high frequencies. O oscillator, D detector coupled to the electric field, F ferrite ring (according to [Bu 1]).

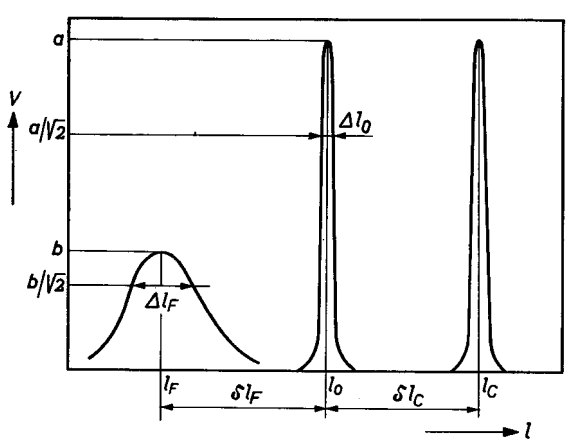

Fig. 28.8. The changes δl_F and δl_C in the length l_0 of a tuned coaxial quarter-wave line as a result of introducing a ferrite or copper ring respectively. The frequency is kept constant.

inserted in the line. The field inside the copper is zero, so that the ring can be described as having $\mu = 0$, which can be used for calibration. If the quality of the line with ferrite ring is high enough (>10) and if the relative detuning $\delta l_F/l_0$ is small with respect to 1, we may write:

$$\begin{aligned} \mu' - 1 &\cong -\delta l_F/\delta l_C \\ \text{and } \mu'' &\cong (\Delta l_F - \Delta l_0)/2\delta l_C \end{aligned} \tag{28.14}$$

For the definitions of the symbols see Fig. 28.8. The measurements can also be carried out by varying the frequency and keeping l_0 constant. The line can be terminated by a variable capacitance, so that the frequency range is extended to lower values; see [Bu 1]. Since the ferrite ring fills only a very small part of the line it is possible to measure ferrites with large loss angles, the quality factor of the line remaining higher than about 10. To avoid the presence of an electric field in the ring, the axial dimension of the ring must be small. At very high frequencies care must be taken that the radius of the outer conductor remains smaller than 1/3 of the wavelength, since otherwise a wave guide mode can appear in the coaxial line in addition to the principal mode, which would give rise to radiation losses and make accurate measurement impossible.

(b) Standing Wave Method

A method of simultaneously measuring the complex dielectric constant and magnetic permeability at centimetric waves has been developed by Roberts and Von Hippel [Ro 2]. A coaxial line is terminated, as in Fig. 28.9, by a ferrite ring. The ring must fit closely into the coaxial tube. The line is first short-circuited immediately behind the ferrite ring (situation I), and

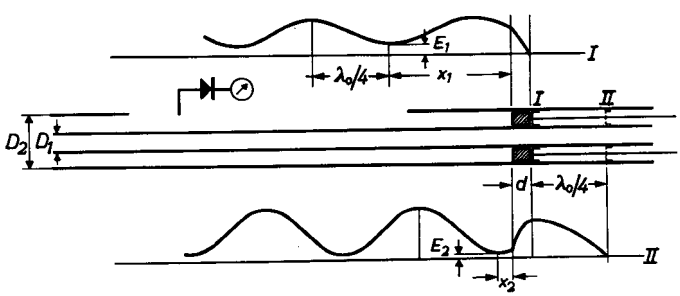

Fig. 28.9. A coaxial line terminated at one end by a ferrite ring. The waveform of the voltage in the line is given for situation I, in which the line is short-circuited by a plunger immediately behind the ferrite ring, and for situation II, in which the plunger is at a distance of $\lambda/4$ behind the ferrite.

afterwards at a quarter-wave distance from the specimen (situation II). What is now measured for situation I as well as for situation II is the distance from the first voltage minimum to the ferrite ring, x_1 and x_2 respectively, together with the voltage standing-wave ratios, E_1 and E_2 respectively. (That is to say the ratio between the voltage in the minimum and that in the maximum.) The impedances Z_1 and Z_2 in both cases can be computed as:

$$Z_j/\zeta = (E_j - i \tan 2\pi x_j/\lambda_0)/(1 - iE_j \tan 2\pi x_j/\lambda_0), \; j = 1,2$$

where ζ is the characteristic impedance of the line, which depends on the ratio of the diameters D_2/D_1, and λ is the wavelength; see [Sl 1]. From the complex impedances Z_i we can calculate ϵ and μ with the help of the relations:

$$\begin{aligned} \tan(2\pi d/\lambda_0)\sqrt{\mu\epsilon} &= \sqrt{Z_1/Z_2} \\ \sqrt{\mu/\epsilon} &= (1/\zeta)\sqrt{Z_1 Z_2}, \end{aligned} \tag{28.15}$$

where d represents the height of the ring. For maximum accuracy the height of the ring should fulfil the condition $d \cong \lambda/8\sqrt{\epsilon\mu}$, provided the losses are small; where the losses are larger the ring must be thinner. Considerable errors can be made if the ring does not fit tightly into the coaxial line.

(c) *Cavity Resonator*

At wavelengths smaller than about 30 cm the permeability of a ferrite can be measured on small rods in a cavity resonator, as shown in Fig. 28.10. With this method, as with the quarter-wave resonator, the detuning and the change in quality caused by the ferrite rod are measured. The specimen should be sufficiently thin to ensure that the electric field in the rod will be small. The theory of electromagnetic waves in resonant cavities is given in [Ca 1].

The permeability of ferrite spheres can also be measured with resonant

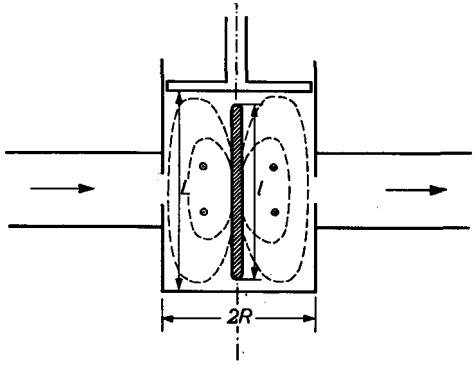

Fig. 28.10. The TE 011 cavity resonator for measuring the permeability of ferrite rods at centimetre waves. The ferrite rod is mounted axially. The electric ($\odot$, $\otimes$) and magnetic (broken curves) lines of force are indicated.

cavities, although at large permeabilities this is difficult owing to demagnetization. In the case of a sphere the apparent permeability μ_{app} is related to the true permeability of the material according to (28.1) as $\mu_{app} - 1 = 2(\mu - 1)/(\mu + 2)$. However, with small spheres ferromagnetic resonance experiments can readily be carried out in a cavity in the presence of an external magnetic field (see [Be 1]). Such experiments also provide information on line widths (hence on the damping in the ferrite) and on g factors (see § 20). At resonance the resonant cavity is detuned and, above all, damped.

The properties of the material, provided the sphere is small enough, can be derived from the complex detuning, which according to perturbation theory is given by:

$$\delta\omega/\omega = (\boldsymbol{H}_0\boldsymbol{M} + \boldsymbol{E}_0\boldsymbol{P})/4W \tag{28.16}$$

where $\boldsymbol{H}_0$ and $\boldsymbol{E}_0$ are the field strengths at the position of the sphere in the empty cavity, W the energy content of the empty cavity and $\boldsymbol{M}$ and $\boldsymbol{P}$ the magnetic and electric dipole moments respectively of the sphere. For constant μ and ϵ these are therefore proportional to M and P, although the demagnetizing and depolarizing effects must be taken into account. For example, with a small sphere of radius R, we may write:

$$\boldsymbol{M} = \frac{\mu - 1}{\mu + 2} R^3\boldsymbol{H}_0 \text{ and } \boldsymbol{P} = \frac{\epsilon - 1}{\epsilon + 2} R^3\boldsymbol{E}_0. \tag{28.17}$$

For the general susceptibility tensor (28.16) becomes

$$\delta\omega/\omega = [\chi_{xx}|h_x|^2 + \chi_{xy}h_x^*h_y + \chi_{yx}h_yh_x^* + \chi_{yy}|h_y|^2]/4W, \tag{28.18}$$

where V is the volume of the specimen. The condition for the validity of these formulas is that $\boldsymbol{H}_0$ and $\boldsymbol{E}_0$ should be uniform over the sphere, as well as the $\boldsymbol{H}$ and $\boldsymbol{E}$ thereby generated. This is the case if the wavelength employed inside the specimen is large with respect to the dimensions. It is precisely at resonance that this condition is not always satisfied. From (23.9) it then follows th at χ'' is of the order of $M_s/\Delta H$, hence for ferrites with $M_s = 300$ gauss, μ'' is of the order of 100 when $\Delta H = 50$ gauss. Furthermore, ϵ is of the order of 10, so that the wave length in the material can be roughly 30 times smaller than in vacuo. For $\lambda = 3$ cm, then, the diameter of the sphere must not be much larger than a few tenths of a millimetre and even less for shorter wave lengths ([Be 2] and [Ya 2]). This requirement of smallness need not be satisfied if the material has the form of a disc and is fixed against a wall. In that case the requirement need only be fulfilled by the thickness of the plate, which can

easily be made small by grinding. A further requirement is that the sphere should not be placed too close to the wall, in view of the image effect. With the platelet in question it is also necessary to take into account the fields produced in the wall by the precessing magnetization. The magnetic lines of force of the high-frequency field must remain parallel to the conductive wall. Polder [Po 2] has pointed out that this can be taken into account by including the mirror image of the ferrite platelet in the considerations. The demagnetizing coefficients in the resonance condition (18.12) are then slightly altered. The static demagnetizing field in the x direction does not change, and is put equal to NM. The demagnetizing fields N_yM and N_zM, which increase the resonance frequency, are now no longer determined by the small demagnetizing factor N of the round platelet, but by the demagnitizing factor of the platelet plus its mirror image; for the alternating magnetizing parallel and perpendicular to the wall they are $2N$ and 4π respectively. When the applied static field H lies in the plane of the disc, the resonance frequency is given by:

$$\omega_r = \gamma\sqrt{[H + (4\pi - N)M][H + NM]}. \tag{28.18}$$

§ 29. Loss Phenomena Related to the Dimensions of the Specimen

29.1. SKIN EFFECTS AND DIMENSIONAL RESONANCES

The propagation of an alternating magnetic field in a conducting dielectric is governed by Maxwell's equations:

$$\begin{aligned} \text{curl } \boldsymbol{H} &= 0.4\pi\sigma\boldsymbol{E} + i\omega(\epsilon' - i\epsilon'')\boldsymbol{E}/300c \\ \text{curl } \boldsymbol{E} &= -i\omega(\mu' - i\mu'')\boldsymbol{H}.10^{-8} \end{aligned} \tag{29.1}$$

In the following we replace $\epsilon'' + 120\pi c\sigma/\omega$ by ϵ'', and we obtain for the wave equation:

$$c^2\Delta\boldsymbol{H} = -\omega^2|\epsilon||\mu|e^{-i(\delta e + \delta m)}\boldsymbol{H}, \tag{29.2}$$

where $|\epsilon|$ and $|\mu|$ are the absolute values of the total dielectric constant and the permeability, respectively. Further δ_e is the total electric loss angle and δ_m the magnetic loss angle. When a plane electromagnetic wave (propagating in the positive x direction), with magnetic field H_y falls normally upon the plane surface of an isotropic medium, we have the solution:

$$H_y = H_y{}^0\, e^{-x/d - 2\pi ix/\lambda}, \tag{29.3}$$

giving for the skin depth d:

$$1/d = (\omega/c)(|\epsilon||\mu|)^{\frac{1}{2}} \sin \tfrac{1}{2}(\delta_e + \delta_m), \tag{29.4}$$

and for the wavelength λ within the material:

$$2\pi/\lambda = (\omega/c)(|\epsilon|\cdot|\mu|)^{\frac{1}{2}} \cos \tfrac{1}{2}(\delta_e + \delta_m). \tag{29.5}$$

The conditions for magnetic metals with negligible magnetic losses are

$$\begin{gathered} |\epsilon| \cong 120\pi c\sigma/\omega;\ \delta_e \cong \pi/2 \text{ and } \delta_m = 0, \text{ so that} \\ 2\pi/\lambda = 1/d = (0.2\pi\mu\omega\sigma)^{\frac{1}{2}} \cdot 10^{-4} \end{gathered} \tag{29.6}$$

Brockman *et al.* [Br 1] discovered that under certain conditions the apparent permeability and dielectric constant of ferrites can be strongly frequency-dependent. In these cases the wavelength of the electromagnetic waves inside the material, see (29.5), is about twice the minimum dimension of the core in which wave propagation takes place, so that these dimensional resonances are already found at relatively low frequencies in ferrites showing at the same time a high value of ϵ and of μ. Fig. 29.1 represents relative values of the real part of ϵ and μ as measured by Brockman *et al* for samples of manganese zinc ferrites with different dimensions. The dispersions found for ϵ' and μ' depend on the dimensions of the specimen, and are completely absent for the very thin specimen. The frequency-dependence of μ' found in a laminated core is caused by the ferromagnetic resonance phenomenon to be discussed in § 50.1. A static magnetic field shifts the dimensional re-

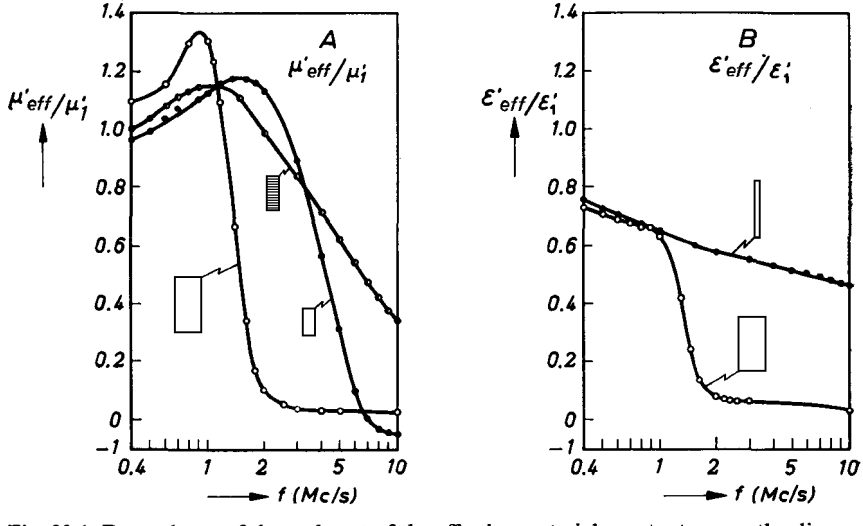

Fig. 29.1. Dependence of the real part of the effective material constants upon the dimensions of the specimen (experimental). Specimen cross-sections drawn to scale for each curve. Data given as the ratio of the effective constant to the real part of the corresponding constant at 1000 cycles. (*A*) Permeabilities. (*B*) Dielectric constant (according to [Br 2]).

sonance phenomena to higher frequencies [Mo 1] as a consequence of the resulting decrease in permeability. This provides a means of measuring at high frequencies the dielectric constant of ferrites having a high initial permeability, without any interference from dimensional effects.

29.2. EDDY-CURRENT LOSSES

Where the skin depth d is very large compared with the thickness of the sample, the influence of eddy currents on the magnetic field is entirely negligible, and the losses due to eddy currents can be calculated easily. The amplitude of the electric field strength E_x at a distance x from the axis of a cylinder (see Fig. 29.2) in which a magnetic induction varies sinusoidally in time with an amplitude B_{max} is given by:

$$E_x = \pi f x \; B_{max} \cdot 10^{-8} \text{ volt/cm.} \tag{29.7}$$

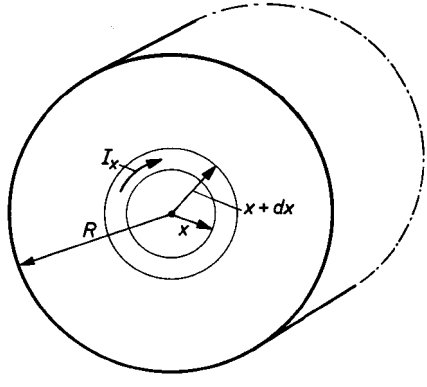

Fig. 29.2. Rectangular cross-section through a cylinder with radius R. Eddy current I_x in the hollow cylinder with radius x, thickness dx and length 1 cm.

When the magnetic material has a resistivity ρ, the energy dissipation in a cylinder with radius R is:

$$W = (\pi^2 f^2 B^2_{max} R^2/4\rho) \cdot 10^{-16} \text{ watt/cm}^3,$$

corresponding to a loss factor tan δ_e:

$$\tan \delta_e = (\pi^2 f \mu R^2/\rho) \cdot 10^{-9}.$$

Analogous expressions for plates and spheres are given in Table 29.I. To give some idea of the order of magnitude of the eddy-current loss factor, a survey for some materials is given in Table 29.II.

It appears of that the amount of eddy-current losses derived from loss measurements of ferromagnetic materials is always larger than is calculated from the resistivity. This discrepancy (eddy-current anomaly) can be ascribed to the inhomogeneity of the flux changes, due to Weiss-domain

TABLE 29.I

EDDY-CURRENT LOSSES W AND EDDY-CURRENT LOSS FACTOR TAN δ_e FOR SOME SIMPLE BODIES (B_{max} EXPRESSED IN GAUSS, R IN CM, AND ϱ IN OHM CM)

Body	W 10^{-16} watt/cm^3	tan δ_e	R
plate	$(2\pi^2/3) f^2 B^2_{max} R^2/\rho$	$(8\pi^2/3)(fR\mu^2/\rho) \cdot 10^{-9}$	thickness $2R$
cylinder	$(\pi^2/4 f^2 B^2_{max} R^2/\rho$	$\pi^2(f\mu R^2/\rho) \cdot 10^{-9}$	radius
sphere	$(\pi^2/5) f^2 B^2_{max} R^2/\rho$	$(4\pi^2/5)(f\mu R^2/\rho) \cdot 10^{-9}$	radius

TABLE 29.II

EDDY-CURRENT LOSS FACTORS FOR SOME MAGNETIC CORES IN THE SHAPE OF PLATES AT A FREQUENCY f.

Material	μ_0	ρ ohm cm	f kc/s	Thickness	tan δ_e
Permalloy	7000	$2 \cdot 10^{-5}$	5	10 micron	10^{-2}
$Mn_{0.48}Zn_{0.48}Fe_{2.04}O_4$	1000	10^2	100	2 cm	10^{-2}
$NiFe_2O_4$	10	10^6	100,000	2 cm	10^{-5}

structure (magnetization by wall displacements) and the polycrystalline state of the sample [St 1, Wi 2]. Suppose that in the cylindrical rod the Weiss domains or grains are very small as compared with the outer dimensions of the sample. For the magnetically homogeneous material a varying axial magnetic field will produce the tangential electric field E according to (29.7), which has at any instant of time a constant magnitude along a concentric circle perpendicular to the axis of the rod. In the real material the contour integral $\int E_l \mathrm{d}l$ along this circle is the same as in the homogeneous material, but E fluctuates both in magnitude and in orientation. Consequently the energy dissipation W, obeying

$$W = (1/\rho) \int E^2 \mathrm{d}V = (1/\rho) \int \mathrm{d}S \int E^2 \mathrm{d}l,$$

is greater than in the homogeneous case. Here $\mathrm{d}S$ is a surface element perpendicular to the concentric circle going through it. For a special configuration this anomaly was calculated by Williams *et al.* [Wi 2], and amounted to a factor of about 3.

CHAPTER VIII

INTRINSIC PROPERTIES OF FERRITES WITH SPINEL STRUCTURE

§ 30 Chemical Composition

The general chemical formula of ferrites possessing the structure of the mineral spinel, $MgAl_2O_4$, is $MeFe_2O_4$, where Me represents a divalent metal ion with an ionic radius approximately between 0.6 and 1Å. In the case of simple ferrites, Me is one of the divalent ions of the transition elements Mn, Fe, Co, Ni, Cu and Zn, or Mg and Cd. A combination of these ions is also possible; we then speak of a solid solution of two ferrites, of mixed crystals or, in general terms, of a mixed ferrite. Furthermore, the symbol Me can represent a combination of ions which have an average valency of two; for example Li^{I} and Fe^{III} in lithium ferrite, $Li_{0.5}Fe_{2.5}O_4$. A particular case is the ferrimagnetic γFe_2O_3, which has the spinel structure and whose chemical formula can be written formally as $\square_{1/3}Fe_{8/3}O_4$, the symbol $\square$ representing a vacant lattice site ([Ve 1], [Ha 1]). In this case Me represents the combination of vacancies and trivalent iron ions in the ratio 1 : 2.

The trivalent iron ions (ferric ions) in $MeFe_2O_4$ can completely or partly be replaced by another trivalent ion such as Al^{III} or Cr^{III}, giving rise to mixed crystals with aluminates and chromites. These compounds are also ferrimagnetic at room temperature if the non-magnetic ions are present in not too large concentrations. If the ferric ions are partly replaced by one of the tetravalent ions Ti^{IV} or Ge^{IV}, the valency of an equal part of the ferric ions is lowered by one. A great variety in the chemical composition of ferirmagnetic oxides with spinel structure is possible [Go 3].

Gorter [Go 4] has pointed out that solid solutions of spinels can occur with compounds which either do not exist themselves or possess a different crystal structure: for example ($Na_{0.5}Fe_{2.5}O_4$) does not exist, but can give a solid solution with $Li_{0.5}Fe_{2.5}O_4$; up to 40% of the lithium ions in the latter compound can be replaced by sodium ions. The ferrite $CaFe_2O_4$ has an orthorhombic structure [De 1], but in $ZnFe_2O_4$ at high temperatures up to 35% of the zinc ions can be replaced by calcium ions without altering the structure.

Certain ferrimagnetic spinels are known, where the oxygen is replaced by sulphur [Lo 1]. The Curie temperatures are usually low and we shall not discuss these substances further.

The valency of the metal ions in ferrites can be determined by an analysis of the oxygen concentration. A difficulty is that one is never certain that different ions will not occur in more than one valency state. In the case of $MnFe_2O_4$, for example, an oxygen analysis does not reveal whether the formula is $Mn^{II}Fe_2^{III}O_4$ or $Mn^{III}Fe^{II}Fe^{III}O_4$. The ferrite $Cu_{0.5}Fe_{2.5}O_4$ constitutes an unsolved problem, since it is not known with certainty whether in this substance all iron ions are trivalent and the copper ion monovalent, or whether it is a mixed crystal of $Cu^{II}Fe_2O_4$ and $Fe^{II}Fe_2O_4$ ([Ko 5] and [Be 3]). For a discussion of this substance see [Go 5]. In many cases a magnetic property, in this case the saturation magnetization (§ 33), can decide between the possible chemical formulas. If it appears from oxygen analysis that the sum of the valencies of the metal ions per formula unit is greater than eight, this points to unoccupied metal ion sites, which means that the ferrite is a mixed crystal with γFe_2O_3.

§ 31. Crystal Structure

31.1. ELEMENTARY CELL OF THE SPINEL LATTICE

The spinel structure takes its name from the mineral $MgAl_2O_4$, which crystallizes in the cubic system. This crystal structure was first determined by Bragg [Br 3] and by Nishikawa [Ni 1]. The smallest cell of the spinel lattice that has cubic symmetry contains eight "molecules" of $MeFe_2O_4$. The relatively large oxygen ions form an f.c.c. lattice. In this cubic close-packed structure two kinds of interstitial sites occur, the tetrahedral and the octahedral sites which are surrounded by 4 and 6 oxygen ions respectively. In the above-mentioned cubic unit cell, 64 tetrahedral sites and 32 octahedral sites are present, of which only 8 and 16 respectively are occupied by metal ions (called *A* and *B* sites respectively). To describe the structure one can best subdivide this elementary cube with edge *a* into eight octants with edge $\frac{1}{2}a$, as shown in Fig. 31.1. The anions (oxygen ions) are positioned in

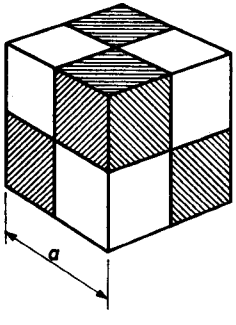

Fig. 31.1. The cube represents symbolically the elementary cell of the spinel lattice. The four shaded and the four non-shaded octants are occupied by the metal ions in the same way as indicated in Fig. 31.2.

the same way in all octants. Each octant contains four anions, which form the corners of a tetrahedron as shown in Fig. 31.2. The edge of the f.c.c. oxygen lattice is $\frac{1}{2}a$. As regards the positions of the cations, the octants in the elementary cube that have only one edge in common are identical (see Fig. 31.1). In Fig. 31.2 the positions of the ions are indicated in two

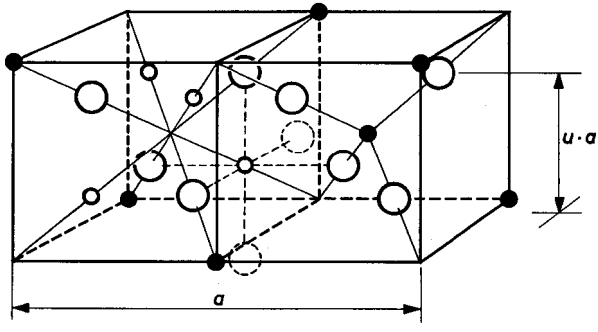

Fig. 31.2. Two octants of the spinel structure. The large spheres represent the oxygen ions. The small black and white spheres represent the metal ions on tetrahedral and octahedral sites, respectively.

adjacent octants. The occupied tetrahedral sites of one of the octants are thus in the centre and on four of the eight corners of the octant. In the adjacent octant the central site is not occupied by a metal ion but, owing to translation symmetry, half of the corner sites are again occupied. It can be seen that the occupied tetrahedral sites (*A* sites) form two interpenetrating f.c.c. lattices having an edge *a*, which are displaced with respect to each other over a distance $\frac{1}{4}a\sqrt{3}$ in the direction of the body diagonal of a cube. The occupied octahedral sites (*B* sites) are found only in the other type of octant. The four metal ions are situated at sites analogous to those of the oxygen ions, *i.e.* on one quarter length of the diagonal from the other ends of the four body diagonals of the octant. Consequently the oxygen and (octahedral) metal ions in this octant together span a cube with edge $\frac{1}{4}a$. All octahedral ions together lie on four interpenetrating f.c.c. lattices with edge *a*, which are displaced with respect to each other over a distance $\frac{1}{4}a\sqrt{2}$ in the directions of the face diagonals of the cube.

The surrounding of a tetrahedral ion by the other ions has strictly cubic symmetry. This is not the case for an individual octahedral ion. The octahedral ions, of course, are cubically surrounded as far as concerns the oxygen ions in the ideal lattice, but not as regards their environment by the neighbouring metal ions. Fig. 31.3 shows the environment of *B* ions by other

B ions. The two cubes shown do not lie each in one octant of Figs. 31.1 or 31.2: four *B* ions lie in one particular octant, the three other *B* ions belong to three different octants. It can be seen from this that the symmetry of the environment of an octahedral site by nearest metal neighbours is lower than cubic, and that only one of the [111] directions is an axis of symmetry. However, in the whole lattice cell all [111] directions occur equally as symmetry axis, so that the overall symmetry nevertheless remains cubic.

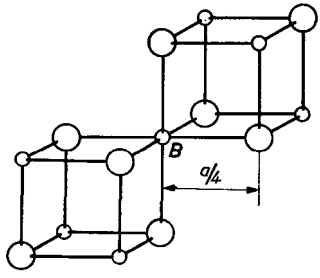

Fig. 31.3. The nearest neighbours of a cation on an octahedral (*B*) site in the spinel structure. Large spheres are oxygen ions, small spheres are metal ions on octahedral (*B*) sites.

While Fig. 31.3 indicates the surrounding of an octahedral ion, Fig. 31.4 gives the environment of an oxygen ion by its nearest (metal) neighbours. These are one *A* ion and three *B* ions. This unit can be regarded as the basic component of the spinel lattice. Each *A* ion belongs to four of such units and each *B* ion to six. The direction O—*A* is one of the body diagonals of the cube, and the directions O—*B* are along the cube edges.

31.2. THE OXYGEN PARAMETER *u*

The statement in § 31.1 that the oxygen ions form an f.c.c. structure is true only in first approximation. In reality slight deviations are found owing to a deformation caused by the metal ions. The tetrahedral sites, which are smaller than the octahedral ones, are in ferrites and many other oxidic spinels too small to contain a metal ion, if we regard the metal ions as well as the oxygen ions as solid spheres. A consequence is that all tetrahedral sites are expanded by an equal displacement of the four oxygen ions outwards

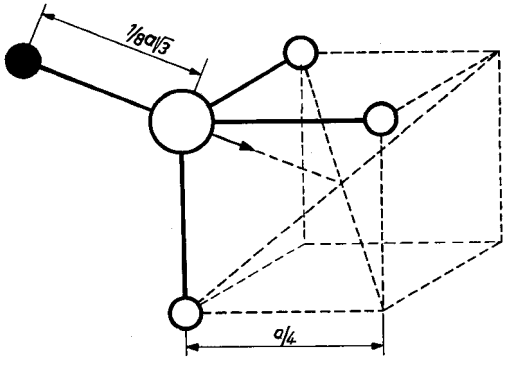

Fig. 31.4. The nearest neighbours of an oxygen ion in the spinel structure. Small open spheres denote metal ions on octahedral (*B*) sites. The black sphere denotes a metal ion on a tetrahedral (*A*) site. The arrow indicates the direction in which the oxygen ion is moved in the case where $u > 3/8$.

along the body diagonals of the cube (see Fig. 31.2). These four oxygen ions thus still occupy the corners of an enlarged tetrahedron, so that the surrounding of each *A* ion retains cubic symmetry. However, the four oxygen ions of the "octahedral octants" in Fig. 31.2 are shifted in such a way that this oxygen tetrahedron shrinks by the same amount as the first expands. This is also the case as regards the oxygen ions indicated in Fig. 31.3. It can be seen that, as a result, the oxygen surrounding of each *B* ion no longer has cubic symmetry, but a symmetry similar to that of the neighbouring *B* ions. In Fig. 31.4 the oxygen ions move along the arrow. A quantitative measure of the displacement is the oxygen parameter *u*, given by the distance shown in Fig. 31.2 between an oxygen ion and a face of the cube, which is put equal to *au*. The ideal f.c.c. parameters correspond to:

$$u_{id} = \tfrac{3}{8}.$$

In the above-mentioned case therefore $u > u_{id}$. Table 31.III gives some values of the parameter *u* found with the aid of X-ray or neutron diffraction. Whereas the displacements of the oxygen ions discussed above make the tetrahedral sites larger, the octahedral sites are reduced in size so that the sizes of the two interstitial sites become more equal. A simple calculation shows that for small displacements the radii of the spheres in both types of interstitial sites are given by:

$$\begin{aligned} r_A &= (u - \tfrac{1}{4})a\sqrt{3} - R_0 \\ r_B &= (\tfrac{5}{8} - u)a - R_0, \end{aligned} \qquad (31.1)$$

where R_0 is the radius of the oxygen ion.

31.3. DISTRIBUTION OF THE METAL IONS OVER OCTAHEDRAL AND TETRAHEDRAL SITES

We have seen that in the elementary cell of the spinel structure eight tetrahedral and sixteen octahedral sites are occupied by metal ions. Now the question may be asked, how are the divalent and trivalent metal ions distributed over the interstitial sites present? Initially this was thought to be no problem. It was believed that the eight divalent ions were in the eight available tetrahedral sites and the sixteen trivalent ions in the sixteen octahedral sites. In many cases this is in fact so, as for example in the mineral spinel, $MgAl_2O_4$, which is therefore known as a *normal* spinel. Barth and Posnjak [Ba 1] have shown, however, that this simple assumption is by no means correct in all cases. By X-ray diffraction studies of a number of spinels in which the two kinds of metal ions show a sufficiently large difference in scattering power, they were able to demonstrate that spinels also occur with

the eight divalent ions in eight of the sixteen available octahedral sites, and with the sixteen trivalent ions uniformly distributed over the remaining sites. The eight divalent and the eight trivalent ions are in this case distributed at random over the sixteen octahedral sites (for exceptions see § 31.4). Spinels having an ionic distribution of this nature are called *inverse* spinels.

Experimentally there are three different ways of acquiring information on the distribution of the ions over the available sites in magnetic compounds, namely, with the aid of X-ray diffraction, neutron diffraction and from the magnitude of the saturation magnetization at the absolute zero of temperature. The scattering cross-section of atoms for X-rays is determined by the number of electrons in the atom. For this reason there is only a slight difference in the scattering power of the atoms of transition elements, and therefore the distribution of these ions amongst the spinel lattice cannot usually be ascertained in this way. The scattering power for thermal neutrons is partly determined by the magnetic moment of the nucleus of the atom, due to interaction with the neutron spin. This often varies considerably for atoms having roughly the same number of electrons, so that neutron diffraction is able to provide information on the occupation of the two spinel sites by ions of the transition elements. It can also provide information on the value of the oxygen parameter and on the magnitude and orientation of the magnetic moments of the ions. From X-ray examinations it has been found [Ba 1] that aluminates and chromites with spinel structure are normal. In the case of ferrites the X-ray scattering power is often not sufficiently different for the various ions to provide any information on the ion distribution. Indirect derivations from lattice constants led to the conclusion [Ve 2] that zinc and cadmium ferrite are normal and the other ferrites inverse. Neutron diffraction experiments have largely confirmed this conclusion. Shull *et al.* [Sh 1] found that Fe_3O_4 is an inverse spinel. Hastings and Corliss [Ha 2] found that $NiFe_2O_4$ is certainly inverse and $ZnFe_2O_4$ normal. It is interesting that the X-ray diagrams of both these substances are identical, since Ni^{II}, Fe^{III} and Zn^{II} have practically the same X-ray scattering properties. The scattering of neutrons on magnetic Ni^{II} is quite different from that on non-magnetic Zn^{II}. Copper ferrite is completely inverse [Pr 1]. For a treatment of the theory of neutron scattering by ferromagnetic media the reader is referred to Bacon [Ba 2]. The relation between cation distribution and saturation magnetization is dealt with in § 32.1.

A completely normal or completely inverse spinel represent extreme cases. The general cation distribution can be indicated as

$$Me^{II}_{\delta}\, Fe^{III}_{1-\delta}\, [Me^{II}_{1-\delta}\, Fe^{III}_{1+\delta}]\, O_4,$$

where the ions on tetrahedral sites are given in front of the square brackets and the octahedral ions between the brackets. For a completely random distribution, $\delta = 1/3$, for a normal spinel $\delta = 1$ and for an inverse spinel $\delta = 0$. The quantity δ is a measure of the inversion. In the case of some ferrites δ depends upon the method of preparation. If these ferrites are quenched from a high temperature δ has a value of about one third. A diffusion mechanism an energetically more favourable state causes to occur at lower temperatures. Depending on whether the diffusion rate is great enough compared to the cooling rate, an ion distribution will be retained at room temperature which is the equilibrium distribution at a temperature that varies from about 150 °C to a much higher temperature. For samples of $MgFe_2O_4$ and $CuFe_2O_4$ quenched from various temperatures, the inversion has been determined by X-ray diffraction [Be 4] and by magnetic measurements, [Ne 6] and [Pa 1]. It was found that the results satisfy the Boltzmann distribution law:

$$\frac{\delta(1+\delta)}{(1-\delta)^2} = e^{-E/kT}, \tag{31.2}$$

where the value of E is approximately equal to 0.14 eV. Neutron diffraction examinations of $MgFe_2O_4$ have yielded a value of δ approximately equal to 0.1 ([Ba 3] and [Co 1]). For $MnFe_2O_4$ an ion distribution has been found [Ha 3] corresponding to the formula $Mn_{0.8}Fe_{0.2}[Mn_{0.2}Fe_{1.8}]O_4$.

The following are some of the factors which can influence the distribution of the metal ions over the A and B sites:

(*a*) *The Ionic Radius*

Since the tetrahedral site is the smaller, one might expect that the smaller ions will prefer to occupy the tetrahedral sites. Trivalent ions are usually smaller than divalent ions (see Table 31.I) and this tends to favour the inverse structure.

(*b*) *The Electronic Configuration*

Certain ions have a special preference for a certain environment. For example, Zn^{II} and Cd^{II} show a marked preference for tetrahedral sites where their *4s,p* or *5s,p* electrons respectively can form a covalent bond with the six 2*p* electrons of the oxygen ion. This produces four bonds oriented towards the corners of a tetrahedron. The marked preference of the ions Ni^{II} and Cr^{III} for an octahedral environment can be explained as being due to the favourable fit of the charge distribution of these ions in the crystal field at an octahedral site ([Sa 1], [Ro 2], [Du 2,3]).

TABLE 31.I

SOME OF THE METAL IONS OCCURRING IN FERROMAGNETIC SPINELS, WITH THEIR GOLDSCHMIDT RADIUS r IN Å UNITS

Ion valency							
I		II		III		IV	
Ion	r	Ion	r	Ion	r	Ion	r
Li	0.78	Mg	0.78	Al	0.57	Ti	0.69
Na	0.98			Sc	0.83		
Ag	1.13			Cr	0.64		
		Mn	0.91	Mn	0.70	Mn	0.52
		Fe	0.83	Fe	0.67	Ge	0.44
		Co	0.82				
		Ni	0.78				
		Cu	0.70				
		Zn	0.82				
		Cd	1.03				

(c) The Electrostatic Energy

Another factor that can determine the distribution of the metal ions over the available interstitial sites is the electrostatic energy of the spinel lattice (denoted as "Madelung energy"). This is the electrostatic energy gained when the ions, at first thought to be infinitely far apart, are brought together to form the spinel lattice. In the normal arrangement the metal ions with the smallest positive charge are surrounded by 4 oxygen ions, and the metal ions with higher positive charge by 6 oxygen ions, which is electrostatically most favourable. With an oxygen parameter larger than the ideal value, this state will be energetically even more favourable. From calculations for the complete lattice made by Verwey *et al.* [Ve 2] and [Bo 1], it follows that for the spinels consisting of divalent and trivalent metal ions the inverse structure has the lowest lattice energy in the case that $u < 0.379$, whereas the normal structure has the lowest lattice energy when $u > 0.379$.

TABLE 31.II

CALCULATED RADII OF THE TETRAHEDRAL AND OCTAHEDRAL SITES, r_{tetr} AND r_{oct} RESPECTIVELY, FOR SOME FERRITES WITH SPINEL STRUCTURE, THE RADIUS OF THE OXYGEN IONS BEING ASSUMED TO BE 1.32 Å. THE GOLDSCHMIDT RADII r_{Me} OF THE DIVALENT METAL IONS HAVE BEEN ADDED FOR COMPARISON.

	Tetrahedral site		Octahedral site	
	r_{tetr}	r_{Me}	r_{oct}	r_{Me}
$MnFe_2O_4$	0.67	0.91; 0.67	0.72	0.67; 0.91
$ZnFe_2O_4$	0.65	0.82	0.70	0.67
$FeFe_2O_4$	0.55	0.67	0.75	0.83; 0.67
$MgFe_2O_4$	0.58	0.67; 0.78	0.72	0.78; 0.67

Table 31.II gives the radii of the tetrahedral and octahedral sites (calculated with the aid of (31.1)) for those ferrites in Table 31.III whose u parameter is fairly accurately known. These are the normal ferrites $MnFe_2O_4$ and $ZnFe_2O_4$, and those with inverse structure Fe_3O_4 and $MgFe_2O_4$. Apart from a large u parameter (0.385) the first two have a large lattice constant a. It can be seen from Table 31.II that this large value of a is practically only used for the purpose of increasing r_{tetr}. This appears most clearly in the case of $MnFe_2O_4$, owing to the large Mn^{II} ion which still partly occupies the B sites. The radius of the octahedral site is larger when it is occupied by the large Fe^{II} ion than by the Mg^{II} ion. The tetrahedral sites are small in this case, although for $MgFe_2O_4$ they are somewhat larger than for Fe_3O_4, possibly because of the partly normal structure of the former.

Table 31.III gives a summary of the metal ion distribution in a number of ferromagnetic spinels as determined mainly by neutron diffraction. The table also gives the cell edges a, the u parameters, molecular weights M and X-ray densities d_x. For the molecular weight the formula $MeFe_2O_4$ is taken as the molecular unit. Since an elementary cell contains eight of these molecules, the relation between the quantities in Table 31.III is given by the formula:

$$d_x = \frac{8\,M}{Na^3}\ \text{g/cm}^3, \tag{31.3}$$

where $N = 6.02 \,.\, 10^{23}\ \text{mol}^{-1}$ represents Avogadro's number.

TABLE 31.III

METAL ION DISTRIBUTION, LATTICE CONSTANT a, u PARAMETER, MOLECULAR WEIGHT M AND X-RAY DENSITY d_x FOR SIMPLE FERRITES WITH SPINEL STRUCTURE.

Ferrite	Metal ion distribution	Reference [ ]	a Å	u	M	d_x g/cm³
$MnFe_2O_4$	$Mn_{0.8}Fe_{0.2}$ $[Mn_{0.2}Fe_{1.8}]$	Ha 3	8.50	0.3846 ± 0.0003	230.6	5.00
Fe_3O_4	Fe $[Fe^{II}Fe]$	Sh 1, Cl 2	8.39	0.379 ± 0.001	231.6	5.24
$CoFe_2O_4$	Fe [CoFe]	Pr 2	8.38	—	234.6	5.29
$NiFe_2O_4$	Fe [NiFe]	Ha 2	8.34	—	234.4	5.38
$CuFe_2O_4$*	Fe [CuFe]	Pr 1, Ve 2	$c = 8.70$ $a = 8.22$	0.380 ± 0.005	239.2	5.35
$ZnFe_2O_4$	Zn $[Fe_2]$	Ha 2	8.44	0.385 ± 0.002	241.1	5.33
$MgFe_2O_4$	$Mg_{0.1}Fe_{0.9}$ $[Mg_{0.9}Fe_{1.1}]$	Ba 3, Co 1	8.36	0.381 ± 0.001	200.0	4.52
$Li_{0.5}Fe_{2.5}O_4$	Fe $[Li_{0.5}Fe_{1.5}]$	Br 4	8.33	0.382 ± 0.005	207.1	4.75

* Copper ferrite shows a tetragonal deformation below 760 °C [Pr 1]. By quenching to room temperature, however, the cubic structure can be maintained. Mixed copper ferrites, for example copper-zinc ferrites with not too high copper concentrations, retain their cubic structure even during slow cooling.

The lattice constants of mixed ferrites can mostly be found in good approximation by a linear interpolation of the lattice constants of the constituent simple ferrites, as for instance is shown for nickel-zinc ferrites in Fig. 31.5.

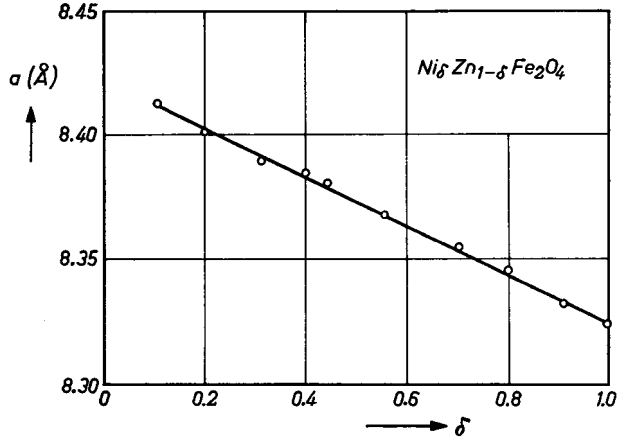

Fig. 31.5. Cell edges a in Å for mixed nickel-zinc ferrites after [Gu 4]

31.4. ORDERING PHENOMENA

In the ferrites with inverse spinel arrangement, ions having different valencies occupy octahedral sites. Ordering of these ions gives rise to a gain in electrostatic energy. Up to now, ordering on octahedral sites has been found in the case of two ferrites, Fe_3O_4 and $Li_{0.5}Fe_{2.5}O_4$. Ordering can also occur at tetrahedral sites if these are occupied by ions of differing valencies. This has been found [Go 3] for the substance $Fe_{0.5}Li_{0.5}[Cr_2]O_4$.

Magnetite

Various experimental indications exist that Fe_3O_4 has a crystallographic transition point at 119 °K, which can be related to an ordering phenomenon. The first indication of a deviation from cubic symmetry was found by Li at 119 °K, [Li 2]. Millar [Mi 1] and Ellefson and Taylor [El 1] discovered an anomaly in the specific heat of this substance at approximately the same temperature. Verwey and Haaijman [Ve 4] studied the conductivity (see § 45) and found that this dropped suddenly upon cooling below 119 °K by a factor of about one hundred. This was ascribed to an electron ordering on the octahedral sites. They predicted an ordering such that successive (001) layers of octahedral sites are occupied alternately by Fe^{II} and Fe^{III} ions, thus giving rise to a crystal with uniaxial symmetry. According to this order the upper two octahedral ions in Fig. 31.2 are, for example, Fe^{II}

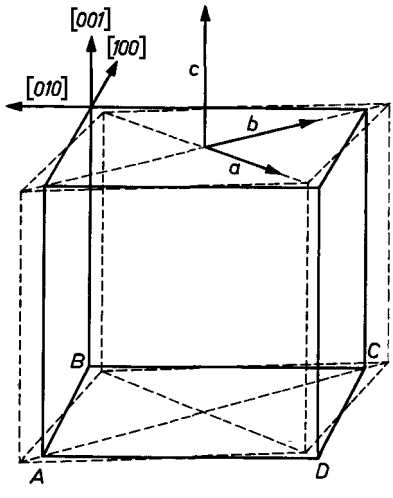

Fig. 31.6. Orthorhombic deformation of the cubic spinel structure of Fe_3O_4 below 119 °K. The spontaneous magnetization is in the [001] direction. After [Bi 2].

ions, and the two lower ones Fe^{III} ions. The drop in the conductivity gradually vanishes as the ferrous-ferric ratio on the octahedral sites deviates from unity. The ordering gives rise to a crystallographic structure with orthorhombic symmetry, as was demonstrated by Bickford [Bi 2] with strain-gauge measurements and by Abrahams and Calhoun [Ab 1] by X-ray analysis. Fig. 31.6 gives a picture of the structure of Fe_3O_4 below the transition point. The transition from the cubic to the orthorhombic structure is indicated in this figure. According to Bickford the changes during the transition are such that the c axis of the orthorhombic phase is parallel to a cube edge, and it is 0.03% smaller than the cube edge. The face diagonal BD becomes 0.07% smaller and the face diagonal AC becomes 0.06% longer. It appears that the edge of the cube along which the crystal is magnetized becomes the new c axis of the crystal below the transition point (see § 34).

According to De Boer *et al.* [Bo 1] the gain in electrostatic energy as a result of the ordering of divalent and trivalent ions at octahedral sites is approximately 1.7 eV, which is much higher than corresponds to the low transition temperature. Van Santen [Sa 2] supposes that this is the consequence of the long range of the Coulomb forces, unlike that of the exchange forces. As a result, strong short-range ordering (cluster formation) takes place also above the transition point. The difference in energy between the "ordered" and "disordered" state is then quite small, which could be the cause of the low transition temperature. The transition apparently is one of the first order, unlike what one would expect for an A—B type of ordering. The large drop in conductivity indicates that the ordering is nearly perfect immediately below the transition point, showing that the ordering forces are much stronger than one would expect from this low transition temperature. Romeyn [Ro 2] assumes that a certain short-range order is always present in all ferrites with spinel structure. In consequence of the low mobility of the ions this transition from short-range to long-range order will not gene-

rally be able to take place at the low temperatures at which this occurs in Fe_3O_4 by electron diffusion.

Guillaud and Creveaux [Gu 3] observed in the case of cobalt ferrite a discontinuity in the conductivity between 85 and 90 °K. At this temperature a fairly abrupt change in the magnetic anisotropy was also found, which could be derived from curves showing the magnetization of cobalt ferrite at various field strengths as a function of temperature. Measurements of crystal structure below this temperature have not been reported.

Lithium Ferrite

Braun [Br4] has shown that lithium ferrite is an inverse spinel, $Fe[Li_{0.5}Fe_{2.5}]O_4$. He found that an ordering of octahedral ions takes place below a temperature lying in the interval of 734° between 755°C. The ordering is such that in rows of octahedral ions with the direction [110] there is an alternate arrangement of successively three ferric ions and one lithium ion. The structure remains cubic. As in Fe_3O_4 the ordering gradually vanishes for deviating compositions according as the ratio Li/Fe on the octahedral sites differs from 1/3. Superstructure lines indicating a similar ordering in γFe_2O_3 are also found by Braun [Br 4]. A complete analysis of the structure of γFe_2O_3 is given by Van Oosterhout and Rooymans [Oo 2].

§ 32. Saturation Magnetization

32.1. MAGNETIC ORDERING AND SATURATION MAGNETIZATION AT 0°K

The exchange energy in ferrites is of the indirect (superexchange) type, described in § 8.1. It has been established experimentally that the predominating exchange energies between the magnetic ions in the ferrites are negative, as would follow from the theory for half-filled or more than half-filled 3*d* shells. These ions include the ferric ions, as well as the divalent metal ions of the first transition series which can be substituted in ferrites with spinel structure (see Table 32.I, p. 157).

The magnitude of the negative exchange energies between two magnetic ions Me and Me′ depends upon the distances from these ions to the oxygen ion O, *via* which the superexchange takes place, and on the angle Me-O-Me′; we shall call these respectively l, l' and ϕ. No quantitative relationship is known between the exchange interactions and these quantities. In § 8.1 it was shown that an angle of 180° will give rise to the greatest exchange energy, and that the exchange energy in general decreases very rapidly with increasing distance. The quantities l, l' and ϕ for different configurations of ion pairs in the spinel structure have been given by Gorter [Go 3]. Fig.

TABLE 32.I

NUMBER OF 3*d* ELECTRONS AND RESULTING SPIN MOMENT OF IONS OF THE FIRST TRANSITION SERIES. THE CURIE CONSTANT C_S PER GRAM-ION ACCORDING TO (6.9) IS GIVEN IN THE LAST COLUMN.

Ions										Number of 3*d* electrons	Spin-only magnetic moment in μ_B	C_S
Sc^{III}	Ti^{IV}									0	0	0
	Ti^{III}	V^{IV}								1	1	0.37
	Ti^{II}	V^{III}	Cr^{IV}							2	2	1.00
		V^{II}	Cr^{III}	Mn^{IV}						3	3	1.87
			Cr^{II}	Mn^{III}	Fe^{IV}					4	4	3.00
				Mn^{II}	Fe^{III}	Co^{IV}				5	5	4.38
					Fe^{II}	Co^{III}	Ni^{IV}			6	4	3.00
						Co^{II}	Ni^{III}			7	3	1.87
							Ni^{II}			8	2	1.00
								Cu^{II}		9	1	0.37
								Cu^{I}	Zn^{II}	10	0	0

32.1 shows the configurations of ion pairs occurring in the spinel lattice for which the distances and angles are most favourable for high exchange energy. The *A* and *B* ions shown in the figure refer to ions occupying tetrahedral and octahedral sites respectively. From a comparison of the different exchange interactions it follows that the *AB* interaction is by far the greatest. For the first of the two *AB* configurations drawn, the distances l and l' (indicated by p and q in the figure) are small and the angle ϕ is fairly large ($\phi \simeq 125°$). The maximum *BB* exchange interaction corresponds to the first *BB* configuration drawn in Fig. 32.1; the angle ϕ, however, is only 90°. The weakest will be the *AA* exchange interaction for which the distance r is relatively large ($\simeq 3.5$ Å) and the angle ϕ unfavourable ($\phi \simeq 80°$). The magnitude of the exchange energies is affected by deviations in the oxygen parameter u from the value 3/8. If $u > 3/8$, which for most ferrites is the case (see Table 31.III), the oxygen ions are displaced in such a way that in the *AB* interaction the distance between the *A* and O ion is increased and that between the *B* ion and the O ion is decreased. Also the angle ϕ is decreased. The resultant influence upon the interaction is not known. The *AA* interaction is reduced, while the *BB* interaction increases owing to the reduction of the distance in p. Because of the relative magnitudes of the exchange interactions one may expect the spins of the *A* and *B* ions in ferrites with spinel structure to be oppositely oriented, so that when $T = 0$ there will be two saturated and oppositely magnetized sublattices present. The resultant magnetization is thus the difference between the magnetization of the

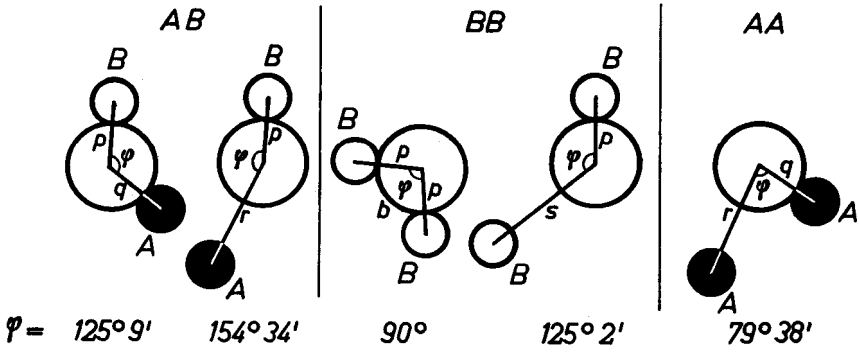

Distances Me-O	Distances Me-Me
$p = a(\frac{5}{8} - u)$	$b = (a/4)\sqrt{2}$
$q = a(u - \frac{1}{4})\sqrt{3}$	$c = (a/8)\sqrt{11}$
$r = a(1 + u)\sqrt{11}$	$d = (a/4)\sqrt{3}$
$s = a(\frac{1}{8}u + \frac{1}{8})\sqrt{3}$	$e = (3a/8)\sqrt{3}$
	$f = (a/4)\sqrt{6}$

Fig. 32.1. Some of the configurations of ion pairs which probably make the greatest contributions to the exchange energy in the spinel lattice. Ions A and B are metal ions on tetrahedral and octahedral sites respectively. The large open circle represents an oxygen ion. The distances between the ions are given in the Table below. The angles ϕ apply to the ideal parameter $u = 3/8$. The figure is drawn for $u > 3/8$. The centre-to-centre distances of the ions, expressed in the lattice constant a and the oxygen parameter u are given below.

octahedral lattice (B) and that of the total tetrahedral lattice (A), whereby the first will generally have the largest value. This was first postulated by Néel [Ne 1], and is experimentally well confirmed, as appears from Table 32.II for a number of simple ferrites. In the last column of this table the

TABLE 32.II

EXPERIMENTAL AND THEORETICAL VALUES OF THE SATURATION MAGNETIZATION OF SIMPLE FERRITES WITH SPINEL STRUCTURE IN BOHR MAGNETONS AT 0 °K.

Ferrite	Postulated ion distribution		Magnetic moment of tetrahedral ions	Magnetic moment of octahedral ions	Magnetic moment per molecule $MeFe_2O_4$	
	tetrahedral ions	octahedral ions			theoretical	experimental
$MnFe_2O_4$	$Fe^{III}_{0.2}+Mn^{II}_{0.8}$	$Mn^{II}_{0.2}+Fe^{III}_{1.8}$	5	5 + 5	5	4.6
Fe_3O_4	Fe^{III}	$Fe^{II}+Fe^{III}$	5	4 + 5	4	4.1
$CoFe_2O_4$	Fe^{III}	$Co^{II}+Fe^{III}$	5	3 + 5	3	3.7
$NiFe_2O_4$	Fe^{III}	$Ni^{II}+Fe^{III}$	5	2 + 5	2	2.3
$CuFe_2O_4$	Fe^{III}	$Cu^{II}+Fe^{III}$	5	1 + 5	1	1.3
$MgFe_2O_4$	Fe^{III}	$Mg^{II}+Fe^{III}$	5	0 + 5	0	1.1
$Li_{0.5}Fe_{2.5}O_4$	Fe^{III}	$Li^{I}_{0.5}+Fe^{III}_{1.5}$	5	0 + 7.5	2.5	2.6

average values are given of the magnetic moments as determined by various authors from the magnitude of the saturation magnetization of polycrystalline specimens, after extrapolation to 0 °K ([Go 3], [Gu 3, 4, 5, 6], [Pa 1, 2, 3]). For inverse ferrites the resultant moment is that of the divalent metal ion. Use is made of Table 32.I, which gives the resultant spin moments of the ions from the first transition series, determined by Hund's rule (see § 5).

There are at least three causes for the deviations of the magnetic moment from the theoretical values. In the first place, the ion distribution may not be the same as that given in the table. As we have seen in § 31.2, this is the case with $MgFe_2O_4$ and $CuFe_2O_4$. For these ferrites the saturation magnetization is greater after quenching than after slow cooling. In the second place the ions may have in addition to a spin moment an orbital moment, which is not completely quenched (see § 3.2); this is particularly the case for cobalt ions. We shall return to this point in § 34. The direction and the magnitude of the average magnetic moments of the ions on the tetrahedral and octahedral sites can in principle be separately determined from neutron diffraction experiments. Thirdly, angles may occur (see § 9.2), which has not yet been proved experimentally. The antiparallel orientation of the magnetic moments of the *A* and *B* ions has been demonstrated for Fe_3O_4 [Sh 1], $NiFe_2O_4$ [Ha 2] and $MgFe_2O_4$ [Ba 2] and [Co 1]. A problem is presented by the magnitude of the saturation magnetization in the case of $MnFe_2O_4$. Neutron diffraction experiments on several specimens have shown [Ha 3] that at 4.2 °K the average magnetic moment of ions on the octahedral sites is twice as large as that of the ions on tetrahedral sites, and that the resultant moment corresponds to 4.6 μ_B. For stoechiometric $MnFe_2O_4$ this value is hard to explain. An explanation for the resultant moment of 4.6 μ_B has been given by Harrison *et al.* [Ha 4] based on the simultaneous occurrence of Mn^{III} and Fe^{II} ions.

An interesting aspect, typical of ferrimagnetism, is exhibited by the mixed zinc ferrites in which the ion distribution is:

$$Zn^{II}_{\delta}\, Fe^{III}_{1-\delta}\, [Me^{II}_{1-\delta}\, Fe^{III}_{1+\delta}]\, O_4.$$

Since, owing to the presence of (non-magnetic) zinc ions, the magnetization of the tetrahedral lattice will be smaller than in the case of the simple ferrite, and since the Fe^{III} ions have the largest moment, the saturation magnetization of a mixed ferrite at the absolute zero point would be expected to increase with rising zinc content. Thus the remarkable fact appears that the substitution of magnetic ions in a ferrimagnetic substance by non-magnetic ions can lead to an increase in the saturation magnetization. Apart from Zn^{II} and Cd^{II}, [Ve 2], the non-magnetic ions Ga^{III} [Ma 1] and In^{III} [Ma 2]

also have a preference (although less pronounced for tetrahedral sites and thus, with small concentrations, increase the saturation magnetization of simple ferrimagnetic spinels at 0 °K. Theoretically the saturation moment should rise linearly with the zinc content and should reach the value 10 μ_B for $\delta = 1$, when all divalent magnetic ions have been replaced by zinc ions. For small concentrations, the linear rise with the theoretical slope has been found experimentally ([Gu 3, 4, 5, 6] and [Go 3]), as appears from Fig. 32.2. For larger concentrations, however, deviations are found. The magnetic moments of the few remaining Fe^{III} ions on the *A* sites are no longer able to align all the moments of the *B* ions antiparallel to themselves, since this is opposed by the negative *B-B* exchange interaction, which remains unaffected. According to the theory described in § 9.2, the *B* lattice will then divide itself into sublattices, the magnetizations of which make an angle with each other differing from 0° or 180°. The criterion for this subdivision is that the ions within one sublattice interact less strongly with each other than with those in the other sublattices. We have seen in § 31.1 that the

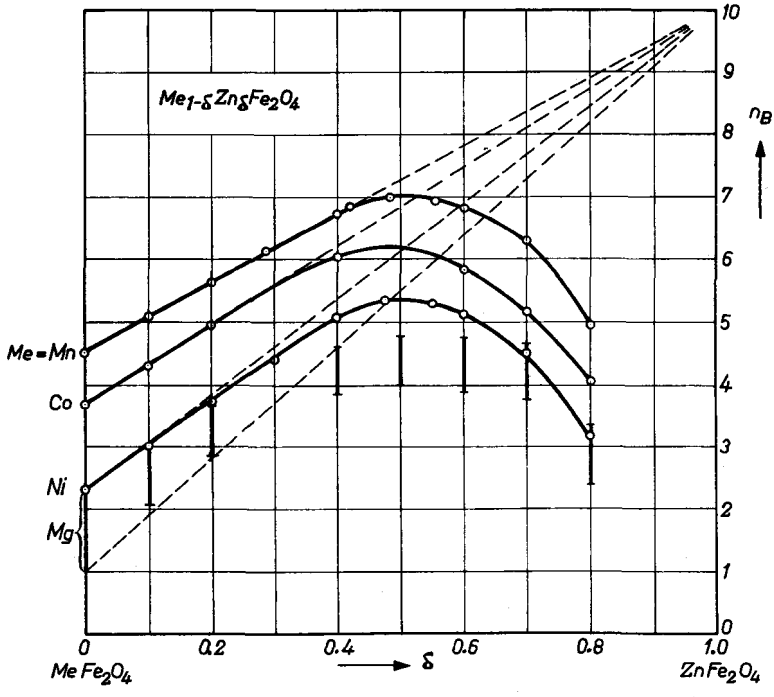

Fig. 32.2. Saturation moment in Bohr magnetons at 0 °K for various mixed crystal series For magnesium-zinc ferrites a region is indicated for the magnetization which is related to the ion distribution. After [Gu3, 4, 5, 6.]

octahedral sites form four interpenetrating f.c.c. lattices having an edge a. Owing to the consideable distances between the ions in one sublattice ($\frac{1}{2}a\sqrt{2} \simeq 6$ Å) the exchange interaction inside a sublattice can be neglected and therefore these sublattices satisfy the above criterion. But there are four B sublattices instead of the two for which the theory was evolved. Identical sublattices, however, can be combined to form two groups in which the magnetizations are mutually parallel [Ya 1], so that in fact we still have the division into two sublattices. This is due to the fact that for constant total magnetization the exchange energy of identical sublattices is independent of their mutual orientation. As regards the interaction of the B lattice with the A lattice this is immediately clear. The sublattices with magnetizations $\boldsymbol{M}_{Bi}$ of equal magnitude but different directions, (see Fig. 32.3*a*), can be combined to form two groups as indicated in Fig. 32.3*b*. The Weiss field exerted by the B sublattices on the magnetic moments of the A lattice are:

$$\boldsymbol{H}_{A,B} = n\Sigma\boldsymbol{M}_{Bi},$$

where $\boldsymbol{M}_{Bi}$ is the magnetic moment of the B_i th sublattice. Evidently this field strength is not affected by a re-arrangement of the orientations of the magnetic moments in the way indicated in Fig. 32.2. For the mutual interaction of the B sublattices an expansion of (9.8) for several identical sublattices is necessary. The Weiss field exerted by the B sublattices on the magnetic moments of the sublattice B_1 is:

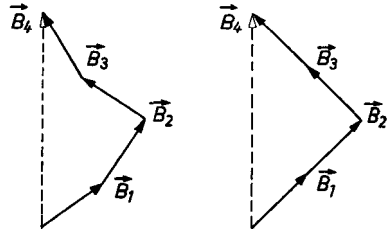

Fig. 32.3. For constant total magnetization B the sublattices $\mathbf{B_i}$ can be combined into two groups in which the netizations are parallel.

$$\boldsymbol{H}_{B1,B} = n_1(\boldsymbol{M}_{B2} + \boldsymbol{M}_{B3} + \boldsymbol{M}_{B4}) + n_2\boldsymbol{M}_{B1},$$

or more generally:

$$\boldsymbol{H}_{Bi,B} = n_1\boldsymbol{M}_B + (n_2 - n_1)\boldsymbol{M}_{Bi}.$$

From this it follows that the exchange energy in the B lattice is also independent of the re-orientation of the magnetic moments as indicated in Fig. 32.3. If, then, we put the four sublattices parallel in pairs and introduce the constants β_1 and β_2, we get $\beta_2 = 2\beta_1$, since each of the four sublattices interacts with another sublattice having parallel magnetization (this has now become an internal exchange interaction), and with two sublattices whose magnetization is not parallel. According to (9.10) we then find:

$$\beta_1 = \frac{2}{3}\beta \text{ and } \beta_2 = \frac{4}{3}\beta. \tag{32.1}$$

For the A lattice a division might possibly take place in the two interpenetrating f.c.c. lattices, so that the difficulties described above for the B lattice do not arise. Here too the interaction within one sublattice can be neglected, so that now:

$$\alpha_1 = 0 \text{ and } \alpha_2 = 2a. \tag{32.2}$$

Since we may expect the A—A exchange interaction to be small, angles will probably never form in the A lattice; no experimental indications of their the existence have so far been encountered.

On the B lattice angles will occur with increasing zinc content, for compositions where, according to (9.12) and (32.1):

$$\beta > 3M_A/4M_B. \tag{32.3}$$

The saturation will then decrease with increasing zinc concentration and, according to (9.14), will be equal to:

$$M_0 = (1 - 3/4\beta)M_A. \tag{32.4}$$

The curves found experimentally for M_0 as a function of the chemical composition (Fig. 32.2) broadly follow the two straight lines predicted by the theory (β being assumed to be constant). According to the theory, angle formation will occur at a certain zinc concentration. The gradual bend of the saturation curves under the dashed lines is explained by Néel [Ne 7] as being due to the occurrence of fluctuations in the ratio of the numbers of zinc and ferric ions on the tetrahedral sites surrounding the various octahedral sites, *i.e.* fluctuations in the tetrahedral-octahedral interaction.

The ferrite $ZnFe_2O_4$ is paramagnetic. From the foregoing it might be expected to be anti-ferromagnetic, having the ordering described with a Néel point of the order of 100 °K or more. Paramagnetic measurements have never, however, revealed a Néel point for this substance. Moreover, neutron examinations at room temperature indicate that no ordering of the magnetic moments of the ferric ions exists [Ha 2], although a peak has been found in the specific heat at about 9.5 °K; see Fig. 32.4 [Gr 2]. It has been suggested by Anderson [An 2] that the non-occurrence of antiferromagnetism in zinc ferrite is due to the fact that the four sublattices on the B sites have to be formed, so that some degeneracy remains. When $ZnFe_2O_4$ is rapidly cooled from a high temperature, it becomes ferrimagnetic because not all the zinc ions occupy tetrahedral sites.

As may be expected, substitution of non-magnetic ions on the octahedral sites of the spinel structure causes a decrease in the saturation magnetization, even at the smallest concentrations. Examples are substitutions of Al^{III} ([Go 3], [Ma 2]), Sc^{III} [Ma 2], $Ni^{II} + Ti^{IV}$ [Go 3] and also the substitution of Cr^{III} for Fe^{III} on octahedral sites [Go 3].

The saturation magnetization of the ferromagnetic spinels can be explained very satisfactorily if one assumes a predominant negative exchange between the magnetic ions on both kinds of lattice sites. A negative exchange is also found in many oxides other than the spinels. The magnetic oxides with perovskite structure, which have been studied by Jonker and Van Santen [Jo 2] are an exception in the group of oxides. The perovskite structure is shown schematically in Fig. 32.5.

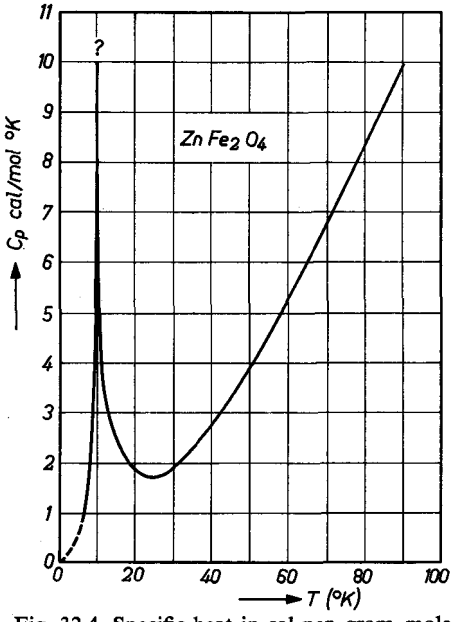

Fig. 32.4. Specific heat in cal per gram molecule for $ZnFe_2O_4$ as a function of temperature. (After [Gr 2].)

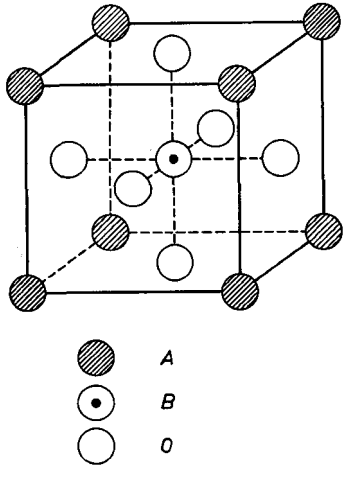

Fig. 32.5. Idealized elementary cell of the perovskite structure.

Large divalent or trivalent ions A occupy the corners of a cube and small trivalent or tetravalent metal ions B occupy the centre of the cube. The oxygen ions are situated centrally on the faces of the cube. The general chemical formula of these substances is ABO_3. The substances with interesting ferromagnetic properties were found in the mixed crystal series $La^{III}Mn^{III}O_3$ — $Ca^{II}Mn^{IV}O_3$, $La^{III}Mn^{III}O_3$—$Ba^{II}Mn^{IV}O_3$, $La^{III}Mn^{III}O_3$ — $Sr^{II}Mn^{IV}O_3$ and in the corresponding series $La^{III}Co^{III}O_3$ — $Sr^{II}Co^{IV}O_3$. These series of compounds are designated respectively as manganites and cobaltites. At sufficiently low temperatures all manganites containing both trivalent and tetravalent manganese ions are

ferromagnetic. In order to explain the saturation magnetization in these oxides, it must be assumed that the magnetic moments of ions *B* (Fig. 32.4) separated by an oxygen ion have parallel orientation. The highest Curie point is 370 °K. The magnitude of the saturation magnetization at low temperature (90 °K) is given in Fig. 32.6 for mixed crystals of (La, Ca)

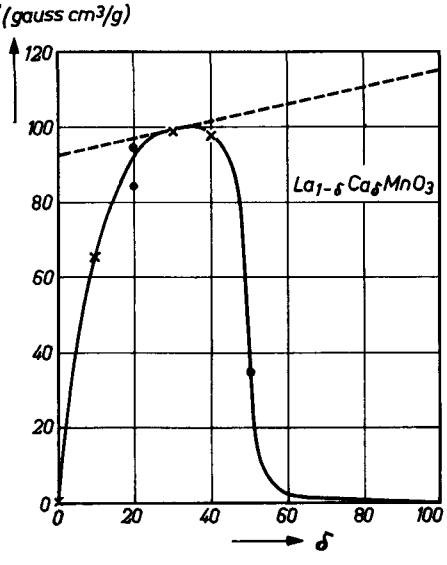

Fig. 32.6. Saturation magnetization at 90 °K of mixed crystals $La_{1-\delta}Ca_{\delta}MnO_3$. The calculated broken line represents the saturation moment in the case where all ionic moments are parallel. (After [Jo 2].)

MnO_3. The broken line in this figure shows the magnitude of the saturation magnetization assuming that the magnetic moments of all ions are parallel. We thus have here for a range of compositions a true ferromagnetism. From the curve in Fig. 32.6 it must be concluded that the exchange energy between the Mn^{III} and Mn^{IV} ions *via* the oxygen ion lying diametrically between them is positive and predominant. A corresponding situation is found with the cobaltites of the (La, Sr)CoO_3 series; see [Jo 3].

32.2. TEMPERATURE DEPENDENCE OF THE SATURATION MAGNETIZATION

According to § 9 various types of curves may be expected for the saturation magnetization M_s as a function of the temperature T for ferrites; see for instance Figs. 9.3 and 9.6. It appears, however, that all simple ferrites with spinel structure and all mixed zinc ferrites show a fairly normal M_s *versus* T curve (see Fig. 32.7). Normalized curves for simple ferrites as given by Pauthenet [Pa 1] are reproduced in Fig. 32.8. In the case of $CuFe_2O_4$ and $MgFe_2O_4$ these curves are highly dependent on the method of preparing

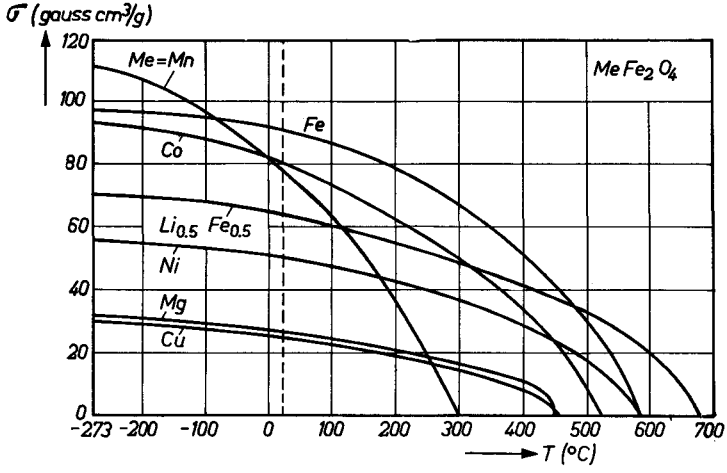

Fig. 32.7. Saturation magnetization per gram, σ, for simple ferrites with spinel structure as a function of temperature T.

the specimen since Cu and Mg ions can occur on both lattice sites. The form of the *M versus T* curves in Fig. 32.8 can be explained with the Weiss field theory. If we assume in first approximation that the exchange interactions between the magnetic moments in each sublattice are zero, $\alpha = \beta = 0$, see (9.6) then the Weiss field at $T = 0$ in the A lattice is approximately twice as large as in the B lattice (inversely proportional to the magnetizations of the sublattices). As a result the M_s *versus* T curves of the A lattice will be much more convex than those for a simple ferromagnetic substance, and the curve for the B lattice will be less convex. The total magnetization is that of the B lattice reduced by that of the A lattice, and the curve will

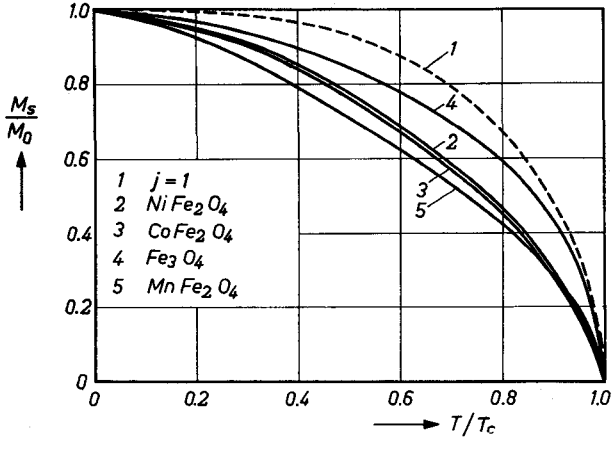

Fig. 32.8. Normalized curves of the saturation magnetization of simple ferrites with spinel structure as a function of temperature, after [Pa 1]. For comparison the Langevin curve is given for the case that elementary magnetic moments of two Bohr magnetons are present ($j=1$).

therefore be less convex than that of a simple ferromagnetic. A finite positive value of β makes the Weiss field in the B lattice even smaller, and will therefore intensify the effect, while a finite positive value of α makes the Weiss field in the A lattice smal ler, and will counteract the effect.

Table 32.III gives a survey of the saturation magnetizations and Curie points, and also indicates the magnetization per gram, $\sigma = M_s/d$; the latter is an intrinsic quantity of the material, which is not the case with M_s in porous substances. The relation between σ at 0 °K and the number of Bohr magnetons n_B per molecule $MeFe_2O_4$ is given by:

$$n_B = \frac{M}{N \cdot \mu_B} \cdot \sigma = \frac{M}{5585} \cdot \sigma, \quad (32.5)$$

where M is the molecular weight of the substance corresponding to one molecule $MeFe_2O_4$, given in Table 31.III.

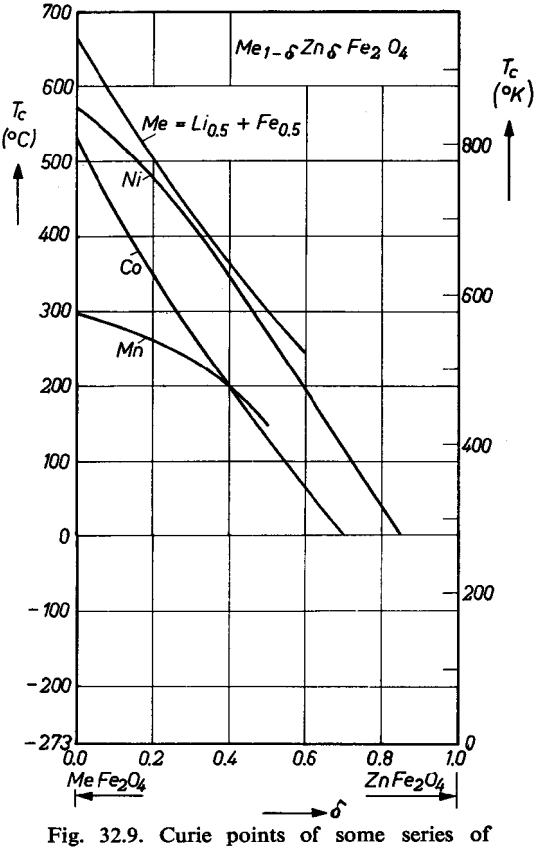

Fig. 32.9. Curie points of some series of mixed zincferrites $Me_{1-\delta}Zn_\delta Fe_2O_4$ as a function of the zinc concentration.

TABLE 32.III

THE SATURATION MAGNETIZATION M_S IN GAUSS AND σ IN GAUSS CM³/G, TOGETHER WITH THE CURIE POINTS T_C OF SOME SIMPLE FERRITES WITH SPINEL STRUCTURE.

Ferrite	0 °K			20 °C			T_C °C
	σ gauss cm³/g	M_s gauss	$4\pi M_s$ gauss	σ gauss cm³/g	M_s gauss	$4\pi M_s$ gauss	
$MnFe_2O_4$	112	560	7000	80	400	5000	300
Fe_3O_4	98	510	6400	92	480	6000	585
$CoFe_2O_4$	90	475	6000	80	425	5300	520
$NiFe_2O_4$	56	300	3800	50	270	3400	585
$CuFe_2O_4$	30	160	2000	25	135	1700	455
$MgFe_2O_4$	31	140	1800	27	120	1500	440
$Li_{0.5}Fe_{2.5}O_4$	69	330	4200	65	310	3900	670

Owing to the reduced A—B exchange interaction with increasing zinc content in the case of mixed zinc ferrites with spinel structure, the Curie point will drop as a result of the substitution of zinc. This was first found by Forestier [Fo 1] and is illustrated by the experimental curves in Fig. 32.9. Since the Curie point decreases with increasing zinc content and the saturation magnetization increases at 0 °K, it cannot be predicted how the saturation of a ferrite will change at an intermediate temperature, for in-

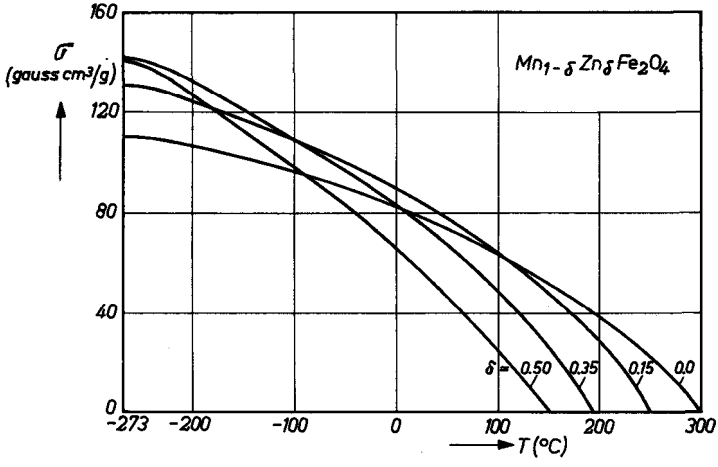

Fig. 32.10. Saturation magnetization per gram, σ, as a function of temperature for some ferrites of the $Mn_{1-\delta}Zn_{\delta}Fe_2O_4$ series.

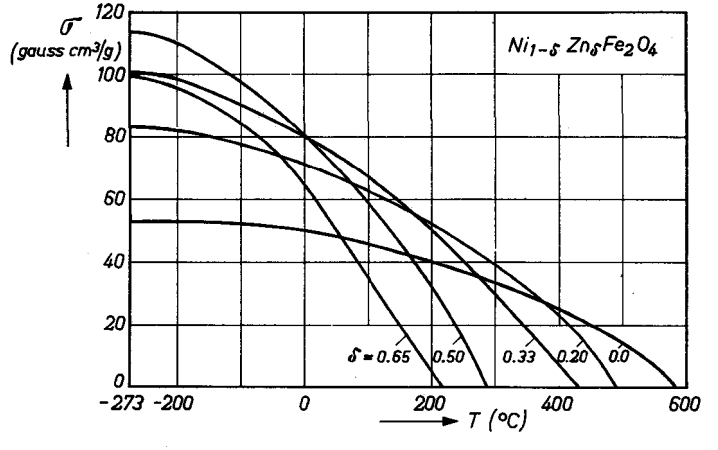

Fig. 32.11. The saturation magnetization per gram, σ, as a function of temperature for some ferrites of the $Ni_{1-\delta}Zn_{\delta}Fe_2O_4$ series.

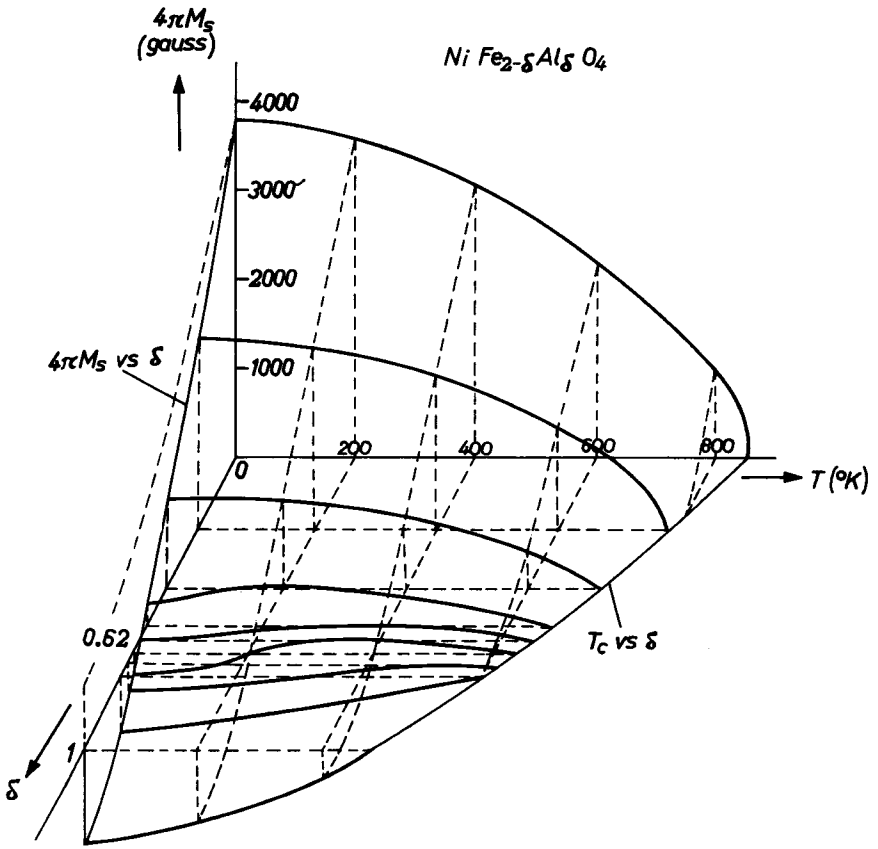

Fig. 32.12. Three-dimensional graph showing $4\pi M_s$ *versus* T curves for different compositions in the series of solid solutions $NiFe_{2-\delta}Al_\delta O_4$, very slowly cooled. The shapes of the curves are all those predicted by theory (see Fig. 9.3). Introduction of Al^{III} *(i.e.*, increasing δ from $\delta = 0$) lowers $4\pi M_s$, at all temperatures. After [Go 4].

stance at room temperature, if magnetic ions are substituted by zinc ions. In Figs. 32.10 and 32.11 it can be seen that in the series $Mn_{1-\delta}Zn_\delta Fe_2O_4$ and $Ni_{1-\delta}Zn_\delta Fe_2O_4$ the saturation at room temperature increases with δ for low zinc concentrations and reaches a maximum when δ is equal to 0.15 and 0.35 respectively.

Although the form of the M_s *versus* T curves of the ferrites discussed so far is still normal, other curves more characteristic of ferrimagnetism are also found, one example having been givenin Fig. 9.2. Curves of this kind also occur in the $NiFe_{2-\delta}Al_\delta O_4$ system, a survey of which is given in Fig. 32.12. The curve in the plane $T = 0$ °K indicates the change in the

saturation magnetization of $NiFe_2O_4$ when part of its Fe ions are substituted by Al ions. Since this substitution is made principally on octahedral sites [Ma 1] and [Sm 3]), the total magnetization M_s decreases with increasing δ, and passes zero at $\delta = 0.62$; see [Go 3] and [Ma 1]. The substitution of non magnetic ions on octahedral sites, like the substitution on tetrahedral sites, causes a decrease in the Curie point, although relatively less, and the M_s *versus* T curves with increasing value of δ have the forms as indicated in Fig. 9.3*a* and 9.3*b*.

§ 33. Paramagnetism above the Curie Point

The $1/\chi$ *versus* T curves of ferrites with spinel structure are convex above the Curie point; this is characteristic of ferrimagnetism (see § 10). Examples for Fe_3O_4 and $MnFe_2O_4$ are given in Fig. 33.1. The Weiss field theory yields for two sublattices the following relation, which can easily be derived from (10.1):

$$1/\chi = \frac{1}{C}\left[T - T_a - \frac{T_b^2}{T - T_a'}\right], \tag{33.1}$$

the Curie constant being $C = C_1 + C_2$, where C_1 and C_2 are the Curie constants of the A and B lattices and are related to the properties of the ions according to (6.9). Fig. 33.1 gives the molar susceptibilities χ_{mol}, so that the

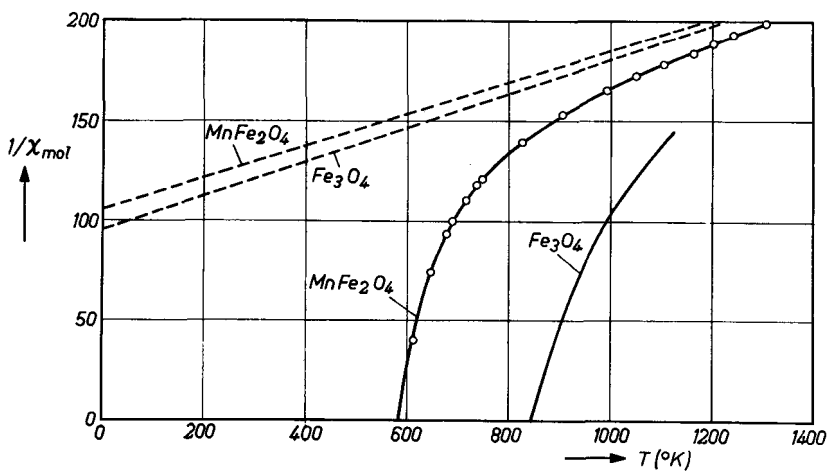

Fig. 33.1. The reciprocal value of the molar susceptibility, $1/\chi_{mol}$, as a function of temperature for $MnFe_2O_4$ (after [Cl 3]) and Fe_3O_4 (after Kopp, see [Ne 1]). The asymptotes for high temperature are drawn in with the theoretical spin-only slope according to the Curie constants in Table 32.I.

C_S values per gram-ion must be taken, as given in Table 32.I, and multiplied by the number of ions on the site in question, as occurring in the formula $MeFe_2O_4$. The equation (33.1) represents a hyperbola the asymptotes of which bisect the T axis at T_a and T_a' given by:

$$T_a = \frac{C_1^2 W_{11} + 2C_1 C_2 W_{12} + C_2^2 W_{22}}{C_1 + C_2} = \frac{-n(\alpha C_1^2 + 2C_1 C_2 + \beta C_2^2)}{C_1 + C_2} \quad (33.2)$$

and

$$T_a' = \frac{C_1 C_2}{C_1 + C_2}(W_{11} - 2W_{12} + W_{22}) = \frac{nC_1 C_2(2 - \alpha - \beta)}{C_1 + C_2}. \quad (33.3)$$

The curvature of the $1/\chi$ *versus* T curve is related to T_b, which is given by:

$$T_b = C_1(W_{11} - W_{12}) + C_2(W_{12} - W_{22}) = n[C_1(1-\alpha) - C_2(1-\beta)]. \quad (33.4)$$

For negative exchange interactions ($\alpha, \beta > 0$) we have $|T_a| > T_a'$. Figure 33.1 gives the asymptotes for high temperatures with the theoretical spin-only slope. Conversely it should be quite easy to determine the values of α and β from the measured $1/\chi$ *versus* T curves. This has been done for a number of ferrites and the results are reproduced in Table 33.I. The result depends very much on the assumption of the ion distribution over tetrahedral and octahedral sites. A small percentage of zinc ions on octahedral sites will influence the calculated molecular field constants to a high degree.

TABLE 33.I

MOLECULAR FIELD COEFFICIENTS CALCULATED WITH THE WEISS FIELD THEORY FROM MEASURED $1/\chi$ *versus* T CURVES.

Ferrite	α	β	Reference
$MnFe_2O_4$	0.82	0.28	Cl 3
Fe_3O_4	0.51	— 0.01	Ne 1
$NiFe_2O_4$	0.21	0.15	Ne 8
$Ni_{0.8}Zn_{0.2}Fe_2O_4$	0.48	0.16	,,
$Ni_{0.4}Zn_{0.6}Fe_2O_4$	1.16	0.15	,,
$Ni_{0.3}Zn_{0.7}Fe_2O_4$	3.08	0.14	,,

It is, moreover, very doubtful whether such detailed data can be obtained from an approximating theory, which the Weiss field theory is. In § 6.4 and § 10 it was shown how short-range order causes deviations from the Weiss field theory. As a result of the short range order the quantity $1/\chi$ becomes larger, thereby causing a decrease in the Curie point, as illustrated in Fig. 10.3. This decrease can amount to several tens of percents. High-temperature behaviour is not influenced by this, and T_a will therefore

have the correct value, whereas the experimental value of T_a' will be too low. This would accordingly result in a too large value for α and/or β when applying the eqs (33.2) and (33.3), although it cannot be ascertained from these equations whether especially α or β will be too large. It is seen from Fig. 10.3, however, that it is just above the Curie point that the slope of the $1/\chi$ *versus* T curve will be too small, and hence the curvature less. This points to a too large value of $|T_b|$ in (33.4). Now C_2 is approximately equal to $2C_1$, so that a large value of $|T_b|$ corresponds to a too large value of α or a too small value of β. This can be understood from the fact that immediately above the Curie point the magnetizations of the A and B sublattices induced by an external field are still antiparallel. A too large value of χ (high magnetization in external field) is obtained when the Weiss field in the A lattice is too small (α large) or in the B lattice too large (β small). Thus, when applying the Weiss field theory, we may expect a too high value especially for α, which is the interaction within the sublattice with the smallest magnetization. This is precisely what is found, as can be seen from Table 33.I. Having regard to the results shown in § 32.1, one can scarcely assume that $\alpha > \beta$.

§ 34. Crystal Anisotropy

34.1. CUBIC CRYSTAL ANISOTROPY

A review of some of the hitherto published values of the crystal anisotropy constants K_1 and K_2 (defined in (11.1)) for ferrites with spinel structure, is given in Table 34.I. A striking fact is that all K_1 values are negative, except those for cobalt ferrite and for ferrites containing a large percentage of divalent cobalt ions. Bozorth [Bo 2] found that the ageing of cobalt ferrites has an influence on K_1. It has been found that the anisotropy constants obtained by a static method of measurement (§ 26.1) may differ from those obtained with the help of microwaves (§ 26.4) if the single crystal contains ferrous ions as well as ferric ions.

Table 34.II gives the results of measurements [Bo 3] carried out on $Ni_{0.8}Fe_{2.2}O_4$ having a resistivity of only 1 ohmcm (which points to a certain concentration of ferrous ions) and on the ferrite $MnFe_{1.9}O_4$, which is deficient in iron and thus probably contains no ferrous ions. The authors attribute the difference in the case of the nickel ferrite at $-196°$ to rearrangements of electrons on the iron ions when the orientation of the magnetization changes. The values of K_1 will then depend on whether the measurement has been carried out at a frequency which is much larger or much smaller than the reciprocal of the time constant which determines the electron

TABLE 34.I

CRYSTAL ANISOTROPY CONSTANTS K_1 AND K_2 OF A NUMBER OF FERRITES WITH SPINEL STRUCTURE AT 20 °C AND −196 °C.

Composition	Temperature °C	K_1 erg/cm³	K_2 erg/cm³	Reference
Fe_3O_4	20	-110×10^3	-280×10^3	Bi 3
$MnFe_2O_4$	20 (*b*)	-28×10^3	—	Bo 2
	−196 (*b*)	-187×10^3	—	,,
$Mn_{0.98}Fe_{1.86}O_4$	−269	-210×10^3 *a*	-100×10^3	Di 2
	−196	-200×10^3 *a*	-3×10^3	,,
	27	-28×10^3 *a*	-2×10^3	,,
$CoFe_2O_4$	90	$+0.9\times10^6$	—	Ta 2
	200	$+66\times10^3$	—	,,
	280	$\cong 0$	—	,,
$Co_{0.8}Fe_{2.2}O_4$ *)	−196	$+4.4\times10^6$	—	Bo 2
	20	$+2.9\times10^6$	—	,,
$Co_{1.1}Fe_{1.9}O_4$	20	$+1.8\times10^6$	—	Bo 2
$NiFe_2O_4$	−196	-87×10^3	—	Ga 1
	20	-62×10^3	—	Ga 1, Ya 2
$CuFe_2O_4$	−196	-206×10^3 *a*	—	Ok 1
	20	-60×10^3 *a*	—	,,
	400	-1×10^3 *a*	—	,,
$MgFe_2O_4$ **)	20	-25×10^3	—	Ra 2
$Mn_{0.45}Zn_{0.55}Fe_2O_4$	20	-3.8×10^3 *a*	—	Ga 2

a Obtained from microwave measurements; the values not denoted by *a* were found from static measurements.

b The values denoted by a bracket apply to the same specimen.

* These values apply to a specimen aged for three days at 150 °C. After quenching the specimen in air from 400 °C the same authors found $K_1 = +3.9\times10^6$ erg/cm³.

** Value extrapolated to zero ferrous content.

TABLE 34.II

THE CRYSTAL ANISOTROPY CONSTANT K_1 AND THE ANISOTROPY FIELD $2|K_1|/M_s$ AS DEPENDENT ON TEMPERATURE AND FREQUENCY ACCORDING TO [Bo 3].

Temperature	Method of measurement	$Ni_{0.8}Fe_{2.2}O_4$		$MnFe_{1.9}O_4$	
		K_1 erg/cm³	$2\|K_1\|/M_s$ oersted	K_1 erg/cm³	$2\|K_1\|/M_s$ oersted
20 °C	static	-39×10^3	260	-34×10^3	180
	microwave	-43×10^3	280	-33×10^3	175
−196 °C	static	-42×10^3	260	-240×10^3	840
	microwave	-74×10^3	468	-233×10^3	812

transitions. A similar electron ordering is also proposed to explain an excessive width of the ferromagnetic resonance line and also as the cause of relaxation losses occurring at entirely different temperatures and frequencies [Cl 4]; see § 36.1 and § 54.3 respectively.

An extensive investigation of Fe_3O_4 has been carried out to determine the change of the crystal anisotropy constants K_1 and K_2 with temperature. Fig. 34.1 gives the result of the static measurements by Bickford [Bi 3]. Results obtained earlier by the same author, but from microwave measurements, are virtually no different from these. The variation of K_1 with temperature is quite anomalous: a change of sign takes place at 130 °K: below this temperature K_1 is positive, above this temperature it is negative. This temperature does not coincide with the transition point for Fe_3O_4, discussed in § 31.4, which point lies at a temperature approximately 10° lower. In the orthorhombic structure the c axis is the preferred direction of magnetization. Upon cooling below the transition point of 119 °K the cube edge along which the magnetization is aligned is the orthorhombic axis (see [Do 2]).

Bickford [Bi 3] has examined the change in the crystal anisotropy constants of Fe_3O_4 when small percentages of ferrous ions are replaced by cobalt ions. In Fig. 34.2 and Fig. 34.3 the quantities K_1 and K_2 respectively are plotted as a function of temperature for mixed cobalt ferrous ferrites $Co_\delta Fe_{3-\delta}O_4$ where $\delta = 0$, 0.01 or 0.04. The cobalt contribution to the anisotropy for these small concentrations is found to be proportional to the cobalt content. For higher cobalt concentrations the anisotropy increases less rapidly, [Pe 1]. By the addition of cobalt ferrite the zero point in the crystal anisotropy of magnetite is shifted towards higher temperatures; for example

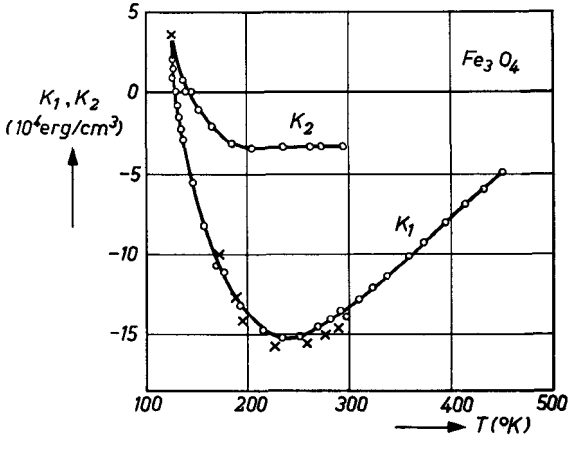

Fig. 34.1. Temperature variation of crystal anisotropy constants K_1 and K_2 of magnetite. (After [Bi 3]).

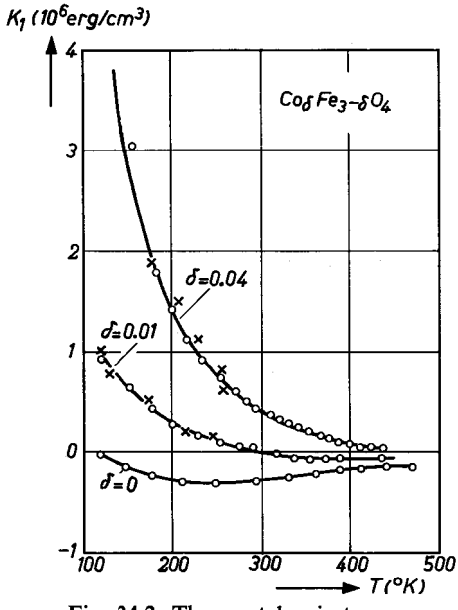

Fig. 34.2. The crystal anisotropy constant K_1 *versus* temperature for magnetite and cobalt-substituted magnetite $Co_\delta Fe_{3-\delta}O_4$. (After [Bi 3]).

in the case of the compound $\delta = 0.01$ it lies at room temperature. Van der Burgt [Bu 2] has also found that the crystal anisotropy of mixed ferrites with cobalt ferrite has generally not the value as is derived simply from the contributions of the compounds. He found moreover that for instance the introduction of cobalt in $Ni_{0.5}Zn_{0.5}Fe_2O_4$ gives per cobalt ion a change in the anisotropy which is only one sixteenth of that when the same amount of cobalt is introduced in Fe_3O_4. The cobalt contribution to the anisotropy depends of course on the site the cobalt ions occupy in the structure and also on the kind of the surrounding ions.

The cause of the crystal anisotropy must be sought mainly in the spin-orbit interaction in the divalent metal ions, since the ferric ions have a half-filled shell, that is to say they have no orbital moment in the ground state.

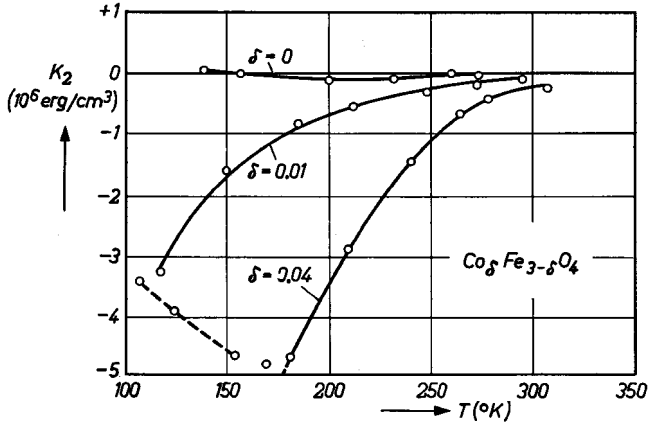

Fig. 34.3. The crystal anosotropy constant K_2 *versus* temperature for magnetite and cobalt-substituted magnetite $Co_\delta Fe_{3-\delta}O_4$. After [Bi 3].

With most ions (Mn^{II}, Fe^{II}, Ni^{II}, Cu^{II}) the orbital moment is quenched (§ 3.2) and the spin-orbit interaction introduces only a relatively small anisotropy. In Co^{II}, however, the crystal field is not able to remove the orbital degeneracy, and the orbital moment is of the same order of magnitude as the spin moment. This must be regarded as the cause of the large anisotropy of cobalt [Sl 2], which manifests itself also in the field-cooling effect (to be dealt with in the following section), in magnetostriction and in the g factor. Yosida and Tachiki [Yo 1] examined theoretically the various mechanisms that can give rise to crystal anisotropy in the ferrites with spinel structure and came to the conclusion that dipole energy, as treated at the end of § 12.1, and mechanism (*b*) of § 12.1, cannot explain the anisotropy observed in nickel ferrite; they can, however, explain the order of magnitude in Fe_3O_4. Mechanism (*a*) of § 12.2 was not, however, considered.

34.2. INDUCED UNIAXIAL ANISOTROPY

In ferrites with cubic crystal structure a uniaxial anisotropy can be brought about by subjecting the material to an annealing treatment in a magnetic field. If a single crystal of a ferrite specimen has a sufficiently high Curie point, for example above 250 °C, and if it is allowed to cool slowly from this temperature to room temperature, one finds in many cases that a uniaxial magnetic anisotropy is superimposed on the cubic anisotropy. The effect occurs particularly in ferrites containing cobalt. Bozorth *et al.* [Bo 2] found for a single crystal, denoted by the formula $Co_{0.32}Zn_{0.24}Fe_{2.18}O_4$, that the direction of the magnetic field becomes the easy direction of magnetization for the uniaxial anisotropy, irrespective of the direction of this field with regard to the axis of the crystal. Penoyer and Bickford [Pe 1] found that in single crystals of magnetite with low cobalt concentrations ($Co_\delta Fe_{3-\delta}O_4$, where $\delta < 0.15$) the direction of the induced uniaxial anisotropy does not generally coincide with the direction of the magnetization during magnetic annealing, and moreover that the magnitude of the uniaxial anisotropy depends on the direction of the magnetic field during the magnetic annealing process with respect to the crystallographic axes. From an analysis of the results of their measurements it appears that the coefficients F and G introduced in (11.9) depend respectively quadratically and linearly upon the cobalt concentration δ (see Fig. 34.4). The same figure indicates the results of measurements performed by Bozorth *et al.* [Bo 2] to determine the uniaxial anisotropy of polycrystalline specimens. A maximum effect occurs in compositions with larger concentrations of both cobalt and ferrous ions. The ferrous ion and cation-vacancy concentration appear to be important for promoting diffusion. The magnitude of the uniaxial anisotropy depends

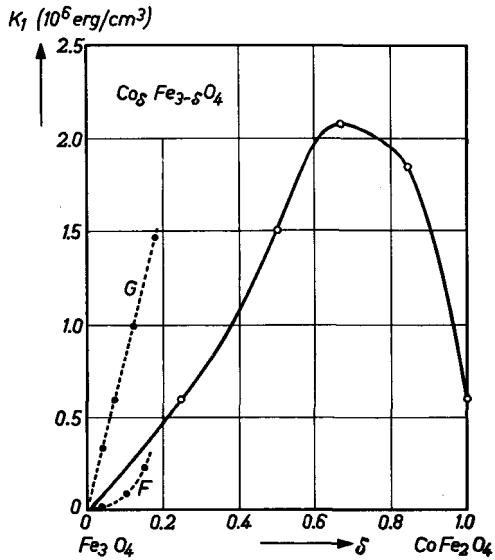

Fig. 34.4. Drawn curve — uniaxial crystalline anisotropy energy K_1 as a result of magnetic annealing of specimens of $Co_\delta Fe_{3-\delta}O_4$, after [Bo 2]. The broken curves represent the coefficients F and G of eq. (11.9), after [Pe 1].

upon the duration of the magnetic annealing and on the temperature at which it is carried out. Bozorth *et al.* [Bo 2] have found the same activation energy of 0.94 eV for this process in the case of single crystals and a polycrystalline specimen of different compositions. The greatest anisotropy is found when the specimen has been aged for three days at the lowest temperature which, in their case, is 150 °C. For small cobalt concentrations the annealing process is much more rapid; in the method adopted by Penoyer and Bickford the annealing time was 5-10 minutes at 100 °C.

The phenomenon of magnetic annealing has long been familiar as far as alloys are concerned, and various theories have been put forward to explain it. It does not seem probable that the anisotropy arises from anisotropic magnetostriction, because the phenomenon is also found with single crystals which can deform freely without the occurrence of stresses. The separation of a second phase in needle or disk form is a possible cause. In § 11.2 a theory was given in which the ordering of ion pairs in a certain direction under the influence of the magnetic field is described as the cause of the uniaxial anisotropy. When discussing the spinel structure in § 31.2 it was pointed out that the surrounding of a single octahedral site by the metal ions, and also by the oxygen ions when $u \neq 3/8$, possesses no cubic symmetry but becomes uniaxial with a symmetry axis along one of the [111] directions (see Fig. 31.3). The occurrence of crystal fields having this symmetry may therefore be expected. According to mechanism (*b*) in § 12.2, this could give rise to a magnetic anisotropy with this particular [111] direction as the axis

of symmetry. The total anisotropy, then, will depend on the occupation of the four possible kinds of octahedral sites by foreign ions. With this mechanism Penoyer and Bickford [Pe 1] explain the term G in (11.9) which has the appropriate symmetry. Since this is a property of a single ion the effect in first approximation will be proportional to the concentration, and this was in fact found. The term F, which was found to be proportional to δ^2, is then to be explained by pair orientation. The connecting lines lie along the [110] directions which, in alloys, would give rise to an f.c.c. symmetry of the anisotropy ($G = 4F$) so that then $G - 4F$ and not G would be proportional to the concentration of cobalt ions. This is not found experimentally. It must therefore be assumed that pair orientation gives rise to a simple cubic symmetry. This is plausible, since the exchange interaction between two cobalt neighbours is not direct but takes place *via* the two intermediate oxygen ions (see Fig. 31.3). These four ions lie in a cube face. For each exchange interaction we can therefore expect an anisotropy along the line connecting the Co ion and the oxygen ion. Since there are two such lines for each Co pair, there is no anisotropy in the said cube face, but the easy (or difficult) direction is perpendicular to the cube face determined by the two Co ions. Hence we must in fact expect an anisotropy of the simple cubic type, corresponding to the F term in (11.9). This crystal anisotropy, then, is of the type (*a*) of § 12.2. During cooling in the absence of a field a preferred direction will also arise owing to diffusion in each Weiss domain in the case of the mixed cobalt ferrites.

§ 35. Linear Magnetostriction

The magnetostriction constants λ_{100} and λ_{111} have been measured on single crystals of ferrites with the aid of strain gauges [Go 2]. The results are given in Table 35.I. On the manner in which the magnostriction constants change

TABLE 35.I

MAGNETOSTRICTION CONSTANTS OF FERRITES WITH SPINEL STRUCTURE AT 20 °C.

Ferrite	$10^6.\lambda_{100}$	$10^6.\lambda_{111}$	Reference
Fe_3O_4	— 20	+ 78	Bi 4
$Co_{0.8}Fe_{0.2}Fe_2O_4$	—590	+120	Bo 2
$Ni_{0.8}Fe_{0.2}Fe_2O_4$	— 36	— 4	Bo 2

with temperature little is known. Fig. 35.1 gives the constants λ_{100}, λ_{111} and λ_{110} for a synthetic single crystal of Fe_3O_4 according to Bickford [Bi 4]. The values of the saturation magnetostriction λ_s measured on polycristalline specimens of simple ferrites and on a series of nickel-zinc ferrites are given in Table 35.II.

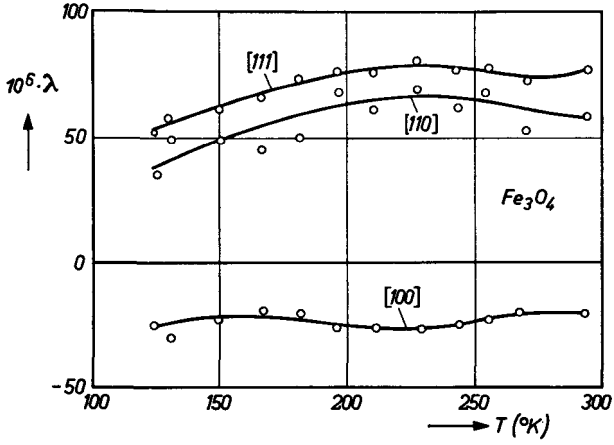

Fig. 35.1. The magnetostriction constants λ_{100}, λ_{111} and λ_{110} *versus* temperature for synthetic magnetite single crystal. (After [Bi 4]).

TABLE 35.II

LINEAR SATURATION MAGNETOSTRICTION λ_s FOR SIMPLE FERRITES AND MIXED NICKEL-ZINC FERRITES WITH SPINEL STRUCTURE AT 20 °C.

Ferrite	$\lambda_s.10^6$	Reference
$MnFe_2O_4$	—5	
Fe_3O_4	+40	
$CoFe_2O_4$	—110	Gu 7
$MgFe_2O_4$	— 6	Sm 4
$Li_{0.5}Fe_{2.5}O_4$	— 8	En 1
$Ni_{0.36}Zn_{0.64}Fe_2O_4$	— 5	
$Ni_{0.50}Zn_{0.50}Fe_2O_4$	—11	
$Ni_{0.64}Zn_{0.36}Fe_2O_4$	—16	
$Ni_{0.80}Zn_{0.20}Fe_2O_4$	—21	
$NiFe_2O_4$	—26	Sm 4

The magnetostriction at room temperature is positive only for the electrically conductive Fe_3O_4. This is because λ_{111} is relatively highly positive; see (13.3). It may be expected that in the case of mixed crystals of a ferrite with Fe_3O_4 it must be possible to have a ratio of components such that the saturation magnetostriction will be zero. In Fig. 35.2 the magnetostriction λ is plotted as a function of the magnetic field H for polycrystalline specimens consisting of mixed crystals of Fe_3O_4 and $NiFe_2O_4$. It appears that the saturation magnetostriction varies gradually with the composition and has a value of zero at about the composition $Ni_{0.56}Fe^{II}_{0.44}Fe_2O_4$. For the simple ferrites the λ *versus* H curves are monotonic. For specimens with

a composition of approximately $Ni_{2/3}Fe^{II}_{1/3}Fe_2O_4$ the magnetostriction as a function of the field strength shows a reversal point, as found in the case of the metal iron (Villari reversal point). The reason for this is that the magnetostriction in small fields, of the order of magnitude of the coercive force, is mainly the result of irreversible wall displacements which turn the magnetization towards a new preferred direction lying closer to the direction of the applied magnetic field. Where, for example, the cube diagonal is the preferred direction of the magnetization, this process is connected with the magnetostriction constant λ_{111}. For all field strengths there is superimposed on this magnetostriction a contribution caused by the rotation of the magnetization in each Weiss domain out of the preferred direction towards the direction of the applied magnetic field. This magnetostriction is also determined by λ_{100} in the case considered, and it predominates at field strengths that are large compared with the coercive force of the material. If λ_{111} and λ_{100} have different signs, then one can expect curves of the different types shown in Fig. 35.2. Conversely, such curves point to the magnetostriction having a different sign in the easy and difficult directions of the magnetization. Thus, from the trend of the λ *versus* H curve for small fields in polycristalline specimens we can get an idea of the magnitude of the magnetostriction in the crystallographic preferred direction of the magnetization. In the mixed crystal series of manganese ferrite and magnetite, compounds with very small values of magnetostriction have

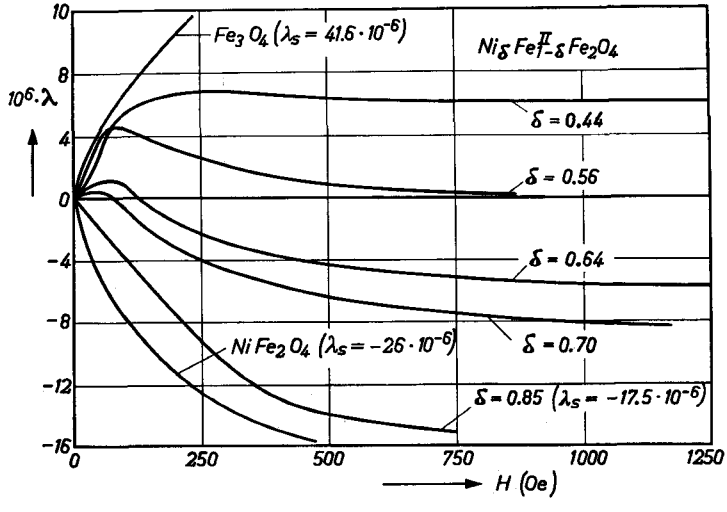

Fig. 35.2. Magnetostriction *versus* magnetic field for polycrystalline specimens of mixed crystals of the $Ni_\delta Fe_{1-\delta}Fe_2O_4$ series. (After [Wi 4]).

been found. Since the crystal anisotropy is also small, very high initial permeabilities can be realized with thes ferrites (see§ 48.1). The manganese-zinc ferrites, much used in practice, always contain so much ferrous ferrite that the magnetostriction at all field strengths has an absolute value lower than approximately 1×10^{-6}.

§ 36. Dynamic Properties

36.1. INDUCED FERROMAGNETIC RESONANCE

Fig. 36.1 gives an example of the absorption line caused by ferromagnetic resonance in a single crystal of a ferrite with spinel structure, in this case $Mn_{0.98}Fe_{1.86}O_4$ (see [Di 2]). A measurement was made of the energy absorption in a cavity by a single-crystal sphere with a diameter of about $\frac{1}{4}$ mm; μ'' was determined from the result with the aid of (23.2). The orientation of the single crystal was such that, for each curve, one of the crystallographic principal axes was parallel to the strong external magnetic field. The magnitude of the magnetic fields H_1, H_2 and H_3, which, at a given frequency f, are needed for resonance in the [100], [110] or [111] directions, is given by the eqs (26.10). From the magnitude of H_i and M_s the values of K_1 and g are determined; the results are given in Tables 34.I and 36.I. These tables include the g factors and anisotropies found in this way for several kinds of single crystals.

The width of the ferromagnetic resonance line is determined to a great extent by the ferrous concentration in the single crystal. Crystals of ferromagnetic spinels having a low ferrous content can yield minimum linewidths of approximately 50 Oersteds (see for example Fig. 36.1). The results of line-width measurements on nickel-ferrite single crystals containing ferrous

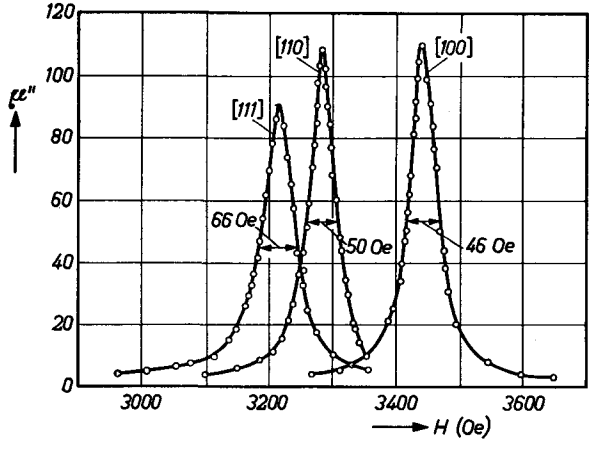

Fig. 36.1. Ferrimagnetic resonance line shapes measured with the d.c. magnetic field along the principal crystallographic directions. Measurements were made on a sphere of $Mn_{0.89}Fe_{1.86}O_4$ with a diameter of approximately $\frac{1}{4}$ mm at 9.3 kMc/sec, at room temperature. (After [Di 2]).

ions are reproduced in Fig. 36.2 [Ya 4]. A dimensional effect occurs since the line width in the case of too large spheres is increased by eddy current losses. It can be seen from the figure that the line width increases with the ferrous ion concentration. As a function of temperature a maximum appears at 160 °K. On the basis of a thermodynamic theory on the relaxation of electron transitions $Fe^{II} \rightleftarrows Fe^{III}$ the authors arrive at a relaxation time τ which depends upon the temperature according to $\tau = \tau_\infty e^{\epsilon/kT}$. From the results of the measurement it follows that $\epsilon = 0.022$ eV and $\tau_\infty = 1.0 \times 10^{-12}$

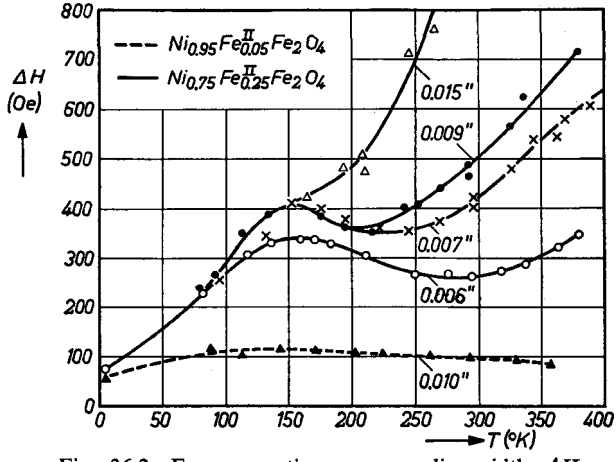

Fig. 36.2. Ferromagnetic resonance line width ΔH as a function of temperature for two single crystals containing ferrous ions. The d.c. magnetic field was in the [111] crystal direction. The drawn curves apply to various diameters of the ferrite sphere. The size effect is attributed to the eddy current losses. (After [Ya 4]).

sec. This activation energy is in agreement with that found for the conductivity of crystals of the same kind.

For crystals containing no ferrous ions the line width depends upon the orientation of the crystal (see Fig. 36.1) and it increases towards low temperatures (see Fig. 36.3). The magnitude of the damping parameter α in (23.10) is related, according to (23.13), with the line width ΔH and the resonance field H in accordance with the equation:

$$2\alpha = \Delta H/H. \tag{36.1}$$

From the results in Figs 36.1 and 36.3 it follows that α is of the order of magnitude of $\alpha = (50/2) \times 3000 = 0.008$ for spinels containing no ferrous ions and rises to a value approximately 10 times higher in the spinels of

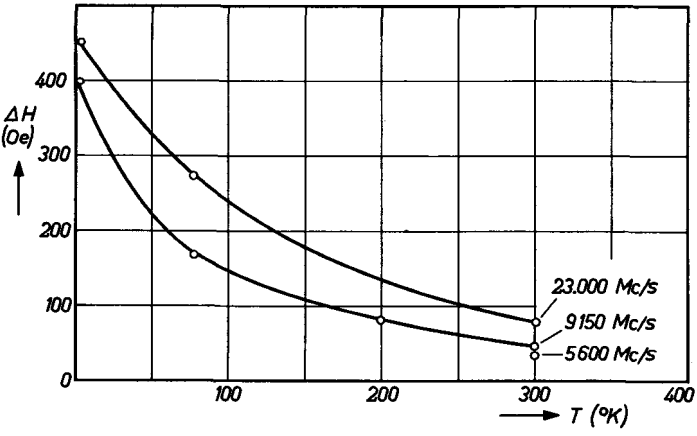

Fig. 36.3. Temperature dependence of the line width ΔH in a Mn-Zn ferrite containing a small (but unknown) amount of zinc and having a resistivity of about 10^4 ohm-cm. (After [Ta 3]).

higher ferrous content. The damping can also be indicated by a characteristic relaxation time τ:

$$\tau = 2H/\omega\Delta H = 1/\alpha\omega, \tag{36.2}$$

which in these two cases is of the order of magnitude of 10^{-9} and 10^{-10} sec respectively.

The shape of the narrow ferromagnetic resonance curves strongly resembles that which is to be expected from (23.12). The difference is that at equal half-value width and peak height the measured curve lies entirely within the calculated curve (see, for example, [Ta 3]). If the amplitude of the high-frequency waves in a ferromagnetic resonance experiment is increased, the shape of the resonance line changes [Bl 2]. The maximum value of μ'' is decreased and a second absorption peak appears at lower frequency for spheres of nickel-ferrite (see Fig. 36.4). An explanation of this phenomenon as given by Suhl was dealt with in § 23.4.

In the case of the ferrimagnetic spinels in which the magnetic moments of the ions on tetrahedral and octahedral sites are mutually parallel, the g factor according to (20.3) is given by

$$g_{\text{eff}} = 2\frac{(M_{\text{total}})_B - (M_{\text{total}})_A}{(M_{\text{spin}})_B - (M_{\text{spin}})_A}, \tag{36.3}$$

from which it follows that, for a completely inverse spinel, the measured value of g_{eff} is equal to the value of g for the divalent magnetic ion on the

octahedral site. Results of measurements carried out on single crystals and on polycrystalline specimens at different temperatures and frequencies are collected in Table 36.I. The fairly high value of the g factors for $NiFe_2O_4$ and $Co_2Fe_2O_4$ can explain the difference between the spin-only value for

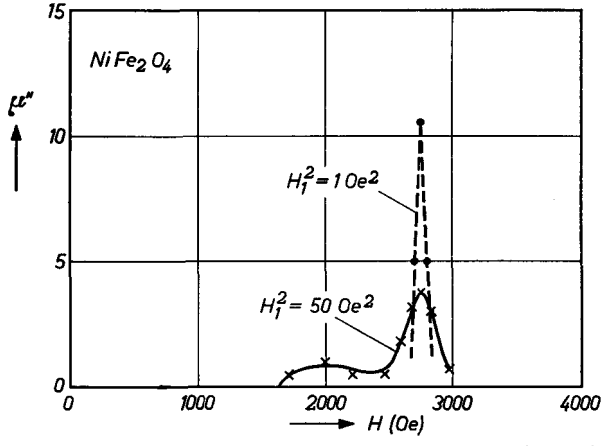

Fig. 36.4. The value of μ'' in arbitrary units as a function of the d.c. magnetic field H at 300 °K. At high microwave power level, indicated by the square of the microwave amplitude H_0, an anomalous absorption appears, especially at the low-field side of the resonance. (After [Bl 2]).

the magnetic moment of these compounds and the measured saturation magnetizations in Table 32.II. The result for $MnFe_2O_4$ is very satisfactory, since the carriers of the magnetic moments here are Mn^{II} and Fe^{III}, both

TABLE 36.I

EXPERIMENTAL VALUES OF THE EFFECTIVE g FACTOR OF SIMPLE FERRITES

Ferrite	Temperature °C	Wavelength cm	g_{eff}	Reference
$MnFe_2O_4$	—269	3.2	2.060	Di 2
	—196	,,	2.019 ± 0.003	,,
	27	,,	2.004 ± 0.002	,,
	—269 to 20	various	2.00	Ta 3
Fe_3O_4	—153	3.35	2.06	Bi 5
	—143	3.35	2.08	,,
		1.25	2.09	,,
	20	3.35	2.17	,,
		1.25	2.13	,,
$CoFe_2O_4$	90	1.25	2.7 ± 0.3	Ta 2
	200	1.25	2.27	,,
$NiFe_2O_4$	20	1.25	2.19	Ya 3
$CuFe_2O_4$	—195	1.25	2.20	Ok 1
	450	1.25	2.05	,,
$MgFe_2O_4$	20	1.24	2.03 — 2.06 *)	Ya 2
$Li_{0.5}Fe_{2.5}O_4$	20	3.18	2.08	Be 5

*) From measurements on polycrystalline samples

of which have a half-filled $3d$ shell and are thus in a ^6S state. In the case of spinels for which the saturation magnetization as a function of temperature shows a zero point at a temperature below the Curie point, anomalies occur in the value of the effective g factor (see § 19 and Fig. 19.2).

If, apart from Fe^{III}, there are two other kinds of metal ions present in a ferrite, it is no longer possible to determine from the magnitude of the saturation magnetization alone how the ions are distributed over the two lattice sites. Gorter [Go 6] and Smart [Sm 5] have indicated that the ion distribution can nevertheless be determined from the measured value of g_{eff} and from known values of the g factors for the ions on both kinds of lattice site. This has been applied to the spinel $Ni^{II}_{1.5}Fe^{III}Ti^{IV}_{0.5}O_4$, for which is found an extrapolated value $g_{eff} = 2.90$ at 0 °K. Assuming that $g_{Ni^{II}(oct)} = 2.3$ on octahedral sites and that $g_{Fe^{III}} = 2.00$ irrespective of the lattice site, then the ion distribution is $Fe_{0.7}Ti_{0.3}[Ni_{1.5}Fe_{0.3}Ti_{0.2}]O_4$. In order to apply this method it is necessary to know the g factors of the different ions on tetrahedral and octahedral sites, except for the above example. A similar analysis has been carried out by Smart [Sm 5] in the $NiFe_{2-\delta}Al_\delta O_4$ system. From susceptibility measurements on nickel-aluminate Smart deduced a g value $g_{Ni^{II}(tetr)} = 3.5$ for nickel ions on tetrahedral sites.

36.2. DOMAIN WALL RELAXATION

The movement of individual domain walls can be studied on so-called "window frames", which are made from a single crystal and whose sides are parallel to preferred directions of the magnetization. It is possible to create in these specimens a simple pattern of domain walls; an example is given in Fig. 36.5. Galt [Ga 3] has observed the movement of a domain wall parallel to the surface of the crystal in the case of Fe_3O_4 and a nickel ferrite having a composition $(NiO)_{0.75}(FeO)_{0.25}Fe_2O_3$. A typical example of a measured curve is given in Fig. 36.6, where the wall velocity is plotted as a function of the magnitude of an applied magnetic field. Oscilloscopic observation of the secondary voltage across a coil shows that this voltage remains constant for a long time, indicating that the wall has a uniform velocity and that therefore the mass m_w in the equation of motion (24.9) can be neglected. Equation (24.9) is then

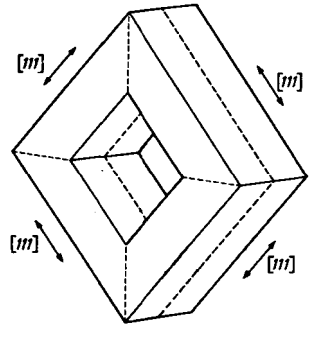

Fig. 36.5. Single-crystal ferrite sample used to study motion of individual ferromagnetic domain walls. The broken lines indicate positions of the domain walls. (After [Ga 3].)

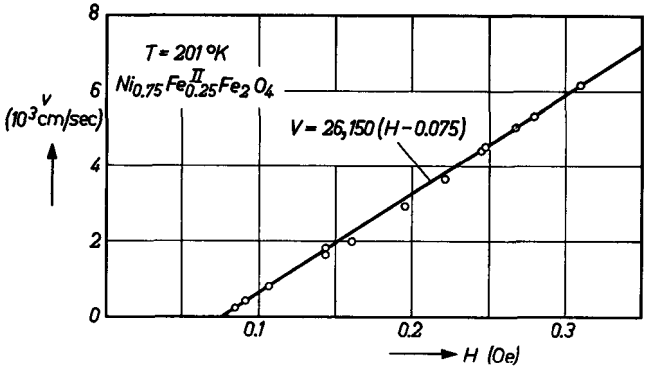

Fig. 36.6. Typical plot of actual data for domain wall velocity v as a function of applied field. (After [Ga 3]).

satisfied if the applied magnetic field is reduced by a critical field below which no wall movement takes place. This critical field corresponds in good approximation to the coercive force of the crystal. From the slope of the straight line in Fig. 36.6 a damping coefficient β for the domain wall displacement can be determined with (24.9) and from this coefficient, after making a correction for eddy current damping (see [Wi 2]) a damping coefficient α can be determined with (24.10) for the spin motion as given by (23.10). Some results of measurements on ferrous ferrites, in which the damping is probably caused by electron relaxation, are collected in Table 36.II. Compared with the damping coefficient α, as found from the width of the ferromagnetic resonance line, there exists a difference of only about a factor two.

TABLE 36.II

THE DAMPING COEFFICIENT α OF (23.10) DETERMINED FROM DOMAIN-WALL MOTION AND FROM THE WIDTH OF THE FERROMAGNETIC RESONANCE LINE ACCORDING TO [Ga 3].

Ferrite	α Domain wall	α Ferromagnetic resonance
Fe_3O_4	0.066	0.11
$(NiO)_{0.75}(FeO)_{0.25}Fe_2O_3$	0.008	0.018

CHAPTER IX

INTRINSIC PROPERTIES OF FERRITES WITH HEXAGONAL CRYSTAL STRUCTURE

§ 37. Chemical Compositions and Crystal Structures

37.1. CHEMICAL COMPOSITIONS

A group of ferromagnetic oxides exists possessing closely related hexagonal crystal structures ([We 2], [Jo 4]). Fig. 37.1 shows a diagram in which the chemical compositions of the substances to be discussed can be indicated. The corners of the diagram represent the oxides BaO, MeO and Fe_2O_3. The symbol Me represents a divalent ion from the first transition series, or it may represent Zn, Mg, or a combination of for instance Li^{I} and Fe^{III}, just as can occur in the spinel structure. The compounds to be described are

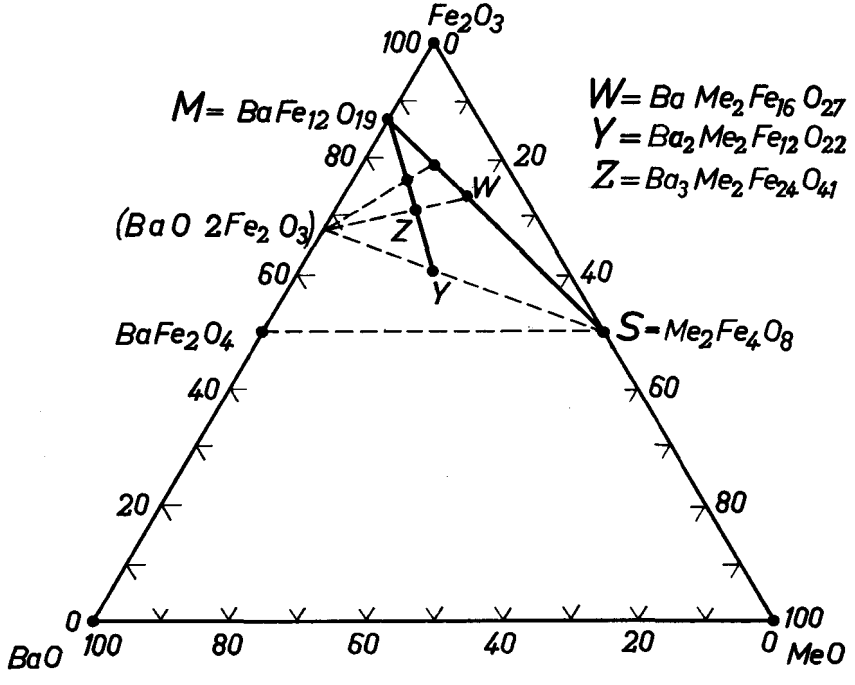

Fig. 37.1. Composition diagram for the ferromagnetic ferrites. The symbol Me represents a divalent ion (or a combination of divalent ions)

produced by firing at a temperature above 1000 °C the appropriate mixture of the oxides represented by the corners of the composition diagram. It is also possible to start from mixtures of compounds, for example carbonates of the metal ions. The method of preparation is analogous to that for ferromagnetic spinels. On the line connecting BaO and Fe_2O_3 in the diagram there is a point which represents the non-ferromagnetic barium ferrite $BaFe_2O_4$. At an equivalent position is found the point **S** on the line between the oxides MeO and Fe_2O_3, which represents $Me_2Fe_4O_8$ with the cubic spinel crystal structure (see Chapter VIII). The point **M** represents the oxide with chemical composition $BaFe_{12}O_{19} = BaO.6Fe_2O_3$ ([Ad 1], [We 2]), which has a hexagonal crystal structure and which is one of the ferromagnetic oxides to be dealt with in this chapter. Another important compound is represented by point **Y**, having the chemical formula $Ba_2Me_2Fe_{12}O_{22} = 2(BaO.MeO.3Fe_2O_3)$. This compound possesses a hexagonal crystal structure differing from the **M** structure [Jo 4]. In order to establish the position of **Y**, the diagram also indicates the hypothetical $BaO.2Fe_2O_3$. Twice the simplest chemical formula unit has been chosen for the composition of the compounds **S** and **Y**. As we shall see later, this has the advantage that the simplest crystallographic blocks, from which the different hexagonal structures can be built up, contain exactly the number of ions indicated by this chemical formula. Many chemical compounds are found on the lines **M-S** and **M-Y**, ([Wi 5], [Br 1], [Jo 4, 5]). However, the elementary cells of these crystal structures can be built up in a simple way from those of **S**, **M** and **Y**. We shall therefore deal first with the crystal structures of the latter compounds. In most cases the Ba ion can partly or completely be substituted by a Ca, Sr or Pb ion, which have approximately the same ionic radii (see Table 37.I), or by a trivalent ion, such as La^{III}. In the latter case

TABLE 37.I

GOLDSCHMIDT IONIC RADII

Ion	Radius in Å
O^{II}	1.32
Ca^{II}	1.06
Sr^{II}	1.27
Ba^{II}	1.43
Pb^{II}	1.32

an equivalent amount of the ferric ions become ferrous ions. It is also possible in these crystal structures to replace the trivalent ferric ion by the trivalent ions of Al or Ga, or by an equivalent amount of a combination of divalent and tetravalent ions. For example, 2δ ferric ions in the **M** compound re-

placed by δ cobalt ions and δ titanium ions yield a compound with chemical formula: $BaCo_{\delta}^{II}Ti_{\delta}^{IV}Fe_{12-2\delta}O_{19}$ (see [Ca 2]).

37.2. HEXAGONAL CLOSE-PACKED STRUCTURE

The hexagonal close-packed structure is represented schematically in Fig. 37.2*a*. The centres of the ions *B* lie in a horizontal plane and form equilateral

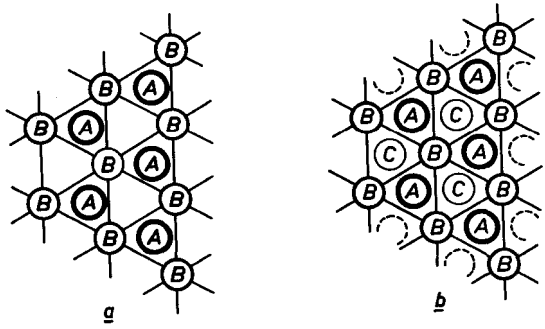

Fig. 37.2. Schematic representation of the close-packed hexagonal structure (a) and the close-packed cubic structure (b) of identical ions. In (a) the ions A are in the interstices in a plane both above and below the plane containing the ions B, thus forming the sequence vertical ABAB *etc.* In (b) the ions A and C in the layers adjacent to the B layer do not lie vertically above each other, resulting in the vertical sequence ABCABC *etc.*

triangles. On this layer can now be placed a new layer of identical ions, shown in the diagram as *A*. These ions are also closely packed in a horizontal plane. With a hexagonal close-packed structure there exists under the layer with *B* ions another layer of ions whose centres lie vertically below those of the ions in the *A* layer. Continuing in the vertical direction we thus obtain in a hexagonal structure the sequence of layers *ABABA* and so on. It is evident that this produces a uniaxial hexagonal crystal structure in which the *c* axis is perpendicular to the oxygen layers.

The cubic close-packed structure is represented in a corresponding manner in Fig. 37.2*b*. The sequence of layers, proceeding vertically, is here *ABCABCA etc.*, where the ions *A* and *B* have positions similar to these in Figure *a*, and where the ions *C* lie closely packed in one plane at the same distance below the plane of the drawing as the *A* ions lie above it. This cubic close-packed oxygen structure occurs in the spinels. Fig. 37.3 gives a perspective drawing of the spinel structure, the [111] axis being set out vertically. The top and

bottom ion layers are identical, also as regards their environment, so that sufficient information is present for continuing the structure in the vertical direction. The distance between two successive oxygen layers is approximately 2.30 Å, and varies only in the third decimal place for the various metal ions. Fig. 37.3*b* gives a cross-section through a mirror plane containing the [111] axis. The vertical lines are axes of threefold symmetry. This means that all ions not lying on one of these axes occur three times.

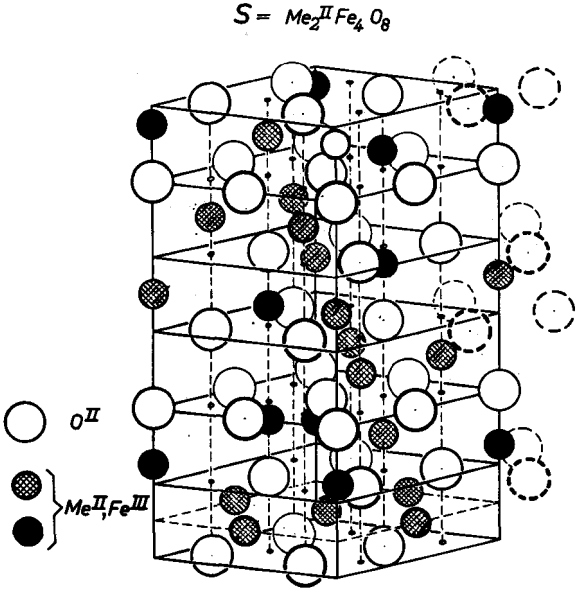

Fig. 37.3a Perspective representation of the spinel structure with the [111] axis vertical. The hatched and black circles represent ions on octahedral and tetrahedral sites respectively.

The ferromagnetic oxides to be discussed all consist of closely packed oxygen ions. The structures are built up from sections having alternately a cubic and a hexagonal structure. It is evident that in such a case the crystal structure will again have hexagonal symmetry. In certain layers in these substances some oxygen ions are replaced by barium ions, which are approximately of the same size as oxygen ions (see Table 37.I). For a complete description of the crystal structures the reader is referred to "Crystal Structures of a New Group of Hexagonal Ferromagnetic Compounds" by Braun [Br 6].

37.3. THE MAGNETOPLUMBITE STRUCTURE M

The compound M, with a chemical composition $BaFe_{12}O_{19}$, has a crystal structure which, according to Adelsköld [Ad 1], is equal to that of the min-

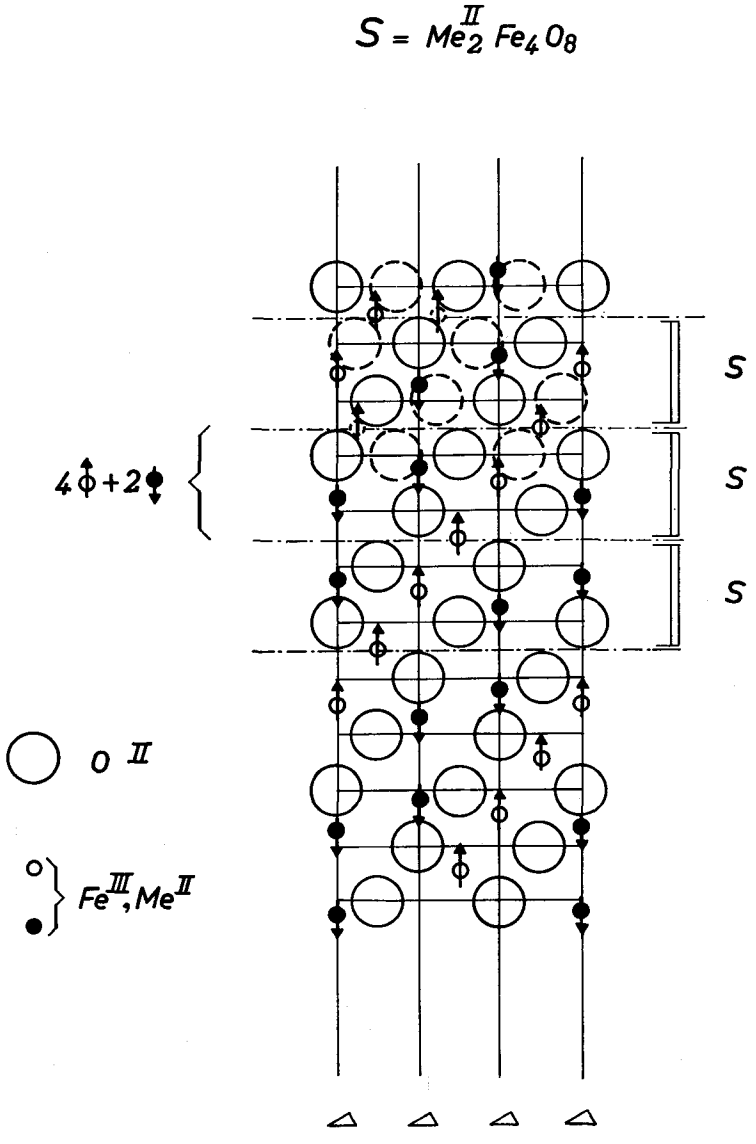

Fig. 37.3b. Cross-section through a mirror plane of the spinel structure with the [111] axis vertical, drawn for the ideal value of the parameter u. The vertical lines are axes of threefold symmetry. All ions not lying on one of these axes occur three times, as shown schematically by broken circles in the top layers. The small white and black circles represent respectively ions on octahedral and tetrahedral sites. The arrows indicate the relative orientation of the magnetic moments of the ions on these sites.

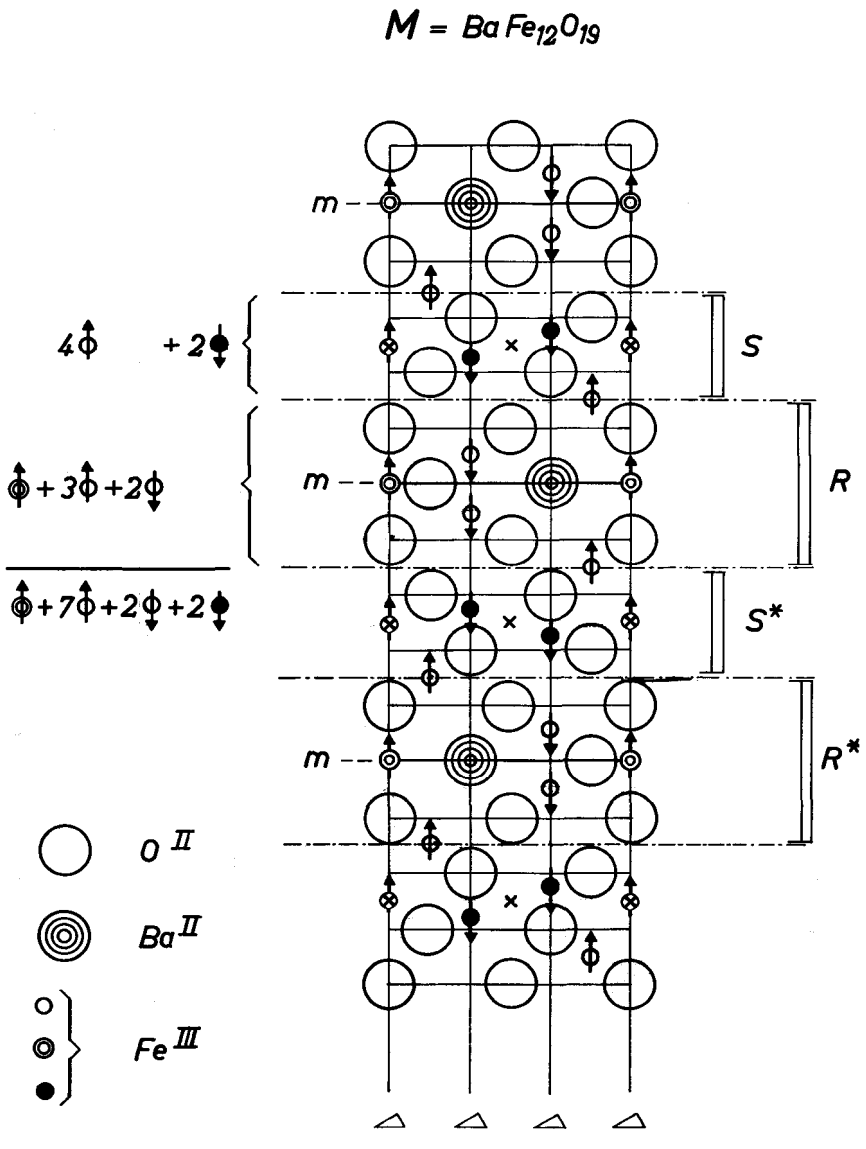

Fig. 37.4. Cross-section of the magnetoplumbite structure M, with the c axis vertical. The arrows indicate the spin orientations. The drawn vertical lines are axes of three-fold symmetry. A cross indicates a centre of symmetry. All layers containing barium are mirror planes, and are denoted by m. This structure consists of the same S blocks as in Fig. 37.3b separated by R blocks containing barium. The asterisk indicates a rotation of a block by 180° about the c axis.

eral magnetoplumbite, the composition of which is approximately $PbFe_{7.5}Mn_{3.5}Al_{0.5}Ti_{0.5}O_{19}$. The hexagonal elementary cell consists of 10 oxygen layers. The length of the *c* axis corresponding to this is 23.2Å and that of the *a* axis is 5.88 Å. A schematic representation of the **M** structure is given in Fig. 37.4. In an elementary cell each layer contains four large ions. There are in four successive layers always four oxygen ions, but each fifth layer contains three oxygen ions and one barium ion. The magnetoplumbite structure can be built up from spinel blocks of two oxygen layers (Fig. 37.4), being blocks **S** and **S***, which are connected by a block **R** (for a perspective drawing of this block see Fig. 37.5*a*) containing the barium ion. Blocks

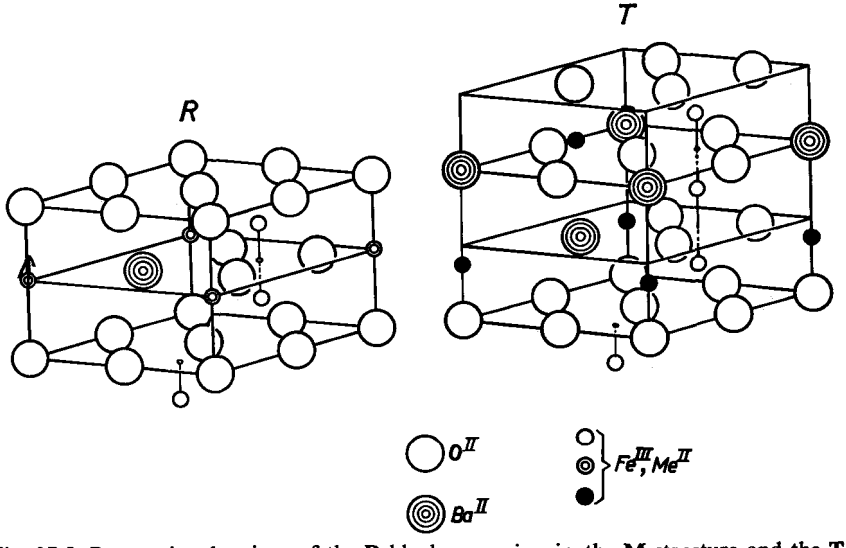

Fig. 37.5. Perspective drawings of the **R** block occurring in the **M** structure and the **T** block occurring in the **Y** structure. The latter block contains two adjacent barium layers.

R* and **S*** are obtained from blocks **R** and **S**, respectively, by rotation over 180° around the *c* axis. The layer containing barium is hexagonally packed with respect to two oxygen layers at each side. The four oxygen layers between those containing barium are cubically packed. There is an overlap of cubically and hexagonally packed sections in the structure. The basal plane containing the barium ion is a mirror plane of the **R** block, and consequently the blocks preceding and succeeding the **R** block (**S** and **S***) must be rotated over 180° with respect to each other. This is also the reason why the elementary cell of the **M** structure contains 10 and not 5 oxygen layers. In general it can be said that when one **R** block is passed in a structure the following blocks must be rotated over 180° around the

c axis. Only after a second **R** block is passed is the original situation found again. The crystallographic structure can thus be described as **RSR*S***, and the elementary cell contains a number of ions corresponding to $2(BaFe_{12}O_{19})$. The unit **S**, then, contains two molecules $MeFe_2O_4$. It would be possible to say that in the **M** structure the spinel block consists of two more oxygen layers [Br 6], but the block then obtained would not contain the metal and oxygen ions in the ratio 3 : 4.

For the ferric ions there are three different kinds of interstitial sites present. Along with octahedral and tetrahedral sites there exists a new type of interstitial site which is not found with spinels and which is surrounded by five oxygen ions constituting a triagonal bipyramid. These sites occur in the same layer as the barium ion, and they can be compared with tetrahedral sites. In the hexagonal structure two tetrahedral sites are adjacent to each other, and for these two only one metal ion is available. This metal ion now occupies a position halfway between them, amidst the three oxygen ions. According to the ideal parameters the available space is extremely small. This means that the three oxygen ions are certainly displaced outwards, as it is also the case with the more spacious tetrahedral sites in the spinel lattice (see § 31.2). In the **R** block two adjacent octahedral sites are occupied by ferric ions. There are now, however, two ions available, so that in this case there is no abnormal environment. The fact that it is not the other way round, *i.e.* two tetrahedral sites occupied and one ion available for the two octahedral sites together, is because an octahedral environment is energetically more favourable than a tetrahedral one (higher coordination number, compare with the situation in spinels). Moreover two ions in the octahedral sites lie further apart than they would do if they had occupied the two tetrahedral sites.

37.4. THE CRYSTAL STRUCTURE OF THE COMPOUND Y = $Ba_2Me_2Fe_{12}O_{22}$

The crystal structure, as determined by Braun [Bi 6], of the compound **Y**, chemical composition $Ba_2Me_2Fe_{12}O_{22}$, is represented schematically in Fig. 37.6. The smallest elementary cell with hexagonal symmetry consists of 18 oxygen layers, the length of the *c* axis being 43.56Å. If, however, the upright edges of the parallelepiped are not taken vertically but along the oblique lines indicated in the figure, it is possible to find an elementary cell, having rhombohedral symmetry, with a repeat distance extending through only six oxygen layers. In the hexagonal elementary cell each layer again contains four large ions. There are four successive layers of four oxygen ions, followed by two layers each containing three oxygen ions and one barium ion. The **Y** structure can be built up from spinel blocks of two oxygen

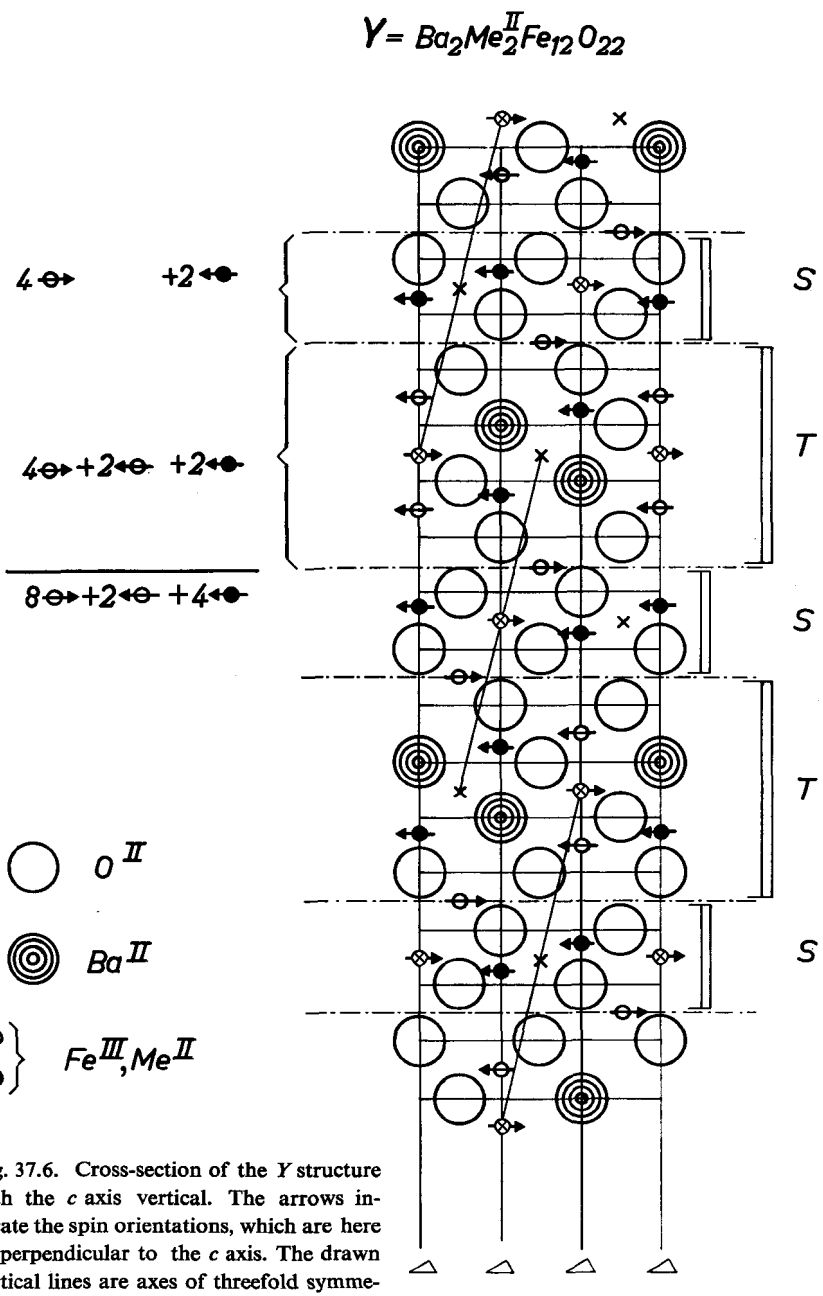

Fig. 37.6. Cross-section of the *Y* structure with the *c* axis vertical. The arrows indicate the spin orientations, which are here all perpendicular to the *c* axis. The drawn vertical lines are axes of threefold symmetry. A cross indicates a centre of symmetry. The structure is composed of alternating *S* and *T* blocks. The rhombohedral repeat distance is indicated.

layers: the blocks **S** in Fig. 37.3*b*, which are connected by a block **T** in which there are now, one above the other, two layers with barium ions; for a perspective drawing of the **T** block see Fig. 37.5*b*. The layers containing barium are hexagonally packed with respect to their adjacent oxygen layers. These barium ions are somewhat larger than the oxygen ions (see Table 37.I). Therefore the distance between the layers with barium ions is greater than between the oxygen layers which contain no barium ions; the distances are 2.40 and 2.32 Å respectively. The projection of the distance between the centres of the barium ions on to the *c* axis is 2.90 Å, from which it follows that the centres of the barium ions lie at a distance of 0.25 Å out of the plane of the nearest oxygen layer. The distance, too, between a layer with a barium ion and the first following oxygen layer is slightly increased, namely up to 2.35 Å. In the **Y** structure, only tetrahedral and octahedral sites are occupied by the metal ions. Per formula unit $Ba_2Me_2Fe_{12}O_{22}$, four ions occupy tetrahedral sites and ten octahedral sites. The **T** block might be regarded as a combination of the innermost layers of two **R** blocks from Fig. 37.5*a*. To the two octahedral ions lying one above the other a second pair is added from the adjacent barium layer, of which two of the octahedral ions coincide. In this way one obtains three octahedral ions one above the other. The two sites surrounded by five anions are no longer occupied either, because one of the tops of the adjacent tetrahedrons is now occupied by a Ba ion. The metal ion is pushed towards the centre of the other oxygen tetrahedron. The **T** block does not contain a mirror plane, so that now the preceding and succeeding **S** blocks are not rotated with respect to each other. The crystallographic build-up of the **Y** structure is thus represented by **TS**. It may be noted that the chemical composition of the **T** block is given by the hypothetical $BaO.2Fe_2O_3$ indicated in Fig. 37.1.

37.5. MIXED COMPOUNDS

Apart from the three structures discussed, **S**, **M** and **Y**, there also occur on the sides **M-Y** and **M-S** of the triangle formed by these three points in Fig. 37.1 a number of crystal structures whose elementary cells can be built up from those of the compounds at the corners. The structure can again be given by the stacking of **R**, **S** and **T** blocks. For all these compounds the *a* axes are the same (= 5.88 Å) and the *c* axes are approximately additive. The compounds listed in Table 37.II have been prepared and identified by X-ray analysis. It is very remarkable that regularities of this order can occur in the sequence of **R**, **S** and **T** blocks. The most important of these compounds are denoted by the letters **W** and **Z**. By way of illustration the cross-sections through mirror planes containing the *c* axis of **W** and **Z**

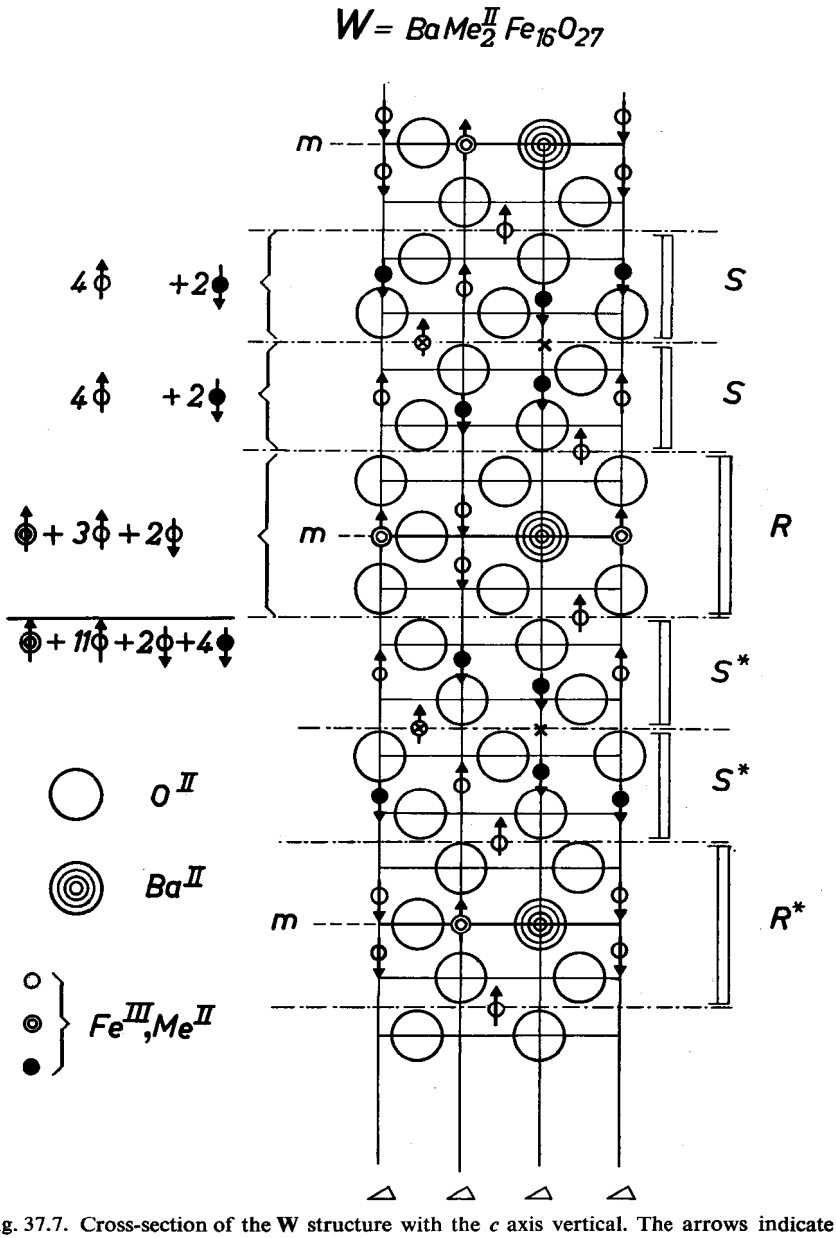

Fig. 37.7. Cross-section of the W structure with the *c* axis vertical. The arrows indicate the spin orientations. The drawn vertical lines are axes of threefold symmetry. A cross indicates a centre of symmetry. The asterisk indicates a rotation of a block by 180° about the *c* axis. The structure can be thought to be the sum of the S and the M structures (Figs. 37.3b and 37.4 respectively).

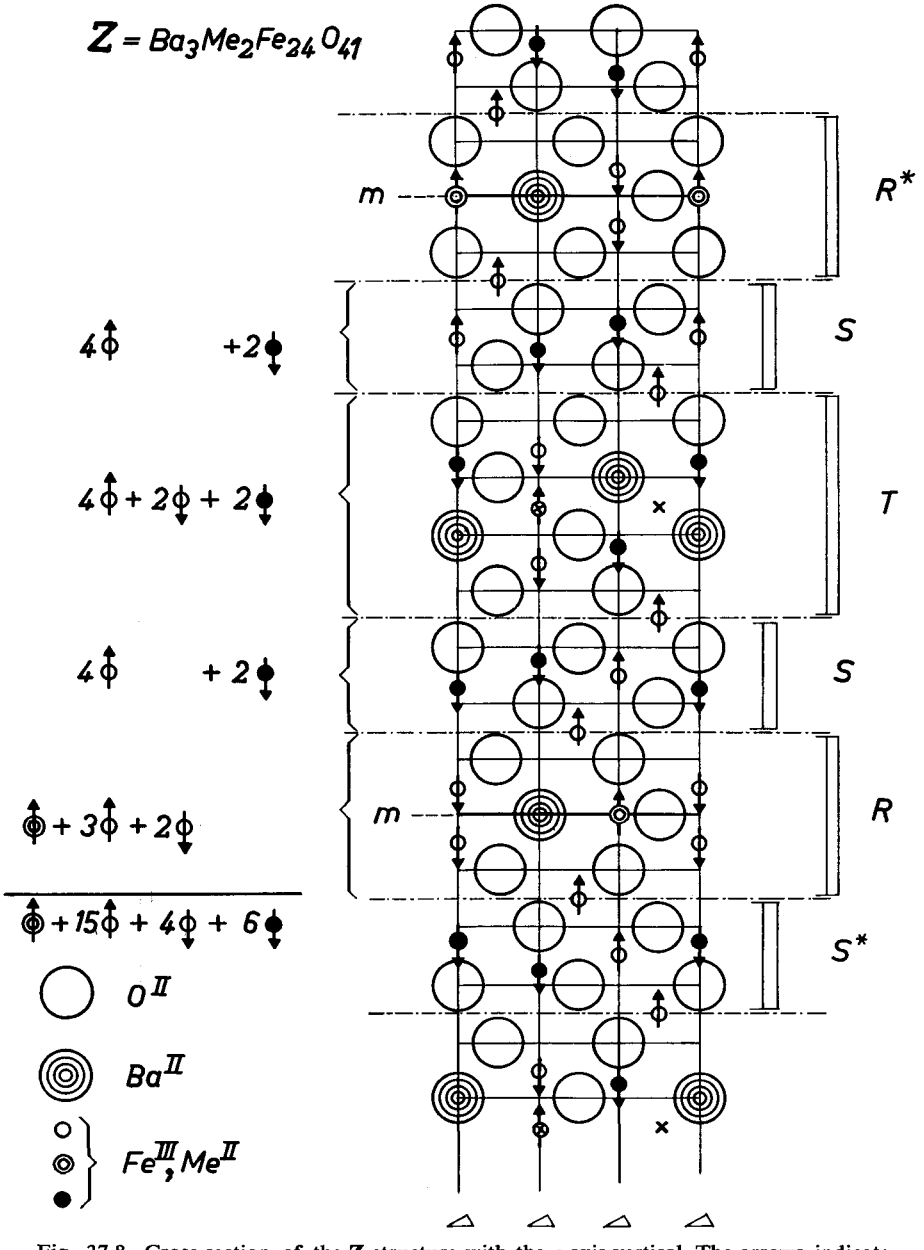

Fig. 37.8. Cross-section of the **Z** structure with the *c* axis vertical. The arrows indicate the spin orientations. The drawn vertical lines are axes of threefold symmetry. A cross indicates a centre of symmetry. The asterisk indicates a rotation of a block by 180° about the *c* axis. The structure can be thought to be the sum of the **M** and the **Y** structure (Figs. 37.4 and 37.6 respectively).

TABLE 37.II

FERROMAGNETIC OXIDES WITH HEXAGONAL CRYSTAL STRUCTURES

Chemical composition	Symbol	Crystallographic build-up	Number of layers per hexagonal elementary cell	c axis *) in Å	Molecular weight	X-ray**) density g/cm³
$BaFe_{12}O_{19}$	M	RSR*S*	10	23.2	1112	5.28
$Me_2Fe_4O_8$	S	S	—	—	232	5.24
$Ba_2Me_2Fe_{12}O_{22}$	Y	$(TS)_3$	3×6	3×14.5	1408	5.39
$BaMe_2Fe_{16}O_{27}$	MS(W)	$RS_2R^*S_2^*$	14	32.8	1575	5.31
$Ba_2Me_2Fe_{28}O_{46}$	M_2S	$(RSR^*S_2^*)_3$	3×12	3×28.0	2686	5.29
$Ba_3Me_2Fe_{24}O_{41}$	MY(Z)	RSTSR*S*T*S*	22	52.3	2520	5.33
$Ba_4Me_2Fe_{36}O_{60}$	M_2Y	RSR*S*TS*	16	38.1	3622	5.31

are given in Figs. 37.7 and 37.8 respectively. For the metal ions Me about the same variety of divalent ions can be taken as for the ferrites with spinel structure. Which these are will be indicated by short notation, as for example: Co_2Z, $Ni_{1.5}Zn_{0.5}W$, Zn_2Y, etc. The molecular weights and X-ray densities of the most important of these compounds are given in Table 37.III.

TABLE 37.III

X-RAY DENSITY d_x AND MOLECULAR WEIGHT M OF SOME OXIDES WITH HEXAGONAL CRYSTAL STRUCTURE.

Me	W = $BaMe_2Fe_{16}O_{27}$		Z = $Ba_3Me_2Fe_{24}O$		Y = $Ba_2Me_2Fe_{12}O_{22}$	
	d_x g/cm³	M	d_x g/cm³	M	d_x g/cm³	M
Mg	5.10	1512	5.20	2457	5.14	1346
Mn	5.31	1573	5.33	2518	5.38	1406
Fe	5.31	1575	5.33	2520	5.39	1408
Co	5.31	1577	5.35	2522	5.40	1410
Ni	5.32	1580	5.35	2526	5.40	1414
Cu	5.36	1590	5.37	2536	5.45	1424
Zn	5.37	1594	5.37	2539	5.46	1428

37.6. IDENTIFICATION OF THE HEXAGONAL OXIDES

The materials are prepared by firing specific mixtures of oxides for a certain time at a temperature ranging between 1200 and 1400 °C, so that a sintered ceramic product is obtained. Their crystal structures are determined by X-ray

*) Independent of the type of Me ions in the approximation given here.

**) In the case where Me represents a ferrous ion. For the other compositions see Table 37.III.

analysis. However, since the compounds **M** and **W**, for example, have a closely related structure, small quantities of **M**, which can occur as by-product in incomplete chemical reaction, are not easy to distinguish in the X-ray powder diagrams from **W**. This difficulty can be circumvented in the following way.

Many **W** compounds, like **M** compounds, are ferromagnetic with a preferred direction of magnetization parallel to the hexagonal axis (see § 39). The crystallites in a powdered material will therefore orient themselves in a magnetic field such that the hexagonal axis of each crystallite will be more or less parallel to the lines of force. A few drops of a suspension of a powdered specimen in a solution of a binder are now applied on a small glass plate, and a strong magnetic field is applied perpendicularly to the glass plate. When the binder is left to dry and afterwards the magnetic field switched off, the crystallites are left with their hexagonal axes perpendicular to the surface of the glass. In the X-ray diffraction diagram of such specimens, recorded with a diffractometer *), the X-ray reflections from the planes perpendicular to the hexagonal axis [001], appear much intensified, whereas the other reflections have almost vanished. This greatly simplifies the diagram; see Fig. 37.9 (page 199). These simplified diagrams are characteristically different for **M** and **W**, and this makes it easy to distinguish a small quantity of one of these compounds from a large quantity of the other. Moreover, the powder diagrams of the other hexagonal compounds, for example **Y** and **Z**, also resemble those of **M** and **W**, so that with powder diagrams alone it is not easy to ascertain in which composition of the oxide mixtures these compounds occur in a pure state. In these cases, too, the method of alignment in a magnetic field is employed, and here again one finds a characteristic simplification of the X-ray diagrams. It appears from these diagrams of aligned specimens (Fig. 37.10 [page 200]) that in most **Z** specimens the hexagonal axis (*c* axis) is parallel to the magnetic field; thus, the spontaneous magnetization of these compounds is also parallel to the *c* axis. As is the case with **M** and with many representative oxides of the **W** group, this axis is a preferred direction. With all **Y** specimens, on the other hand, the hexagonal axis lies perpendicular to the magnetic lines of force, the directions of the other axes being arbitrary; this means that the spontaneous magnetization of the **Y** compounds lies in a plane at right angles to the *c* axis. The result is that after a magnetic treatment as described above, only *hko* reflections appear in the X-ray diagram.

*) In diffraction experiments with a diffractometer it is precisely such *flat* specimens that are used. See [Pa 1].

§ 38. Saturation Magnetization

38.1. THE PREDOMINANT SUPEREXCHANGE INTERACTIONS IN THE VARIOUS STRUCTURES

It is assumed that the relative orientation of the magnetic moments of the ions in the S blocks of the hexagonal ferrites is the same as in the ferrites with spinel structure. In each S block, then, there are four octahedral ions and two tetrahedral ions with oppositely oriented magnetic moments; this is indicated by arrows in Figs 37.3*b*, 37.4, 37.6, 37.7 and 37.8. To indicate the predominant superexchange interactions in the interlying blocks **R** and **T**, these blocks are again reproduced schematically in Fig. 38.1, but now taking into account the correct parameters for the ions in the environment of the layers containing barium. In the **R** block (occurring for example in the half elementary cell of the **M** structure) the direction of the magneticmoment of the ion 1 in the layer containing barium is chosen, parallel to the *c* axis in an upward direction *). The starting premise is

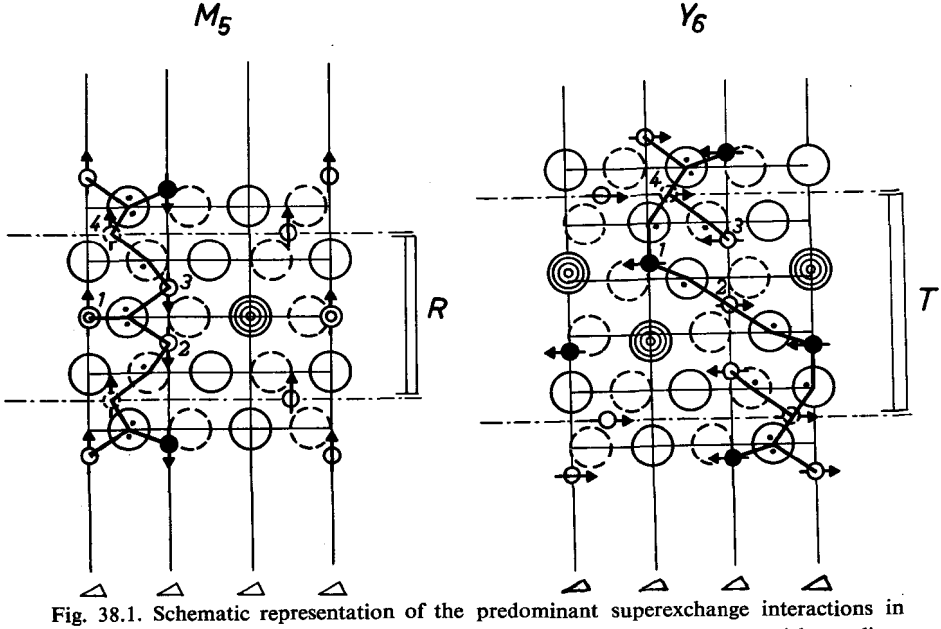

Fig. 38.1. Schematic representation of the predominant superexchange interactions in the **M** and the **Y** structures. Each interaction is indicated by two connected heavy lines with a dot included in the angle between them.

*) The direction of the magnetic moments with respect to the crystal lattice is dealt with in § 39. We are only concerned with the mutual direction of the magnetic moments of the ions.

again that the superexchange interactions between the magnetic ions take place *via* the intermediate oxygen ions, and it is assumed that this is again a negative exchange interaction (number of *d* electrons $\geqslant 5$) see § 8.1. As for the spinels (see § 32.1) Gorter estimates the magnitude of the exchange interactions from the magnitude of the distances l = Me-O-Me and the angles ϕ = MeOMe (see [We 2]). This leads to the assumption that the magnetic moments of the metal ions 2 and 3, which lie closest to the layer containing barium, are directed downwards. The reason is that the 1-oxygen-2 interaction is large because the appertaining angle ϕ is large (approximately 140°), whereas the other interaction, the 2-oxygen-3 interaction, which attempts to align the magnetic moments of these ions antiparallel, is smaller because the appertaining angle is unfavourable (approximately 80°). Moreover, the distances from the ion to the three surrounding oxygen ions in the basal plane is very small (1.3 Å) and this promotes a high 1-oxygen-2 interaction. The coupling with the **S** block is brought about by the interaction between the magnetic moments of the octahedral ions 3 and 4. Interaction between octahedral ions also occurs in the spinel structure (its magnitude is indicated by the quantity β, see § 33), but there it is relatively small owing to the unfavourable angle (90°). The distances here to the oxygen ions are the same, but because of the different oxygen stacking in the **R** block, the angle is now larger (130°). This is the most important interaction between the **R** and the **S** blocks. The interaction between the ions 1 and 4 opposes the drawn spin configuration. This interaction will be small because of the considerable distance between ion 1 and the oxygen ion vertically above it (2.3 Å). From the fact that the Curie point of the **M** compound is high (450 °C) it may be deduced that the octahedral-octahedral interaction will increase sharply with increasing angle.

In the case of the **T** block (occurring, for instance, in the elementary cell of the **Y** structure, (see Fig. 37.6) the starting point [Go 7] is the octahedral ion 2 which lies between the two layers containing barium. If the magnetic moment of this ion is oriented perpendicularly to the *c* axis towards the right, the magnetic moment of the tetrahedral ion 1 will be oriented to the left. In the **R** block the 1-oxygen-3 interaction was equal to the 1-oxygen-2 interaction. This is not the case now because the ion is displaced in such a way that the angle 1-oxygen-2 is larger than the angle 1-oxygen-3. Moreover, according to Braun [Br 6], the ion 3 is shifted upwards, so that the distance from this ion to the oxygen ions in the layer containing barium has become relatively large (2.33 Å), and this reduces the 1-oxygen-3 interaction (now comparable to the 1-oxygen-4 interaction in the **R** block). The 1-oxygen-4 interaction is now important and is of the tetrahedral-

octahedral type occurring in the spinel lattice. The magnetic moment of the ion 3 is now oriented in accordance with the 3-oxygen-4 interaction, which was also important in the **R** structure, and in this case would probably be even stronger since the ion 3 is closer to the oxygen ion between ions 3 and 4. As a result, the moment of ion 3 is now antiparallel to that of ion 2. Consequently the **T** block contains as many ions (4) pointing to the right as pointing to the left, and therefore, if all these ions are of the same kind, there will be no net resultant moment. The **T** block may then be called "antiferrimagnetic". It is found experimentally, in agreement with the above, that the saturation magnetization of the **Y** crystals is relatively low, being about half that of ferrimagnetic spinels. A survey of the relative directions of the magnetic moments of the metal ions in the various blocks is given in Table 38.I.

TABLE 38.I

NUMBER OF METAL IONS ON THE VARIOUS SITES IN THE BLOCKS R, S AND T. THE RELATIVE DIRECTION OF THEIR MAGNETIC MOMENTS IS INDICATED BY ARROWS.

Block	Tetrahedral ions (surrounded by 4 oxygen ions)	Octahedral ions (surrounded by 6 oxygen ions)	Ions with fivefold coordination
R	—	3 ↑ 2 ↓	1 ↑
S	2 ↓	4 ↑	—
T	2 ↓	4 ↑ 2 ↓	—

38.2. SATURATION MAGNETIZATION OF COMPOUNDS WITH M STRUCTURE

The resultant magnetic moment per formula unit $BaFe_{12}O_{19}$ is equal to the sum of the moments of the seven octahedral ions and the ion in the layer containing barium, reduced by the moments of two octahedral and two tetrahedral ions, which are oppositely oriented to them; this is schematically indicated by arrows in Fig. 37.4. In the case of $BaFe_{12}O_{19}$, all magnetic ions have a magnetic moment of 5 Bohr magnetons, so that the magnetization per formula unit is equal to $(1 + 7 - 2 - 2) \times 5 = 20$ Bohr magnetons. Measurements on polycrystalline $BaFe_{12}O_{19}$ at liquid hydrogen temperature and in fields up to 26,000 oersteds result in exactly this value [St 1].

In Fig. 38.2 the saturation magnetization is given as a function of temperature for $BaFe_{12}O_{19}$ (corresponding to $\delta = 0$ in the figure). The satura-

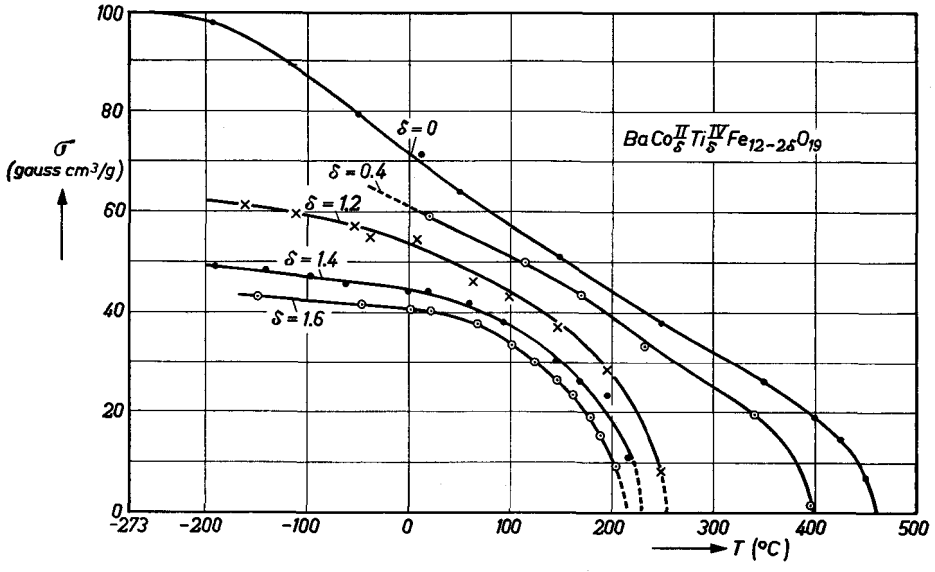

Fig. 38.2. Saturation magnetization as a function of temperature for a number of compounds with the magnetoplumbite structure **M**.

tion magnetization decreases approximately linearly with temperature in a wide temperature range. At $T = 20$ °C one finds $\sigma = 72$ gauss cm³/g, corresponding to $4\pi M_s = 4775$ gauss. The Curie point is 450 °C. Some information is available on how the saturation magnetization is affected by the substitution of other ions in the **M** structure [Ca 2]. The curves in Fig. 38.2 give the saturation magnetization for the case where some of the ferric ions are replaced by a combination of Co^{II} and Ti^{IV} ions according to the formula $BaCo_\delta^{II}Ti_\delta^{IV}Fe_{12-2\delta}O_{19}$. The measurements were carried out on polycrystalline specimens at the relatively low field strength of 6600 oersteds. It can be seen that both the Curie point and the saturation magnetization at low temperature decrease rapidly with increasing δ. From measurements at liquid hydrogen temperature and in magnetic fields up to 25,000 oersteds a saturation magnetization has been found of approximately 14 and 12 Bohr magnetons per formula unit for values of δ equal to 1.2 and 1.4 respectively.

38.3. SATURATION MAGNETIZATION OF COMPOUNDS WITH W STRUCTURE

In Fig. 38.3 the saturation magnetization σ per gram for a number of simple and mixed **W** compounds is plotted as a function of temperature. In the

case of these W compounds, too, almost straight lines are found over a large temperature range, as had already been found for the compound $BaFe_{12}O_{19}$ with M structure. It appears from the figure that the substitution of zinc gives the highest saturation magnetization at low temperature; evidently in this case, just as with spinels, the zinc ion occupies tetrahedral sites and consequently lowers the average moment of the ions on these sites. Table 38.II gives the saturation magnetization at room temperature, σ_{20}, and the Curie points T_C of a number of W compounds.

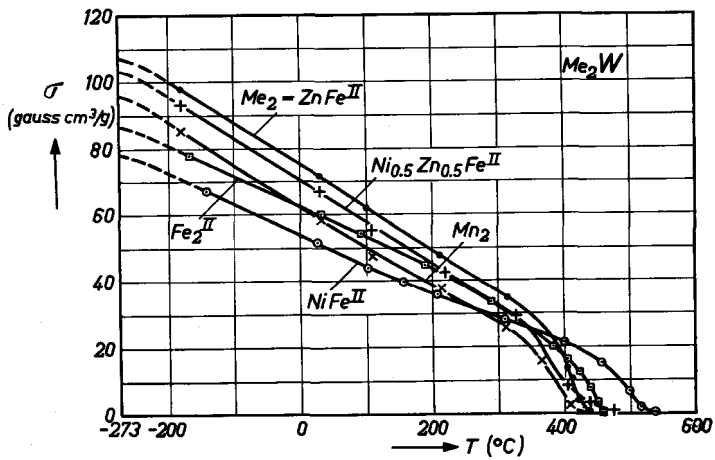

Fig. 38.3. Saturation magnetization as a function of temperature for a number of compounds with W structure, measured on polycrystalline specimens at a field strength of 6600 oersteds.

TABLE 38.II

SATURATION MAGNETIZATIONS AT 20 °C AND CURIE POINTS T_C OF Me_2W COMPOUNDS.

Me_2	σ_{20} gauss cm³/g	$4\pi M_s$ gauss	T_C °C
Mn_2	59	3900	415
Fe_2^{II}	78	5220	455
$NiFe^{II}$	52	3450	520
$ZnFe^{II}$	73	4800	430
$Ni_{0.5}Zn_{0.5}Fe^{II}$	68	4550	450

By extrapolation to the absolute zero point of the σ *versus* T curves in Fig. 38.3 an approximate value of σ_0 at 0 °K can be estimated. This value is given in Table 38.III, together with the derived number of Bohr magnetons (n_B)W per molecule Me_2W. From the way in which the W structure is built up from double spinel blocks S and blocks R, it follows that the saturation

magnetization of a **W** compound should be simply related to the saturation magnetization of $BaFe_{12}O_{19}$ (denoted by $(n_B)_M$) and the corresponding spinel compound Me_2S (denoted by $(n_B)_S$); that is:

$$[(n_B)_{W,}]_{theor} = (n_B)_M + 2(n_B)_S \qquad (38.1)$$

The values of the saturation magnetizations of the **W** compounds shown in the last column of Table 38.III are calculated from (38.1) assuming that $(n_B)_M = 20$ and that the values from Table 32.II are applicable for $(n_B)_S$. The measured values are found to be in reasonably good agreement with the expected values. Deviations can be due to the fact that the Me ions also occupy sites in the **R** block, and they are certainly also partly due to the small fields with which the measurement was carried out, *viz.* about 6600 oersteds. For the compound Fe_2W, the values are given in the table hold for a measuring field of 25.000 oersteds.

TABLE 38.III

SATURATION MAGNETIZATION σ_0 OF Me_2W COMPOUNDS AT THE ABSOLUTE ZERO POINT, AND A COMPARISON OF THESE VALUES WITH THOSE OF THE COMPOUNDS M AND S ACCORDING TO (38.1), ASSUMING $(n_B)_M = 20$.

Me_2W	σ_0	$(n_B)_W$	$(n_B)_S$	$[(n_B)_W]_{theor} =$
Me_2	gauss cm^3/g	experimentally	from Table 32.II	$20+2(n_B)_S$
Mn_2	97	27.4	4.6	29.2
Fe_2^{II}	98	27.4	4.0	28
$NiFe^{II}$	79	22.3	3.2	26.4
$ZnFe^{II}$	108	30.7	5.8	31.6
$Ni_{0.5}Zn_{0.5}Fe^{II}$	104	29.5	4.6	29.2

38.4. SATURATION MAGNETIZATION OF COMPOUNDS WITH Y STRUCTURE

Fig. 38.4 gives the saturation magnetization of a number of simple **Y** compounds as a function of temperature. In Table 38.IV a survey is given of the saturation magnetizations at room temperature and the Curie points of these **Y** compounds. It was seen in § 38.1 that the **T** block contains an equal number of oppositely oriented magnetic moments. If, then, we were to assume, as in the case of the **W** structure in § 38.3, that the Me ions are contained only in the spinel block, the magnetic moment would result from this block alone. The corresponding values of n_B are given in the last column of Table 38.V and compared with the measured values, as found from the σ *versus* T curves by extrapolation to $T = 0$. In this case the measured values

TABLE 38.IV

SATURATION MAGNETIZATIONS AT 20 °C AND THE CURIE POINTS OF SOME SIMPLE Me_2Y COMPOUNDS.

Me_2Y	σ_{20}	$4\pi M_s$	T_C
Me	gauss cm³/g	gauss	°C
Mn	31	2100	290
Co	34	2300	340
Ni	24	1600	390
Zn	42	2850	130
Mg	23	1500	280

TABLE 38.V

THE SATURATION MAGNETIZATION σ_0 OF COMPOUNDS Me_2Y AT THE ABSOLUTE ZERO. THE NUMBER OF BOHR MAGNETONS $(n_B)_Y$ PER UNIT CELL IS COMPARED WITH THE VALUE $(n_B)_S$ OF THE CORRESPONDING FERRITES WITH SPINEL STRUCTURE.

Me_2Y	σ_0	$(n_B)_Y$	$2(n_B)_S$
Me	gauss cm³/g		from Table 32.II
Mn	42	10.6	9.2
Co	39	9.8	7.4
Ni	25	6.3	4.6
Cu	28	7.1	2.6
Mg	29	6.9	2.2
Zn	72	18.4	(20)

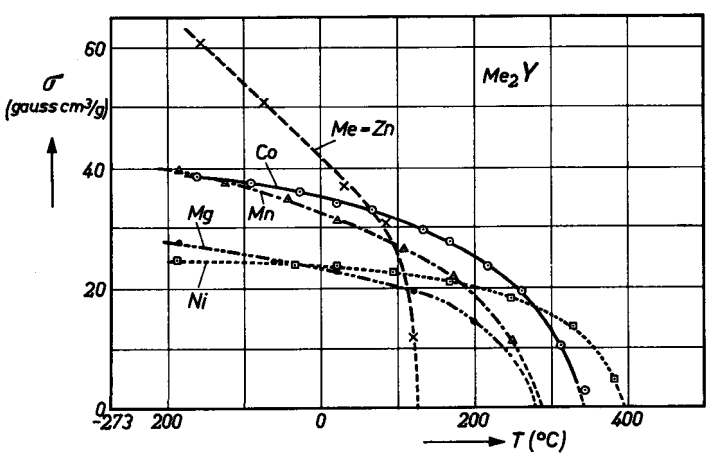

Fig. 38.4. Saturation magnetization as a function of temperature for a number of compounds with Y structure, measured on polycrystalline specimens at a fieldstrength of 11000 oersteds.

are seen to be somewhat higher than those of the spinel block, contrary to what is found in the case of **W**. This gives no cause to doubt the correctness of the spin configuration of the **T** block as postulated in § 38.1, since any deviation from this would result in much greater deviations in the number of Bohr magnetons. For example, if in Fig. 38.1*b* the spin moments of the ions 3 in the **Y** structure were to be reversed, this would give a resultant moment corresponding to $n_B = 4$ for each **T** block, which would have to be added to that of the **S** block, and therefore σ_0 would increase by a factor of three. It must rather be assumed that the divalent Me ions are also contained in the **T** block. If the cobalt or nickel ions, which have a moment lower than that of the ferric ions, also occupy the sites 3 in the **T** block of Fig. 38.1*b*, the result is an increase in the magnetization. To explain the moment of the Co_2Y compound, still assuming the moment of the cobalt ion to be 3.7 μ_B, then of the two Co ions 1.2 ions must occupy the sites 3 in Fig. 38.1*b*. For the nickel ferrite this figure would be only 0.3.

The case of the Zn_2Y compound is particularly interesting, because one must assume that the zinc ions in the **Y** structure too must occupy tetrahedral sites, the moments of which are all parallel. It is evident that the zinc ions cannot all be contained in the spinel block, because otherwise the block would become antiferromagnetic or paramagnetic. The lowering of the resultant moment in spinels with high Zn content is caused by the formation of angles between the moments of the octahedral ions (see § 32.1). This is due to the negative exchange interaction between the moments of these ions. The measured value of the saturation magnetization suggests that this angle formation, without which n_B would be equal to 20, is less pronounced in the **Y** structure. This is clear for the following reasons. The moments of the octahedral ions 2 and 3 in Fig. 38.1*b* are already antiparallel, so that the interaction 2-3 favours this orientation. The same holds for ions 3 and 4. Moreover, since each ion 3 interacts with six ions 4, and since the 3-4 interaction is strong, this will have the effect of favouring the parallel orientation of the moments of all ions 4. A further result of this is that the angle formation between the moments of the octahedral ions in the **S** block will be opposed.

38.5. SATURATION MAGNETIZATION OF COMPOUNDS WITH **Z** STRUCTURE

In Fig. 38.5 the saturation magnetization is plotted as a function of temperature for polycrystalline specimens of Me_2Z. Table 38.VI gives their Curie points and the saturation magnetization at 20 °C.

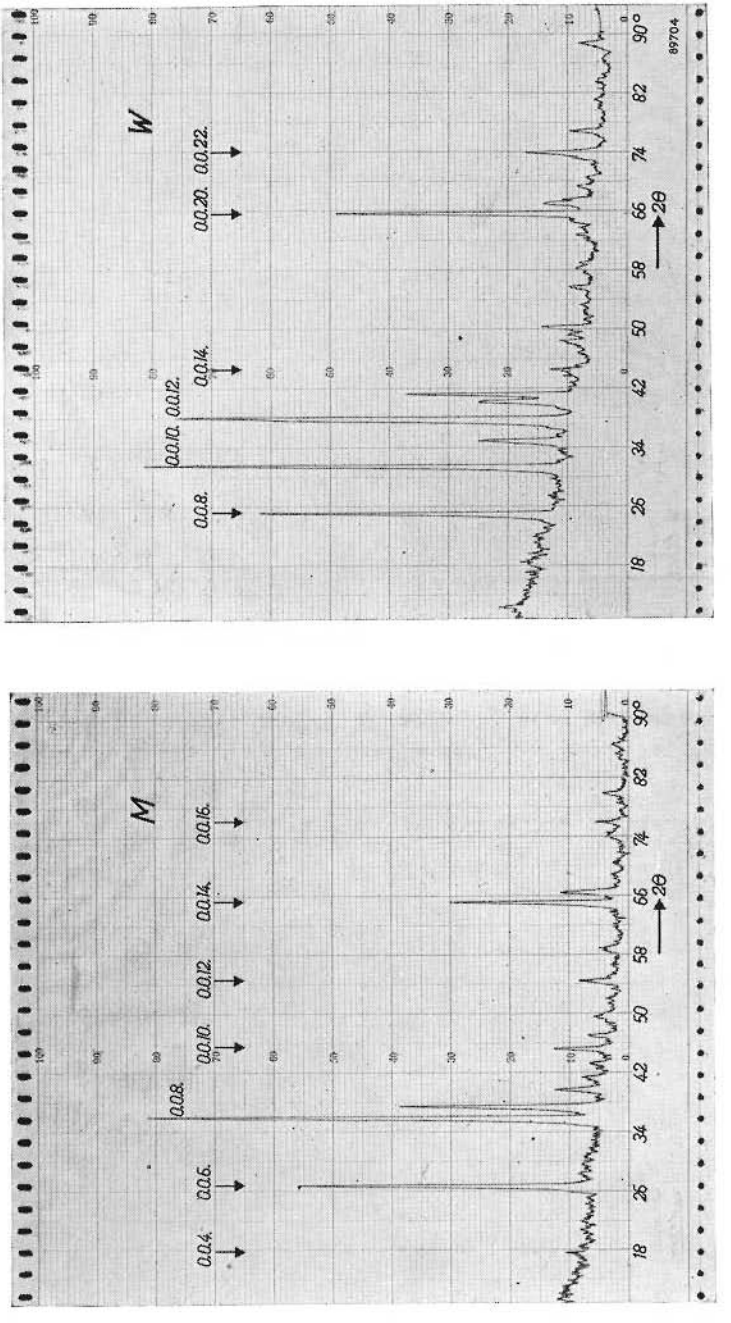

Fig. 37.9. X-ray diffraction diagrams of magnetically oriented powder of M and W compounds taken with CoKα radiation. The c-axes are parallel, so that the reflexions from the basal planes o.o.l. are intensified with respect to those obtained for a powder of crystals with random orientation.

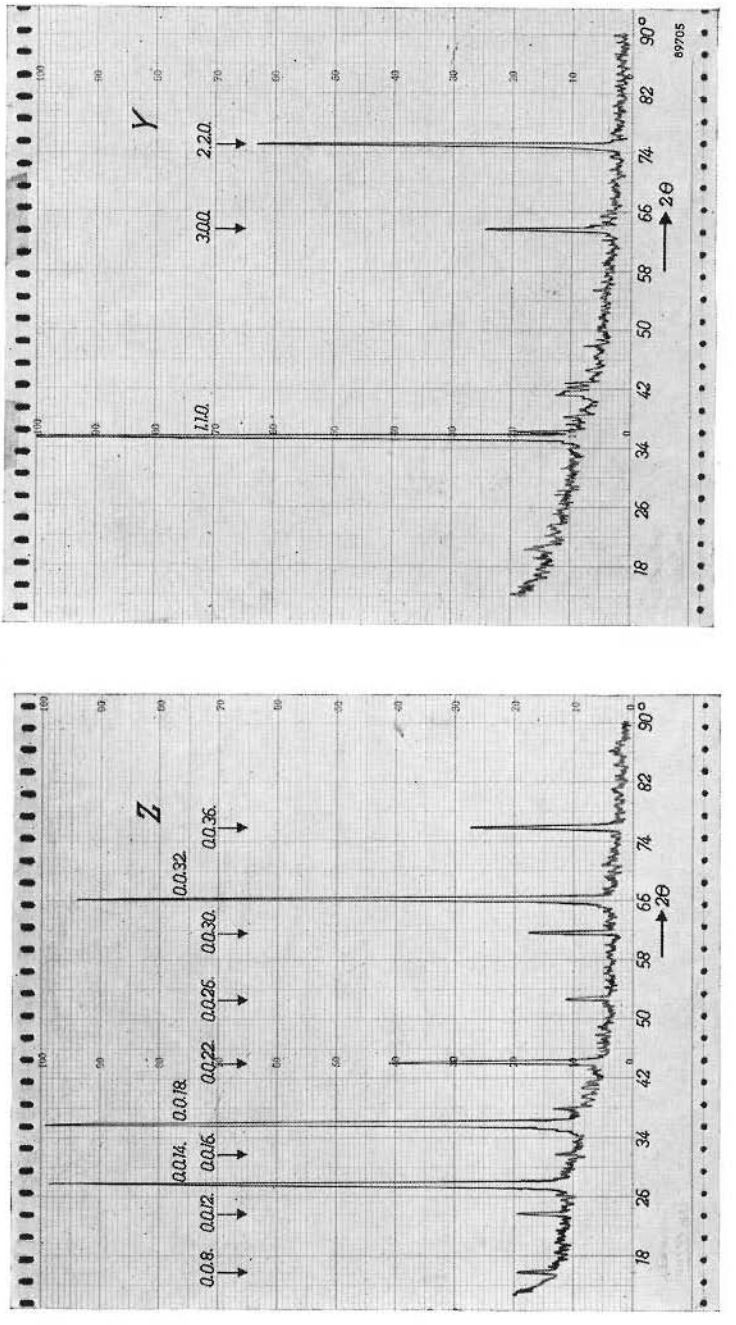

Fig. 37.10. X-ray diffraction diagrams for aligned powders of **Z** and **Y**. For **Z** the (o.o.l.) reflections are strong as in Fig. 37.9. For **Y** the reflections from the (h.k.o.) planes (parallel to the hexagonal axis) are intensified, indicating that the c axes are normal to the reflecting plane.

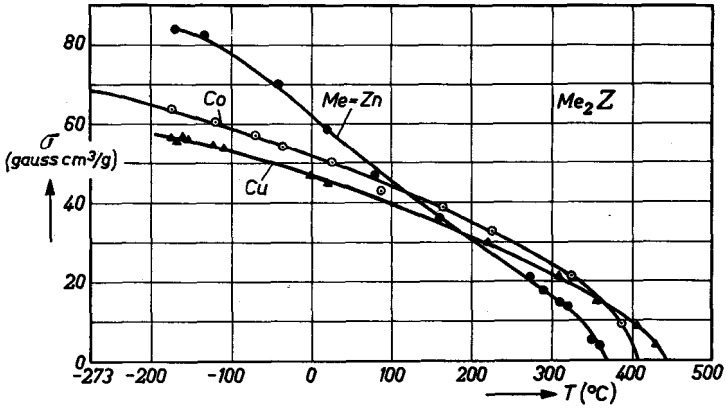

Fig. 38.5. Saturation magnetization as a function of temperature for compounds with Z structure, measured on polycrystalline specimens at a fieldstrength of 11000 oersteds for Co_2Z and Zn_2Z and of 18000 oersteds for Cu_2Z.

TABLE 38.VI

THE CURIE POINT AND THE MAGNETIZATION OF SOME COMPOUNDS Me_2Z AT $T = 20$ °C.

Me_2Z Me	σ_{20} gauss cm³/g	$4\pi M_s$ gauss	T_C °C
Co	50	3350	410
Cu	46	3100	440
Zn	58	3900	360

Since the Z structure can be considered crystallographically as a superposition of the structures M and Y, the experimentally found values for the saturation magnetization per unit cell of substances with Z structure is compared in Table 38.VII with the sum of those found for the M structure and the corresponding Y structure. The value $n_B = 20$ is taken for

TABLE 38.VI

THE SATURATION MAGNETIZATION σ_0 OF COMPOUNDS Me_2Z AT THE ABSOLUTE ZERO POINT. THE NUMBER OF BOHR MAGNETONS $(n_B)Z$ PER UNIT CELL IS COMPARED WITH THE SUM OF THESE OF THE M COMPOUND, $(n_B)M = 20$, AND THE CORRESPONDING Y COMPOUND, $(n_B)Y$. THE LATTER VALUES HAVE BEEN TAKEN FROM TABLE 38.V.

Me_2Z Me	σ_0 gauss cm³/g	$(n_B)_Z$ experimentally	$[(n_B)_Z]_{theor} = 20 + (n_B)_Y$
Co	69	31.2	29.8
Ni	54	24.6	26.1
Cu	60	27.2	27.1
Mg	55	24	26.9

M, and the values for **Y** are obtained from Table 38.5. Deviations can occur owing to the Me ions also occupying sites in the **R** blocks of the **M** structure, as in the case of the **W** structure.

§ 39. Crystal Anisotropy

39.1. BINDING OF THE MAGNETIZATION TO THE c AXIS

The crystal anisotropy of hexagonal crystals can be described with (11.6), where the values of the coefficients K_1 and K_2 determine the direction of the magnetization as indicated in Fig. 11.2. The sign of the anisotropy can easily be determined by the method described in § 37.6, that is by aligning powdered particles of the compound in a magnetic field and then determining their orientation by X-ray diffraction. The magnitude of the crystal anisotropy energy can be found by measuring the magnetization of a single crystal as a function of the field in both the direction of the hexagonal axis and at right-angles thereto. Results of measurements on $BaFe_{12}O_{19}$, Co_2Y and Co_2Z are given in Figs. 39.1, 39.2 and 39.3 respectively. At room tem-

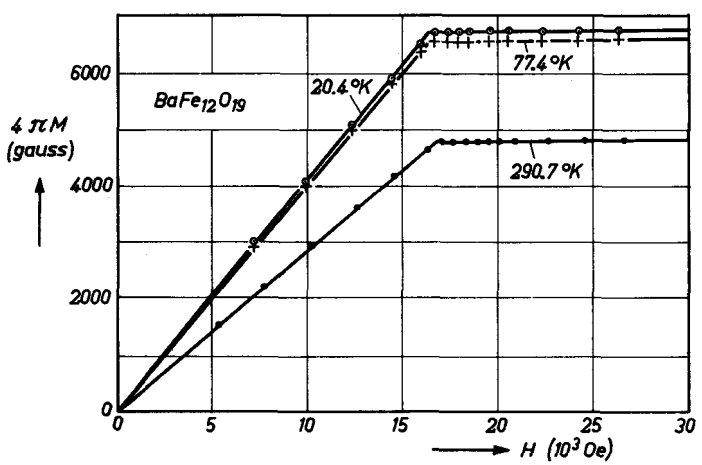

Fig. 39.1. Magnetization curves for a single crystal of $BaFe_{12}O_{19}$ as a function of an applied field perpendicular to the *c* axis at different temperatures, after [St1].

perature the compound $BaFe_{12}O_{19}$ can be saturated with a relatively small field parallel to the *c* axis, and the compounds Co_2Y and Co_2Z with a relatively small field perpendicular to the *c* axis. The magnetization curves in the difficult direction of magnetization are almost straight lines, from which it would follow that at room temperature all higher order anisotropy con-

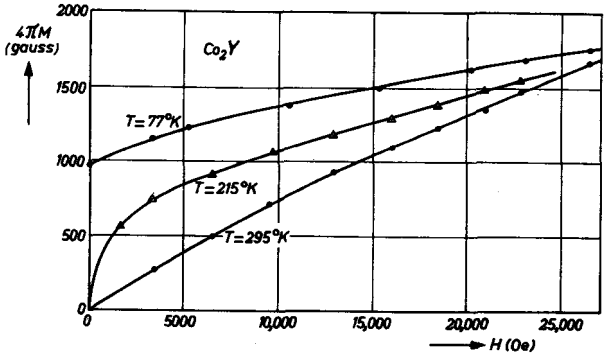

Fig. 39.2. Magnetization curves for a single crystal of Co_2Y as a function of an applied field along the c axis at different temperatures, after [Ca2].

stants are small compared to K_1. As stated in § 26.1, the magnetization curve in the difficult direction will differ from a straight line if $K_2 \neq 0$. This case is found below room temperature for ferrites containing cobalt [Ca 2].

Anisotropy constants of hexagonal oxides have also been measured by the torsion pendulum method described in § 26.3. From the description of

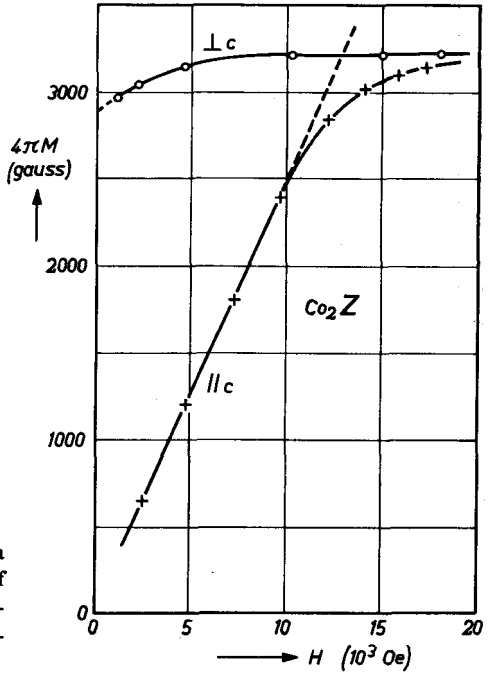

Fig. 39.3. Magnetization curves of a single crystal of Co_2Z as a function of an applied field both parallel and perpendicular to the c axis at room temperature.

the method it follows that where the c axis is a preferred direction of magnetization the quantity K_1 from (11.6) will be measured, whereas in the case of a preferred plane the combination $K_1 + 2K_2$ is measured. Measurements have been carried out on single crystals and on specimens consisting of crystals whose c axes were, to a fairly high degree, in parallel alignment (for the preparation of these specimens see § 44). Table 39.I gives values found at room temperature for the anisotropy constants together with the anisotropy field strength H_θ^A defined by (11.7). For $BaFe_{12}O_{19}$ the value of K_1 was also determined by ferromagnetic resonance measurements [Sm 2], the results being the same as found by direct (static) magnetic measurement.

TABLE 39.I

ANOSOTROPY CONSTANTS K_1 OR $K_1 + 2K_2$, SATURATION MAGNETIZATION M_s AND ANISOTROPY FIELD H_θ^A OF SOME HEXAGONAL OXIDES AT 20 °C.

Compound	Symbol	K_1 10^6 erg/cm³	K_1+2K_2 10^6 erg/cm³	M_s gauss	H_θ^A oersted
*) $BaFe_{12}O_{19}$ [We 1]	M	+3.3		380	17,000
*) $BaFe_{18}O_{27}$ [We 1]	Fe_2W	+3.0		314	19,000
$BaZnFe_{17}O_{27}$	FeZnW	+2.4		380	12,500
$BaZn_{1.5}Fe_{17.5}O_{27}$	$Fe_{0.5}Zn_{1.5}W$	+2.1		380	11,100
$BaMnFe_{16}O_{27}$	MnZnW	+1.9		370	10,200
$BaNi_2Fe_{16}O_{27}$	Ni_2W	+2.1		330	12,700
$BaNi_{0.5}ZnFe_{16.5}O_{27}$	$Fe_{0.5}Ni_{0.5}ZnW$	+1.6		350	9,100
$BaCo_{0.75}Zn_{0.75}Fe_{16.5}O_{27}$	$Fe_{0.5}Co_{0.75}Zn_{0.75}W$		—0.4	360	2,200
$Ba_2Mg_2Fe_{12}O_{22}$	Mg_2Y		—0.6	119	10,000
$Ba_2Ni_2Fe_{12}O_{22}$	Ni_2Y		—0.9	127	14,000
$Ba_2Zn_2Fe_{12}O_{22}$	Zn_2Y		—1.0	227	9,000
*) $Ba_2Zn_{1.5}Fe_{12.5}O_{22}$	$Fe_{0.5}Zn_{1.5}Y$		—0.9	191	9,500
*) $Ba_2Co_2Fe_{12}O_{22}$	Co_2Y		—2.6	185	28,000
*) $Ba_3Co_2Fe_{24}O_{41}$	Co_2Z		—1.8	270	13,000

*) Measurements on single crystals.

Fig. 39.4 shows the saturation magnetization $4\pi M_s$, the anisotropy field H_θ^A and the crystal anisotropy constant K_1 for $BaFe_{12}O_{19}$ as a function of temperature. The same quantities for Co_2Y are given in Fig. 39.5. For this ferrite [Ca 2] a remarkable decrease in the anisotropy occurs near 215 °K. The anisotropy field becomes here almost zero: what remains is perhaps due to inhomogeneities of the crystal. For temperatures below 215 °K the ferrite Co_2Y has a preferred cone for the magnetization with the c axis as the axis of the cone (see § 11.1). The top angle θ_0 of the cone is represented as a function of temperature in Fig. 39.6. Above 215 °K the basal plane of

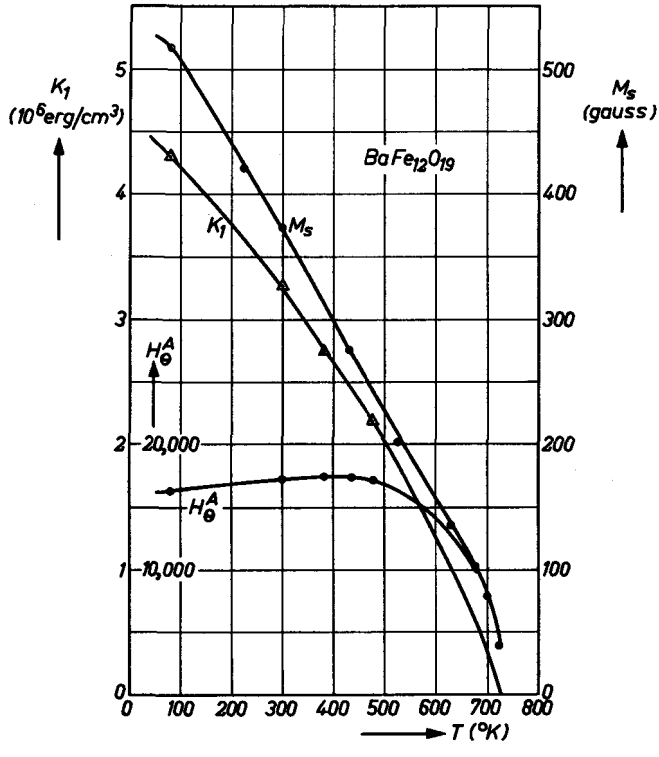

Fig. 39.4. Saturation magnetization M_s, crystal anisotropy K_1 and anisotropy field H_θ^A of $BaFe_{12}O_{19}$ as a function of temperature.

the hexagonal structure is a preferred plane of magnetization. The magnetization curves for various directions of the crystal also show a trend which is characteristic of a preferred cone of the magnetization. At 77 °K there is already a magnetization in the direction of the c axis for a field strength $H = 0$, (see Fig. 39.2).

As shown in Fig. 39.7 the compound Co_2Z represents the remarkable case of having three types of crystal anisotropy [Ca 2]. Above 480 °K the c axis is a preferred direction, between 220 °K and 480 °K the basal plane is a preferred plane and below 220 °K the material exhibits a preferred cone for the magnetization.

Mixed hexagonal ferrites can be made which, at a specific temperature, possess an anisotropy that is found to lie between the extremes of $BaFe_{12}O_{19}$ and Co_2Y. An example is the series of mixed crystals of the compounds $Co_\delta Zn_{2-\delta}Z$ The anisotropy constants at room temperature are given in Fig. 39.8 as a

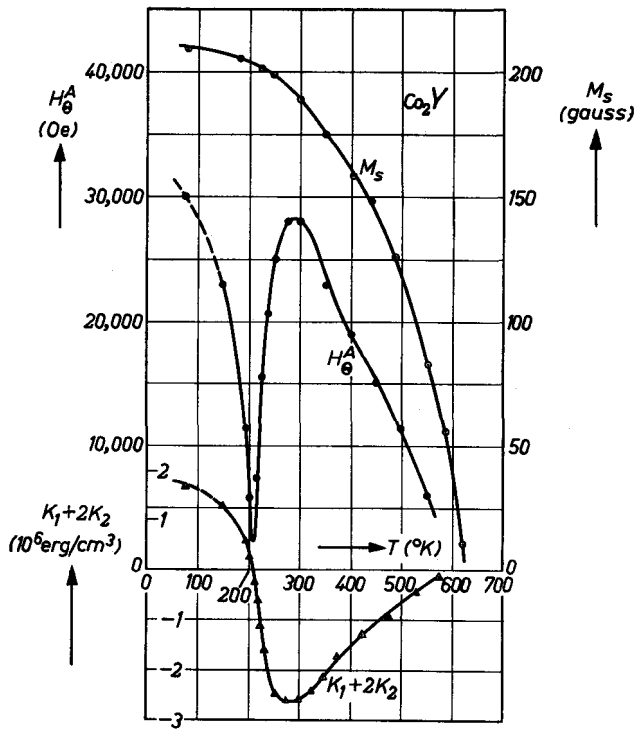

Fig. 39.5. Saturation magnetization M_s, crystal anisotropy ($K_1 + 2K_2$) and anisotropy field H_θ^A of Co_2Y as a function of temperature.

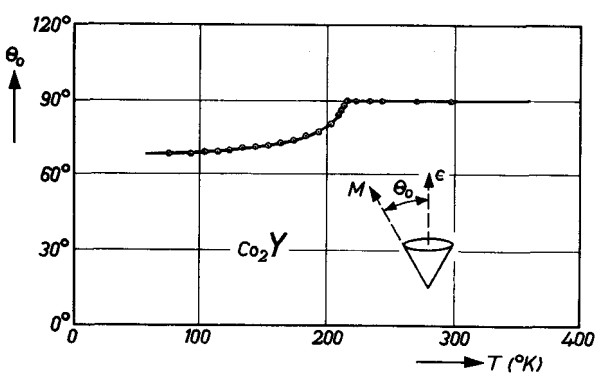

Fig. 39.6. Equilibrium orientation with respect to c axis of the magnetization vector of Co_2Y as a function of temperature.

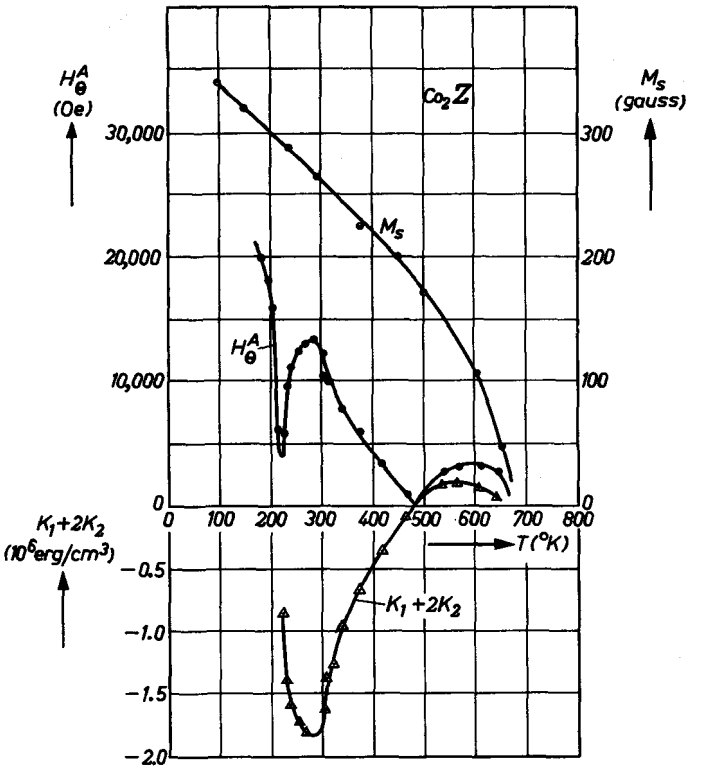

Fig. 39.7. Saturation magnetization M_s, crystal anisotropy (K_1+2K_2) and anisotropy field H_θ^A of Co_2Z as a function of temperature.

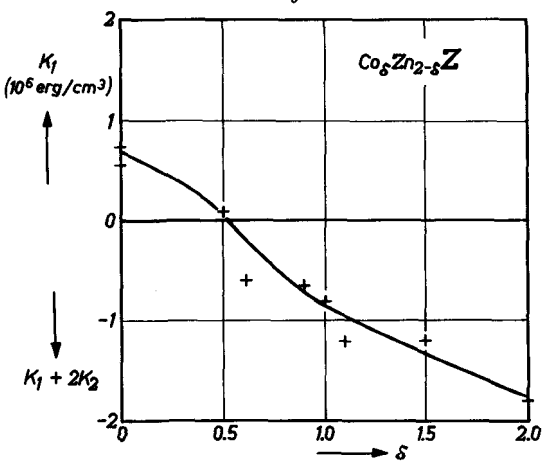

Fig. 39.8. Crystal anisotropy K_1 of cobalt-zinc Z compounds as a function of the cobalt content.

function of the composition parameter δ. The compounds at the ends of the diagram, Zn_2Z and Co_2Z, have respectively a preferred direction and a preferred plane for the spontaneous magnetization. For the mixed crystals a gradual transition is found as a function of δ from the one kind of anisotropy to the other.

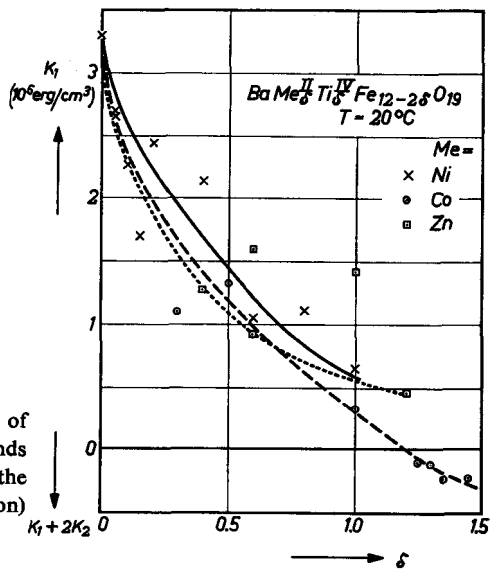

Fig. 39.9. Crystal anisotropy K_1 of several titanium-substituted compounds with M structure as a function of the titanium (or divalent metal ion) content.

In the compound M, divalent ions can also be introduced, together with the same number of tetravalent ions. An example of the effect on the crystal anisotropy is given in Fig. 39.9. It appears that relatively small quantities of Ti^{IV} and Me^{II} ions can considerably reduce the crystal anisotropy. In the case where Me represents the nickel or zinc ion the c axis remains a preferred direction. In the case where Me = Co the compounds $BaCo_\delta Ti_\delta Fe_{12-2\delta}O_{19}$ with $\delta > 1.1$ have a preferred plane of magnetization.

39.2. ANISOTROPY IN THE BASAL PLANE

Where the spontaneous magnetization lies in the basal plane of the crystal with hexagonal structure, the anisotropy energy in the basal plane is determined by the magnitude of K_3 from equation (11.6). It appears that K_3 is smaller than K_1 by at least a factor of the order of magnitude 10^3. In Fig. 39.10a the stiffness c is plotted for a single crystal of $Co_{1.92}Fe^{II}_{0.08}Z$ as a function of the angle ϕ which a fixed direction in the preferred plane of the crystal platelet makes with the direction of the field, the stiffness c being given by an equation analogous to (26.3):

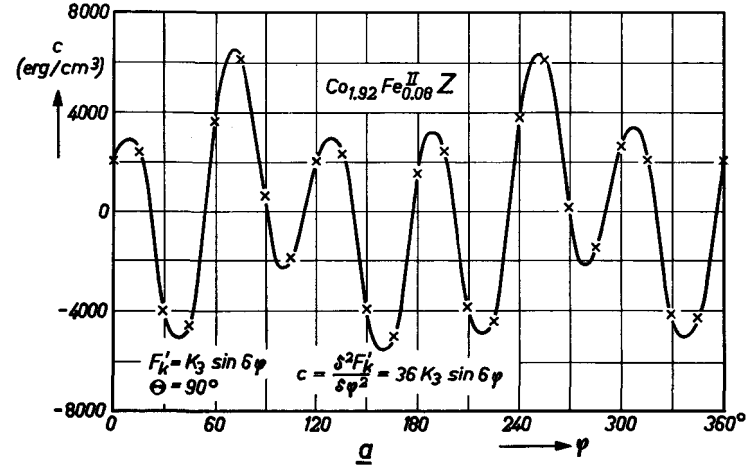

Fig. 39.10a. The rotational stiffness of the magnetization vector in the basal plane of $Co_{1.92}Fe_{0.08}Z$ as a function of the orientation in this plane (indicated by ϕ).

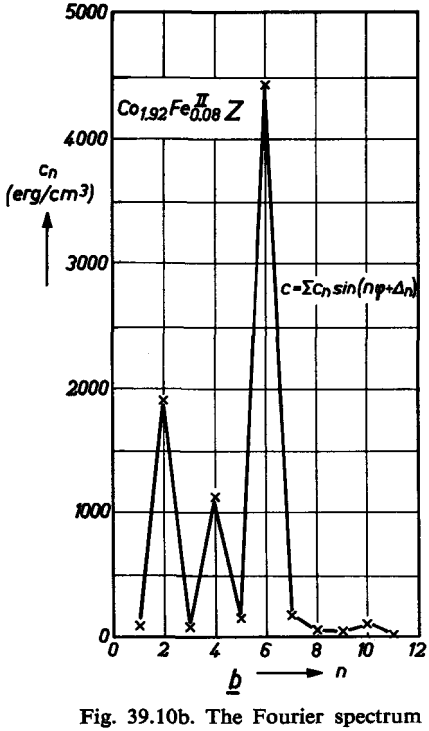

Fig. 39.10b. The Fourier spectrum of the stiffness data of Fig. 37.10a.

$$c = \frac{\partial^2 F_K}{\partial \phi^2} = 36 K_3 \sin 6\,\phi. \qquad (39.1)$$

The measurement was carried out in a field strength of 3300 oersteds. The Fourier analysis of the curve in Fig. 39.10*a* gives the spectrum shown in Fig. 39.10*b*. The sixth harmonic component has a strikingly high amplitude; this component corresponds to the term K_3 in (11.6), and is equal to 120 erg/cm³. The appearance of the second harmonic is due to the fact that the crystal platelet is not exactly parallel to the direction of the lines of force of the homogeneous magnetic field. Consequently a very small part of the large anisotropy K_1 is also measured. Table 39.II gives some values of K_3

TABLE 39.II

THE CRYSTAL ANISOTROPY CONSTANT K_3 AND THE ANISOTROPY FIELD H_ϕ^A FOR SOME HEXAGONAL FERROMAGNETIC OXIDES.

Material	Temperature °C	M_s gauss	K_3 erg/cm³	H_ϕ^A oersted
Co_2Y	—196	210	2000	340
	20	187	800	155
	170	145	150	37
$Co_{1.5}Fe^{II}_{0.5}Z$	20	280	55	7
	158	220	≈9	≈2
$Co_{1.92}Fe^{II}_{0.08}Z$	20	280	120	16
$CoZn_{0.5}Fe^{II}_{0.5}Z$	20	290	25	3
$Zn_{1.5}Fe^{II}_{0.5}Y$	20	190	<6	<1

measured on various crystals at different temperatures, together with the corresponding anisotropy field $H_\phi^A = 36\ K_3/M_s$. It is seen that K_3 is larger the greater is the cobalt content in the material; for $Zn_{1.5}Fe_{0.5}Y$ a value of K_3 which may possibly be present falls within the measuring error. The compound Co_2Y contains relatively the most cobalt and has by far the largest K_3. The anisotropy field strengths H_ϕ^A are small compared with the field strength of approximately 3000 oersteds at which the measurement is carried out, so that in these cases no great error is made if the extrapolation to an infinitely large measuring field is omitted.

39.3. ORIGIN OF CRYSTAL ANISOTROPY IN HEXAGONAL OXIDES

In hexagonal crystals the characteristic dipole-dipole interaction can in principle give rise to uniaxial anisotropy (see § 12.1), in which case only $K_1 \neq 0$. The spin configuration in the **Y** structure favours the occurrence of a preferred plane. A complete calculation of the dipole sums has been made [Ca 2] and yields:

$$(K_1)_{dip} = -(0.044\ \mu_t^2 + 0.0006\ \mu_t \mu_0 + 0.240\ \mu_0^2).10^6\ \text{erg/cm}^3, \quad (39.2)$$

where μ_t and μ_0 are the averaged magnetic moments, expressed in Bohr magnetons, of the tetrahedral and octahedral ions respectively. Equation (39.2) yields values ranging from -5 to -7×10^6 erg/cm³ for the various **Y** compounds (at $T = 0$ °K), so that it is probable that the negative crystal anisotropy of compounds with the **Y** structure is caused by the magnetic dipole-dipole energy.

In the **M** structure, on the other hand, it is not to be expected that the dipole-dipole energy will be at all substantial. It is true that the two ions one above the other in the **R** block (see Fig. 37.4) are parallel, and this makes a positive contribution to K_1 of about 1×10^6 erg/cm³, but the nega-

tive contribution of the ions on the boundary plane of an **R** and **S** block still remains. The calculation reveals indeed that the resultant contribution to K_1 is negative (-1.5×10^6 erg/cm^3) and therefore cannot explain the observed positive value of K_1 of about 4.5×10^6 erg/cm^3 at $T = 0$ °K. It is possible that spin-orbit interaction may yet be able to explain the anisotropy observed. In this case it would have to be spin-orbit interaction in an excited state. Presumably K_2 is small because in this case the simple theory of § 12.2, which states that it should differ by a factor $(\lambda/\Delta E)^2$, is applicable here, inasmuch no fluctuations in ΔE occur.

The anisotropy caused by the cobalt ions is probably of the same kind as that appearing in magnetic annealing. The sign of the anisotropy energy was not apparent in these experiments. In the hexagonal oxides the sign of the anisotropy will depend on the sites which are occupied by the cobalt ions, but which are not precisely known. In § 34.2 we saw that the uniaxial anisotropy per cobalt ion is of the order of 50 cm^{-1}. From Table 39.I it follows that the contribution of cobalt in the **Y** structure is about 2×10^6 erg/cm^3, corresponding to approximately 3 cm^{-1} per cobalt ion. It appears that the distribution over the available sites is such as to give rise to considerable cancelling of the anisotropy. In the **W** structure, the contribution of each cobalt ion is roughly twice as large.

In ferrites with spinel structure the cubic crystal anisotropy is positive for cobalt ions, that is to say the [111] direction is an abhorred direction. In the hexagonal structure this direction is equivalent to the c axis, which is also an abhorred direction for the spins of the cobalt ions. These facts, however, are not directly connected, since the cubic K_1 corresponds to the hexagonal K_2. Thus, if the same mechanism is effective for the anisotropy energy of the cobalt ions in the cubic and in the hexagonal crystals, one would expect K_2 in hexagonal crystals containing cobalt to be positive. This agrees with the experimental finding in Co_2**Y** and in Co_2**Z** at low temperatures, (see § 39.1) and is then the cause of the occurrence of a preferred cone for the magnetization vector.

CHAPTER X

INTRINSIC PROPERTIES OF FERRITES WITH GARNET STRUCTURE

§ 40. Chemical Composition and Crystal Structure

Yoder and Keith [Yo 2] showed in 1951 that substitutions can be made in the ideal mineral garnet $Mn_3Al_2Si_3O_{12}$. By substituting $Y^{III} + Al^{III}$ for $Mn^{II} + Si^{IV}$ they obtained the first silicon-free garnet $Y_3Al_5O_{12}$. In 1956 Bertaut and Forret [Be 6] reported the preparation and magnetic properties of $Y_3Fe_5O_{12}$, and Geller and Gilleo [Ge 2] prepared and investigated $Gd_3Fe_5O_{12}$, which compound is also ferromagnetic. It appeared [Be 6] that the yttrium ion could be replaced by the rare-earth ions Pm, Sm, Eu, Gd, Tb, Dy, Ho, Er, Tm, Yb, or Lu, owing to their nearly equal ionic radius. There are no other trivalent ions known with about the same ionic radius.

The crystal structure is quite complicated. The iron ions, having the smallest radii, all occupy tetrahedral (Fe_3) and octahedral (Fe_2) sites just as in the spinel structure, although they are somewhat distorted. According to Geller and Gilleo [Ge 3] the tetrahedral-oxygen distance in yttrium garnet is 1.88 Å and the octahedral-oxygen distance is 2.00 Å, which is about the same as in the spinel structure. Nevertheless the aluminium ions now preferentially occupy tetrahedral sites, whereas they occupy preferentially octahedral sites in the spinel structure [Ge 2]. A difference compared with the spinel structure is also that all existing octahedral and tetrahedral sites occurring in the garnet structure are occupied by the metal ions. Perhaps this fact contributes to the very great stability of the structure. The yttrium or rare-earth ions are too large to occupy tetrahedral and octahedral sites, which are in 4-fold and 6-fold coordination respectively, but are, on the other hand, too small to be substituted for an oxygen ion, each of which is surrounded by 12 oxygen ions. The close-packed structure of the oxygen ions is therefore not retained, but the yttrium or rare-earth ions occupy sites which are rather irregularly surrounded by eight oxygen ions of which four are at a distance of 2.37 Å and four at 2.43 Å. The edges of the cubic unit cell, which contains 8 molecules $Y_3Fe_5O_{12}$, are 12.37 Å. The X-ray density of *e.g.* $Y_3Fe_5O_{12}$ is 5.17 g/cm³.

§ 41. Saturation Magnetization

The iron ions on the octahedral and tetrahedral sites are coupled antiferro-

magnetically by the superexchange mechanism as in the other ferrites. In this case the resultant magnetic moment of the iron ions is due to the ions in tetrahedral coordination. The rare-earth ions, which have a magnetic moment, are coupled antiferromagnetically to the net moment of the iron ions. This coupling usually is much weaker than that between the iron ions. As a consequence the magnetization of the rare-earth ions drops very quickly with increasing temperature, approximately as $1/T$. Because most of these ions have a saturation moment which is much larger than the resultant magnetic moment of the iron ions, (Table 41.I) the moment of the rare-earth ions predominates at low temperatures and that of the iron ions at temperatures near the Curie temperature. Therefore a compensation point of the magnetization is observed (Fig. 41.1), as in the case of LiCr ferrite (see § 9.1). The intrinsic susceptibility, observed in high fields, is very high in these ferrites at not too low temperatures and is caused by the unsaturated magnetization of the rare-earth ions. The Curie point is determined by the superexchange interactions

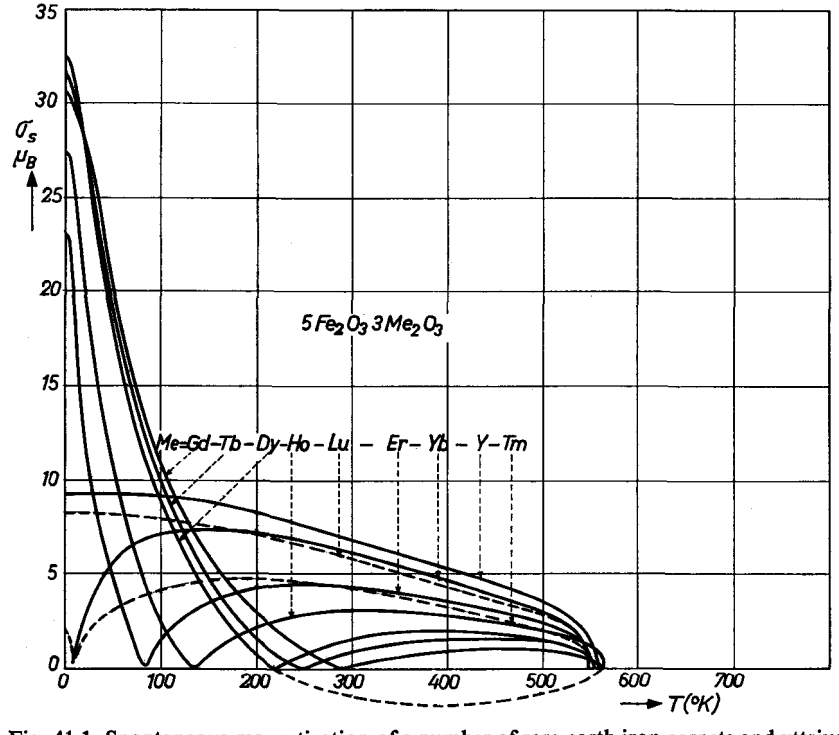

Fig. 41.1. Spontaneous magnetization of a number of rare-earth iron garnets and yttrium-iron garnet, expressed in number of Bohr magnetons as a function of temperature, after Bertaut [Be 7]).

between the iron ions and is almost the same for all rare-earth garnets (560 °K). The magnetic moments of the rare-earth ions is between that of pure spin and that of spin and orbit together, owing to partial quenching of the orbital angular momentum. This quenching is less complete than in the ions of the iron group because the partly filled $4f$ shell is not the outer filled shell of the ion, the $5s$ and $5p$ shells being are occupied. The crystalline fields, which should cause such quenching, are therefore more screened off.

The curve representing the reciprocal value of the susceptibility as a function of temperature above the Curie point is hyperbolic, as should hold for a ferrimagnetic substance. Aleonard *et al.* [Al 1] have determined for $Y_3Fe_5O_{12}$ from the $1/\chi$ curve the molecular field constants n, α and β where $n\alpha$ represents the molecular field constant within the octahedral sublattice and $n\beta$ that within the sublattice containing the iron ions on tetrahedral sites. The calculated values of α and β are 0.474 and 0.284 respectively. This corresponds to fairly strong interactions between the spin magnetic moments of the ions on equivalent lattice sites. The distance between the ions is, however, rather large (5.4 Å) and moreover a superexchange interaction *via* one oxygen ion is scarcely possible. The interaction has to take place *via* at least two oxygen ions, and should therefore be very small. It is accordingly very likely, as in the case of the spinels (§ 33), that the large values of α and β are erroneous, and are due to the fact that the molecular field theory does not strictly apply. It was shown in § 33 that in particular this gives rise to excessive values of the interaction constants inside the sublattice with the smallest magnetization. In the present case this is the interaction between the ions on the octahedral sites (here a), in agreement with the observed values.

§ 42. Crystal Anisotropy and Ferromagnetic Resonance Properties

The great interest of ferrites with garnet structure, and chiefly of yttrium garnet, resides in the small ferromagnetic resonance line width. The smallest line width on carefully polished spheres reported so far is 0.6 oersted [Le 2] at 3 cm wavelength at room temperature. This is presumably due, referring to the theory of Clogston *et al.* [Cl 1], to the fact that only trivalent magnetic ions of one kind occur, having no orbital angular momentum, so that no fluctuating perturbing fields are present. The high value of the resistivity also arises from this fact. The saturation magnetization at room temperature is rather low ($4\pi M_s = 1700$ gauss) so that losses due to incomplete saturation do not occur at microwave frequencies. The garnets containing rare-earth ions invariably have broad resonance lines, and are therefore not very interesting from a technical point of view.

The crystal anisotropy of yttrium garnet is rather low at room temperature, $-K_1/M_s = 40$ Oe, as has been measured by Dillon [Di 3] and can be quite well described with a single constant K_1. Below 100 °K the anisotropy strongly increases and varies approximately as $1/T$. At still lower temperatures, below 10 °K, the situation becomes quite complex, anisotropy fields of the order of 3000 oersteds occur and the preferred direction is no longer along one of the simple crystallographic directions, so that anisotropy constants of higher order are necessary to describe such a behaviour. This is contrary to what one should expect from the simple theory developed, because the g factor is very close to 2, and therefore the anisotropy ought to be small and a power series expansion of the energy in the direction cosines should converge very rapidly. Moreover, since only one type of magnetic ion is present, there are no fluctuations which should tend to make higher terms important.

TABLE 41.I

ELECTRONIC STRUCTURE AND ANGULAR MOMENTUM OF YTTRIUM AND RARE-EARTH IONS.

	Y	Nd	Pm	Sm	Eu	Gd
At. el. conf.	$4d5s^2$	$4f^46s^2$	$4f^56s^2$	$4f^66s^2$	$4f^76s^2$	$4f^75d6s^2$
Ion el. conf.	$4p^6$	$4f^3$	$4f^4$	$4f^5$	$4f^6$	$4f^7$
S	0	3/2	2	5/2	3	7/2
L	0	—6	—6	—5	—3	0
$L + 2S$	0	—3	—2	0	3	7

	Tb	Dy	Ho	Er	Tm	Yb	Lu
At. el. codf.	$4f^75d6s^2$	$4f^{10}6s^2$	$4f^{11}6s^2$	$4f^{12}6s^2$	$4f^{13}6s^2$	$4f^{14}6s^2$	$4f^{14}5d6s^2$
Ion el. conf.	$4f^8$	$4f^9$	$4f^{10}$	$4f^{11}$	$4f^{12}$	$4f^{13}$	$4f^{14}$
S	3	5/2	2	3/2	1	1/2	0
L	3	5	6	6	5	3	0
$L + 2S$	9	15	10	9	7	4	0

CHAPTER XI

STRUCTURE OF POLYCRYSTALLINE FERRITES

§ 43. Isotropic Samples

43.1. PREPARATION

Polycrystalline samples of ferrites are prepared by a sintering proces as commonly used in the ceramic industry. Broadly speaking this process comprises the following operations. The metal oxides, carbonates or other compounds which are to form the ferrite by a solid state reaction are mixed homogeneously and wet-milled, usually in a steel ball mill. The dried powder which may or may not have been pressed into a particular shape, is prefired at a temperature of about 1000 °C in order to bring about the initial chemical reaction between the constituents. In order to produce a chemically homogeneous sample, the prefired powder is again intensively milled and mixed. This powder, after the addition of a binder, is pressed into the required shape, or is extruded as a plastic mass in the form of tubes or rods. The pressed or extruded products are sintered at a temperature between 1200 and 1400 °C, the precise temperature depending upon the properties of the ferrite that are wanted, (see for example [Sn 3] and [Ec 1]). During this sintering process, a shrinkage of up to approximately 20% can occur, a fact which has to be taken into account when dimensioning the press mould. In the final sintering process the gas atmosphere in the furnace plays an essential role, since it determines the degree of oxidation of the product which is in many cases important for the magnetic properties (see for instance § 54.3).

The sintering process does not produce an entirely dense material, but a product having a certain porosity. The porosity p of a ferrite is the relative volume of the pores it contains, and it is derived from a comparison of the X-ray density d_x with the apparent density d of the ferrite. Fig. 43.1 shows a photomicrograph of the polished and etched surface of a manganese-zinc ferrite with porosity $p = 0.1$. The firing programme was such that the sample was held for five minutes at the maximum temperature of 1375 °C. If the material is held for one minute at a maximum temperature of 1435 °C a denser product with larger crystals is obtained ($p = 0.05$), a picture of which is shown in Fig. 43.2. The firing temperature necessary in order to obtain a dense product depends on the chemical composition of the ferrite.

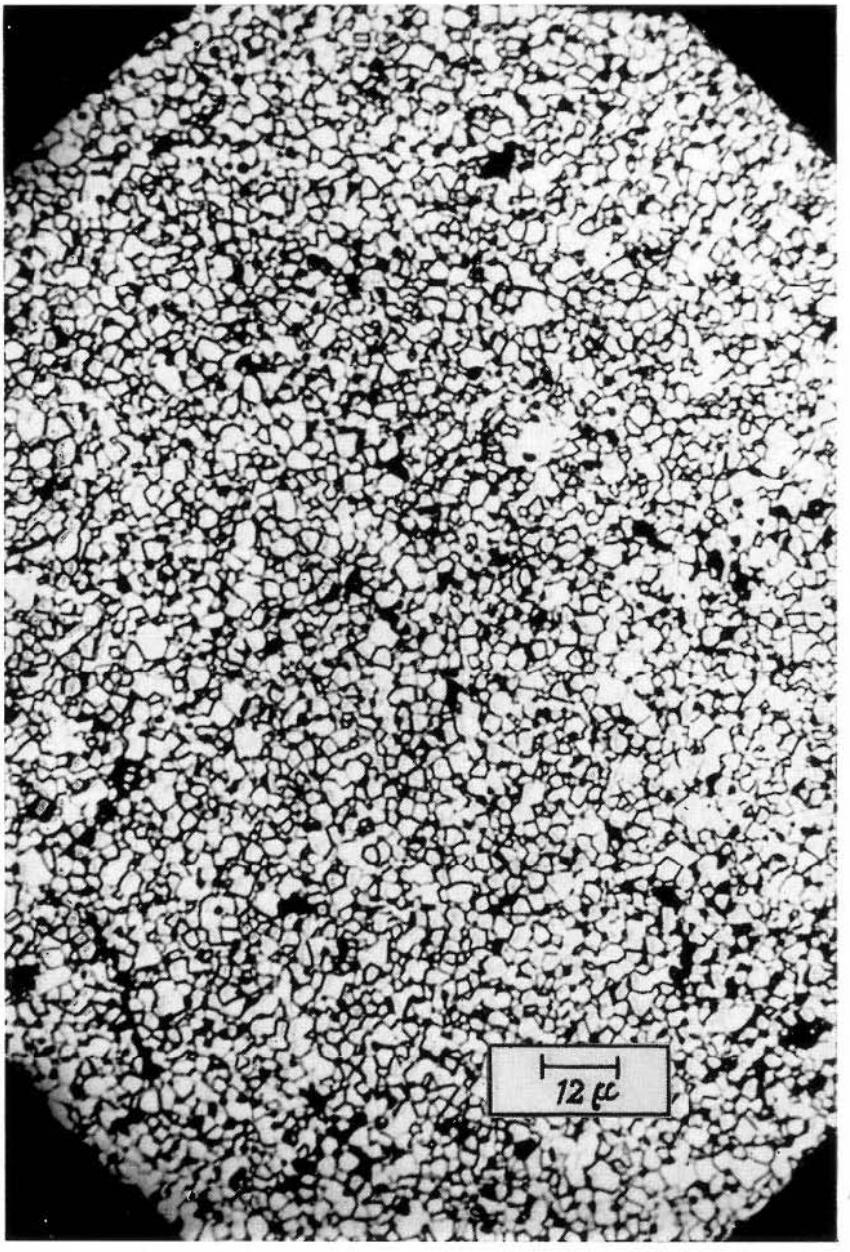

Fig. 43.1. Polished and etched surface of a manganese-zinc ferrite, sintered for five minutes at 1375 °C. Porosity $p = 0.1$.

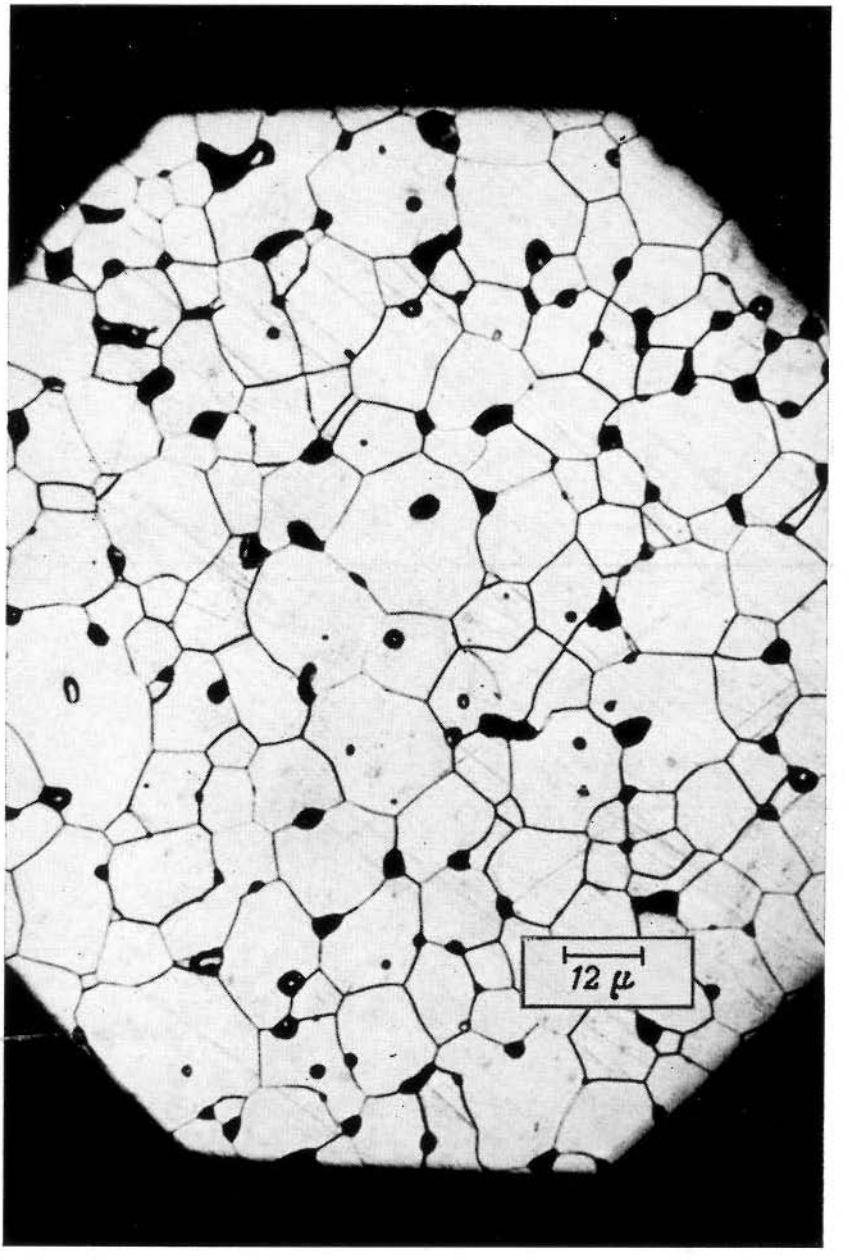

Fig. 43.2. Same ferrite as in Fig. 43.1, but now sintered for one minute at a temperature of 1435 °C. Porosity $p = 0.05$.

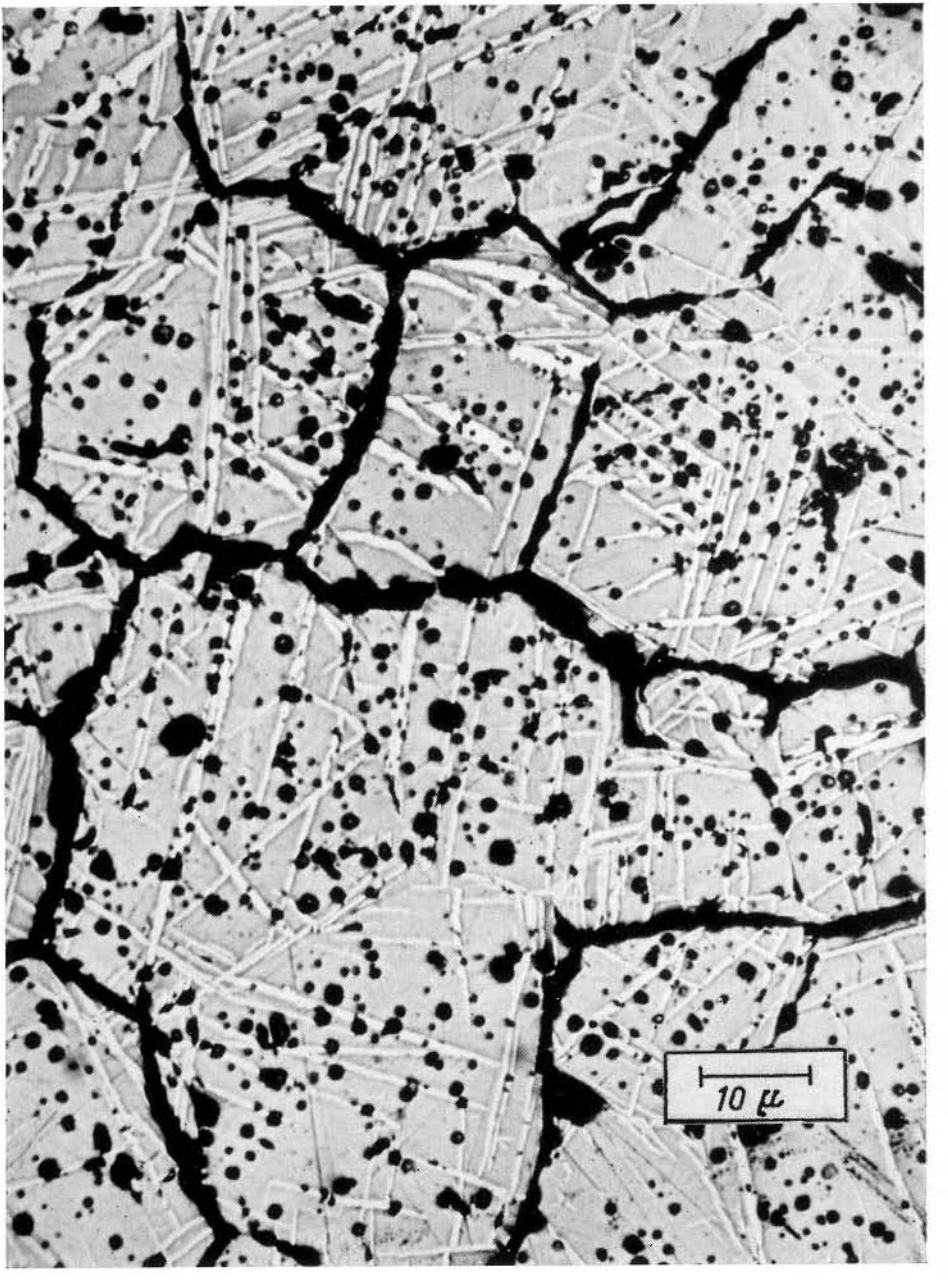

Fig. 43.3. Polished and etched surface of MnFeO a magnanese ferrite with a segregation of a second phase of αFe_2O_3.

For instance a porosity of less than 0.1 is obtained for $CuFe_2O_4$, $MnFe_2O_4$ and $NiFe_2O_4$ if the sintering takes place at temperatures of about 1100, 1200 and 1400 °C respectively. These temperatures are related to the melting points, which are 1300°, 1500° and 1650 °C respectively. It seems that nickel ions in particular do not diffuse easily in ferrites. The addition of zinc lowers the firing temperature of most ferrites. If samples of $Me_\delta Zn_{1-\delta}Fe_2O_4$ with various values of δ are sintered at the same temperature, the sample with the highest zinc content will have the greatest density. The temperature at which good sintering takes place depends to a large extent also on the grain size and grain shape of the starting material. A very fine-grained powder gives dense products at a lower firing temperature. For this reason the ball milling of the compounds or of the prefired ferrite is often replaced by a treatment of the powder in a vibration mill which leads to a smaller particle size.

43.2. PHASE DIAGRAMS

Many ions can occur in a ferrite in different valency states; iron for example can occur as a divalent or a trivalent ion. In order to obtain a certain chemical composition of the ferrite it may be necessary for some types of the ions to occur in different valencies. If either the gas atmosphere during firing is not sufficiently oxidizing, or the ratio of the quantities of metal ions in the starting materials is not correct, the wanted concentration cannot be obtained. Where the deviations are considerable a second phase segregates from the ferrite. This can have an adverse effect on the magnetic properties. Under the microscope this second phase is often clearly visible on polished ferrite surfaces. Fig. 43.3 (see page 235) gives an example of a second phase of αFe_2O_3. This is the result of an attempt to make a spinel from Fe_2O_3 and MnO as basic materials having a molar ratio of 55 : 45. The light-coloured segregations of the αFe_2O_3 phase, clearly visible on the photograph, result from a firing in a too oxidizing atmosphere. The light colour is characteristic of αFe_2O_3. If the ferrite is fired in a reducing atmosphere, single-phase manganous-ferrous ferrite may be produced. Inhomogeneous oxidation or reduction of the sample will take place if there is no equilibrium between the sample and the atmosphere. Often a so-called surface layer will be the result; an exaggerated case is shown in Fig. 43.4 (see page 336). Phase diagrams of the iron-oxygen and manganous-iron-oxygen systems have been given by Darken [Da 1] and by Gurry [Gu 8] respectively.

Where the compositions are complicated it is important to study the complete phase diagram. For instance in the case of Mn,Zn-ferrites the series of mixed crystals of $MnFe_2O_4$ and $ZnFe_2O_4$ form only one single line of

compositions in the large spinel field of the quaternary system Mn-Zn-Fe-O. The compositions Fe_3O_4, Mn_3O_4 and $ZnMn_2O_4$ also belong to this system, and for a complete understanding at least a large part of the spinel region has to be investigated. These investigations have only been carried out in a few cases, *e.g.* in the system Mg-Mn-Fe-O where the first compositions with rectangular hysteresis loops were found. An important point is to represent phase diagrams in the appropriate way. In the quaternary system, which can be represented as a tetrahedron, all so-called stoichiometric compositions $(Mg,Mn,Fe)_3O_4$ are found in one triangular plane. In order to obtain a simple diagram it is necessary to place equal amounts of comparable compounds in the corners. This is done in Fig. 43.5, thoug in one corner of the triangle no spinel compound exists but rather a mixture $3MgO + \frac{1}{2}O_2$. In this method of representation, introduced by Jonker [Jo 6], the three different metal ions appear with equal weight and the simple compositions as $MgFe_2O_4$ $MnFe_2O_4$, $MgMn_2O_4$ and $MgMnFeO_4$ are found on simple locations in the diagram. In the MgO-MnO-Fe_2O_3 or MgO-Mn_3O_4-Fe_2O_3 diagrams, which are often used, spinel compounds, apart from the simple ones, cannot be represented. The region of spinel compounds is large in this system (it covers the area within the drawn contour in Fig. 43.5). For different parts different methods of preparation are needed, for instance for Fe_3O_4 a high temperature and a reducing atmosphere, for $MgMn_2O_4$ a low temperature and a high oxygen pressure. The spinel compounds obtained by firing at 1350 °C and slow cooling in air lie within the hatched area of Fig. 43.5. The compounds containing Fe^{II} and Mn^{IV} ions are for the greater part not included and even $MnFe_2O_4$ does not belong to this region. There are of course also non-stoichiometric compounds with an excess or a deficiency

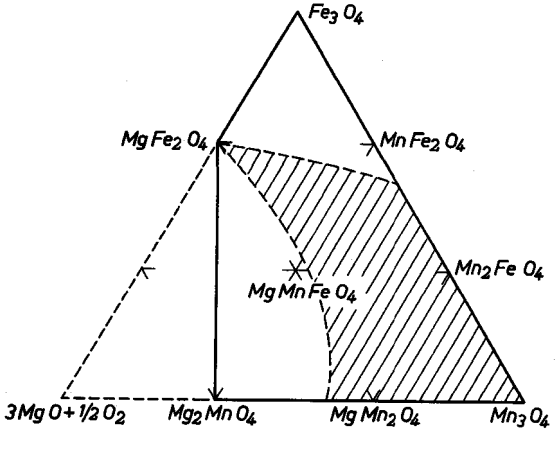

Fig. 43.5. Example of a phase diagram of a ternary oxide system. The area between the solid lines represents crystals with spinel structure. The smaller shaded region represents spinels obtained by firing at 1350 °C in air followed by slow cooling.

of oxygen. These compositions can only be represented in the three-dimensional diagram.

43.3. INTERNAL DEMAGNETIZATION

In the magnetization of polycrystalline ferrite specimens internal demagnetizing fields occur owing to the porosity of the specimens. An impression of the demagnetization due to pores is obtained by measuring the so-called ideal magnetization curve; see § 28.1. From the slope of this curve an internal demagnetizing factor N_i can be derived. It appears that a relationship exists between N_i and the porosity p which is fairly independent of the chemical composition of the spinel. For $Ni_{0.5}Zn_{0.5}Fe_2O_4$ this is represented by curve *a*) in Fig. 43.6. When, however, we determine in the same way the relation between N_i and p for various specimens of hexagonal ferrites for which the basal plane is a preferred plane of magnetization (see § 39.1), we then obtain an entirely different picture [St 3], as can be seen from curve *b*) in the same figure, which holds for Co_2Z. Even for very dense materials a fairly large value for the factor N_i is obtained, and it increases rapidly with the porosity; curve *b*) is seen to be shifted towards the left with respect to curve *a*). This anomalous behaviour can be understood by reference to Fig. 43.7; a crystal lying crosswise affects the pattern of the lines of force in the same way as an air cavity would. The demagnetizing influence is even greater: in the surrounding crystals the lines of force must continue to run parallel to the preferred plane, *i.e.* in the plane of the

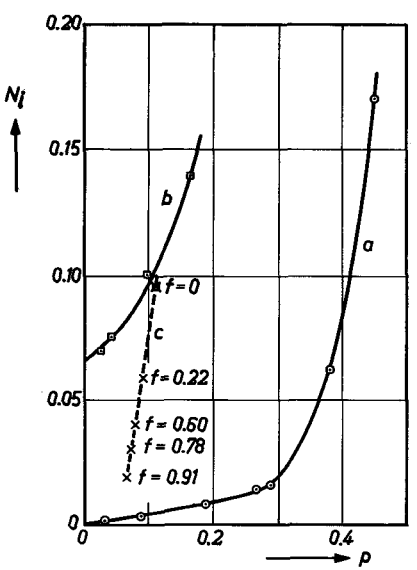

Fig. 43.6. Internal demagnetizing coefficient N_i as a function of porosity p; curve *a*) for the ferrite with spinel structure $Ni_{0.5}Zn_{0.5}Fe_2O_4$, curve *b*) for isotropic specimens of Co_2Z with a hexagonal crystal structure and a preferred plane of magnetization, curve *c*) for anisotropic specimens of Co_2Z having different degrees of orientation.

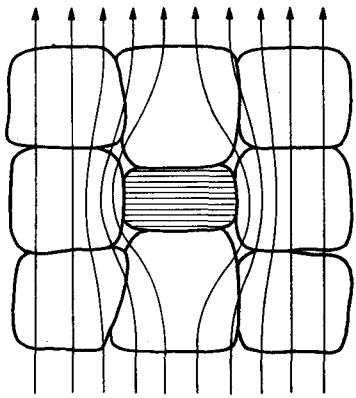

Fig. 43.7. Demagnetization caused by a wrongly oriented crystal in ferrites in which the crystals have a preferred plane of magnetization (for instance the basal plane in the hexagonal crystal structure). The preferred plane of the crystals lies in the plane of the drawing; that of the hatched crystal is perpendicular to the plane of the drawing and parallel to the hatching. Magnetic lines of force have to bend round the sides of this crystal.

drawing. They can thus only bend around the wrongly oriented crystal towards the left and right and not backwards and forewards. It is understandable, therefore, that the internal magnetization of such a fairly dense material is comparable to that of a cubic ferrite having a porosity p of about one third.

43.4. MECHANICAL PROPERTIES

By sintering ferrites at high temperatures the material gets mechanical properties which greatly resemble those of earthenware. Thus, while it cannot be worked with a cutting tool, it can be ground and lapped. When grinding, the same precautions should be taken as with other ceramic materials: wet grinding is necessary with small feed and with suitable grinding discs. Very accurate dimensions and cleanly fitting surfaces are obtained by face-grinding and centreless rotary grinding. The ground surfaces can be very well cemented together with adhesives such as plastics of the aethoxyline group which harden at a temperature of about 180 °C. The air gap need not be greater than a few microns. In this way more complicated shapes can be built up from simple ferrite components. Although ferrites are not sensitive to water or brine, it is advisable, if the ferrites are to be used in high-quality circuits, to impregnate the components in order to prevent dielectric losses through absorption of moisture.

The mechanical strength of sintered samples depends on the porosity. In Fig. 43.8 the compressive strength for uniaxial pressure and the tensile strength of nickel zinc ferrites with spinel structure are plotted as a function of p [Bu 2]. It is well known that the ultimate unidirectional compressive stress of ceramic materials exceeds their ultimate tensile stress by a factor of

10 to 30. When using these data it must be taken into account that the tensile strength of ceramic materials is a function of the cross-sectional area — or better, of the volume of the material, since fracture in ceramic materials is essentially a matter of statistics. Fracture is initiated at the weakest point in the volume under load: the probability of there being a weak point increases as the volume increases. There are various indications that the tensile strength, as given in Fig. 43.8, should be reduced by a factor of 2 to 3 for very large cross-sections in order to obtain the correct value.

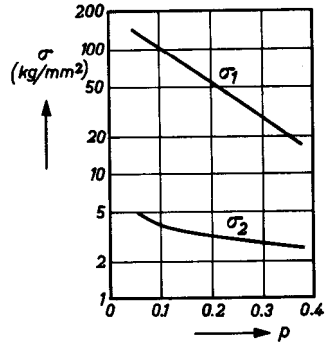

Fig. 43.8. The compressive strength, σ_1, and the tensile strength, σ_2, as functions of the porosity p. The curves refer to a cross-section of 2 mm × 3 mm, and they are roughly the same for the various types of ferrites, after [Bu 2].

Young's modulus for sintered ferrites of all chemical compositions has the order of magnitude 10^{12} dyne/cm². It depends on the porosity as shown by Fig. 43.9. The temperature dependence of this quantity can be influenced to a large extent by minor variations in the chemical composition, (see [Bu3]). Other properties which are fairly independent of the chemical compositions are the thermal conductivity, about 1.5×10^{-2} cal/sec-cm-deg, and the heat capacity, about 0.2 cal/g-deg.

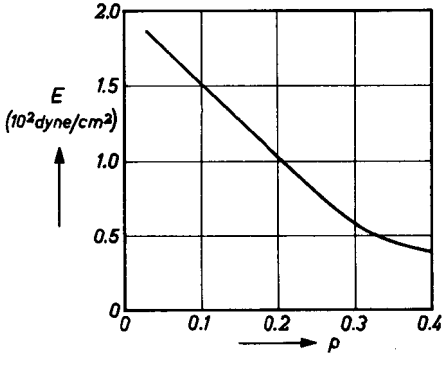

Fig. 43.9. Young's modulus of nickel-zinc ferrites with spinel structure as dependent on the porosity p, after [Bu 3].

§ 44. Crystal-Oriented Samples

Various methods of preparation are known by means of which a magnetic material is obtained with a textural alignment of the crystallites. In the ceramic materials use might be made, for instance, of the non-spherical shape of the powder particles of the hexagonal oxides. These crystals grow preferentially in the basal plane and much less in the direction of the c axis. By packing the powder in steel tubes sealed tightly at both ends and rolling these

at high temperature, it has been found [St 2] possible to produce a slight anisotropy.

A more elegant method [St 2] is to make use of the magnetic crystal anisotropy of the hexagonal oxides. Particles that can rotate freely, and for which the c axis is the preferred direction of magnetization, will be aligned by an externally applied magnetic field such that their preferred axes of magnetization are parallel (see Fig. 44.1). The aligning torque exerted on the crystal of Fig. 44.1 is:

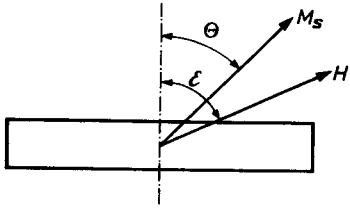

Fig. 44.1. Equilibrium orientation for the magnetization M_s in a fixed particle with uniaxial magnetic anisotropy when an external field H is applied at an angle ϵ to the preferred direction.

$$T = K_1 \sin 2\theta. \qquad (44.1)$$

This torque is equal to K_1 for $\theta = 45°$ or 135° and equal to zero for $\theta = 0°$, 90° or 180°. If for $\epsilon = 90°$ the field strength is greater than $2K_1/M_s$, the magnetization rotates in the direction of H, ($\theta = 90°$), while the orientation of the crystal axes remains unchanged. The mechanical torque is then zero. The rotation of the magnetization is momentary, so that in general the particle will not rotate with the magnetization when the field is applied. Even when the field is further increased, the particle will therefore remain unoriented. If, however, $H = \sqrt{2}\, K_1/M_s$, the sudden application of the field will give rise to the state with $\theta = 45°$, *i.e.* with a maximum torque. In that case the particle will be oriented. The conclusion is that the value of a suddenly applied external magnetic field should be approximately $H = \sqrt{2}\, K_1/M_s$; in the case of $BaFe_{12}O_{19}$ for instance, this is about equal to 11,000 oersteds. This process is most effective if the powder consists of separate particles which are unicrystalline. For an optimum result the particles should hinder each other as little as possible in their orientation. In this respect the platelet-shaped crystals of hexagonal oxides are unfavourable. The powder subjected to treatment with the magnetic field should thus not be too closely packed. After the particles have been oriented in the magnetic field, they must be fixed in this state without loosing the texture obtained. A simple method would be one in which the powder is first mixed with warm, molten paraffin wax, the suspension then being placed in the magnetic field and the paraffin wax allowed to solidify. This method, however, is often not practicable, since the magnetic material in most cases must also have a high density. Fixation together with a high density can be obtained with ceramic substances by compressing the powder suspension in a magnetic field and by subsequent sintering. Although the forces arising during

the compression process are much greater than the orienting force of the magnetic field, a good texture is nevertheless obtained.

Finally, the texture must not be lost by a recrystallization process at the high temperature at which sintering is carried out and which is far above the Curie point. Surprisingly enough it has been found that the texture of the starting material is even improved by sintering at a temperature where crystal growth occurs. This so-called foliate texture of such a crystal-oriented material can clearly be seen in Fig. 44.2*a* and *b* (see page 237), which shows photomicrographs of the faces of a cube of this material. In Fig. 44.2*a* the direction of the magnetic field applied during compression is perpendicular to the plane of the figure, whereas in Fig. 44.2*b* it is parallel to the figure.

It appears that the greatest improvement is obtained in the texture when the density of the sintered material is about 90% of the X-ray density. The phenomenon of the improvement of a preferred orientation by grain growth has been extensively studied on metals, where it could more directly be followed with an electron emission microscope [Ra 2]. It is found that in a matrix of identically or almost identically oriented crystals, which contains a differently oriented crystal, the latter crystal generally disappears while the boundary planes between the identically oriented crystals remain unchanged. It also appears that the wrongly oriented crystal can only grow if it is large with respect to the crystals of the matrix. This behaviour can be understood from surface energy considerations.

In the hexagonal oxides, in which the basal plane is a preferred plane of magnetization, the foliate structure can be obtained [St 3] if a powder of a material of this kind, the particles of which are single crystals, is subjected to a magnetic field which varies in direction but remains parallel to the same plane. This may be, for example, a rotating magnetic field, obtainable by mechanical rotation of a yoke magnet. A rotating magnetic field can also be obtained with a stationary magnet, making use of for instance the three phases of the a.c. mains. Fig. 44.3 (see page 238) shows two electron photomicrographs; the foliate texture of the samples is clearly visible. In Fig. 44.3*a* the preferred planes, which are also the basal planes of the crystals, lie parallel to the plane of the paper, while in Fig. 44.3*b* they lie at right angles.

The magnetization curves of a specimen with foliate texture can be plotted for magnetization in a preferred direction and in a difficult direction. In the case of an ideally oriented sample the area between both curves corresponds to the crystal anisotropy energy of the material. When the sample is not ideally oriented the two curves lie more closely together and include an area which is a fraction f of the area between the corresponding curves of the single crystal. We shall call this fraction the degree of orientation of

the anisotropic material. The degree of orientation of oriented specimens of $BaFe_{12}O_{19}$ or of Co_2Z, for example, is found to have values up to over 90%. Results of measurements of the internal demagnetizing factor N_i for crystal-oriented specimens of Co_2Z are plotted in Fig. 43.6, curve *c*), showing the relevant degree of orientation *f*. It is seen that N_i drops sharply with increasing degree of orientation, entirely as expected: we thus approach the ideally oriented state where, as in the case of the spinels, N_i is determined exclusively by the porosity.

The orientation of crystals by a magnetic field can only occur provided the crystal anisotropy field H^A is not too weak. The result is poor for materials with a composition where H^A is in fact too weak, as for instance in the case of certain mixed crystals of Co_2W with other Me_2W compounds. Substances of this kind can be oriented by a method developed by Lotgering [Lo 2] in which the materials are prepared from a ferromagnetic oxide whose crystals are oriented with help of one of the above-mentioned methods. An example of such a reaction is:

$$BaFe_{12}O_{19} + 0.8\ CoO + 1.2\ ZnO + 2\ Fe_2O_3 \rightarrow BaCo_{0.8}Zn_{1.2}Fe_{16}O_{27}.$$

The starting materials are mixed together and, during compression, are placed in a uniform magnetic field, as a result of which the *c* axes of the crystals of $BaFe_{12}O_{19}$ are aligned mutually parallel. The reaction during sintering is now such that the *c* axes of the product $Co_{0.8}Zn_{1.2}W$ are also parallel, as can clearly be seen from X-ray diagrams similar to those of Figs. 37.9 and 37.10. The basal plane of the product $Co_{0.8}Zn_{1.2}W$ is a preferred plane of magnetization, so that the specimen obtained has a magnetic anisotropy corresponding to this. The anisotropy of this compound, however, is much too weak for orienting in the more conventional way. Several of such so-called topotactical reactions have been described by Lotgering [Lo 2].

CHAPTER XII

ELECTRICAL PROPERTIES

§ 45. D.C. Resistivity

The d.c. resistivity of oxide materials can be fairly reliably measured by means of a sonde method as illustrated schematically in Fig. 45.1. The same current is passed through a resistor R and the ferrite rod F. The voltage between points B_1 across a part of the ferrite rod is compared with the voltage between points B_2 across the known resistance R. For an accurate measurement the internal resistance of the voltmeter V should be high as compared with the resistance of the ferrite rod and the resistances of the contacts B_i. It is also possible to measure the resistance directly between two electrodes on a ferrite rod, provided the contacts are properly

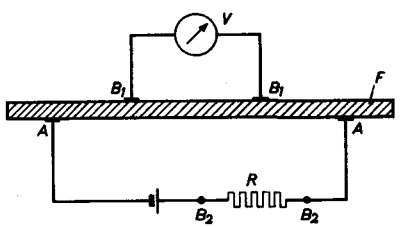

Fig. 45.1. Four-contact method for measuring the electrical resistivity of a ferrite rod F. The voltage drop across the points B_1B_1 is compared with the voltage drop between the points B_2B_2 across a known resistance R.

applied. Indium-amalgam contacts [Ui 1] which are obtained by rubbing indium, moistened with mercury, against a clean and preferably freshly ground surface, are very well suited for the purpose. Grinding is necessary because difficulties may be presented by a surface layer formed during firing. This layer is shown in Fig. 43.4 for an extreme case; it can have either a higher resistivity than the bulk, owing to re-oxidation, particularly at the surface of the product during cooling, or a lower resistivity than the bulk, as found for example with mixed nickel-zinc ferrites of spinel structure [Ui 1]. In the latter case the explanation is that zinc has evaporated from the surface layer at the high sintering temperature and as a result ferrous ions have formed.

For ferrites the resistivity at room temperature can vary, depending on the chemical composition between about 10^{-2} ohm-cm and higher than 10^{11} ohm-cm. It has long been known [Ve 5] that low resistivities are caused in particular by the simultaneous presence of ferrous and ferric ions on equivalent lattice sites (octahedral sites). For example, Fe_3O_4 at room temperature has a resistivity of approximately 7.10^{-3} ohm-cm, and $NiFe_2O_4$ with

TABLE 45.I

RESISTIVITY ρ AND DIELECTRIC CONSTANT ϵ MEASURED AT A FREQUENCY OF 1 KC/S ON SPECIMENS OF $Ni_{0.4}Zn_{0.6}Fe_2O_4$, COOLED FROM THE SINTERING TEMPERATURE IN DIFFERENT WAYS (AFTER [KO 6]).

Ferrite	Sintering temp. °C	Sintering atmos.	Method of cooling	FeO % by weight	ρ ohm-cm	ϵ
1*a*	1300	Oxygen	Slowly in oxygen	0.10	540,000	1,710
1*b*	1300	Oxygen	Rapidly in air	0.38	1,300	28,200
2*a*	1300	Air	Slowly in air	0.07	136,000	4,300
2*b*	1300	Air	Rapidly in air	0.42	1,100	39,000
3	1280	Air	Slowly in air	$\leqslant$0.05	960,000	1,090

some deficiency in iron and sintered in a sufficiently oxidizing atmosphere so that the product contains no ferrous ions, can have a resistivity higher than 10^6 ohm-cm. Intermediate values of resistivity have been given by Koops [Ko 6] among others, for specimens of $Ni_{0.4}Zn_{0.6}Fe_2O_4$ fired in different gas atmospheres; the results are shown in Table 45.I. A relatively low resistivity is found to be associated in these ferrites with a high dielectric constant. An extensive investigation into the origin of the electrical conductivity of spinels has been carried out by Verwey *et al.* [Ve 6] and later by Van Uitert [Ui, 1, 2 and 3] and Jonker [Jo 7], who were concerned especially with obtaining ferrites of high resistivity. Specimens with a varying ferrous content can be obtained by using as starting materials mixtures

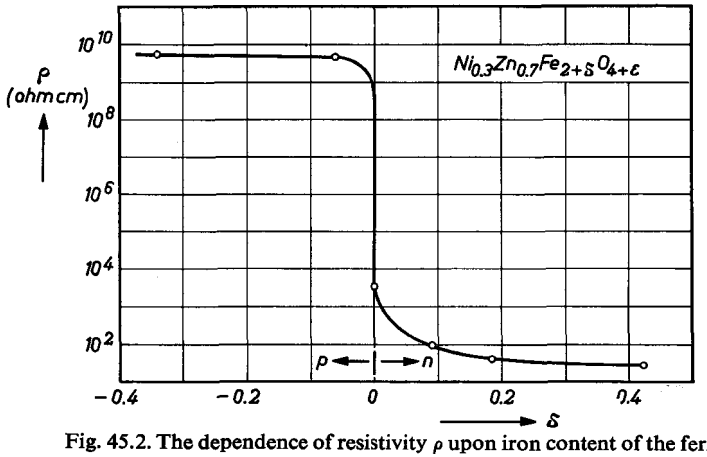

Fig. 45.2. The dependence of resistivity ρ upon iron content of the ferrites $Ni_{0.3}Zn_{0.7}Fe_{2+\delta}O_{4-\epsilon}$ fired at 1250 °C in oxygen. The value of δ is determined by the starting material and the value of ϵ by the firing conditions, after [Ui 3].

with different iron concentrations and by sintering all these in the same way. For the ferrites $Ni_{0.3}Zn_{0.7}Fe_{2+\delta}O_{4+\epsilon}$ Fig. 45.2 gives the resistivity in dependence on the surplus or deficiency δ of iron ions for the case where the ferrites are sintered in an oxygen atmosphere at 1250 °C. The value of δ is determined by the starting material, the value of ϵ by the sintering conditions. With ferrites of the series $Co_{1-\delta}Fe_{2+\delta}O_4$, Jonker [Jo 7] has obtained the results of Fig. 45.3*a*. Two regions of conductivity are found; one region of compositions containing Co^{II} and Co^{III} and having

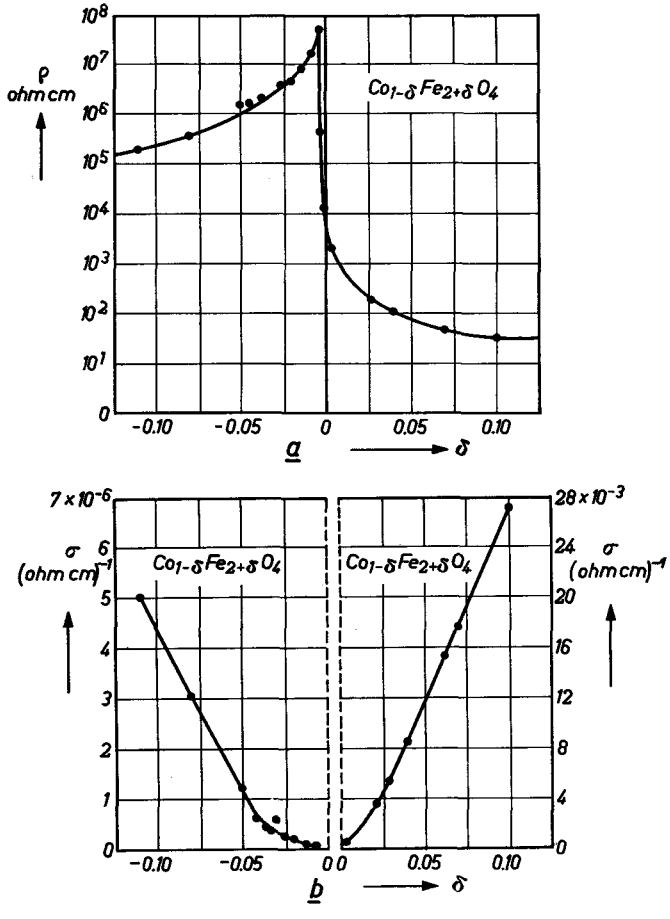

Fig. 45.3*a*. The dependence of resistivity ρ upon iron content of the ferrites $Co_{1-\delta}Fe_{2+\delta}O_4$, after [Jo 7].
b. A replot of the measuring points of Fig. 45.3*a*. The conductivity σ is now given on a linear scale as a function of iron content of the ferrites.

a high resistivity, and one region of compositions containing Fe^{II} and Fe^{III} and having a low resistivity. Measurements of the thermo-e.m.f. show that where there is an excess of cobalt ions, hole conduction occurs (*p* type semiconductor) and in the case of excess iron there is electron conduction (*n*-type semiconductor) [Ui 1]. In Fig. 45.3*b* the results of Fig. 45.3*a* have been replotted so that it can be seen that the conductivity increases somewhat more than linearly with the electron or hole concentration of the ferrite. In the ferrites of Figs. 45.2 and 45.3 the electron concentration can reach a value of almost 10^{22} cm^{-3}, which is much higher than found in normal semiconductors (about 10^{19}—10^{20} cm^{-3}). This figure combined with the results of the resistivity measurements leads to an abnormally low mobility for electrons and holes in ferrites, namely about 10^{-4} and 10^{-8} cm^2/V sec, respectively.

A low resistivity due to the simultaneous presence of ferrous and ferric ions on equivalent lattice sites can also be obtained in stoichiometric oxides by applying the principle of controlled valency [Ve 6]. If small quantities, up to about 1%, of foreign ions, can be incorporated in an oxide of very high resistivity, and if these ions have a valency which differs from that of the ions already present, (for instance titanium ions in Fe_2O_3), then it is possible to force some of the ions present into a different valency state. The result is that ions of the same atom are now again present in different valencies, so that the electrical resistivity of the oxide is reduced ([Ve 6] and [He 2]).

It is often important to make ferrite samples with a high resistivity. It is evident from what is said above that it is then necessary to ensure that there are no ferrous ions in the stoichiometric ferrite. However, it appears that stoichiometric $NiFe_2O_4$ or $MgFe_2O_4$, for example, has a resistivity which is only slightly higher than 10^6 ohm-cm. Van Uitert assumes that this is due to a slight dissociation in the ferrite, for instance according to:

$$Ni^{II} + Fe^{III} \rightleftarrows Ni^{III} + Fe^{II},$$

which in turn makes conductivity possible between Fe^{II} and Fe^{III} ions and between Ni^{II} and Ni^{III} ions. Van Uitert [Ui 1] obtained an appreciable increase in the resistivity of the ferrite by adding to it small quantities of manganese or cobalt ions. Fig. 45.4 gives a picture of this improvement, which results in resistivities higher then 10^{11} ohm-cm. The explanation of this substantial effect [Ui 3] is that in the case, for example, of the addition of Mn to $NiFe_2O_4$ for the purpose of obtaining a stoichiometric ferrite with the formula $NiFe_{1.9}Mn_{.1}O_4$, the concentration of Fe^{II} ions is kept

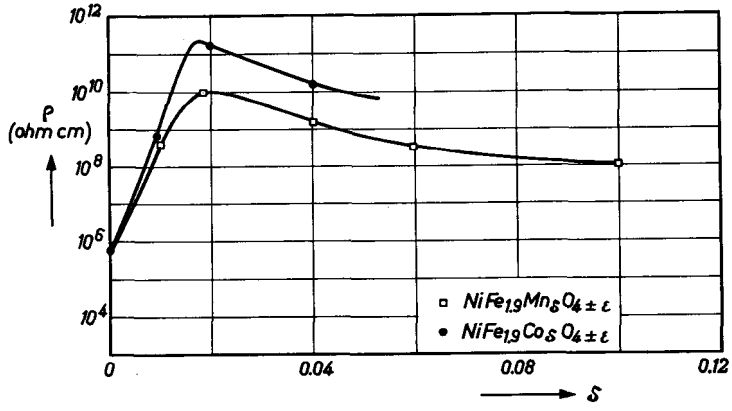

Fig. 45.4. The increase of the resistivity of $NiFe_2O_4$ samples as a result of additions of manganese or cobalt. Firing for 10 hours at 1250 °C in O_2. The value of ϵ is determined by the firing conditions. After [Ui 3].

low by the Mn^{III} ions, while the concentration of any Ni^{III} that may be present remains low owing to the presence of Mn^{II} ions:

$$Fe^{II} + Mn^{III} \rightarrow Fe^{III} + Mn^{II}$$

and

$$Ni^{III} + Mn^{II} \rightarrow Ni^{II} + Mn^{III}.$$

This is related to the increase in the third ionization potential for the ions in the series Cr-Fe-Mn-Co-Ni. Since Mn and Co occur between Fe and Ni in this series, small quantities of these two kinds of ions have the same effect in opposing the formation of Fe^{II} and Ni^{III} ions.

If we use the method of raising the resistivity by adding small quantities of, say, Mn ions, then these ions will occur in two valencies and probably also on equivalent lattice sites. Nevertheless, this results in only a small contribution to the conductivity, owing to the low concentration of these ions.

Ferrites are semiconductors, and their resistivity decreases with increasing temperature according to the relation

$$\rho = \rho_{\infty}\, e^{E_{\rho}/kT}, \tag{45.1}$$

where E_{ρ} represents an activation energy which, according to Verwey and De Boer [Ve 6] is the energy needed to release an electron from the ion for a jump to the neighbouring ion, so giving rise to electrical conductivity. Upon an electron jump, a displacement occurs of the ions in the neighbourhood of the electron in question (see also [He 2]). The mean free path is only about 3 Å. It has been pointed out by Jonker [Jo 7] that in these non-

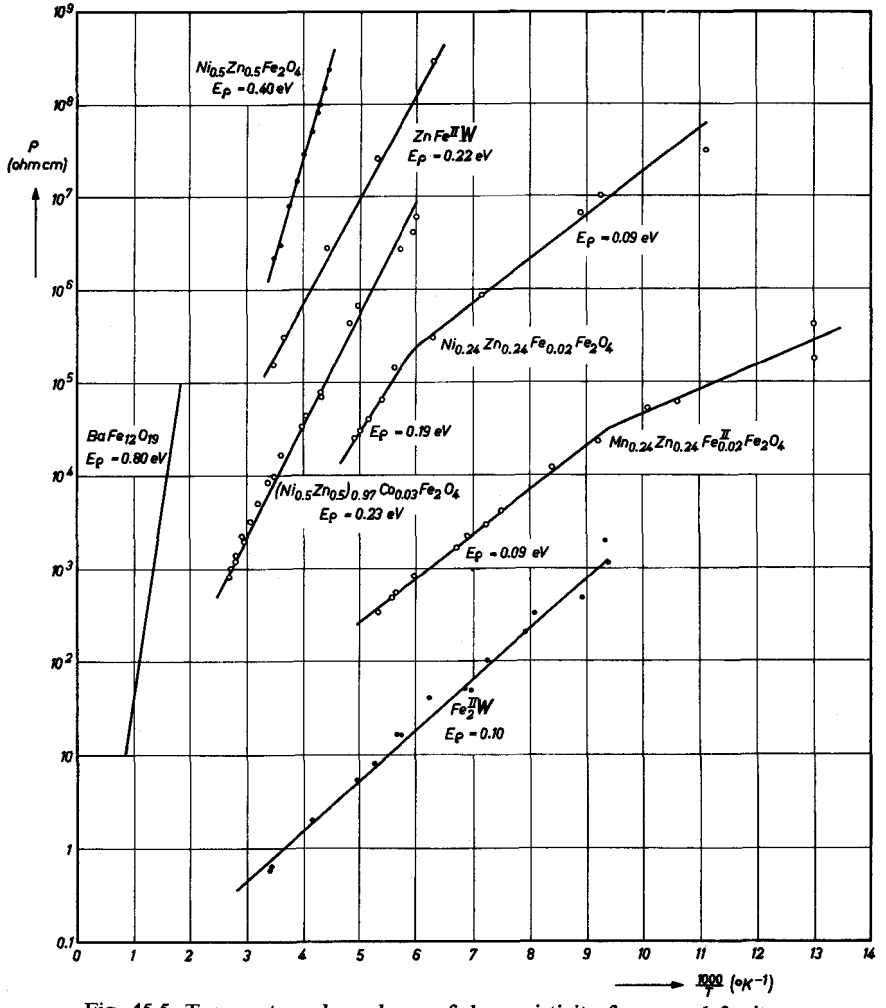

Fig. 45.5. Temperature dependence of d.c. resistivity for several ferrites.

impurity (intrinsic) semiconductors the influence of temperature on the concentration of the conduction carriers is relatively small. This means that the temperature influence on the conductivity is only a result of the change of the mobility of the electrons or holes with temperature. Fig. 45.5 gives the relation between log ρ and $1/T$ for various ferrites. In most cases a straight line is found in a wide temperature range, with a slope corresponding to E_ρ according to the relation:

$$E_\rho = 0.198.10^{-3} \,.\, \mathrm{d}(\log\rho)/\mathrm{d}(1/T). \qquad (45.2)$$

The values for E_ρ lie between 0.1 and 0.5 eV. A high activation energy E_ρ always goes hand in hand with a high resistivity of the ferrite at room temperature. In a few cases a change in slope is found in the curve, which points to two parallel conductivity mechanisms with differing activation energies. Similar changes have also been found at the Curie points of $MnFe_2O_4$, $NiFe_2O_4$ and $CuFe_2O_4$; (see [Ko 7]). As regards the curve of resistivity *versus* temperature, a special case among the ferrites is pure Fe_3O_4 and Fe_3O_4 which is not entirely stoichiometric or in which a small concentration of foreign ions has been substituted. Curve I in Fig. 45.6, as found by Verwey and Haaijman [Ve 4], shows log ρ plotted against $1/T$ for highly stoichiometric Fe_3O_4. The jump in the resistivity at 119 °K is caused by the electron ordering described in § 31.4, which is associated with a transition from cubic to orthorhombic crystal structure below 119 °K. It can be seen from the same figure that an excess of γFe_2O_3 in Fe_3O_4 reduces the jump in resistivity and shifts it towards lower temperatures. The same effect is found for minor substitutions of Ni, Co, Mg, Mn and Zn ions [Ep 1]. Domenicali [Do 2] found on a single crystal of Fe_3O_4

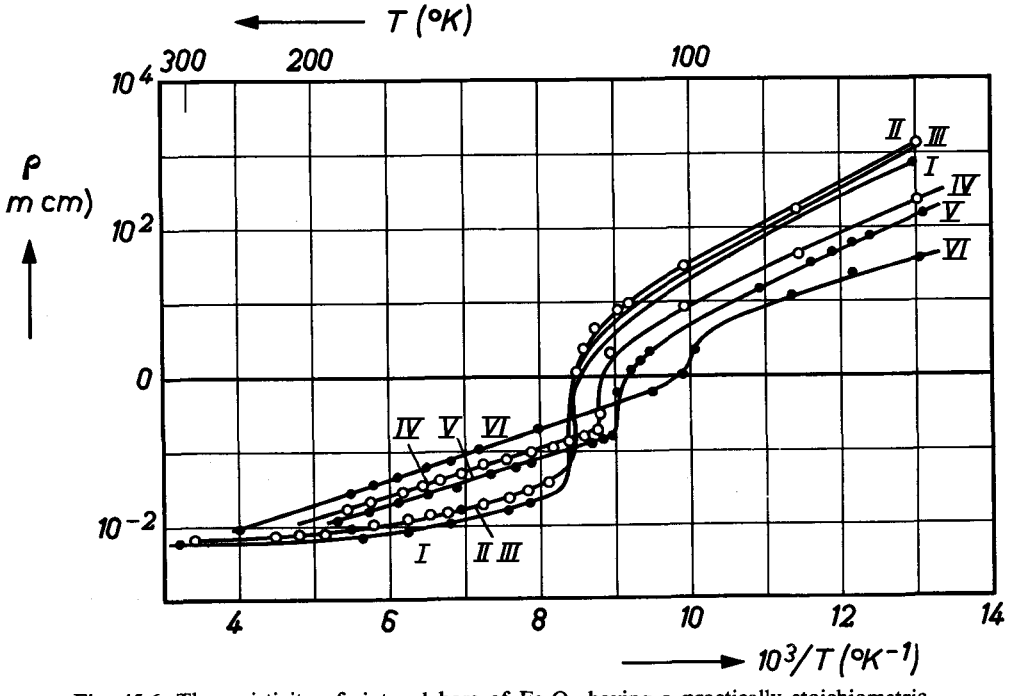

Fig. 45.6. The resistivity of sintered bars of Fe_3O_4 having a practically stoichiometric composition (curve I) and with small quantities of γFe_2O_3 (increasing from II to VI) dissolved in the lattice, after [Ve 4].

for the resistivity in the three principal crystallographic directions a similar jump as indicated in Fig. 45.6. Above room temperature the resistivity of Fe_3O_4 does not continue to drop, but shows a minimum at 80 °C (see Fig. 45.7), above which the conductivity of Fe_3O_4 shows a metallic behaviour.

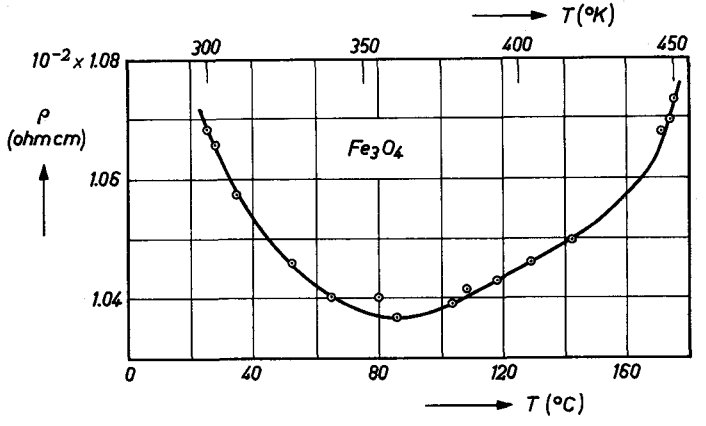

Fig. 45.7. Resistivity of a natural magnetite single crystal in the [100] direction above room temperature, after [Do 2].

§ 46. Frequency-Dependence of Conductivity and Dielectric Constant

46.1. EXPERIMENTAL RESULTS

Up to a frequency of about 100 kc/s measurements of the conductivity and the dielectric constant of ferrites can be carried out on a bridge, as described for example by Köhler and Koops [Ko 4]. For much higher frequencies, resonance methods are used, such as described by Gevers [Ge 2]. An ideal capacitor C_p (with loss-free dielectric) in parallel with a resistor R_p is taken as the equivalent circuit of a capacitor with a dielectric having a certain conductivity. The resistor R_p can be considered as built up from two parallel resistors, one representing the finite ohmic resistance of the dielectric (ferrite) and the other representing an equivalent resistance of such a value that the energy dissipated in it is equal to the dielectric losses in the dielectric. It is not possible by a measurement at a single frequency to determine these two resistances separately, and for this reason it is usual to apply the simple equivalent circuit of Fig. 46.1 for a capacitor with dielectric. For the impedance Z between points P and Q we can write:

$$Z^{-1} = j\omega C_p + R_p^{-1}. \tag{46.1}$$

Putting ϵ'_p as the real part of the dielectric constant and σ as the conductivity

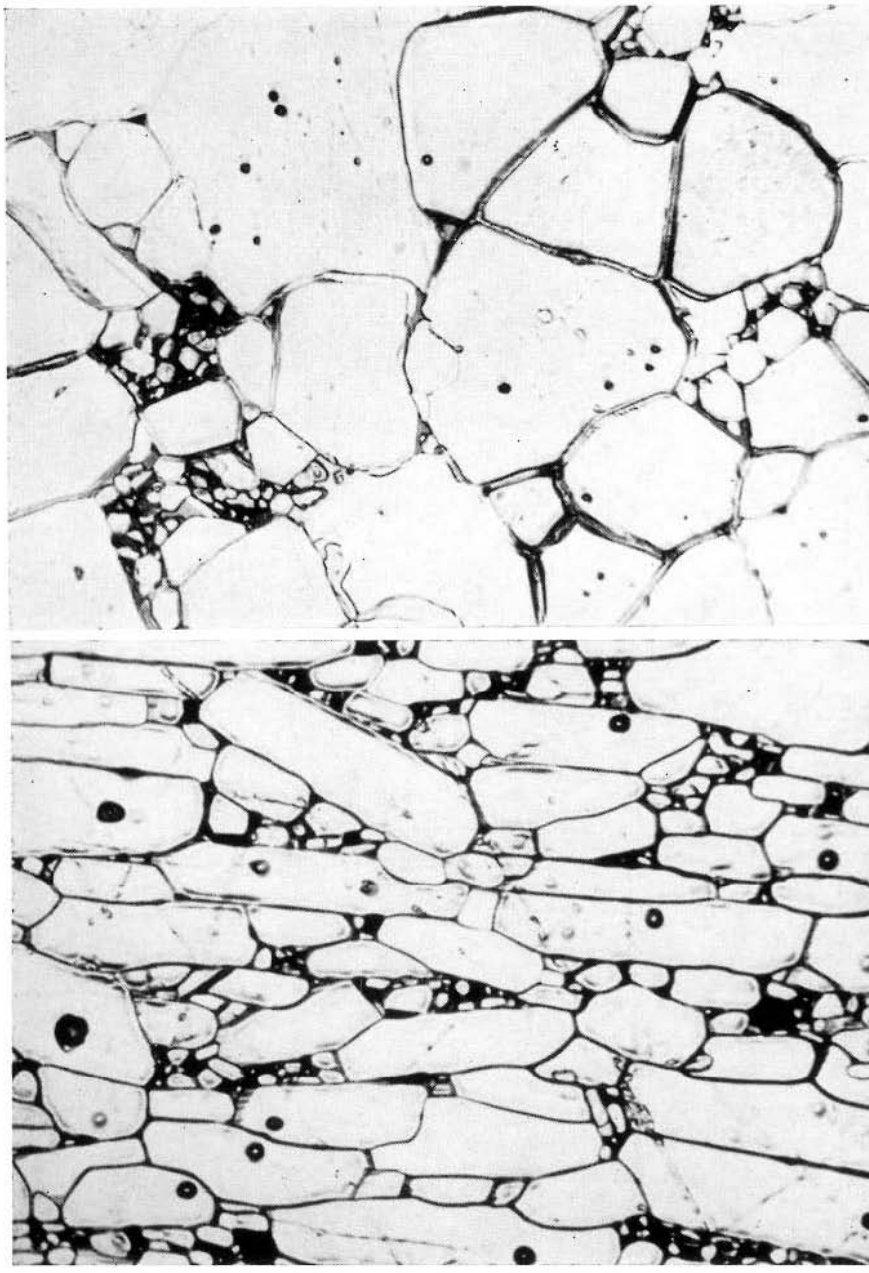

(a)

(b)

Fig. 44.2. Photomicrographs of sintered specimens of $BaFe_{12}O_{19}$ with oriented crystals. The crystals with a preferred direction of magnetization have been oriented in a uniform magnetic field. In (*a*) the hexagonal basal planes lie in the plane of the paper; in (*b*) the basal planes are perpendicular thereto. 1 cm of the figure corresponds to 18 microns.

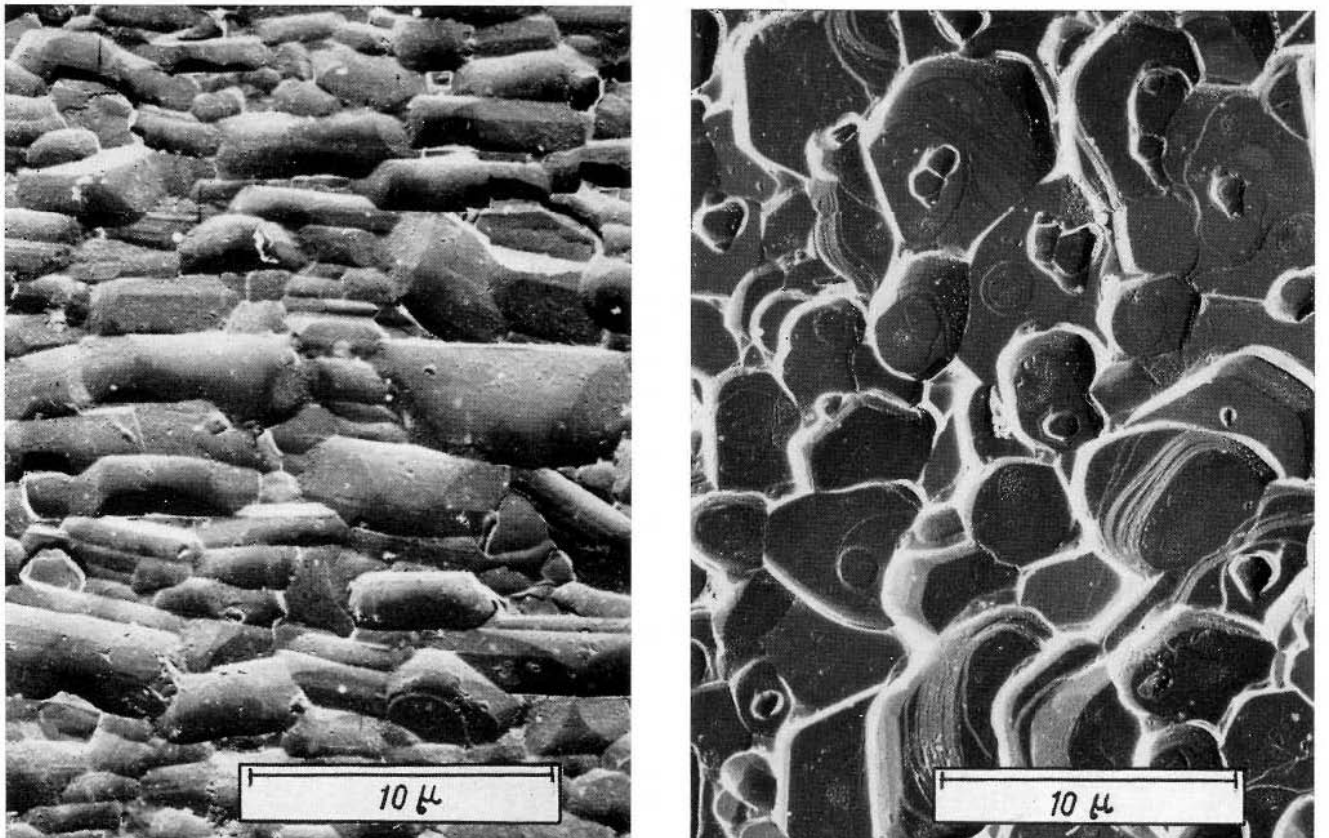

a *b*

Fig. 44.3. Electron-microscope photographs of sintered specimens of crystal-oriented Co_2Z. The crystals having a preferred plane of magnetization have been oriented in a rotating magnetic field. In (*a*) the basal planes, *i.e.* the preferred planes of magnetization, are parallel to the plane of the paper; in (*b*) they are perpendicular to this plane: the directions of the *c* axes lie approximately from top to bottom of the figure (**after [St 3]**)

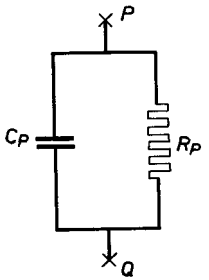

Fig. 46.1. Equivalent circuit of a capacitor with a lossy dielectric.

we have $C_p = 1.11.10^{-12}\epsilon_p' A/4\pi d$ farad, and $R_p = d/A\sigma$ ohm, where A expressed in cm^2 is the area of the capacitor plates, and d expressed in cm is the distance between the plates, which is entirely filled with the dielectric under investigation. (The plates are electrodes applied to the dielectric.) The fact that the dielectric is not loss-free can generally be denoted by a complex dielectric constant ϵ, hence:

$$\epsilon = \epsilon_p' - i\epsilon_p'', \tag{46.2}$$

where

$$\epsilon_p'' = 11.3 \times 10^{12}\, \sigma/\omega. \tag{46.3}$$

The dielectric loss factor is given by:

$$\tan \delta = (\omega C_p R_p)^{-1} = 4\pi\sigma/\omega\epsilon_p'. \tag{46.4}$$

Brockman *et al.* [Br 2] have discovered that sintered ferrites with a high conductivity at low frequencies (below about 1 Mc/s) always have a high dielectric constant ($\epsilon \cong 10^5$). Koop's results in Table 45.I give an impression

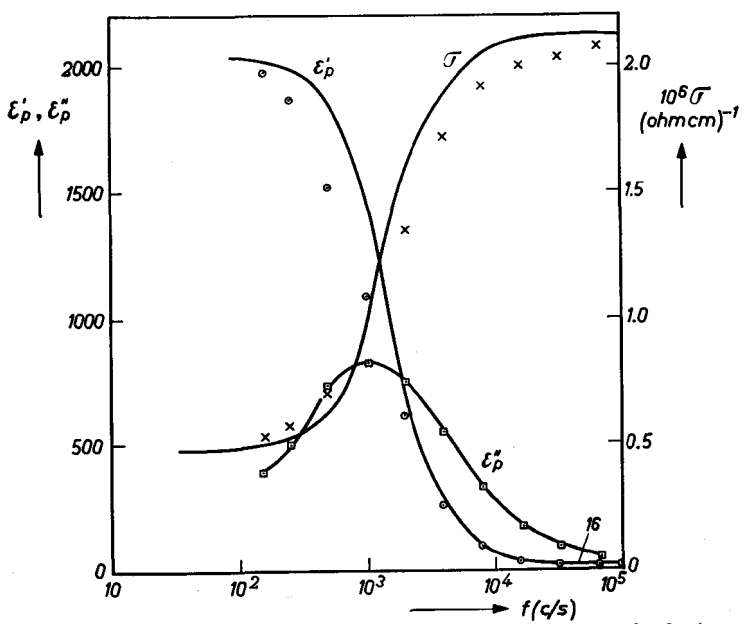

Fig. 46.2. Dielectric constant ϵ'_p and specific conductivity σ of a ferrite $Ni_{0.4}Zn_{0.6}Fe_2O_4$, sample No. 3 from Table 45.I. Measuring points after [Ko 6]. Drawn curves according to (46.5). The ϵ''_p curve is calculated according to (46.3) with correction for the d.c. conductivity.

of the relationship between σ and ϵ. In general it is found that ϵ is roughly inversely proportional to the square root of σ. Both quantities depend on the measuring frequency, as may be seen, for example, from the measuring points in Fig. 46.2. The relaxation in ϵ and σ can be described in terms of the relaxation formula:

$$\sigma = \sigma_\infty + \frac{\sigma_0 - \sigma_\infty}{1 + \omega^2\tau^2}$$
$$\epsilon_p' = \epsilon_\infty + \frac{\epsilon_0 - \epsilon_\infty}{1 + \omega^2\tau^2}, \qquad (46.5)$$

where the indices 0 and ∞ indicate the limiting values at very low and at very high frequency respectively, and where the relaxation time τ is a characteristic time constant of the ferrite. The relaxation frequency ($\propto 1/\tau$) for the different materials appears to be approximately proportional to the low-frequency value of the dielectric constant. The true low-frequency level for ϵ has never been reached according to the data recorded in literature; for this purpose measurements are needed at frequencies below 10^{-1} c/s. Table 46.I gives a survey of the quantities ϵ and σ as found for diverse substances. A constant high-frequency level for ϵ has not been reached for the ferrites mentioned in the table, which have a high dispersion frequency. At 9300 Mc/s the dielectric constant of all ferrites has decreased to about 10, which is a value corresponding to the polarizability for oxygen ions [Fa 2]. It has been found that at field strengths above 1 volt/cm and at low frequency

TABLE 46.I

DATA CONCERNING DISPERSION IN THE DIELECTRIC CONSTANT ϵ AND THE CONDUCTIVITY σ OF A NUMBER OF FERRITES WITH SPINEL STRUCTURE.

Ferrite	Low-frequency value *)		High-frequency value		Relaxation frequency (in kc/s)	
	ϵ_0	σ_0 (ohm-cm)$^{-1}$	ϵ_∞	σ_∞ (ohm-cm)$^{-1}$	Measured	According to (46.7)
No. 3 from Table 45.I	1,980	$0.5 \cdot 10^{-6}$	16	$2.1 \cdot 10^{-6}$	1.7	2.0
No 1*a* ,,	1,710	$2 \cdot 10^{-6}$	13.8	$14 \cdot 10^{-6}$	4	15
No. 1*b* ,,	28,200	$0.8 \cdot 10^{-3}$	$\simeq 42$	$2 \cdot 10^{-3}$	200	130
$Hi_{0.48}Zn_{0.48}Fe^{II}_{0.04}Fe_2O_4$	100,000	$7.7 \cdot 10^{-3}$	†)	>1 †)	2000	—
$Ni_{0.5}Zn_{0.5}Fe_2O_4$	2,100	$0.5 \cdot 10^{-6}$	15	$2 \cdot 10^{-6}$	1	1.8
$MgFe_2O_4$, after [Fa 1]	30,000	$0.3 \cdot 10^{-6}$	22	$4.8 \cdot 10^{-6}$	11	0.3

*) The figures represent the results of measurements at the lowest frequency.

†) With this ferrite no constant level for ϵ and σ has yet been reached at 50 Mc/s.

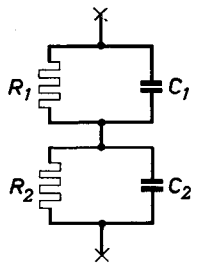

Fig. 46.3. Equivalent circuit for a ferrite core showing relaxation dispersions in ϵ and σ with a single time constant.

the quantities ϵ and σ^{-1} (*i.e.* the resistivity) become smaller with increasing field strength, particularly for ferrites with a high dielectric constant. It appears that in sufficiently high measuring fields the low-frequency value of ϵ does not differ much from the high-frequency value.

46.2. PHENOMENOLOGICAL THEORY

It may be assumed that a polycrystalline sintered ferrite consists of large domains of fairly well conducting material (R_1 and C_1 in Fig. 46.3) which are separated by thin layers of a relatively poorly conducting substance (R_2 and C_2). These boundary layers can have arisen by superficial reduction or oxidation of the crystals in the porous material as a result of their direct contact with the firing atmosphere. In this case the relaxation time τ is given by:

$$\tau = \frac{C_1 + C_2}{1/R_1 + 1/R_2} = \frac{\epsilon_1 + \epsilon_2/a}{4\pi(\sigma_1 + \sigma_2/a)} \cdot \frac{1}{9.10^{11}}, \tag{46.6}$$

where $a(\ll 1)$ is the ratio between the thickness of the boundary layer and that of the large domain. Koops [Ko 6] has assumed that the intrinsic dielectric constant of the large domain has approximately the same value as that of the boundary layer ($\epsilon_1 = \epsilon_2$). This will be approximately equal to the ϵ caused by the oxygen ions. If it is assumed, moreover, that $R_2 \gg R_1$, we then have, if σ_∞ is expressed in (ohm-cm)$^{-1}$:

$$\begin{aligned} \epsilon_\infty &\cong \epsilon_1 \\ \sigma_\infty &\cong \sigma_1 \\ \epsilon_0 &\cong \epsilon_2/a \\ \sigma_0 &\cong \sigma_2/a \\ \tau &\cong 0.0855 \times 10^{-12}\, \epsilon_0/\sigma_\infty . \end{aligned} \tag{46.7}$$

In Fig. 46.2 the values of ϵ and σ of the ferrite No. 3 in Table 45.I are plotted as a function of frequency. The crosses and the circles in the figure denote the measuring results, while the curves are drawn in accordance with (46.5), it being assumed that $\tau = 0.94 \times 10^{-4}$ sec. The thickness ratio*) is then $a = 0.78 \times 10^{-2}$ ($a \cong \epsilon_2/\epsilon_0 \cong \epsilon_\infty/\epsilon_0$). In those cases where ϵ is very high ($\epsilon \cong 10^5$), a becomes so small that the boundary layers can only be a few

*) Koops [Ko 6] did not disregard the high-frequency conductivity in (46.7) and therefore found a different value: $a = 0.45 \cdot 10^{-2}$.

Ångstroms thick. It is found then that where the ferrous content is high, this boundary layer will be only a few lattice spacings thick, whereas with a lower ferrous content it would be a factor of 100 thicker. Also plotted in Fig. 46.2 is the quantity ϵ_p'', which is calculated according to (46.3). The assumption is made that the direct current conductivity also makes a contribution to the losses at high frequencies, for which reason the values inserted for σ in (46.3) are the differences between σ measured at a specific frequency and its low-frequency value, σ_0. Kamiyoshi [Ka 2], Volger [Vo 1] and Fairweather and Frost [Fa 1] found the same activation energy E_ρ for the temperature-dependence of the d.c. conductivity ($\propto 1/R_2$) and for the relaxation time τ. However, according to (46.3), the relaxation time τ is proportional to the high-frequency level of the resistivity ($\propto R_1$), so that we come to the conclusion that the activation energies for the conductivity of the boundary layers and the large domains are equal. Volger and Fairweather and Frost assume therefore that the grains make poor contact with each other. The field-dependence of σ and ϵ may, according to this model be connected with electrical breakdown in the layers.

CHAPTER XIII

STATIC INITIAL PERMEABILITY

§ 47. Static Initial Permeability at Room Temperature

47.1. FERRITES WITH ISOTROPIC ROTATIONAL PERMEABILITY

As explained in Chapter V, the initial permeability of a ferromagnetic substance can be due either to a simultaneous rotation of the spins in each Weiss domain or to a reversible displacement or bulging of domain walls. The initial permeability due to rotations is determined by the anisotropies discussed in Chapter IV. For the general case that the binding of the magnetization to a preferred direction is described in terms of two anisotropy fields H_ϕ^A and H_θ^A, we may write according to (17.4) for the components of the rotational permeability in the three principal directions of a crystal with the magnetization vector in the x direction (see Fig. 47.1):

$$\mu_{xx} = 1;\ (\mu_{yy} - 1)/4\pi = M_s/H_\phi^A;\ (\mu_{zz} - 1)/4\pi = \mathrm{M}_s/H_\theta^A. \quad (47.1)$$

For a polycrystalline specimen consisting of randomly oriented crystallites without any magnetic interaction, the average value of the initial permeability μ_0 is given by the expression:

$$(\mu_0 - 1)/4\pi = (1/3)(M_s/H_\theta^A + M_s/H_\phi^A). \quad (47.2)$$

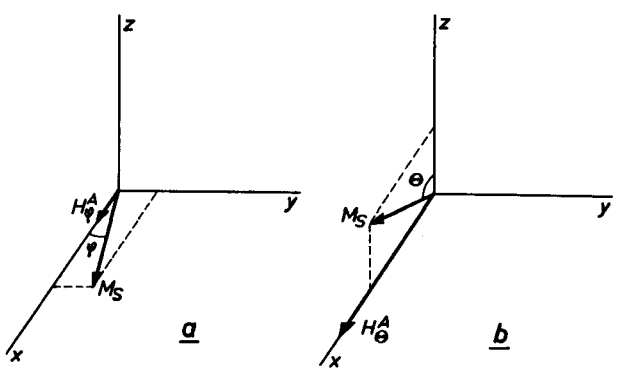

Fig. 47.1. Anisotropic rotational permeability. The x direction is the preferred direction of magnetization. A rotation of the magnetization M_s in the xy plane over a small angle ϕ out of the preferred direction is opposed by a relatively small anisotropy field H_ϕ^A; see figure *a*. A rotation in the xz plane is opposed by the larger anisotropy field H_θ^A; see figure *b*.

For the ferrimagnetic spinels, and for the hexagonal ferrimagnetic oxides having the c axis as the preferred direction of magnetization, we may write $H_\theta^A = H_\phi^A$ $(=H^A)$; the rotational permeability is then isotropic, so that (47.2) reduces to:

$$(\mu_0 - 1)/4\pi = (2/3)M_s/H^A. \tag{47.3}$$

If the crystal anisotropy is predominant the anisotropy field H^A is related to the crystal anisotropy constants according to Table 11.I and eq. (11.7). In a polycrystalline material the crystals are not free to deform. As a consequence the rotation of the magnetization vector will induce stresses which in their turn give rise to an anisotropy of the type (13.8). For cubic crystals this is [Ki 2] (see page 58):

$$F_\sigma = \tfrac{3}{4}\,[(c_{11} - c_{12})\,\lambda_{100}^2 - 2c_{44}\lambda_{111}^2]\,. \tag{47.4}$$

If the internal mechanical stresses in a polycrystalline specimen are so great that the stress anisotropy predominates, the situation for determining the permeability due to rotations is complicated. Assuming for the sake of simplicity that the magnetostriction is isotropic and positive, then according to [Be 8] the permeability due to rotations, at an average stress value $|\sigma_i|$, will be of the order of magnitude of:

$$(\mu_0 - 1)/4\pi = (2/9)M_s{}^2/|\lambda||\sigma_i|. \tag{47.5}$$

The reversible bulging of the domain wall does not change the Weiss domain pattern as a whole, and as stated in § 16.1 the stiffness of the domain walls is determined by the energy increase due to the enlargement of the wall area. The permeability corresponding to this is given by (16.3). According to this formula the permeability depends not only on the anisotropies determining the magnitude of the specific wall energy, but also substantially upon the span D of the wall.

For simple spinels one can calculate an initial permeability for rotations according to (47.3) with the aid of the crystal anisotropy and saturation magnetization data given in Tables 34.I and 32.III. The result is always at least a factor of two lower than the value measured for polycrystalline specimens. Naturally, the measured permeability varies within a wide range, since it depends closely on the method of preparing the specimen. The size and distribution of the pores, as well as the average size of the crystallites, have a pronounced effect on μ_0. However, the permeability of the sintered specimens is always appreciably higher than that which is to be expected from the magnitude of the anisotropy for the case of rotations alone. This may be the consequence of a contribution from reversible wall dis-

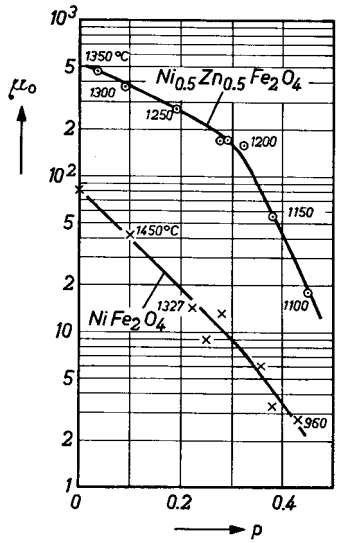

Fig. 47.2. The initial permeability μ_0 of polycrystalline ferrite samples as a function of their porosity p. The porosity was varied by varying the sintering temperature. The sintering temperature for each sample is indicated.

placements. Assuming the span D to be equal to the distance between the domain walls and equal to 5 microns, which, in ferrites fired at high temperature, corresponds approximately to the distance between the pores, and assuming further $M_s \simeq 300$ gauss and $\sigma_w \simeq 1$ erg/cm^2, which is an average value for the ferrites with spinel structure, we find according to (16.3) that $\mu_0 \simeq 200$ and according to (16.4) that $\mu_0 \simeq 60$ for $K = 5 \cdot 10^4$ erg/cm^3. It appears from this that in the case of ferrites whose porosity is not too great and whose pores are not too finely distributed, the reversible bulging of domain walls can make a contribution to μ_0 which is greater than that originating from rotations. Fig. 47.2 gives the relation between initial permeability μ_0 and porosity p for specimens of nickel ferrite [Br 7] and nickel-zinc ferrite with spinel structure which have been fired at different temperatures. For $p = 0$ the figure shows the result of a measurement made on a nickel ferrite single-crystal by Galt [Ga 4]. It can be seen that there is an appreciable increase in the permeability with increasing density of the material, which appears to be connected with an increase in the contribution from domain wall displacements.

An investigation of the influence of crystal size on the magnitude of μ_0 has been carried out by Guillaud [Gu 9] on manganese-zinc ferrites (the firing composition in mol % was 52.5 Fe_2O_3, 28.3 MnO and 19.2 ZnO). Care was taken to ensure that the pores occurred as much as possible only on grain boundaries, so that each crystallite would be free of pores. The result is reproduced in curve *a* of Fig. 47.3. It can be seen that there is a considerable increase in μ_0 when the average diameter of the crystallite is greater than about 5 microns. Guillaud assumes that from this crystal size onwards the permeability is due not only to rotations of the magnetization but also to wall displacements. In the preparation of samples with crystallites larger than 20 microns, pores also occur in the crystals, and these, according to the author, limit the permeability. Curve *b* in Fig. 47.3 gives similar results for a nickel-zinc ferrite.

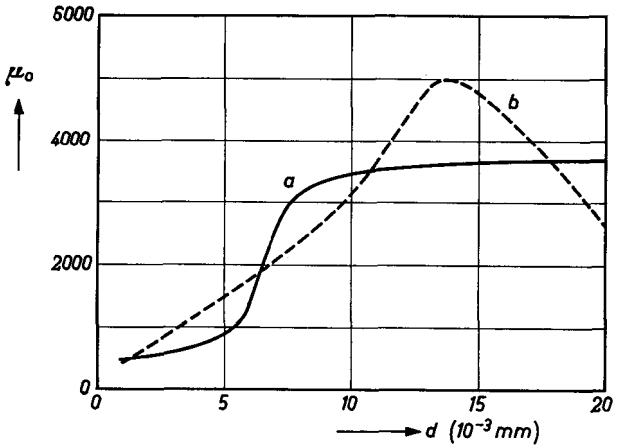

Fig. 47.3. Dependence of the initial permeability μ_0 on the diameter d of the crystals in *a*) manganese-zinc ferrites with spinel structure, made from the oxide mixture 52 mol % Fe_2O_3 28.3% MnO and 19.2% ZnO and *b*) nickel-zinc ferrite with spinel structure: 50.3 mol% Fe_2O_3, 15% NiO and 34.7% ZnO. After [Gu 9].

For making polycrystalline specimens with a high initial permeability it is a prerequisite that the magnetic anisotropies, such as the crystal anisotropy and the stress anisotropy, should be small. The crystal anisotropy and the magnetostriction are determined by the chemical composition of the ferrite. With cubic crystals the internal stresses may be small, since these crystals have an isotropic coefficient of expansion. In order to obtain a high permeability it is also necessary that the specimen should have as few pores as possible and that the crystallites should have a sufficiently large size. These conditions can be fulfilled by suitable technological procedure in the preparation of the ferrite.

A particular case is the ferrite with very small magnetic anisotropies, for example a manganese-zinc-ferrous spinel, which has been sintered in such a way that it has only a small porosity consisting of a large number of finely distributed cavities. In this case the domain-wall thickness may be of the order of magnitude of the distance between the cavities. It is questionable whether in such a case one can still speak of a Weiss domain structure, or whether one should speak of a gradual variation of the direction of magnetization throughout the entire specimen.

47.2. FERRITES WITH ANISOTROPIC ROTATIONAL PERMEABILITY

For the ferrites with hexagonal crystal structure, whose basal plane is a preferred plane of magnetization, we have $H_\theta^A \gg H_\phi^A$, so that the rotational permeability of such crystals is anisotropic according to (47.1). The anisotropy field H_ϕ^A is often a factor of 1000 smaller than H_θ^A, so that, neglecting the magnetic interaction between the crystals, we can write for a polycrystalline specimen in good approximaton:

$$(\mu_0 - 1)/4\pi \cong (1/3)M_s/H_\phi^A. \tag{47.6}$$

Since H_ϕ^A is of the same order of magnitude as the anisotropy field in the case of spinels, hexagonal ferrites with a preferred plane of magnetization can, in principle, also show appreciable values of permeability. Results of measurements on polycrystalline isotropic specimens are represented in the third column of Table 47.I. The initial permeability of a sintered polycrystalline sample of these ferrites also depends strongly on the method of preparation. It is striking, however, that the measured values for μ_0 are appreciably smaller than those which may be deduced from the magnitude of the crystal anisotropy in the basal plane (for the anisotropy energy see Table 39.II). Only in the case of Co_2Y is the crystal anisotropy comparatively high, so that here this anisotropy probably determines the permeability.

It is possible that, during the cooling of polycrystalline samples, appreciable stresses arise in the hexagonal crystals in consequence of the anisotropic coefficient of expansion. Assuming these internal stresses to be so large that they approach the crushing strength of the ferrite ($\sigma_i \cong 10^9$ dyne/cm^2), it follows that for a saturation magnetostriction value of 10^{-5} (which is a quite normal value for hexagonal ferrites) the maximum value of the initial permeability μ_0 will be approximately equal to 10. Such a value is found experimentally in many cases, so that it is not unlikely that

TABLE 47.I

INITIAL PERMEABILITY μ_0 OF SINTERED SPECIMENS OF HEXAGONAL OXIDES WITH A PREFERRED PLANE OF MAGNETIZATION, AT 20 °C.

Ferrite	Isotropic specimen		Anisotropic specimen	
	Calculated according to (47.6)	Measured	Calculated	Measured
Co_2Z	75	12	$^3/_2\times$ 75	29
$Co_{0.8}Zn_{1.2}Z$	$\cong$ 700	24	$\cong {}^3/_2\times 700$	55
$Co_{1.0}Zn_{1.0}Z$	$\cong$ 400	20	$\cong {}^3/_2\times 400$	43
Zn_2Y	$>$ 750	16	$> {}^3/_2\times 750$	35
Co_2Y	5	5	$\cong {}^3/_2\times$ 5	7

the stress anisotropy has a substantial influence on the magnitude of μ_0 for polycrystalline specimens of hexagonal ferrites with a preferred plane of magnetization. There are no indications that domain wall displacements make any appreciable contribution in these ferrites. It is easy, however, to form walls parallel to the basal plane. The energy will be low and the thickness large, since these are both determined by K_3 from (11.6), which is small.

Internal demagnetization due to pores is also appreciably larger in the case of ferrites with a preferred plane of magnetization than in the case of spinels, and internal demagnetization exists even in the absence of pores, owing to crystal platelets whose basal plane is at right angles to the magnetic flux; see § 43.6 and Fig. 43.7. A substantial reduction of internal demagnetization is obtained in specimens in which the crystallites are oriented with the basal planes mutually parallel (curve *c*) in Fig. 43.6. The permeability in these specimens is found to increase with the degree of orientation of the crystals; see Fig. 47.4. For these samples of Co_2Z and CoZnZ with foliate texture (§ 44) the degree of orientation is varied by using different currents which produce the rotating field used for orienting the crystals. All specimens have approximately the same density. The figure clearly shows the considerable gain in permeability obtained in particular at a high percentage of orien-

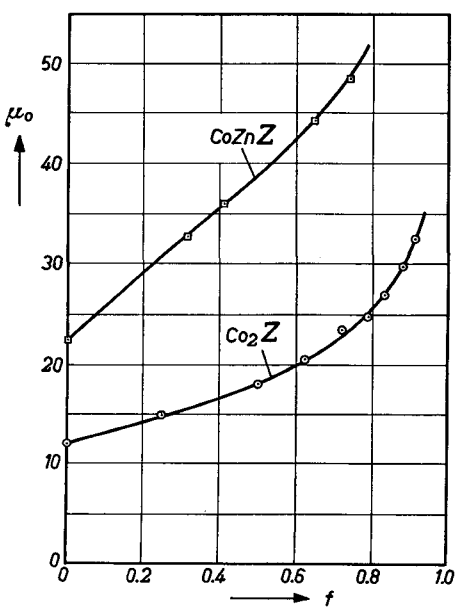

Fig. 47.4. Initial permeability μ_0 of samples of Co_2Z and CoZnZ with different degrees of crystal orientation *f*.

tation. In Table 47.I the gain in permeability obtained by crystal orientation is given for several different compositions. For the measurement of the permeability the applied field strength is parallel to the preferred planes. For a measurement where the field strength is perpendicular to these planes, a lower permeability than in the isotropic material is to be expected. In fact, by measuring in this way the Co_2Z specimen with $f = 0.91$, a permeability of only 2.5 is found. For an ideally oriented sample the value derived from the uniaxial anisotropy is 1.3.

In Fig. 47.5 the initial permeability at room temperature is given for the ferrites of the series $Co_\delta Zn_{2-\delta}Z$. For $\delta < 0.65$ the c axis of these ferrites is a preferred direction of magnetization (see Fig. 39.8) and μ_0 is determined by the magnitude of K_1. The susceptibility due to rotations is then extremely small since K_1 is of the order of magnitude of 10^5 to 10^6 erg/cm^3 or higher. In specimens with low porosity a further contribution to μ_0 may be expected from the domain wall displacements. That is why an initial permeability $\mu_0 \cong 4$ may still be found for specimens corresponding to $\delta < 0.65$. The compounds corresponding to $\delta > 0.65$ have a preferred plane of magnetization (see Fig. 39.8) and thus in principle have a greater value of μ_0, which is in fact found. The decrease in permeability when δ increases from 0.65 to 2.0 is related to the increase of anisotropy in the basal plane (K_3) with increasing cobalt content; see, for example, Table 39.II.

A curve of permeability as a function of the composition, similar to that of Fig. 47.5, is found for all series of mixed ferrites which exhibit a change in the sign of the principal anisotropy constant K_1, as for example the series $Co_\delta Me_{2-\delta}Z$ and $Co_\delta Me_{2-\delta}W$, where Me represents one of the divalent ions that can occur in Z and W compositions.

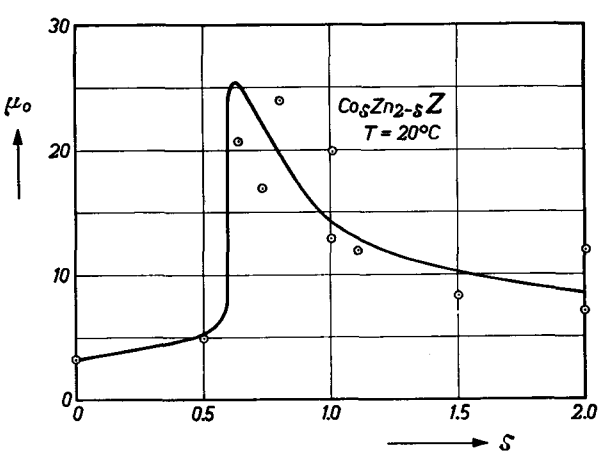

Fig. 47.5. Initial permeability μ_0 at room temperature in dependence on the cobalt content for ferrites of the series $Co_\delta Zn_{2-\delta}Z$.

§ 48. Temperature Dependence of Initial Permeability

48.1. FERRITES WITH SPINEL STRUCTURE

Simple Ferrites

The magnitude of the initial permeability of a magnetic material as a result of rotations is proportional to the square of the saturation magnetization and inversely proportional to the magnetic anisotropy energy. Both quantities vary with temperature, so that μ_0 can be a complicated function of temperature. In § 11 it was pointed out that the anisotropy is related in general to the second or a higher power of M_s. The permeability will thus, as a rule, increase up to the Curie point. For a number of simple ferrites with spinel structure the curves of μ_0 *versus* T are drawn in Fig. 48.1. The curves represent measurements on sintered samples, so that the same restrictions concerning the reproducibility of the curves apply as in § 47. Since the density of the sample may influence the permeability, it is mentioned in the figure for each ferrite. In general, μ_0 increases with temperature and shows a maximum just below the Curie point.

For Fe_3O_4 a second peak appears in the curve at approximately 130 °K. This peak is related with a zero point in the crystal anisotropy; see Fig. 34.1. The height of this maximum may be limited not only by some inhomogeneity of the specimen but also by the shape and stress anisotropy still present.

Mixed Zinc Ferrites

Among the technically important ferrites are the mixed zinc ferrites with a high initial permeability. After Forestier [Fo 1] had discovered that the Curie points of mixed crystals of ferrites with zinc ferrite are lower than those of the corresponding simple ferrite (see, for example, Fig. 32.9), Snoek made a broad investigation into the behaviour of the initial permeability of these ferrites. In doing so he was the first to prepare specimens with an initial permeability well above 50 and even of the order of magnitude of 1000. He found not only that the maximum in the μ_0 *versus* T curves of Fig. 48.1 shifts with the Curie point towards lower temperatures, and accordingly may lie at room temperature or immediately above it, but also that, in most mixed zinc ferrites, appreciably higher values of μ_0 appear in this maximum the lower is the Curie point. Examples are given in Fig. 48.2 and Fig. 48.3 for the series of ferrites $Mn_{1-\delta}Zn_\delta Fe_2O_4$ and $Ni_{1-}\ Zn_\delta Fe_2O_4$. The effect is less pronounced for the series $(Li_{0.5}Fe_{0.5})_{1-\delta}Zn_\delta Fe_2O_4$ (Fig. 48.4). Also in this case, however, μ_0 is maximum for the lowest possible Curie point.

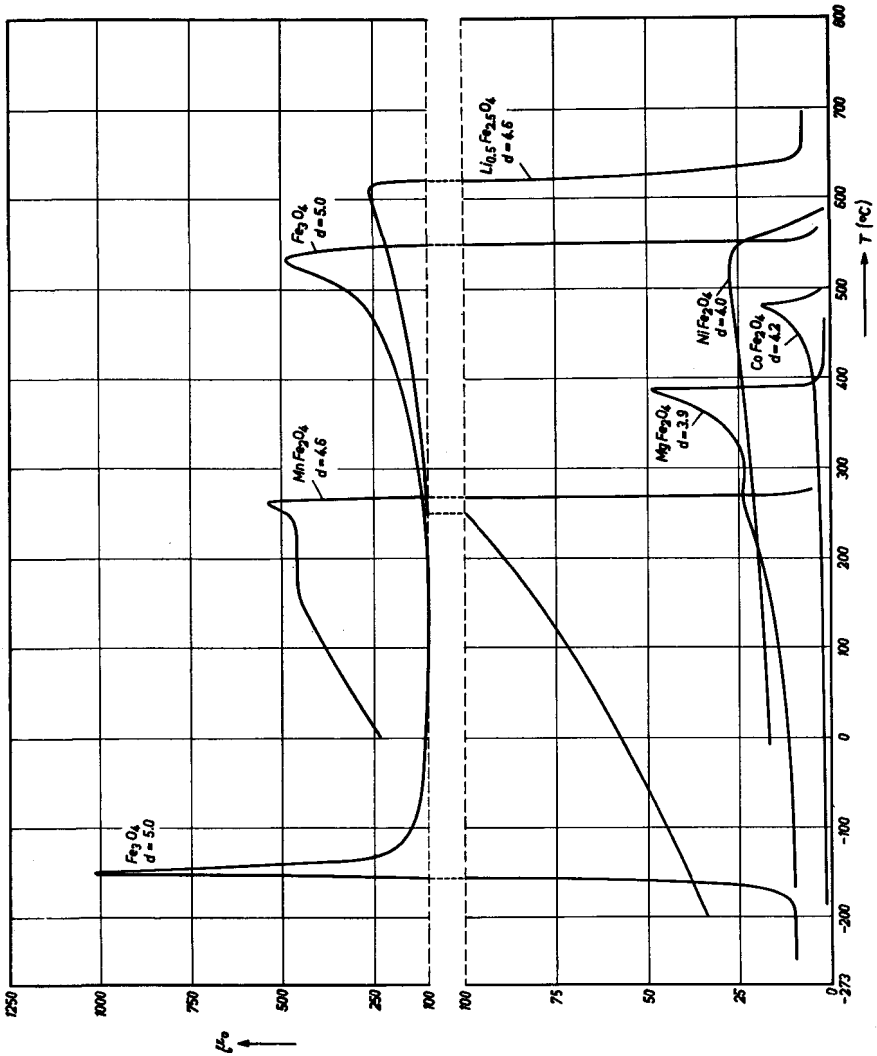

Fig. 48.1. Initial permeability of some polycrystalline specimens of simple ferrites with spinel structure as a function of temperature. The density d in g/cm³ is given for each sample.

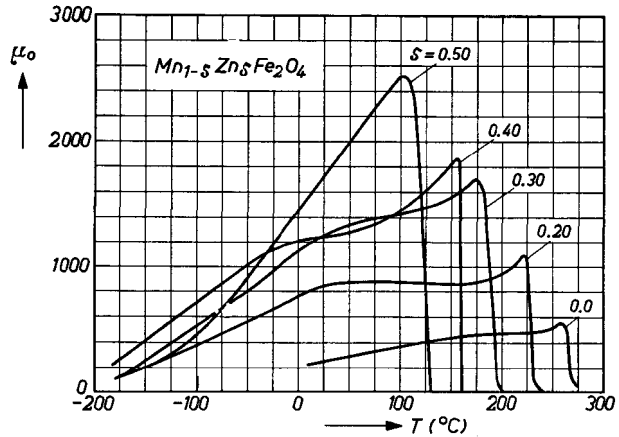

Fig. 48.2. Initial permeability μ_0 as a function of temperature for mixed manganese-zinc ferrites with spinel structure $Mn_{1-\delta}Zn_\delta Fe_2O_4$. These specimens also contain a small ferrous ion content.

As examples for the manganese zinc ferrites experimental data are given for specimens which also contain a low concentration of ferrous ions; these are ternary manganese-zinc-ferrous ferrites in which the Fe_3O_4 content can amount to 5%.

Mixed Cobalt Ferrites

Mixed crystals between ferrites having a negative crystal anisotropy and the cobalt ferrite having a positive crystal anisotropy can be made with such proportions of the components that the crystal anisotropy of the mixed crystal is zero at a desired temperature. Owing to the high anisotropy of cobalt ferrite, only a small concentration of this ferrite is needed.

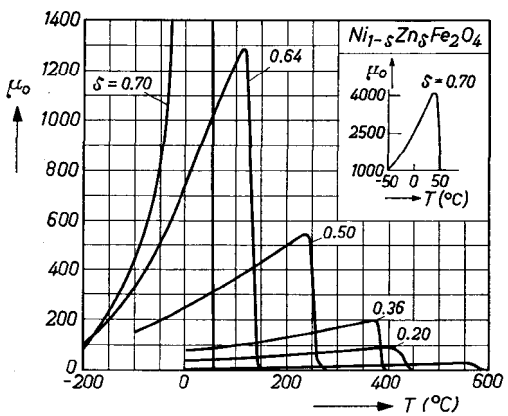

Fig. 48.3. Initial permeability μ_0 as a function of temperature for mixed nickel-zinc ferrites with spinel structure, $Ni_{1-\delta}Zn_\delta Fe_2O_4$.

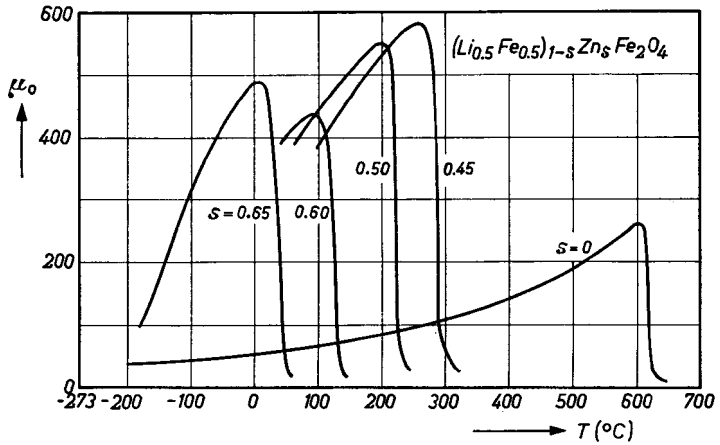

Fig. 48.4. Initial permeability μ_0 a as function of temperature for mixed lithium-zinc ferrites with spinel structure, $(Li_{0.5}Fe_{0.5})_{1-\delta}Zn_\delta Fe_2O_4$.

In § 34.1 it was shown that the zero point in the crystal anisotropy of magnetite (at 130 °K) can be shifted towards higher temperatures by the formation of a mixed crystal with cobalt ferrite. For the compound $Co_{0.01}Fe_{2.99}O_4$ this zero point already lies near room temperature. By substituting cobalt the maximum in the μ_0 *versus* T curve for polycrystalline magnetite specimens is also shifted towards a higher temperature (see Fig. 48.5). The zero points in the crystal anisotropy for varying cobalt content are found at the same temperatures as the maxima in the μ_0 *versus* T curves. The peak value of μ_0 is found to decrease the more the composition differs from Fe_3O_4; this may be related to the fact that there are two anisotropies of opposite sign, the absolute values of which are greater the higher is the temperature of the zero point for the crystal anisotropy of the mixed ferrite.

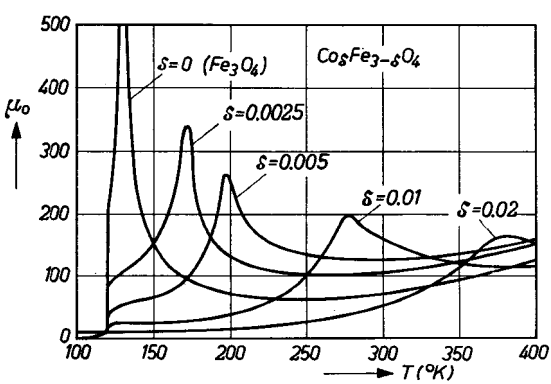

Fig. 48.5. Initial permeability of cobalt-substituted magnetite $Co_\delta Fe_{3-\delta}O_4$ measured at a frequency of 10 kc/s, after [Bi 4].

In order to make certain that that the anisotropy in each part of the specimen is zero at the same temperature, it is necessary to ensure a uniform distribution of the cobalt ions. For equimolar lithium zinc ferrites, Fig. 48.6 gives the initial permeability as a function of temperature for various cobalt contents [Bu 2]. A pronounced second maximum is seen in these curves far below the Curie point, and the position of this maximum shifts with the cobalt content. In this case too, the relatively low value of μ_0 in the maximum will be attributable to chemical inhomogeneities and possibly to stress and shape anisotropy. Similar results have been reported for lithium ferrites and nickel-zinc ferrites [Bu 2] and [Bu 3]. Van der Burgt found, however, that the effect of cobalt substitution on the permeability differs from one ferrite to another. In other words, one may find that the simple

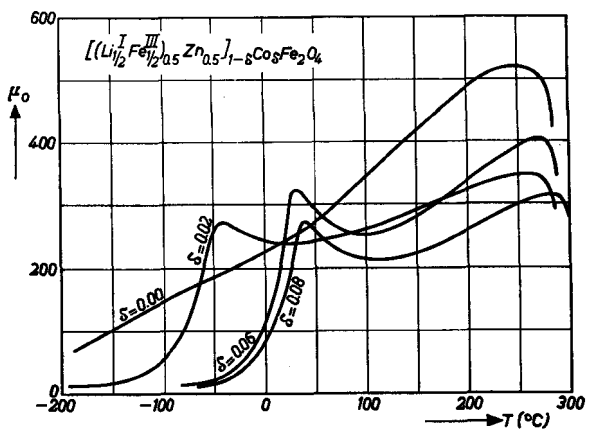

Fig. 48.6. Temperature dependence of the initial permeability μ_0 of cobalt-substituted equimolar lithium-zinc ferrites, after [Bu 2].

relation $K_1(\delta) = (1 - \delta)\, K_1(\delta = 0) + \delta\, K_1(\delta = 1)$ does not hold at a given temperature. For instance, where Me stands for the divalent metal ions Fe and Mn the cobalt content required to make the crystal anisotropy zero at room temperature appears to be respectively about $^1/_4$ and 4 times the cobalt content predicted by the above relation [Bu 3].

Manganese-Ferrous Ferrites

Figure 48.7 shows the permeability *versus* temperature curves of some polycrystalline specimens of manganese-ferrous ferrites $Mn_{1-\delta}Fe^{II}_{\delta}Fe_2O_4$. Here, too, a second maximum is found besides the maximum at the Curie point. The position of this second maximum depends only slightly on the ferrous content. In the same figure a curve of similar shape (dashed) is shown for a

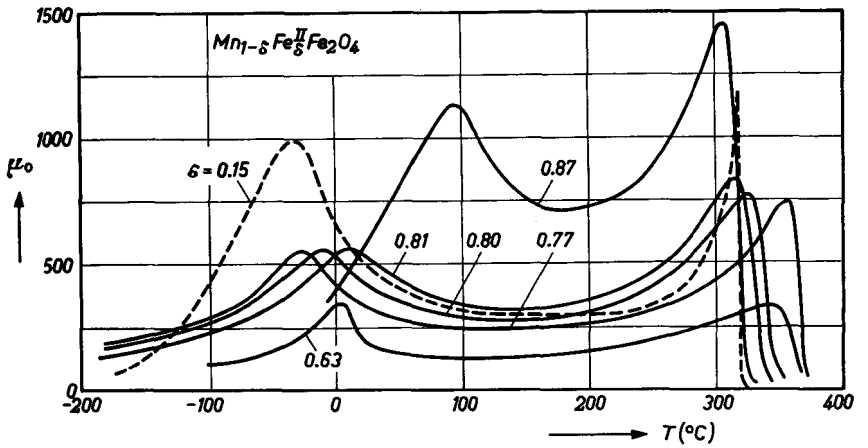

Fig. 48.7. Initial permeability of manganese-ferrous ferrites as a function of temperature. Fully drawn lines for polycrystalline specimens, the dashed curve for a single crystal, after [En 2].

single crystal with the composition $Mn_{0.85}Fe_{2.15}O_4$. Measurements on this single crystal by Enz [En 2] indicate that the second maximum in the curve is not related to zero points in crystal anisotropy or magnetostriction. It was found, however, that after demagnetization, the permeability of the single crystal is very time-dependent. The disaccommodation of this crystal is represented for various temperatures in Fig. 48.8. As a consequence of the disaccommodation the μ_0 *versus* T curve also depends on the measuring time. It is highly probable that the special form of the μ_0 *versus* T curve, which was measured in a relatively short time, is connected with the increase in the disaccommodation rate at higher temperature. In the case of the polycrystalline specimens an appreciable disaccommodation is found also, but it is not yet certain whether this is sufficiently large to explain completely the additional peak in the μ_0 *versus* T curve.

The manganese-zinc ferrites have a fairly high initial permeability, which can be further increased by making a ternary ferrite with Fe_3O_4; in Fig. 48.9 the saturation magnetostriction λ_s and the initial permeability μ_0 of such ferrites are plotted as a function of the ferrous concentration at room temperature. It can be seen that, for a given composition of the ternary ferrite, λ_s is zero, and that for the same material the greatest value of μ_0 occurs. This result indicates that, in order to obtain very high permeabilities in ferrites, the magnetostriction must also be made small. The fact that the maximum in μ_0 is found for a certain ferrous content does not necessarily point to a magnetostriction effect, since it is known [St 4] that an excess of

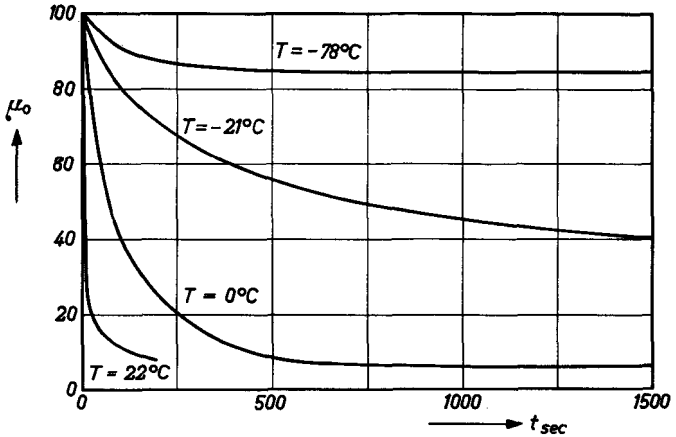

Fig. 48.8. Disaccommodation of the initial permeability for the single crystal $Mn_{0.85}Fe_{2.15}O_4$ from Fig. 48.7 at different temperatures. The permeabilities immediately after demagnetization have been normalized to 100.

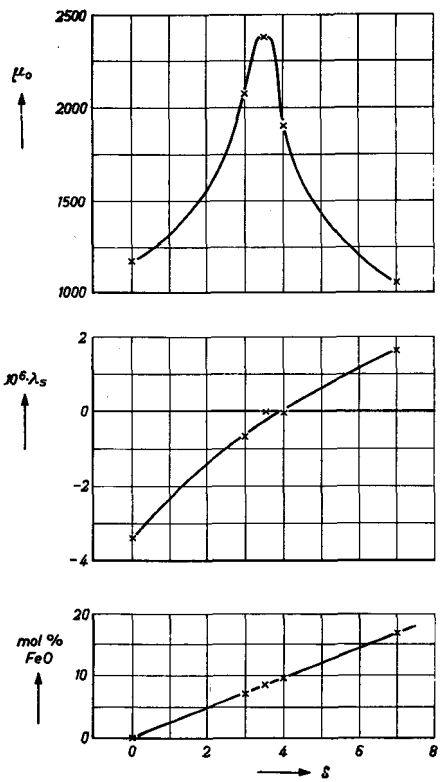

Fig. 48.9. Oxide mixtures consisting of 18 mol% ZnO, (50 + δ) mol% Fe_2O_3, balance MnO, were fired for two hours at 1290 °C in nitrogen atmosphere. The three graphs from the bottom upwards give respectively the ferrous content expressed in mol% FeO, the saturation magnetostriction λ_s and the initial permeability μ_0 of the samples, [Lo 3].

divalent oxides above the stoichiometric composition leads to better sintering, which can also give rise to higher permeabilities.

48.2. FERRITES WITH HEXAGONAL CRYSTAL STRUCTURE

Ferrites having a hexagonal crystal structure and whose c axis is a preferred direction of magnetization will have an initial permeability of the order of magnitude of unity if the crystal anisotropy is large ($K_1 \simeq 10^6$ erg/cm^3). For ferrites where the basal plane is a preferred plane such high values of K_1 may be accompanied by higher values of permeability as a consequence of rotations of the magnetization in the basal plane; Fig. 48.10 gives the μ_0 *versus* T curves for a number of simple compounds of this kind. These curves show the normal behaviour of an increase in μ_0 with temperature up to the Curie point. An exception is Co_2Z, for which there is a sudden drop in μ_0 at approximately 250 °C, while the Curie point is much higher, being approximately 400 °C (see Fig. 38.5). The explanation is that, at 250 °C, the first-order crystal anisotropy constant changes sign (see Fig. 39.7). Below 250 °C the compound Co_2Z has a preferred plane of magnetization, hence in principle a higher permeability owing to the possibility of rotations of the magnetization in the basal planes of the crystals. Above 250 °C the material has a preferred direction of magnetization, and the magnitude of μ_0 is determined by that of K_1, and is therefore small. The saturation magnetization σ, the crystal anisotropy and the initial permeability of Co_2Z are plotted together as a function of temperature in Fig. 48.11 in order to illustrate this relation.

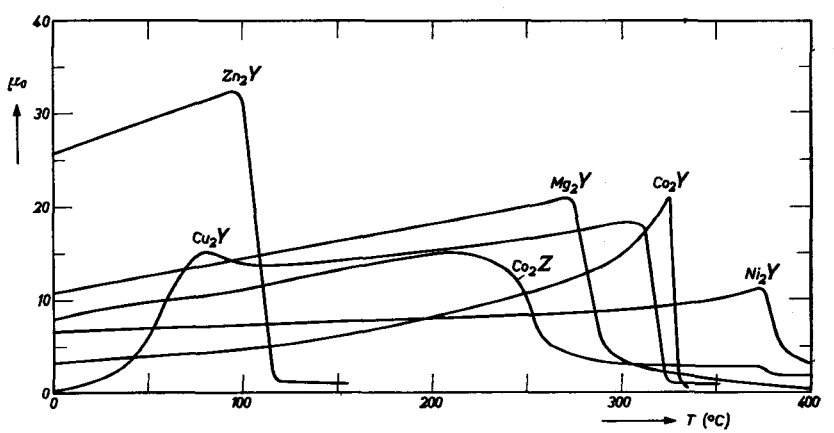

Fig. 48.10. Initial permeability *versus* temperature for a number of polycrystalline specimens of simple hexagonal oxides.

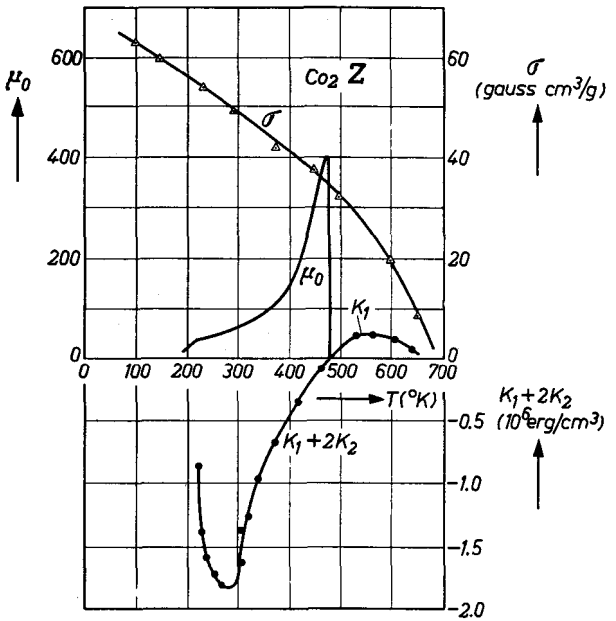

Fig. 48.11. Temperature dependence of the saturation magnetization σ, the crystal anisotropy and the initial permeability of a single crystal of Co_2Z.

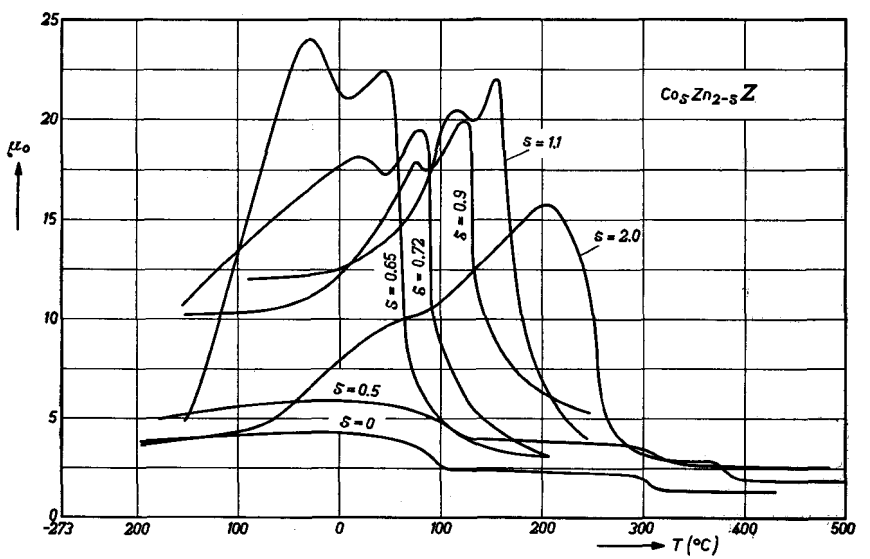

Fig. 48.12. Initial permeability *versus* temperature curves for ferrites of the series $Co_\delta Zn_{2-\delta}Z$.

In § 39.1 we saw that, at room temperature, Co_2Z has a preferred plane of magnetization and Zn_2Z a preferred direction and that in the series of mixed crystals $Co_\delta Zn_{2-\delta}Z$ a change of sign in the crystal anisotropy occurs at a chemical composition corresponding to about $\delta = 0.6$, (see Fig. 39.8). For the other compositions this change of sign will occur at a different temperature. In the μ_0 *versus* temperature curves of some of these ferrites one finds therefore a temperature range in which μ_0 drops rapidly with increasing temperature (Fig. 48.12). With T_0 defined as the temperature at which μ_0 has fallen to half of its peak value, Fig. 48.13 gives this temperature as a function of the composition parameter δ. In the same figure the

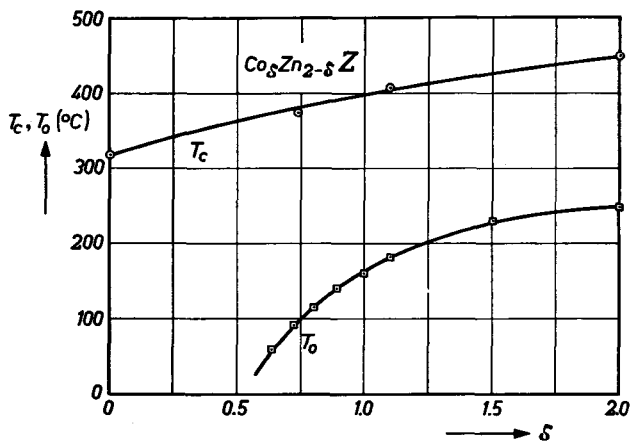

Fig. 48.13. The Curie temperature T_c and the temperature T_0 at which the initial permeability has dropped to half its maximum value (see Fig. 48.12) in dependence on the chemical composition of the ferrites $Co_\delta Zn_{2-\delta}Z$.

Curie point T_C is plotted for some of these compounds. For the mixed ferrites with $\delta = 0.65 - 2.0$ it is evident that the drop in μ_0 with increasing temperature is not caused by the approach to the Curie point but, as in the case of Co_2Z, by the change in sign of the first crystal anisotropy constant. For the two specimens $\delta = 0$ and $\delta = 0.5$ the sharp drop of μ_0 with increasing temperature is not found. This is in agreement with what is to be expected by extrapolation of the T_0 *versus* δ curve for these ferrites in Fig. 48.13. Moreover it can be deduced from this figure that, in the case of the specimen with a composition corresponding to a value of δ of approximately 0.5 to 0.6, the anisotropy changes sign at room temperature. This is the same composition, as follows from direct measurement of the crystal anisotropy;

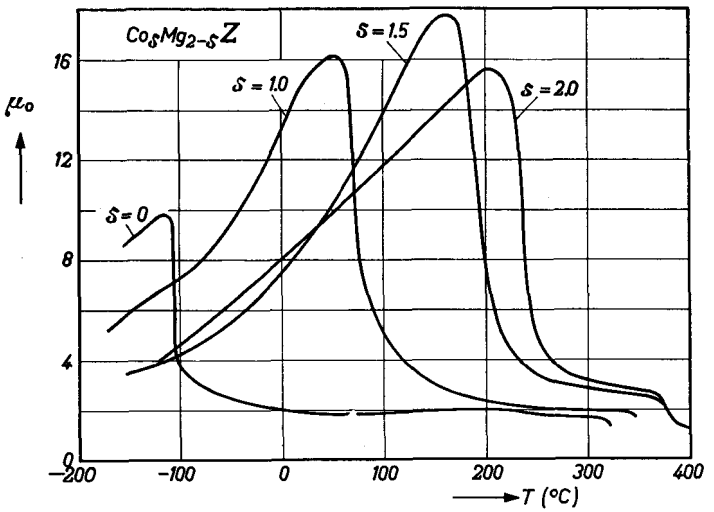

Fig. 48.14. As Fig. 48.12, but now for compounds $Co_\delta Mg_{2-\delta}Z$.

see Fig. 39.7. In the μ_0 *versus* T curves of some $Co_\delta Zn_{2-\delta}Z$ compounds in Fig. 48.12 a second maximum occurs, for which no explanation has been given.

In Fig. 48.14 the initial permeability is plotted against temperature for a number of specimens from the series $Co_\delta Mg_{2-\delta}Z$. As in the series of cobalt-zinc Z compounds, the sharp drop in μ_0 corresponds here to a transition from preferred plane to preferred direction. It appears that Mg_2Z (which contains no cobalt ions) also has a preferred plane at low temperature (below −95 °C). The slight drop in μ_0 at high temperature takes place exactly at the Curie point. Properties corresponding to those mentioned above are also found in other mixed cobalt Z and cobalt W compounds, since all simple Z and W compounds, apart from Co_2Z and Co_2W, have a preferred direction of magnetization at room temperature.

§ 49. External Influences on the Permeability

49.1. THE REVERSIBLE PERMEABILITY IN A BIASED STATE

The permeability of a magnetic core measured with a very small field strength is generally called the reversible (or differential) permeability μ_{rev}. When the core is in the demagnetized state, $\mu_{rev} = \mu_0$. In all other cases μ_{rev} depends on both the magnetic polarization (magnetization) of the core, and, owing to hysteresis phenomena, on the sequence of applied biasing fields which have caused this steady magnetization. The solid curves in

Fig. 49.1 show μ_{rev} in dependence on a polarizing field H_p, in the case of polycrystalline $Ni_{0.36}Zn_{0.64}Fe_2O_4$, when the permeability is measured in a direction parallel to this field. The arrows indicate the cycle of the polarizing field after demagnetization of the core. The maximum value for μ_{rev} is found when H_p is approximately equal to H_c; this value differs but little from μ_0. A magnetic field $H_{p,\perp}$ perpendicular to the direction in which the reversible permeability is measured, reduces the latter less than a field $H_{p,//}$ parallel to the direction of measurement; this is indicated by the dashed curves in Fig. 49.1. In the case of fields H_p which are large with respect to the internal anisotropy fields of the material, the transversal reversible permeability is given by $\mu_{rev,\perp} - 1 = 4\pi M_s/H_{p,\perp}$. The hyperbola corresponding to this is the dotted curve in Fig. 49.1, which approaches the measured curve at high strengths of the transversal polarizing field. To obtain large variations of permeability with relatively small polarizing fields it is necessary to polarize parallel to the direction of measurement. For small variations of permeability, perpendicular biasing is more favourable since

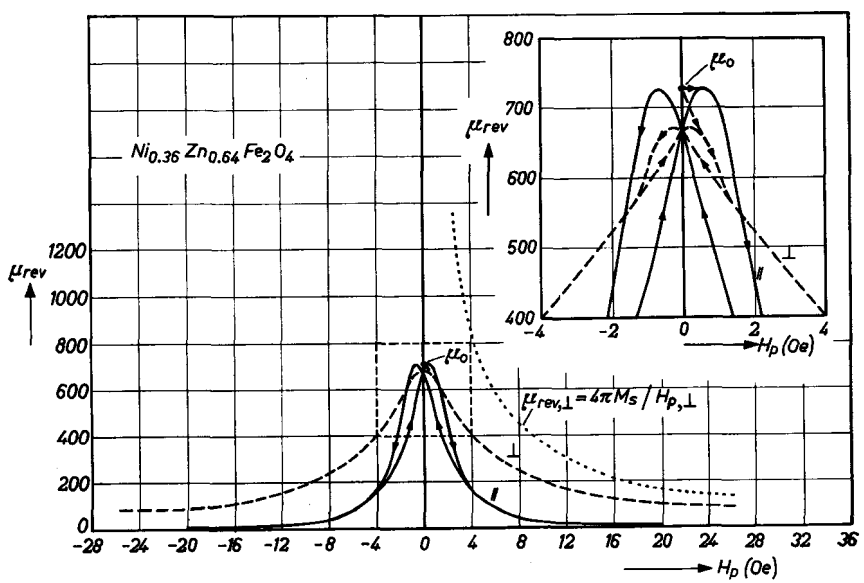

Fig. 49.1. The reversible permeability of a sample of $Ni_{0.36}Zn_{0.54}Fe_2O_4$ as a function of the polarizing field-strength H_p. The solid curves and the broken curves apply to the cases where measuring and polarizing fields are parallel or perpendicular to each other respectively. The arrows indicate the cycle of the polarizing field. The dotted curve represents the permeability to be expected in the case where the material has no magnetic anisotropies and where the permeability is only determined by a biasing field perpendicular to the direction of measurement. The inset shows a part of the curves on an enlarged scale.

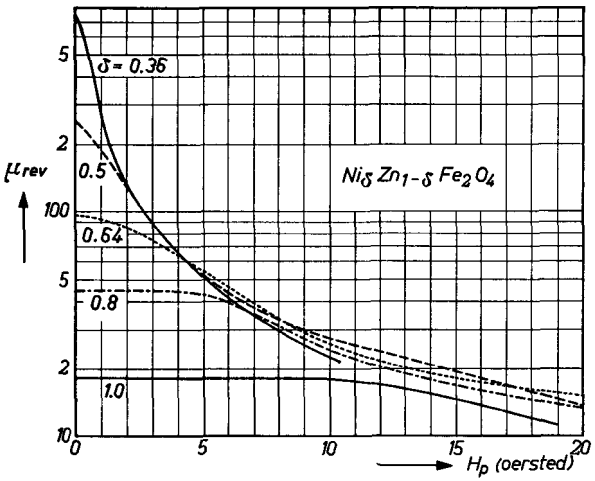

Fig. 49.2. The reversible permeability of ferrites $Ni_\delta Zn_{1-\delta} Fe_2O_4$ as a function of the polarizing field strength. Measuring field and polarizing field are mutually parallel.

in that case there are no difficulties from coupling between the two circuits.

In Fig. 49.2, μ_{rev} for ferrites of the series $Ni_\delta Zn_{1-\delta} Fe_2O_4$ is shown for the case commonly occurring in practice, where the field H_p is parallel to the direction in which μ_{rev} is measured. The demagnetized state was taken as the starting point of the measurement. For $H_p = 0$ the curve must be parallel to the H axis, because the change in permeability does not depend on whether the biasing field is parallel or antiparallel to the measuring field.

49.2. THE INFLUENCE OF UNIDIRECTIONAL MECHANICAL STRESS ON THE INITIAL PERMEABILITY

Owing to the phenomenon of magnetostriction, internal stresses in a ferrite can influence the permeability. The stress anisotropy, discussed in § 13.2, will limit the permeability. The influence of stress can be investigated quantitatively by applying external uniaxial tensile or compressive stresses to the ferrite. In the case of ferrites with a negative saturation magnetostriction, the magnetization will orient itself at right angles to the tensile stress, as illustrated in Fig. 49.3*a*. The initial permeability μ_0 measured in the direction of the tensile stress σ_e, in the case where the stress anisotropy prevails over the other anisotropies, is determined by domain rotations, and is related to the magnitude of the tensile stress according to:

$$\mu_\sigma - 1 = (4\pi/3)(M_s^2/\sigma_e)|\overline{\lambda^{-1}}|, \text{ (large } \sigma), \qquad (49.1)$$

in which $\overline{\lambda^{-1}}$ is the average of the reciprocal values of the magnetostriction

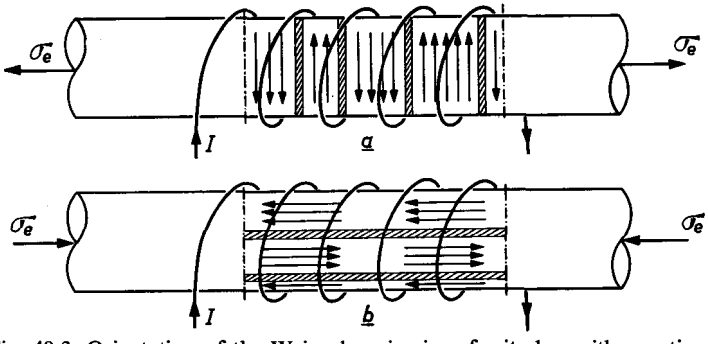

Fig. 49.3. Orientation of the Weiss domains in a ferrite bar with negative magnetostriction; the bar is subjected to a uniaxial tensile stress (*a*) or a uniaxial compressive stress (*b*).

constants in the various crystal directions. Equation (49.1) was first derived for the case of nickel under tensile stress [Be 8]. In the case of the porous ferrites a factor $(d_x/d)^{1/3}$ must be added to the right-hand side, d_x being the X-ray density and d the apparent density of the ferrite. Fig. 49.4 gives the initial permeability μ_0 of four ferrites as a function of the reciprocal tensile stress $1/\sigma_e$. For $Ni_{0.36}Zn_{0.64}Fe_2O_4$ with a saturation magnetostriction -3.7×10^{-6} it is found that, before the tensile strength of the ferrite is reached (this is reached at a tensile stress of approximately 4 kg/mm^2), a range of

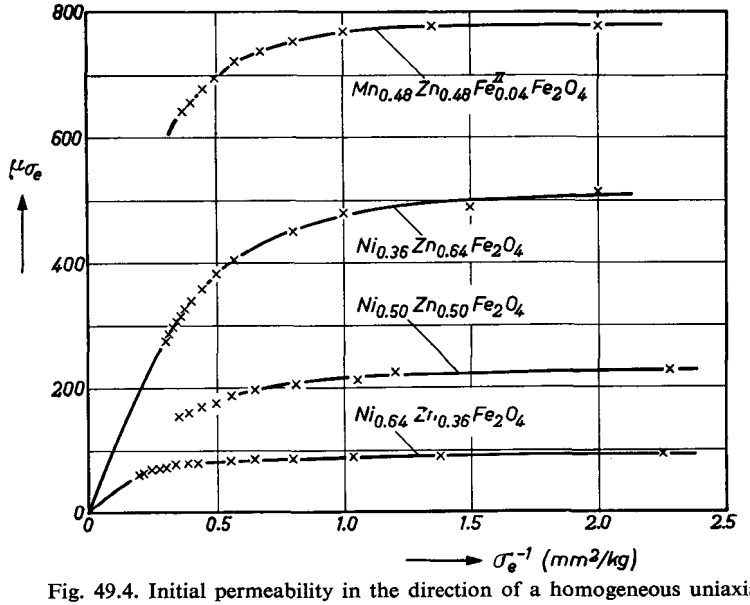

Fig. 49.4. Initial permeability in the direction of a homogeneous uniaxial tensile stress as a function of that stress for four polycrystalline ferrite bars.

stresses exists in which $\mu_0 - 1$ is inversely proportional to σ_e, in agreement with (49.1). From the slope of this straight line it follows that $1/|\overline{\lambda^{-1}}| = 5.0 \times 10^{-6}$, which is in reasonably good agreement with the earlier-mentioned value of the saturation magnetostriction. The difference between the two values is, at least partly, due to the different values of the magnetostriction constants for the various crystallographic directions, as for example indicated in Fig. 35.1 for magnetite. For the nickel-zinc ferrites with a low zinc concentration ($\delta = 0.50$ and 0.36) the initial permeabilities are small and the internal anisotropies large. It can be seen from the figure that in this case the stress anisotropy caused by the greatest tensile stress is not large enough to predominate, so that a linear relationship between μ_0 and $1/\sigma_e$ cannot be established. The values of the saturation magnetostriction are -11×10^{-6} and -16×10^{-6}, which is larger than in the case of the higher zinc content. It is evident that μ_0 in these ferrites is not determined by stresses. The ferrite $Mn_{0.48}Zn_{0.48}Fe^{II}_{0.04}Fe_2O_4$ has in fact a small internal anisotropy and therefore a high μ_0, but no linear relationship is found to exist for this ferrite between μ_0 and $1/\sigma_e$ since the magnetostriction in this case is exceptionally small, $|\lambda_s| < 10^{-6}$; this means here, then, that tensile stresses larger than the tensile strength are necessary in order to obtain a predominating homogeneous stress anisotropy.

When a uniaxial compressive stress is exerted on ferrites having a negative magnetostriction, the magnetization will orient itself parallel to the compressive stress and a Weiss-domain distribution will arise as in Fig. 49.3*b*. The change in the initial permeability of a polycrystalline specimen on which a small, homogeneous mechanical compressive or tensile stress is exerted, is given for the case where μ_0 is determined only by domain rotations, by the expression:

$$\mu_\sigma - 1 = (\mu_0 - 1)[1 + 0.072\lambda_s\sigma_e(\mu_0 - 1)/M_s^2], \text{ (small } \sigma_s). \quad (49.2)$$

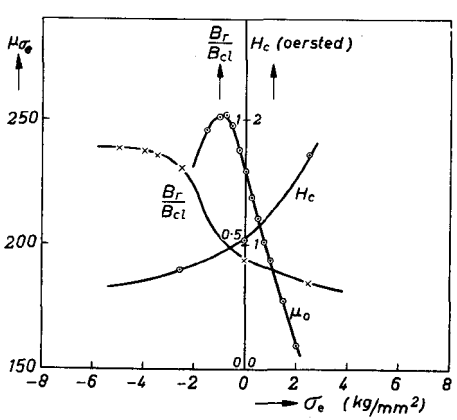

Fig. 49.5. Initial permeability μ_{σ_e}, relative remanent induction B_r/B_{cl} and coercive force H_c for a polycrystalline rod of $Ni_{0.5}Zn_{0.5}Fe_2O_4$ as a function of externally applied stress. B_r is the remanent induction and B_{cl} is the induction at which the hysteresis loop closes. Tensile stresses are positive, pressure is negative.

In this expression, σ_e must be taken negative in the case of pressure. A small compressive stress raises the initial permeability of ferrites with negative magnetostriction. For greater compressive stresses the initial permeability again becomes smaller. In Fig. 49.5 the initial permeability of $Ni_{0.5}Zn_{0.5}Fe_2O_4$ is plotted as a function of an externally applied tensile or compressive stress [Ra 4]; it shows clearly the slight increase in μ_0 with low pressures.

In the case of ferrites having positive saturation magnetostriction, what is said above for tensile stress applies for compressive stress and *vice versa*.

49.3. THE INITIAL PERMEABILITY AS DEPENDENT ON THE METHOD OF DEMAGNETIZATION

A ferromagnetic material can be demagnetized in two different ways. The ferromagnetic core can either be heated to a temperature above the Curie point and then cooled slowly to room temperature, or it can be subjected to an alternating magnetic field the amplitude of which decreases monotonically to zero. Using the latter method of demagnetization, the direction of the demagnetizing field can also be varied with respect to the direction of the field with which the permeability is measured. Above the broken line in Table 49.I some results are given of investigations carried out by Rathenau and Fast [Ra 5] into the influence of the method of demagnetization on the magnitude of the initial permeability in the case of $Ni_{0.5}Zn_{0.5}Fe_2O_4$; it is probable that their results hold, at least qualitatively, for other kinds of sintered ferrites also. The fact that, after cooling from the Curie point, the initial permeability is greater than after demagnetizing by an alternating field at room temperature may, according to (15.4), be due to the increase of the number of domain walls at higher temperature.

TABLE 49.I

THE INITIAL PERMEABILITY AT ROOM TEMPERATURE OF FERRITE BARS ($Ni_{0.5}Zn_{0.5}Fe_2O_4$) AFTER DIFFERENT METHODS OF DEMAGNETIZATION. DATA ON METALLIC NICKEL BARS ARE GIVEN FOR COMPARISON. VALUES AT ROOM TEMPERATURE, AFTER [Ra 5].

Method of demagnetization	Sintering temperature of the ferrite		Metallic nickel [Sn 4]
	1230 °C	1330 °C	
a) Heating above Curie point (265 °C)	400	380	600
b) Alternating field with monotonically decreasing amplitude. Measuring field parallel to demagnetizing field.	284	300	280
c) Demagnetization as under a) or b) followed by mechanical shocks until a stable value is reached	252	258	220

Some of these additional walls may persist at room temperature [Ra 6], so that the difference between the *a* and *b* values in Table 49.I should be regarded as a difference in the contribution made by reversible domain wall displacements to the initial permeability. The influence of the direction of the demagnetizing field with respect to the measuring field on the magnitude of the initial permeability can be seen from Table 49.II. It appears that the largest values for the initial permeability are obtained when the measuring and demagnetizing directions are parallel. This is again explained by assuming that alternating current demagnetization gives rise to domain walls in a particular direction, which can make a special contribution to the reversible magnetization in this direction.

TABLE 49.II

THE INITIAL PERMEABILITY OF A TUBE OF $Ni_{0.5}Zn_{0.5}Fe_2O_4$ IN DEPENDENCE ON THE DIRECTION OF MEASUREMENT WITH RESPECT TO THE DEMAGNETIZING DIRECTION. SINCE IT IS DIFFICULT TO DETERMINE EXACTLY THE DEMAGNETIZING COEFFICIENT IN THE DIRECTION OF THE TUBE AXIS, THE VALUES (d) AND (a) HAVE BEEN EQUALIZED, AFTER [Ra 5].

Measuring direction	After prior demagnetization along the	
	circumference of the tube	axis of the tube
Along the circumference	185 (a)	167 (b)
Along the axis	167 (c)	185 (d)

49.4. THE STABILITY OF THE INITIAL PERMEABILITY

It is important to know whether the initial permeability of a ferrite core, after having been demagnetized by an alternating field, remains constant for a long time, and what external perturbations can influence it. A change in the initial permeability with time, without any external cause, is called disaccommodation, as already mentioned (see Fig. 48.8). The initial permeability of a core can be permanently changed by the application of a transient mechanical deformation, for instance as a result of bending or dropping; this is known as shock effect.

Disaccommodation

The phenomenon of disaccommodation in ferrites has been described by Snoek [Sn 3]. It is found particularly in manganese-zinc ferrites containing an excess of Fe_2O_3 and which are fired in an oxidizing atmosphere. Fig. 49.6 gives a result which is always found with ferrites of this kind, but for which the explanation is as yet unknown. At each temperature there exists a kind of spectrum of relaxation times. The relaxation time becomes longer at lower temperature. After demagnetization the same variation of μ_0

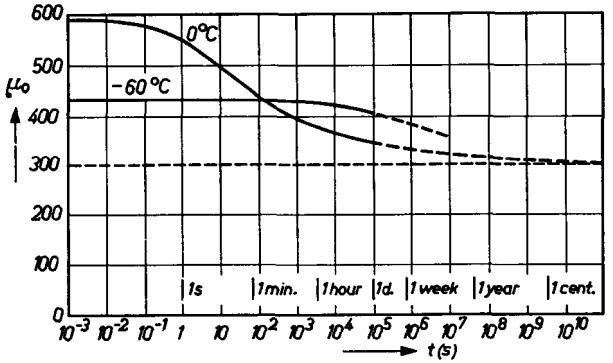

Fig. 49.6. Initial permeability μ_0 *versus* (the logarithm of) time at two different temperatures for a ferrite with spinel structure and molar composition 23.5% MnO, 22.5% ZnO and 54% Fe_2O_3, after [Sn 3].

with time is always measured. When these ferrites are fired in a reducing atmosphere, for example in nitrogen, mixed crystals of manganese-zinc-ferrous ferrites are produced which often show little or no disaccommodation. In the case of manganese ferrite or manganese-zinc ferrite without excess iron for example, disaccommodation is absent at room temperature, just as in the case of nickel-zinc ferrites with a surplus or deficiency of Fe_2O_3. An indication of disaccommodation of some significance has been found at −196 °C in a nickel-zinc ferrite fired in an oxidizing atmosphere. In 15 minutes the initial permeability at −196 °C was found to drop by about 5%. Exceptionally high disaccommodation occurs in a single crystal of $Mn_{0.85}Fe_{2.15}O_4$; see Fig. 48.8.

Shock Effect

Sensitivity of the initial permeability to shock is found mainly in those ferrites which combine a high magnetostriction with a high value of μ_0, in which case mechanical stresses can cause substantial changes in the Weiss domain structure of the ferrite core. Rathenau and Fast [Ra 5] found that, when nickel-zinc ferrites with spinel structure were subjected to shocks, the in itial permeability steadily decreased and reached a final value which was independent of the method of demagnetization; see for instance Table 49.I below the dashed line. The manganese-zinc ferrites are fairly insensitive to shocks.

CHAPTER XIV

FREQUENCY-DEPENDENCE OF THE INITIAL PERMEABILITY

§ 50. The Magnetic Spectrum of Ferrites with Spinel Structure

50.1. DISPERSION FREQUENCY

Although, in many applications of ferrites, eddy currents are negligible up to the highest frequencies, the initial permeability of these substances is nevertheless dependent on frequency. The dispersion due to dimensional resonance (see § 29.1) is here left out of consideration.

By the magnetic spectrum of a ferrite we mean the curves which give the real part μ' and the imaginary part μ'' of the initial permeability as a function of frequency for the case where the magnetization of the core is so small that hysteresis may be neglected.

If we know only one of the quantities μ' or μ'' in the whole frequency range we can determine the other quantities with the aid of the Kramers-Kronig equations (23.3), so that in principle it is sufficient to measure one curve. In practice, both quantities are measured in a limited frequency range.

The magnetic spectra up to $f = 10{,}000$ Mc/s of a number of ferrites with spinel structure from the series of chemical compositions $Ni_\delta Zn_{1-\delta} Fe_2O_4$ is given in Fig. 50.1. The general characteristic of the spectra is that μ' remains constant in a certain frequency range, while at higher frequencies, after a small rise, it drops fairly rapidly to a very small value. There always exists a frequency above which $\mu' < 1$. From this initial rise of μ' with frequency, and from the fact that the susceptibility becomes negative, it follows that the dispersion is caused, it least in part, by resonance phenomena. Owing to the logarithmic scale, the maximum in the μ' curves of the figure is not so striking, although on a linear scale it is in many cases very pronounced. The losses indicated by the μ'' curves are maximum at the frequency at which μ' has fallen to approximately half the static value. The μ'' curve is very asymmetrical with a large tail towards the high frequencies. For relaxation processes $\mathrm{d} \log \mu''/\mathrm{d} \log f > 1$.

The peak of the loss curve appears at a lower frequency the higher is the static initial permeability μ_0, which means that high-permeability ferrites can be used as cores in high-quality coils only in a small frequency range. This relationship was explained by Snoek [Sn 1] in 1948 by means of ferro-

magnetic resonance in the anisotropy field H^A. Snoek assumed that the magnetization in very small fields is the result of domain rotations, the magnetization in each domain being bound to a preferred direction by an effective anisotropy field H^A. In order to calculate the resonance frequency we shall use the picture of § 18.1, according to which the grains or other re-

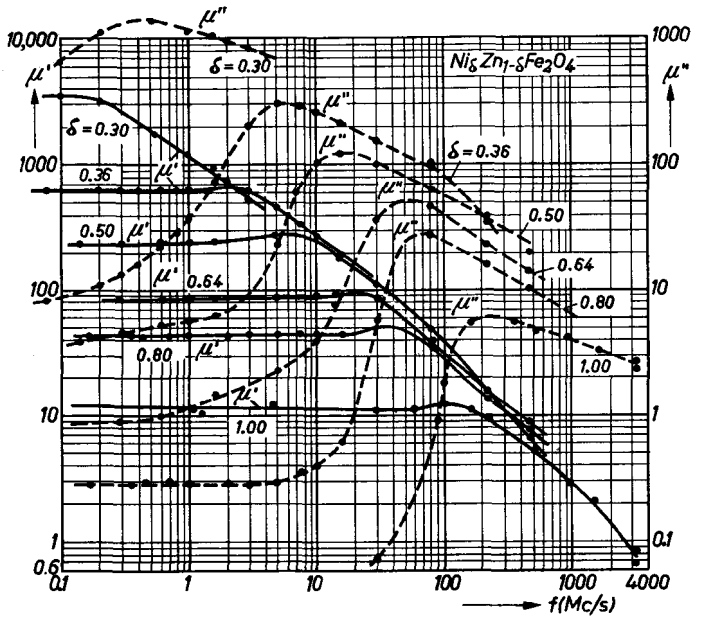

Fig. 50.1. Frequency dependence of the real and the imaginary parts of the initial permeability, μ' and μ'' repsectively, for polycrystalline specimens of ferrites having chemical compositions which are determined by the different values of the parameter δ in the formula $Ni_\delta Zn_{1-\delta} Fe_2O_4$. Note the scale shift by a factor of 10 between the μ' and the μ'' scale.

gions with a regular Weiss domain structure are represented by ellipsoids. In the case of high-permeability materials the demagnetization of these regions is not effective, and they are comparable with ellipsoids imbedded in a material having a susceptibility χ. The effective demagnetization coefficients are then

$$N_{\text{eff}} = \frac{N}{1 + (4\pi - N)\chi}. \tag{50.1}$$

For small N this expression reduces to N/μ which is small at low frequencies. We may then assume in this case that, according to (47.3), μ_0 is given by:

$$\mu_0 - 1 = (8\pi/3)M_s/H^A. \tag{50.2}$$

Under the same conditions ferromagnetic resonance will occur, beginning at a frequency:

$$\omega_r = \gamma H^A \tag{50.3}$$

for regions in which the alternating field has a component perpendicular to the domain boundaries. In that case practically no demagnetization occurs at the domain boundaries, but only at the edges of the ellipsoid which, according to (50.1), is again reduced by its surroundings. Thus, an important part of the material will resonate at a frequency given by (50.3), whereas for the rest of the material the resonance frequency will be appreciably raised, since the poles on the domain boundaries are not neutralized by the surroundings. We may expect, then, a maximum in the losses whose frequency,

TABLE 50.I

THE RELATION BETWEEN THE MAGNITUDE OF THE INITIAL PERMEABILITY μ_0 AND THE FREQUENCY $(f_r)_{exp}$ AT WHICH μ'' IS AT MAXIMUM, FOR VARIOUS FERRITES WITH SPINEL STRUCTURE. THE LAST COLUMN BUT ONE GIVES THE RATIO BETWEEN THE MEASURED DISPERSION FREQUENCY AND THE RESONANCE FREQUENCY CALCULATED ACCORDING TO (50 4)

Ferrite	Porosity p	μ_0	M_s gauss	$(f_r)_{exp}$ Mc/s	$\frac{(\frac{2}{3})(\mu_0-1)(f_r)_{exp}}{\gamma M_s}$	Figure or Ref
$Ni_{0.30}Zn_{0.70}Fe_2O_4$	0.10	3800	182	0.5	0.4	50.1
$Ni_{0.36}Zn_{0.64}Fe_2O_4$	0.08	640	292	5.5	0.5	,,
$Ni_{0.50}Zn_{0.50}Fe_2O_4$	0.15	240	332	15	0.5	,,
$Ni_{0.64}Zn_{0.36}Fe_2O_4$	0.22	85	321	50	0.5	,,
$Ni_{0.20}Zn_{0.80}Fe_2O_4$	0.24	44	283	80	0.5	,,
$NiFe_2O_4$	0.25	12	197	250	0.6	,,
$NiFe_2O_4$	0.24	13	205	200	0.5	50.4
$NiFe_2O_4$	0.25	7.7	196	450	0.7	,,
$NiFe_2O_4$	0.36	4.5	168	700	0.6	,,
$NiFe_2O_4$	0.38	2.3	162	1500	0.5	,,
$NiFe_2O_4$	0.43	1.7	149	2000	0.4	,,
$MgFe_2O_4$	0.43	9	69	80	0.4	—
$Mg_{0.5}Zn_{0.5}Fe_2O_4$	0.23	120	190	30	0.8	—
$Mg_{0.97}Fe^{II}_{0.03}Fe_2O_4$	0.06	36	183	20	0.2	Ra 2
$Mg_{0.81}Fe^{II}_{0.19}Fe_2O_4$	0.21	23	123	50	0.4	,,
$Mn_{0.5}Zn_{0.4}Fe^{II}_{0.1}Fe_2O_4$	0.10	4300	350	1.0	0.5	—
$Mn_{0.48}Zn_{0.47}Fe^{II}_{0.05}Fe_2O_4$	0.04	1760	266	1.5	0.4	—
$Mn_{0.7}Zn_{0.2}Fe^{II}_{0.1}Fe_2O_4$	0.06	800	407	5	0.4	—
$Li_{0.5}Fe_{2.5}O_4$	0.08	33	285	50	0.2	—
$Li_{0.2}Zn_{0.6}Fe_{2.2}O_4$	0.1	250	293	20	0.7	—
$Li_{0.5}Fe_{1.0}Cr_{1.5}O_4$	0.2	1.35	9	500	0.8	—
$Cu_{0.4}Zn_{0.6}Fe_2O_4$	0.14	150	206	18	0.6	—
$Ni_{0.26}Co_{0.16}Zn_{0.58}Fe_2O_4$	0.19	17	370	400	0.7	—
γFe_2O_3	0.6	2.8	123	1200	0.4	Bl 3

according to (50.2) and (50.3), is related with the static initial permeability according to:

$$f_r(\mu_0 - 1) = \frac{4}{3}\gamma M_s, \tag{50.4}$$

where M_s is the saturation magnetization per cm³ measured for the porous material. This equation applies very well to many ferrites with spinel structure, as appears from Table 50.I. The last but one column of this table gives the ratio between the experimentally found frequency at which μ'' is at maximum $(f_r)_{exp}$ and the resonance frequency determined with (50.4). The relation (50.4) can also be tested by measuring the spectrum of a ferrite with a very different value of M_s, as for example $Li_{0.5}Fe_{1.0}Cr_{1.5}O_4$, for which $M_s = 9$ gauss (see for a similar material Fig. 9.2). The spectrum of this ferrite is given in Fig. 50.2. To an initial permeability $\mu_0 - 1 = 0.35$ corresponds according to (50.4), a resonance frequency of 600 Mc/s, which is what is approximately found. In order to make a ferrite with spinel structure having the highest possible initial permeability up to a high frequency, the saturation magnetization according to this picture must be as high as possible. For spinels containing cobalt it is found [Sc 1] that $(f_r)_{exp}$ can be approximately a factor of 2 higher than for spinels with corresponding values of μ_0 and M_s, but which contain no cobalt. The unsatisfactory aspect of the situation, however, is that the initial permeability of, say, sintered nickel ferrite is greater than one might expect from the magnitude of the crystal anisotropy constant K_1, if μ_0 is determined by domain rotations only. For single crystals of $NiFe_2O_4$ it is found (see Table 34.I) that $K_1 = -62{,}000$ erg/cm³. If we neglect mutual coupling between the magnetization in the different crystals and also demagnetizing effects, the magnitude of the initial permeability for the specimen from Fig. 50.1, in the case where this is due solely to simultaneous rotations of the spins, is found to be:

$$\mu_0 - 1 = 2\pi(d_x/d)M_s^2/|K_1| = 2\pi(5.38/4.0)197^2/62000 = 5.3.$$

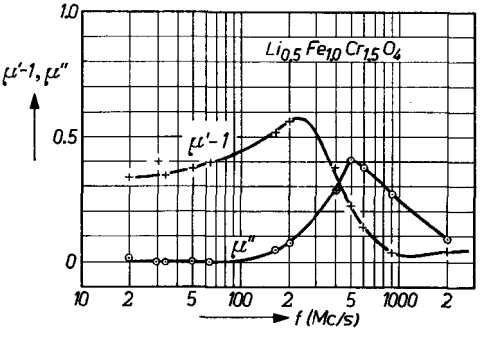

Fig. 50.2. Magnetic spectrum of $Li_{0.5}Fe_{1.0}Cr_{1.5}O_4$. The dispersion frequency is appreciably lower than is usually found at this low value of the initial permeability, owing to the exceptionally low saturation magnetization of this ferrite (σ = 2.2 gauss cm³/g and d = 4.0 g/cm³).

The measured susceptibility is thus a factor of 2 larger than may be expected for rotation processes alone.

This discrepancy is more serious still in the case of a number of magnesium-ferrites investigated by Rado *et al.* [Ra 2]. The magnetic spectrum was measured on sintered specimens and the crystal anisotropy, K_1, determined with the aid of torsion measurements on single crystals from the same range of compositions. An example of the nature of the spectra of these ferrites is reproduced in Fig. 50.3. In all cases, two dispersion regions are

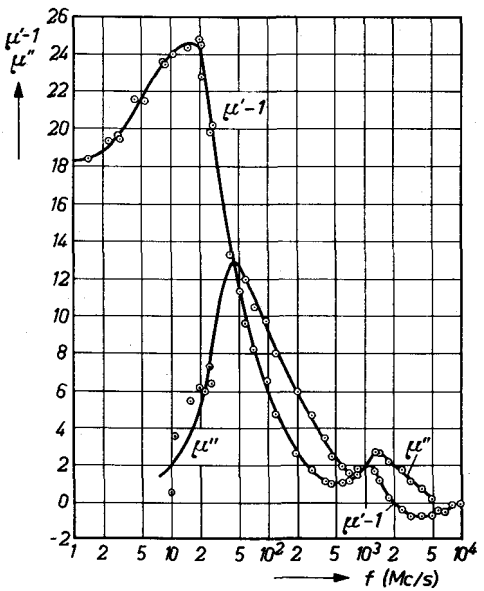

Fig. 50.3. Magnetic spectrum of a sintered ferrite consisting primarily of magnesium ferrite, showing two natural resonances at room temperature, after [Ra 2].

found. The low-frequency dispersion for these ferrites, too, satisfies Snoek's relation. From the measured crystal-anisotropy constants, however, it follows that a possible initial permeability due to rotations is approximately a factor of six smaller than the value found by experiment for μ_0. The resonance frequency f_{K1}^{rot} determined from the magnitude of K_1 is higher by an even larger factor than the experimentally found main dispersion frequency (see Table 50.II).

Since the second dispersion region found by Rado *et al.* [Ra 7] in a large number of ferrites has a dispersion frequency $(f_r)_{exp}$ in the microwave range, which is of the same order of magnitude as the resonance frequency determined from K_1, this is attributed to ferromagnetic resonance. Consequently, there remains as the cause of the low-frequency dispersion, according to these authors, only the domain wall resonance. The fact that in many sintered ferrites only one dispersion range is observed would then be due

TABLE 50.II

DISPERSION FREQUENCIES MEASURED ON FERRITES $Mg_{1-\delta}Fe^{II}_{\delta}Fe_2O_4$, AFTER RADO *ET AL.* [RA 2]. THE THREE FREQUENCIES INDICATED ARE: $(f_r)_{exp}$, BEING THE DISPERSION FREQUENCY MEASURED FOR THE MAIN DISPERSION, DEFINED AS THE FREQUENCY AT WHICH μ'' HAS AN ABSOLUTE MAXIMUM; $(f_{mw})_{exp}$, BEING THE DISPERSION FREQUENCY FOR THE SECOND DISPERSION WHICH IN THESE SPECIMENS APPEARS AT A HIGHER FREQUENCY (SEE FIG. 50.3); AND $f^{rot}_{K_1}$, BEING THE LARMOR PRECESSION FREQUENCY DETERMINED FROM THE CRYSTAL ANISOTROPY CONSTANT K_1 AND SATURATION MAGNETIZATION.

$Mg_{1-\delta}F^{II}_{\delta}Fe_2O_4$	Temperature °C	K_1 erg/cm³	$(\mu_0-1)_{rot}$	M_s gauss	H^A oersted	$(\mu_0-1)_{exp}$	$(f_r)_{exp}$ Mc/s	$(f_{mw})_{exp}$ Mc/s	f^{rot}_{K1} Mc/s
$\delta = 0.03$	26	— 31,000	6	183	225	35	20	1100	640
0.05	26	$\simeq$— 33,000	3	131	335	—	43	1400	940
,,	—196	$\simeq$—113,000	—	183	820	—	100	3900	2300
0.19	26	— 43,000	2.2	123	470	22	50	1700	1300
,,	—196	—117,000	—	151	1030	—	200	4000	2900

to the coincidence of both dispersion ranges. If this is a resonance of domain walls, we can apply to it the theory from § 24.3 and ascertain whether the resonance frequency theoretically to be expected for these ferrites is in agreement with the value found by experiment. A combination of the equations (24.12) and (24.13) gives for the resonance frequency of domain walls:

$$(\mu_0 - 1)^{\frac{1}{2}} \cdot f_r = c(\delta_w/l)^{\frac{1}{2}} \gamma M_s, \tag{50.5}$$

where c is a constant of the order of magnitude of unity, depending on the kind of walls. If we take for the distance l between domain walls the distance determined by (14.4), which is equal at maximum to 10 microns, we find for the magnesium ferrites mentioned in Table 50.II a domain-wall resonance of approximately 100 Mc/s, to be compared with the experimental value of 30 Mc/s. In the right-hand side of (50.5) there is also a variable quantity $(\delta_w/l)^{\frac{1}{2}}$, the dependence of which upon K_1 is as $K_1^{-3/8}$ according to (15.1). Since an increase of K_1 will give rise to a decrease in μ_0, one ought to find in reality that for a series of ferrites the product $f_r(\mu_0-1)^{\alpha}$, in which $\alpha < \frac{1}{2}$, is proportional to M_s. The series of NiZn ferrites, however, are found to satisfy nicely the equation (50.4), for a variation in μ_0 by a factor of 300.

For a given chemical composition it is possible to vary the initial permeability by powdering the ferrite, so that each particle consists of one or only a few Weiss domains. The magnetization process in this case will only take place *via* domain rotation. Fig. 50.4 gives an illustration of the change in the magnetic spectrum when samples with various densities are made from the same powder of $NiFe_2O_4$, using different degrees of sintering [Br 7]. Compressed powder consisting of particles of 0.5 to 1 micron and fired at 960 °C results in a sample having a very low initial permeability: $\mu_0 - 1 = 1.7$. The higher the temperature to which the sample is fired the more this value rises, until for a firing temperature of 1327 °C one obtains $\mu_0 - 1 = 13$. In Fig. 50.4 it can be seen that the rise in permeability is associated with a lowering of the main dispersion frequency in the spectrum. The relation between the measured dispersion frequency and the resonance frequency to be expected according to (50.4) is given for these ferrites in Table 50.I. The same agreement is found as when varying the chemical composition. In a denser specimen (fired to a higher temperature) having a higher permeability, the dispersion extends towards a much lower frequency than in a specimen that is very porous. At the high-frequency side of the dispersion there is not much difference between the spectra of the specimens; for frequencies higher than about 10^4 Mc/s the losses in all cases are very small. If we take as our starting point that in the nickel-ferrite powder with the smallest grains only domain rotations contribute to μ_0, and that in the

denser specimens a contribution is also made by wall displacements, then for this last magnetization process we should expect an additional dispersion region. This, however, is not found. The dispersion frequency drops continuously with increasing density. It is as if μ_0 in the less porous specimen is larger because the rotation of the magnetiztation becomes easier: lowered porosity results in less internal shape anisotropy, and hence in higher rotational permeability and a lower ferromagnetic resonance frequency. If the density is very high, as in some examples reported [Kr 1], where

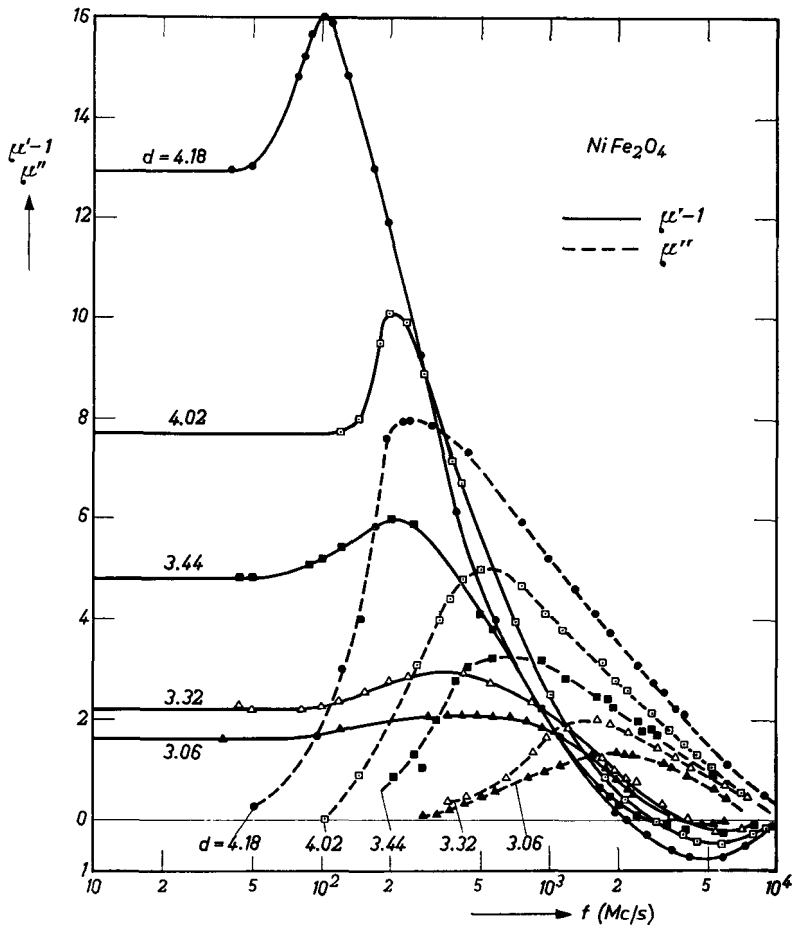

Fig. 50.4. Permeability spectra of incompletely sintered samples of nickel ferrite $NiFe_2O_4$. The five samples were sintered at progressively higher maximum temperatures in the range 960-1327 °C. The densities d of the samples indicated in the figure should be compared with an X-ray density $d_x = 5.38$. After [Br 7].

$p = 0.02$, wall displacements are presumably the main magnitization process at low frequencies.

50.2. WIDTH OF THE DISPERSION REGION

The broadening of the loss curves towards higher frequencies is due to the fact that the alternating measuring field possesses a component parallel to the domain walls and also perpendicular to the saturation magnetization. Consequently, in the case of resonance, as in Fig. 18.3*b*, poles also appear on the walls, thereby appreciably increasing the effective demagnetizing factors and hence the resonance frequency. Moreover, at these frequencies a large part of the material will be above resonance; this means that the permeability of the surrounding material will be small and therefore N_x and N_y will not be reduced according to (50.1). This increases the resonance frequency still further. At very high frequencies the ellipsoid of Fig. 18.3*b* may be regarded as isolated, so that the largest demagnetizing field to be expected in the y direction is that for a flat plate, *i.e.* $4\pi M_s$. The highest resonance frequency which, according to this description, will occur in a sintered specimen, is given according to (18.18*b*) by:

$$\omega_{r,\max} = \gamma(H^A + 4\pi M_s). \tag{50.6}$$

Above this frequency there should be no magnetic losses. For many magnetically soft spinels the demagnetizing field is about $4\pi M_s = 4000$ gauss, against which the small anisotropy fields H^A are negligible. In these ferrites, then, losses due to the Weiss domain structure may be expected up to a frequency of the order of magnitude of 10^4 Mc/s. For $NiFe_2O_4$ the relevant values are: $g = 2.19$, $H^A = 450$ oersteds and $4\pi M_s = 3400$ gauss, hence $f_{r,\max} = 7400$ Mc/s, in reasonably good agreement with what is found by experiment (see Fig. 50.4).

The fact that the losses are low above the frequency determined by (50.6) has been illustrated by an experiment carried out by Beljers *et al.* [Be 9]. The losses were measured at 9300 Mc/s as a function of temperature on a nickel-zinc ferrite with spinel structure (molar composition approximately 18% NiO, 32% ZnO and 50% Fe_2O_3). Fig. 50.5*a* gives for this ferrite the quantity $(\gamma/2\pi)4\pi M_s$ as a function of temperature (this is a frequency which is proportional to the saturation magnetization M_s, and which would fall to zero at the Curie point, that is at about 200 °C). The same figure indicates the resonance width Δf of a resonant cavity filled with a bar of this ferrite and measured at a frequency of 9300 Mc/s. It is found that Δf also becomes smaller at higher temperature, and at about 60 °C becomes equal to Δf for the case where the bar is magnetically saturated and thus

no longer subject to losses due to the Weiss domain structure. Below a temperature of 60 °C, $4\pi M_s$ is sufficiently large to be able to cause losses in the ferrite at 9300 Mc/s, according to (50.6); above 60 °C, $4\pi M_s$ has become too small. The anisotropy field H^A is small with respect to $4\pi M_s$.

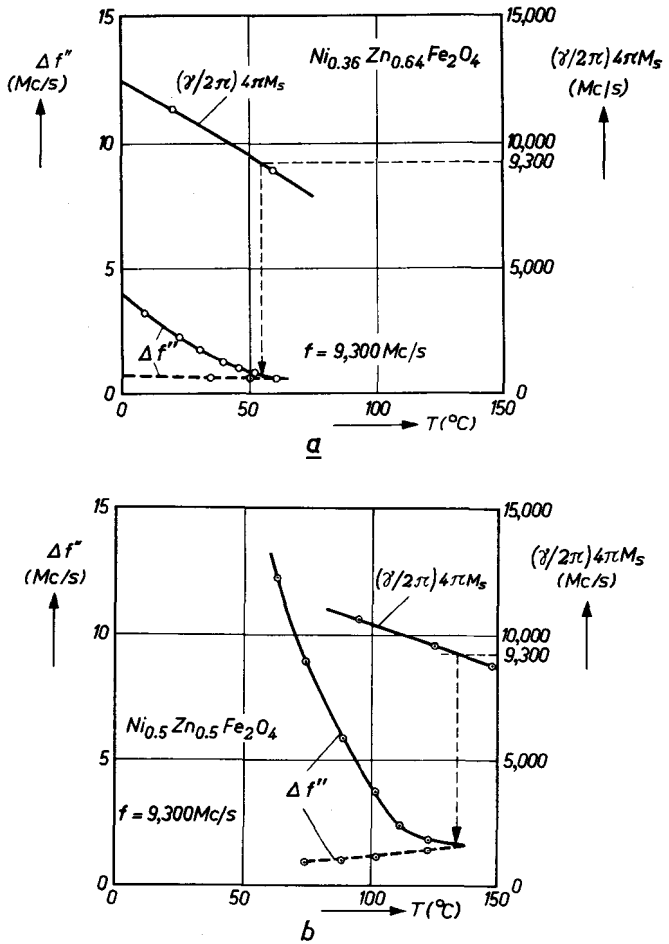

Fig. 50.5. High-frequency losses $\Delta f''$ measured at a frequency of 9300 Mc/s as a function of temperature for a ferrite in the demagnetized state (drawn curve), and for the case that the ferrite is magnetically saturated, broken curve. The saturation magnetization, M_s, is also given, expressed in the quantity $(\gamma/2\pi) \cdot 4\pi M_s$.

The figures *a*) and *b*) show for two ferrites of different chemical compositions that the losses disappear if $(\gamma/2\pi) \cdot 4\pi M_s$ is smaller than the measuring frequency.

The same result, but at different temperature is obtained for a specimen with a molar composition of approximately 25% NiO, 25% ZnO and 50% Fe_2O_3 (see Fig. 50.5*b*). With this ferrite we again find the losses vanishing at a temperature at which $4\pi M_s$ has fallen to the same value as in the case of the ferrite in Fig. 50.5*a*. Since the losses in this frequency range are due to the Weiss domain structure, they disappear when the material is magnetized.

§ 51. The Magnetic Spectrum of Hexagonal Ferrites with the Basal Plane as the Preferred Plane of Magnetization

The magnetic spectrum of ferrites with hexagonal crystal structure and having a preferred plane of magnetization resembles that of the spinels. One finds, however, for the same value of initial permeability a higher dispersion frequency than in the case of spinels. As an example, Fig. 51.1

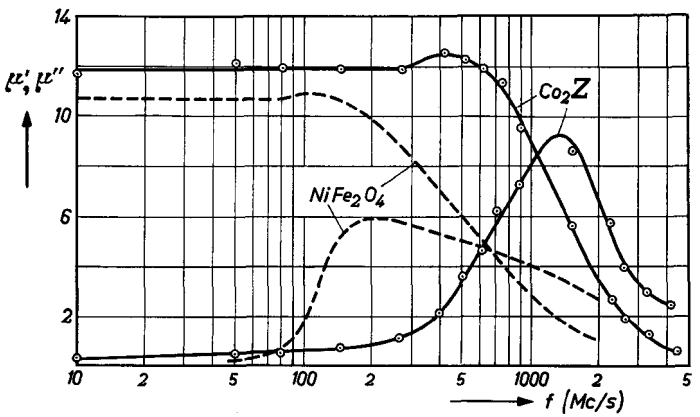

Fig. 51.1. The magnetic spectrum of a polycrystalline specimen of Co_2Z. For comparison, the spectrum of $NiFe_2O_4$ with approximately the same low-frequency permeability is given.

shows the initial permeability of the compound Co_2Z plotted as a function of the frequency. This figure also gives the permeability of the spinel $NiFe_2O_4$ It can clearly be seen that, although the permeability at low frequency is approximately equal for both compounds, the dispersion in the case of Co_2Z is substantially higher than in the case of the spinel. Corresponding results are found with many other ferrites with hexagonal crystal structure and a preferred plane of magnetization. The dispersion may be the result of ferromagnetic resonance. In these materials the natural ferromagnetic resonance frequency will be determined by the rotational stiffness of the magnetization in the preferred plane as well as by the rotational stiffness

of the magnetization out of the preferred plane. By analogy to (18.14) it can be derived from (18.10) and is given by:

$$2\pi f_{\text{res}} = \gamma\sqrt{H_\phi^A \cdot H_\theta^A}. \tag{51.1}$$

According to (11.7) the field H_θ^A is connected with the crystal anisotropy constants K_1 and K_2, and can have very high values, as we have seen in § 39.1. The field H_ϕ^A is connected with the crystal anisotropy constant K_3, which is a measure of the stiffness of the rotations in the preferred plane, or, if K_3 is small, then stress anisotropy and shape anisotropy can determine H_ϕ^A. Assuming that μ_0 is due solely to rotations, H_ϕ^A will be related to μ_0 according to (47.6).

In Table 51.I the values of the resonance frequency calculated according to (51.1) are compared with those found directly by experiment. The resonance frequency taken for the experiments is that at which μ'' is maximum. Contrary to the spinels (see *e.g.* Fig. 50.1), at this frequency the permeability μ' is found to have fallen to half of its value at low frequency. The theoretically determined frequencies, for the case where the dispersion is due to ferromagnetic resonance, and the experimentally measured frequencies, differ by the same factor 2 as is found for the spinels. The fields H_ϕ^A in Table 51.I, which are derived from the magnitude of the initial permeability of the sintered polycrystalline specimens, are much greater than the equi-

TABLE 51.I

VALUES OF THE DISPERSION FREQUENCY OF HEXAGONAL OXIDES WITH A PREFERRED PLANE OF MAGNETIZATION, AS CALCULATED WITH (51.1) AND AS FOUND BY EXPERIMENT.

Ferrite	$\mu_0 - 1$ at low frequency	$4\pi M_s$ gauss	H_θ^A oersted	H_ϕ^A oersted	f_{res} in 10^3 Mc/s	
					according to (51.1)	measured
Co_2Z	11	3350	13,000	112	3.4	1.4
Mg_2Y	9	1500	10,000	62	2.2	1.0

valent crystal anisotropy fields H_ϕ^A which are given in § 39.2 for single crystals of the same compounds. This indicates that the initial permeability in these polycrystalline specimens is not primarily limited by the crystal anisotropy in the preferred plane, but by shape or stress anisotropy. Thus, in the crystal-oriented samples H_ϕ^A will be much smaller, causing a decrease of the resonance frequency. We shall return to this subject at the end of this section.

The improvement as regards high-frequency behaviour which these ferrites with a preferred plane of magnetization offer as compared with the ferrites

with spinel structure can be illustrated by combining equations (47.2) and (51.1):

$$f_{\text{res}}(\mu_0 - 1) = (4/3)\gamma M_s[\tfrac{1}{2}\sqrt{H_\theta^A/H_\phi^A} + \tfrac{1}{2}\sqrt{H_\phi^A/H_\theta^A}]. \qquad (51.2)$$

For ferrites with spinel structure the factor between brackets is always equal to unity, since $H_\phi^A = H_\theta^A$, so that for a given value of the initial permeability the resonance frequency depends only upon M_s. In the case $H_\theta^A \neq H_\phi^A$, the factor between square brackets is greater than unity. At comparable values of permeability this factor is equal to the ratio of the resonance frequency of a hexagonal ferrite with preferred plane of magnetization and that of a spinel.

The highest resonance frequency which, according to (18.18*b*), can occur in a sintered specimen is:

$$\omega_{r,\max} = \gamma\sqrt{4\pi M_s(4\pi M_s + H_\theta^A)}, \qquad (51.3)$$

analogous to (50.6). For example, in the series of compositions denoted by the general formula $Co_\delta Zn_{2-\delta}Z$, the factor H_θ^A/H_ϕ^A can be continuously varied from a high value to the value 1 by changing the chemical composition. Figure 51.2 shows the magnetic spectrum for some specimens of this series having a preferred plane of magnetization. The low-frequency value of the initial permeability increases very little with the zinc content, indicating that H_ϕ^A is substantially constant, whereas it follows from Fig. 39.5 that H_θ^A is highly dependent on δ. The dispersion frequency, however, changes considerably; the maximum of the μ'' curve is found respectively at 1400 Mc/s for Co_2Z and at about 200 Mc/s for $Co_{0.65}Zn_{1.35}Z$, which represents

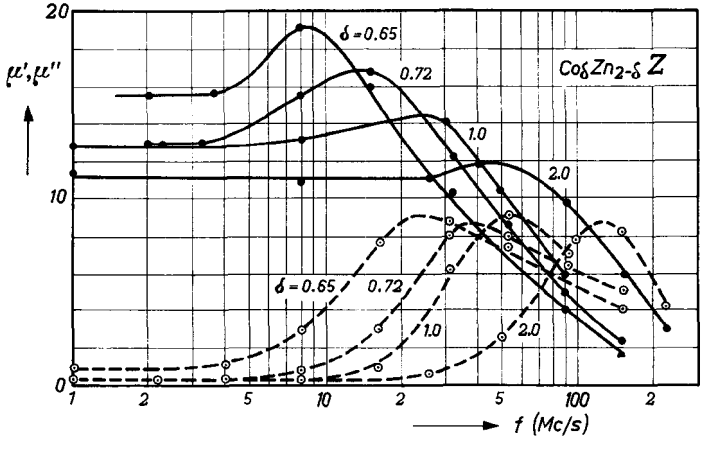

Fig. 51.2. Magnetic spectrum of some ferrites from the series $Co_\delta Zn_{2-\delta}Z$.

a change by a factor 7. The saturation magnetizations $4\pi M_s$ of these ferrites at room temperature are respectively 3350 and 3720 gauss. The considerable change in the dispersion frequency with the chemical composition does not appear to be related to variations in μ_0 or $4\pi M_s$, but is presumably due to the change in the anisotropy field H_θ^A. For the specimen $\delta = 0.65$ the anisotropy field H_θ^A is of the same order of magnitude as the anisotropy fields determining μ_0. The particular effect of a preferred plane is then no longer present in the crystals of this specimen. The dispersion frequency is therefore equal to that which is found for a spinel with the same initial permeability and approximately the same saturation magnetization (about 200 Mc/s for $NiFe_2O_4$).

Fig. 51.3 shows the magnetic spectra of two specimens of the same compound Co_2Z. The preparation of the specimens differs only in as much as the basal planes of the crystals in the specimen with the highest permeability are oriented mutually parallel owing to the fact that during the pressing of the sample a rotating magnetic field was applied, as described in § 44. The result of this crystal orientation is an increase of $(\mu_0 - 1)$ from the value 11 for the isotropic specimen to 27 for the crystal-oriented one. A striking fact revealed by the magnetic spectra is that this appreciable increase in initial permeability is accompanied by only a slight decrease of the dispersion frequency. A better comparison of the spectra is possible by dividing the measured values of $\mu' - 1$ and μ'' by the low frequency value of $\mu' - 1$. The now "normalized" spectra for the same specimens are shown in Fig. 51.4, from which it can clearly be seen that the dispersion frequency for the anisotropic

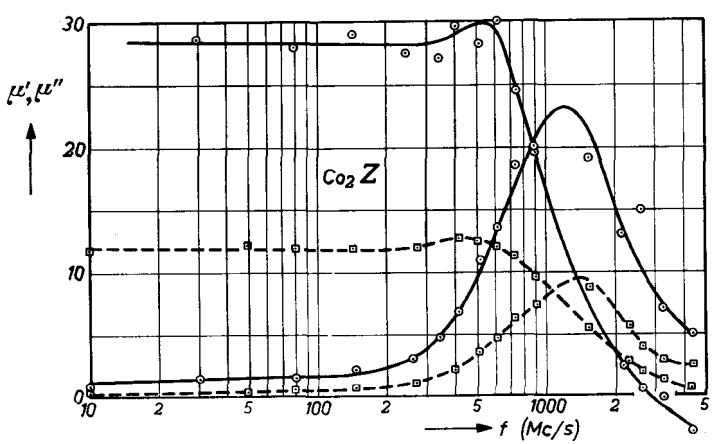

Fig. 51.3. Magnetic spectrum of two Co_2Z samples. The broken lines apply to an anisotropic and the solid lines to a crystal-oriented sample.

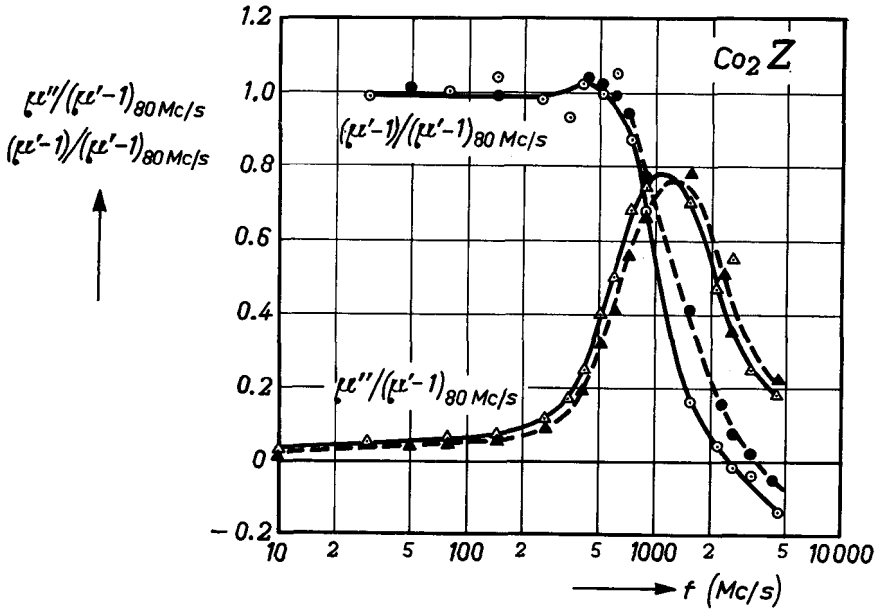

Fig. 51.4. Comparison of the normalized spectra of the Co_2Z specimens of Fig. 51.3. The broken curves again apply to the isotropic sample, the solid curves to the crystal-oriented sample. The measured values of $\mu' - 1$ and μ'' of Fig. 51.3 have been normalized by dividing them by the low-frequency permeability. For this purpose the values of $\mu' - 1$ at 80 Mc/s have been taken, being respectively 11 and 27.

specimen is only slightly lower than that for the isotropic specimen. This slight change can be explained on the basis of the theory of ferromagnetic resonance. For if the basal planes of all crystals are parallel one would have, according to (47.2) and (47.6), a gain in susceptibility by a factor of 1.5. (In that case the applied magnetic field-strength is parallel to the basal plane in all crystals.) Accordingly, for the anisotropic specimen one may expect $\mu_0 - 1 = 1.5 \times 11 = 16.5$. This increase in μ_0 will not be associated with a change in the dispersion frequency. As explained in § 47.2, owing to the orientation of the crystals the permeability increases more than by the said factor of 1.5, because the stress anisotropy and internal shape anisotropy are smaller in the case of oriented crystals. The resultant gain obtained for the permeability is an extra factor of 27/16.5. This lowering of anisotropy is accompanied by a lowering of the resonance frequency. The resonance frequency is determined by the two anisotropy fields H_θ^A and H_ϕ^A in accordance with (51.1). Of these, H_θ^A — the large crystal anisotropy which determines the preferred plane — will scarcely be changed by the orientation (although at relatively small values of H_θ^A there may be some influence from

the changed shape-anisotropy due to the orientation of the crystals). The equivalent internal anisotropy field H_ϕ^A is thus reduced owing to orientation by a factor of 16.5/27, assuming that $\mu_0 - 1$ is a measure of H_ϕ^A. Consequently the dispersion should be lowered by a factor $\sqrt{16.5/27} = 0.8$, which is in reasonable agreement with what is found by experiment. This unappreciable lowering of the dispersion frequency with a substantial increase in μ_0 due to the orientation of the crystals is found for all kinds of hexagonal ferrites having a preferred plane of magnetization [St 3].

§ 52. The Magnetic Spectrum of Hexagonal Ferrites with the *c* Axis as the Preferred Direction of Magnetization

In the case of a polycrystalline specimen of a hexagonal ferrite, where the *c* axis is the preferred direction of magnetization, the initial permeability due to rotations is generally small and is given by (47.3). For $BaFe_{12}O_{19}$ this is $\mu_0 - 1 = 0.17$. However, owing to a contribution from reversible domain-wall displacements the permeability becomes appreciably larger if the specimens are fired at higher temperatures (for instance above 1300 °C), which increases the size of the crystallites and hence reduces the porosity. This additional contribution to the initial permeability is found to be frequency-dependent. In Fig. 52.1, the idealized textures of three ring-shaped samples of $BaFe_{12}O_{19}$ are illustrated by *a*), *b*) and *c*) respectively. In *a*) the hexagonal axes of the crystallites are parallel to the axis of the ring; in *b*) the basal planes of all crystallites pass through the axis of the ring, and in *c*) the crystallites are in random orientation. The crystal-oriented samples were made by compressing the ring in the presence of a magnetic field, as discussed in § 44. If the crystallites in the cores were ideally oriented, as in case *a*), a tangential magnetic field in the core would only produce a magnetization by domain rotation and not by domain-wall displacements, whereas

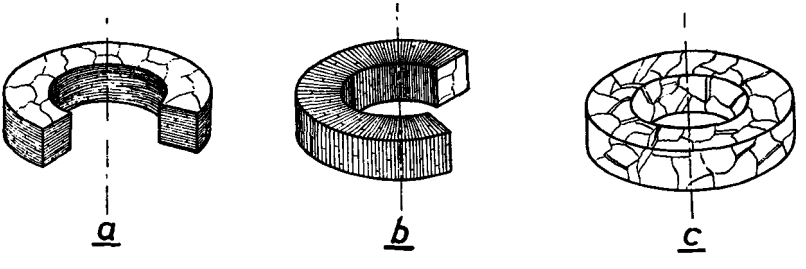

Fig. 52.1. Illustration of the crystal orientation in three samples of $BaFe_{12}O_{19}$; the magnetic spectra measured for these rings are reproduced in Fig. 52.2.

in case *b*) a magnetization in a small field can only be brought about by 180° domain-wall displacements. For a ring of type *a*) a permeability is found of $\mu_0 - 1 = 0.6$, which indicates that the texture is not ideal, for if it were one would expect a permeability originating from rotations: $\mu_0 - 1 = 4\pi M_s/H^A = 0.28$. For a ring of type *c*) without texture, $\mu_0 - 1 = 1.6$, and for a ring of type *b*) whose texture is such that the initial permeability may be large if many reversible domain-wall displacements contribute to it, one finds $\mu_0 - 1 = 5$. The magnetic spectra of these rings is given in Fig. 52.2. It can clearly be seen that there are two dispersion regions for the permeability, one being in the frequency range from 20 to 50 Mc/s and the other in the frequency range from 200 to 500 Mc/s. Above the highest dispersion frequency, the permeability approaches a final value which is approximately equal to the permeability to be expected for each of the rings, provided it is caused only

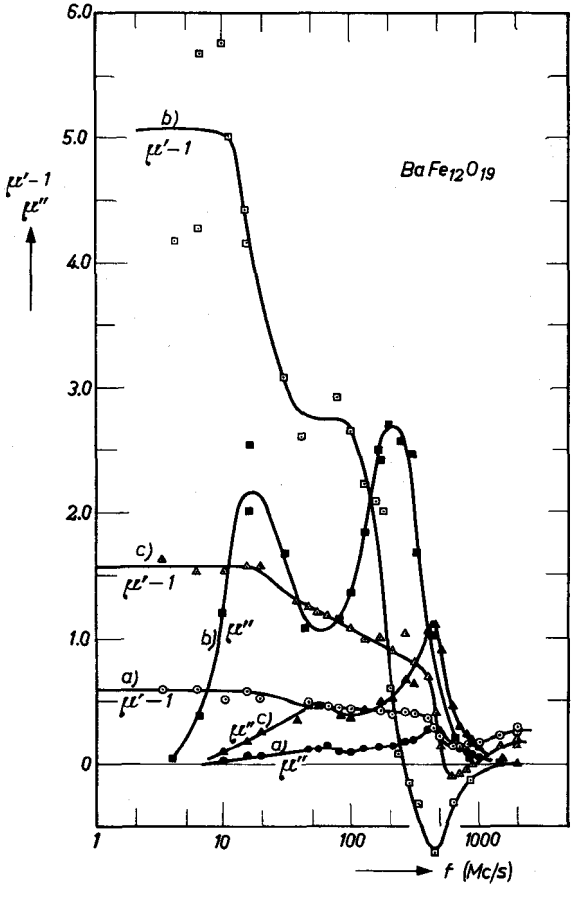

Fig. 52.2. Magnetic spectra of the rings *a*), *b*) and *c*) of Fig. 52.1. The rings have the same chemical composition and differ only in their crystal texture.

by simultaneous rotations of the spins in the Weiss domains. This permeability will show a further dispersion as a result of the natural ferromagnetic resonance at 50,000 Mc/s.

The high-frequency dispersion at about 200-500 Mc/s is presumably associated with resonance of the domain walls, since negative values are measured for $(\mu_0 - 1)$. The domain-wall resonance frequency is given by (24.12). To ascertain whether the value found experimentally for the resonance frequency is in agreement with the value to be expected according to the theory, it is thus necessary to make an estimate of the equivalent mass m_w and stiffness constant a introduced for the domain wall. The equivalent wall mass m_w is given by (24.7). In this equation only the wall thickness δ_w is not accurately known for $BaFe_{12}O_{19}$. From the Curie point, $T_C = 450$ °C, and the minimum distance between the magnetic ions, approximately 3×10^{-8} cm, we arrive according to (15.1) at the very rough approximation $\delta_w \cong 10^{-6}$ cm, leading to $m_w \cong 10^{-10}$ g/cm^2. In this case the change in the crystal anisotropy for the moving wall is more important than the change in its demagnetizing energy. The stiffness constant a is related to the initial permeability and to the distance l between parallel walls. For the configuration of Fig. 52.1*b* we have $a = 16\pi M_s^2/(\mu_0 - 1)l$. The distance l can be determined from Bitter figures on polished surfaces. From these one finds 5×10^{-4} cm. A probable value for a is then $a \cong 7 \times 10^9$ dyne/cm. This leads, according to (24.12), to a resonance frequency for the domain walls in these $BaFe_{12}O_{19}$ specimens of about 1000 Mc/s, which, in view of the rough approximation, particularly as regards the determination of δ_w, is in reasonable agreement with the value found by experiment.

For the dispersion in the frequency range from 20 to 50 Mc/s no satisfactory explanation has been given. If ring *b*) is measured in the remanent state the permeability is found to be approximately half the permeability in the demagnetized state. This means that in this ring with imperfect texture there are also many walls present in the remanent state, with the result that in this state, too, the domain-wall displacements make a substantial contribution to the permeability. A special feature, however, is that in the spectrum of the ferrite in the remanent state the low-frequency dispersion has vanished, whereas the high-frequency dispersion is scarcely different from that found in the demagnetized state.

The temperature of the specimen has little influence on the low-frequency dispersion. Fig. 52.3 shows for a specimen of $BaFe_{12}O_{19}$ without texture the low-frequency dispersion at 20 °C and at −183 °C. The temperature change is accompanied by a slight decrease of μ_0 and an increase in the dispersion frequency by about a factor of 2.

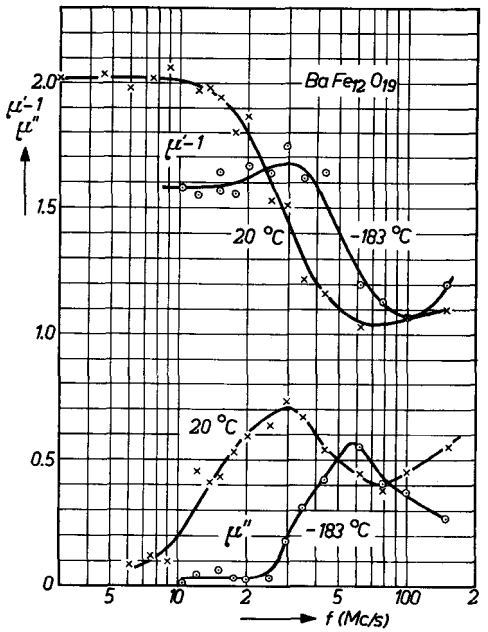

Fig. 52.3. The low-frequency dispersion in an isotropic specimen of $BaFe_{12}O_{19}$ at 20 °C and −183 °C.

The permeability of finely powdered materials subsequently fired at low temperature drops to the rather low value of 1.7, so that wall displacements are to a great extent suppressed. The dispersions in μ_0 occur at 200 and 900 Mc/s respectively. Both dispersion frequencies are higher than was found for the isotropic specimen of Fig. 52.1*c* and 52.2*c*. This may be in agreement with the lower value for μ_0, which points to a stronger binding of the walls to their equilibrium position. For this material the losses expressed in tan δ are given as a function of frequency in Fig. 52.4. In this curve both the above-mentioned dispersions are conspicuous, and it is also striking that this material has low residual losses at audio frequencies. The loss angle at 20 kc/s is only tan $\delta = 4 \times 10^{-4}$.

Magnetic spectra similar to those described for the compound $BaFe_{12}O_{19}$ are found for the other hexagonal oxides whose *c* axis is a preferred direction of magnetization. As an example, Fig. 52.5 shows the spectra of two rings of the compound $NiFe^{II}W$ having a crystal anisotropy of about $K_1 = 1.8 \times 10^6$ erg/cm^3. The broken curves *a*) and the solid curves *b*) were measured on rings having a texture according to Fig. 52.1 *a* and *b* respectively. The measuring fields were therefore respectively perpendicular and parallel to the *c* axes of the crystals. The rings were simultaneously sintered for one

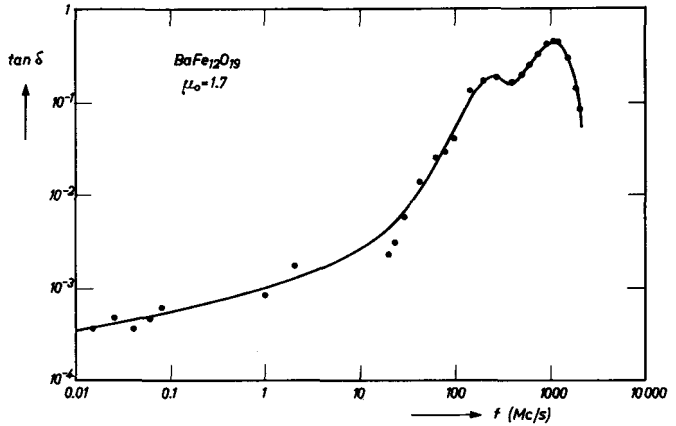

Fig. 52.4. Loss factor tanδ as a function of frequency for $BaFe_{12}O_{19}$ which has been finely powdered and subsequently sintered at low temperature.

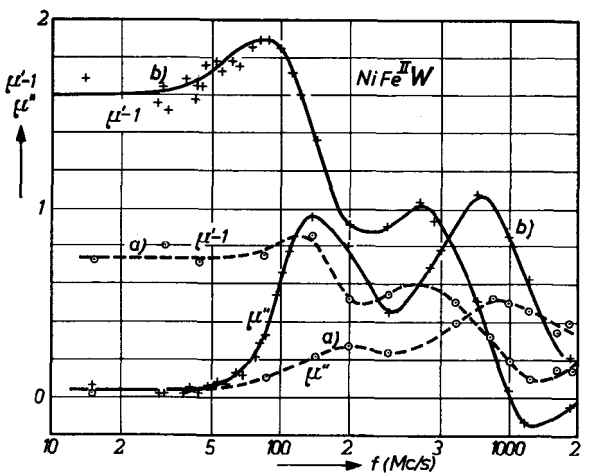

Fig. 52.5. Magnetic spectra of two rings of crystal-oriented $NiFe^{II}W$. The curves *a*) and the curves *b*) were measured on rings having a crystal texture as in Fig. 52.1*a* and *b* respectively.

hour at 1360 °C in an oxygen atmosphere. The spectra again show two dispersions, entirely as given in Fig. 52.2 for $BaFe_{12}O_{19}$.

§ 53. Effect of Mechanical Stresses on the Spectrum

An example of a situation where either only rotations or only wall displacements can contribute to the permeability in ferrites is obtained by applying an external mechanical stress to a ferrite rod as indicated in Fig. 49.3*a*. If a tensile stress is applied to a material having negative magnetostriction,

the magnetic moments will orient themselves perpendicular to the tensile stress. For $Ni_{0.36}Zn_{0.64}Fe_2O_4$ the internal anisotropy is relatively small, so that for large tensile stresses σ_e the stress anisotropy $^3/_2\lambda_s\sigma_e$ may be predominant, as described in § 49.2 and as indicated in Fig. 49.4. The magnetic spectrum of this ferrite is given for two different tensile stresses in Fig. 53.1 and compared with the spectrum of the same ferrite without stress. The low-frequency level of the permeability is reduced by the tensile stress, while at the same time the frequency at which μ'' is at maximum becomes higher. The reduction of μ_0 from 640 to 320 is accompanied by an increase of the dispersion frequency from 5 Mc/s to about 15 Mc/s. This is more than corresponds to the relation (50.4). This difference may be due to the fact that, at a stress $\sigma_e = 2.7$ kg/mm² in this ferrite, most of the spins are perpendicular to the direction in which μ_0 is measured (see § 49.2). In order to calculate the anisotropy field in this state from μ_0 it is therefore necessary to omit the factor 2/3 in (47.3), so that the same factor disappears in the right-hand side of (50.4).

The μ'' *versus* frequency curve in the case of an applied tensile stress becomes broader; towards low frequencies the dispersion is particularly broadened. If the magnetic moments are oriented perpendicularly to a tensile stress, then all directions in a plane perpendicular to that tensile

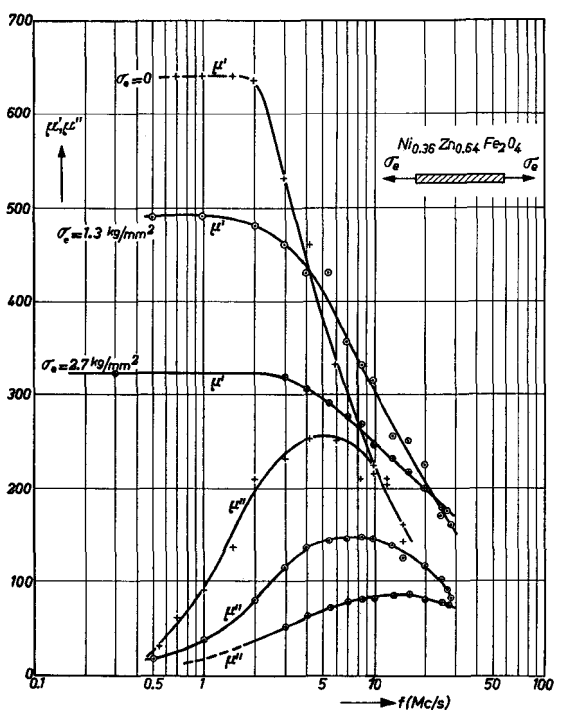

Fig. 53.1. Magnetic spectra of a rod of $Ni_{0.36}Zn_{0.64}Fe_2O_4$ measured at different values of a uniform tensile stress σ_e, after [Wi 6].

stress are equivalent, and therefore rotation of the magnetization in this plane is not limited by the anisotropy due to the tensile stress. The ferromagnetic resonance frequency is in this case determined by the geometrical mean of the stiffness of rotations in the plane and out of the plane, analogous to (51.1), and since the anisotropies in this plane are smaller than the stress anisotropy that determines the magnitude of μ_0, we may therefore expect dispersions at lower frequencies than would follow from the simple relation (50.4). This phenomenon may also be the reason for the fact that in ferrites with high internal stresses, substantial losses occur [Sn 1] far below the resonance frequency determined by (50.4).

§ 54. Relaxation Losses

54.1. IDENTIFICATION OF RELAXATION LOSSES

In many ferrites one often finds in addition to the main dispersion described in § 50, which is probably due to ferromagnetic resonance, a second dispersion arising from a relaxation. In Fig. 54.1 an example is given of the

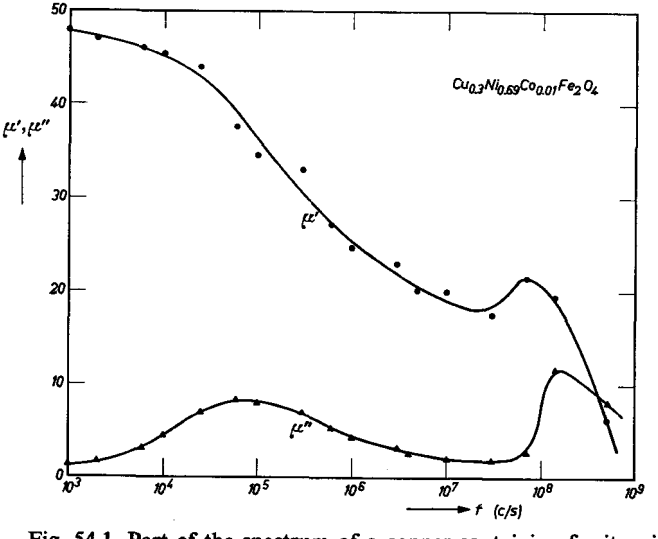

Fig. 54.1. Part of the spectrum of a copper-containing ferrite with spinel structure, $Cu_{0.3}Ni_{0.69}Co_{0.01}Fe_2O_4$, showing two dispersion ranges.

spectrum of a spinel containing copper ($Cu_{0.3}Ni_{0.69}Co_{0.01}Fe_2O_4$) measured with alternating fields of very small amplitude. In the μ'' *versus* frequency curve the dispersion at about 200 Mc/s can be seen which is accompanied by a drop in μ'; this dispersion shows all the characteristics of the resonances

discussed in the foregoing sections. In an extensive frequency range around 100 kc/s the value of μ'' is fairly high, whereas μ' becomes gradually smaller. This phenomenon, which seems to be connected with a relaxation, is discussed at greater length in this section. Losses of this kind are found to occur in all copper-containing ferrites with spinel structure [Sn 3] and also in those ferrites which contain divalent iron ions. Such dispersions are also found in ferrites with garnet structure and in ferrites with hexagonal crystal structure.

54.2. PHENOMENOLOGICAL DESCRIPTION OF THE RELAXATION PROCESS

The relaxation process can be described by postulating that after the application of a magnetic field H the magnetization M does not immediately reach its final equilibrium value M_∞. The simplest picture is that the change of the magnetization is proportional to its deviation from the equilibrium value:

$$\dot{M} = (1/\tau)\,(M_\infty - M). \tag{54.1}$$

The change of M with time is then given by an exponential function:

$$M = \chi_\infty\,(1 - e^{-t/\tau})H = (1 - e^{-t/\tau})M_\infty\,. \tag{54.2}$$

This function is plotted in Fig. 54.2. The relaxation time τ is the time that

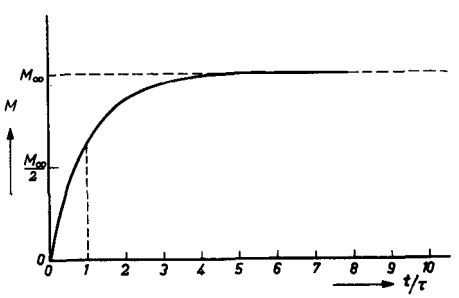

Fig. 54.2. Exponential increase of the magnetization M to its final value M_∞ with a relaxation time τ according to (54.2).

elapses after the application of a field H before the magnetization differs by less than $1/e$ from its equilibrium value, and χ_∞ is defined by the relation $M_\infty = \chi_\infty H$. If an alternating field $H = H_0 e^{i\omega t}$ is applied, then the appertaining magnetization is:

$$M = \frac{\chi H}{1 + i\omega t}\,. \tag{54.3}$$

From this the permeability follows as:

$$\mu' = 1 + \frac{4\pi\chi_\infty}{1 + \omega^2\tau^2}\,;\quad \mu'' = \frac{4\pi\chi_\infty\,\omega\tau}{1 + \omega^2\tau^2}\,. \tag{54.4}$$

Normalized curves of μ' and μ'' as a function of frequency are given in Fig. 54.3. Another method of representation is the so-called Argand diagram or Cole and Cole diagram, in which μ' and μ'' are used as coordinates. The relation between μ' and μ'' for variable frequencies is given, according to (54.4), by a semi-circle, as in Fig. 54.4; see for instance [Br 8]. For a ferrite

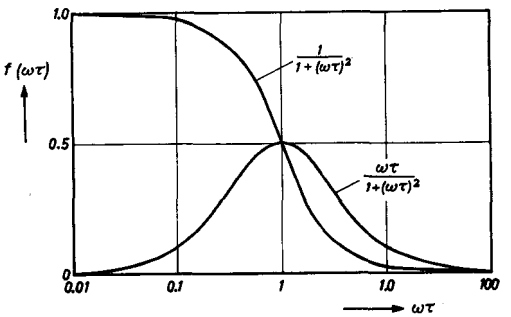

Fig. 54.3. Normalized curves according to (54.4) of $\mu' - 1$ and μ'' *versus* frequency for the case of a relaxation dispersion with one time constant τ.

$Cu_{0.5}Zn_{0.5}Fe_2O_4$, fired for $2\frac{1}{2}$ hours at 1000 °C in an oxygen atmosphere (density 5 g/cm³, resistivity $\rho = 6 \times 10^5$ ohm-cm) Figs. 54.5*a* and *b* show for different frequencies the real and the imaginary part of the permeability as a function of temperature. Measuring at various fixed frequencies as a function of temperature is much simpler than measuring at various fixed temperatures as a function of frequency. The value of τ at a certain temperature is equal to the reciprocal value of the angular frequency ω, for which the μ'' *versus* T curve at this temperature touches the broken curve of Fig. 54.5*b*, which is the envelope of the μ'' *versus* T curves. One can also plot a Cole and Cole diagram from the measuring results as shown in Fig. 54.6. This figure gives the relation between μ' and μ'' for various frequencies at a number of different temperatures. In the case of one relaxation time τ at each temperature one would expect a number of semi-circles. The observed deviations are probably due to a spread in the relaxation times. The distribution laws governing relaxation times, and their influence on the Cole and Cole diagrams, have been extensively

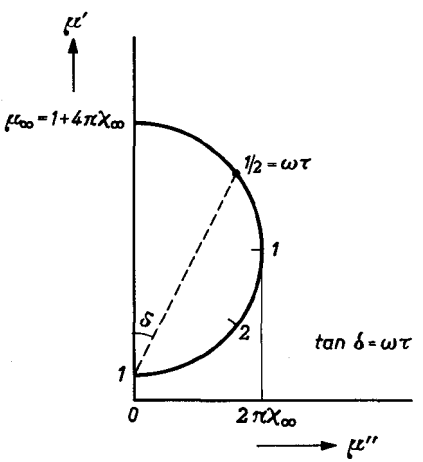

Fig. 54.4. The relation between μ' and μ'' in the case of a relaxation dispersion with one time constant τ (so called Argand or Cole and Cole diagram).

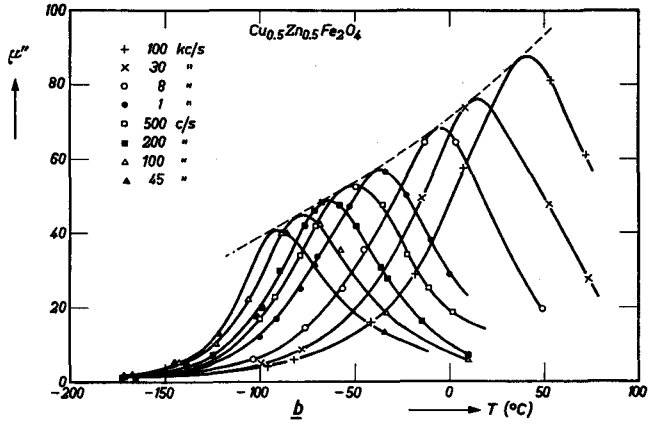

Fig. 54.5. The real and imaginary part of the complex permeability, μ' and μ'' respectively, measured at various frequencies as a function of temperature for a sample of $Cu_{0.5}Zn_{0.5}Fe_2O_4$ that has been fired for $2^1/_2$ hours at 1000 °C in an oxygen atmosphere.

treated in publications on dielectric relaxation losses; see for example [Br 8].

The relaxation time τ decreases with increasing temperature, and if we plot for this ferrite, as is done in Fig. 54.7, the values of log τ^{-1} against the reciprocal value of the temperature, we obtain a practically straight line. The relation between these two quantities can therefore be described by the equation:

$$\tau = \tau_\infty \, e^{E_m/kT} \tag{54.5}$$

where τ_∞ is the relaxation time at an infinite temperature and E_m is the activation energy controlling the process. The slope of the straight line for $Cu_{0.5}Zn_{0.5}Fe_2O_4$ in Fig. 54.7 corresponds to an activation energy $E_m \cong 0.32$ eV. The relaxations described here for a copper ferrite are phenomelogically entirely similar to the relaxation losses found in carbonyl iron containing a small percentage of carbon [Sc 2].

54.3. RELAXATIONS IN FERROUS FERRITES

Considerable relaxation losses are found in ferrous ferrites, where the relaxation strength appears to be very closely connected with the ferrous content. In Fig. 54.8 the loss factor tan δ at frequencies of 25, 600 and 1000 kc/s is plotted as a function of temperature for a magnanese-zinc ferrous ferrite having a chemical composition of approximately $Mn_{0.66}Zn_{0.28}Fe^{II}_{0.06}Fe_2O_4$ (at room temperature, $\mu_0 \cong 500$, $d \cong 5.0$ g/cm^3 and $\rho \cong 10^2$ ohm-cm). These results are also typical of a relaxation phenomenon. The relaxation time as a function of temperature can be calculated from the straight line

in Fig. 54.7, appertaining to this ferrite and is equal to $E_m = 0.17$ eV. This small activation energy points to an electron diffusion process in this ferrite. For a ferrite with a high resistivity, $Ni_{0.5}Zn_{0.5}Fe_2O_4$ (fired in oxygen at 1250 °C, resistivity $\rho = 10^6$ ohm-cm, $d \cong 5$ g/cm³ and $\mu_0 \cong 200$), the results are given in Fig. 54.9. It can be seen that in the temperature range covered, $\tan\delta$ does not show the high values observed for the manganese zinc ferrite. However, $\tan\delta$ is not a constant and the variations with temperature and frequency can again be ascribed to a relaxation process. Corresponding values of the logarithm of the frequency and the reciprocal of the temperature at which the $\tan\delta$ curves for this ferrite have a maximum are therefore also plotted in Fig. 54.7. An activation energy is calculated of 0.40 eV. Refiring of this ferrite in the same atmosphere but at a higher temperature, 1525 °C, causes a concentration of 0.4 % by weight of ferrous ions in the ferrite, leading to a decrease of the resistivity from 10^6 to 10^3 ohm-cm. As we shall see in § 62, the firing of this ferrite at such a high temperature causes $\tan\delta$ to increase with increasing field, which means that hysteresis is important. For this reason μ' and μ'' of this ferrite were measured at field strengths of 5 and 2.5 mOe, permitting an extrapolation to zero field strength.

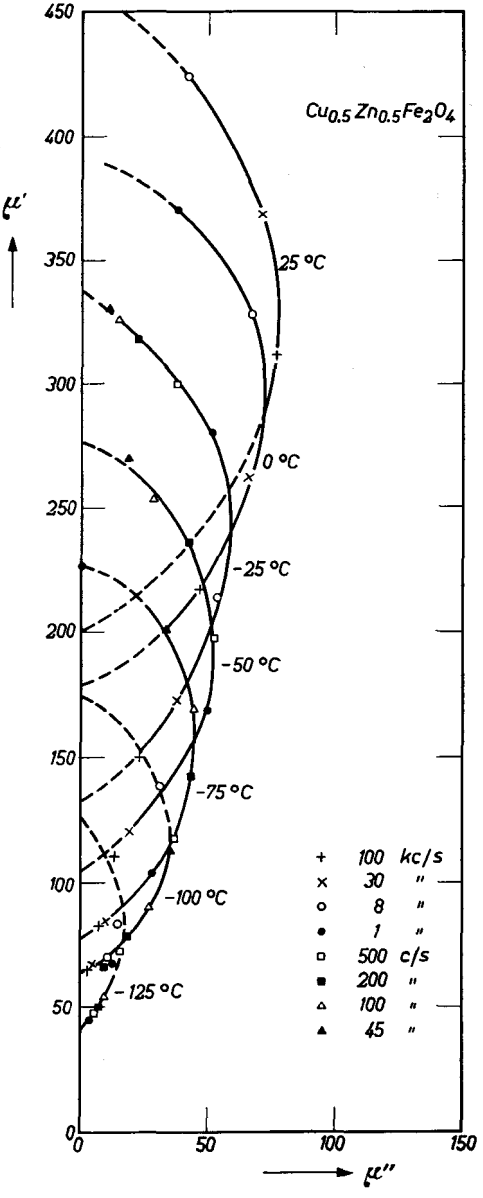

Fig. 54.6. Argand or Cole and Cole diagram for the copper-zinc ferrite of Fig. 54.3.

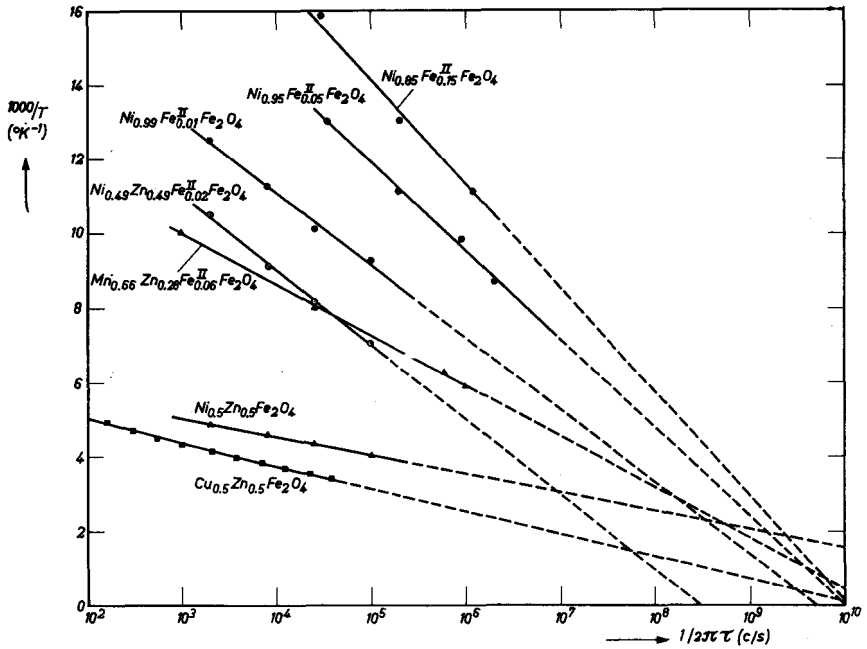

Fig. 54.7. The relation between relaxation time τ and temperature T for various ferrites from Table 54.1.

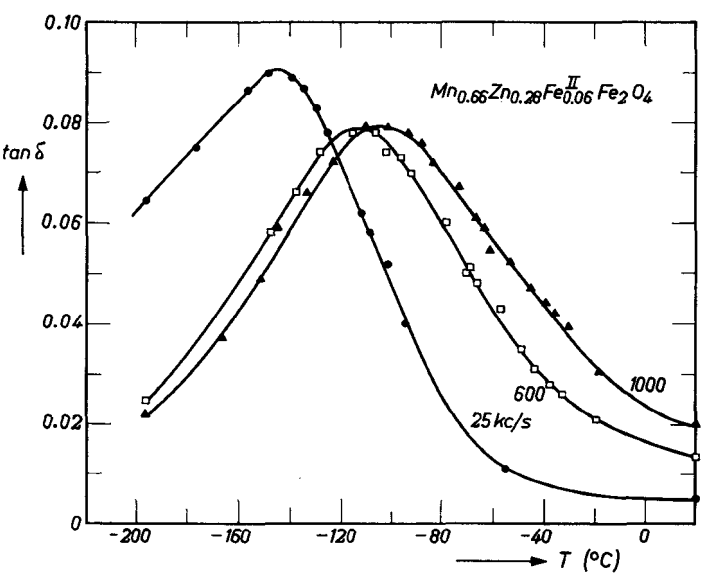

Fig. 54.8. The loss factor tanδ of $Mn_{0.66}Zn_{0.28}Fe^{II}_{0.06}Fe_2O_4$ as a function of temperature, measured for various frequencies at a field strength of about 5 millioersteds.

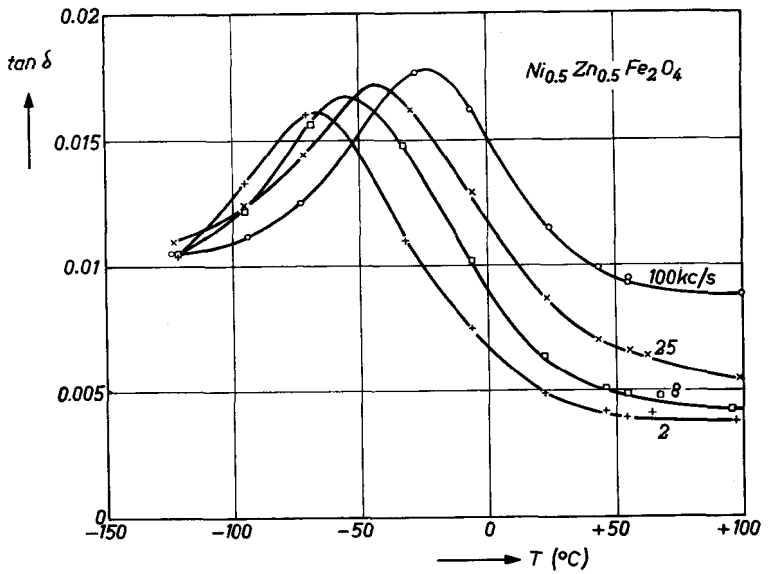

Fig. 54.9. The loss factor $\tan\delta$ of a ferrite $Ni_{0.5}Zn_{0.5}Fe_2O_4$ (fired for two hours at 1250 °C in oxygen) as a function of temperature, measured at a field strength of 2.5 millioersteds.

The values of μ'' measured at these field strengths for 2, 8, 25, and 100 kc/s are plotted as a function of temperature in Fig. 54.10. After a linear extrapolation to zero field strength, the drawn lines are obtained. The variation of μ' with the field strength proves to be less than one per cent, so it suffices to give the values of μ' measured at 2.5 mOe, neglecting the extrapolation. From the values of μ' and the extrapolated values of μ'' a residual loss factor $\tan\delta_r$ has been calculated: the result is given in Fig. 54.11, which shows the temperature dependence of $\tan\delta_r$ for various frequencies. It can be seen that results are obtained similar to those for the manganese-zinc ferrite, which also contains both ferric and ferrous ions. Also the activation energies of the relaxation processes in both ferrites are about equal (see Fig. 54.7 and Table 54.I). Relaxation times τ are also given in Fig. 54.7 as a function of temperature for a number of mixed nickel-ferrous ferrites $Ni_{1-\delta}Fe^{II}_{\delta}Fe_2O_4$. It can be seen, as is also evident from Table 54.I, that E_m decreases with increasing ferrous content. The relaxation frequency at an infinite temperature is of the order of magnitude of 10^{10} c/s. For the nickel-zinc ferrite fired at low temperature, which is porous and consists of small crystallites, this relaxation frequency is much higher, being about 10^{13} c/s, whereas for the nickel-zinc ferrite fired at high tem-

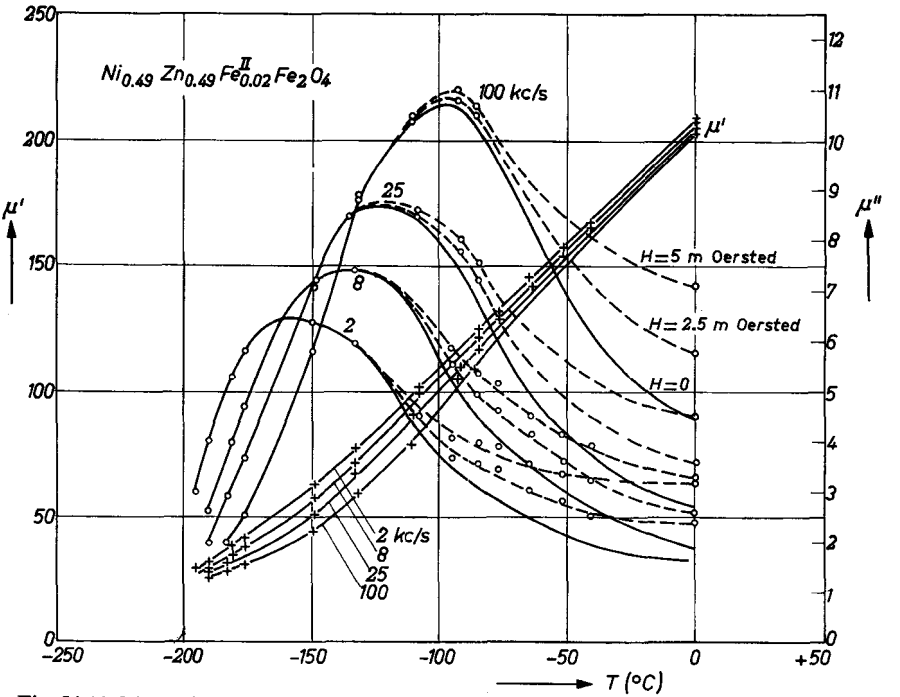

Fig. 54.10. The real and imaginary part of the complex permeability, μ' and μ'' respectively measured at various frequencies as a function of temperature for the ferrite of Fig. 54.9. This ferrite was fired additionally for two hours at 1525 °C in oxygen, so as to introduce ferrous ions.

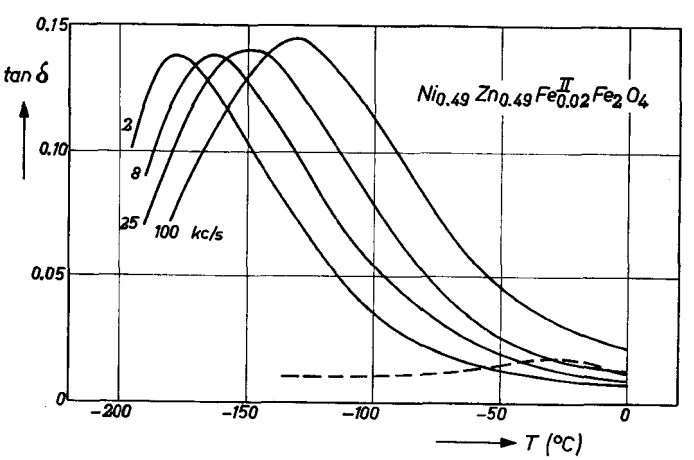

Fig. 54.11. The residual loss factor tan δ derived from the measuring results of the preceding figure. The broken curve represents the loss factor at 100 kc/s of the same ferrite before the additional firing at 1525 °C (compare Fig. 54.9).

perature and consisting of large crystals, this frequency is on the low side, being about 3×10^8 c/s.

Table 54.I gives a survey of the activation energies, E_m, derived from the magnetic loss measurements on ferrous ferrites as well as the activation energies E_p of their d.c. resistivities. A comparison of both activation energies permits the conclusion that they are related to the same dissociation phenomenon, and it is fairly probable that the magnetic after-effect found in ferrites in which atoms of the same element occur as ions of different valencies is due to an electron diffusion process. The activation energies found can be divided into two classes: for ferrites having a relatively high conductivity, E_m is about 0.1 eV, and for ferrites that are almost insulators, E_m is about 0.4 eV.

TABLE 54.I

THE ACTIVATION ENERGY E_m OF THE MAGNETIC RELAXATION PHENOMENON COMPARED WITH THE ACTIVATION ENERGY E_ρ OF THE D.C. RESISTIVITY FOR SOME FERRITES. AN APPROXIMATE VALUE OF THE RELAXATION STRENGTH, TAN δ_{max}, IS ALSO GIVEN.

Ferrite	Resistivity at room temp. (ohm-cm)	E_m eV	E_ϱ eV	$\tan\delta_{max}$	Figure
$Ni_{0.50}Zn_{0.50}Fe_2O_4$	10^6	0.40	0.41	0.02	54.9
$Ni_{0.49}Zn_{0.49}Fe^{II}_{0.02}Fe_2O_4$	10^3	0.10	0.10	0.13	54.10 and 54.11
$NiFe_2O_4$	$>10^9$	*)	—	—	
$Ni_{0.99}Fe^{II}_{0.01}Fe_2O_4$	30	0.10	—	0.33	
$Ni_{0.95}Fe^{II}_{0.05}Fe_2O_4$	500	0.08	—	0.10	
$Ni_{0.85}Fe^{II}_{0.15}Fe_2O_4$	5	0.07	—	0.10	
$Mn_{0.66}Zn_{0.28}Fe^{II}_{0.06}Fe_2O_4$	150	0.17	0.16	0.10	54.8
$MgFe_2O_4$	10^6	0.37	0.32	0.03	
$Cu_{0.5}Zn_{0.5}Fe_2O_4$	6×10^5	0.32	0.29	0.30	54.5
$Cu_{0.5}Li_{0.25}Fe_{2.25}O_4$	500	0.20	—	0.40	

*) No maxima found in the $\tan\delta$ *versus* temperature curves. The ferrite shows abnormally low residual losses: $\tan\delta = 0.0017$ at 100 kc/s at room temperature.

§ 55. Induced Ferromagnetic Resonance

The ferromagnetic resonance in a ferrite saturated in an applied static field differs for sintered polycrystalline materials from that in single crystals. In the first place the peak in the losses as a function of the applied field is seen to be very broad and asymmetrical (Fig. 55.1), and in the second place the mean resonance field does not satisfy the simple relation $\omega = \gamma H$ when the frequency is varied. The latter phenomenon was first discovered

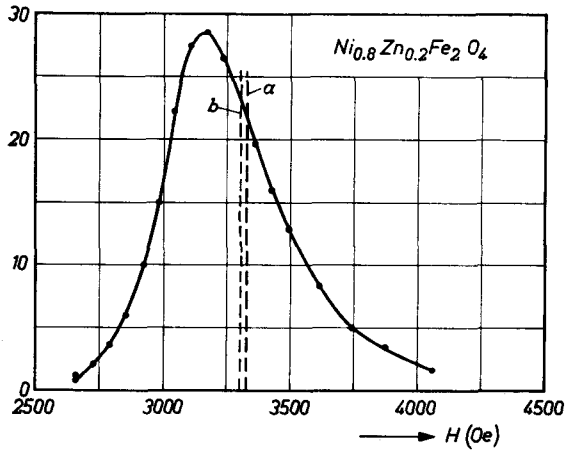

Fig. 55.1. Induced ferromagnetic resonance in a polycrystalline sphere of $Ni_{0.8}Zn_{0.2}Fe_2O_4$. Diameter of sphere 0.75 mm; measuring frequency $f = 9400$ Mc/s, porosity $p = 0.2$. The broken line (a) indicates the resonant field for the true g factor ($g = 2.02$). The broken line (b) is through the centre of gravity of the peak. The losses are given on an arbitrary scale.

by Okamura [Ok 2], who, on the basis of the results of his measurements, assumed instead

$$\omega = \gamma(H + H_i), \tag{55.1}$$

where H_i is a frequency-independent internal field (see Fig. 55.2). It is always found that $H_i > 0$. In practice this phenomenon appears as an increase in the g factor, which becomes larger the lower is the frequency. For example, a ferrite with a "true" g factor according to (55.1) of 2.1 at $\lambda = 3$ cm may have an apparent g factor of 2.4. Snieder [Sn 5] has brought this anomaly in sintered Ni-Zn ferrites into relation with their porosity. If we substitute his experimental results in the Okamura equation (55.1) we find the values for g_{real} and H_i as given in Table 55.I.

TABLE 55.I

APPARENT g FACTORS AND VALUES OF THE REAL g FACTOR AS CALCULATED FROM THE OKAMURA EQUATION (55.1), TOGETHER WITH INTERNAL FIELDS H_i OF Ni-Zn FERRITES WITH SPINEL STRUCTURE AT ROOM TEMPERATURE.

Ferrite $Ni_\delta Zn_{1-\delta}Fe_2O_4$	porosity p	g apparent		g real	H_i
		f=9320 Mc/s	f=24000Mc/s		
$\delta = 0.36$	0.166	2.16	2.06	2.01	250
0.50	0.110	2.17	2.06	2.00	270
0.64	0.162	2.29[5]	2.10[5]	2.00	430
0.80	0.262	2.46[5]	2.17	2.02	600
1.00	0.295	2.47[5]	2.22[5]	2.13	500

In Fig. 55.3 the internal field H_i from Table 55.I is plotted as a function of $p.4\pi M_s$, the magnetization taken being that of the dense material. A linear relationship is found, which, for these materials, is:

$$H_i \simeq 0.5\, p.4\pi M_s. \tag{55.2}$$

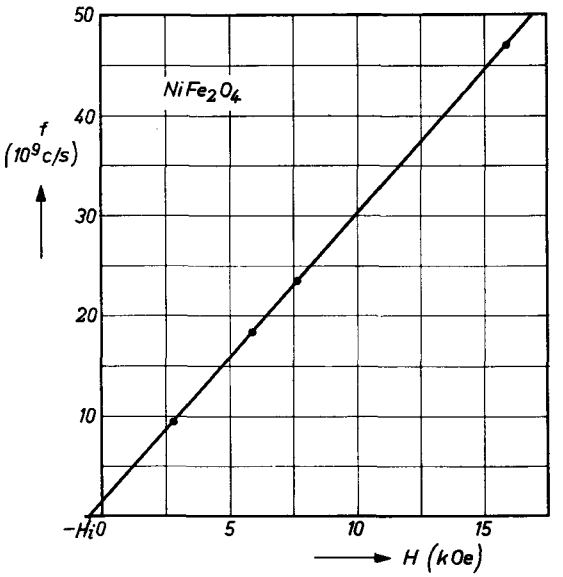

Fig. 55.2. Relation between the ferromagnetic resonance frequency f, and the corresponding magnetic field H for a polycrystalline sphere of $NiFe_2O_4$, after [Ok 2].

The true g factor for the Ni-Zn ferrites with high Zn content has almost the spin-only value; only for Ni ferrite is an essentially higher value found. This, however, is smaller than that found for single crystals (see Table 36.I).

It is noteworthy that for ferrites with high values of H_i the line width ΔH is also large (see Fig. 55.1), whereas the absorption peak has a tail towards the high field side. According to recent theories of Clogston [Cl 5] and Schlömann[Sc 3] concerning the line width of polycrystalline samples, the

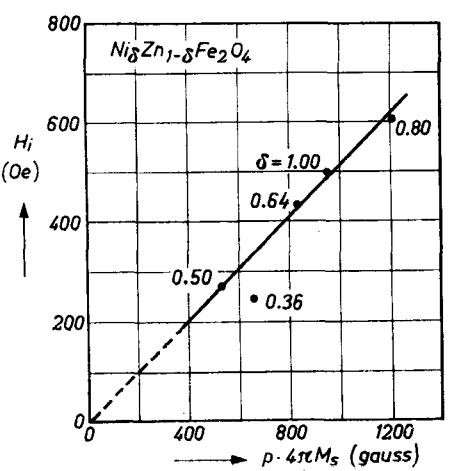

Fig. 55.3. Relation between the internal field H_i, defined by (55.1) and the product $p \cdot 4\pi M_s$, for polycrystalline specimens of $Ni_\delta Zn_{1-\delta}Fe_2O_4$.

dipolar interaction between the magnetic moments of different points of the material leaves the centre of gravity of the absorption peak unchanged. If we take for the resonance field the field at which maximum absorption occurs, as is usually done, then the resonance field is too low, and should be corrected by a field of the type H_t. It is seen in Fig. 55.2 that if instead the field of the centre of gravity is taken, the resultant H_t is very small. Such a correction should be dependent on porosity, as the line width is due to stray fields near the pores. According to Clogston the line-width is of the order of magnitude $(H^A)^2/M_s$, in which case H^A should be the mean square root of the stray fields. According to (2.7) and (2.8) this $(H^A)^2$ is of the order of $4\pi N M_s^2 p$, where N is an averaged demagnetization factor of the pores. An expression for H_t of the type (55.2) is then plausible.

CHAPTER XV

STATIC HYSTERESIS LOOPS

§ 56. The Coercive Force

As described in § 16 and § 17 a ferromagnetic substance becomes magnetized as a result of domain-wall displacements and rotations. Both processes can take place irreversibly, which is the cause of hysteresis. Rotation processes are mainly associated with intrinsic properties of the material and are therefore fairly independent of the structure; this is not the case, however, as regards the contribution of wall displacements to the magnetization. Consequently the shape and width of the hysteresis loop of a ferrite depend not only on the chemical composition, which determines the intrinsic properties, but also on various factors connected with the sintering process, such as porosity, the size and shape of the pores and the size and shape of the crystals. Fig. 56.1 gives an example of the way in which the coercive force H_c depends on the porosity p in the case of sintered samples of $Ni_{0.5}Zn_{0.5}Fe_2O_4$. The samples were obtained by compressing powder consisting of grains with an average diameter of about 1 micron and by sintering at a temperature varying from 1100 to 1450 °C. In this case H_c increases linearly with p, as it should according to (16.8). The deviation from linearity at high values of p may be caused by the fact that in the very porous samples fewer domain walls are present. Some of the grains will consist of a single domain, which leads to greater coercive forces. The quantity K_1/M_s from (16.8) becomes smaller with increasing zinc content in the series of nickel-zinc ferrites $Ni_\delta Zn_{1-\delta}Fe_2O_4$, since the initial permeability becomes larger (see Table 56.I). At the same time the coercive force also becomes smaller, as appears from the column last but one in Table 56.I. The last column gives the value of H_c calculated with (16.8), the anisotropy constant according to (47.3) being derived from the value of μ_0. Here, too, the calculated values are probably on the high side, since only pores with a diameter comparable with the thickness of the domain wall make a contribution

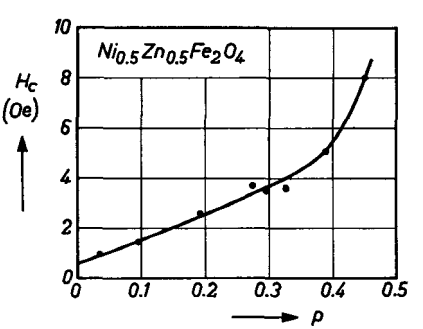

Fig. 56.1. Relation between the coercive force and the porosity of sintered samples of $Ni_{0.5}Zn_{0.5}Fe_2O_4$.

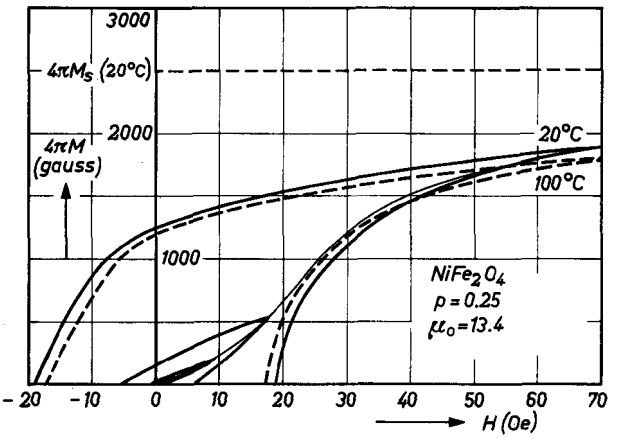

Fig. 56.2. Virgin curve and hysteresis loops of a polycrystalline sample of $NiFe_2O_4$ at 20 °C. The dashed curve is a hysteresis loop at 100 °C.

TABLE 56.I

RELATION BETWEEN INITIAL PERMEABILITY AND COERCIVE FORCE FOR FERRITES OF THE SERIES $Ni_\delta Zn_{1-\delta}Fe_2O_4$. THE LAST COLUMN GIVES THE VALUE OF H_c CALCULATED WITH THE AID OF (16.8), WHERE THE QUANTITY K_1/M_s ACCORDING TO (47.3) IS DERIVED FROM μ_0.

Ferrite $Ni_\delta Zn_{1-\delta}Fe_2O_4$	p	M_s gauss	μ_0	H_c oersted	
				measured	according to (16.8)
$\delta = 1$	0.25	196	17	13.7	16.1
0.80	0.24	283	45	6.8	10.4
0.67	0.22	321	90	4.0	6.2
0.50	0.15	332	230	1.4	2.0
0.33	0.09	292	650	0.4	0.4

to H_c. A better comparison is complicated by the fact that, although all samples are fired at the same temperature, the average diameter of the pores varies from sample to sample, as a consequence of the fact that a higher zinc content promotes sintering.

The solid curves in Figs 56.2 and 56.3 represent the virgin curve, the major loop and two minor loops of $NiFe_2O_4$ and $Ni_{0.5}Zn_{0.5}Fe_2O_4$, respectively. An example of a magnetically really soft ferrite is $Mn_{0.65}Zn_{0.35}Fe_2O_4$, for which $\mu_0 \simeq 1500$ and $H_c \simeq 0.2$ oersteds. The hysteresis loop of this ferrite is shown in Fig. 56.4 In all these cases the relative remanent magnetization is low, being no more than half the saturation magnetization. By means of special preparation techniques it is possible to make ferrites for which some

loops have a rectangular shape, as is shown for example in Fig. 56.5 for $Mg_{0.45}Mn^{II}_{0.55}Mn^{III}_{0.23}Fe_{1.77}O_4$. A general rule for making ferrites with such rectangular minor loops cannot be given. With many chemical compositions it is possible to arrange the conditions during preparation so as to produce loops of this kind; see [Wi 4]. Even samples of the simple ferrites $NiFe_2O_4$ and $MnFe_2O_4$ have been made with rectangular minor loops [Ec 1]. It is

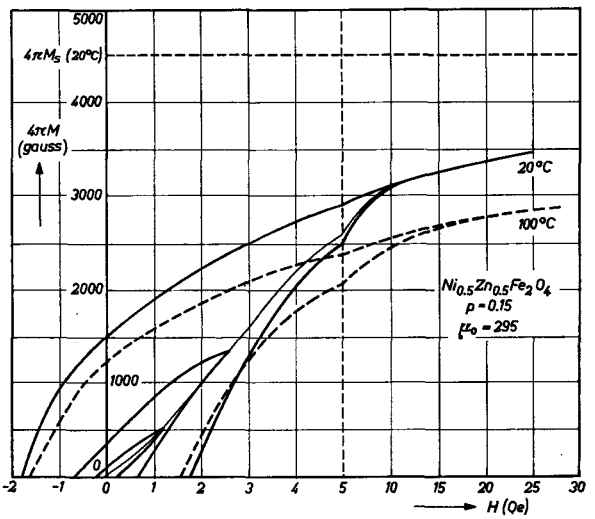

Fig. 56.3. The same as Fig. 56.2, but now for $Ni_{0.5}Zn_{0.5}Fe_2O_4$.

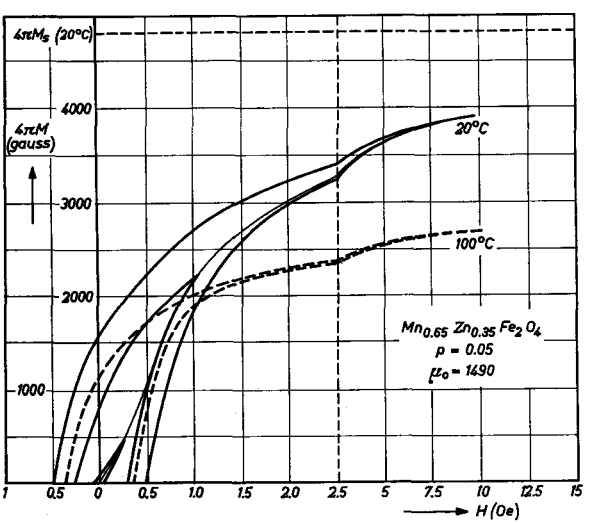

Fig. 56.4. The same as Fig. 56.2, but now for $Mn_{0.65}Zn_{0.35}Fe_2O_4$.

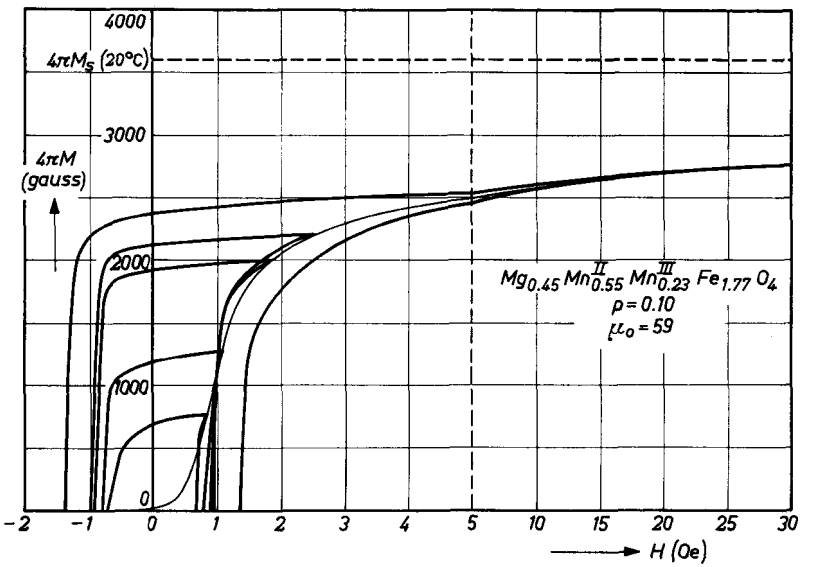

Fig. 56.5. The same as Fig. 56.2, but now for $Mg_{0.45}Mn^{II}_{0.55}Mn^{III}_{0.23}Fe_{1.77}O_4$, showing some rectangular minor hysteresis loops.

probable that in order to obtain ferrites with such loops, a small initial permeability, and hence a small permeability in the remanent state, must be associated with a low coercive force. It is also thought [Go 8] that the critical field strength needed to produce domain walls must be greater than the field strength needed for the irreversible displacement of these walls.

Most polycrystalline sintered samples of ferrites with spinel structure have a relatively low coercive force. Exceptions are the simple and mixed cobalt ferrites, for which H_c can be larger than 1000 oersteds.

The ferrites with hexagonal crystal structure and a preferred plane of magnetization also have a low coercive force. See, for example, Fig. 56.6*a* and *b*, showing families of hysteresis loops for an isotropic and a crystal-oriented sample of $Co_{0.8}Zn_{1.2}Z$. The crystal-oriented sample has the higher remanence. In this sample the basal planes of the hexagonal crystals are as near as possible mutually parallel (see § 44), and for measuring the hysteresis loop the field is parallel to these magnetically preferred planes of the crystals. In the case of the hexagonal oxides with a preferred direction of magnetization the coercive force is generally very high, being of the order of magnitude of 100 oersteds and more. By a special method of preparation it is possible to make permanent magnets of many of these compositions (see § 60).

The virgin curve determines the amplitude permeability μ. This is defined as the ratio between the maximum value of the induction B_{max} and the corresponding value of the field strength H_{max}, when a minor loop is described: $\mu = B_{max}/H_{max}$. In Fig. 56.7 the relation between the normalized amplitude permeability (μ/μ_0) and H_{max} is given for the ferrites of Figs 56.2 to 56.6. At a field strength slightly higher than the coercive force, μ reaches a maximum value, μ_{max}, and at a much higher value of H_{max} it approaches asymptotically the value 1. If the ratio μ_{max}/μ_0 as a function

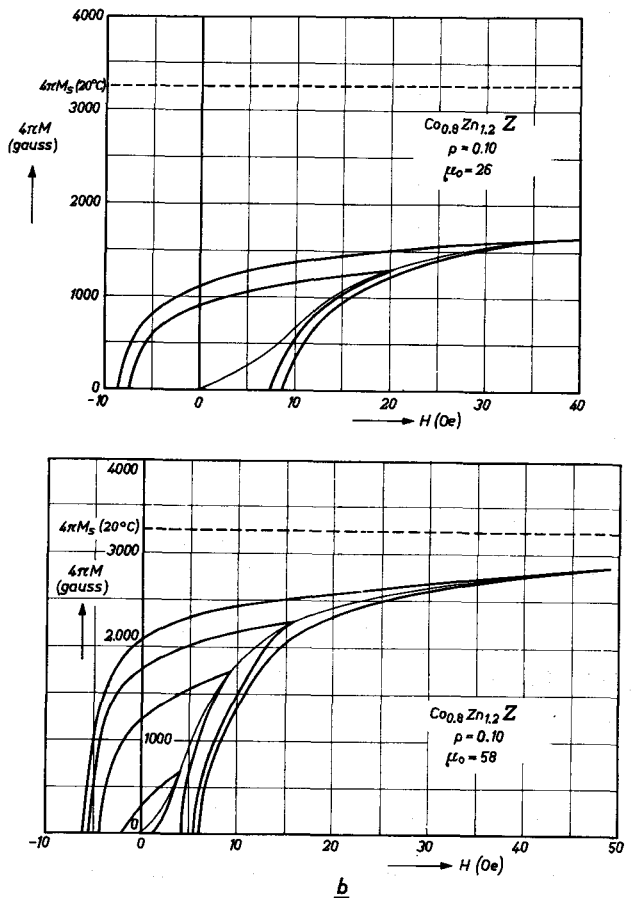

Fig. 56.6. Hysteresis loops and virgin curve of polycrystalline samples of $Co_{0.8}Zn_{1.2}Z$.
a) isotropic sample,
b) crystal-oriented sample.

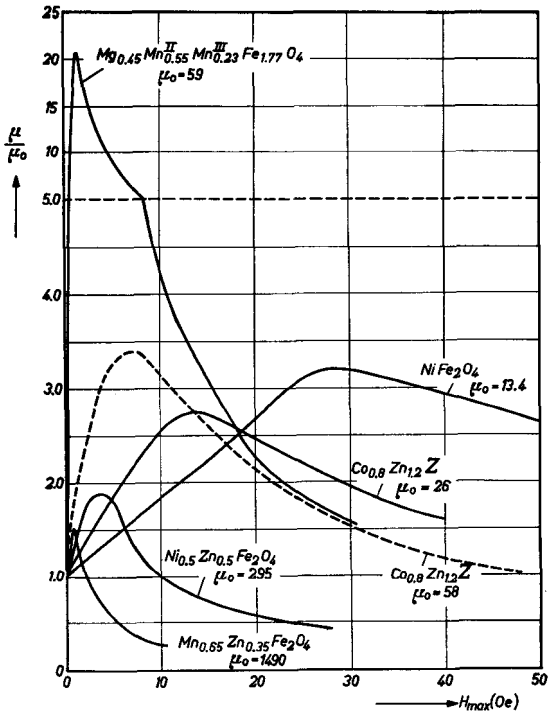

Fig. 56.7. The normalized values of the amplitude permeability of the ferrites of Figs. 56.2 to 56.6 as a function of the amplitude H_{max} of the measuring field-strength. The value of μ_0 of each ferrite is marked beside the curve.

of H differs little from unity, this means that when such ferrites are used as cores in a circuit they cause little distortion.

In Figs. 56.2 to 56.4 the broken curves indicate the hysteresis loops at 100 °C. It is known that, in general, the initial permeability increases (§ 48.1) and the saturation magnetization decreases (§ 32.2) with increasing temperature, so that the virgin curves for different temperatures intersect. At the field strength corresponding to this point of intersection the magnetization caused by this field is almost independent of temperature. This also applies to the reversible permeability, μ_{rev}, at a particular value of the biasing field strength.

§ 57. Remanent Magnetization

In the process of demagnetization the material divides itself into Weiss domains, such that the average magnetization over all domains is zero. The preferred direction of the magnetization vector in each domain is determined by the three anisotropies: crystal, stress and shape anisotropy. If, after saturation of the material in a very strong field, the field is allowed

to return slowly to zero, the magnetization vectors rotate out of the field direction towards the nearest preferred direction, which is determined by one or a combination of the above-mentioned anisotropies. For a field $H = 0$ a remanent magnetization M_{rem} is left. In this state the susceptibility in the case of small fields is χ_{rem}. We shall now examine in turn what the magnitude of the ratios M_{rem}/M_s and χ_{rem}/χ_0 will be when one of the three types of anisotropy is predominant.

(a) Crystal Anisotropy

If a crystal is subjected to a strong magnetic field, which is subsequently reduced to zero, the magnetization vector will stick in that preferred direction which is nearest to that of the applied field. This will also occur in a polycrystalline material, provided the magnetic coupling between the individual crystals can be neglected. In the case of a cube whose edges are preferred directions of magnetization, there are six preferred directions in each crystal. In the remanent state the magnetization vectors then distribute themselves over a solid angle of $2\pi/3$ steradians. Where the eight body-diagonals are the preferred directions, the solid angle is $\pi/2$ steradians. In Table 57.I will be found the relative values of the remanent magnetization and the rotational susceptibility in the remanent state as calculated for these cases by Gans [Ga 5].

TABLE 57.I

RELATIVE REMANENT MAGNETIZATION M_{rem}/M_s AND SUSCEPTIBILITY χ_{rem}/χ_0 FOR ISOTROPIC POLYCRYSTALLINE SPECIMENS WITH VARIOUS CRYSTAL-STRUCTURES AND CRYSTAL ANISOTROPIES. THE INTERACTION BETWEEN THE CRYSTALS IS NEGLECTED.

Crystal structure	Crystal anisotropy, preferred direction	M_{rem}/M_s	χ_{rem}/χ_0
cubic	cube edge	0.83	0.45
cubic	body diagonal	0.87	0.36
hexagonal	*c* axis	0.5	1
hexagonal	basal plane		
	a. uniaxial anisotropy in basal plane	0.5	0.33
	b. hexagonal symmetry in basal plane	0.75	0.06

In the case of hexagonal crystal structure and a preferred direction of magnetization (*c* axis) the magnetization vectors in the remanent state are distributed (again neglecting interaction) in a solid angle of 2π steradians and the remanent magnetization is half the saturation magnetization. In this state $\chi_{\text{rem}}/\chi_0 = 1$. Where the plane at right-angles to the *c* axis is a

preferred plane, the anisotropy in this basal plane determines the remanent magnetization. If $2\phi_0$ is the angle between two successive preferred directions of magnetization in the basal plane, the relative remanent magnetization and the relative susceptibility are given by:

$$\frac{M_{\text{rem}}}{M_s} = \frac{\pi}{4}\frac{\sin\phi_0}{\phi_0}. \tag{57.1}$$

and

$$\frac{\chi_{\text{rem}}}{\chi_0} = \frac{1}{3}\left[1 - \frac{\sin 2\phi_0}{2\phi_0}\right]. \tag{57.2}$$

In the case of anisotropic samples with oriented crystals the above-mentioned quantities depend on the direction of the applied magnetic field with respect to the anisotropy directions in the samples. If the preferred directions of magnetization of all crystallites in a sample are in parallel orientation, the relative remanent magnetization, neglecting interaction, will be equal to unity in the preferred direction; at right-angles thereto it would be equal to zero. In the case of hexagonal crystals with a preferred plane of magnetization and hexagonal anisotropy in the basal plane, the relative remanent magnetization for a sample consisting of crystals with mutually parallel c axes, will be equal to $3/\pi$ for all directions in the basal plane and equal to zero in the direction of the c axis.

(b) Stress Anisotropy

When stresses due to elastic deformation are present in a magnetic material with magnetostriction, the magnetization tries to orient itself such that the accompanying changes in length eliminate these stresses as far as possible. If stress anisotropy predominates, then in the case of positive magnetostriction, a plane at right-angles to a compressive stress is a preferred plane of magnetization, and the direction of a tensile stress is a preferred direction. With negative magnetostriction the reverse is the case. Once again, after a strong field is switched off, a Weiss domain distribution will arise in such a way that the magnetization vectors rotate out of the direction of the field back to the nearest preferred direction. With a random stress-distribution in the material it is not possible to determine the remanent magnetization by simple means.

If there are no mechanical stresses present in the material after preparation and demagnetization by cooling from a temperature above the Curie point, the direction of the magnetization vector in each Weiss domain is determined by the crystal anisotropy (shape anisotropy, which is dealt with under (*c*), is disregarded here). When the material is brought into the remanent

state this means that most magnetization vectors are turned out of a magnetically preferred crystallographic direction towards another preferred direction which makes a smaller angle with the direction of the field. In an isolated crystal this would be accompanied by a change in the shape of the crystal, but a crystal in an agglomerate polycrystalline sample will suffer stresses. In the remanent state no stresses will arise if the magnetostriction in the preferred direction (λ_{111} or λ_{100} for a cubic ferrite) is zero. Only in that case can we expect a remanent magnetization as given in Table 57.I; otherwise it will be lower.

(c) Shape Anisotropy

Although, seen macroscopically, the hysteresis loop is measured on a magnetically closed circuit of the material, there is nevertheless an appreciable degree of internal demagnetization due to shape anisotropy arising from the more or less porous structure of the sintered ferrite (see § 43.3).

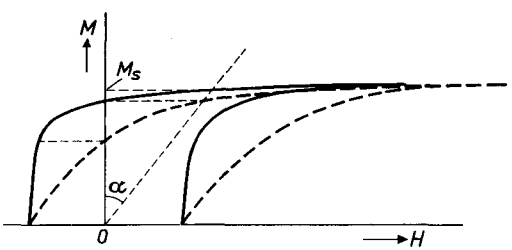

Fig. 57.1. Effect of demagnetization on the shape of a hysteresis loop. The internal demagnetizing factor $N_i = \tan \alpha$.

In Fig. 57.1 the magnetization M is plotted against both the externally applied magnetic field H_0 (broken curve) and the average internal magnetic field H_i (solid curve). It is assumed that:

$$H_0 - H_i = N_i M, \tag{57.3}$$

where N_i denotes the internal demagnetizing factor (see § 43.3). It can be seen from the figure that the ratio M_{rem}/M_s is greatly reduced by the demagnetization, and also that the ratio μ_{rem}/μ_0 approaches unity. This demagnetizing field will have a greater influence on the hysteresis loop the smaller is the coercive force of the ferrite.

For the ferrites of Figs. 56.2 to 56.6 the relative remanent magnetization and the relative permeability in the remanent state are given in Table 57.II. The table also indicates the properties of the isotropic and crystal-oriented samples of $BaFe_{12}O_{19}$ to be discussed in § 60.

The values of the remanent magnetizations are much lower than those that might be expected according to Table 57.I, which is probably due to the phenomenon of "shearing" as a result of internal demagnetization.

TABLE 57.II

RELATIVE REMANENT MAGNETIZATION, M_{rem}/M_s, RELATIVE PERMEABILITY, μ_{rem}/μ_0, AND POROSITY p OF THE FERRITES IN FIGS. 56.2 TO 56.6.

Ferrite	p	μ_0	μ_{rem}/μ_0	M_{rem}/M_s	Figure
$NiFe_2O_4$	0.25	13	1.0	0.5	56.2
$Ni_{0.5}Zn_{0.5}Fe_2O_4$	0.15	300	0.80	0.33	56.3
$Mn_{0.65}Zn_{0.35}Fe_2O_4$	0.05	1500	0.84	0.33	56.4
$Mg_{0.45}Mn^{II}_{0.55}Mn^{III}_{0.23}Fe_{1.77}O_4$	0.10	55	0.32	0.67	56.5
$Co_{0.8}Zn_{1.2}Z$					
isotropic	0.10	26	0.64	0.38	56.6*a*
crystal-oriented	0.10	58	0.52	0.65	56.6*b*
$BaFe_{12}O_{19}$					
isotropic		$\simeq$1.5	—	0.46	60.5*a*
crystal-oriented		$\simeq$2	—	0.94	60.5*b*

This is particularly important when high porosity is combined with low coercive force (the coercive force is generally inversely proportional to μ_0). In the case of the isotropic samples of $Co_{0.8}Zn_{1.2}Z$ the effective internal demagnetization is high owing to the anisotropic permeability of each crystallite (see § 43). Accordingly isotropic samples of these hexagonal ferrites with a preferred plane of magnetization always have a low remanence, even when the porosity is small. For anisotropic (*i.e.* crystal-oriented) specimens the remanence is appreciably higher in a direction parallel to that of the preferred plane. Nevertheless their remanence values by no means reach the high values given in Table 57.I. This may be due to the fact that the crystallites are far from ideally oriented, and for the small coercive forces in question it will also be due to the porosity.

The remanent magnetization of the isotropic polycrystalline sample of $BaFe_{12}O_{19}$ with a high coercive force and whose crystallites show a large uniaxial anisotropy, is only slightly less than half the saturation value, as is theoretically to be expected. For the crystal-oriented sample the remanence measured in the preferred direction of the crystals differs little from the saturation magnetization. The mutual interaction of the magnetizations of the crystals has little effect since the crystallites of both samples are so small that most of them are single-domain particles (see also § 60).

§ 58. Constricted Hysteresis Loops and Magnetic Annealing

A special shape of the hysteresis loop is often found in polycrystalline samples of mixed crystals of ferrites with spinel structure if one of the components is cobalt ferrite. As an example, Fig. 58.1 shows loops as found for a number of rings of cobalt-ferrous ferrites $Co_\delta Fe^{II}_{1-\delta}Fe_2O_4$, which were slowly

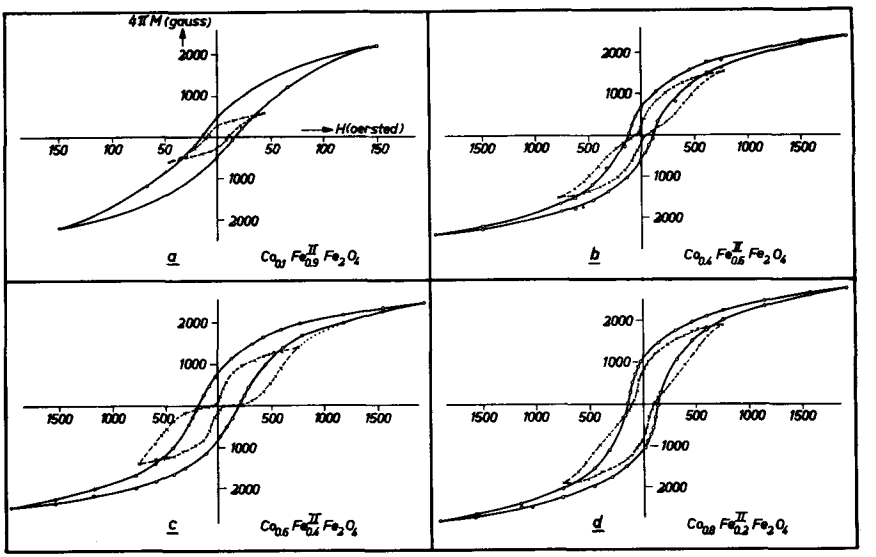

Fig. 58.1. Major and minor hysteresis loops for ferrites $Co_\delta Fe_{1-\delta}Fe_2O_4$ which have been cooled slowly in the absence of a magnetic field.

cooled to room temperature from above the Curie point (for the whole series of ferrites this temperature lies between 500 and 600 °C). In most samples the minor loops show a constriction near the origin. This is not found in the major loops. It is remarkable that the tips of the minor loop fall outside the major loop, which is equivalent to the fact that the virgin curve runs mainly outside the major loop, as indicated by the dotted curve in Fig. 58.1*c*. In these ferrites the virgin state is very stable. At small fields no hysteresis is found; at somewhat larger fields hysteresis phenomena appear, but when the field drops again to zero the virgin state is approximately restored. The difference as compared with ferrites containing no cobalt is probably that, during slow cooling, a very stable domain pattern arises owing to ionic diffusion. Rapid cooling, *i.e.* quenching, gives rise to normal loops; the time for diffusion seems in that case to have been too short. The Curie point of the compound must also be sufficiently high (higher than 150 to 200 °C) in order for the diffusion to be influenced by the magnetization. The family of hysteresis loops measured after slow cooling from the Curie point is in practice not influenced by demagnetization at room temperature by a field whose amplitude is gradually decreased. The shape of the minor loop changes with temperature, as can be seen in Fig. 58.2. Above room temperature the constriction in the loop is generally somewhat more pro-

nounced, but disappears at a temperature higher than 100 °C. At temperatures below 20 °C the constriction rapidly becomes smaller and vanishes at liquid-air temperature.

It is generally found that ferrites with constrictions in their hysteresis loops are sensitive to so-called magnetic annealing, that is to say the shape of the hysteresis loop changes when the ferrite, placed in a sufficiently strong magnetic field (a.c. or d.c.), is slowly cooled to room temperature from the Curie point. If one measures the hysteresis loop in fields which are parallel to the field present during cooling, one finds rectangular loops, both for a minor and for the major loop. Fig. 58.3 gives the loops found after the process of magnetic annealing in an a.c. field has been applied to the samples of Fig. 58.1. In some samples the rectangularity is so marked that a minor loop exists consisting of two lines which are approximately parallel to the H axis. The magnetization jumps discontinuously from the one to the other level when the magnetic field is gradually made only very little larger (less than 0.5%) than a certain critical value (see the solid curve in Fig. 58.4). A particular feature of these ferrites is that asymmetry with respect to the B axis (and sometimes also with respect to the H axis) is caused by annealing in a d.c. magnetic field; this is shown by the broken curve in Fig. 58.4. The fact that this heat treatment of cobalt-ferrous ferrites makes the hysteresis loop more rectangular was discovered by Kato and Takei

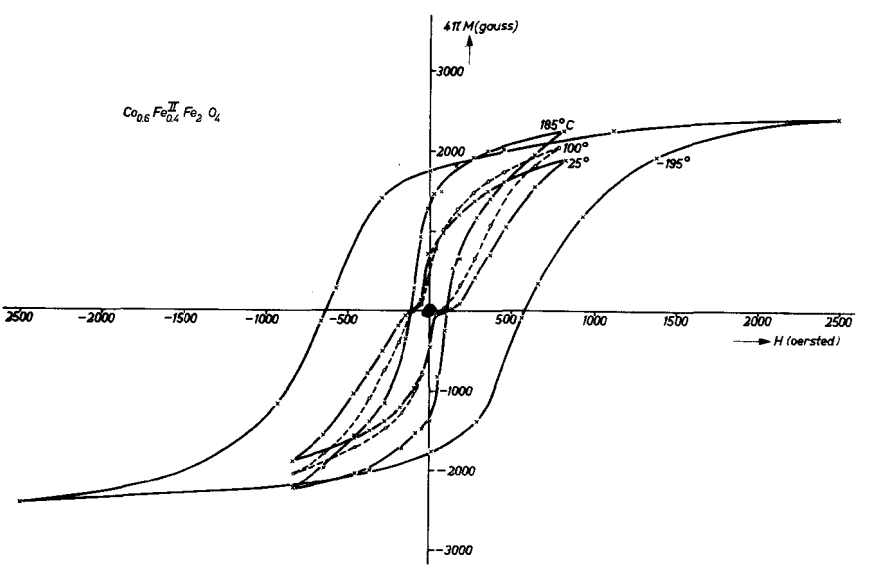

Fig. 58.2. Minor hysteresis loops of $Co_{0.6}Fe_{0.4}Fe_2O_4$, measured at various temperatures.

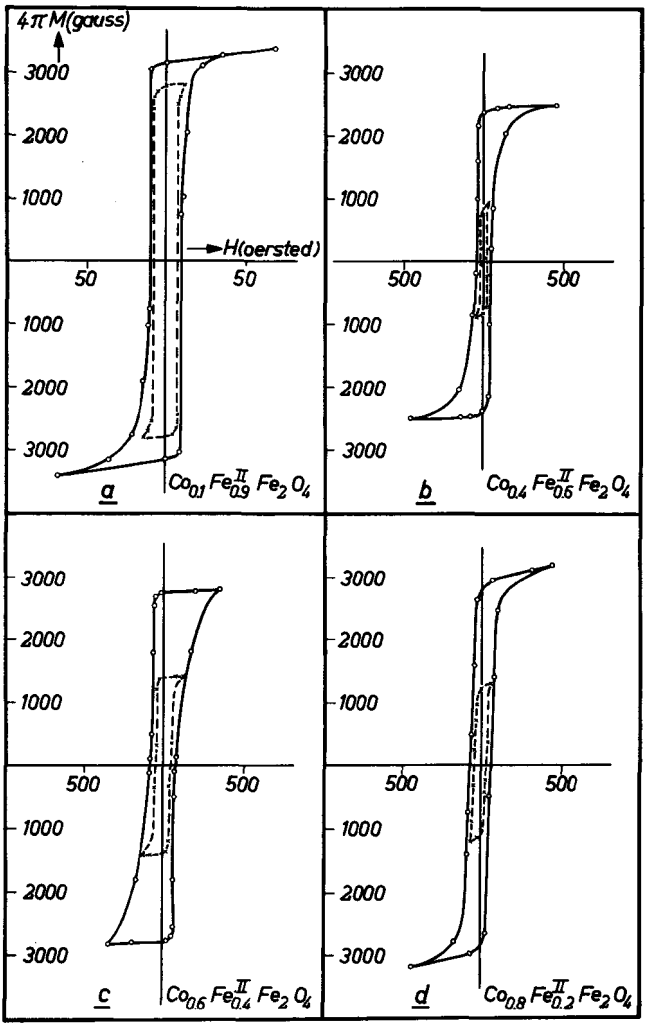

Fig. 58.3. Major and minor hysteresis loops for the same samples as those of Figs. 58.1, but now measured after magnetic annealing of the samples.

[Ka 3] and led to the development of a permanent magnetic material known as "Vectolite".

Many other ferrites having spinel structure, and a sufficiently high Curie point, and containing a small concentration of cobalt ions show a constricted hysteresis loop and are sensitive to magnetic annealing. Examples are ferrous-

manganese, ferrous nickel, ferrous magnesium and nickel-magnesium ferrites [Go 9] (see Fig. 58.5), magnesium-zinc ferrites [Ko 8] and nickel-zinc ferrites [Ec 2] which contain a small percentage of divalent cobalt. Bozorth [Bo 2] and Eckert [Ec 2] found that at 150 °C annealing effects still take place. The magnitude of the effects depends both on the temperature and on the duration of the treatment. The constriction of the loop and the phenomenon of magnetic annealing are both related to the uniaxial anisotropy discussed in § 43.2, which arises in the field-cooling of single crystals of ferrites containing cobalt and which is the result of a directional ordering of cobalt ions under the influence of the magnetization. If no external magnetic field is present, this ordering will still take place along the direction of the spontaneous magnetization in each domain. A non-180° wall will then be bound more rigidly to its equilibrium position since the ion ordering is along different directions in the adjacent Weiss domains (see [Ta 4]). In Fig. 58.6 the potential energy per cm² of a 90° wall is plotted as a function of its position for the case where a uniaxial anisotropy K is present in the adjacent domains in the direction of the magnetization. The ion ordering in the wall itself has also taken place along the direction of the spins in the wall. Normalized coordinates are used. The potential energy is expressed in $K\delta_w$ units, where δ_w is the wall thickness, and the displacement z is measured

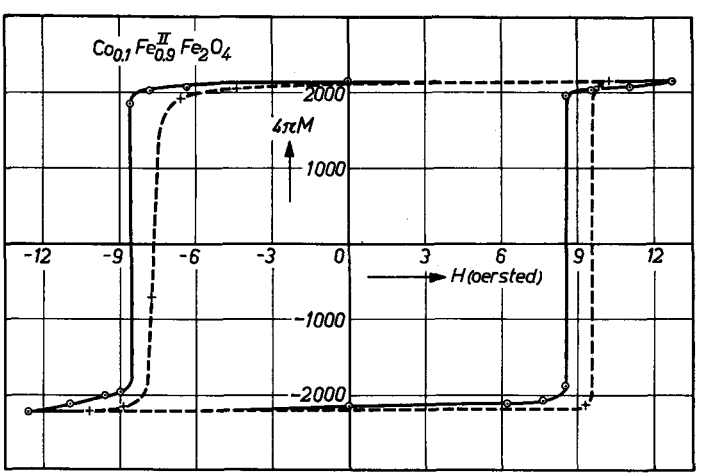

Fig. 58.4. The solid curve describes a rectangular minor hysteresis loop of $Co_{0.1}Fe_{0.9}Fe_2O_4$ after magnetic annealing in an a.c. field. A single large Barkhausen jump causes the magnetization to change sign. The broken curve shows the asymmetric curve obtained for the same ferrite after magnetic annealing in a d.c. field.

in δ_w units. For the directional distribution of the spins in the wall we assume for the sake of simplicity a linear relationship between ϕ and z instead of (15.3). It can be seen that no hysteresis occurs; as a result of this phenomenon the wall returns reversibly to the position of equilibrium. The broken curve in the figure shows the potential energy assuming that the ions have oriented themselves at the position of the wall at a higher temperature than the temperature at which the measurement was performed. It is assumed that the ion orientation in and near the wall corresponds to a wall thickness $2\delta_w$. For the case of a 180° wall the additional potential energy is represented in Fig. 58.7. The most important anisotropy effect caused by the directional ordering of the ions is now to be found in the wall itself. For wall-displacements over a distance which is small compared with the wall thickness the permeability will thus be small. If the wall has once been displaced by a large field over a distance equal to the thickness of a wall, it will be able, under the influence of this field, to cover a much greater distance. The coercive force for this irreversible wall-movement is determined by the maximum slope of the curve in Fig. 58.7. In order of magnitude this is equal to K/M_s. In the case of the sample in Fig. 58.1*c* the value of K can be derived from Fig. 34.4. From this one finds $H_c \simeq 10^4$ oersteds, which is much greater than found by experiment (the abnormal increase in the amplitude permeability takes place at about 500 oersteds). The phenomenon des-

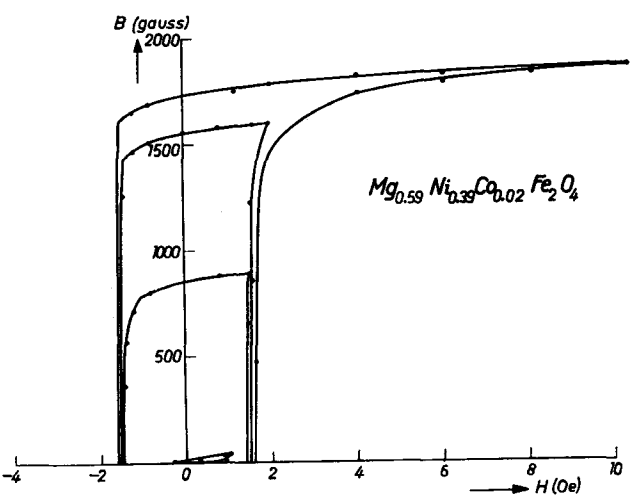

Fig. 58.5. A family of hysteresis loops of a ferrite $Mg_{0.59}Ni_{0.39}Co_{0.02}Fe_2O_4$ which has been annealed in a magnetic field.

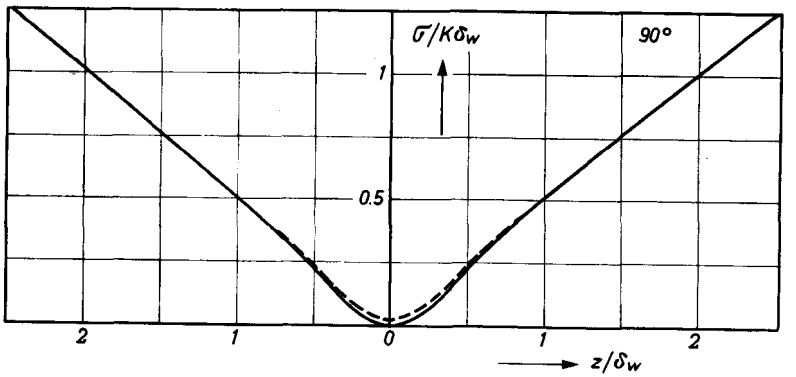

Fig. 58.6. The additional potential energy of a 90° wall as a result of a directional ordering of ions in the wall itself and in the adjacent domains where it causes a uniaxial anisotropy K along the direction of the magnetization. The potential energy and the position of the wall are expressed in units $K\delta_w$ and δ_w respectively, where δ_w is the wall thickness. The solid and the broken curve apply respectively to an ordering of the ions in the wall corresponding to the directional distribution of the magnetic moments and to the case where the ionic ordering in and near the wall corresponds to the directional distribution of the magnetic moments in a wall with thickness $2\delta_w$.

cribed occurs on an atomic scale and hence must influence all walls equally.

Since the walls are only in the deep potential wells in the demagnetized state, this wall pattern will be particularly stable, and this is reflected in the constriction in the hysteresis loop at a field $H = 0$ after this ferrite has only been partly magnetized. If the material is magnetized by such a strong field that the domain walls disappear, then it will be purely coincidental if the walls which form while this field returns to zero resume

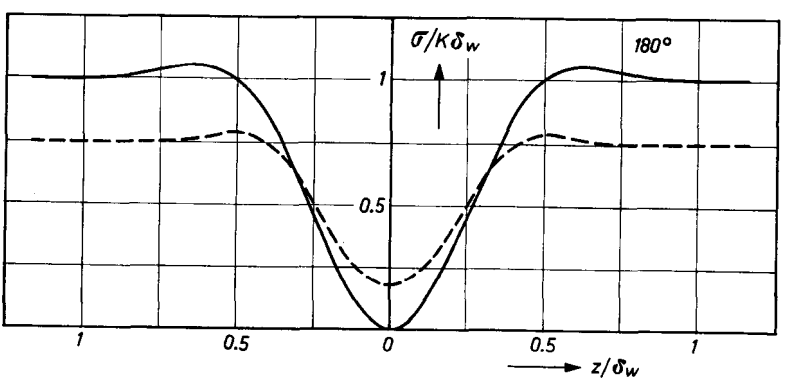

Fig. 58.7. The same as Fig. 58.6, but now for a 180° wall.

their former positions. The new domain pattern will generally be quite different from that originally obtained after demagnetization. A minor loop can thus have a constriction, the major loop cannot.

At low temperatures the domain walls are thinner than at the temperature at which the directional ordering of the ions took place as a result of diffusion, so that the ion ordering in the domain wall does not match the spin directions. On the other hand the other anisotropies which determine the hysteresis are usually larger at lower temperature. This may be the reason for the disappearance of the constriction in the loop at low temperatures. At high temperature, far above room temperature, the ordering changes during the measurement, as a result of which the constriction disappears in this case too. For a sample at a temperature of about 200 °C the change in the hysteresis loop with time can be followed on an oscilloscope, and a constriction originally present can be seen to disappear gradually. If the field is switched off for a while, the constriction reappears in about the same relaxation time as it took to disappear.

§ 59. Effect of Uniform Mechanical Stresses on the Form of the Hysteresis Loop

As described in § 49.1 and illustrated in Fig. 49.3, a sufficiently large uniform mechanical stress, either tensile or compressive, can bring about a special Weiss-domain configuration in ferrites. This influences the form of the hysteresis loop in a manner as illustrated in Fig. 59.1 for $Ni_{0.5}Zn_{0.5}Fe_2O_4$ ($\mu_0 \cong 220$ and $\lambda_s = -8 \times 10^{-6}$). Without external stress ($\sigma_e = 0$) a loop of normal shape is measured (the demagnetization measured on a rod is kept small by, for example, closing the magnetic flux with a yoke of a material having a high permeability). In the presence of a compressive stress the loop changes in such a way that the remanent magnetization increases; see the curves for compressive stresses σ_e from 2.5 to 5 kg/mm² in the Figure. If the compressive stress is so high that the stress anisotropy is predominant, the remanent magnetization measured in the direction of the rod axis will be equal to the saturation magnetization. A compressive stress makes the remanence smaller — see the broken curve in Fig. 59.1. The reason is that during the measurement of the hysteresis loop the magnetization is turned out of the preferred direction determined by the stress anisotropy, towards a direction at right angles thereto. In the extreme case where the tensile stress is so large that the stress anisotropy is predominant, a linear relationship without hysteresis would be found between magnetization and field strength. For field strengths of the order of magnitude of the coercive force

of the ferrite and larger, tensile and compressive stresses thus have an opposite influence on the amplitude permeability μ. At smaller field strengths the relation between permeability and tensile or compressive stress is somewhat more complicated, as described in § 49.2. The variation in the coercive force H_c, the low amplitude permeability and the relative remanent magnetization M_{rem}/M_{c1} with tensile and compressive stresses is shown in Fig. 49.5 for a polycrystalline sample of $Ni_{0.5}Zn_{0.5}Fe_2O_4$. The quantity M_{c1} denotes the magnetization at a field strength above which hysteresis phenomena no longer occur in the ferrite. In the case of ferrites with positive magnetostriction what is said above for compressive stresses applies to tensile stresses and *vice versa*. The extent to which the form of the hysteresis loop of a ferrite can be influenced by external stresses is further illustrated by the curves in Fig. 59.2. The polycrystalline ferrite ring (composition $Ni_{0.34}Zn_{0.66}Fe_2O_4$, $\mu_0 \cong 650$ and $\lambda_s = -4 \times 10^{-6}$) is surrounded by a ring of glass with a somewhat higher thermal expansion coefficient than the ferrite. When the glass ring is fitted around the ferrite ring at a high temperature, the ferrite after being cooled to room temperature will be subjected to a uniaxial tangential compressive stress. The figure shows that the hysteresis loops consequently become rectangular [Ra 4].

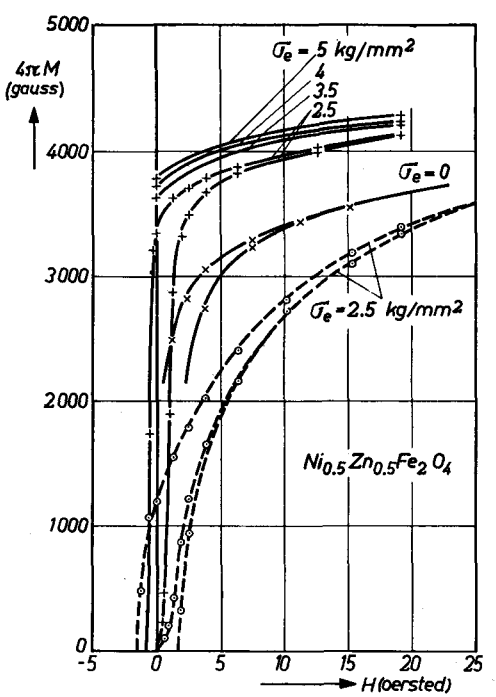

Fig. 59.1. The change in the hysteresis loop of a polycrystalline sample of $Ni_{0.5}Zn_{0.5}Fe_2O_4$ with negative magnetostriction when subjected to an external stress. The solid curves apply to different values of a compressive stress σ_e. The broken curve applies to a tensile stress $\sigma_e = 2.5$ kg/mm².

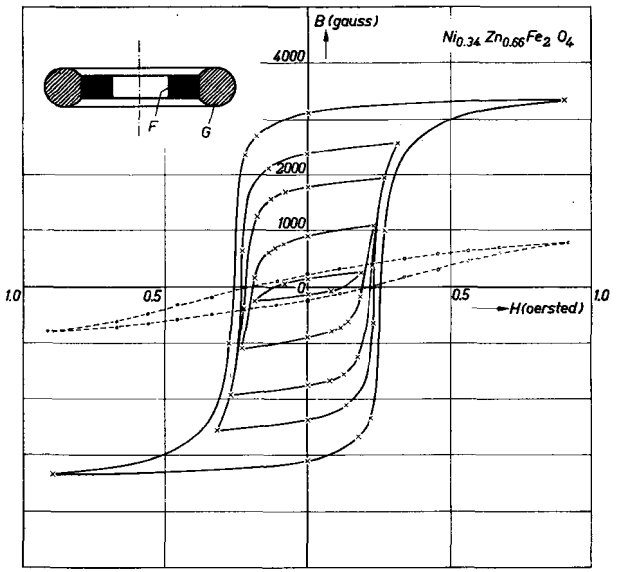

Fig. 59.2. Family of hysteresis loops for a glass-covered ferrite ring. The ferrite, with negative magnetostriction, is under a tangential compressive stress. For comparison the dotted curve represents a minor loop for the unstressed ferrite. The inset shows a cross-section of the glass-covered ferrite ring *F*, with glass *G*.

§ 60. Permanent Magnets

60.1. FIGURES OF MERIT FOR PERMANENT MAGNETS

Among the spinel ferrites containing cobalt, and in the series of ferromagnetic oxides with hexagonal crystal structure having the *c* axis as the preferred direction of magnetization, are found a number of compounds from which permanent magnets can be made. In order to make a comparison of various permanent magnetic materials, we shall first consider what characteristics in quantitative form are important for various applications.

(a) Generation of Magnetic Fields by Magnets

Making use of equation (2.4) with $\boldsymbol{a} \equiv \boldsymbol{H}$ and $\boldsymbol{b} \equiv \boldsymbol{B}$, we may write for systems in which the field is due to permanent magnets alone:

$$\int \boldsymbol{H}\boldsymbol{B}\,\mathrm{d}V = 0, \tag{60.1}$$

where integration is carried out over the total volume. Assuming that the

system consists of magnets plus "magnetically soft" materials and air, the integral (60.1) can be split into the following parts:

$$\int \boldsymbol{H}\,\boldsymbol{B}\,\mathrm{d}V = \int_{\text{magnet}} \boldsymbol{H}\,\boldsymbol{B}\,\mathrm{d}V + \int_{\text{air}} H^2\,\mathrm{d}V = 0,$$

since the contribution of the magnetically soft material ($H \cong 0$) can be neglected. For a given value of the volume integral over the air it follows that the required volume of magnetic material will be inversely proportional to the value of the product BH. The maximum value of this product can be taken as the figure of merit of the magnetic material for this type of application. In practice, at smaller values of $(BH)_{\max}$ the required magnetic volume will increase relatively more than $(BH)_{\max}$ decreases, since the extensiveness in space increases and therefore more ineffective space will be filled by stray fields.

(b) Attractive Forces of Magnets

For the magnitude of the forces which various magnetic systems exert on each other, as for example in sticking magnets, a different figure of merit should be used. This can be derived by calculating the work which must be done in order to bring about a small change in the configuration, as would be caused by the magnetic force. This energy consists of:

$$\delta A = \frac{1}{4\pi} \int_{\text{magnet}} \boldsymbol{H}\delta\boldsymbol{B}\mathrm{d}V + \frac{1}{8\pi}\,\delta \int_{\text{air}} H^2\,\mathrm{d}V, \tag{60.2}$$

where $\delta\boldsymbol{B}$ is the change in $\boldsymbol{B}$ in a fixed point of the magnet, while the last term is the change in the total integral. Let us now eliminate the contribution from air, so that δA is expressed only in quantities which refer to the magnet. For this purpose we make use of (60.1), remembering that the change in this integral due to the change in the configuration must then also be zero. This gives:

$$\int_{\text{magnet}} (\boldsymbol{H}\delta\boldsymbol{B} + \boldsymbol{B}\delta\boldsymbol{H})\,\mathrm{d}V + \delta \int_{\text{air}} H^2 \mathrm{d}V = 0. \tag{60.3}$$

Combining (60.2) and (60.3) gives

$$\delta A = \frac{1}{8\pi} \int_{\text{magnet}} (\boldsymbol{H}\delta\boldsymbol{B} - \boldsymbol{B}\delta\boldsymbol{H})\,\mathrm{d}V. \tag{60.4}$$

Assuming that the relation between B and H is linear, the magnitude of δA, except for the factor 8π, is given by the hatched area in Fig. 60.1. The maximum value of δA, which is a linear measure of the work that can be done by a magnet, is equal to $B_r H_m$, where H_m, is the maximum permissible

value of the field at which the magnet is still reversible. This product which, except for a factor 8π, represents the work to be performed in order to open a short-circuited magnetic system, we shall use as a figure of merit for magnets for these applications.

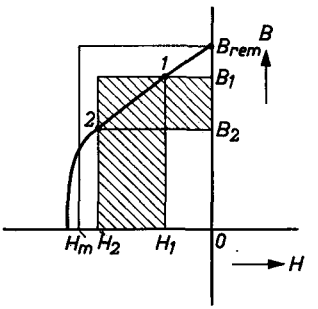

Fig. 60.1. The hatched area represents 8π times the work per cm³ of magnetic material needed for changing the configuration of a magnetic system so as to cause the working point to go from 1 to 2.

60.2. PERMANENT MAGNETIC PROPERTIES OF HEXAGONAL OXIDES

The origin of the permanent magnetic properties of some hexagonal oxides is to be found in the high value of the uniaxial anisotropy field H^A. In § 17 it was calculated that a field of the order of H^A is needed in order to cause an appreciable rotation of the magnetization vector in a Weiss domain. If the crystal is large enough to contain several Weiss domains, the movement of the walls will usually require a substantially lower field. A high coercive force can therefore be expected in these substances only when the crystallites consist of single Weiss domains. It is found that the crystals are mainly in the shape of platelets. For single domain behaviour the thickness must therefore be smaller than that which follows from (14.4). In the case of $BaFe_{12}O_{19}$ the wall energy is large because K_1 is large. Assuming a to be 3.10^{-8} cm, the wall energy is found according to (15.2) to be of the order of $\sigma_w \cong 5$ erg/cm². It then follows from (14.5) that the critical thickness of the platelets for single domain behaviour is $D_{cr} \cong 0.5 \times 10^{-4}$ cm; this is much larger than the wall thickness, which is approximately 2×10^{-6} cm. Samples having grains of about 1 micron or smaller consequently have a large coercive force, whereas a material having grains of about 10 micron in diameter or more have a low coercive force (Fig. 60.2). Since the quantities that determine the critical diameter (14.5) depend on the temperature, the critical diameter will also be temperature-dependent. One finds

$$D_{cr} \propto \sqrt{K_1}/M_s, \tag{60.5}$$

it being assumed that the exchange energy, in agreement with the Weiss-field theory of ferromagnetism, varies with temperature as M_s^2 does. The quantity $\sqrt{K_1}/M_s$ for $BaFe_{12}O_{19}$ is shown as a function of temperature in Fig. 60.3. As can be seen, it increases by almost a factor of 2 going from low to high temperatures. This is in agreement with the variation of the coercive force as a function of temperature (Fig. 60.4); at low temperature

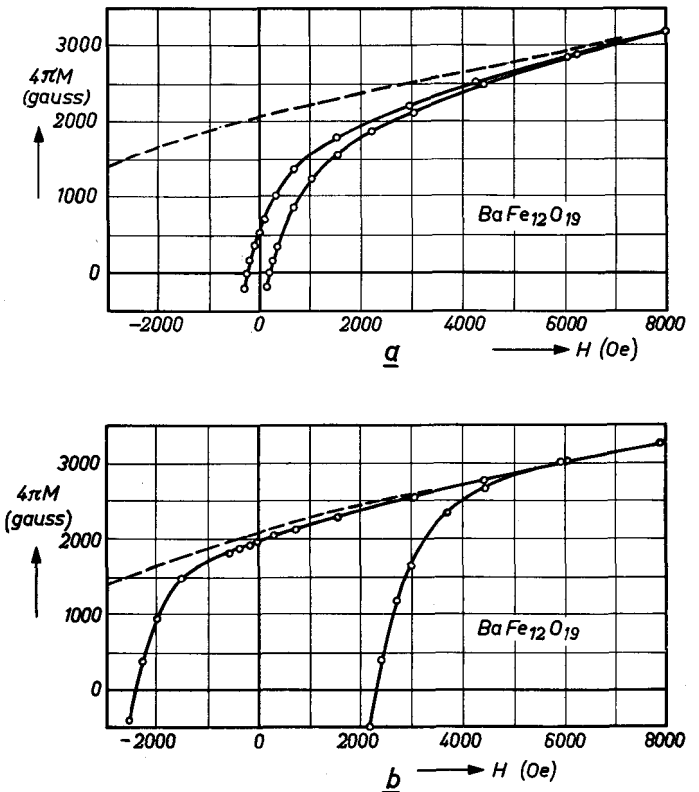

Fig. 60.2. Hysteresis loops at room temperature of $BaFe_{12}O_{19}$ with random crystal orientation, sintered at 1350 and 1400 °C, so that the average grain sizes are about 10 and 1 microns, respectively. After [Ra 7]. Dashed: demagnetization curves for pure rotation.

some wall formation still occurs, which reduces the coercive force. Stoner and Wohlfahrth [St 5] have calculated the magnetization curves for pure rotational processes, neglecting the interaction between the grains. The demagnetization curves according to this model are given by the broken lines in the Figures 60.2. The corresponding coercive force (in this case the field strength at which $M = 0$) is 0.96 K_1/M for random orientation of the crystals. In the case of $BaFe_{12}O_{19}$ at room temperature, this would be approximately 8000 oersteds. The fact that the coercive force found by experiment is smaller is probably attributable to the formation of walls in a negative field. It seems therefore desirable to make the grains even smaller (by longer milling of the powder). It is found, however, that in that case the

coercive force again decreases, probably owing to plastic deformation of the grains; this can be eliminated by annealing at 1000 °C, at which temperature no noticeable sintering takes place (see Table 60.I).

TABLE 60.I

DEPENDENCE OF THE COERCIVE FORCE OF A POWDER OF $BaFe_{12}O_{19}$ ON THE MILLING TIME AND HEAT TREATMENT.

Milling time in hours	${}_MH_c$ oersteds
0	100
2	500
4	700
8	1000
18	1570
38	1600

Additional heat treatment of 1 hour in air at various temperatures

Temperature °C	${}_MH_c$ oersteds
200	1600
700	1900
1000	3400
1100	3900
1200	3440

The high coercive force in Table 60.I can occur only in loose powders. In denser materials the tiny grains have grown as a result of the sintering process into bigger units, in which walls are formed. Moreover in dense materials the interaction between neighbouring grains cannot be neglected, so that a correlation between the Weiss domain patterns occurs (*e.g.* walls do not stop at the boundary between two grains). Thus with the formation

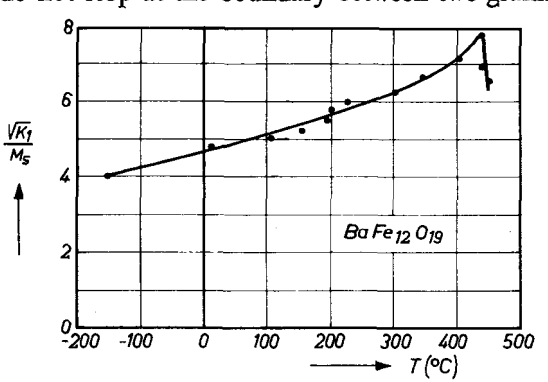

Fig. 60.3. The quantity $\sqrt{K_1}/M_s$ of $BaFe_{12}O_{19}$ as a function of temperature. This quantity is proportional to the critical diameter for single-domain behaviour. After [Ra 6].

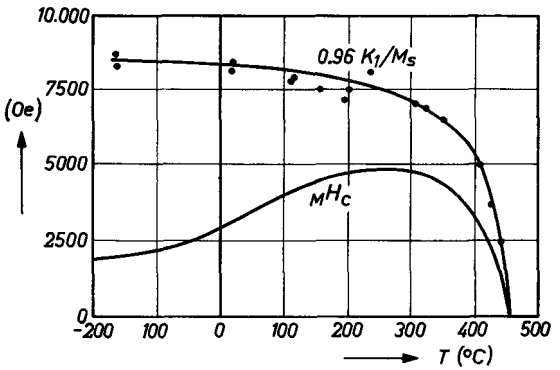

Fig. 60.4. The intrinsic coercive force ${}_{M}H_c$ as measured for fine-grained $BaFe_{12}O_{19}$ as a function of temperature, compared with the quantity $0.96\ K_1/M_s$.

of a wall more energy is gained than without this interaction, and consequently walls will already occur in smaller grains. It can be seen that a certain degree of porosity is indispensable.

For practical purposes the B-H curve of permanent magnetic material is of prime importance. In the case of high-coercive materials, where H_c is at least of the order of magnitude of B_r (for example the hexagonal compounds with uniaxial anisotropy) the B-H curve differs essentially from the $4\pi M$-H curve. For instance, ${}_{B}H_c$ can never be larger than B_r. As shown in Table 57.I, $M_r/M_s = {}^1/_2$ for the polycrystalline material with random crystal orientation. The quantities $(BH)_{\max}$ or $B_rH_m = B_rH_c$ can thus be increased by orienting the crystallites, resulting approximately in $M_r \simeq M_s$. The figures of merit mentioned can then rise by a maximum factor of 4. This orientation in a magnetic field during the pressing process is described in § 44. A drawback to this orientation is that it promotes the formation of Weiss domains, owing to the fact that the preferred direction of magnetization (c axis) in adjacent grains has approximately the same orientation, so that Weiss domains can easily continue from one crystal to the other and there is thus a danger that the graininess of the material, which should be the reason for the absence of domain walls, will be lost. A high remanence is thus associated with a low coercive force. A microphotograph of a cross-section parallel to the c axes of the crystals of a sample having large crystals is shown in Fig. 14.6. A deposition of a colloidal solution of Fe_3O_4 powder marks the position of the domain walls. Examples of the $4\pi M$-H curves and demagnetization curves for both an isotropic and a crystal-oriented sample of $BaFe_{12}O_{19}$ are given in Figs. 60.5 and 60.6. The corresponding figures of merit are given in Table 60.II. Comparable results can be obtained with compounds of the W structure; for example an isotropic permanent magnet of Fe_2^{II} W can have a value of $(BH)_{\max} = 10^6$ gauss oersted. The

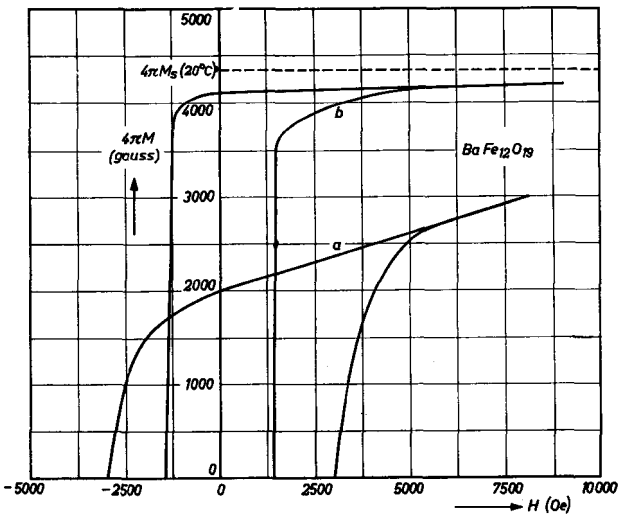

Fig. 60.5. Hysteresis curves of $BaFe_{12}O_{19}$ for *a*) isotropic and *b*) crystal-oriented magnets of $BaFe_{12}O_{19}$.

TABLE 60.II

SOME FIGURES OF MERIT OF PERMANENT MAGNETS OF $BaFe_{12}O_{19}$.

Polycrystalline sample	B_r gauss	${}_MH_c$ oersted	${}_BH_c$ oersted	$(BH)_{max}$ gauss oersted	B_rH_m gauss oersted
isotropic	2000	3000	1650	$0.8 \cdot 10^6$	$3.3 \cdot 10^6$
crystal-oriented	4080	1450	1360	$3.0 \cdot 10^6$	$5 \cdot 10^6$

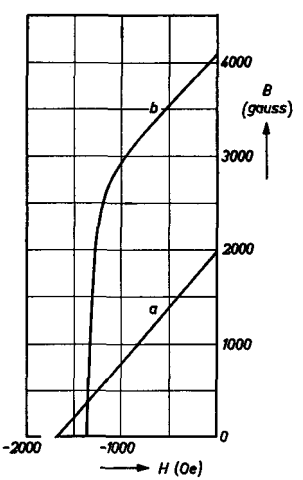

Fig. 60.6. Demagnetization curves of the magnets in Fig. 60.5.

saturation magnetization at room temperature of this compound is about 8% higher than that of $BaFe_{12}O_{19}$, which is important for obtaining optimum properties.

The highest value of $(BH)_{max}$ theoretically to be expected for a material corresponds to a remanence $M_r = M_s$ and an infinite coercive force. This can only occur in the impossible case of ideally oriented crystals without mutual interaction, and moreover with a sample having no porosity. For $BaFe_{12}O_{19}$ in this case, $(BH)_{max} = {}^1/_4(4\pi M_s)^2 = 6.10^6$ gauss oersted.

A useful property of these oxide magnets is that the coercive force is comparable with the remanence. This allows a considerable free-

dom in the shape of the magnets, since demagnetizing fields will not irreversibly demagnetize the magnet. This applies particularly to the unoriented material, where ${}_{M}H_c > {}_{B}H_c$. A further consequence of the large crystal anisotropy is that the susceptibility is small both perpendicular and parallel to the c axis (about 1.4).

CHAPTER XVI

DYNAMIC PROPERTIES AT HIGH FIELD STRENGTHS

§ 61. Hysteresis Losses and Distortion in the Rayleigh Region

61.1. HYSTERESIS RESISTANCE AND DISTORTION

The distortion caused in a network by a coil containing a ferromagnetic core is a consequence of the non-linear relation between the induction B and the field strength H in the core. This non-linearity can have two reasons:

(a) The induction B is a single-valued non-linear function of H

The function $B(H)$, then, has the origin ($H = 0$, $B = 0$) as point of symmetry, so that $B(H) = -B(-H)$. For small values of H the function $B(H)$ can be expanded into a series:

$$B(H) = \mu_0 H + \nu H^3 + \lambda H^5 + \ldots, \tag{61.1}$$

from which it follows that for a sinusoidal field ($H = H_{\max}\cos \omega t$) the distortion $D = V_3/V_1$ is proportional to $H_{\max}^2$ (where V_1 and V_3 are respectively the fundamental and third harmonics of the voltage across a coil with ferromagnetic core when a sinusoidal current passes through the coil).

(b) Hysteresis

When the induction in the core is not a single-valued function of H, hysteresis phenomena will occur. The simplest representation of the lower branch (1) of the hysteresis loop of Fig. 61.1 is given by the equation:

$$b(h) = \mu_0 h + \nu h^2, \tag{61.2}$$

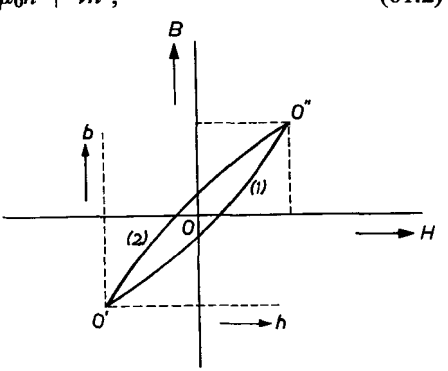

Fig. 61.1. Hysteresis loop at low induction consisting of two quadratic curves.

the point O′ being the origin of the coordinates b and h. To the upper branch (2) an analogous equation applies, with reference to a coordinate system having O'' as its origin. After a simple transposition to coordinates B and H with O as origin, both branches are represented by the expression:

$$B(H) = \pm\nu H_{\max}^2 + (\mu_0 + 2\nu H_{\max})H \mp \nu H^2, \tag{61.3}$$

the upper signs referring to the upper branch of the hysteresis loop. It should be noted in this connection that, in principle, the coefficients μ_0 and ν can be a function of $H_{\max}$. In the case of a sinusoidal field $H = H_{\max}\cos\omega t$, the distortion $D = V_3/V_1$ will be proportional to $H_{\max}$ (in as much as μ_0 and ν do not depend on $H_{\max}$). In ferromagnetic materials there is practically always some hysteresis, so that where the field strengths are sufficiently small the distortion is entirely caused by this hysteresis and not by the non-linear character of the B-H curves [Pe 2]. The energy dissipated per cycle and per unit of volume is according to (2.2) proportional to the area of the hysteresis loop:

$$W = (1/4\pi)\int H\,\mathrm{d}B \text{ erg.} \tag{61.4}$$

Integration of the two series (61.3) yields for (61.4) the result:

$$W = (2/3\pi)\nu H_{\max}^3 + \ldots \tag{61.5}$$

It appears, then, that the hysteresis losses per period and per cm³ of material are proportional in first approximation to the third power of the amplitude of the field strength. The total heat per second generated in a core by hysteresis is:

$$W = (2/3\pi)\nu H_{\max}^3 f V \text{ erg}, \tag{61.6}$$

where f is the frequency of the applied field and V the volume of the core in cm³. We can now define a hysteresis resistance R_h by $W = I_{\text{eff}}^2 R_h$, hence according to (61.4)

$$R_h = (4\sqrt{2}/3\pi)\nu c_1^3 I_{\text{eff}} f V\, 10^{-7} \text{ ohm}, \tag{61.7}$$

where the geometric factor c_1 denotes the relation between coil current and the magnetic field strength in the core: $H_{\max} = c_1 I_{\max}$. For a toroidal core with cross-section A and mean diameter d_m, and provided with N turns, one finds:

$$\begin{aligned} &c_1 = (0.4\,N)/d_m \quad \text{and} \quad V = \pi A\, d_m. \\ &R_h = (1.21/d_m^2)N^3 A f I_{\text{eff}}\, \nu \cdot 10^{-8} \text{ ohm}. \end{aligned} \tag{61.8}$$

The distortion caused by the core can be brought into relation with the hysteresis resistance given in (61.7). In the case of sinusoidal fields ($H =$

$H_{max} \cos \omega t$) of small amplitude, equation (61.3) becomes:

$$B(t) = (\mu_0 + 2\nu H_{max})H_{max} \cos \omega t \pm \nu H^2_{max} \sin^2 \omega t =$$

$$= (\mu_0 + 2\nu H_{max})H_{max} \cos \omega t +$$

$$+ (8/\pi)\nu H^2_{max}\left(\frac{\sin \omega t}{1.3} - \frac{\sin 3\omega t}{1.3.5} - \frac{\sin 5\omega t}{1.3.5.7} - \cdots\right).$$

The induction is directly related to the voltage across the coil:

$$10^8 E/c_2 = -\mathrm{d}B(t)/\mathrm{d}t = (\mu_0 + 2\nu H_{max})\omega H_{max} \sin \omega t +$$

$$- (8/\pi)\nu\omega H^2_{max}(\tfrac{1}{3} \cos \omega t - \tfrac{1}{5} \cos 3\omega t - \cdots), \qquad (61.9)$$

where c_2 is again a constant depending on the core and coil dimensions. The loss factor $\tan\delta_h$ that determines the hysteresis losses in the coil is defined as:

$$\tan \delta_h = \frac{8\nu H_{max}}{3\pi(\mu_0 + 2\nu H_{max})}, \qquad (61.10)$$

and the distortion D is:

$$D = V_3/V_1 = \frac{8\nu H_{max}}{5\pi(\mu_0 + 2\nu H_{max})}. \qquad (61.11)$$

From (61.9) and (61.10) follows the simple relation:

$$D = 0.6 \tan\delta_h = 0.6\, R_h/\omega L, \qquad (61.12)$$

in which L is the self-inductance of the coil with core. From (61.9) the relation between the reactance of the coil with core ($X = \omega L$) and the hysteresis resistance R_h is found to be

$$X = \omega\mu_0 c_1 c_2 + (3\pi/4)R_h. \qquad (61.13)$$

The resistance of a coil containing a ferromagnetic core is often plotted as a function of the appertaining hysteresis resistance R_h for different values of H_{max}; this is done in Fig. 61.2. If μ_0 is independent of H_{max}, the relation between both quantities (each measured as a function of the coil current) is given by a straight line which makes an angle β of 23° with the ordinate. If the relation (61.13) applies, it is then said that the material satisfies Rayleigh's law. Lord Rayleigh found that μ_0 and ν in several iron samples are independent of H_{max} when the samples are magnetized to about 1% of the saturation magnetization. In the case of ferrites, equation (61.13) does not apply. The angle β is always smaller than the Rayleigh value. For a polycrystalline ferrite $Mn_{0.5}Zn_{0.5}Fe_2O_4$ ($\mu_0 = 1090$) the loss factor $\tan\delta$ and

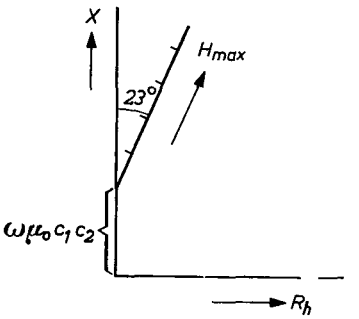

Fig. 61.2. The reactance X as a function of the hysteresis resistance R_h in the case where the core material obeys Rayleigh's law. The straight line carries a linear magnetizing-force scale.

the selectively measured distortion V_3/V_1 (see § 62) are given in Fig. 61.3 as a function of the amplitude $H_{\max}$ of a sinusoidal measuring-field having a frequency of 2 kc/s. Both quantities are seen to be linearly dependent on the field strength up to about 30 millioersteds, as expected according to (61.10) and (61.11). The relation (61.12) holds fairly well, especially for low values of $H_{\max}$, as can be seen from the comparison of the dashed curve, giving 0.6 $\tan\delta_h$, with the curve for V_3/V_1. At higher field strengths, however, the field-dependent contribution to the loss factor, ($\tan\delta - \tan\delta_r$), seems to be not only the consequence of hysteresis. The discrepancy between distortion and hysteresis losses is generally found to be larger the higher is the measuring frequency. In Figs. 62.1 and 62.2 it is shown that in the case of a ferrite with high initial permeability, the magnetization curves and the distortion depend on the frequency. The selectively measured distortion becomes smaller at higher frequencies, but the field-dependent part of the loss factor generally becomes larger [Sm 4].

61.2. HYSTERESIS CONSTANTS

As appears from the foregoing, in order to calculate the hysteresis resistance

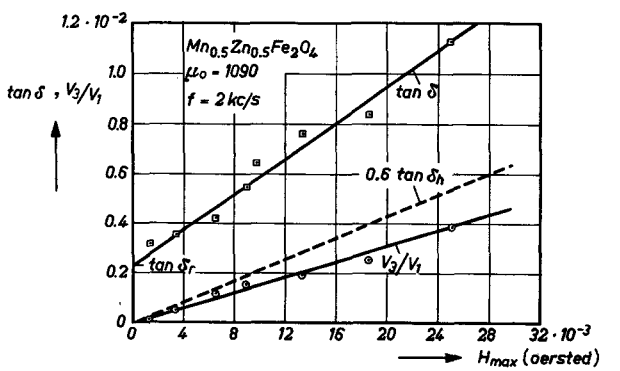

Fig. 61.3. The loss factor $\tan\delta$ and the selectively measured distortion V_3/V_1 as a function of the amplitude H_{max} of a sinusoidally varying measuring-field. The broken curve indicates the distortion calculated with (61.12) from the hysteresis losses.

or the distortion of a coil containing a ferromagnetic core it is necessary to know the quantities μ_0 and ν of the core material as a function of H_{max}, together with the dimensions of the core and the number of turns around the coil, comprised in the constants c_1 and c_2. Where the core material obeys Rayleigh's law, that is where μ_0 and ν are independent of H_{max}, a hysteresis constant of the core material can be given by means of which the hysteresis resistance and the distortion of the coil with core can be determined as a function of the coil current at a given value of self-inductance. This simplifies the comparison of various core materials to be used for the same purpose, and it also simplifies the calculation of hysteresis losses or distortion when cores with air gaps are used. In the latter case the relations (61.6) or (61.11) are complicated, since H_{max} then refers to the internal magnetic fields.

Hysteresis constant a

Legg [Le 1] introduced a hysteresis constant a according to the equation*):

$$(\tan\delta_h)/\mu_0 = a\, B_{max}/2\pi, \tag{61.18}$$

where B_{max} is the maximum induction in the core for a sinusoidal magnetic field in the core with amplitude H_{max}. From (61.10) it follows that for small field-strengths ($\nu H_{max} \ll \mu_0$) and at constant frequency, the hysteresis loss factor $\tan\delta_h$ ($= R_h/2\pi fL$) is proportional to the induction in the core. Since the quantity $(\tan\delta)/\mu$ undergoes, to the first approximation, no change when an air gap is introduced in the core, see (28.8), the hysteresis constant a in (61.18) will also not depend on air gaps, and it is related to μ_0 and ν:

$$a = \frac{16}{3}\,\frac{\nu}{\mu_0^3} \tag{61.19}$$

It will be clear that the hysteresis constant according to (61.18) cannot reasonably be introduced unless it is independent of B_{max}. Apart from a very special case, however, this condition is fulfilled only if ν and μ_0 are independent of B_{max}, which means that the hysteresis constant can only be introduced for those substances that obey Rayleigh's law; only in those cases is a a material constant.

One can find the relation between the distortion V_3/V_1 and the hysteresis constant a for a ring-shaped core of constant cross-section, in which an air

*) The symbols c_h and C_h are also used, being defined as:

$$c_h = a$$
$$C_h = 10^6.a$$

gap is introduced at right-angles to the magnetic lines of force. It is assumed that the air gap is small enough to allow the stray magnetic flux to be neglected, so that the induction in the core is homogeneous and the core volume is given in good approximation by $V = \pi A d_{\text{mean}}$. Let μ_{app} be the apparent permeability of the core with air gap, then from (61.18) we get:

$$R_h = aLf\mu^2_{\text{app}} c_1 I_{\max} \text{ ohm},$$

which can also be written as:

$$R_h = 0.2\sqrt{10\pi}\, a \frac{L\sqrt{L}}{\sqrt{V}} . f . \mu^{3/2}_{\text{app}} . I_{\max} . 10^4 \text{ ohm}. \tag{61.21}$$

This in combination with (61.12) yields:

$$D = 600\sqrt{10\pi}\sqrt{L/V}\, a\, \mu^{3/2}_{\text{app}} \cdot I_{\max}. \tag{61.22}$$

This equation can be read in the following way. What is wanted in a small volume V is a large self-inductance L with low losses, such that the loss angle δ is small. For this purpose a particular core material is selected and an air gap is introduced such that the loss factor $(\tan\delta)_{\text{app}}$ of the coil with core is sufficiently low at a given frequency or in a given frequency band. From the apparent value of the permeability and the values L and V one can now, with the aid of (61.22), calculate the expected third harmonic components in the voltage as a function of the coil current, given the hysteresis constant a of the core material. Equation (61.22) indicates that the hysteresis constant a is a particularly good measure for comparing core materials as regards the distortion which they will cause in circuits. In cores of various magnetic materials but of the same dimensions (same value of V), air gaps can be introduced in such a way that μ_{app} will be the same for all cores. The quantity a then gives directly the ratio between the amounts of distortion caused by the various cores for equal coils and coil currents. The hysteresis constant a can best be measured on an a.c. bridge (*e.g.* Maxwell bridge, see § 28.2) on which L and R_h of a coil with core can be determined as a function of the current $I_{\max}$. The core should then preferably have no air gap, so that μ_{app} will be equal to the known true initial permeability of the material.

Hysteresis Constants h and q_2

Another method of introducing a hysteresis constant has been worked out by Jordan [Jo 8]. He introduced the quantity h, which represents the ratio of the equivalent hysteresis loss-resistance R_h to the self-inductance L of a coil containing a ferromagnetic core, if both are measured at a frequency

of 800 c/s and at a magnetic field-strength corresponding to 1 ampere turn per cm core length:

$$R_h/L = h, \text{ when } f = 800 \text{ c/s and } (N/l) \cdot I_{\text{eff}} = 1 \text{ A/cm}. \quad (61.23)$$

According to (61.7) it follows from this, for an arbitrary frequency f and an arbitrary field strength, corresponding to a current I_{eff} that:

$$R_h/L = h(N/l)I_{\text{eff}}f/800.$$

Brought into relation with (61.10) this gives for the hysteresis constant h the expression:

$$h = 750\, \nu/\mu_0. \quad (61.24)$$

A reference frequency of 1000 c/s is also often used, resulting in a different value for the hysteresis constant h of a magnetic core.

For loading coils for telephony applications the quality-factor q_2 is used for determining the amount of distortion. In conformity with the requirements of the C.C.I.F. [Co 2], q_2 is defined as the increase of the resistance of a coil with core, having a self-inductance of 1 henry, when the coil current is increased from 1 to 2 mA. This increase is measured at a frequency of 800 c/s. Table 61.I gives the relation between the various hysteresis constants in use for magnetic cores, and also their connection with the quantities μ_0 and ν. The indices of q_2 indicate that this quality factor is given for a core with a uniform cross-section having a volume of 24 cm^3 and an apparent permeability of 100 (these were once the usual figures for loading coils). The lowest values of hysteresis constants can be achieved in the case of magnetically very soft manganese-zinc ferrites with spinel structure, where for instance $a < 0.5 \cdot 10^{-6}$ (or $q_{\substack{2.800 \\ 24.100}} < 1$).

TABLE 61.I

RELATION BETWEEN THE VARIOUS HYSTERESIS CONSTANTS USED IN LITERATURE.

$a = (16/3)\nu/\mu_0^3$	$= 0.71 \cdot 10^3 h/\mu_0^2$	$= 0.39 \cdot 10^{-6}\, q_{\substack{2.800 \\ 24.100}}$	
$h = 750\, \nu/\mu_0$	$= 1.4 \cdot 10^3\, \mu_0^2 a$	$= 0.54 \cdot 10^{-3}\, \mu_0^2 q_{\substack{2.800 \\ 24.100}}$	
$q_{\substack{2.800 \\ 24.100}} = 13.8 \cdot 10^6\, \nu/\mu_0^3$	$= 2.6 \cdot 10^6\, a$	$= 1.85 \cdot 10^3\, h/\mu_0^2$	

§ 62. Frequency-Dependence of the Magnetization Curve

The single-valued function which gives the relation between the amplitude $H_{\max}$ of a sinusoidal magnetic field and the maximum value $B_{\max}$ of the induction in a ferrite core will be called the alternating current magnetiza-

tion curve of the ferrite at a fixed frequency of the field H. This definition is only useful for materials having a high resistivity, as the a.c. magnetization curve is otherwise highly influenced by eddy currents, depending on the dimensions of the sample. Measurements at high inductions and under continuous-wave conditions have been made on ferrites with spinel structure to a frequency of 1.5 Mc/s. It is found [Wi 7] that ferrites with high initial permeability ($\mu_0 > 400$) have frequency-dependent magnetization curves in a frequency range below that of the ferromagnetic resonance. As an example Fig. 62.1 shows the data for a manganese ferrite with spinel structure (43.5 mol% MnO, balance Fe_2O_3 + FeO; initial permeability $\mu_0 = 860$; ferromagnetic resonance frequency about 5 Mc/s). The inset shows the change with frequency for the amplitude permeability μ at $H_{max} = 0.6$ oersted. An obvious interpretation of this behaviour is that there are two magnetization processes. One process which gives rise to μ_0 is frequency-independent up to at least 626 kc/s, and a second process makes an important contribution to the magnetization at field strengths of about the coercive force. This second process is already very frequency-dependent from 100 kc/s onwards.

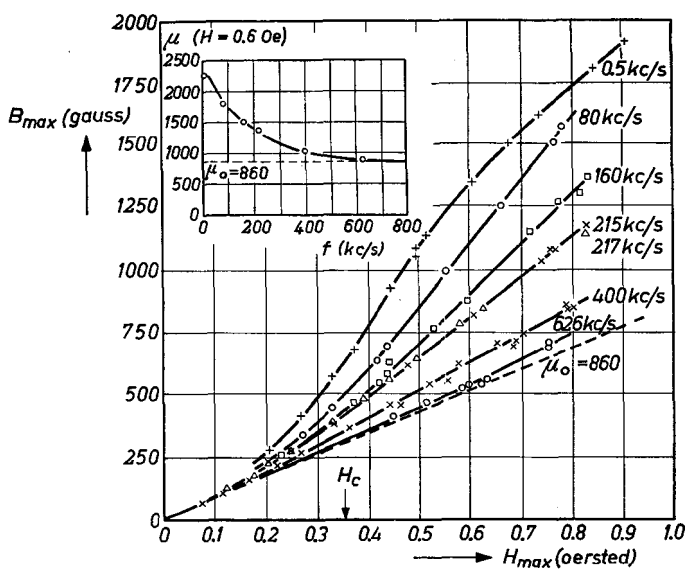

Fig. 62.1. Magnetization curves of a manganese-ferrous ferrite with spinel structure (43.5 mol % MnO balance Fe_2O_3 + FeO). Inset: the amplitude permeability μ for $H_{max} = 0.6$ oersted as a function of frequency.

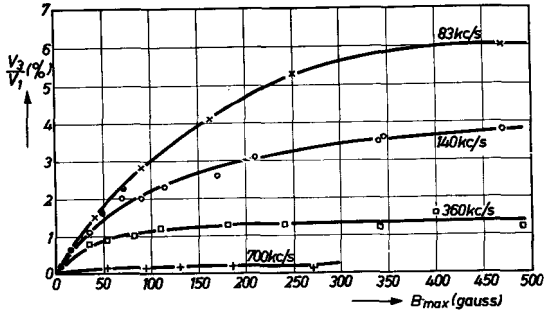

Fig. 62.2. The distortion V_3/V_1 *versus* the maximum value of the induction B_{max} caused by a sinusoidally varying field strength in a core of the ferrite of Fig. 62.1. The encircled crosses represent the distortion calculated according to (61.12) from the hysteresis resistance at a frequency of 2 kc/s.

We shall define the distortion of a core material as the ratio of the amplitudes of the third harmonic V_3 and the fundamental V_1 of the secondary voltage of an open transformer completely filled with this core material, when the primary current is sinusoidal. The distortion measurement provides information on the loop that gives the relation between the field strength and the induction in the core during one period of the sinusoidal field H. It is to be expected that this loop will also depend on frequency when the magnetization curve does. Fig. 62.2 gives for the manganese ferrite of Fig. 62.1 the results of the distortion measurements at four frequencies. It is seen that this quantity depends very much on frequency, being almost absent at 700 kc/s. Thus the shape of the hysteresis loop for this ferrite must likewise change with frequency: at low frequency it is the well-known loop with sharp tips, whereas at high frequency B is a linear function of H and only a phase shift between the two can occur, giving rise to an elliptical loop.

In ferrites for which the initial permeability is lower than about 400, little or no dispersion in the a.c. magnetization curve is found in this range of frequencies and field strengths, if they are sintered at the relatively low temperature of 1250 °C. When fired at about 1450 °C the porosity of the material is lower and a much larger ratio μ_{max}/μ_0 is found; compare, for instance, the low-frequency curves in Fig. 62.3*a* and *b*. This additional contribution to the magnetization at field-strengths of the order of magnitude of the coercive force appears to have a frequency dependence similar to that shown in Fig. 62.1. The distortion curves for these ferrites are given in Fig. 62.4*a* and *b*. The three curves in Fig. 62.4*b* are similar to those for a ferrite having a high initial permeability, but with one exception, namely

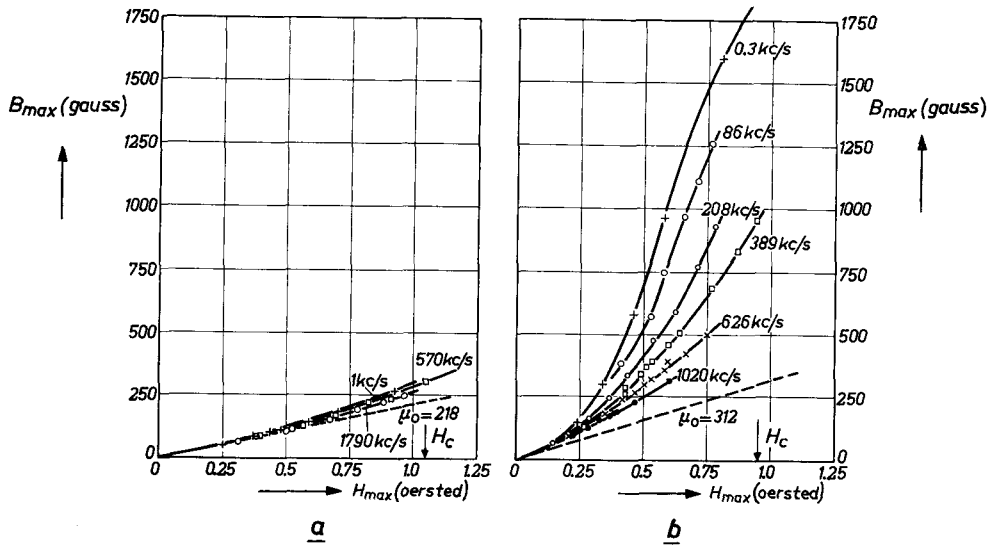

Fig. 62.3. *a*) Magnetization curves of $Ni_{0.5}Zn_{0.5}Fe_2O_4$ fired at 1250 °C in oxygen. *b*) Magnetization curve of the same ferrite after additional firing at 1450 °C in oxygen.

that, besides the frequency-dependent distortion, a frequency-independent distortion arises at low inductions. At 590 kc/s the distortion curve is easily divided into two parts, given by the curves *OA* and *ODE*. Subtracting the distortion given by the curve *ODE* from the measured curves at 80 and 360 kc/s we get the dotted lines *OA'* and *OA''* in the figure. It is to be concluded that the distortion caused by ferrites sintered at relatively high temperature (*e.g.* 1450 °C) is brought about by two magnetization processes. The exceptionally high distortion at low inductions seems to be caused by the fact that the high-temperature firing is done in a reducing atmosphere. A large distortion is also found [Sm 4] for a nickel ferrite fired at the relatively low temperature of 1050 °C but in an atmosphere of CO_2, which should be considered as a reducing atmosphere for the ferrite at this temperature. It seems that the distortion caused by a ferrite core at low inductions depends to a great extent on the presence of ferrous ions.

Microscopic eddy-currents might be the cause of the damping. It is known that the high-frequency level of the resistivity of ferrites is often much smaller than the d.c. resistivity (see § 46.1). However, it appears that the dispersion in the magnetization curve takes place in the same frequency region for ferrites for which the high-frequency resistivity is varied by a factor of 10^6. Moreover a calculation of this micro eddy-current effect results in a much higher relaxation frequency than is found experimentally.

A damping of the irreversible domain-wall displacements by eddy currents will not take place in these ferrites in the frequency range considered.

The relaxation of the irreversible domain-wall displacements means that a moving wall suffers a friction which prevents it from covering the same distance in the short time available at high frequency as it would at the same maximum field-strength at low frequency. In these samples the walls move under the influence of an applied field of about 1 oersted, at a frequency of about 0.5 Mc/s. If the wall displacement is equal to the domain width, which is of the order of magnitude of 10^{-4} or 10^{-3} cm, their velocity would

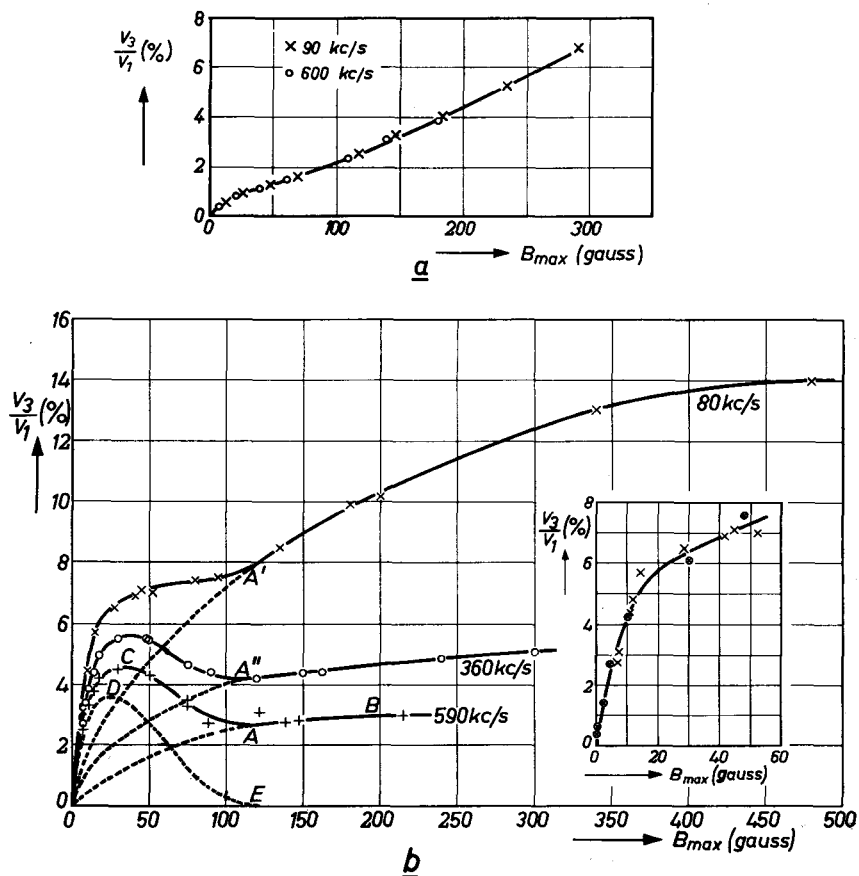

Fig. 62.4. *a*) Frequency-independent distortion curves for the ferrite of Fig. 62.3*a*. *b*) Frequency-dependent distortion curves for the ferrite of Fig. 62.3*b*. The encircled crosses in the inset denote the distortion calculated according to (61.12) from the hysteresis resistance at a frequency of 2 kc/s.

be about 10^2 or 10^3 cm/sec, respectively. Accordingly, the damping coefficient β from (24.10) has to be smaller than unity. For Fe_3O_4 Galt [Ga 3] has found that $\beta = 0.4$, whereas for nickel-ferrous ferrite $\beta = 0.02$. Thus it is possible that the same unknown wall-damping mechanism applies to the experiments with polycrystalline samples as to experiments with single crystals.

§ 63. Ferrites under Pulse Conditions

63.1. THE SHAPE OF THE PULSE RESPONSE CURVES

A current pulse applied to the primary winding of a transformer with a ferrite core will cause a voltage V_s to appear across the terminals of a secondary winding (see Fig. 63.1). The length of the voltage pulse is short compared with the duration of the current pulse. The voltage V_s varies with time in a way that depends on the changes with time of the magnetization in the core. The pulse response curves, which give V_s as a function of time, are measured with an oscilloscope; see for instance [He 3].

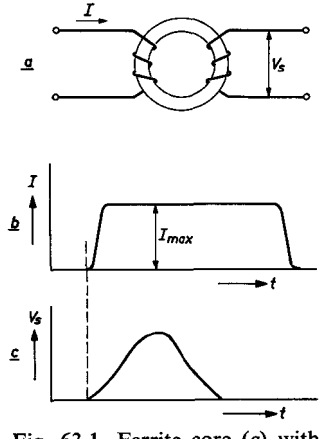

Fig. 63.1. Ferrite core (*a*) with two windings. A current pulse (*b*) in the primary gives rise to a voltage pulse (*c*) in the secondary.

The shape of the pulse-response curve of a ferrite depends on the amplitude H_m of the applied pulse. For the ferrite with hysteresis loops as reproduced in Fig. 56.5, pulse-response curves at various values of H_m are given in Fig. 63.2. In the case of low pulse amplitudes ($H_m < 1$ oersted) only one maximum occurs very shortly after the start of the pulse (0.1 μsec). At higher pulse amplitudes a second maximum in the curve appears. This second peak shifts to shorter times when H_m is increased, and for a sufficiently large value of H_m the second peak merges into the first. This situation is almost obtained in Fig. 63.2 for $H_m = 2.6$ oersteds. The area of the voltage-response curve is proportional to the total change of flux in the ferrite core caused by the switching field. When all dimensions are known, it is possible to calculate the corresponding change of the magnetization of the core (or of the induction B, since $H_m \ll B$). The integration, carried out electronically, yields the result reproduced in Fig. 63.3. For this ferrite, where the remanent magnetization is approximately equal to the magnetization in a

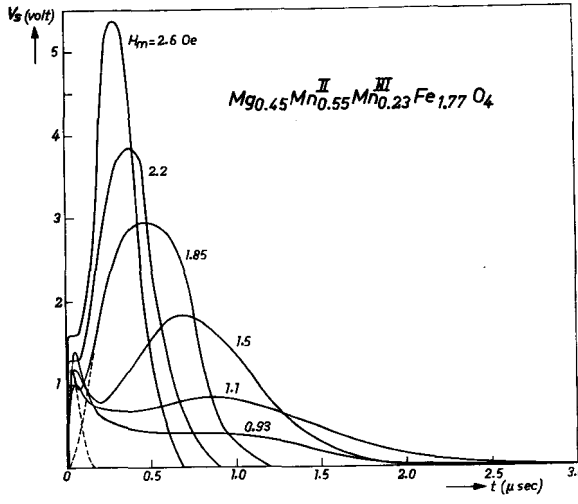

Fig. 63.2. Family of pulse-response curves for the ferrite $Mg_{0.45}Mn^{II}_{0.55}Mn^{III}_{0.23}Fe_{1.77}O_4$ of Fig. 56.5. The amplitudes of the various pulses correspond to the maximum field strengths for which the hysteresis loops of that figure were obtained.

field H_m, the curve giving the total change of the induction (*i.e.* ΔB in Fig. 63.3 for infinite time) as a function of H_m corresponds to the virgin magnetization curve.

The two maxima in some of the curves in Fig. 63.2 might be related to two different types of magnetization processes, each of which gives rise to a time-dependent secondary voltage as indicated for one case by the dashed curves. A relatively small change of the magnetization occurs fairly rapidly in this square-loop ferrite, and the major part of the magnetization reverses only slowly. It seems possible to associate these changes of magnetization with reversible rotation processes and with irreversible domain-wall displacements respectively. Suppose that the permeability of the ferrite in the remanent state, μ_{rem}, is the result of simultaneous rotations of the magnetizations in each Weiss domain. A field H_m will then

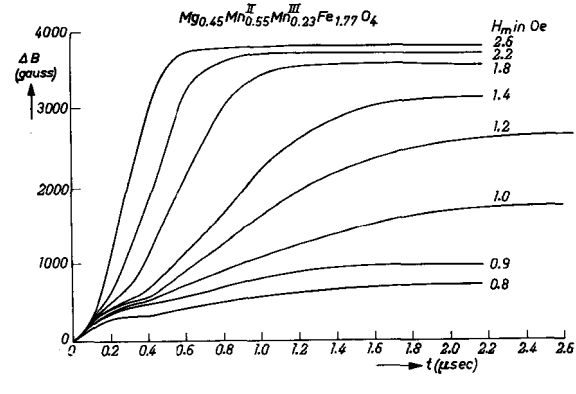

Fig. 63.3. The reversal of the magnetization of the ferrite as a function of time, for various amplitudes of the applied pulses.

cause in the ferrite a change of induction as a result of rotations, ΔB, which is about equal to $\mu_{rem} \cdot H_m$. For the ferrite under consideration $\mu_{rem} = 22$, so that $\Delta B \cong 40$, for $H_m = 1.85$ oersteds. This induction change is in fairly good agreement with that corresponding to the smaller area below the dotted curves in Fig. 63.2. Pulse-response curves of a ferrite $Ni_{0.36}Zn_{0.64}Fe_2O_4$ having a hysteresis loop similar to those in Figs 56.2 and 56.3 and an initial permeability $\mu_0 = 600$, do not show two maxima; see for instance the curve marked 0 in Fig. 63.4, which is found for $H_m = 1.5$ oersteds. However, if a tangential pressure is applied to the ring, the shape of the hysteresis loop will change as a consequence of magnetostriction (see § 59). This behaviour is reflected in the voltage-response curve.

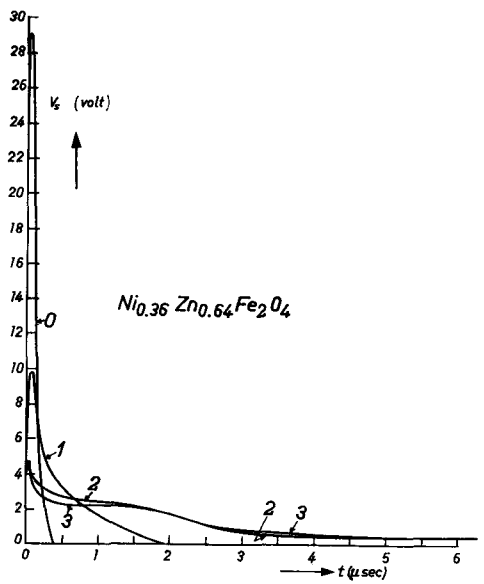

Fig. 63.4. Voltage-response curves for a nickel-zinc ferrite $Ni_{0.36}Zn_{0.64}Fe_2O_4$. Curve 0 is obtained in the absence of pressure. Curves 1, 2 and 3 are obtained at increasing values of an applied tangential pressure, which correspond to increased rectangularity of the hysteresis loop.

The curves denoted by 1, 2 and 3 in Fig. 63.4 are obtained at increasing values of an applied pressure. It is seen that in the case of the largest pressure, when the flux reversal is mainly brought about by domain-wall displacements, a second maximum apears.

A more pronounced distinction between the two maxima in the pulse-response curves may be found with a magnetically annealed sample of the ferrite $Co_{0.1}Fe^{II}_{0.9}Fe_2O_4$; see § 58. In the remanent state the permeability of this ferrite is very small, *i.e.* $\mu_{rem} \cong 2$. The reversal of the magnetization is brought about by a single Barkhausen jump. The pulse-response curves are reproduced in Fig. 63.5. There is a clear distinction between the first narrow peak, corresponding to the small change of the magnetization caused by

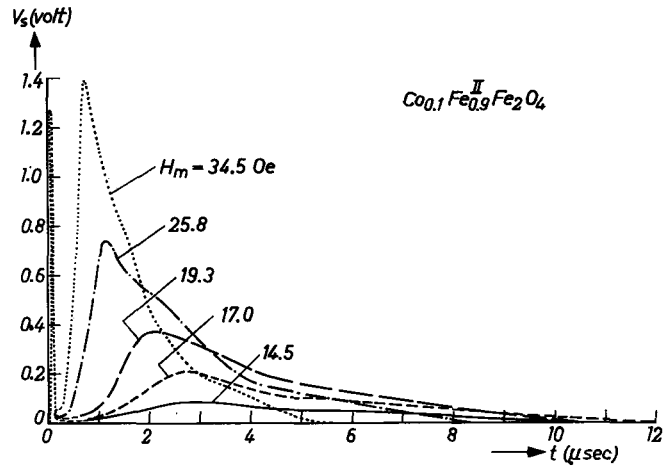

Fig. 63.5. $Co_{0.1}Fe^{II}_{0.9}Fe_2O_4$ annealed in a magnetic field: pulse response curves recorded for various amplitudes H_{max} of the field pulse.

rotations, and the following broad curve, corresponding to the bulk change of the magnetization caused by the Barkhausen jump (which is a domain-wal displacement). In the figure the first peak in the response curve is given only for the pulses of amplitude $H_m = 34.5$ oersteds. The lower-amplitude pulses give rise to correspondingly high voltage peaks within the first few tenths of a microsecond after the application of the pulse.

63.2. SWITCHING TIMES

The switching time of a core is ussually defined as the time needed for a complete reversal of the magnetization, *i.e.* the time that elapses before V_s drops to, say, one tenth of its maximum value (see Fig. 63.2). However, according to this definition, the switching time of a material is governed by the slowest reversal, which might lead to wrong interpretations. Moreover, for practical purposes the time that elapses between the moment of applying the field and the moment that V_s reaches its maximum value is very important. From a more physical point of view a comparison can be made with the definition of the coercive force H_c. Instead of being defined as the field strength needed to obtain, say, 90% magnetization in the reversed direction of a remanent magnetization, H_c is defined as the field strength needed to annihilate a remanent magnetization in the core. Accordingly we shall define the switching time as the time taken for the remanent magnetization to be annihilated, or, put more generally, the time that elapses during a half reversal of the magnetization. After this time, the area

between the V_s *versus* time curve and the abscissa has reached half its final value.

From Fig. 63.2 it can be seen that the switching time depends on the amplitude H_m of the applied pulse. For this ferrite the value of τ^{-1} is plotted *versus* H_m in Fig. 63.6. It appears that if the reversal of the magnetization takes place predominantly as a result of irreversible domain wall displacements, the following relation exists:

$$(H_m - H_0)\tau = s \text{ microsecond oersteds}, \tag{63.1}$$

where H_0 and s are constants for a ferrite.

This equation has been given by various authors, for instance [Ga 3] and [Me 1]. The threshold field strength H_0 is usually slightly smaller than the coercive force of the ferrite. The motion of a domain wall is governed by (24.11). The inertia is small and can be neglected compared with the viscous damping term. Moreover if we suppose that under the influence of a field H_m the walls come into uniform motion, the elastic term can also be neglected. The switching constant s is then proportional to the distance d between the domain walls and also proportional to the friction determined by the damping coefficient β. Because the pressure on the wall is proportional to the amplitude of the vector difference between the magnetizations of the Weiss domains at each side of the domain wall, s will be inversely proportional to M_s hence:

$$s \propto d/M_s, \tag{63.2}$$

where M_s is the saturation magnetization. For the ferrite in Fig. 63.6 the constants H_0 and s are 0.9 oersted and 0.4 microsec.oersted respectively.

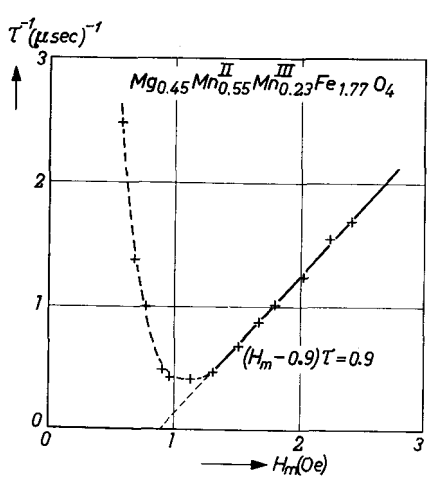

Fig. 63.6. The reciprocal of the switching time, $1/\tau$, as a function of the pulse amplitude, H_m, for the curves of Fig. 63.2.

A small value of s denotes a ferrite with a rapid pulse response. Materials for which H_m is smaller than H_0 do not have a rectangular hysteresis loop. In these cases the contribution of the irreversible domain-wall displacements to the reversal of the magnetization is no longer predominant and τ will be determined by the fast changes of the magnetization due to domain rotations. This explains the rise in the curve in Fig. 63.6 at field strengths below H_0.

In order to make a comparison between different rectangular-loop ferrites as regards their time response, the quantities H_0 and s of (63.1) can be used. H_0 is a kind of threshold field strength for wall movement or for wall nucleation [Go 10] and s can be considered as the additional field strength required for a full reversal of the magnetization in 1 microsecond. A survey of these two quantities is given in Table 63.I for rectangular-hysteresis-loop ferrites with widely varying chemical composition [He 3]. It is noteworthy that the switching coefficients for almost all these ferrites are of the order of magnitude of unity, the only exceptions being two samples with a high coercive force and exhibiting the extreme rectangularity as shown in Fig. 58.4, for which s is much higher.

Variation of the temperature of a core involves a change in the electrical resistivity and in the magnetic anisotropies of the ferrite. Both factors might influence the switching time. The resistivity of the ferrite $Cu_{0.25}Mn_{0.75}Fe_2O_4$ is only about 1500 ohm-cm, so that damping of wall motions by micro eddy currents might be important. In the temperature range investigated (*i.e.* from −115 to +250 °C) the rectangularity of the hysteresis loop

TABLE 63.I

THE THRESHOLD FIELD H_0 AND THE SWITCHING COEFFICIENT s FOR SOME FERRITES WITH RECTANGULAR HYSTERESIS LOOPS

Ferrite	H_0 oersted	s microsec-oersted
$Mg_{0.45}Mn^{I}_{0.55}Mn^{III}_{0.23}Fe_{1.77}O_4$	0.9	0.4
$Cu_{0.25}Mn_{0.75}Fe_2O_4$	0.85	0.4
$Mg_{0.6}Ni_{0.4}Fe_2O_4$	3.6	1.1
$Li_{0.47}Ni_{0.06}Fe_{2.47}O_4$	2	0.5
MF1312B, ref. [Me 1]	0.6	0.5
$MnFe_2O_4$	0.5	1.6
$(Mg_{0.6}Ni_{0.4})_{0.985}Co_{0.015}Fe_2O_4$	*) 1.4	2.0
$Ni_{0.39}Mg_{0.59}Co_{0.02}Fe_2O_4$	*) 2.5	1.3
$Ni_{0.5}Fe^{II}_{0.4}Co_{0.1}Fe_2O_4$	*) 12	13
$Mn_{0.18}Fe^{II}_{0.8}Co_{0.02}Fe_2O_4$	*) 2.5	4
$Co_{0.1}Fe^{II}_{0.9}Fe_2O_4$	*) 8	50

*) These ferrites show the rectangular hysteresis loop after a magnetic annealing process.

of this ferrite is such that by far the major part of the magnetization reversal is brought about by domain-wall displacements. The switching time was measured as a function of the applied field at various temperatures. For each temperature a straight line similar to the drawn line of Fig. 63.6 was obtained, and from these lines the threshold field-strength H_0 and the switching coefficient s were calculated, the results being given as a function of temperature in Fig. 63.7. As can be seen, the threshold field H_0 decreases slightly with increasing temperature, which was to be expected since this is similar to what is found for the coercive force. However, the switching coefficient s also varies only slightly with temperature, the total change in s in the temperature range investigated being not more than about a factor of 2. Eddy currents cannot possibly, therefore, play any part in the damping process, since the resistivity changes according to an exponential law with temperature, and hence in the temperature range mentioned above it will vary by several factors of 10, giving rise to a variation of s with temperature in the opposite sense to that actually found. The ferrite $Co_{0.1}Fe^{II}_{0.9}Fe_2O_4$ of Table 63.I shows an abnormally high switching coefficient ($s = 50$). Although this ferrite has a resistivity of only about 5 ohm-cm, the long switching time is not caused by eddy current damping, since, in this case also, s increases by about a factor of 3 in the temperature range from -130 °C to $+200$ °C.

More information about the origin of the magnitude of s is provided by the curves in Fig. 63.8. This figure applies to the ferrite $Mg_{0.6}Ni_{0.4}Fe_2O_4$ to which 1.5% of cobalt is added. As a result the mixed ferrite shows a

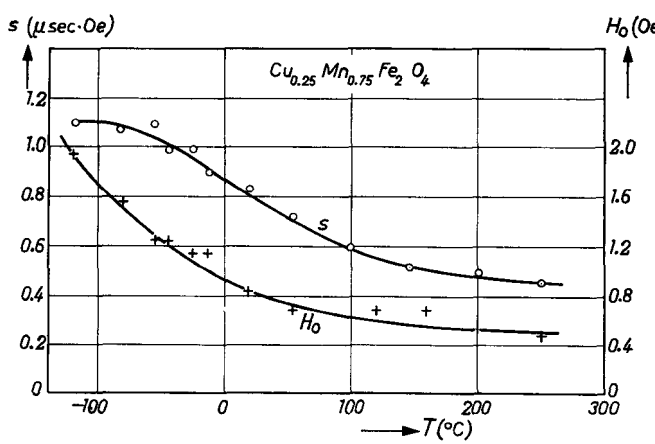

Fig. 63.7. The quantities H_0 and s, see (63.1), measured as a function of temperature for the ferrite $Cu_{0.25}Mn_{0.75}Fe_2O_4$ of Table 63.I.

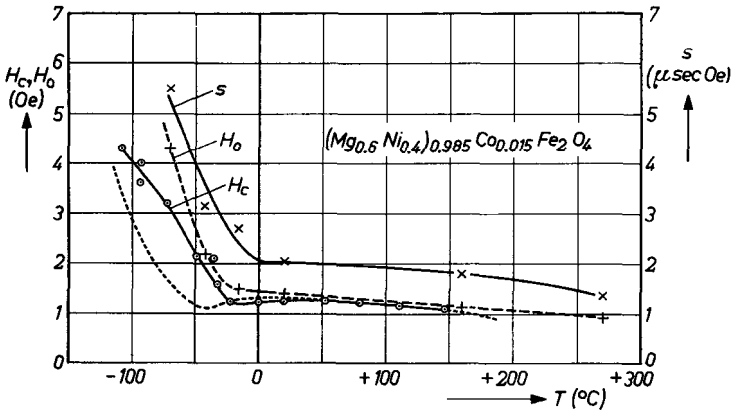

Fig. 63.8. The quantities H_0 and s, see (63.1), measured as a function of temperature for the ferrite $(Mg_{0.6}Ni_{0.4})_{0.985}Co_{0.015}Fe_2O_4$ after magnetic annealing. The coercive force H_c measured as a function of temperature is also given. The dotted curve represents the coercive force calculated according to (16.8). Porosity $p = 0.035$.

maximum in the μ_0 *versus* T curve at about −40 °C (see § 48.1). It appears that correspondingly both the coercive force and the critical field strength H_0, derived from switching times at various temperatures according to (63.1), also show a characteristic behaviour as a function of frequency. The great similarity of these curves indicates that the two field strengths are closely related. From the known trend of μ_0 *versus* T and of M_s *versus* T a coercive force of this ferrite can be calculated with the equations (16.8). For a porosity of 3.5% the dashed curve in Fig. 63.8 is obtained, which in fact is found to agree satisfactorily with the curve actually measured. A remarkable fact is that the switching coefficient s as a function of temperature also shows the same characteristic trend. The combination of the equations (63.1), (24.10) and (15.4) gives:

$$s \propto \frac{\beta d}{M_s} \propto \frac{\alpha M_s}{\gamma d_w} \cdot \frac{K\delta_w}{M_s^2} \cdot \frac{1}{M_s} \propto \frac{\alpha}{\gamma} \cdot \frac{K}{M_s^2}. \tag{63.3}$$

According to the theory put forward by Clogston *et al.* (§ 23.3) the damping coefficient α is proportional to the saturation magnetization; this is in fact approximately the case as found by experiments on single crystals. This being so, it follows from (63.3) that s is proportional to an anisotropy field, which might explain the similarity in the variation of s and H_c with temperature.

§ 64. Total Losses

Total losses can be measured directly with a calorimeter in calories per cubic centimetre. It is also possible to measure the real and imaginary part of the permeability as a function of frequency and induction by a coaxial line method or to measure directly the quality of a resonant circuit of which the self-inductance is formed by the ferrite core with coil [Bu 1] .In calculating the losses from these measurements it is assumed that the distortion of the signal by the ferromagnetic core can be neglected. The latter methods are therefore especially adapted for small inductions (up to about 100 gauss) and high frequency (0.1 to 10 Mc/s). We include the equation giving the relation between the loss factor $\tan\delta$ and the amount of energy dissipated per cubic centimetre of ferrite per second:

$$W_{\text{tot}} = (10^{-7}/4)B^2_{\max} f(\tan\delta)/\mu' \text{ watt/cm}^3. \tag{64.1}$$

Data for the total losses of the nickel-zinc ferrites of Fig. 50.1 are collected in Fig. 64.1. For each ferrite the loss factor $\tan\delta$ is given as a function of

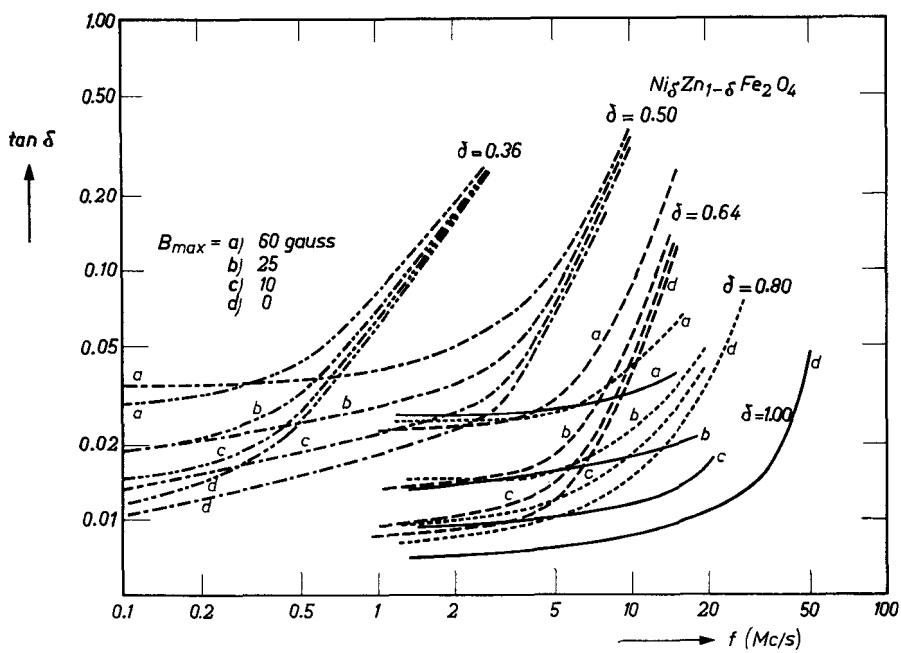

Fig. 64.1. Total losses (expressed as $\tan\delta$) for nickel-zinc ferrites $Ni_\delta Zn_{1-\delta}Fe_2O_4$ as a function of frequency. The four loss-curves for each ferrite correspond to induction amplitudes of 60, 25, 10 and 0 gauss.

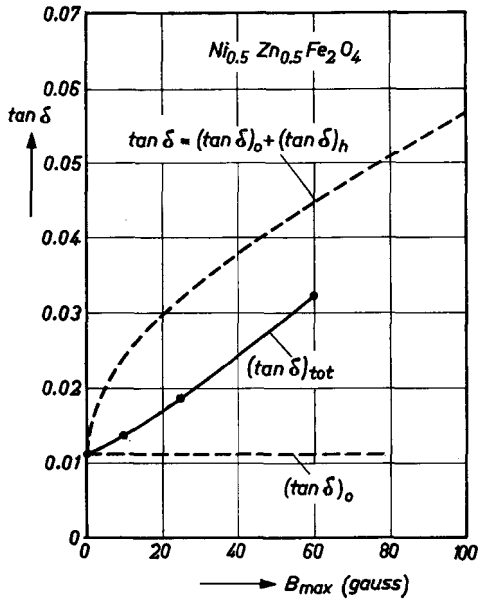

Fig. 64.2. Comparison between the total loss factor $\tan\delta_{tot}$ and the sum of the residual loss factor $\tan\delta_0$ and the hysteresis loss factor $\tan\delta_h$ for a sample of $Ni_{0.5}Zn_{0.5}Fe_2O_4$.

frequency at maximum inductions B_{max} of 60, 25 and 10 gauss. The graph also includes the curve for vanishingly small amplitude of the induction, as derived from the μ' and μ'' curves of Fig. 50.1.

One might expect the total losses to consist of the sum of residual and hysteresis losses (eddy current losses can be neglected when the resistivity is higher than about 10^4 ohm-cm). For $Ni_{0.5}Zn_{0.5}Fe_2O_4$ the residual losses $\tan\delta_0$ and hysteresis losses, $\tan\delta_h$, were measured separately, and their sum compared with the measured total losses $\tan\delta_{tot}$ at 100 kc/s; see Fig. 64.2. The residual loss factor was measured at 100 kc/s and the hysteresis loss factor was calculated from ballistically measured hysteresis loops. It was found that the total losses measured were less than the sum of the separately measured hysteresis and residual losses. It looks as if very slow after-effects cause an increase in the ballistically measured hysteresis losses. It appears to be unjustified to derive total losses at high frequency from the ballistically measured losses. The same holds of course for the distortion (see § 62).

REFERENCES

		§
Ab 1	S. C. Abrahams and B. A. Calhoun, Acta Cryst. **6,** 105-106 (1953) *The Low-Temperature Transition in Magnetite* and **8,** 257-260 (1955) *A Magneto-X-Ray Study of Magnetite at* 78 °*K.*	31.4
Ad 1	V. Adelsköld, Arkiv Kemi, Min. Geol. **12***A*, No. 29, 1-9 (1938) *X-ray Studies on Magnetoplumbite* $PbO.6Fe_2O_3$ *and other Substances Resembling "Beta-Alumina",* Na_2O-$11Al_2O_3$.	37.1 37.3
Ak 1	A. Akhieser, J. Phys. U.S.S.R., **10,** 217-230 (1946). *Theory of the Relaxation Processes in Ferromagnetics at Low Temperatures.*	23.3
Al 1	R. Aléonard, J. C. Barbier and R. Pauthenet, C. R. Paris, **242,** 2531-2533 (1956). *Propriétés magnétiques du ferrite d'yttrium* $5Fe_2O_3.3Y_2O_3$ *du type grenat.*	41
An 1	P. W. Anderson and H. Hasagawa, *quoted by* T. Nagamiya, K. Yosida en R. Kubo, Advances in Physics **4,** nr. 13, 1-112 (1955). *Antiferromagnetism.*	8.1
An 2	P. W. Anderson, Phys. Rev. **102,** 1008-1013 (1956). *Ordering and Antiferromagnetism in Ferrites.*	32.1
Ba 1	T. F. W. Barth and E. Posnjak, Zs. f. Kristallographie, **82,** 325-341 (1932). *Spinel Structures: with and without Variate Atom Equipoints.*	31.3
Ba 2	G. E. Bacon, *Neutron Diffraction,* Clarendon Press, Oxford (1955).	32.1 31.3
Ba 3	G. E. Bacon and F. F. Roberts, Acta Cryst. **6,** 57-62 (1953). *Neutron Diffraction Studies of Magnesium Ferrite-Aluminate Powders.*	31.3
Ba 4	F. Barson, S. Legold and F. H. Spedding, Phys. Rev. **105,** 418-424 (1957). *Thermal Expansion of Rare Earth Metals.*	13
Be 1	H. G. Beljers, Physica, **14,** 629-641 (1949). *Measurements on Gyromagnetic Resonance of a Ferrite using Cavity Resonators.*	28.3
Be 2	H. G. Beljers and D. Polder, Nature, **165,** 800 (1950). *g-Factors in Ferrite Materials.*	28.3
Be 3	F. Bertaut and C. Delorme, C. R. Acad. Sc. **236,** 74-76 (1953). *Etude de* Fe_5CuO_8.	30

		§
Be 4	F. Bertaut, J. de Phys. Rad. **12,** 252-255 (1951). *Sur quelques progrès récents dans la cristallography des spinelles, en particulier des ferrites.*	31.3
Be 5	H. G. Beljers, Unpublished data.	36.1
Be 6	F. Bertaut and F. Forrat, C. R. Paris **242,** 382-384 (1956). *Structure des ferrites ferrimagnetiques des terres rares.*	40
Be 7	F. Bertaut and R. Pauthenet, Proc. I. E. E. *B* **104,** 261-164 (1957). *Crystalline structure and Magnetic Properties of Ferrites Having the General Formula* $5Fe_2O_3.3M_2O_3$	41
Be 8	R. Becker and M. Kersten, Zs. Phys. **64,** 660-681 (1930). *Die Magnetisierung von Nickeldraht unter starkem Zug.*	47.1 49.2
Be 9	H. G. Beljers, W. J. van der Lindt and J. J. Went, J. Appl. Phys. **22,** 1506 (1951). *A new Point of View on Magnetic Losses in Anisotropic Bars of Ferrite at Ultra-High Frequences.*	50.2
Bi 1	L. R. Bickford, Phys. Rev. **76,** 137-138 (1949). *Ferromagnetic Resonance Absorption in Magnetite.*	26.4
Bi 2	L. R. Bickford, Revs. Mod. Phys. **25,** 75-79 (1953). *The Low Temperature Transformation in Ferrites.*	31.4
Bi 3	L. R. Bickford, J. M. Brownlow and R. F. Penoyer, Proc. Inst. Electr. Eng. *B* **104,** 238-244 (1957). *Magnetocrystalline Anisotropy in Cobalt-substituted Magnetite Single Crystals.*	34.1
Bi 4	L. R. Bickford, J. Pappis, and J. L. Stull, Phys. Rev. **99,** 1210-1214 (1955). *Magnetostriction and Permeability of Magnetite and Cobalt-Substituted Magnetite.*	35 48.1
Bl 1	N. Bloembergen, Proc. I.R.E. **44,** 1259-1269 (1956). *Magnetic Resonance in Ferrites.*	
Bl 2	N. Bloembergen and S. Wang, Phys. **93,** 72-83 (1954). *Relaxation Effects in Para- and Ferromagnetic Resonance.*	50.1
Bl 3	J. C. Bluet, I. Epelboin, D. Quivy, C. R. Acad. Sc. **246,** 246-249 (1958). *Sur les Spectres Electrique et Magnétique des Oxydes* $Fe_2O_3\gamma$	50.1
Bo 1	F. de Boer, J. H. van Santen and E. J. W. Verwey, Jr. Chem. Phys. **18,** 1032-1034 (1950), *The Electrostatic Contribution to the Lattice Energy of Some Ordered Spinels.*	31.3 31.4
Bo 2	R. M. Bozorth, E. F. Tilden and A. J. Williams, Phys. Rev. **99,** 1788-1798 (1955). *Anisotropy and Magnetostriction of Some Ferrites.*	34.1 34.2 35 58

		§
Bo 3	R. M. Bozorth, B. B. Cetlin, J. K. Galt, F. R. Merritt and W. A. Yager, Phys. Rev. **99,** 1898 (1955). *Frequency Dependence of Magnetocrystalline Anisotropy.*	34.1
Br 1	F. G. Brockman and W. G. Steneck, Philips techn. Rev. **16,** 79-87 (1954). *A new automatic Hysteresis Curve Recorder.*	25.1
Br 2	F. G. Brockman, P. H. Dowling and W. G. Steneck, Phys. Rev. **75,** 1440 (1949). *Anomalous Behaviour of the Dielectric Constant of a Ferromagnetic Ferrite at the Magnetic Curie Point,* and **77,** 85-93 (1950). *Dimensional Effects Resulting from a high Dielectric Constant Found in a Ferromagnetic Ferrite.*	29.1
Br 3	W. H. Bragg, Nature **95,** 561 (1915), Phil. Mag. **30,** 305-315 (1915). *The Structure of the Spinel Group of Crystals.*	31.1
Br 4	P. B. Braun, Nature **170,** 1123 (1952). *A Superstructure in Spinels.*	31.3 31.4
Br 5	P. B. Braun, Nature, **170,** 708 (1952). *Crystal Structure of* $BaFe_{18}O_{27}$.	37.1
Br 6	P. B. Braun, Philips Res. Rep. **12,** 491-548 (1957). *The Crystal Structure of a new Group of Ferromagnetic Compounds.*	37.4 38.1
Br 7	F. Brown and Ch. L. Gravel, Phys. Rev. **97,** 55-59 (1955). *Domain Rotation in Nickel Ferrite.*	47.1 50.1
Br 8	W. F. Brown Jr., Hb. Phys. Bd XVII *Dielektrika* Springer Berlin (1956) 1-54. *Dielectrics.*	54.2
Bu 1	C. M. van der Burgt, M. Gevers and H. P. J. Wijn, Philips techn. Rev. **14,** 245-256 (1953). *Measuring Methods for some Properties of Ferroxcube Materials.*	28.3 28.2 64
Bu 2	C. M. van der Burgt, Philips Res. Rep. **12,** 97-122 (1957). *Controlled Crystal Anisotropy and Controlled Temperature Dependence of the permeability and Elasticity of various Cobalt-Substituted Ferrites.*	34.1 43.4 48.1
Bu 3	C. M. van der Burgt, Proc. Inst. El. Eng. **104***B,* 550-557 (1957). *Ferrites for Magnetic and Piezomagnetic Filter Elements with Temperature-Independent Permeability and Elasticity.*	43.4 48.1
Ca 1	H. B. G. Casimir, Philips Res. Rep. **6,** 162-182 (1951). *On the Theory of Electromagnetic Waves in Resonant Cavities.*	28.3

		§
Ca 2	H. B. G. Casimir *et al.*, J. Phys. Rad. (January 1959). *Rapport sur quelques Recherches dans le Domaine du Magnetisme aux Laboratoires Philips.*	37.1 38.2 39.1
Cl 1	A. M. Clogston, H. Suhl. L. R. Walker and P. W. Anderson, Phys. Rev. **101,** 903-905 (1956). *Possible Source of Line Width in Ferromagnetic Resonance.*	23.3
Cl 2	A. Claassen, Proc. Phys. Soc. **38,** 482-487 (1925-1926). *The Scattering Power of Oxygen and Iron for X-rays.*	31.3
Cl 3	C. A. Clark and W. Sucksmith, Proc. Royal Soc. *A* **225,** 147-159 (1954). *The Spontaneous Magnetization of Alloys and Compounds.*	33
Cl 4	A. M. Clogston, Bell System Techn. J. **34,** 739-760 (1955). *Relaxation Phenomena in Ferrites.*	34.1
Cl 5	A. M. Clogston, J. Appl. Phys. **29,** No. 3, 334-336 (1958). *Inhomogeneous Broadening of magnetic Resonance Lines*	55
Co 1	L. M. Corliss, J. M. Hastings and F. G. Brockman, Phys. Rev. **90,** 1013-1018 (1953). *A Neutron Diffraction Study of Magnesium Ferrite.*	31.3 32.1
Co 2	16e Assemblée Plénière du C.C.I.F., Firenze Tome III bis. 228 (1951).	66.2
Da 1	L. S. Darken, and R. W. Gurry, Jr. Am. Chem. Soc. **67,** 1398-1412 (1945). *The System Iron-Oxygen I. The Wüstite Field and Related Equilibria;* and **68,** 798-816 (1946). *The System Iron Oxygen II. Equilibrium and Thermodynamics of Liquid Oxides and other Phases.*	45.2
De 1	B. F. Decker and J. S. Kaspar, Acta Cryst. **10,** 332-337 (1957). *The Structure of Calcium Ferrite.*	30
Di 1	L. J. Dijkstra and C. West, Phys. Rev. **79,** 979-985 (1950). *Effect of Inclusions on Coercive Force of Iron.*	16.1
Di 2	J. F. Dillon, S. Geschwind and V. Jaccarino, Phys. Rev. **100,** 750-752 (1955). *Ferrimagnetic Resonance in Single Crystals of Manganese Ferrite.*	34.1 36.1
Di 3	J. F. Dillon, Phys. Rev. **105,** 759-760 (1957). *Ferrimagnetic Resonance in Yttrium Iron Garnet.*	42
Do 1	W. Döring, Z. Naturforschung **3***a*, 374-379 (1948). *Uber die Trägheit der Wände zwischen Weiszschen Bezirken.* R. Becker, J. Phys. Rad. **12,** 332-338 (1951). *La Dynamique de la Paroi de Bloch et la Perméabilité en haute Fréquence.* G. T. Rado, Phys. Rev. **83,** 821-826 (1951). *On the Inertia of Oscillating Ferromagnetic Domain Walls*	24.1

		§
Do 2	C. A. Domenicali, Phys. Rev. **78,** 458-467 (1950). *Magnetic and Electric Properties of Natural and Synthetic Single Crystals of Magnetite.*	34.1 45
Du 1	F. K. du Pré, Philips. Res. Rep. **10,** 1-10 (1955). *On the Microwave Cotton-Mouton Effect in Ferroxcube.*	22.2
Du 2	J. D. Dunitz and L. E. Orgel, J. Phys. Chem. Solids, **3,** 20-29 (1957). *Electronic Properties of Transition Metal Oxides I. Distortions from Cubic Symmetry.*	31.3
Du 3	J. D. Dunitz and L. E. Orgel, J. Phys. Chem. Solids, **3,** 318-323 (1957). *Electronic Properties of Transition Metal Oxides II. Cation Distribution amongst Octahedral and Tetrahedral Sites.*	31.3
Ec 1	G. Economos Jr., J. Amer. Cer. Soc. **38,** 241-244, 292-297, 335-340, 353-357 and 408-411 (1955). *Magnetic Ceramics: I. General Methods of Magnetic Ferrite Preparation. II. Properties of Magnetite and Manganese Ferrite Fired in Various Atmospheres. III. Effects of Fabrication Techniques on Magnetic Properties of Magnesium Ferrite. IV. Development of a Complex Ferrite with a Rectangular Hysteresis-Loop Characteristic. V. Magnetic Properties of Square-Loop Ferrites within the System* $MgOMnOFe_2O_3$.	43.1 56
Ec 2	O. Eckert. Proc. Inst. elect. Eng. **104***B*, 428-432 (1957). *Ferrites with Constricted Loops and Thermal Magnetic Treatment.*	58
El 1	B. S. Ellefson and N. W. Taylor, J. Chem. Phys. **2,** 58-64 (1934). *Crystal Structures and Expansion Anomalies of* MnO, MnS, FeO, Fe_3O_4, *between* 100 °K *and* 200 °K.	31.4
En 1	U. Enz, *Erzeugung von Ultraschall mit Ferriten,* Thesis, Zürich (1955).	35
En 2	U. Enz, Physica, **24,** 609-624 (1958). *Relation between Disaccomodation and Magnetic Properties of Manganese-Ferrous Ferrite.*	48.1
Ep 1	J. H. Epstein, Progress Report M.I.T. **14,** 46-48 (December 1953). *The Effect of Substitution on the Low-Temperature Transition of Magnetite.*	45
Fa 1	A. Fairweather and E. J. Frost. Proc. Inst. Electr. Engrs. (London), **100,** 15-22 (1953). *Dielectric Behaviour of Granular Semi-conducting Aggregates with Special Reference to some Magnesium Ferrites.*	46.1 46.2

		§
Fa 2	A. Fairweather, F. F. Roberts and A. J. E. Welch, Repts. Prog. in Phys. **15, 142-172** (1952). *Ferrites.*	46.1
Fo 1	H. Forestier, Annales Chimie Xe Serie Tome IX, 316-401, (1928). *Transformations Magnétiques du Sesquioxyde de Fer, de ses Solutions, et de ses Combinaisons Ferromagnetiques*	32.2 48.1
Ga 1	J. K. Galt, B. T. Matthias and J. P. Remeika, Phys. Rev. **79,** 391-392 (1950). *Properties of Single Crystals of Nickel Ferrite.*	47.1
Ga 2	J. K. Galt, W. A. Yager, J. P. Remeika and F. R. Merritt, Phys. Rev. **81,** 470 (1951). *Crystalline Magnetic Anisotropy in Zinc Manganese Ferrite.*	34.1
Ga 3	J. K. Galt, Bell Syst. Techn. Jr. **33,** 1023-1054 (1954). *Motion of Individual Domain Walls in a Nickel-Iron Ferrite.*	36.2 62 63
Ga 5	R. Gans, Ann. Physik **15,** 28-44 (1932). *Uber das Magnetische Verhalten isotoper Ferromagnetika.*	57
Ge 1	L. H. Germer, Phys. Rev. **62,** 295 (1942). *Stray Magnetic Fields from Cobalt.*	14
Ge 2	S. Geller and M. A. Gilleo, Acta Cryst. **10,** 239 (1957). *Structure and Ferrimagnetism of Yttrium and Rare-Earth-Iron Garnets.*	40
Ge 3	S. Geller and M. A. Gilleo, Acta Cryst. **10,** 787 (1957). *The Crystal Structure and Ferrimagnetism of Yttrium-Iron Garnets,* Y_3Fe_2 $(FeO_4)_3$.	40
Go 1	E. W. Gorter and J. A. Schulkes, Phys. Rev. **90,** 487-488 1953). *Reversal of Spontaneous Magnetization as a Function of Temperature in* LiFeO *Spinels.*	9.1
Go 2	J. E. Goldman, Phys. Rev. **72,** 529-530 (1947). *Magnetostriction of Annealed and Cold Worked Nickel Rods.*	27.2
Go 3	E. W. Gorter, Philips Res. Rep. **9,** 295-320, 321-365 and 403-443 (1954). *Saturation Magnetization and Crystal Chemistry of Ferrimagnetic Oxides.*	30 31.4 32.1 32.2
Go 4	E. W. Gorter, Proc. I.R.E. **43,** 1945-1973 (1955). *Some Properties of Ferrites in Connection with their Chemistry.*	30 32.2
Go 5	E. W. Gorter, Adv. in Physics, **6,** 23 336-361 (1957). *Chemistry and Magnetic Properties of some Ferrimagnetic Oxides like those Occurring in Nature.*	30
Go 6	E. W. Gorter, Nature **173,** 123-124 (1954). *Ionic Distribution decided from the g-Factor of a Ferrimagnetic Spinel:* Ti^{4+} *in Fourfold Co-ordination.*	36.1

		§
Go 7	E. W. Gorter, Proc. Inst. El. Eng. **104***B*, 255-260 (1957). *Saturation Magnetization of some Ferrimagnetic Oxides with Hexagonal Crystal Structures.*	38.1
Go 8	J. B. Goodenough. Phys. Rev. **95,** 917-932 (1954). *A Theory of Domain Creation and Coercive Force in Polycrystalline Ferromagnetics.*	56
Go 9	E. W. Gorter and C. J. Esveldt, Proc. Inst. Electr. Eng. **104***B*, 418-421 (1957). *Square-Loop Ferrites obtained by Magnetic Annealing of New Compositions.*	58
Go 10	J. B. Goodenough, Proc. Inst. Electr. Eng. **104,** 400-411 (1957). *The Influence of Chemistry on B-H Loop Shape, Coercivity and Flux-reversal Time in Ferrites.*	
Gr 1	J. H. E. Griffith, Nature **158,** 670-671 (1946). *Anomalous High-Frequency Resistance of Ferromagnetic Metals.*	18.1
Gr 2	D. M. Grimes and E. F. Westrum, Pittsburgh Conference on Magnetism and Magnetic Materials 64 (Oct. 1955).	32.1
Gu 1	T. R. McGuire, Phys. Rev. **97,** 831-832 (1955). *Observation of Exchange Resonance near a Ferrimagnetic Compensation Point.*	19
Gu 3	C. Guillaud and H. Creveaux, Compt. R. Ac. Sc. Paris, **230,** 1256-1258 (1950). *Préparations et propriétés magnétiques des ferrites de manganese et de cobalt.*	31.4 32.1
Gu 4	C. Guillaud, J. Phys. Rad. **12,** 239-248 (1951). *Propriétés magnétiques des ferrites.*	31.2 32.1
Gu 5	C. Guillaud and H. Creveaux, Compt. R. Ac. Sc. Paris, **230,** 1458-1460 (1950). *Propriétés Ferromagnétiques des Ferrites Mixtes de Cobalt et de Zinc et de Manganése et de Zinc.*	32.1
Gu 6	C. Guillaud and M. Sage, Compt. R. Ac. Sc. Paris, **232,** 944-946, (1951). *Propriétés Magnetiques des Ferrites Mixtes de Magnesium et de Zinc.*	32.1
Gu 7	C. Guillaud, Revs. Mod. Phys. **25,** 64-74 (1953). *Elementary Mechanisms of Magnetizations in Mixed Oxides of Iron and Cobalt.*	35
Gu 8	R. W. Gurry and L. S. Darken, Jr. Am. Chem. Soc. **72,** 3906-3910 (1950). *The Composition of* CaO-FeO-Fe_2O_3 *and* MnO-MFeO-Fe_2O_3 *Melts at Several Oxygen Pressures in the Vicinity of* 1600°.	43.2
Gu 9	C. Guillaud, Proc. Inst. El. Eng. **104***B*, 165-173 (1957).	

		§
	The Properties of Manganese-Zinc Ferrites and the Physical Processes governing them.	47.1
Ha 1	G. Hägg, Zs. für physik. Chemie, **29***B*, 95-103 (1935). *Die Kristallstruktur des magnetischen Ferrioxyds* γ-Fe_2O_3.	30
Ha 2	J. M. Hastings and L. M. Corliss, Revs. Mod. Phys. **25,** 114-119, (1953). *Neutron Diffraction Studies of Zinc Ferrite and Nickel Ferrite.*	31.3 32.1
Ha 3	J. M. Hastings and L. M. Corliss, Phys. Rev. **104,** 328-331 (1956). *Neutron Diffraction Study of Manganese Ferrite.*	31.2 32.1
Ha 4	F. W. Harrisson, W. P. Osmond and R. W. Teale, Phys Rev. **106,** 865-866 (1957). *Cation Distributions and Magnetic Moment of Manganese Ferrite.*	32.1
He 1	W. E. Henry, Phys. Rev. **88,** 559-562 (1952). *Spin Paramagnetism of* Cr^{III}, Fe^{III} and Gd^{III} *at Liquid Helium Temperatures and in Strong Magnetic Fields*	6.1
He 2	R. R. Heikes and W. D. Johnston, J. Chem. Phys. **26,** 582-587 (1957). *Mechanism of Conduction in* Li-*substituted Transition Metal Oxides.*	45
He 3	H. van der Heide, H. G. Bruijning and H. P. J. Wijn, Philips techn. Rev. **18,** 336-346 (1956). *Switching Time of Ferrites with Rectangular Hysteresis Loop.*	63
Jo 2	G. H. Jonker and J. H. van Santen, Physica, **16,** 337-349, (1950). *Ferromagnetic Compounds of Manganese with Perovskite Structure.*	32.1
Jo 3	G. H. Jonker and J. H. van Santen, Physica, **19,** 120-130 (1953). *Magnetic Compounds with Perovskite Structure.* III. *Ferromagnetic Compounds of Cobalt.*	32.1
Jo 4	G. H. Jonker, H. P. J. Wijn and P. B. Braun, Philips techn. Rev. **18,** 145-154, (1956/1957). *Ferroxplana, Hexagonal Ferromagnetic Iron-Oxide Compounds for very high Frequencies.*	37.1 37.6
Jo 5	G. H. Jonker, unpublished.	37.1
Jo 6	G. H. Jonker, private communication.	43.2
Jo 7	G. H. Jonker to appear in J. Phys. and Chem. of Solids *Analysis of the Semiconducting Properties of Cobalt Ferrite*	45
Jo 8	H. Jordan, Elektr. Nachr. Techn. **1,** 7-29 (1924). *Die ferromagnetischen Konstanten für schwache Wechselfelder.*	61.2
Ka 1	H. Kaplan, Phys. Rev. **86,** 121 (1952). *A Spin-Wave Treatment of Saturation Magnetization of Ferrites.*	10

		§
Ka 2	K. Kamiyoshi, Phys. Rev. **84,** 374-375 (1951). *Low Frequency Dispersion in* Ni- *and* Co-*Ferrites.*	46.2
Ka 3	Y. Kato and T. Takei, J. Inst. Electr. Eng. Japan **53,** 408 (1953).	58
Ke 1	F. Keffer, Phys. Rev. **100,** 1692-1698 (1955). *Temperature Dependence of Ferromagnetic Anisotropy in Cubic Crystals.*	11.1
Ke 2	M. Kersten, Zeitschrift für Physik, **8,** 313-322 *Die Wölbung der Blochwand als Elementarvorgang Reversibler Magnetisierungsänderungen (Anfangspermeabilität und ΔE-Effekt)* and 382-386 (1956). *Zur Deutung des Temperaturganges der Anganfspermeabilität* (Mn_2Sb *Kobalt, Eisen, Nickel).*	16.1
Ki 1	C. Kittel, *Introduction to Solid State Physics,* J. Wiley & Sons, New York, Appendix A **195** (1956).	12.1
Ki 2	C. Kittel, Rev. Mod. Phys. **21,** 541-583 (1949). *Physical Theory of Ferromagnetic Domains.*	14 47.1
Ki 3	C. Kittel, Phys. Rev. **73,** 155-161, (1948). *On the Theory of Ferromagnetic Resonance Absorption.*	18.1
Ki 4	C. Kittel, Phys. Rev. **76,** 743-748 (1949). *On the Gyromagnetic Ratio and Spectroscopic Splitting Factor of Ferromagnetic Substances.*	20
Ki 5	C. Kittel and E. Abrahams, Rev. mod. Phys. **25,** 233-238 (1953). *Relaxation Processes in Ferromagnetism.*	23.3
Kl 1	D. de Klerk, Thesis Leiden (1948). *Onderzoekingen over Adiabatische Demagnetisatie.*	28.2
Ko 1	C. Kooy, Phil. Techn. Rev. **19,** 286-289 (1957/58). *Direct Observation of Weiss Domains by Means of the Faraday Effect.*	14
Ko. 2	J. S. Kouvel, Phys. Rev. **102,** 1489-1490 (1956). *Specific Heat of a Magnetite Crystal at Liquid Helium Temperatures.*	22.3
Ko. 3	J. W. L. Köhler and C. G. Koops, Philips Res. Rep. **2,** 454-467 (1947). *Absolute Measurement of the Time Constant of Resistors.*	28.2
Ko 4	J. W. L. Köhler and C. G. Koops, Philips Res. Rep. **1,** 419-446 (1946). *A new Alternating Current Bridge for Precision Measurements.*	28.2 46.1
Ko. 5	E. Kordes and E. Röttig, Zs. Anorg. Chem. **264,** 34-47 (1951). *Neue Mischoxyde mit Spinellstruktur.*	30

		§
Ko 6	C. G. Koops, Phys. Rev. **83,** 121-124 (1951). *On the Dispersion of Resistivity and Dielectric Constant of some Semiconductors at Audio-Frequencies.*	45 46.1 46.2
Ko 7	A. P. Komar and V. V. Klivshin, Bull. Ac. Sc. USSR, Physics **18,** (1954). *Temperature Dependence of the Electrical Resistivity of Ferrites.*	45
Ko 8	N. Kornetzki, J. Brackmann and J. Frei, Naturwissenschaften **42,** 482 (1955) *Magnetische Ferrite mit Perminvarschleife,* and Siemens Zs. **29,** 434-440 (1955). *Ferritkerne mit Perminvarschleife.*	58
Kr 1	C. J. Kriessman, S. E. Harrison and S. R. Black, Phys. Rev. **110,** No. 4, 844-849 (1958). *Magnetic Spectra of Manganese Ferrites.*	
La 1	L. Landau and E. Lifshitz, Phys. Z. Soviet Un. **8,** 153-169 (1935). *On the Theory of the Dispersion of Magnetic Permeability in Ferromagnetic Bodies.*	14
Le 1	V. E. Legg, Bell Syst. Techn. J. **15,** 39-62 (1936). *Magnetic Measurements at Low Flux Densities using the Alternating Current Bridge.*	61.2
Le 2	R. C. Lecraw, E. G. Spencer and C. S. Porter, Phys. Rev. **110,** 1311-1313 (1958). *Ferromagnetic Resonance Line Width in Yttrium Iron Garnet Single Crystals.*	
Li 1	J. H. Lindenhovius and J. C. van der Breggen, Philips Res. Rep. **3,** 37-45 (1948). *The Measurement of Permeability and Magnetic Losses on Non-conducting Ferromagnetic Material at High Frequencies.*	28.3
Li 2	Li Ching Hsien, Phys. Rev. **40,** 1002-1012 (1932). *Magnetic Properties of Magnetite Crystals at Low Temperatures.*	31.4
Lo 1	F. K. Lotgering, Philips Res. Rep. **11,** 190-249 (1956). *On the Ferrimagnetism of some Sulphides and Oxides.*	9.2 30
Lo 2	F. K. Lotgering, to be published.	44
Lo 3	M. Louwerse, Unpublished results.	48.1
Ma 1	L. R. Maxwell and S. J. Pickart, Phys. Rev. **92,** 1120-1126 (1953). *Magnetization in Nickel Ferrite-Aluminates and Nickel Ferrite-Gallates.*	32.1 32.2
Ma 2	L. R. Maxwell and S. J. Pickart, Phys. Rev. **96,** 1501-1505 1954). *Magnetic and Crystalline Behavior of Certain Oxide Systems with Spinel and Perovskite Structures.*	32.1
Me 1	N. Menyuk and J. B. Goodenough, J. Appl. Phys. **26,** 8-18 (1955). *Magnetic Materials for Digital-Computer*	

§

Components. IA: *Theory of Flux Reversal in Polycrystalline Ferromagnetics.* 63.2

Mi 1 R. W. Millar, Jr. Am. Chem. Soc. **51,** 215-222 (1929). *The Heat Capacities at low Temperatures of "Ferrous Oxide", Magnetite and Cuprous and Cupric Oxides.* 31.4

M o 1 G. Möltgen, Zs. angew. Phys. **4,** 216-224 (1952). *Dielektrische Untersuchungen an Ferriten.* 29.1

Mo 1 H. Moser, Phys. Z. **37,** 737-753 (1936). *Messung der wahren spezifischen Wärme von Silber, Nickel, β-Messung, Quarzkristall und Quarzglas zwischen* +50 *und* 700 °C *nach einer verfeinerten Methode.* 7.1

Ne 1 L. Néel, Ann. de Phys. **3,** 137-198 (1948). *Propriétés magnétiques des ferrites: Ferrimagnétisme et Antiferromagnétisme.* 8.2 9.1

Ne 2 L. Néel, C.R. **237,** 1468-1470, 1613-1616 (1953). *L'Anisotropie Superficielle des Substances Ferromagnétiques. Les Surstructures d'Orientation.* J. Phys. Rad. **15,** 225-239 (1954). *Anisotropie Magnétique Superficielle et Surstructures d'Orientation.* 11.2

Ne 3 L. Néel, Cah. Phys. **25,** 21-44 (1944). *Effect of Cavities and Inclusions on the Coercive Force.* 14

Ne 4 L. Néel, Ann. Univ. Grenoble **22,** 299-300 (1946). *Bases d'une Nouvelle Théorie Generale du Champ Coercitif. Nouvelle Théorie du Champ Coercitief.* Physica **15,** 225-234 (1949). 16.1

Ne 5 L. Néel, J. Phys. Rad. **9,** 184-192 (1948). *La loi d'Approche en a : H et une Nouvelle Théorie de la Dureté Magnétique.* 17

Ne 6 L. Néel. Comptes R. Ac. Sc. Paris, **230,** 190-192 (1950). *Aimantation à Saturation de Certains Ferrites.* 31.3

Ne 7 L. Néel, Compt. R. Acad. Sc. Paris, **230,** 375-377 (1950). *Aimantation à Saturation des Ferrites Mixtes de Nickel et de Zinc.* 32.1

Ne 8 L. Néel and P. Brochet, Compt. R. Ac. Sc. Paris, **230,** 280-282 (1950). *Les Coefficients de Champ Moléculaire des Ferrites Mixtes de Nickel et de Zinc.* 33

Ni 1 S. Nishikawa, Proc. Tokyo Math. Phys. Soc. **8,** 199-209 (1915). *Structure of Some Crystals of the Spinel Group.* 31.1

Ok 1 T. Okamura and Y. Kojima, Phys. Rev. **86,** 1040-1041 (1952). *Ferromagnetic Resonance in Copper Ferrite.* 34.1 36.1

		§
Ok 2	T. Okamura, Y. Torizuka and Y. Kojima, Phys. Rev. **88,** 1425-1226 (1952). *The g-Factor of Ferrites.*	55
Oo 1	G. W. van Oosterhout, Appl. Sci. Res. *B.* **6,** 101-104, (1956). *A Rapid Method for Measuring Coercive Force and other Ferromagnetic Properties of very small Samples.*	25.1
Oo 2	G. W. van Oosterhout and C. J. M. Rooymans, Nature, **181,** 44 (1958). *A New Superstructure in Gamma-Ferric Oxide.*	31.4
Ow 1	D. Owen, Proc. Phys. Soc. **27,** 39-55 (1915). *A Bridge for the Measurement of Self-Induction in Terms of Capacity and Resistance.*	28.2
Pa 1	R. Pauthenet, Compt. R. Ac. Sc. Paris, **230,** 1842-1843 (1950). *Variation Thermique de l'Aimantation Spontanée des Ferrites de Nickel, Cobalt, Fer et Manganèse.*	31.3 32.1 32.2
Pa 2	R. Pauthenet and L. Bochirol, J. Phys. Rad. **12,** 249-251 (1951). *Aimantation Spontanée des Ferrites.*	32.1
Pa 3	R. Pauthenet, Ann. Phys. Paris, **7,** 710-747 (1952). *Aimantation Spontanée des Ferrites.*	32.1
Pa 4	W. Parrish, E. A. Hamacher and K. Lowitzsch, Philips techn. Rev. **16,** 123-133 (1954/1955). *The "Norelco" X-ray Diffractometer.*	37.6
Pe 1	R. F. Penoyer and L. R. Bickford Jr., Phys. Rev. **108,** 271-277 (1957). *Magnetic Annealing Effect in Cobalt-Substituted Magnetite Single Crystals.*	34.1 34.2
Pe 2	E. Peterson, Bell Syst. Techn. J. **7,** 762-796 (1928). *Harmonic Production in Ferromagnetic Materials at Low Frequencies and Low Flux Densities.*	61.1
Po 1	D. Polder, Phil. Mag. **40,** 99-115 (1949). *On the Theory of Ferromagnetic Resonance.*	20
Pr 1	E. Prince and R. G. Treuting, Acta Cryst. **9,** 1025-1028 (1956). *The Structure of Tetragonal Copper Ferrite.*	31.3
Pr 2	E. Prince, Phys. Rev. **102,** 674-676 (1956). *Neutron Diffraction Observation of Heat Treatment in Cobalt Ferrite.*	31.3
Ra 1	G. W. Rathenau and J. L. Snoek, Philips Res. Rep. **1,** 239 (1946). *Apparatus for Measuring Magnetic Moments.*	25.2
Ra 2	G. T. Rado, V. J. Folen and W. H. Emerson, Proc. I.E.E. **104,** 198-205 (1956). *Effect of Magnetocrystalline Anisotropy on the Magnetic Spectra of* Mg-Fe *Ferrites.*	34.1 50.1
Ra 3	G. W. Rathenau and G. Baas, Physica **17,** 117-128 (1951).	

		§
	Grain Growth in a Texture, studied by means of Electron-Emission Microscopy.	44
Ra 4	G. W. Rathenau, Unpublished results.	49.2 59
Ra 5	G. W. Rathenau and J. F. Fast, Physica **21**, 964-970 (1955). *Initial Permeabilities of Sintered Ferrites.*	49.3 49.4
Ra 6	G. W. Rathenau, Revs. Mod. Phys. **25**, 297-301 (1953). *Saturation and Magnetization of Hexagonal Iron Oxide Compounds.*	49.3
Ra 7	G. W. Rathenau, J. Smit and A. L. Stuijts, Zs. für Phys. **133**, 250-260 (1952). *Ferromagnetic Properties of Hexagonal Iron Oxide Compounds with and without Preferred Orientation.*	60
Ra 7	G. T. Rado, Revs. Mod. Phys. **25**, 81-89 (1953). *Magnetic Spectra of Ferrites.*	50.1
Ro 1	B. W. Roberts, Proc. Conf. Magnetism, Pittsburgh, 192-197 (1955). *Observation of the Magnetic Domains and Domain Wall in* BiMn *by the Kerr Magneto-Optic Effect.*	14
Ro 2	S. Roberts and A. von Hippel, J. Appl. Phys. **17**, 610-616 (1946). *A new Method for Measuring Dielectric Constant and Loss in the Range of Centimeter Waves.*	28.3
Ro 3	F. C. Romeyn, Philips Res. Rep. **8**, 304-342 (1953). *Physical and Crystallographical Properties of some Spinels.*	31.3 31.4
Sa 1	J. H. van Santen and J. S. van Wieringen, Rec. trav. chim. Pays Bas, **71**, 420-430 (1952). *Some Remarks on the Ionic Radii of Iron-Group Elements. The Influence of Crystalline Fields.*	31.3
Sa 2	J. H. van Santen, Philips Res. Rep. **5**, 282-287 (1950). *Order-Disorder for Coulomb Forces.*	31.4
Sc 1	F. J. Schnettler and F. R. Monfort, J. Appl. Phys. **29**, 477-478 (1958). *Effect of Cobalt on the Relaxation Frequency of Nickel-Zinc Ferrite.*	50.1
Sc 2	H. Schultze, see *Probleme der Technischen Magnetisierungskurven* p. 114 edited by R. Becker, Springer Verlag, Berlin (1938).	54.2
Sc 3	E. Schlömann, Phys. of. Chem. Solids, **6**, 242-256 (1958). *Spin-Wave Analysis of Ferromagnetic Resonance in Polycrystalline Ferrites.*	55
Sh 1	C. G. Shull, E. O. Wollan and W. C. Koehler, Phys. Rev. **84**, 912-921 (1951). *Neutron Scattering and Polarization by Ferromagnetic Materials.*	31.3 32.1

		§
Sh 2	W. Shockley, Bell Syst. Techn. J. **18,** 645-723 (1939). *The Quantum Physics of Solids,* and more especially p. 720, *Magnetism and Thermal Expansion.*	13.1
Si 1	D. B. Sinclair, Proc. I.R.E. **28,** 497-503 (1940). *A Radio-Frequency Bridge for Impedance Measurements from* 400 *Kilocycles to 60 Megacycles.*	28.2
Sl 1	J. C. Slater, *Microwave Electronics,* 3rd ed. Van Nostrand Cy. New York (1954) p. 29.	28.3
Sl 2	J. C. Slonczewsky, Phys. Rev. **110,** 1341-1348 (1958). *Origin of Magnetic Anisotropy in Cobalt-Substituted Magnetite.*	34.1
Sm 1	J. S. Smart, Phys. Rev. **101,** 585-591 (1956). *Application of the Bethe-Weiss Method to Ferrimagnetism.*	10
Sm 2	J. Smit and H. G. Beljers, Phil. Res. Rep. **10,** 113-130 (1955). *Ferromagnetic Resonance Absorption in* $BaFe_{12}O_{19}$, *a Highly Anisotropic Crystal.*	18.1 39.1
Sm 3	J. S. Smart, Phys. Rev. **94,** 847-850 (1954). *Cation Distributions in Mixed Ferrites.*	32.2
Sm 4	J. Smit and H. P. J. Wijn, Adv. in Electronics and Electr. Phys. **6,** 69-136 (1954). *Physical Properties of Ferrites.*	35 61.1 62
Sn 1	J. L. Snoek, Physica, **14,** 207-217 (1948). *Dispersion and Absorption in Magnetic Ferrites at Frequencies above one Megacycle.*	18.2 50.1 53
Sn 2	J. L. Snoek, Physica, **8,** 426-438 (1941). *The influence of Eddy Currents on the Apparent Hysteresis Loop of Ferromagnetic Bars.*	25.1
Sn 3	J. L. Snoek, *New Developments in Ferromagnetic Materials,* Elsevier Publishing Comp. New York-Amsterdam (1947).	43.1 49.4 54.1
Sn 4	J. L. Snoek and J. F. Fast, Nature, **161,** 887 (1948). *Metastable States of Nickel Characterized by a High Initial Permeability.*	49.1
Sn 5	J. Snieder, Appl. Sci. Res. *B.* **7,** 185-232 (1957). *Ferromagnetic Resonance in Polycrystalline Ferrites.*	55
So 1	I. H. Solt, R. L. White and J. E. Mercereau, J. A. P. **29,** 324-325 (1958). *Multiplicities of the Uniform Precessional Mode of Ferrimagnetic Resonance.*	18.3
St 1	K. H. Stewart, Proc. Inst. Electr. Eng. (London) Part 2, **97,** 121-125 (1950). *Losses in Electrical Sheet Steel.*	29.2
St 1	A. L. Stuijts and P. Jongenburger, unpublished.	38.2

		§
St 2	A. L. Stuijts, G. W. Rathenau and G. H. Weber, Philips Techn. Rev. **16,** 141-147 (1954). *Ferroxdure II and III, Anisotropic Permanent Magnet Materials.*	43.3 44
St 3	A. L. Stuijts and H. P. J. Wijn, Philips Techn. Rev. **19,** 209-217 (1957/58). *Crystal-Oriented Ferroxplana.*	44 50.2
St 4	A. L. Stuijts, Transact. Brit. Cer. Soc. **55,** 57 (1956).	48.1
St 5	E. C. Stoner and E. P. Wohlfahrt, Philos. Trans. **240A,** 599-842 (1948). *A Mechanism of Magnetic Hysteresis in Heterogenerous Alloys.*	60
Su 1	W. Sucksmith and J. E. Thompson, Proc. Roy. Soc. **225***A*, 362/375 (1954). *The Magnetic Anisotropy of Cobalt.*	11.1 26.1
Su 2	H. Suhl, Phys. Rev. **97,** 555-557 (1955). *Ferromagnetic Resonance in Nickel Ferrite between One and Two Kilomegacycles.*	18.1
Su 3	H. Suhl, Proc. I.R.E. **44,** 1270-1284 (1956). *The Nonlinear Bahavior of Ferrites at High Microwave Signal Levels.*	23.4
Ta 1	S. Taniguchi, Sci. Rep. Res. Inst. Tohoku Univ. Ser. *A***7,** 269-281 (1955). *A Theory of the Uniaxial Ferromagnetic Anisotropy Induced by Magnetic Annealing in Cubic Solid Solutions.*	11.2
Ta 2	P. E. Tannenwald, Phys. Rev. **99,** 463-464 (1955). *Multiple Resonances in Cobalt Ferrite.*	34.1 36.1
Ta 3	P. E. Tannenwald, Phys. Rev. **100,** 1713-1719 (1955). *Ferromagnetic Resonance in Manganese Ferrite Single Crystals.*	36.1
Ta 4	S. Taniguchi and M. Yamamoto, Sc. Rep. R.I.T.U. *A***6,** 330-332 (1954). *A Note on a Theory of the Uniaxial Ferromagnetic Anisotropy Induced by Cold Work or by Magnetic Annealing in Cubic Solid Solutions.*	58
Tr 1	A. A. Th. M. van Trier, App. Sci. Res. *B***3,** 305-371 (1953). *Guided Electromagnetic Waves in Anisotropic Media.*	22.2
Ui 1	L. G. van Uitert, Jr. Chem. Phys. **23,** 1883-1887 (1955). *dc Resistivity in the Nickel and Nickel-Zinc Ferrite System.*	45
Ui 2	L. G. van Uitert, Jr. Chem. Phys. **24,** 306-310 (1956). *High-Resistivity Nickel Ferrites. The Effect of Minor Additions of Manganese or Cobalt.*	45
Ui 3	L. G. van Uitert, Proc. I.R.E. **44,** 1294-1303 (1956). *Dielectric Properties of and Conductivity in Ferrites.*	45

		§
Va 1	J. H. van Vleck, J. Phys. Rad. **12,** 262-274 (1951). *Recent Development in the Theory of Antiferromagnetism.*	8.1
Va 2	J. H. van Vleck, Phys. Rev. **52,** 1178-1198 (1937). *On the Anisotropy of Cubic Ferromagnetic Crystals.*	11.1
Ve 1	E. J. W. Verwey, Zs. für Kristallographie, **91***A*, 65-69 (1935). *The Crystal Structure of* γ-Fe_2O_3 *and* γ-Al_2O_3.	30
Ve 2	E. J. W. Verwey and E. L. Heilmann, Jr. Chem. Phys. **15,** 174-180 (1947). *Physical Properties and Cation Arrangement of Oxides with Spinel Structures.*	31.3 32.1
Ve 3	E. J. W. Verwey, F. de Boer and J. H. van Santen, Jr. Chem. Phys. **16,** 1091-1092 (1948). *Cation Arrangement in Spinels.*	31.3
Ve 4	E. J. W. Verwey and P. W. Haaijman, Physica, **8,** 979-987 (1941). *Electronic Conductivity and Transition Point of Magnetite* (Fe_3O_4).	31.4 45
Ve 5	E. J. W. Verwey and J. H. de Boer, Rec. trav. chim. Pays Bas, **55,** 531-540 (1936). *Cation Arrangement in a Few Oxides with Crystal Structures of the Spinel Type.*	45
Ve 6	E. J. W. Verwey, P. W. Haaijman and F. C. Romeyn, J. Chem. Phys. **15,** 181-187 (1947). *Physical Properties and Cation Arrangement of Oxides with Spinel Structures.*	45
Ve 6	E. J. W. Verwey, P. W. Haaijman, F. C. Romeyn and G. W. van Oosterhout, Philips Res. Rep. **5,** 173-187 (1950). *Controlled Valency Semiconductors.*	45
Vo 1	J. Volger, *Semi-Conducting Materials,* Butterworth Scientific Publications Ltd, London (1951) 162-171. *Some Properties of Mixed Lanthamum and Strontium Manganites.*	46.2
Wa 1	L. R. Walker, J. A. P. **29,** 318-323 (1958). *Ferromagnetic Resonance: Line structures. Resonant Modes of Ferromagnetic Spheroids.*	18.3
Wa 2	R. K. Wangsness, Phys. Rev. **93,** 68-71 (1954). *Magnetic Resonance in Ferrimagnetics.*	19
We 1	P. Weiss and R. Forrer, Ann de Phys. **5,** 153-213 (1926). *Aimantation et phénomène magnétocalorique du nickel.*	7.2
We 2	J. J. Went, G. W. Rathenau, E. W. Gorter and G. W. van Oosterhout, Philips techn. Rev. **13,** 194-208 (1951/1952). *Ferroxdure, a Class of New Permanent Magnet Materials.*	37.1 38.1
Wi 1	J. S. van Wieringen, Phys. Rev. **90,** 488 (1953). *Anomalous Behaviour of the g-Factor of* LiFeCr *Spinels as a Function of Temperature.*	19

		§
Wi 2	H. J. Williams, W. Shockley and C. Kittel, Phys. Rev. **80,** 1090-1094 (1950). *Studies of the Propagation Velocity of a Ferromagnetic Domain Boundary.*	29.2
Wi 3	H. J. Williams, R. M. Bozorth and Matilda Goertz, Phys. Rev. **91,** 1107-1115 (1953). *Mechanism of Transition in Magnetite at Low Temperatures.*	31.4 56
Wi 4	H. P. J. Wijn, E. W. Gorter, C. J. Esveldt and P. Geldermans, Philips techn. Rev. **16,** 49-58 (1954). *Conditions for Square Hysteresis Loops in Ferrites.*	35
Wi 5	H.P. J. Wijn, Nature, **170,** 707-708 (1952). *A New Method of Melting Ferromagnetic Semiconductors,* $BaFe_{18}O_{27}$, *a New Kind of Ferromagnetic Crystal with High Crystal Anisotropy.*	37.1
Wi 6	H. P. J. Wijn and H. van der Heide, Revs. Mod. Phys. **25,** 98-99 (1953). *A Richter Type After-Effect in Ferrites Containing Ferrous and Ferric Ions.*	53
Wi 7	H. P. J. Wijn and J. J. Went, Physica, **17,** 976-992 (1951). *The Magnetization Process in Ferrites.*	62
Ya 1	Y. Yafet and C. Kittel, Phys. Rev. **87,** 290-294, (1952). *Antiferromagnetic Arrangements in Ferrites.*	8.2 9.2 32.1
Ya 2	W. A. Yager, F. R. Merritt and C. Guillaud, Phys. Rev. **81,** 477-478 (1951). *Ferromagnetic Resonance in Various Ferrites.*	28.3
Ya 3	W. A. Yager, J. K. Galt, F. R. Merritt and E. A. Wood, Phys. Rev. **80,** 744-748 (1950). *Ferromagnetic Resonance in Nickel Ferrite.*	34.1 36.1
Ya 4	W. A. Yager, J. K. Galt and F. R. Merritt, Phys. Rev. **99,** 1203-1210 (1955). *Ferromagnetic Resonance in Two Nickel-Iron Ferrites.*	36.1
Yo 1	K. Yosida and M. Tachiki, Prog. Theor. Phys. **17,** 331 (1957). *On the Origin of Magnetic Anisotropy in Ferrites.*	34.1
Yo 2	H. S. Yoder and M. L. Keith, Am. Mineralogist **36,** 519 (1951).	40
Ze 1	C. Zener, Phys. Rev. **96,** 1335-1337 (1954). *Classical Theory of the Temperature Dependence of Magnetic Anisotropy Energy.*	11.1

INDEX